FACULTY
OF MATHEMATICS
AND PHYSICS
Charles University

DOCTORAL THESIS

Michal Lacko

Studies of reactions of ions with water molecules in the gaseous phase for trace gas analysis

Department of Surface and Plasma Science

Supervisor of the doctoral thesis: Prof. RNDr. Patrik Španěl, Dr. rer. nat.

Study programme: Physics (P1701)
Study branch: Physics of Plasma and Ionized Media

Prague 2022

I declare that I carried out this doctoral thesis independently and only with the cited sources, literature and other professional sources.

I understand that my work relates to the rights and obligations under the Act No. 121/2000 Coll., the Copyright Act, as amended, in particular the fact that Charles University has the right to conclude a license agreement on the use of this work as a school work pursuant to Section 60 paragraph 1 of the Copyright Act.

In Prague date 15.8.2022 Mgr. Michal Lacko, PhD.

"Man, he took his time in the sun
Had a dream to understand
A single grain of sand … "

(Nightwish)

Acknowledgements

First, would like to thank my supervisor Prof. Patrik Španěl for his help and guidance during my studies as well as all members of his group making my work and life in Prague awesome. Dear Ksenia, Anatoli, Krystina, Violet, Pavel, Jan, Niki, thank you. Massive thanks also go to Stephan, who helped me with the language aspect of the thesis. Additionally, I would like to thank all members of the IMPACT project for their unforgivable experiences and great memories. Also, thanks to the members of my faculty for their patience, as the preparation of this work took more time than expected. Finally, the biggest thanks belong to my patient wife and children, for accompanying me during my complicated path to knowledge.

Title: Studies of reactions of ions with water molecules in the gaseous phase for trace gas analysis
Author: Michal Lacko
Department / Institute: Department of Surface and Plasma Science, Faculty of Mathematics and Physics, Charles University in Prague

Department of Chemistry of Ions in Gaseous Phase, J. Heyrovský Institute of Physical Chemistry of the CAS, v. v. i.

Supervisor of the doctoral thesis: Prof. RNDr. Patrik Španěl, Dr. rer. nat.,
J. Heyrovský Institute of Physical Chemistry of the CAS, v. v. i.

Abstract: Chemical ionization mass spectrometry (CI-MS) is a powerful analytical technique, capable to detect trace levels of organic molecules diluted in air samples in real-time. Processes leading to ionization of organic molecules, necessary for their detection and identification, are however often strongly affected by the presence of water vapours in form of sample humidity. In the present work, I studied the influence of water vapours on ion chemistry and, subsequently, the respective influence on sensitivity and selectivity of CI-MS techniques.

Studies were carried out using several soft chemical ionization mass spectrometry instruments, including Selected Ion Flow Tube Mass Spectrometry (SIFT-MS), Proton Transfer Reaction Mass Spectrometry (PTR-MS) and Selected Ion Flow-Drift Tube Mass Spectrometry (SIFDT-MS). Experimental studies were also supplemented by theoretical simulation of proposed ion chemistry using the Kinetic of Ion-Molecular Interaction simulator (KIMI), developed by the author.

In this thesis, I present a study of formaldehyde, glyoxal and phthalates ion chemistry with H_3O^+, NO^+ and O_2^+ reagent ions, focusing on secondary reactions with water vapours. Additionally, I also studied secondary reactions of protonated hydrated acetic acid with acetone. Finally, I have carried out experiments with fast gas chromatography (CG) coupled with the SIFT-MS instrument, to reduce humidity influence and improve the selectivity of monoterpenes.

Keywords: Soft chemical ionization mass spectrometry, selected ion flow tube mass spectrometry, proton transfer reaction mass spectrometry, selected ion flow drift tube mass spectrometry

Název práce: Studium reakcí iontů s molekulami vody v plynné fázi pro stopovou analýzu

Autor: Michal Lacko

Katedra/Ústav: Katedra fyziky povrchů a plazmatu Matematicko-fyzikální fakulty, Univerzity Karlovy v Praze

Oddělení chemie iontů v plynné fázi, Ústav fyzikální chemie J. Heyrovského AV ČR, v. v. i.

Vedoucí disertační práce: Prof. RNDr. Patrik Španěl, Dr. rer. nat., Ústav fyzikální chemie J. Heyrovského AV ČR, v. v. i.

Abstrakt: Metoda hmotnostní spektrometrie pomocí chemické ionizace je účinná analytická technika, umožňující detekovat v reálném čase stopová množství organických těkavých látek přítomné ve vzduchu. Procesy vedoucí k ionizaci organických molekul, nutné k jejich detekci a následnou identifikaci, jsou bohužel často ovlivněné přítomností vodní páry. V představené práci jsem studoval vliv vodní páry na chemii iontů a její následní vliv na citlivost a selektivitu metod hmotnostní spektrometrie pomocí chemické ionizace.

Pro studium jsme využili několik hmotnostně-spektrometrických přístrojů, mimo jiné techniku hmotnostní spektrometrie v proudové trubici s vybranými ionty (SIFT-MS), techniku hmotnostní spektrometre pomocí reakce přenosu protonu (PTR-MS) a techniku hmotnostní spektrometrie v proudově-driftové trubice s vybranými ionty (SIFDT-MS). Experimentální stude je doplněná teoretickými simulacemi studovaných procesů pomocí autorem vytvořeným simulačním programem KIMI.

V disertační práci prezentuji výsledky zkoumání iontové chemie molekul formaldehydu, glyoxalu a ftalátů pomocí H_3O^+, NO^+ and O_2^+ reakčních iontů, přičemž se zaměřuji na pochopení sekundárních reakci iontových produktů s vodní párou. Následně jsem také studoval sekundární reakce protonovaných a hydratovaných molekul kyseliny mravenčí s acetonem. V práci jsem nakonec zkoumal analýzu monoterpenů kombinací rychlé plynové chromatografie a SIFT-MS, která mimo jiné umožnuje redukovat vliv vodní páry na iontovou chemii.

Klíčová slova: hmotnostní spektrometrie pomocí měkké chemická ionizace, hmotnostní spektrometrie v proudové trubici s vybranými ionty, reakce přenosu protonu

Contents

Preface

The dissertation thesis deals with specific problems of chemical ionisation mass spectrometry and its applications for trace gas analysis, mainly focusing on the influence of water molecules on ion chemistry in soft chemical-ionisation mass-spectrometry (SCIMS). The study was carried out as a part of the Interactional Training Network "IMPACT" program, connecting several leading European academic institutions and companies in the area of chemical ionisation, analytical chemistry and instrumental development. The international team, containing 10 PhD students, have been focusing on the identification and solving of specific SCIMS problems as well as the development of new analytical solutions. Present work is an integral part of the IMPACT network, dealing with the fundamental theoretical and experimental research of SCIMS. This thesis reflects on the problems of the SCIMS techniques which were found from interactional and interdisciplinary discussions, which are still ongoing.

The main objective of this thesis is to study the reactions of specific reagent ions H_3O^+, NO^+ and O_2^+ (usually presented in SCIMS), with various molecules in the gas phase and to determine the influence of sample humidity on these reactions. This was achieved by experimental research on individual SCIMS instruments and theoretical simulation of ion molecular interactions.

This thesis consists of four main Chapters. The first part introduces ion chemistry and its application to trace gas analysis, identifying the specific problems connected with SCIMS techniques influencing their sensitivity and selectivity, as well as formulation of objectives dealing with these specific problems.

In the second section, we present the construction of the fast gas chromatography (GC) unit used to pre-separate molecular isomers in a gas sample, along with its coupling with selective ion flow tube mass spectrometry (SIFT-MS). This combination of techniques was used to analyse monoterpenes in several coniferous needle samples.

The following chapter focuses on the development of an interactive numerical model capable of simulating ion chemistry in individual SCIMS analytical techniques which in turn enables us to improve the interpretation of our results. This model was then successfully applied to several studies, describing and compensating for the effect of sample humidity.

The final chapter presents the main results of the thesis. Firstly, the thesis deals with the ion chemistry surrounding glyoxal molecules in the flow and drift tubes, which were studied using several SCIMS experimental techniques. Later, the ion chemistry of phthalate isomers dimethyl phthalate, dimethyl isophthalate and dimethyl terephthalate together with diethyl phthalate were studied by the SIFT technique. In both studies, we investigated effect of sample humidity on ion chemistry and, using the numerical model, we were capable of identify secondary reactions forming new product ions. Secondary reactions influencing ion chemistry are, however, not exclusively induced by presence of water vapours. In our next study, we studied secondary reactions of protonated acetic acid hydrates induced by presence of acetone vapours. Acetone vapours, similar to water vapours, reacts with primary product ions via association and ligand switching reactions, reducing selectivity and sensitivity of SCIMS analysis. Finally, we demonstrated applicability of SCIMS techniques on inorganic hydrides of arsene and selene, in highly humidified environment of atomizers. This study can help to understand decomposition processes in atomizers and eventually may lead into new analytical applications of SCIMS techniques.

1. Introduction to gas phase ion processes for trace gas analysis

The term ion processes (or ion chemistry) refers to ion-neutral reactions between ionised and neutral molecules (or atoms) in the gas phase. This form of interaction is typical for low-temperature plasmas and ionised gasses which can be found in many technical applications as well as in the environment (planetary ionosphere, interstellar clouds).

The study of ion-molecular reactions started in the middle of the 20th century after the development of quantum chemistry. Development of new materials, improvements in electronics together with new techniques for vacuum generation and mass spectrometry, allowed for the construction of accurate experimental systems capable of carrying out investigations of individual ion-neutral reactions.

The interest in ion-neutral reactions was supported by early astronomical observations, which indicated the presence of the diatomic molecules CH, OH, NH, CN and C_2 in interstellar space. [1, 2] The formation of various diatomic molecules in low-density plasmas under heavy radiation was expected to be carried out by occasional ion-neutral reactions over a long period of time. [3] Nowadays, we know that ion chemistry together with electron-ion recombination are the main processes generating complex molecules in interstellar space, such as dense and diffuse molecular clouds or nebulas. [4-6]

The second area of research where ion chemistry was considered important was the Earth's ionosphere. This topic has become particularly interesting for the development of long-range radio communication; explanation of rare atmospheric phenomena; as well as the future development of space technologies. Initial measurements of ion concentrations in the Earth's ionosphere were carried out on a rocket-borne mass-spectrometer, launched in Canada [7], which observed the presence of NO^+, O_2^+ ions at altitudes above 100 km. Shortly after this initial *in situ* measurement, an intensive experimental study of atmospheric ion chemistry started.

The first pieces of experimental data were obtained using time-resolved stationary afterglow techniques. [8, 9] The mass-spectrometric analysis of ion decay in stationary afterglows provided the first measurements of ion-neutral reaction rate constants at

Maxwellian kinetic energy distributions, defined by gas temperature. These experiments were more useful compared to the direct ion-neutral cross-section estimation carried out by cross beam experiments, as said previous experiments were only able to effectively achieve interaction energies over 1 eV, thus were not reproducing experimental conditions characteristic for either atmospheric or interstellar plasmas. [10] The discharge in stationary afterglow may however ionise not only the gas mixture but also produce a high population of excited neutrals which may interfere with studied ion-neutral processes. [11] Secondly, the presence of electrons in the afterglow allows for the production of an ambipolar diffusion field, preventing the flow of negative ions into the plasma and thus can only be used for the study of cation-neutral reactions.

Significant progress in an experimental study of ion chemistry was achieved by the development of the flowing afterglow (FA) technique by Ferguson and Fehsenfeld [12] at the National Oceanic and Atmospheric Administration (NOAA) in the U.S. The discharge was generated in the stream of carrier gas in a flow tube. Generated ions and radical species were carried by the gas stream from the active discharge region, where they thermalized. A specific gas might be introduced into the fresh afterglow (e.g. a small amount of a specific electronegative gas such as SF_6 to attract remaining free electrons) to adjust the afterglow properties as well as ion formation. The targeted ion chemistry was then studied by injecting molecules of interest into the afterglow. Ions presented in the afterglow interact with the injected sample neutrals, generating product ions which are detected by the mass spectrometer. Reaction times can be reconstructed by changing the positions of the gas injection and detection orifices, as well as the afterglow gas velocity. However, as a limitation, more than one primary ion is often present in such a system and some metastable species (often in Helium) may influence the studied ion chemistry by Penning ionization. Nevertheless, the FA was a popular technique for the determination of reaction rate constants for ion-neutral reactions. [13-17]

Building from the FA, the newly developed flow-drift-tube type (FDT) technique allowed for the study of ion chemistry and estimating ion motilities for both positive and negative ions over a wide range of interaction energies. [18-20] Here, the uniform electric field was applied along the flow tube, accelerating the ion swarm and increasing the relative interaction energy between ions and neutrals. The technique allowed for the determination of reaction rate constants from thermal energies up to several eV. For higher values of reduced electric field (*E/N*), however, the non-Maxwellian and non-Boltzmann distributions of energy and internal excitation could be achieved. [21]

The possibility to selectively choose specific reagent ions while keeping the ion-neutral reactions at thermal conditions was achieved by the development of the selective ion flow tube (SIFT), developed by Adams and Smith [22]. The SIFT technique uses a mass selective ion injection system providing high ion transmission from a plasma discharge into the flow tube while keeping sufficient resolution of ions (with the mass-to-charge ratios of O_2^+ (*m/z* 32) and NO^+ (*m/z* 30) produced in the discharge being very close in value). The construction was possible due to the unique solution of the flow tube ion injection orifice, providing ion transmission from the low-pressure region of the injection quadrupole mass filter (10^{-5} mbar) into the medium-pressure region of the flow tube (1 mbar). [23] The orifice is made of specifically shaped and orientated injection nozzles placed symmetrically around the ion orifice. Helium gas injected through the nozzles creates a conical gas stream, minimalizing the back flow of gas into the low-pressure injection quadrupole while generating turbulences afterwards, which helps to mix injected ions with carrier gas. The remaining parts of the technique were similar to the FA, including the injection needle for sampled gas at the point where helium flow is laminar and the second quadrupole mass spectrometer for analysis of ion concentrations at the downstream end of the flow tube. The initial concept consisted of a 100 cm long flow tube that required a substantial pumping speed of the main flow tube pump (100 Torr $l.s^{-1}$) to reduce diffusion losses of ions to the flow tube wall. The initial instrument thus achieved a room-size dimension, high operational cost, and despite its popularity, was used rather rarely.

Besides the limitations of FA and SIFT, both techniques were actively used to determine ion products and rate coefficients for many reactions of positive and negative ions [24, 25]. Accumulated data were afterwards compared with theoretical predictions. [13, 26] As a result, SIFT quickly became a standard method for the study of ion-neutral reactions at and near thermal interaction energies. [23]

As stated before, SIFT was initially used to study the ion chemistry of interstellar clouds, planetary atmospheres [27-29] and laboratory plasmas for technical use. [30] The idea of using SIFT for analytical applications became visible after a series of studies related to terrestrial atmospheric chemistry. The concentration of neutral reactants needs to be changed over a wide range to determine the rate constants for studied ion-molecular reactions. Studies showed that when processes occur at the collisional rate, ion products become visible even at low concentrations of neutral reactants. Thus, it should be possible to analyse a gas sample with unknown composition and concentration based on the specific chemical ionization of gas components within the flow tube. Additionally, reagent ions should be chosen on the basis that they do not react with the main components of air, but would react rapidly with trace components of the sample gas (such as organic molecules) and thus allowing for the analysis of their concentration. The idea of using chemical ionization for the detection of trace gas components in air was not new. It was shown previously that organic molecules become protonated after their reaction with specific ions such as CH_5^+. [31] Additionally, Kr^+ and Xe^+ were once used for the analysis of air sample, as their ionization potential lay below the ionization threshold for N_2, thus it was possible to analyze minor air components without interference from the major components. [32] This was beneficial over classical electron ionization mass spectrometry (EI-MS), where only components with partial pressures at the percentage or fraction of percentage levels can be analysed. (i.e. oxygen or carbon dioxide). [33]

The benefit of the SIFT technique was its simple principle. The reaction time is well defined by carrier gas velocity; thus, the concentration of specific neutral components can be directly determined from the abundance of the ion product and known rate constants. Studies of ion chemistry in the Earth’s ionosphere provided information about stable ions (H_3O^+, NO^+ and O_2^+) which do not interact with the major components of the Earth’s atmosphere. Additionally, data was obtained on their reactions with a series of molecules which could be used for the analysis of trace compounds in it. The possibility to select multiple reagent ions in SIFT has opened new analytical opportunities for SIFT-MS, which was then demonstrated by lab air and breath analysis. [34-36]

Successful introduction of chemical ionization into analytical applications provided benefits over conventional analytical techniques such as gas chromatography-mass spectrometry (GC-MS). Demonstration of detection limits in the range of 1 ppbv for several volatile organic compounds (VOCs) allows one to analyse complex mixtures without pre-concentration, allowing for the analysis of the gas sample in real-time. [37] As a result of this, chemical ionization techniques are an excellent choice for analysis of breath or samples from environments requiring quick response times (i.e. homeland security).

The potential of chemical ionization for trace gas analysis became even more dominant after the introduction of new analytical techniques. The Proton Transfer Reaction Mass Spectrometry (PTR-MS) technique replaces a flow tube presented in SIFT-MS with a drift tube. [38] The axial electric field presented in the flow tube carries ions instead of drifting carrier gas. The full volume of the drift tube can be filled with a gas sample which increases the sensitivity of the technique down to the pptv region. The next step involved the installation of the axial electric field into the SIFT, creating a flow-drift tube reaction region. So-called Selected Ion Flow-Drift Tube Mass Spectrometry (SIFDT-MS) has the potential to further improve the analytical possibilities of chemical ionization. [39]

In parallel to low-pressure chemical ionization, atmospheric pressure chemical ionization (APCI) was developed, where ion chemistry occurs at atmospheric or near-atmospheric pressure. [40] The absence of powerful vacuum pumps allows APCI to inhabit much smaller instruments. APCI is also often combined with measurements of ion mobility (APCI-IMS) [41] instead of classical mass spectrometry. [42] The latest development is called secondary electrospray ionization (SESI), which ionizes ambient gas by secondary ions formed by the electrospray technique [43]. Although APCI is an important variant of CI, used globally, we will not focus on it in the present work. Instead, we focus on the low-pressure CI occurring in the SIFT, PTR and IMS instruments. The obtained results and surrounding principles, however, may also be applied to APCI.

1.1. Chemical ionisation of organic molecules

Chemical ionisation is a process achieved through the chemical reaction between ions and molecules. Compared to other ionisation techniques (such as electron ionisation or photoionization), the chemical ionisation here cannot be described by Franck-Condon's vertical electronic transition. Rather, the slower adiabatic approximation has to be considered, assuming adjustment of electronic states and atomic position during the interaction. [44] The amount of energy required to overcome an ionisation threshold is contained in the potential of electronic states of one of the reactants and not necessarily in the kinetic energy of particles. Chemical ionisation can thus be efficient even at low temperatures, characteristic, for example, for interstellar space.

Chemical ionization requires at least two reacting species, A and B, with one of the species carrying a positive or negative charge:

$$A^{+/-} + B \rightarrow products. \qquad (1)$$

Such interaction may result in several reaction channels based on the individual properties of both reactants. Apart from elastic collisions and trivial non-elastic collisions, where reactants thermalize by adjustment of their vibrational and rotational excitation states, we are interested in reactions where reactants change their electronic states. This can lead to rearrangement of electron positions, leading to transfer of charge on the second particle, or eventually initiate atomic rearrangement leading to the formation of new products.

The formation of such products is described by the reaction rate coefficient, individual for each reaction path:

$$k_{\mathrm{exp}}(T) \sim k_{\mathrm{col}}(T)\omega(T), \qquad (2)$$

where $k_{\mathrm{col}}(T)$ is the collisional rate of both reactants and $\omega(T)$ is the thermal reaction probability. While the collisional rate is a property shared between all possible reaction channels, depending on the collision cross-section between reactants, the thermal reaction probability is unique for each reaction channel, determined by its reaction potential. Therefore, both reaction kinetics and thermodynamics have to be considered.

Collision rate of ion – molecular reactions

The initial theory describing the interaction between ions and molecules was created by Langevin. [45] A moving charged particle generates an electric field, creating a long-range interaction via the formation of an induced dipole moment on a neutral molecule. The interaction potential between a point ion and spherical molecule at distance r takes the form:

$$V(r) = -\frac{1}{4\pi\varepsilon_0}\frac{\alpha q^2}{2r^4}, \tag{3}$$

where q represents the charge of the ion, α is the polarizability of the neutral molecule and ε_0 is the permittivity of the vacuum. The ion-molecular interaction potential decreases with distance (due to the r^{-4} term) much slower than classical Lennard-Jones' potential for neutral-neutral collision [46], influenced by Van der Vaal interaction (which decreases as r^{-6}). The crucial parameter is the polarizability (α), which will force the neutral to move towards the ion. Higher polarizability will directly lead to a stronger interaction between particles. The reaction cross-section of such interactions can be determined by a simple collision model as a function of relative ion velocity v [47], also referred to as the capture cross-section,

$$\sigma(v) = \frac{\pi}{v}\left(\frac{4\alpha q^2}{\mu}\right)^{1/2}, \tag{4}$$

where $\mu = m_1 m_2/(m_1 + m_2)$ represents the reduced mass of colliding particles, where m_1 stands for the ion mass and m_2 for the mass of the neutral molecule. This cross-section represents the associated area around the molecule on which a reaction will occur in the event of a collision. For Maxwellian distribution of particle velocities, the cross-section leads to the temperature-independent Langevin reaction rate coefficient:

$$k_L = \sqrt{\frac{\pi\alpha q^2}{\mu\varepsilon_0}}. \tag{5}$$

This reaction model may however only predict the ion-molecular interaction accurately for atomic ions reacting with small non-polar molecules.

For polar molecules containing permanent dipole moments, the shape of the interaction potential differs from Eq. 1. Charge-dipole potential depends on the angle, Θ, between the vector of the permanent dipole moment relative to the mutual orientation of both interacting particles as:

$$V(r,\Theta) = -\frac{1}{4\pi\varepsilon_0}\frac{\alpha\mu_D}{2r^2}\cos\Theta, \tag{6}$$

where μ_D represents the value of the permanent dipole moment of the neutral molecule. The range of the potential is much greater as now it falls as a function of r^{-2}. For most ion-molecular interactions, both permeability and permanent dipole moment will be non-zero values. Thus, dipole forces cannot be ignored, and both potentials have to be considered. [48] The issue which surrounds modelling is that the mean value of the relative dipole orientation, Θ, depends on the specific molecular system and differs between molecules in a non-trivial way. Two main approaches have been developed to describe the effect of permanent dipole moments; the average dipole orientation (ADO) theory and the parametrised trajectory calculation.

The ADO theory uses a specific locking constant, C, to reflect the effect of the permanent dipole moment. Modelling of such systems shows that for Maxwell-Boltzmann distribution of relative velocities, the locking constant can be parametrised as a function of $\mu_D/\alpha^{1/2}$ for a temperature range 150 – 500 K. [49-51] Using this approach, the collision rate constant for the specific thermal energy is

$$k_{\mathrm{ADO}}(\mathrm{therm}) = \sqrt{\frac{\pi\alpha q^2}{\mu\varepsilon_0}} + \frac{C\mu_D q}{\varepsilon_0}\sqrt{\frac{1}{2\pi\mu k_B T}}. \tag{7}$$

Even for large values of dipole moment, the locking constant C does not exceed the value of 0.3. However, in such a situation, it may still enhance the rate constant by a factor of 2 to 4 compared to the Langevin reaction rate coefficient. Numerous experimental studies showed that even ADO theory tends to underestimate reaction rates by 10 – 25%. [52].

The parametrised trajectory calculation model's ion-molecular interactions via a series of classical trajectory calculations rather than looking for an exact interpretation of dipole interaction. The extensive modelling provided by Chesnavich, Su and Bowers show a good estimation of an upper bound for the true capture rate coefficients. [53] Assuming that the actual reaction rate is always lower or equal to the collisional or capture rate, the theory provides a good estimation of the upper reaction rate limit. The capture rate coefficient was then parametrised by the quantity $K_{\mathrm{cap}}(T_{\mathrm{R}}, I^*)$, depending on the polarizability, α, and dipole moment, μ_{D}, of the neutral molecule

$$\begin{aligned} k_{\mathrm{cap}}(T) &= k_L \times K_{cap}(T_{\mathrm{R}}, I^*), \\ T_{\mathrm{R}} &= 4\pi\varepsilon_0 \frac{2\alpha k_{\mathrm{B}} T}{\mu_{\mathrm{D}}^2}, \\ I^* &= \frac{\mu_D I}{\alpha q \mu}, \end{aligned} \tag{8}$$

where k_{L} is the Langevin reaction rate coefficient and I is the moment of inertia of the neutral molecule. [54]

Both theories can be applied to determine collisional rate coefficients, as they only require the available values of polarizability and permanent dipole moment. Nowadays, such values can be easily obtained by using density functional theory (DFT) calculations and thus the collisional rates can be estimated for a large number of molecules. [55]

Thermodynamics of ion-molecular reactions

Based on the thermodynamic properties of reagents, several reaction channels can be observed, as summarized in Table 1. At the low pressures (below 10 mbar), the most important are bimolecular reactions, as they are usually very fast and occur at rates comparable to the collisional rate. This is true if the chemical energy of the reaction sufficiently exceeds the specific reaction barrier. Such reactions are very important for chemical ionization as they occur in almost every single collision. Some reactions, however, may require a specific mutual orientation of reactants described by a steric factor, which is often much less than 1.

The reactions of positive ions can be divided into five main reaction channels (Table 1, a-e). Most of them can be supplemented by additional dissociation if the chemical potential is high enough to excite the molecule after ionization (into a repulsive state) and thus overcome the bounding energy which leads to dissociation.

Table 1 List of ion-molecular reactions used for CI.

	Reactants		Products	Condition
Positive CI				
a,	$A^{+\cdot} + B$	→	$B^{+\cdot} + A$	$IE(A) > IE(B)$
b,	$AH^{+} + B$	→	$BH^{+} + A$	$PA(B) > PA(A)$
c,	$A^{+\cdot} + BH$	→	$B^{+\cdot} + AH$	if exothermic
	$A^{+\cdot} + BR$	→	$B^{+} + AR$	if exothermic
d,	$A^{+} + B + C$	→	$AB^{+} + C$	if exergonic
e,	$AL^{+} + B$	→	$BL^{+} + A$	if exergonic
Negative CI				
f,	$A^{-} + B$	→	$B^{-} + A$	EA(B) > EA(A)
g,	$A^{-} + BH$	→	$B^{-} + AH$	$PA(A^{-}) > PA(B^{-})$
h,	$A^{-} + BL$	→	$B^{-} + AL$	if exergonic
i,	$A^{-} + B + C$	→	$AB^{-} + C$	if exergonic

The first typical process is a charge transfer (Table 1, a), where a cation radical $A^{+\cdot}$ takes an electron from a neutral molecule B, leaving molecule B ionised. The process is exothermic if the ionization energy of neutral B is lower than the recombination energy of the reactant ion, $A^{+\cdot}$. As reactions often occur at thermal conditions, only a negative difference in respective adiabatic ionization energies, IE(A) > IE(B) is required. In practical applications, the reaction is triggered by using ions of noble gases, as their IE exceeds most of the IE of other atoms and molecules. [56] $O_2^{+\cdot}$ ions are often used as they can be easily produced by a discharge in air, for which the IE(O_2) = 12.07 eV exceeds the IE of most organic molecules. [57] As the difference in ionization energies for both A and B often exceed 2 eV, reactions are frequently accompanied by the dissociation of the B^{+} molecular ion. The dissociation pattern is very similar to electron ionization, as both reactions form an odd-electron molecular ion by removing the electron from the highest occupied molecular orbital (HOMO). The fragmentation rates will however differ as the energy distribution for charge transfer is strictly limited by the exothermicity of the process (usually 2-3 eV for the charge transfer which compares to 70 eV for electron ionization). The reaction rates for charge transfer are very dependent on the electronic and vibrational state of the reactants, as the charge transfer (similar to electron ionization) abides by the Franck-Condon principle. If the electronic states of the reactant neutrals are accessible, the reaction will occur as a fast reaction with reaction rates close to the collisional rate. If not (i.e. HOMO is not accessible), the reaction will either form a long-lived intermediate complex where the reaction may be triggered after isotropic redistribution of energies or as more frequently seen, the reaction would result in elastic or non-elastic scattering (even though the reaction is exothermic). We will discuss this scenario later. In summary, in such a situation, the reaction rate is much slower than the collisional rate.

An additional process which is very characteristic for CI, is proton transfer (Table 1, b) from a conjugated base (AH^+) to a neutral base (B). The ability of a molecule to bind a proton is represented by its basicity, defined as the negative change of the Gibbs free energy (ΔG) when a neutral molecule accepts a proton. During the reaction, a proton is more likely to be attached to a base with higher associated basicity, while the reaction equilibrium rises with a larger basicity difference. However, as the transfer of a single proton from one base to another does not significantly change the entropy ($T\Delta S$), only the enthalpy change (ΔH) is usually important. The condition for successful proton transfer is for the proton affinity of the neutral molecule (B) to exceed the proton affinity of the neutral (A) currently binding the proton; $PA(B) > PA(A)$. As the proton transfer does not face a potential barrier, the process will be spontaneous after the condition is fulfilled. A series of experiments showed that proton transfer is extremely efficient as the reaction rate almost equals the collisional rate, meaning that a reaction occurs on almost every single collision if the reaction is exothermic by at least 20 kJ/mol. [58] This makes proton transfer the most used CI process for analytical applications. A variety of reagent ions can be used, although should be chosen based on their PA and how easily they may be generated in a discharge. Initially, CH_5^+ together with $C_2H_5^+$ was used as reagent ions as they were easily generated by electron bombardment of methane gas in a discharge yielding approximately a 1:1 ratio. [44] The proton affinity of methane $PA(CH_4) = 543.5$ kJ/mol and ethylene $PA(C_2H_4) = 680.5$ kJ/mol were sufficient for proton transfer to almost all organic molecules. [57] However, the low PA of methane represents a significant chemical potential for most reactions as the PA of organic molecules is around 800 kJ/mol. [57] The energy difference of around 250 kJ/mol

(~2.6 eV) triggers the repulsive behaviour and molecules tend to dissociate. More consistent formation of protonated products can be achieved by hydronium (H_3O^+), easily generated in by discharge in pure water vapours. As PA(H_2O) = 691 kJ/mol [57], hydronium can protonate most organic molecules (except for light alkanes from methane to propane, and a few others), and the dissociation probability is significantly reduced. The last considered ion is NH_4^+, produced by discharge in pure ammonia gas. The use of NH_4^+ is however limited as the PA(NH_3) = 853.6 kJ/mol is above the PA of most organic molecules. It was shown that NH_4^+ can be used for the specific identification of some molecules, demonstrated when distinguishing between pinenes and 2-ethyl-3,5-dimethylpyrazine. [59] However, except for specific applications, the use of NH_4^+ as a proton donor is limited, as for most organic molecules it forms ion adducts via an association reaction. [60, 61]

The next process (Table 1, c) indicates a series of different ratio channels, where the reagent ion $A^{+\cdot}$ removes hydrogen or a radical R from the neutral molecule B. The molecule B then remains charged (although with a lighter mass due to the transferred radical, R, or the proton, H). The initial reagent ion becomes neutral as it reacts with the removed fragments. An example of such hydride ion abstractions is found in the reactions of unsaturated hydrocarbon ions with other hydrocarbons, such as $C_3H_5^+$ + neo-$C_5H_{12} \rightarrow C_5H_{11}^+ + C_3H_6$ [62]. However, hydrocarbon ions are not frequently used for analytical applications due to their rapid proton transfer to H_2O molecules, and therefore the reaction between hydrocarbons and NO^+ is of greater use. NO^+ may also induce hydrogen transfer on reaction with sample molecules by forming NOH when reacting with ethers [63], aldehydes [64], amines [65] and alcohols [66]. The hydrogen transfer reaction is determined by the difference in hydrogen affinity between the reagent ions and B (where BH is the neutral reactant molecule, as shown in Table 1). Again, if the reagent ion has a higher hydrogen affinity, the reaction is exothermic and can proceed.

In addition to hydride ion abstraction, more complex radicals from the neutral may be transferred onto the reagent ion. A typical example of this is found in the transfer of OH^- hydroxide ions which has been observed for alcohols [66] and diols [67]; or carboxylic acids [68] observed for hydronium (H_3O^+) and NO^+ reagent ions, respectively. For alcohols reacting with hydronium, the reaction results in the elimination of an additional H_2O neutral from the molecule, producing a dehydrated ion (typical for heavier alcohols). For the NO^+ reagent ion, the reaction produces HNO_2 as a neutral product alongside the dehydrated molecular ion. This reaction is very important for the use of chemical ionisation in an analytical setting. This is because if this process is exothermic, then this reaction would most likely be dominant over other processes.

Last but not least, the association (or adduct formation) reaction (Table 1, d), where the colliding particles A^+ and B form a short-lived ion-neutral complex AB^{+*}, is discussed. The complex exists due to the presence of a resonance structure formed by a centrifugal barrier, as the charge can be partially located on both molecules. The complex can spontaneously dissociate back to its original form or be stabilized by the emission of a photon, or more likely in CI, by a collision with a third particle, C. The third particle removes part of the potential energy from the excited transition complex and acquires this energy itself, in the form of kinetic energy. The reaction complex may thus become bounded inside the barrier. The efficiency of the energy transfer during the collision depends on the reduced mass of the complex, as well as on the mass and the number of degrees of freedom of the C particle. The bound energy can be small or significantly high, depending on the type of the reactants defining the enthalpy and the entropy change between the free and bounded states. For hydronium, the enthalpy difference changes from 33 kJ/mol to 60 kJ/mol for the association reaction with non-polar CH_4 and CO_2, respectively. These differences reach up to 92 kJ/mol and 136 kJ/mol for the association reactions between hydronium with polar SO_2 and H_2O, respectively. [57] Polar molecules tend to form even larger structures, as the reaction complex after stabilisation may react with more neutrals, thus forming bigger clusters. However, the bound energy between elements of such a cluster decreases with each new neutral added to the cluster. The size of the cluster is based on the temperature and pressure of the gas, as larger clusters will spontaneously dissociate under thermal collisions with other molecules. The association rate drops rapidly for higher temperatures, as T^{-n}, where n ranges from 3-5. [69]

Association is a third-order reaction with the unit $cm^{-6}s^{-1}$. As the reaction often occurs in a drift or a flow tube at constant pressure and temperature, it is practical to consider this as an effective second-order reaction. As an example, for a carrier gas at 1.3 mbar and 300 K, the number density is 3.22×10^{16} cm^{-3}. A third-order association rate constant of 1x10^{-25} cm^{6}s^{-1} corresponds to an effective second-order rate of 3.22x10^{-9} cm^{-3}s^{-1}.

Ligand switching (Table 1, e) is often not considered as a primary reaction channel, as it cannot proceed from the injected reagent ions. However, the reaction is important for its presence as a secondary process occurring in the ion–molecular system. The reaction often involves neutral or ionised clusters, from which one or more cluster ligands can be transferred to the other reactant. An example of this is when hydronium water clusters [70] react with organic molecules in the system:

$$\mathrm{H_3O^+ + H_2O + He \rightarrow H_3O^+.H_2O + He}, \tag{9a}$$

$$\mathrm{H_3O^+H_2O + M \leftrightarrow M.H_3O^+ + H_2O}. \tag{9b}$$

The thermochemistry of the process (9b) depends primarily on the different affinity of the transferred ligand (H_3O^+ affinity in the present example). However, as the reaction system contains many molecules, the change in entropy becomes significant. Therefore, describing the reaction only as the difference in particular affinities (otherwise sufficient for proton transfer reactions) is not possible and the total Gibbs free energy must be considered. Additionally, in practical applications, the fact that the reaction is exergonic or endergonic does not necessarily define the reaction equilibrium. That is mainly established by the difference in the number densities of particular neutrals. In typical analytical applications, the number density of the H_2O is six orders of magnitude higher than the number density of the organic molecule, M. Therefore, the reaction will run heavily in favour of hydronium cluster production even if the process is endergonic, as seen in the case of the reaction between formaldehyde and hydronium clusters. [71, 72]

Finally, it is necessary to mention reactions which involve negative ions. However, as we have not used negative ions in the present work, we will only briefly summarize some important reactions. In the environment, negative ions may naturally occur in the upper level of atmosphere as free electrons (generated by solar radiation) are captured by surrounding molecules. [73] Therefore, the study of molecular reactions with negative ions is highly relevant to the ion chemistry of planetary atmospheres in our solar system. [74-76] For analytical applications, using negative ions as reagents are not as popular as positive ions. This is because reactions involving negative ions are more selective and thus are not universal for all applications. However, they can serve as a beneficial supplement to the analysis with positive ions as well as be used for the analysis of specific molecules (especially halogenated molecules).

A set of four of the most important reactions is listed in Table 1, f-i. Electron transfer (or charge exchange) (f) is the reaction equivalent to the charge transfer reaction observed for positive ions. The exothermicity of the process is defined by the difference between the electron affinity (EA) of the reacting molecules. If the EA of the neutral molecule (B) is greater than the EA of the reacting molecular ion in the neutral state (A), the process is exothermic and may proceed. In the stable negative ion, the electron is captured in the Feshbach resonance state and occupies the lowest unoccupied molecular orbital (LUMO) of the neutral molecule. This electron state is usually easily accessible and the reaction may proceed at the reaction rate close to the collisional rate. However, if the difference between the geometries of the neutral molecule and the negative ion is too great, the reaction rate may be reduced. This is due to the formation of a potential barrier as the neutral reagent becomes ionised. [77]

All remaining reactions share many similarities with the reactions of positive ions. For proton transfer reaction (Table 1, g), exothermicity depends on the difference between the respective PAs of the negative ions, A^- and B^-. If the PA of A^- is greater than the PA of B^-, the proton will be transferred from BH on A^-, leaving the B^- ion. The reaction rate behaves similar to positive proton transfer. If the PA difference is above 10 kcal.mol^{-1}, the reaction rate becomes almost identical to the collisional rate. [69] This, however, may not be true for the anions where electrons are delocalized. [78] The ligand switching (or the displacement reaction) (Table 1, h) will proceed in the absence of the effective proton transfer reaction if the displacement process is exothermic. An interesting example is the reaction of OH^- with CH_3CN, where a displacement of CN^- is suppressed by proton transfer. [79] Finally, association (Table 1, i), as a third-order reaction, is also common for negative ions, especially in the presence of polar molecules. The mechanism and reaction rate are comparable with the equivalent association for positive ions.

In conclusion, molecular ions react with neutral molecules in various ways, based on the thermodynamic and physical properties of the reaction system. The effect of the physical parameters (i.e. gas temperature) was not discussed carefully in this chapter, as we will focus on it later in the work. However, it may be seen that ion products of the reactions carry information about the neutral reactant (M) on the formation of ions such as M^+, $(M+H)^+$, $(M-H)^+$, that can be detected using mass spectrometry. The presence of such ions can be thus used to retrospectively determine the presence of the neutral reactant M in the system. This fact led to the development of chemical ionization mass spectrometry (CI-MS). Unlike electron ionization mass spectrometry (EI-MS) often used for analytical applications, CI-MS cannot provide useful information about molecular structure due to a lack of fragmentation of molecules. However, a small amount of reaction products that are closely related to the neutral reactants can be effectively used to analyse complex molecular systems containing several molecules.

The effect of an external electric field

So far, we have described various types of ion molecular reactions and collisional reaction rates for thermalized systems. The energy distribution of the internal energy states, as well as the kinetic energy of all involved particles, is defined by the gas temperature. Most laboratory applications occur at temperatures around 300 K and below, thus we may assume all involved particles are presented in their ground energetic states. In such a situation it is easy to determine or predict the reactions, as we can simply compare important thermodynamic parameters of reactants and products and assume the thermodynamic availability of the selected process (for example difference in proton affinity of ionization energy) and also determine the collisional rate, representing the upper limit for the reaction rate.

The Boltzmann distribution may however be disrupted by external factors. One practical example is the injection of ions from an ion source into the reactor. Ions are often generated in a discharge – an energy-dense environment – from where they can preserve a range of electronically excited states. The high internal energy of such excited ions has to be first dissipated into the gas via (in the best scenario) inelastic collisions for the ion to be thermalized. Until that point, excited ions carry much more chemical energy and classical determination of the collisional rate nor the determination of the thermodynamic availability may be applied. In most applications, this effect is not significant as instrumental design tends to avoid or minimize such situations by letting ions “relax” and thermalize before reacting with molecules of interest.

The external electric field is an additional source of potential disruption. In the presence of an electric field, ions in the gas phase accelerate along the vector of the electric field, *E*. Collisions with gas molecules cause ions to maintain a mean ion drift velocity, v_d, characterized by ion mobility, μ, as:

$$v_d = \mu E. \tag{10}$$

For low electric fields (comparable to or below the thermal velocity), the ion mobility is constant. However, for higher electric fields it acquires a non-linear form:

$$\mu(E) = \mu(0)[1 + \alpha_1(E/N)^2 + \alpha_2(E/N)^4 + \cdots] \tag{11}$$

The ion mobility depends on a collisional cross-section between ions and a buffer gas but is also highly sensitive on gas pressure and temperature. Determination of ion drift velocity, as well as ion mobility, is important for the calculation of ion transit time through the drift tube. Both parameters can be obtained by their direct measurement in the drift tube if the apparatus is capable of generating short pulses of ions entering the drift tube. Alternatively, ion mobility can be found in the literature [80-82] for the most common ions, from which the drift velocity may be calculated.

Increased ion velocity has a direct effect on the kinetic energy of the ion and thus on the reaction cross-section. Collisions of ions with neutrals thus do not occur at thermal energies. To describe this effect, we defined the mean collisional energy (KE_{CM}) as the relative kinetic energy available for the reaction process at the centre-of-mass, which is related to the two interacting particles through:

$$KE_{CM} = \frac{1}{2}\left(\frac{m_n m_{ion}}{m_n + m_{ion}}\right)(v_{ion}^2 + v_n^2), \tag{12}$$

where m_{ion} and m_n refer to the mass of the colliding ion and neutral. The v_{ion} and v_n represent the mean velocities of the colliding ion and neutral at the centre-of-mass, respectively defined as:

$$\frac{1}{2}m_i v_{ion}^2 = KE_{ion}, \tag{13}$$

$$\frac{1}{2}m_n v_n^2 = \frac{3}{2}k_B T. \tag{14}$$

Eq. 12 is then often expressed in a more convenient form

$$KE_{CM} = \frac{m_n}{m_n + m_{ion}}\left(KE_{ion} - \frac{3}{2}k_B T\right) + \frac{3}{2}k_B T. \tag{15}$$

The ion reactions often take place in a system where the analyte molecule is diluted in a buffer (or carrier) gas. The reagent ions thus mainly collide with the buffer gas molecules, while the main interest is to describe the reaction with the analyte. The kinetic energy of the reagent ion is thus characterised by the mass of the buffer gas, m_b, and can be calculated from its drift velocity using the Wannier formula [83]:

$$KE_{ion} = \frac{3}{2}k_BT + \frac{1}{2}m_{ion}v_d^2 + \frac{1}{2}m_bv_d^2. \tag{16}$$

The KE_{CM} can be thus defined for collisions with both buffer gas, $KE_{CM,b}$, and the analyte (neutral reactant), $KE_{CM,r}$:

$$KE_{CM,b} = \frac{m_b}{m_b + m_{ion}}\left(KE_{ion} - \frac{3}{2}k_BT\right) + \frac{3}{2}k_BT, \tag{17}$$

$$KE_{CM,r} = \frac{m_r}{m_r + m_{ion}}\left(KE_{ion} - \frac{3}{2}k_BT\right) + \frac{3}{2}k_BT, \tag{18}$$

where m_r represents the mass of the neutral reactant molecule. The $KM_{CM,b}$ is related to the internal excitation of the reagent ions. An increase of the $KM_{CM,b}$ over the thermal energy causes a redistribution of the rotational and vibrational equilibrium into energetically higher states, resulting in a change in ion reactivity. The $KM_{CM,r}$ then represents the translational collision energy of the reagent ion with the analyte.

The energy transfer at the centre-of-mass depends on the mass of the neutral particle and is less effective for lighter neutral reactants (see Figure 1). For the reaction of hydronium (*m/z* 19) with helium (4 amu) and argon (40 amu), the mass coefficient is 0.17 and 0.68, respectively. This rapid increase in the effectivity of energy transfer, however, is not that significant, due to ion mobility and thus an ion mean drift velocity decrease for a heavier buffer gas. At this point, it would be convenient to recap on the situation introduced previously, where ions were injected from the ion source into the buffer gas. In such a situation, the mean velocity of the particle is defined by the potential difference between the ion source and the reaction region (and may achieve several eV). Reagent ions in the injection region, before deceleration, collide with the buffer gas regardless of ion mobility. The mass of the buffer gas molecules thus significantly influences the collisional energy.

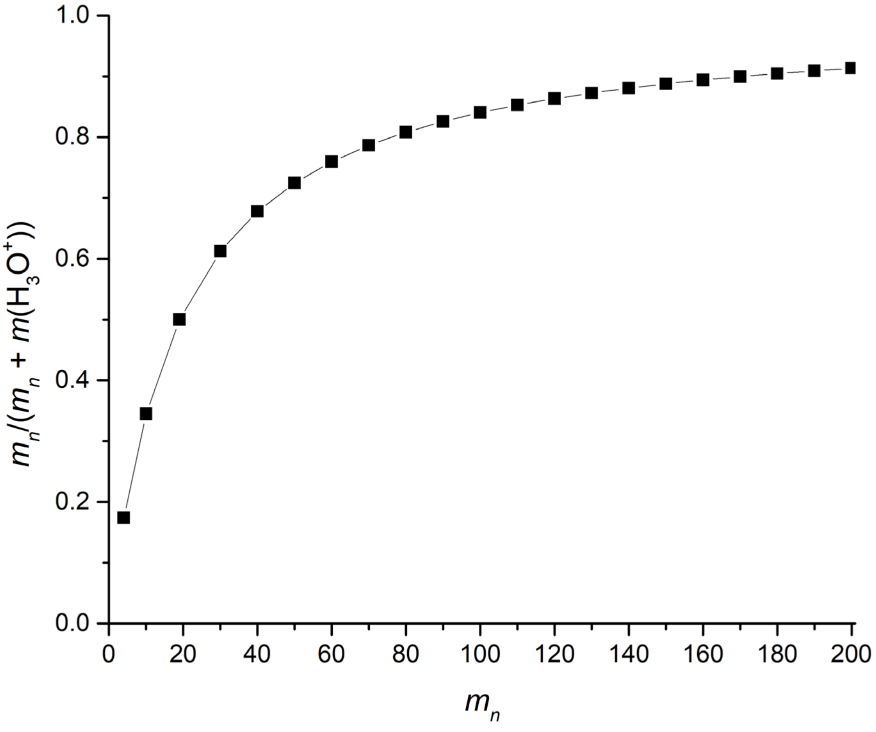

Figure 1 The mass coefficient for conversion of the laboratory ion kinetic energy into the centre-of-mass collisional energy (see Eq. 15). The profile represents the energy conversion for the hydronium ion colliding with neutrals from 4 up to 200 amu.

The $KM_{CM,r}$ is a crucial parameter for ion-molecular reactions and describes the amount of translational energy in addition to the internal chemical energy which is available for that particular reaction. This significantly affects the thermodynamics of the reaction as well as the reaction cross-sections. To visualize this effect, we may consider the typical drift velocity of hydronium in PTR-MS (see Section 1.2), of 995 ms^{-1}. The translational collisional energy with neutral particles of molar mass 30 g/mol, 60 g/mol and 100 g/mol is 0.19 eV, 0.35 eV and 0.55 eV, respectively. At the temperature T = 300 K, the mean thermal energy is 0.039 eV. The collisional energy may exceed the average thermal energy and thus significantly affect ion-molecular reactions. The increase in the reaction energy affects both the collisional cross-section as well as the thermodynamics of individual reactions and thus the reaction cross-section.

The influence of an electric field (and therefore KM_{CM}) on the collisional rate was in most cases determined indirectly. Assuming Maxwellian ion velocity distribution, we can define an effective temperature of the system, T_{eff}, as:

$$\frac{3}{2}k_B T_{eff} = KE_{ion} = \frac{3}{2}k_B T + \frac{1}{2}m_{ion}v_d^2 + \frac{1}{2}m_b v_d^2. \tag{19}$$

Thus, T_{eff} is the kinetic temperature corresponding to three degrees of freedom in the centre-of-mass system of the ion and reactant molecule, where the first term represents the thermal energy; the second term represents the energy absorbed from the field which is converted into the ion drift motion; and the last term represents the energy of random motion from collisions with gas molecules. [21, 84] This assumption allows us to simplify the reaction rate function from $k(T, E, p)$ to $k(T_{\mathrm{eff}})$. It should however be stressed that Eq. 19 represents only the first-order approximation, derived by Wannier. [83] The higher orders of Eq. 19 are usually ignored, as their effect on the calculated value is below 15%. [84] The conclusions also apply only to an atomic ion drifting in an atomic buffer gas, where internal excitations do not affect reactions.

Looking back at the Langevin reaction rate coefficient, k_L, (Eq. 5), we see that it is temperature independent. Thus, the collisional rate of non-polar molecules is not affected by elevated collisional energy. For polar molecules, the ADO theory, Eq. 7, predicts the temperature dependence as $T^{-1/2}$. Su [85] also developed a parametric representation of the ion-polar molecular collision rate for kinetic energy dependence, where:

$$\begin{aligned} &k_{\mathrm{cap}} = k_L \times K_c(\tau, \varepsilon), \\ &\tau = \frac{\mu_D}{\sqrt{\alpha T}}, \\ &\epsilon = \frac{\mu_D}{\sqrt{\alpha KE_{cm}}}. \end{aligned} \tag{20}$$

The parametric representation of Su was tested for the rotational temperature T up to 1000 K and KE_{cm} up to several eV, achieving good agreement with available experimental data. Additionally, Su concluded that the parametric representation is sufficient without introducing the dipole–induced dipole potential. [86] A trajectory calculation approach may also be used, but good agreement with experimental data has only been reported at low temperatures and low relative kinetic energies. [87] In conclusion, all theories predict the reduction of the collisional reaction rate for polar molecules, as KE_{cm} increases as a function of $T_{eff}{}^{-1/2}$, or eventually with a slightly faster reduction when also considering higher orders of Eq. 19.

The reaction rate however differs from the collisional rate and the dependence on KE_{cm} and T_{eff} changes with the type of reaction. Multiple studies can be found investigating ion molecular reaction rates under variable electric fields, or more frequently, under variable gas temperatures. Also, reactions shall be divided into several sub-categories, reflecting the different natures of ion-molecular reactions which include whether the reaction is exothermic or endothermic; slow or fast (compare to collisional rate); unimolecular or bimolecular; and if ions react with non-polar or polar neutrals.

The most common are bimolecular reactions:

$$\mathrm{A}^{+} + \mathrm{B} \leftrightarrow \mathrm{AB}^{*+} \rightarrow \text{products}. \tag{21}$$

Fast bimolecular reactions are exothermic, proceeding at reaction rates close to the collisional rate. The distribution and stabilisation of atoms and charge in the formed AB^{*+} nascent complex have to occur rapidly. A good example is a charge or proton transfer, that is very rapid and can effectively proceed even as the interaction time (the time interval for when both reactants are in close proximity to each other and a reaction can occur) decreases due to increased relative ion velocity. These reactions follow the profile of the collisional reaction rate, thus there is no thermal dependence for non-polar neutral reactants and small negative temperature dependence for polar molecules, as predicted by theory. [73] As an example, we may choose a dissociative charge transfer reaction $He^+ + N_2 \rightarrow N^+ + N + He$ with a reaction rate 1.5×10^{-9} cm^3s^{-1} and with no thermal dependence [88-90]. Also, the proton transfer reaction $N_2H^+ + CH_4$ with a reaction 1.3×10^{-9} cm^3s^{-1} shows no thermal dependence. [91] For polar reactants, the exothermic proton transfer reaction $N_2H^+ + CH_3CHOH$ follows the negative thermal dependence as predicted by ADO theory. [91]

Slow bimolecular reactions have reaction rates significantly lower than the collisional rate, even at normal laboratory temperatures. This may occur when a reaction is endothermic (or endogenic) and thus an energetic barrier is present. The thermal dependence of a reaction rate consists of a combination of collisional rate thermal dependence and the Arrhenius function, describing the increase of reactivity when temperatures or collisional energies close the difference in the activation energy:

$$k_r = k_{cap} \times exp\left(-\frac{E_a}{k_B T_{eff}}\right). \quad (22)$$

The reaction rate of such a reaction may have negative thermal dependence (at the beginning); however, it will change into positive thermal dependence when the reaction channel starts to open up as the translational or internal energy of the reactant can overcome the reaction barrier. After the reaction channel opens, the reaction becomes fast. An example is the charge transfer reaction CO_2^+ + O_2 which has a negative thermal dependence on reaction rate up to 740K, where it changes into a positive thermal dependence. [92]

Some reactions are however slow naturally. A reaction may become less effective when a reagent ion is excited from its ground vibrational state (due to collisions with buffer gas, Eq. 17) or when the reverse reaction channel occurs faster than the forward reaction, transferring the products back into the reactants. This may happen for reactions of small molecules with high exothermicity, while the nascent reaction intermediate AB^{*+} does not have an accessibly fast reaction potential towards new products. In other words, the nascent intermediate requires a longer period of time to rearrange the electronic or atomic distribution. The lifetime of the nascent intermediate must be long enough to allow for the statistical redistribution of energy into all degrees of freedom and thus favour the most exothermic channel. However, the lifetime of the nascent intermediate decreases with the total energy. Thus, an increase in the translational energy results in a higher probability of elastic scattering

$$\mathrm{A}^+ + \mathrm{B} \rightarrow \mathrm{AB}^{*+} \rightarrow \mathrm{A}^+ + \mathrm{B}. \quad (23)$$

An example of this is the charge transfer reaction $O^+ + O_2$, where the reaction rate was estimated to be $3.4 \times 10^{-15} \times T^{-0.48}$. [93, 94]

The thermal dependence for slow reaction, however, does not necessarily follow the $T^{-1/2}$ profile. Often, the exponent is much larger than 0.5. This can happen if, for example, during processes involving the exchange or relocation of massive particles. The proton transfer reaction of t-$C_4H_9^+$ conversion to benzyl acetate follows a temperature dependence from T^{-6} to T^{-10}. [95] Also, for the proton transfer from CH_4D^+ to CH_4, the data suggest a thermal dependence of T^{-8}. [96, 97] Similar thermal profiles can be found also for association reactions, where in the first reaction step a nascent intermediate is also formed, followed by its stabilisation via collision with a third particle. [73]

$$\mathrm{A}^{+} + \mathrm{B} \rightarrow \mathrm{AB}^{*+},$$
$$\mathrm{AB}^{*+} + \mathrm{M} \rightarrow \mathrm{AB}^{+} + \mathrm{M}. \tag{24}$$

As an example, the association reaction $N_2^+ + 2N_2$ forming $N_4^+ + N_2$ proceeds with a third-order rate constant of 8×10^{-29} cm^6s^{-1} at 300 K, (while following a thermal dependence of T^{-4}). [98]

H^- transfer reactions are unique to certain processes, an example being s-$C_3H_7^+$ + i-$C_4H_{10} \rightarrow C_3H_8 + C_4H_9^+$, which requires little or no activation energy. These reactions occur rapidly at low temperatures, but after a critical temperature, a strong negative thermal dependence ranging from $T^{-1.5}$ to $T^{-6.8}$ appears. [91, 99] The exponent is smaller for the increasing exothermicity of the reaction.

The strong thermal dependence originates in the presence of the nascent intermediate AB^{*+} and a long reaction time. These reactions thus need to be thought of as unimolecular decompositions of the ions. For H^- transfer reactions, the authors used transition state theory (TST) to explain the negative thermal profile. [91, 100] The TST is however used to describe the neutral chemical reactions in the presence of activation energy. In the general TST, the forward reaction rate constant takes the Eyring form:

$$k_f = \kappa \frac{kT}{h} \frac{Q_{tr}^{\ddagger} Q_{rot}^{\ddagger} Q_{vib}^{\ddagger} Q_{elec}^{\ddagger}}{\prod_{i=1}^{n} (Q_i)_{tr} (Q_i)_{rot} (Q_i)_{vib} (Q_i)_{elec}} exp\left(\frac{-E_a}{kT}\right), \tag{25}$$

where κ is the transmission coefficient, $Q^{\ddagger}$ and Q_i are the respective partition functions for the transition complex AB^{*+} and the reactants, respectively. Assuming the activation energy is negligible, the exponential factor is unity. The influence of electronic and vibrational terms may be neglected at moderate temperatures. Thus, the forward rate constant may be expressed as:

$$k_f = CT \frac{\left(T_{trans}^{\ddagger}\right)^{3/2} \left(T_{rot}^{\ddagger}\right)^{3/2}}{\prod (T_{trans})^{3/2} (T_{rot})^{3/2}} T_{int.rot}^{-r/2} = CT^{-\left(2+\frac{r}{2}\right)}, \tag{26}$$

where r represents the change in the number of internal rotations upon the formation of the transient complex and C is a constant. Note that the exponent of 3/2 in the rotational temperature terms is for nonlinear molecules, whereas for linear molecules a 2/2 exponent is used. The r term may be positive or negative if more or less internal rotors are hindered upon the formation of the complex compared to new internal rotors formed in the process. The TST represents a simple explanation, that follows the observed T^{-n} profile of thermal dependence and explains the changes in reaction rates for changing complexity of the reactions. However, the TST does not account for changes in the exothermicity or the kinetic parameters. [73]

The more universal approach to this problem is the application of RRK [101] or RRKM [102] theory. Their theories represent a semi-classical approach to unimolecular decomposition of transient ion species, first described by Rice-Ramsperger-Kassel and later reformulated by Marcus-Rice. Both theories assume that the molecule behaves as a harmonic oscillator with Boltzmann energy distribution. The molecule may undergo unimolecular decomposition when the critical energy, ε_0, is achieved, allowing the molecule to isomerize into a transition complex, $X^\ddagger$, of which decomposition is inevitable: $X^* \leftrightarrow X^\ddagger \rightarrow$ *products*. Also, the distribution of energy between oscillators is much faster than the reaction itself.

Kassel (RRK theory, [101]) assumes a system of s classical harmonic oscillators (s = $3n$-6 for non-linear molecules, where n represents the number of atoms). The distribution function in such discrete systems at a given energy, ε, takes the form:

$$P(\varepsilon) = \frac{\varepsilon^{s-1}}{(kT)^s}\frac{exp(-\varepsilon/kT)}{(s-1)!}. \tag{27}$$

The energy-dependent microscopic rate constant for decomposition is

$$k(\varepsilon) = A\left(\frac{\varepsilon - \varepsilon_0}{\varepsilon}\right)^{s-1}, \tag{28}$$

where ε_0 is the zero-point energy difference between $X^\ddagger$ and X^*, $\varepsilon_0 = \varepsilon_{ZPE}(X^\ddagger) - \varepsilon_{ZPE}(X^*)$, ε is the excitation energy of X^* and A is a constant factor representing the lifetime of the transition complex, in the order of magnitude of the vibrational frequency. [103]

Marcus (RRKM theory, [102]) assumes that the density of energy states in the excited complex X^* is high, so the distribution function is continuous. In addition, only a few vibrational states of the transient complex $X^\ddagger$ (located above the threshold) need to be considered. Also, the initial energy ε of the excited complex X^* is distributed between the vibrational energy $\varepsilon^\ddagger_v$ and the reaction coordinate translational energy $\varepsilon^\ddagger_t$ of the transient complex $X^\ddagger$: $\varepsilon - \varepsilon_0 = \varepsilon^\ddagger = \varepsilon^\ddagger_v + \varepsilon^\ddagger_t$. The reaction thus proceeds as $X^*(\varepsilon) \leftrightarrow X^\ddagger(\varepsilon^\ddagger_v) \rightarrow$ *products*, where the microscopic rate constant k is a function of $f(\varepsilon, \varepsilon^\ddagger_v)$. In such systems, the distribution function takes the form:

$$P(\varepsilon) = \frac{\Omega(\varepsilon)}{Q} exp(-\varepsilon/kT), \tag{29}$$

and the energy-dependent microscopic rate constant for decomposition is:

$$k(\varepsilon) = \sum_{0 \le \varepsilon_v^{\ddagger} \le \varepsilon^{\ddagger}} \frac{1}{h\Omega(\varepsilon)} = \frac{1}{h}\frac{W(\varepsilon_v^{\ddagger})}{\Omega(\varepsilon)}, \tag{30}$$

where Q represents the corresponding partition function, $\Omega(\varepsilon)$ is the density of the considered active vibrational (or rotational) states per unit of energy at energy ε; and $W(\varepsilon^{\ddagger}{}_v)$ is the total number of active states in the transient complex in the energy range ε - ε_0. [103]

It is important to point out that the RRKM approach is better, mainly in the near-threshold region. [103] Furthermore, in the RRK theory, the s parameter is often not consistent. [104] Moreover, both previous forms of the microscopic rate constant (Eyring and Kassel forms, Eq. 25 and Eq. 28) can be reduced from the Marcus representation. The reader may thus ask why we have also discussed these previous theories? Both Eyring and Kassel forms are good first-order approximations. Both clearly indicate a trend with increasing temperature, which is not obvious in the Marcus representation.

Considering an association reaction

$$\mathrm{A}^{+} + \mathrm{B} \underset{k_{-1}}{\overset{k_1}{\longleftrightarrow}} \mathrm{AB}^{+*}, \quad \mathrm{AB}^{+*} + \mathrm{M} \overset{k_2}{\rightarrow} \mathrm{AB}^{+} + \mathrm{M}, \tag{31}$$

the forward reaction rate takes the form

$$k_f = \frac{k_1 k_2 [\mathrm{M}]}{k_{-1} + k_2 [\mathrm{M}]}, \tag{32}$$

which at low pressures ($k_{-1} >> k_s[\mathrm{M}]$) reduces to:

$$k_f = \frac{k_1 k_2}{k_{-1}} [M]. \tag{33}$$

Considering the substitution $\varepsilon - \varepsilon_0 = \varepsilon^{\ddagger} = rkT$ for r squared terms contributing to the internal energy of the transient complex AB^{+*}; and $\varepsilon_0 = D_e$ to represent the dissociation energy of AB^{+*}, Eq. 28 may be integrated into Eq. 33 as:

$$k_f = k_1 k_2 [M] \left(\frac{rkT}{D_e + rkT}\right)^{-(s-1)}, \tag{34}$$

for which the approximation $D_e >> rkT$, may be applied, assuming the reaction rates k_1 and k_2 do not significantly depend on T:

$$k_f = k_1 k_2 [M] \left(\frac{rkT}{D_e}\right)^{-(s-1)} \sim CT^{-n}. \tag{35}$$

Clearly, this interpretation uses several assumptions. Also, contributions from the rotational excitations may be significant. However, processes lacking a fast reaction channel will undergo a unimolecular decomposition back to the reactants with a temperature dependence T^{-n}, where n depends on the degrees of freedom in the produced transient complex.

In this extensive discussion, we should finally compare how the predicted profiles of temperature-dependent rate coefficients apply to ion molecular reactions under the presence of an electric field. In the typical application, the ion translational energy is between 0.04 eV up to (1-2) eV.

For fast ion-molecular reactions characterised by the lack of the internal energy barrier, there is no significant dependence of the reaction rate on EK_{CM}. [105, 106] This includes fast charge transfer reactions as well as fast proton transfer reactions with the exothermicity above 10 kJ/mol. Reactions thus follow the expected profiles of the collision rate. As an example, we can present the study of Lindinger et al. [107], studying the reactions of metastable $O_2^+(a\ ^4\Pi_u)$ with N_2, Ar, H_2, O_2. All reaction rates are close to Langevin collisional rate. The proton transfer reaction $H_3O^+ + CH_2O$ studied by Hansel et al. follows a steady decay expected for the interaction of polar molecules. [108] Some reactions have, however, even positive trends where the reaction rate overcomes the Langevin limit. [105] This interesting behaviour was discussed by Smith et al. [109], showing that at sufficiently high energies the shape of the interaction potential described by Langevin (Eq. 5) changes into a hard-spherical potential, leading to a $k_c \sim T^{1/2}$ profile of collision rate.

In practical applications for trace gas analysis, proton transfer reactions that are exothermic at zero-field conditions are affected only minimally, as the higher relative kinetic energy results in a minor decrease of the collisional cross-section. However, added collisional energy may open new reaction channels that were not previously possible due to lower PA. For example, propane or i-butane both have PA values lower than that of water (PA(propane) = 6.49 eV, PA(i-butane) = 7.03 eV, PA(water) =

7.16 eV, from [57]) and in flow tube experiments do not react with hydronium. In the presence of an electric field, however, the reaction is possible. Furthermore, the increased collisional energy opens new and changes existing dissociation channels, mainly for more complex molecules. For example, hydronium reacting with 3-pentanone at zero-field conditions in SIFT-MS produces only a protonated 3-pentanone ($C_5H_{11}O^+$) molecule [64], while in PTR-MS at 140 Td, 20 % of the protonated 3-pentanone dissociates into $C_2H_5O^+$ [110]. A similar conclusion applies to charge transfer reactions. Fast charge transfer reactions between reagent ions and neural analyte molecules remain stable. The increased collisional energy, however, may also open new dissociative channels. The profile of dissociative channels will then follow the Arrhenius form.

For slow ion-molecular reactions, the negative energy dependence was of course also observed, following the previous assumption of transient complex formation. However, some differences need to be discussed. Typically, the reaction rate profile for ion-molecular processes follows a “U” shape. Initially decreasing, following the power-law profile of $EK_{CM}{}^{-n}$ and after reaching the reaction rate minimum, the reactivity increases. This character was observed for many reactions, where the formation of an intermediate complex is expected. [105] For very low temperatures, reaction rates reach the collisional rate. However, an increase in temperature results in negative energy dependence. The negative energy dependence is present until the lifetime of the transient complex is above the typical vibrational time constant. If the lifetime of the transient complex is shorter, then there is no sufficient statistical randomisation of the energy between vibrational modes. This induces a change in the energy from an isotropic to an anisotropic distribution and in turn causes a change in the reaction mechanism, resulting in the opening of a new (“direct”) reaction channel. [19] In other words, the generated reaction potential has a double-minima shape, where one minimum generates a “loose” complex and the second minimum a “tight” complex. For low energy interaction, the long-lived “loose” complex is formed and is sensitive to unimolecular decomposition. However, after reaction energy exceeds the central barrier between the two states and a “tight” complex is formed, this results in the opening of a new reaction channel. [106] This behaviour can be practically demonstrated by the work of Glosik et al. [111], who studied the reactions of several ions with an HCl molecule as a function of the centre-of-mass energy. Reactions forming intermediate complexes, showing transitions from the "loose" to the "tight" arrangement in the studied energy range, were described as a combination of two independent reaction channels, I and II, where the total reaction rate may be described as:

$$k(KE_{CM}) = k_I + k_{II}$$
$$= k_1 \frac{1}{1+\left(\frac{KE_{CM}}{KE_{CM,1}}\right)^m} + k_{II,0} \exp\left[\frac{-\Delta E_a}{\left({}^2\!/_3\, KE_{CM}\right)}\right]. \tag{36}$$

In this interpretation, k_I represents the low energy reaction rate for the indirect process forming the "loose" complex and $k_{II,0}$ represents the total reaction rate for the direct process proceeding via the formation of the "tight" complex. The power dependence of k_I originates from the assumption [105]:

$$\frac{k_1}{k_{-1}} = \left(\frac{KE_{CM}}{KE_{CM,1}}\right)^m, \tag{37}$$

where m is a constant exponent describing the unimolecular decomposition and $KE_{CM,1}$ is the value of energy where $k_1 = k_{-1}$. This concept was afterwards also implemented in several of the following studies. [112, 113]

The parameter, m, can be found by interpolating experimental data using a $\log(k_{-1}/k_f - 1)$ versus $\log(KE_{CM})$ plot. To obtain a predicted value of m, the Eyring form (Eq. 26) is frequently used [114] and considers the total forward reaction rate:

$$k_f = f k_c \frac{Q^{\ddagger}(\mathrm{AB}^{+*})}{Q_{rel} Q_{rot}(\mathrm{A}^+) Q_{rot}(\mathrm{B})} \sim \frac{T_c^{r_c/2}}{T_t^{3/2} T_i^{r_i/2} T_n^{r_n/2}}, \tag{38}$$

where $Q^{\ddagger}$ and Q represent partition functions of the intermediate complex and the reactants, respectively. In the final notation, the translational temperature is T_t; the temperature of the reaction complex is T_c; the reaction ion temperature is T_i; the reaction neutral temperature is T_n. Also, r_c, r_i and r_n refer to the respective number of rotational degrees of freedom. We discuss before that the Eyring interpretation is not a correct approach to unimolecular dissociation, however, some important conclusions about ion-molecular interactions should be pointed out. For thermalized systems (under isotropic energy distribution) the reaction rate should decay as a function of $T^{-r/2}$, considering only rotational excitation (and as $T^{-(r/2 + 2)}$ considering also vibrational modes, Eq. 26). Under the presence of an electric field, the translational temperature is mainly determined by $EK_{CM,r}$ (Eq. 18), $3/2kT_t = EK_{CM,r}$. The temperature of reaction neutrals, T_n, is represented by the true temperature of the gas, T, and the temperature of reaction ions is determined by the centre-of-mass energy between ions and the buffer gas $EK_{CM,b}$ (Eq. 17), $3/2kT_i = EK_{CM,b}$. [114] The temperature of the transient complex, T_c, can originate in all related forms of energy, thus we have to consider the major contributor. In the drift field, T_t and T_i will be larger than T_n. Thus, the reaction will be mainly driven by direct collision via the translational energy, $EK_{CM,r}$, or via the internal excitation of the reagent ion, $EK_{CM,b}$. Both parameters depend on the type of reaction neutral as well as the buffer gas. For example, the reaction of CH_3^+ with N_2 in He buffer gas results in $EK_{CM,r} > EK_{CM,b}$ (as mass $m(N_2) > m(He)$) and T_c is mainly determined by T_t. However, for the same reaction with H_2 instead of N_2, $EK_{CM,r} < EK_{CM,b}$ and T_c are mainly determined by T_i. This leads to the cancellation of the temperature component in Eq. 38. Therefore (considering the three rotational degrees of freedom for CH_3^+) $k_f \sim EK_{CM,b}^{-3/2}$ is associated with this particular reaction for N_2; and $k_f \sim EK_{CM,r}^{-3/2}$ is associated with this reaction with H_2. The change in the characteristics of this reaction was also observed experimentally. [114] Similar results were shown by Glosik et al. who studied the reaction of CH_3^+ with HCl in He and Ar buffer gas. [115] In He buffer gas $EK_{CM,r} > EK_{CM,b}$, whereas in the Ar buffer gas $EK_{CM,r} \approx EK_{CM,b}$. The study showed that the reaction in He buffer gas followed the power law of $k_f \sim EK_{CM,b}^{-1.7}$, whereas the field-free variable temperature found in the SIFT study depended on the "true" temperature, T, as a result of $k_f \sim T^{-2.1}$. The predicted value of the exponent (Eq. 38, not considering vibrational excitation) $m = -2.5$, close to the thermal studies. Comparing the effect of He and Ar buffer gases, the authors showed that for the same value of $EK_{CM,r}$ (and thus T_t), the reaction rate for the Ar buffer gas is larger than for the He buffer gas. This is a significant observation as the total reaction energy (sum of the internal and translation energy) in the Ar buffer gas is higher than in He. In our theoretical discussion above, we assumed isotropic energy distribution among all energy states of the formed transient complex. This clearly does not correspond with the observation of Glosik et al. [115], where the translational energy reduces the reaction rate (where the internal ion energy has a positive effect on the reaction rate). The positive effect of internal excitation was also observed and discussed by Ferguson et al. [105], McFarland et al. [19] and Viggiano et al. [106]. According to these authors, both vibrational and rotational excitation may influence the formation of transient ions. This is often present in charge transfer reactions, where the Franck-Condon principle and energy resonance have a direct effect. In many situations, internal excitation has no or little effect on reactivity. However, if one of the reactants has a large rotational constant or if the reaction is endothermic but the reaction threshold is energetically similar, the effect is recognizable. Moreover, if the vibrational mode is located on the anticipated reaction coordinate, the effect is dramatic. [116]

We should note that slow charge transfer reactions are not highly significant for trace gas analysis. However, some slow reactions like association reactions or ligand switching reactions can be abundant and important. Association reactions are mentioned separately, as the formation and decomposition of the ion adducts is a characteristic feature of analytical applications of chemical ionisation, in the presence of an electric field. As we already understand, the reaction rates for the formation of ion adducts (Eq. 31 – 33) are known to be at low pressures for third-order reactions, where the forward reaction rate depends on the energy, as $k_f \sim KE_{CM}{}^{-n}$.

We can make an interesting comparison between the power-law exponent of the reaction rate obtained in the presence of an electric field (as a function of KE_{CM}), in variable temperature experiments (as a function of true temperature, T) and with the exponent predicted by theory. The study of Adams and Smith [114] predicted non-linear reagent molecules in drift field $k_f \sim EK_{CM}{}^{-3/2}$ (not considering vibrational excitation) and $k_f \sim T^{-5/2}$ in the thermalized environment. Experimental data for CH_3^+ association with N_2, CO and H_2 in He buffer gas agrees with the prediction. However, different experiments do not agree with the prediction well. H_3O^+ association with H_2O in He follows the $EK_{CM,b}{}^{-1}$ profile, whereas in the thermalized system T^{-3} decay is expected. [39] In a study of $H_3O^+(H_2O)_n$ (n = 2,3,4) association with deuterated ammonia in He, the reaction rates' fall-offs were estimated as $EK_{CM,r}{}^{-0.7}$ for n = 2, $EK_{CM,r}{}^{-1.1}$ for n = 3 and $EK_{CM,r}{}^{-1.2}$ for n = 4. [117] Finally, NO^+ association with ketones in He should follow an $EK_{CM,b}{}^{-1}$ profile, as $r = 2$ for the linear NO^+ molecule. However, much faster decay was observed in the experiments: $EK_{CM,b}{}^{-2.5}$ for acetone; $EK_{CM,b}{}^{-2.3}$ for 2-butanone and 3-pentanone. [118]

To summarize, the presence of a drift electric field influences ion chemistry. The reactions are affected not only by elevated translation energy of reacting ions but also via the internal rotational and vibrational excitations resulting from their frequent collisions with the neutral buffer gas. The significance of such excitations and the translational energy for ion molecular interactions has to be evaluated individually for every reaction, as it differs depending on the reactants and buffer gasses. In the context of chemical ionization for trace gas analysis, the application of an electric field has the following consequences:

1, The reaction rates for the main ionization processes (charge transfer and proton transfer) are affected only slightly. However, for increased collisional energies a new dissociation channel may open, producing ion fragments.

2, Slow ion molecular reactions will have their reaction rates reduced following the power-law decay. However, for higher collisional energies the internal excitation of the reagent ion may change the character of the reaction resulting in the reaction becoming fast and thus significant.

3, Ligand switching reactions (when slow) also undergo a negative energy dependence.

4, The reaction rate for association reactions also follows the power-law decay. Additionally, the formed ion complex is usually weakly bounded. Therefore, a reversed collisional-induced dissociation reaction reduces the abundance of the associated complexes, even more. Thus, for collisional energies above the cluster bound energy, the abundance of ion clusters decays much faster.

5, The energy dependence of reaction rate for slow ion molecular reactions cannot be directly compared with the thermal dependence obtained in thermalized experiments.

6, For collisional energies at around 1 eV and above, slow reactions are no more visible as collisional-induced dissociation. Dissociative charge transfer and dissociative proton transfer reactions dominate over other reaction channels.

1.2. Analytical techniques for trace gas analysis

Chemical ionisation (CI) (described in the previous chapter) can be effectively used for the analysis of various molecules in the gas phase by producing molecular ions, that may be detected by several techniques. With a careful selection of reagent ions, reaction pathways are open for the analysis of targeted molecules. This is crucial as most gas samples are diluted in the air. With the proper selection of reagent ions, any reaction with the main components of air (N_2, O_2, CO_2) will be negligible. In addition, the reagent ions will react rapidly with any remaining molecules diluted in the sample. If the analysis requires the observation of all species within the sample mixture, more aggressive reagent ions (like He^+ or Xe^+) may be needed. The selection of reagent ions depends on individual applications. The most common application is for the analysis of volatile organic molecules (VOCs) presented at trace levels in the air. Therefore, H_3O^+, O_2^+ or NO^+ are often used as the reagent ion of choice as they do not react rapidly with the main components within the air. Additionally, they provide the effective chemical ionisation of most VOCs, as well as other volatile compounds. [37, 52]

Before we start with the description of the chemical ionisation analytical techniques, it is necessary to mention a referential technique. The golden standard for the quantitative analysis of VOCs in the air has always been gas chromatography coupled with electron ionisation mass spectrometry (GC-MS). [119] This approach provides the determination of molecules based on the retention time of a particular species within the column, as well as by the characteristic dissociation pattern in the mass spectrum provided by electron ionisation. Conducting an appropriate preconcentration step, this technique may quantitatively determine the concentration of molecules at the pptv level. [120, 121] However, the downside of this technique is the extensive length of time required for sample analysis (usually several minutes). This technique is also associated with a difficult calibration procedure before any measurement due to the many different influential factors from the instrument. Analytical techniques based on CI are alternative to the classical GC-MS, as will be shown later because they do not require chromatographic separation. However, CI is successfully used with GC as an alternative to EI. This application uses EI to generate reagent ions which go on to react in the ionisation tube, with the gas leaving the GC. This is however not very popular, as the combination of GC with EI is usually enough to analyse most compounds. Nonetheless, it is still useful for compounds with similar MS patterns, such as phthalates [122].

A typical technical solution for chemical ionisation analysis contains three general stages. Firstly, reagent ions are generated by a discharge or another ionization method (e.g. photoionization or radiation). Secondly, reagent ions react with sampled volatiles under specific conditions (pressure, temperature, reaction time, etc.) while producing reaction products characteristic of the studied VOCs. Finally, all ion products are analysed using analytical techniques capable of detecting ions. Until now, various analytical techniques were developed. These techniques are mainly identified by the characteristic pressure in the reaction region. Atmospheric pressure chemical ionisation (APCI) operates near atmospheric pressure, whereas classical CI operates in the order of mbar pressure.

The use of APCI has several benefits. This approach does not require powerful vacuum pumps to generate low pressures and thus such instruments are much easier to construct. Additionally, at atmospheric pressure ions undergo more frequent collisions within the sampled gas, which increases the likelihood of a successful reaction occurring. Moreover, all ions are quickly thermalized and the Boltzmann distribution is established. A typical APCI technique is known as ion mobility spectrometry (IMS). This technique commonly uses radioactive radiation or a corona discharge to produce reagent ions at atmospheric pressure. The reagent ions react with VOCs; products are analysed using the different mobilities of individual ions in a homogenous electric field. As the number of produced ions is high, this technique does not require a sensitive ion multiplier as a detector; instead, a classical Faraday cap with an associated preamplifier is sufficient. This technique is very popular as a result of its compactness and high sensitivity. It is often used in a military and security setting, to detect traces of drugs and explosives. [123, 124] Field Asymmetric Ion Mobility Spectrometry (FAIMS) is a modification worth mentioning. [125, 126] Here, an asymmetric RF field is applied radially to the drift tube alongside the axial field, forcing ions to move towards the wall of the drift tube. Only ions with the correct mobility can penetrate through the modular RF and thus be detected. This unique solution allows for the device to be produced on a chip. [127] The last two techniques necessary to mention (also highly used for analytical applications) include electrospray ionization [128] and secondary electrospray ionization (SESI) [43]. The techniques use a high voltage which is applied on a capillary to disperse the solvent into a fine aerosol. The droplets carry an initial charge (acquired from a high voltage electrode) which continuously evaporates until the droplets meet the Rayleigh limit [129]. The Rayleigh limit is where the Coulomb forces disassemble the droplet to even smaller sizes. In electrospray ionization, the solvent contains a diluted analyte and the combination of evaporation with Coulomb explosion generates the molecular ions (and their associated clusters) which are detected by MS. Therefore, electrospray-MS is often combined with liquid chromatography (LC) to produce a powerful analytical approach for the analysis of various biological molecules. SESI uses electrospray indirectly, first generating droplets of pure solvent. Generated ions and ionized clusters of initial solvents may then react with molecules presented in the surrounding atmosphere, in a secondary reaction. Formed ionised products are then analysed using MS.

Instruments operating at low pressures have already been mentioned. SIFT-MS was developed to study chemical ionisation processes [22], however, it was quickly applied to gas-phase analysis [34, 130]. This technique generates ions in a microwave discharge, for which the reagent ions are selected using a quadrupole mass filter. Reactions with the analyte gas are carried out in helium after which the generated ions are analysed in a mass spectrometer. Following this PTR-MS was developed, optimising previous designs for more sensitive analysis. [59] PTR-MS uses a glow discharge to produce hydronium ions almost exclusively. The H_3O^+ ions are then injected into the reaction region via ion optics. The lack of a mass filter allows for a high ion throughput from the discharge and this, in turn, enhances the probability of a successful reaction occurring. In the reaction region, a drift tube occupied an axial electric field with an intensity of around 130 Td is used instead of a carrier gas to carry ions through into the reaction region. The sampled gas is not diluted within the carrier gas and therefore the full volume of the drift tube may be filled with the gaseous sample. Parasitic association reactions are depressed by the presence of a high drift field increasing the mean reaction temperature above an association threshold. The ions produced are subsequently detected by mass spectrometry. Finally, SIFDT-MS combines both SIFT and PTR [39]. The technique consists of a selected ion source composed of a glow discharge and a quadrupole mass filter, similar to SIFT. However, the flow tube is replaced by a drift tube similar to PTR. This combination allows for the injection of various reagent ions and therefore allows us to determine the sample composition through different reaction channels. Furthermore, the addition of a drift tube allows for the variation of reaction temperature (due to the presence of a homogenous electric field). Higher reaction temperatures are useful for the determination between various isomers. In SIFT, isomers often produce similar molecular ions, however at higher reaction temperatures the product branching ratios for various isomers change, allowing isomers to be distinguished and measured.

Note that we have briefly mentioned only the most important techniques in their most basic form. These techniques may be modified and combined with others, producing unique analytical systems. For example, electrospray and SESI may be combined with tandem mass spectrometry [131, 132]; IMS may be combined with MS, producing 2D IMS-MS spectra [42]. The recent development of IMS has resulted in the production of high kinetic energy IMS (HIKE-IMS), operating within the mbar pressure range, containing a reaction region previously characteristic of PTR-MS or SIFDT-MS. [133] It is beyond the scope of this thesis to fully cover all variations. Thus, we focus only on the relevant ones:

In the present work, we have studied how water vapour affects ion chemistry in the mentioned CI-MS techniques. In this study, we have only used instruments which may provide a direct and detailed study of ion chemistry, such as SIFT-MS, PTR-MS and SIFDT-MS. These instruments operate at ~1 mbar pressure, in which primary reactions dominate over secondary reactions with water, under normal operational conditions. This is important as ion distribution is not in an ideal equilibrium and ions may dynamically respond to a change in the concentration of the neutrals. This therefore allowed for the study of the full set of ion-neutral reactions. Additionally, each technique has a unique construction, allowing one to focus on the different reaction parameters. APCI experiments were not included as they operate near atmospheric pressure where the reaction equilibrium between primary and secondary processes is quickly established due to the high frequency of collisions. Water vapours also affect the ion chemistry in APCI, although they are not ideal for the study of complex reactions. Thus, we will now introduce SIFT-MS, PTR-MS and SIFDT-MS in greater detail.

Selected ion flow tube mass spectrometry (SIFT-MS)

The SIFT technique was developed in 1976 by Adams and Smith [22] and quickly became the standard in the study of ion-neutral reactions, near to thermal interaction energies [23]. For analytical applications, the SIFT technique was implemented into the SIFT-MS instrument. The instrument consists of four main parts: a discharge generating reagent ions; a mass filter selecting one specific ion; a flow tube where selected ions react with gasses in the presence of a carrier gas; and finally, a mass spectrometer at the end of the flow tube.

The setup is characterised by several regions operating at different pressures; ~1 mbar for the discharge and the flow tube; and ~10^{-5} mbar for both the filter and the mass spectrometer. Differential pumping of the system requires a series of orifices, providing the ion transfer between different pressurized regions. The orifices inserted into the SIFT-MS are designed to reduce the back-flow of gases from the flow tube back into the two low-pressure regions. [23] The series of orifices as well as the presence of the mass filter, however, limit the total ion current and number of reagent ions provided by this setup. In the present work, we used a SIFT-MS Profile 3 instrument (see Figure 2) developed by Instrument Science, Crewe, UK, providing ~10^6 ions per cm^3 in the flow tube. The ion current at the injection venturi-type orifice (1mm diameter) leads into the flow tube (tens of nanoamps) and the ion current is reduced by the time it reaches the end of the flow tube (by a factor of 1000). This current drop, partially caused by diffusion to the walls of the flow tube (but mainly occurring during ion transfer through the orifice) represents the main limitation of the instrument.

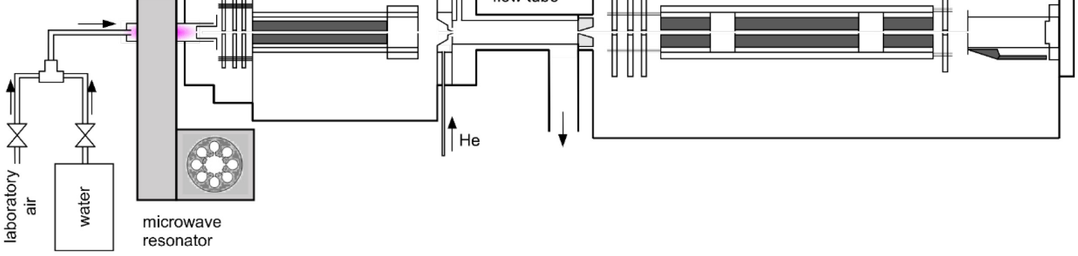

Figure 2 The schema of SIFT-MS experiment. *QMS* - quadrupole mass filter

The SIFT-MS uses a microwave discharge usually within a mixture of water vapour and air. The combination of both gasses allows for the formation of several stable ions, mainly H_3O^+, NO^+ and O_2^+ which may be used in analytical applications. The relevant reaction channels occurring in the RF plasma are listed in Figure 3. In the presence of pure water vapour, the H_3O^+ ions are produced from a series of primary and secondary reactions, mainly by binary reactions of H_2O^+ and OH^+ ions with H_2O (highlighted in blue). By introduction of air into the discharge, the ion reactions also generate O_2^+ and NO^+ ions. The ion composition in the discharge depends strongly on the pressure ratio between individual gaseous components (water vapour and air). Therefore, the ion composition may be optimized to preferentially sift through one of the selected ions, or allow all of the reagent ions through (in comparable concentrations).

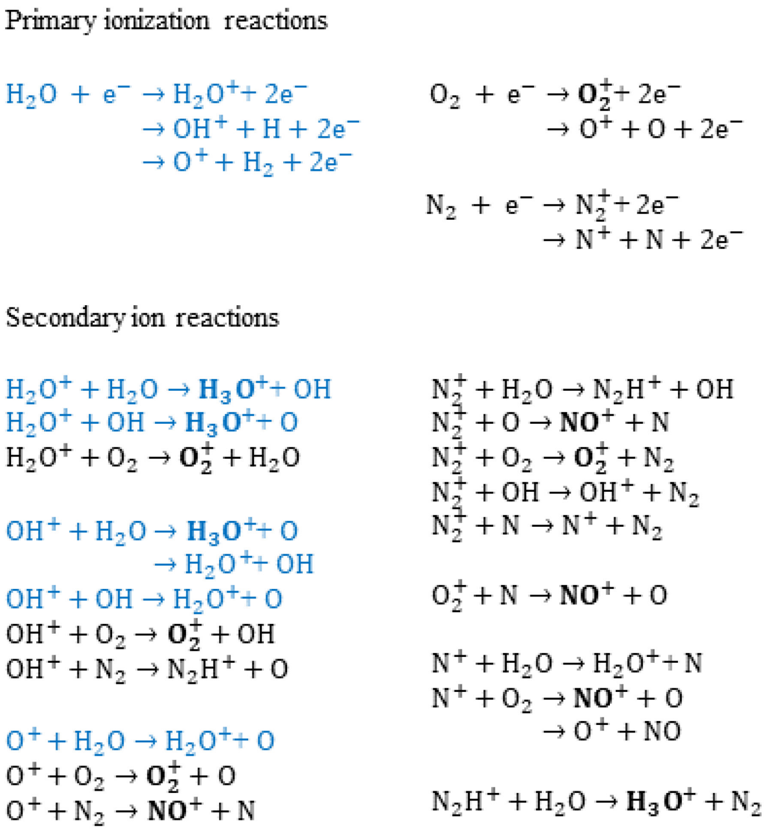

Primary ionization reactions

$H_2O + e^- \rightarrow H_2O^+ + 2e^-$
$\rightarrow OH^+ + H + 2e^-$
$\rightarrow O^+ + H_2 + 2e^-$

$O_2 + e^- \rightarrow \mathbf{O_2^+} + 2e^-$
$\rightarrow O^+ + O + 2e^-$

$N_2 + e^- \rightarrow N_2^+ + 2e^-$
$\rightarrow N^+ + N + 2e^-$

Secondary ion reactions

$H_2O^+ + H_2O \rightarrow \mathbf{H_3O^+} + OH$
$H_2O^+ + OH \rightarrow \mathbf{H_3O^+} + O$
$H_2O^+ + O_2 \rightarrow \mathbf{O_2^+} + H_2O$

$OH^+ + H_2O \rightarrow \mathbf{H_3O^+} + O$
$\rightarrow H_2O^+ + OH$
$OH^+ + OH \rightarrow H_2O^+ + O$
$OH^+ + O_2 \rightarrow \mathbf{O_2^+} + OH$
$OH^+ + N_2 \rightarrow N_2H^+ + O$

$O^+ + H_2O \rightarrow H_2O^+ + O$
$O^+ + O_2 \rightarrow \mathbf{O_2^+} + O$
$O^+ + N_2 \rightarrow \mathbf{NO^+} + N$

$N_2^+ + H_2O \rightarrow N_2H^+ + OH$
$N_2^+ + O \rightarrow \mathbf{NO^+} + N$
$N_2^+ + O_2 \rightarrow \mathbf{O_2^+} + N_2$
$N_2^+ + OH \rightarrow OH^+ + N_2$
$N_2^+ + N \rightarrow N^+ + N_2$

$O_2^+ + N \rightarrow \mathbf{NO^+} + O$

$N^+ + H_2O \rightarrow H_2O^+ + N$
$N^+ + O_2 \rightarrow \mathbf{NO^+} + O$
$\rightarrow O^+ + NO$

$N_2H^+ + H_2O \rightarrow \mathbf{H_3O^+} + N_2$

Figure 3 List of relevant ion-molecular reactions occurring in the RF plasma ion source in the mixture of air and water vapours. [134] Reactions in blue represent those active in pure water vapour discharges. The remaining reactions are active in water vapour/air mixtures. The ions in bold (H_3O^+, NO^+ and O_2^+) are the main reagent ions produced in the discharge at high concentrations.

From the discharge, ions are selected according to their *m/z*, first by a quadrupole mass filter; subsequently by a series of electrostatic lenses focused into the centre of a Venturi-type orifice; and injected into the flow tube. The injection energy, determined by the potential of a quadrupole mass filter, may be several eV. The relatively high energy is necessary for ions to efficiently penetrate into the drift tube. This kinetic energy is then removed from the reagent ions by collisions with a carrier gas, usually helium. Other gasses may be used instead of helium, however, the injection energy must be adjusted to prevent any potential ion-carrier gas reactions within this region.

In the flow tube, reagent ions are mixed with helium and are carried along by the carrier gas stream through the flow tube. At typical conditions (300 K, 1 mbar), the laminar flow distribution is established, while ions are mostly concentrated in the centre of the stream. To minimize diffusion losses, the helium carrier gas flows at a speed of ~10,000 cm/s which requires a powerful vacuum pump. A 5 cm long flow tube used in the present instrument requires a pumping speed of 20 - 30 m^3/h to achieve the required conditions.

The sample inlet is positioned in the flow tube 1 cm downstream from the injection orifice. This distance is sufficient for helium gas to remove any additional energy found in the reagent ions. Therefore, the ion-molecule interaction (with the sample species) will occur at thermal energies. A gaseous sample is introduced through the inlet into the centre of the helium gas stream, where they are mixed with the carrier gas and reagent ions. From this point, the mixture of all components travels to the end of the flow tube, (4 cm from the sample inlet). During this transport, the reagent ions react with the neutral molecules at a defined pressure and temperature, typically 1 mbar and 300 K. The flow tube design does however also allow for ion-molecular experiments to be carried out at varying temperatures, as to determine the temperature dependence on reaction kinetics. [76, 135] At the end of the flow tube, ions are sampled through the exit orifice into the quadrupole mass spectrometer and are detected by a Channeltron detector.

The defined position of the sample inlet and exit orifice, together with the defined ion speed within the helium carrier gas allows a simple calculation of the reaction time t_r, to be conducted (usually 300 μs), schematically illustrated in Figure 4. The known time constant is then used to determine the concentration of neutral molecules if the reaction rate constants are known.

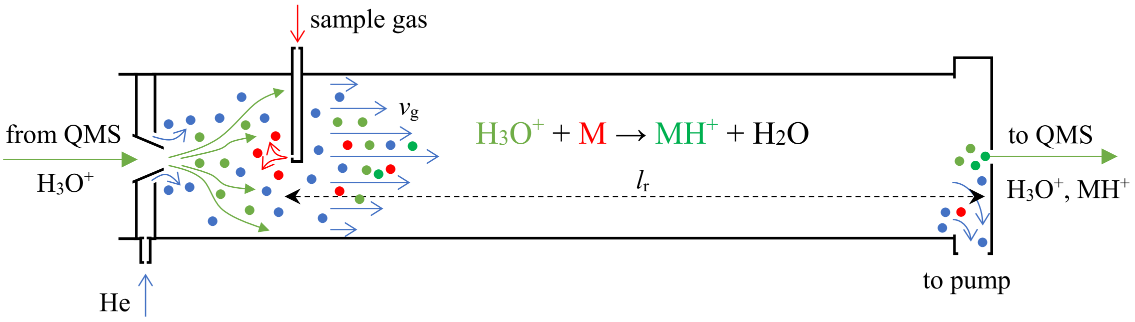

Figure 4 The schematic interpretation of physical and chemical processes in the flow tube. The reagent ions (orange) are injected into the flow tube and mixed with the helium carrier gas. Sample gas (red) is introduced into the mixture as well. The laminar flow of the helium carrier gas transports the reagent ions and sample gas along the defined reaction length l_r, from the injection point up until the end of the flow tube, where neutrals are separated from the ions. Ion-neutral reactions take place along the reaction length (in the flow tube).

For a typical bimolecular exothermic proton transfer reaction between hydronium and an organic molecule M, $H_3O^+ + M \rightarrow MH^+ + H_2O$, the number density of the primary reagent ion $[H_3O^+]$ and protonated product $[MH^+]$ is described by a simple kinetic equation:

$$\frac{d[\mathrm{H_3O^+}]}{dt} = -k[\mathrm{M}][\mathrm{H_3O^+}] - [\mathrm{H_3O^+}]\frac{D_{\mathrm{H_3O^+}}}{\Lambda^2}, \tag{39}$$

$$\frac{d[\mathrm{MH^+}]}{dt} = k[\mathrm{M}][\mathrm{H_3O^+}] - [\mathrm{MH^+}]\frac{D_{\mathrm{MH^+}}}{\Lambda^2}, \tag{40}$$

where k represents the reaction rate constant; $D_{\mathrm{MH^+}}$ and $D_{\mathrm{H_3O^+}}$ stand for the respective MH^+ and H_3O^+ ion diffusion coefficients; and Λ represents the characteristic diffusion length, characterized by the diameter of the flow tube. Integration of Eq. 39 over the reaction time $t_r = l_r/v_d$ leads to an exponential solution showing the concentration of the reagent ion at the end of the flow tube:

$$[\mathrm{H_3O^+}] = [\mathrm{H_3O^+}]_0 exp(-k[\mathrm{M}]t_r), \tag{41}$$

where the reaction rate constant may be determined from a semilogarithmic plot of log[H_3O^+] vs [M]. This same approach may be used for other reagent ions as well. The uncertainty of this method is however augmented by knowing only a rough estimate of the ion reaction time. Thus, the reaction rate constants are determined via a different approach. It was shown that parametrised trajectory calculations give very good results of collisional rate constants [54], which are almost identical to reaction rate constants for proton transfer reactions if the reactions are sufficiently exothermic [69]. Using this fact, we can take the theoretical reaction rate constant as a reference for the rate constants determined by SIFT-MS. In the experiment, we allow all reagent ions to travel into the drift tube simultaneously, which allows for all the investigated primary reactions to happen at the same time. This allows us to determine the slope of the logarithmic curve for the relationship between the reagent ions signal vs the neutral molecule concentration. It also allows us to estimate the relative ratio between the individual primary reaction rate constants. Normalizing the proton transfer reaction rate data to the theoretical values obtained by parametrised trajectory calculations can give an accurate result for reaction rate constant estimates with other reagent ions. This is necessary as one cannot expect the reactions of the neutral molecule with NO^+ or O_2^+ to proceed at the collisional rate. This approach has been used previously on several organic molecules, allowing for the acquisition of calculated reaction rate constants for the reactions of the neutral molecule with NO^+ and O_2^+ ions, as well. [64, 66]

Determination of the analyte concentration in the flow tube may also be achieved by monitoring the decrease in the reagent ions' signal if the reaction rate constant is known. However, if the sample contains several different molecules, they will all react with the reagent ions present and analysis cannot be achieved. Alternatively, we need to focus on Eq. 40 which describes the concentration of product ions. If the reactions of various molecules (in the sample mixture) with the reagent ions result in different product ions and if the reaction rate constants for said reactions are known, all individual molecules within the mixture may be quantified. [136] The first assumption applied in the calculation of neutral molecule number densities in the flow tube is that the concentration of reagent ions is not highly affected by the analyte. In other words, the sample flow rate and therefore the concentration of analyte species in the flow tube is small. Therefore, the reagent ion number density, [H_3O^+] in Eq. 40, may be considered independent from the analyte number density, [M]. An analytical solution for the differential Eq. 40 leads to the time variation of the number density of the product ion [MH$^+$]:

$$[\mathrm{MH^+}]_t = [\mathrm{H_3O^+}]_t\, k[\mathrm{M}]t \frac{exp\left(k[\mathrm{M}]t + \frac{\mathrm{D_{H_3O^+}} - \mathrm{D_{MH^+}}}{\Lambda^2} t\right) - 1}{k[\mathrm{M}]t + \frac{\mathrm{D_{H_3O^+}} - \mathrm{D_{MH^+}}}{\Lambda^2} t}. \tag{42}$$

For a trace amount of [M] in the system we can modify the solution as (as applied in trace gas analysis):

$$\lim_{[\mathrm{M}]\to 0} [\mathrm{MH^+}]_t = [\mathrm{H_3O^+}] k[\mathrm{M}] t D_e\,, \tag{43}$$

where

$$D_e = \lim_{[\mathrm{M}]\to 0} \frac{exp\left(k[\mathrm{M}]t + \frac{\mathrm{D_{H_3O^+}} - \mathrm{D_{MH^+}}}{\Lambda^2} t\right) - 1}{k[\mathrm{M}]t + \frac{\mathrm{D_{H_3O^+}} - \mathrm{D_{MH^+}}}{\Lambda^2} t} = \frac{exp\left(\frac{\mathrm{D_{H_3O^+}} - \mathrm{D_{MH^+}}}{\Lambda^2} t\right) - 1}{\frac{\mathrm{D_{H_3O^+}} - \mathrm{D_{MH^+}}}{\Lambda^2} t} \tag{44}$$

is the differential diffusion enhancement coefficient. [136] If both MH$^+$ and H$_3$O$^+$ ion diffusion coefficients, $\mathrm{D_{MH^+}}$ and $\mathrm{D_{H_3O^+}}$, are similar, D_e converges close to 1. In this case, the product ion number density, as well as the detected ion count rate, are proportional to the neutral analyte gas number density.

It is important to state that if the *m*/*z* value of the product ion differs from the value of the reagent ion, the effect of the differential diffusion coefficient must be considered for the analysis. Fortunately, quadrupole mass spectrometry used in the analysis also provides a mass discrimination correction which is applied to larger ions. As the treated analyte product ions are usually heavier comped to reagent ions, the mass discrimination factor tends to cancel out the effect of the diffusion coefficient. [137] However, for precise analysis, both phenomena must be considered within the SIFT-MS operational software.

Finally, we have to consider the presence of various parallel and secondary reactions. In our previous assumption (Eq. 39, 40), we considered only one primary proton transfer reaction, producing only one product ion MH$^+$. The primary process may however be accompanied by additional reactions including the potential dissociation of product ions into ion fragments. These fragments contribute to the total reaction yield and must be considered in the calculation. Additionally, the presence of water vapour in the system causes the formation of various water clusters, following the association reaction described in the previous chapter. Clusters may be formed not only from reagent ions (making ions like $H_3O^+(H_2O)_{1,2,3}$ or $NO^+(H_2O)$) but also from product ions (like $MH^+(H_2O)$), increasing the overall complexity of the reaction system. Formed reagent ion clusters are also able to react with our analyte molecule, M. We may still treat this problem with the assumption that all reaction products originate from M and thus the overall number density of a neutral analyte is proportional to the sum of product ions intensities produced by individual reaction channels. The neutral number density of the analyte [M] may then be calculated from the corresponding ion count rate [37], following reaction 14 as:

$$[\mathrm{M}] = \frac{1}{t_r} \frac{f_{p1}\, {}^{I_{p1}}\!/_{D_{ep1}} + f_{p2}\, {}^{I_{p2}}\!/_{D_{ep2}} + \cdots}{f_{i1} I_{i1} k_1 + f_{i2}\, {}^{I_{i2}\frac{k_1 + k_2}{2}}\!\Big/_{D_{ei2}} + \cdots}, \tag{45}$$

where I_{p1}, I_{p2}, etc. correspond to the count rates of individual product ions corrected for mass discrimination, I_{i1}, I_{i2}, etc. represent the count rates of individual reagent ions reacting with M. k_1 and k_2 are the reaction rate coefficients for the main and secondary reagent ions, respectively. D_{ep} and D_{ei} are the respective differential diffusion enhancement coefficients, and t_r is the reaction time. Finally, the auxiliary factors f_p and f_i correct for the calculation of non-linear reaction kinetics. For example, f_i coefficients adjust the conversion of hydronium reagent ions into its hydrates, whereas f_p may be used to correct for the calculation of parasitic ions or isotopes (found at the same mass as the analyte ion). [136] This refined determination of the analyte concentration is important, especially for humid air and breath analysis. [138] Even the calculation contains several coefficients and looks difficult to execute, although these calculations have already been integrated into the SIFT-MS software. Differential diffusion enhancement coefficients may be calculated from their ion diffusion coefficients, which may be calculated [139], or just estimated using the ion mass [136]. Mass discrimination may also be interpreted as a simple function of ion mass. The important conclusion is that all parameters may be obtained before analysis and may be universally used in SIFT-MS. Therefore, to achieve quantitative analysis, a calibration for each trace gas species analysed by SIFT-MS is not necessary. [140] However, this only applies if the ion chemistry in the flow tube is fully understood.

The concentration of the trace gas in the sampled air may be determined from the previously calculated number density [M] if both the sample gas flow (Φ_s) and carrier gas flow (Φ_c) are carefully measured. The concentration, *C*, may then be calculated as:

$$C = [\mathrm{M}]\frac{k_\mathrm{b}T_\mathrm{g}}{p_\mathrm{g}}\frac{(\Phi_\mathrm{c}+\Phi_\mathrm{s})}{\Phi_\mathrm{s}}, \tag{46}$$

where k_b is the Boltzman constant, p_g represents the total pressure of the carrier gas and T_g is the gas temperature. One may directly calculate the relative concentration of the trace gas as p_M/p_0, using Loschmidt`s number ($n_0 = 2.687 \times 10^{19}$ cm^{-3}) which represents the reference concentration at standard atmospheric pressure (p_0 = 1,013.25 mbar) and temperature (T_0 = 273.15 K):

$$\frac{p_M}{p_0} = [\mathrm{M}]\frac{p_0}{n_0 p_g}\frac{T_g}{T_0}\frac{(\Phi_\mathrm{c}+\Phi_\mathrm{s})}{\Phi_\mathrm{s}}. \tag{47}$$

The calculated concentration may be converted into the commonly used parts-per-million (ppm) or parts-per-billion (ppb) units, by multiplying by 10^6 or 10^9, respectively.

At this stage, it should be understood that SIFT-MS can quantitatively determine the traces of molecules in sampled air if the ion chemistry of targeted trace molecules is understood. The error of determined concentration depends on all involved instrumental parameters, as gas flow measurements and estimations of diffusion and mass discrimination functions. Therefore, it is difficult to estimate the error directly. However, as most of the parameters for concentration calculation are associated with the instrument, the errors are mostly systematic. Therefore, the relative changes in analyte concentration will always be true. Additionally, the quality of parameters may be tested by providing an analysis of a single volatile molecular standard (i.e. acetone) and therefore clarifies whether the determined concentration agrees with the concentration of the standard.

The sensitivity depends predominantly on the reaction rate of the selected reagent ion with the target molecules. Under standard experimental conditions (using a reaction rate of $3\mathrm{x}10^{-9}$ cm^{3}s^{-1} [64]) and detecting a signal down to 0.1 cps (using longer integration times), this technique is able to detect molecules at the 0.1 ppb level. For the upper limit, we need to guarantee that each ion-molecular reaction does not significantly affect the reagent ion concentration. Therefore, the product ion concentration should be at a maximum of 2 orders of magnitude below the concentration of the reagent ions. Using a count rate of 10^9 cps for the reagent ions and thus 10^7 cps for the product ions (total product ion count rate), one may reach the top molecular concentration at 10,000 ppm. As we see, the instrument may analyse molecular ions in a range of over 7 orders of magnitude.

The concentration of the sample injected into the flow tube may be adjusted by a regulation of the sample flow rate. For highly concentrated samples, the flow rate may always be reduced to achieve the required ion product intensity criteria. For low concentrated samples, the sample flow rate may be increased, however, this possibility is limited. Helium carrier gas needs to be the dominant gas in the system. Therefore, the flow rate of the sample into the flow tube should not exceed 5-10% of the helium flow rate. For the Profile 3 instrument used in this work, the carrier gas flow rate is around 500 sccm. Therefore, we commonly used a sample flow rate of 30 sccm. It is important to note that the present sample flow limitation directly impacts the detection limit. New SIFT-MS instruments use nitrogen gas instead of helium and as a result of this, the flow rate of sampled air may be increased. [141] This however brings other complications which will not be addressed here, as they are outside the scope of the presented work.

Finally, the analysis may be carried out using two methods. Firstly, SIFT-MS may obtain a classical mass spectrum, where we can identify all reagent and product ions. Secondly, the apparatus can monitor the selected *m/z* values and provide real-time analyses of selected molecules. The acquisition time depends only on the integration time and therefore the instrument is able to detect rapid changes in sample concentrations, such as in breath analysis.

Proton transfer reaction mass spectrometry (PTR-MS)

The PTR-MS (see Figure 5) is a technique developed by Lindinger et al. [59], based on discoveries obtained by the FA and SIFT. The initial intention of the authors, however, was to make a purely analytical instrument rather than an instrument capable of investigating ion chemistry and its reaction kinetics. The instrument is tuned to provide a highly sensitive analysis of various organic compounds in real-time with a high level of resolution. Three major upgrades were conducted to achieve such properties which were: an absence of an injection mass filter allowing for a high ion flux of reagent ions; secondly, the absence of a carrier gas but with the full volume of the reaction chamber being filled with the sample gas; and finally, the introduction of an axial homogenous electric field (drift tube) accelerating ions through the reaction region into the detecting mass spectrometer (while increasing the reaction energy of each ion-molecular reaction). As a result, the detection limit of the PTR-MS may be up to three orders of magnitude better than for other SCIMS techniques. Some studies even showed detection limits up to 1 pptv. [142, 143] Now let’s focus on a careful description of the PTR-MS instrument.

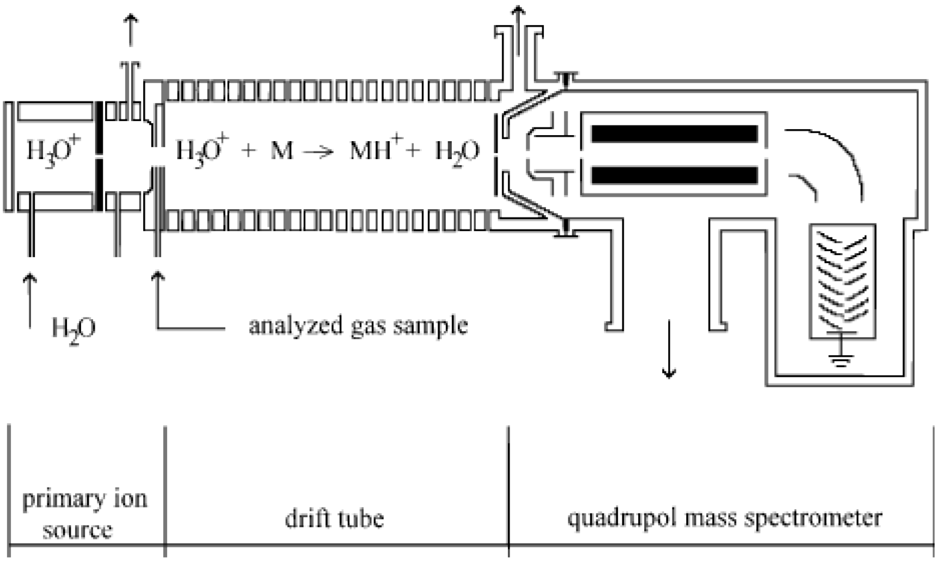

Figure 5 A scheme showing the PTR-MS instrument. [144]

For the ion source, PTR-MS often uses a DC hollow cathode discharge which can achieve higher current densities (several mA) compared to a classical cathode discharge. The plasma in the discharge is generated in pure water vapour at pressures of around 1 mbar, producing a flow of hydronium ions. The ions formed in the discharge pass through a pin hole which introduces them to the next separation chamber. The separation chamber lies between the discharge and the drift tube and is continuously evacuated by a vacuum pump. This region is crucial, as it provides a constant gas flow from both the discharge and the drift tube, preventing gas from the drift tube from entering the discharge (and vice versa). Any gas contamination coming from the drift tube may negatively affect the discharge ion chemistry; and thus, the generation of reagent ions. The chamber also prevents other radicals, generated by the discharge, from entering the drift tube. After entering the separation chamber, reagent ions are injected into the drift tube via a set of electrostatic lenses.

As a final note on the ion source, the PTR-MS is optimised for hydronium as the reagent ion. This is because the water-based discharge produces minimal other undesirable ions which may interfere with the ion chemistry occurring in the drift tube. It is however possible to modify the ion source to produce other reagent ions as well. For this to be possible, the discharge gas and its pressure must change accordingly. It has been demonstrated, that NO^+, O_2^+ and Kr^+ ions may be used for analyses, enhancing the flexibility of the instrument and its capabilities. [145-147] These reagent ions are however rarely used in typical procedures using this instrument as proton transfer from H_3O^+ ions is already highly effective. Additionally, changing over the reagent ion requires time (as the change of gas and its pressure cannot be done rapidly) and thus it is not possible for the conventional PTR-MS instrument to switch between reagent ions in the same way as SIFT-MS. For the first-generation instruments (equipped with quadrupole mass spectrometers) this was considered a limitation as it was difficult to distinguish between isobaric and isomeric molecules. Later generations of the PTR-MS were equipped with powerful time-of-flight mass spectrometers (ToF-MS), providing much better mass resolution of product ions and making isobaric molecules distinguishable. The latest generation of PTR-MS instruments is equipped with a modified ion source containing three separated ion sources placed perpendicular to the axis of the drift tube. All three ion sources can generate different reagent ions, which may be rapidly switched between (using electrostatic optics). [148]

Ions introduced into the drift tube are immediately accelerated along the central axis of the drift tube. The homogeneous electric field is generated by a series of stainless-steel rings, usually isolated by Teflon. The details of the dimensions and a total number of electrodes used differ between producers, but typically a drift tube length is 10 cm. A characteristic parameter used in PTR-MS is the reduced strength of the electric field, *E/N*, accelerating ions along the drift tube. This value is calculated from the drift tube length; applied electric potential; and the pressure of the analysed sample gas in the drift tube. The PTR-MS operates at a pressure of around 2 mbar. The sample inlet is placed at the beginning of the drift tube, where the inlet gas may effectively mix with the reagent ions. The pressure in the drift tube is regulated by the inlet flow controller (with a sample flow of around 20-30 sccm), while the drift tube is continuously evacuated. Using this approach, the pressure in the drift tube remains stable and therefore we can obtain the number density of the sample gas, *N*, as:

$$N = \frac{N_A}{V_M}\frac{273.15}{T_d}\frac{p_d}{101.325}, \tag{48}$$

where N_A is Avogadro`s number (6.022×10^{23} mol^{-1}); V_M is the molar volume of an ideal gas at a temperature of 273.15 K and a pressure of 1 atm (101.325 kPa); T_d is the drift tube temperature; p_d is the drift tube pressure. Knowing the gas number density, *N*, the drift tube length, *d*, and the electric potential across the drift tube, ΔV, we can determine the value of the reduced electric field

$$\frac{E}{N} = \frac{\Delta V}{Nd}, \text{where } \left[\frac{E}{N}\right] = \mathrm{V.m^2} \text{ and } 1\ \mathrm{Td} = 10^{-21}\ \mathrm{V.m^2}. \tag{49}$$

The *E/N* used in PTR-MS ranges from 80 Td to 300 Td, depending on the instrument. The most widely used value (and often used as the reference) of *E/N* is 130 Td.

As mentioned previously, the primary function of the drift field is to carry the reagent and product ions along the drift tube. Additionally, the presence of an electric field also positively affects the ion chemistry in the drift tube, as we will now explain. The presence of the water vapour in the sample gas affects the composition of reagent ions through association reactions, producing water clusters which affect the regent ions' reactivity. In SIFT, the presence of water clusters is limited as the sample gas is diluted in a flow of helium which avoids the water vapour from overwhelming the overall ion chemistry. In other words, hydronium ions are usually dominant over other hydronium water clusters. In PTR-MS, the concentration of water vapours in the drift tube is around two orders of magnitude higher compared to SIFT-MS and hydronium clusters are thus formed more rapidly. This would decrease the reagent ions' reactivity with neutral molecules. Increases in the kinetic energy of ions as a result of the presence of an electric field decreases the reaction rate for association reactions, keeping the main ionization channels unaltered. At *E/N* 130 Td (standard), the kinetic energy of hydronium water clusters is also sufficient to initiate collisional induced dissociation (CID) with buffer gas, thus hydronium ions remain the dominant species. After this initial note, let's carefully describe the interaction of the ion with the electric field.

The drift velocity of ions, v_d, in the drift tube with an electric field (E) is characterized by ion mobility, μ (Eq. 10). The ion mobility depends on the collisional cross-section between the ions and neutral gas particles but is also highly sensitive to neutral gas pressure and temperature. Ion mobility is often expressed in a condensed form for reduced ion mobility, μ_0, scaled on normal pressure (760 Torr, 1013.25 mbar) and temperature (273 K) from where the ion mobility at selected pressure p and temperature T can be obtained as:

$$\mu = \frac{760}{p}\frac{T}{273}\mu_0. \tag{50}$$

Using the reduced ion mobility formula (Eq. 50) together with the reduced electric field (Eq. 48, 49), the ion drift velocity may be expressed as:

$$v_d = \mu_0 N_0 \frac{E}{N}, \tag{51}$$

where $N_0 = 2.6867 \text{ x } 10^{19}$ cm^{-3} represents the gas number density at standard temperature (273.16 K) and pressure (760 Torr). The ion transit time through the drift tube (of length, L) is given by the formula:

$$t_d = \frac{L}{v_d}. \tag{52}$$

In a typical situation for a drift tube with length $L = 10$ cm and $E/N = 130$ Td (operating with hydronium ions in nitrogen), the hydronium reduced ion mobility is ~2.85 cm^2 V^{-1} s^{-1}. The mean ion drift velocity is 995 m s^{-1} and the transit time is 100 µs. Compared to SIFT-MS, the ion drift velocity in PTR-MS is around 10 times larger compared to the ion flow velocity in SIFT-MS. Therefore, it is preferable to increase the length of the drift to compensate for the reduction of ion transit time; and subsequently the reaction time.

Calculation of the absolute concentration of a specific species in PTR-MS follows a similar principle to the one already described for SIFT-MS in the previous chapter. We assume that the concentration of the neutral molecule of interest resides at trace levels and therefore the concentration of reagent ions is not affected by the reactions with it. The higher ion velocity reduces the effect of ion diffusion, increasing ion intensities. The kinetic equation, however, differs from one used for flow tubes (Eq. 39, 40). The transient velocity of ions is defined by ion mobility (different for individual particles) and therefore the transient time of multiple ions is not the same. As a consequence, it is not possible to form a differential equation as a function of time, but rather as a function of the axial position of molecules, x, by applying the substitution dt = dx / v_d. Thus, considering Eq. 51, the differential equation for the simple example of a proton transfer reaction, $H_3O^+ + M \rightarrow MH^+ + H_2O$ takes the form:

$$\frac{d[\mathrm{H_3O^+}]}{dx} = \frac{-k[\mathrm{M}][\mathrm{H_3O^+}] - [\mathrm{H_3O^+}]\frac{D_{\mathrm{H_3O^+}}}{\Lambda^2}}{v_g + \mu_{0,\mathrm{H_3O^+}}(E/N)N_0\frac{E}{N}}, \tag{53}$$

$$\frac{d[\mathrm{MH^+}]}{dx} = \frac{k[\mathrm{M}][\mathrm{H_3O^+}] - [\mathrm{MH^+}]\frac{D_{\mathrm{MH^+}}}{\Lambda^2}}{v_g + \mu_{0,\mathrm{MH^+}}(E/N)N_0\frac{E}{N}}, \tag{54}$$

where v_g is the buffer gas velocity; $\mu_{0,\mathrm{H3O+}}$ and $\mu_{0,\mathrm{MH+}}$ are the reduced field-dependent ion mobilities of H_3O^+ and MH^+ ions; and the remaining parameters have been previously mentioned. If the detected ion signal is corrected by the ion mass discrimination, we may use Eq. 41 and determine the concentration of analyte [M] from the detected ions signals, $i(MH^+)$ and $i(H_3O^+)$, as follows:

$$\frac{[\mathrm{MH^+}]\mu_{0,\mathrm{MH^+}}}{[\mathrm{H_3O^+}]\mu_{0,\mathrm{H_3O^+}}} = \frac{i(\mathrm{MH^+})\mu_{0,\mathrm{MH^+}}}{i(\mathrm{H_3O^+})\mu_{0,\mathrm{H_3O^+}}} = k[\mathrm{M}]t_d, \tag{55}$$

where k represents the reaction rate constant. To determine the concentration of the analyte, we need to know the transition properties of individual ions. For product ions with ion mobilities close to that of the reagent ions, Eq. 55 simplifies and leads to Eq. 42. In most situations, however, the instrument must be calibrated to obtain transition ratio coefficients for individual substances. [149] Once obtained, the absolute concentration of analyte ion in the sampled gas may be calculated (Eq. 46, 47).

Even though the presence of an electric field complicates the determination of the absolute analyte concentration, it is a necessary part of the instrument due to the high concentrations of H_2O vapour present in the discharge and the drift tube. The H_3O^+ ion formed in the discharge reacts with neutral H_2O molecules, forming hydrated hydronium ions $H_3O^+(H_2O)_n$, where $n > 1$. Ions entering the drift tube thus mainly consist of hydronium hydrates. Additionally, the concentration of water vapour in the drift tube induces the continuous formation of hydronium hydrates. Water vapour in the drift tube originates from humidity from within the sample, but also from the ion source due to diffusion. Additionally, as most gas samples consist of mostly diatomic molecules (N_2, O_2), three body association reactions in the drift tube proceed at rates which are faster compared to association reactions in monoatomic noble gasses (He in SIFT-MS). As a result, the distribution of reagent ions would consist mostly of larger clusters of the hydronium hydrates, complicating the analysis (see Chapter 1.4). The introduction of an electric field results in decreased formation of hydronium hydrates in the drift tube (association reaction rates decrease rapidly with collisional energy and *E/N*) and also causes CID of already existing hydrates:

$$\mathrm{H_3O^+.(H_2O)}_n + \mathrm{H_2O} + \mathrm{N} \xrightleftharpoons[k_{diss}(E/N)]{k_{ass}(E/N)} \mathrm{H_3O^+.(H_2O)}_{n+1} + \mathrm{N}, \tag{56}$$

where N represents a neutral molecule presented in the system (in PTR-MS this is often N_2 or O_2). The final reaction equilibrium and therefore the distribution of hydronium hydrates depends on the total water concentration in the drift tube; concentration of the analyte sample; as well as the type of buffer gas used; and *E/N*. As water clusters are usually weakly bounded (see Table 2), for increasing *E/N* the equilibrium quickly shifts towards higher concentrations of H_3O^+. An example of hydronium hydrates distribution at various *E/N* is presented in Figure 6. At *E/N* = 80 Td, the H_3O^+ ion already dominates over its cluster hydrates. An additional increase in *E/N* reduces the number of hydrates even more. Increasing *E/N* to higher values is beneficial for a greater distribution of hydronium hydrates, however, this also causes negative secondary effects. These include a reduction in the reaction time leading to a decreased abundance of product ions and therefore a decrease in the sensitivity as well as an increased probability of dissociation reactions with the analyte affecting the selectivity of the technique. Therefore, in most applications, *E/N* ~ 130 Td is chosen as a compromise between having a sufficient reduction in hydronium hydrates concentration (abundance of $H_3O^+H_2O$ around 10% of H_3O^+ intensity); and fragmentation induced by electric field, of an insignificant level.

Table 2 Selected thermodynamic properties of hydronium hydrates formation $H_3O^+(H_2O)_n + H_2O \leftrightarrow H_3O^+(H_2O)_{n+1}$

n, n + 1	$PA(H_2O(H_2O)_n)^a$	$-\Delta H^b$	$-\Delta S^b$	$-\Delta G^b$	BDE^c
0,1	7.16	1.37	24.3	1.05	1.25
1,2	8.56	0.85	21.7	0.56	0.91
2,3	9.07	0.78	28.4	0.41	0.67
3,4	9.37	0.55	23.4	0.24	0.43

PA, $-\Delta H$, $-\Delta G$, BDE in eV, $-\Delta S$ in cal K^{-1} mol^{-1}, [a] Michalczuk et al. [150], [b] Lau et al. [70], [c] Wróblewski et al. [151]

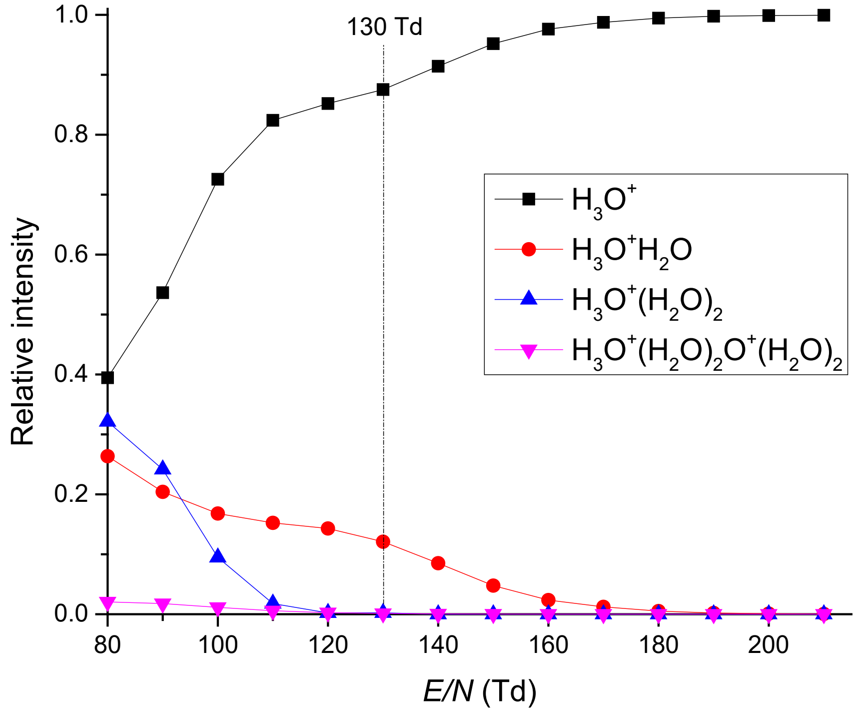

Figure 6 Relative intensity of hydrated hydronium clusters $H_3O^+(H_2O)_n$, $n = 0,1,2,3$ in PTR-MS determined for various *E/N* values for a sample containing 0.6% humidity (absolute).

Selected ion flow-drift tube mass spectrometry (SIFDT-MS)

SIFDT-MS is a compilation of both PTR-MS and SIFT-MS, exploiting the strengths of both instruments. SIFDT-MS is equipped with an injection mass filter, allowing for a specific reagent ion to be selected. Selected ions are then injected into a flow-drift tube reactor. Flow-drift tubes use helium carrier gas in combination with an axial electric field, reducing diffusion losses to the walls as well as pumping speed requirements. The abundance of primary ion hydrates in the carrier gas in SIFDT-MS is lower compared to PTR-MS. Therefore, the *E/N* used in the SIFDT-MS reactor is lower than in the PTR-MS reactor. In the present work, we used a SIFDT-MS instrument developed by Spesyvyi et al. [39] This instrument additionally contains the possibility to directly determine the ion retention time via the application of a modulated signal on the injection ion optics. This therefore allows for the acquisition of ion mobilities and reaction energies data.

For SIFDT-MS used in this work (see Figure 7), the reagent ions are generated in a glowing cathode discharge, operating in a water vapor/synthetic air mixture. After extraction from the discharge, reagent ions are introduced via ion optics into the quadrupole mass filter. Ions with selected *m/z* are injected into the transition ion optics, equipped by the shutter grid. The shutter grid can modulate the ion transmission by applying the Hadamard modulation. [152] From the transition ion optics, ions are injected into the flow-drift tube (as a continuous stream or modulated by Hadamard modulation). The drift tube reactor is 145 mm long; has an ID of 10 mm; and is made of a PHOTONIS resistive glass tube with a total resistance of 14 MΩ. In the flow-drift tube, ions are carried along the tube by a homogenous electric field in a ~150 sccm reverse flow of He (1.5 mbar and 24 °C). Application of the voltage along the resistive layer (100 to 500 V) creates a homogenous electric field (from 10 to 100 Td) inside the cylinder. At the end of the flow-drift tube, ions are introduced via an orifice into the quadrupole mass spectrometer and are detected by the electron multiplier with conversion dynode. Sample gas is introduced into the helium gas stream at the end of the flow-drift tube and is carried through in helium flow reverse to the ion movement.

During the study, the SIFDT-MS instrument was frequently modified. A notable improvement as a result of this study was in the modification of the ion source. [153] In the modification, a hollow cathode discharge operating in a water vapor/synthetic air mixture produces primary reagent ions. Ions are then transferred through to the stacked ring ion guide (SRIG) housed in a polypropylene vacuum chamber, operating in helium buffer gas (5.3 mbar), where they thermalize. Thermalized ions carried by the electric field and helium flow enter the next chamber (with a 50 mm long octupole), with an He pressure of about 0.3 mbar. Using an octupole, ions are guided through an aperture into the quadrupole mass filter. Filtered ions are introduced via the Venturi inlet to the small flow-drift tube (VDT in Figure 8), where ions are mixed with He buffer gas and thermalized again. At the end of the VDT, a series of three meshes are present which are required for Hadamard modulation of the ion current.

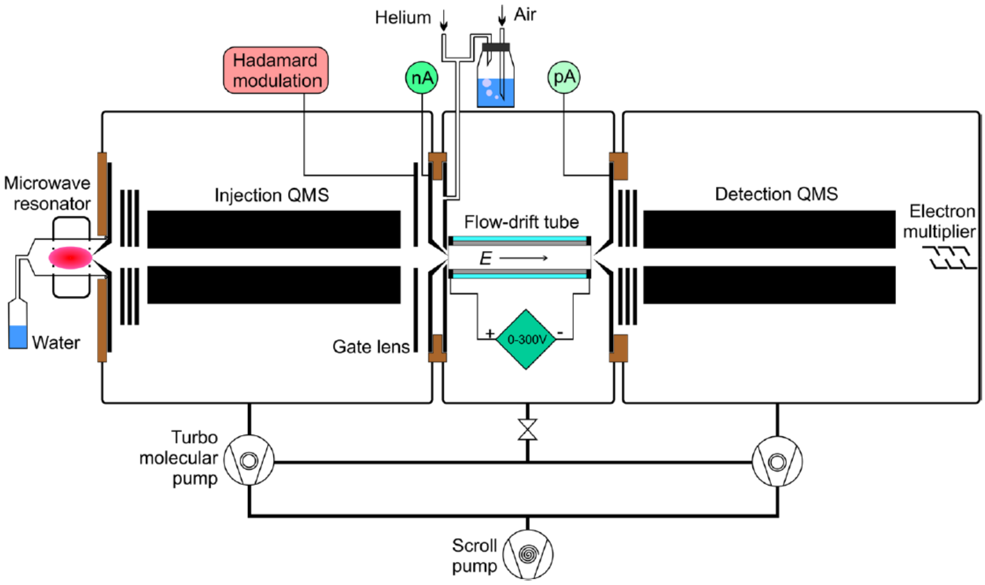

Figure 7 The SIFDT-MS instrument; the initial concept. [39]

The second design was built to generate a wider spectrum of reagent ions. The octupole chamber is equipped with a separate gas inlet. The gas molecules then react with primary reagent ions and become ionized via CI, for example via proton transfer from hydronium hydrates. The newly formed ions may be then introduced into the flow-drift tube via a quadrupole mass filter. This instrumental design allows for the generation of several various ions, allowing for a more in-depth study of particular (mainly secondary) reaction channels.

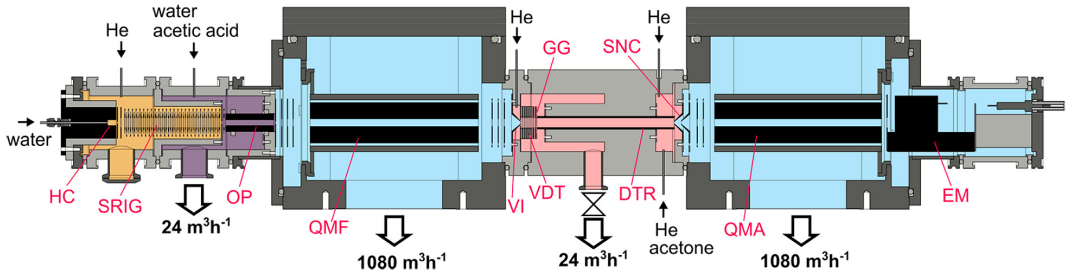

Figure 8 The SIFDT-MS instrument; the final design. [153] The coloured areas represent individual pressure regions: 5 mbar (yellow), 0.3 mbar (violet), 5×10^{-6} mbar (blue), 1.9 mbar (pink). HC - hollow cathode ion source, SRIG – stacked ring ion guide, OP - octupole, QMF - quadrupole mass filter, VI - Venturi inlet, VDT - Venturi flow-drift tube, GG - gating grid, DTR - drift tube reactor, SNC - ion sampling nose cone, QMA - quadrupole mass analyser, EM - electron multiplier with conversion

As ion velocity in the drift field changes with different ion mobilities, is necessary to measure the ion reaction/residence time (Eq. 55) for the precise calculation of trace sample concentrations. Ion residence time is determined by applying a pseudo-random Hadamard modulation on a specific electrode of the ion optics at the front of the flow-drift tube. The residence time is then reduced by the detector transfer time (time interval required for ions to travel from the end of the flow-drift tube to the detector), determined by applying the same modulation on the ion optics directly after the flow-drift tube. Knowing the length of the flow-drift tube, ion velocities may be determined. Ion velocity may then be used to calculate the ion mobility μ (Eq. 10); reduced ion mobility μ_0 (Eq. 50); and the mean reaction energy using the Wannier equation (Eq. 17, 18). It is important to note that application of the Hadamard modulation and the determination of the ion residence time requires ion intensities above 10k cps. The ion residence time therefore cannot always be determined.

The SIFDT-MS used in the present study is an instrument which bridges the SIFT-MS and PTR-MS techniques. The ability of SIFDT-MS to determine the residence time as well as the reaction energy is invaluable for ion chemistry studies under homogenous electric fields.

1.3. Areas of application

In previous sections, we have compared some aspects of SCIMS techniques and the reference technique, GC-MS. Now, we should discuss the benefits of SCIMS related to analytical applications, mainly high sensitivity, selectivity and rapid response time.

To recapitulate, the power of the GC-MS as an analytical technique comes from combining two differing analytical techniques. Firstly, pre-separation of a complex mixture occurs in the chromatographic column where individual components of the gas mixture interact with the active phase of the column and thus progress through the column at different velocities. As a result, each species travels through the column with a different retention time. Secondly, the separation by retention time is combined with EI-MS using an electron energy of 70 eV. The high electron energy induces fragmentation of molecules via dissociative electron ionization. The final fragmentation pattern represents a footprint of the molecular structure. Molecules can thus be identified based on the MS fragmentation pattern as well as on the retention time.

Chromatography is however a time-consuming process requiring tens of minutes to be completed. This clearly disables the possibility of analysing rapidly changing samples and limits sampling frequency. Additionally, if the targeted analyte compounds are at trace levels, pre-concentration of samples is required, usually using absorption or cryogenic traps. [154] This combination of multiple stages of analyses increases not only the complexity, but also requires frequent calibration procedures to be carried out for each analysed component.

Chemical ionization mass spectrometry has its advantages over GC-MS. The reaction energy for chemical ionization (usually 1-2 eV) is significantly lower compared to electron ionization (typically 70 eV), resulting in less fragmentation. Product ions generated by CI via charge transfer, proton transfer, or association reactions, form M^+, MH^+ or MR^+ respectively (where R represents the reactant ion). This carries information about the mass of the reactant neutral, M. It is therefore possible to directly identify the reaction neutrals from the mass spectrum. It is true that isobaric molecules may produce ion products with similar mass-to-charge ratios. This may however be overcome by using multiple reagent ions (commonly used in SIFT-MS) or by implementation of high-resolution mass spectrometry (commonly used in PTR-MS).

As long as the ionization mechanism is a fast reaction (which is usually the analytical aim), ionization occurs close to the collisional rate. Therefore, even for trace concentrations of analytes in the sample, we are able to achieve sufficient abundances of product ions for their MS analysis. This is true for most VOCs. The detection limit is a critical parameter that determines the applicability of individual SCIMS techniques. The first series of instruments had detection limits at levels of ppb. [37] The modern series of instruments however claim to achieve detection limits as low as ppt for SIFT-MS [155] and ppq for PTR-MS [156]. This reduces the need for sample pre-concentration. Low detection limits combined with high selectivity allows for SCIMS techniques to conduct the analyses of complex gas mixtures without pre-separation in a chromatographic column. The analytical time is therefore defined by the velocity of gases and ions in the reactor tube (usually at around tens of milliseconds). The ability to rapidly monitor the concentration of analytes is an important feature of SCIMS. Finally, SCIMS instruments are easily calibrated. The concentration of product ions in the reactor is directly dependent on the concentration of neutral reactants. Thus, knowing the mass discrimination functions of the mass spectrometer and the detector, we can directly relate the ion count rate to the concentration of the reactant molecule. The response is linear as long as the physical parameters of the instruments are constant (pressure, temperature, ion velocity, *E/N*). Therefore, after initial calibration, there is no need to recalibrate the instrument for every analyte species, as is needed for GC-MS. *N.B* This is true unless SCIMS analyses uses a pre-concentration step; is coupled with chromatography; or contains an ion funnel as a part of the ion optics.

GC-MS will always be a much better option for analysis of a completely unknown sample. Combination of precise chromatography, EI-MS and careful calibration provides much better selectivity and analytical quality. However, benefits of SCIMS are excellent for the monitoring of gas samples with known composition. Over the years, SCIMS was successfully recognised as a useful analytical technique, providing real-time quantitative analysis of organic compounds in various applications requiring fast response times. In the following paragraphs we would like to introduce the most promising areas where SCIMS techniques are positively recognised and frequently applied.

Probably the most notable area of application is analysis of human breath. As breath is exhaled through alveoli in lungs (in direct contact with the blood stream) there is potential for obtaining valuable clinical data using a non-invasive approach. For a decade, researchers have been analysing the potential of breath analysis within clinical applications, identifying several characteristic metabolites presented in human breath: ammonia, acetone, methanol, ethanol and isoprene. [157-160] However, it was also found that volatile compounds in breath are not necessarily metabolites originating from blood (endogenous source), but rather originate from exogenous sources, such as from bacteria found in the airways or mouth. Nevertheless, direct breath analysis via SCIMS techniques may be used to monitor (or eventually help diagnose) several diseases. Most typical is the analysis of acetone (as a direct metabolic product) for type 2 diabetes. [161] Targeted analysis and quantification of acetic acid may be used for monitoring patients with gastroesophageal reflux disease. [162] A promising application is the monitoring of VOCs emitted from bacterial infection [163-166] related to cystic fibrosis - autosomal recessive disorder affecting mainly children. [166, 167] This non-invasive approach was also used for the monitoring of advanced chronic kidney disease [168, 169] and chronic liver disease [170, 171]. Asthma is an additional disease which may also be diagnosed by SCIMS. [172, 173] Interestingly and promisingly, it is possible to analyse n-pentane with this method; a metabolite produced from inflammation within the body which may be a valuable in the diagnosis of chronical Crohn’s disease. [174, 175] A big effort has been made to find a biomarker for lung cancer diagnosis, however, little success has been gained so far. [154] It is out of the scope of this thesis to cover all applications of SCIMS in breath research. More details can be found in the literature. [52, 158, 160]

The monitoring of breath volatiles is not restricted only for clinical diagnosis. It was demonstrated that SCIMS may be used to monitor drug levels in the human body. [176-179] This is beneficial in the surgical environment, where doctors may need to monitor the levels of drugs within a patient, (i.e. anaesthetics) from exhaled breath in real time. VOCs are not only emitted by breath but also by the skin [180-182]. In addition, the type and quantity of VOCs emitted from the human body may be directly related to one’s mental state of mind (i.e. happiness, fear). This effect was observed in various studies in which human breath composition was shown to change while participants watched a film in the cinema; and the composition of breath has also been shown to change during other collective activities, like football events. [183-185] The data showed variations in CO_2, isoprene and ethanol related to specific events. Overall, human breath composition may also be analysed in the field of forensics and security. Mobile SCIMS instruments based on IMS technology may be used to detect human presence in restricted areas, (i.e. refugees hiding in cars or lorries). [186, 187]

SCIMS techniques are also highly used in environmental applications. They are used in the identification and monitoring of biogenic VOCs (mainly monoterpenes) emitted from various ecosystems. Several studies were carried out investigating emission cycles in tropical rainforests [188-190], coniferous forests [191-193], deciduous forests [194-196], plantations [197-200], grasslands [201-203] and many more. [204, 205] The aim of such studies is to describe not only the ecosystem itself, but also its influence on atmospheric chemistry. Selective monitoring of individual biogenic VOCs, for example, does not correspond to the total [VOCs] determined from total reactivity measurements (Biogenic VOCs reacting with a controlled concentration of OH radicals, where the reduction on OH concentrations represents the concentration of VOCs in the sample). [206, 207] The study indicates that more than 30% of total reactivity (varying by season) is not described by monitored VOCs. This indicates a significant knowledge gap in environmental and atmospheric science. These environmental studies are also combined with studies of emissions from individual plants. [208, 209] Atmospheric chemistry is a topic directly related to global warming. Studies related to investigating emissions from rural and livestock activities; [210-212] the marine environment including bio-emissions of sea floor [213-215]; as well as industrial contamination; are of significant importance [216, 217].

Besides natural sources, atmospheric chemistry is heavily influenced by anthropogenic emissions which are also frequently studied and monitored by SCIMS. In the urban environment (mainly big cities) VOCs like isoprene, benzene and toluene together with NO_x are an important source of pollution via the production of ground-level ozone. The concentration of VOCs, as well as their secondary products during daytime hours have been investigated in many big cities including Houston [218], Barcelona [219], Tokyo [220], Paris [221, 222] and more. [223, 224] Related research focuses on individual sources of pollutants, such as diesel [225] and aircraft engine emissions [226, 227], as well as industrial sources [228, 229]. Besides outdoor air quality, indoor air quality studies focus on various emissions present in indoor environments. This includes the study of volatiles released from the use of everyday domestic products [230-232], wall paintings [233] and building materials [234]. Apart from the analysis of domestic indoor air quality, SCIMS are also frequently used to monitor the air quality of clean rooms in industrial settings. This is required especially in the semiconductor industry, where even small contamination of specific halogen compounds can damage and decrease the quality of silicon component end products. [235]

Determination of odour and characteristic VOC emissions of products is also applied in food science and emissions related to food market products. The analysis of characteristic volatiles is used either to monitor the quality of products; identify product origin (through characteristic geographical labelling); to develop characteristic artificial odours; and to analyse complex food texture. The typical products with the need for quality assurance and geographical control is coffee [59, 236, 237], tea [238], wine [239] and cheese [240, 241]. These products are often characterised by their unique composition of volatiles, related to their geographic origin. Additionally, specific compounds responsible for the reduction of quality within these foods may be identified (the presence of halogenated anisoles in wine originated form corks, for example). [41, 242] Additionally, SCIMS may be used to monitor the growth of fruit and therefore help estimate the best time for harvesting [243, 244]. Almost every food product has a characteristic profile of volatile compounds, and it is therefore not possible to cover all of these in this thesis. Finally, food processing may also be monitored (i.e. fermentation of milk [245, 246], or yeast activity in beer production [247]).

The final significant application of SCIMS is homeland security and detection of warfare and threat agents. This includes the detection of drugs, explosives or others dangerous chemicals. [248-251] The detection of explosives is dominated by IMS systems, achieving very low detection limits (even though explosives are known for their low volatility). [252] By using PTR-MS, however, much better selectivity of individual explosives may be achieved. [253-255] SIFT-MS is used by customs offices in New Zealand and Canada to screen the shipping containers for the presence of toxic chemicals (fumigants) which may endanger staff during container inspection. [256]

The presented overview reflects the most common applications of SCIMS techniques. Each application has a specific requirement for sensitivity, selectivity and therefore also on the type of SCIMS technique used. For breath analysis, SIFT-MS provides the most consistent results; highly sensitive PTR-MS is often used in environmental applications. The field of applicability of SCIMS is however limited by several factors outlined in the next chapter. The aim of future development is to reduce said limitations and increase the possibility of using SCIMS in new areas of study.

1.4. Limitations of chemical ionization mass spectrometry

The applicability of SCIMS techniques for analytical applications is limited by two main factors: sensitivity and selectivity. Sensitivity describes the minimal concentration of trace gas in the analyte at which the SCIMS instrument is able to determine its presence (and quantify the analyte concentration) with respect to the background noise. Selectivity represents the ability of instruments to distinguish individual analyte components as well as determine their exact molecular composition. The aim of SCIMS instruments is to optimise both sensitivity and selectivity, without losing any of the benefits of using SCIMS. This is namely the use of pre-concentration systems and chromatography affecting the calibration requirements and rapid detection possibility, respectively.

The sensitivity of SCIMS is mainly determined by the design and type of instrument. The new generation of instruments is reaches detection limits up to ppt/ppq levels. This is mainly due to the advanced design of transfer ion optics and their implementation in the drift tube.

Selectivity on the other hand is mainly determined by ion chemistry occurring inside the SCIMS reactor, as well as by the resolution of the mass spectrometer. The characteristic feature of chemical ionization is the formation of product ions which carry information about the mass of the neutral reactant (M), by formation of M^+, MH^+, $M\text{-}H^+$, … ions. This however also occurs for isobaric and isomeric molecules which thus cannot be easily distinguished. For example, using a proton transfer reaction with H_3O^+, both acetone and 1-propanal produce MH^+ (*m/z* 59). [64, 66] The same applies for acetic acid and methyl formate when producing the MH^+ ion (*m/z* 61). [257] With increasing molecular mass, the number of isobaric compounds increase. Both main analytical SCIMS instruments (SIFT-MS and PTR-MS) use different approaches to resolve isobaric molecules. SIFT-MS uses a combination of multiple reagent ions (H_3O^+, NO^+ and O_2^+) that may be selectively introduced into the flow tube. Different types of molecules, producing similar ion products using one reagent ion, tend to react differently with other one. For example, when using NO^+, ketones mainly form $M.NO^+$ while alcohols produce $(M\text{-}H)^+ + HNO$. [64, 66] Early PTR-MS instruments, equipped with a quadrupole mass spectrometer, have limited possibilities to differentiate isobaric compounds. This was solved later by the installation of high-resolution Time-of-Flight mass spectrometry (ToF-MS, resolution power > 10.000), able to differentiate between isobaric molecules.

Even though modern instruments now have the possibility to differentiate between isobaric compounds, secondary effects affecting the selectivity of these instruments are still present. The predominant remaining limitation is the reduced possibility to differentiate between various isomers. Isomeric molecules often produce similar product ions regardless to their reagent ion type. Thus, isomers are difficult to recognize in the obtained mass spectrum. For example, monoterpenes ($C_{10}H_{16}$) emitted by trees and plants react with all main reagent ions, H_3O^+, NO^+ and O_2^+. However, ion products are almost identical among all monoterpenes. [258] This is also true for branching ratios of individual product channels. Furthermore, H_3O^+ and NO^+ are the only reagent ions practical for monoterpene analysis in SIFT-MS as O_2^+ induces dissociative charge transfer, forming multiple ion fragments and in turn reducing selectivity significantly. If ion product branching ratios differ, it is possible to use a pseudoinverse matrix to determine the concentration of individual isomers if branching ratios of individual isomers are known. This approach was used in SIFDT, applying specific potential differences triggering CID in the flow-drift tube at witch ion products of individual monoterpenes started to differ. [259] This is, however, not always possible and can only be used with limited accuracy.

Peak interference is however not only caused by isobaric and isomeric molecules, but also by the presence of various parallel or secondary reactions. Ideally, the aim is to optimise the instrument so that each analyte produces only one product ion, as secondary ion products may interfere with the ion products from the compound. This is however not always possible and represents one of the main challenges of SCIMS. The ion chemistry is affected by the choice of the reagent ion as well as by the composition of the buffer gas. Proton transfer from H_3O^+ is often very rapid and is therefore the preferred ion for CI. Dissociative proton transfer may however also occur (as is seen in the analysis of monoterpenes, which forms $C_6H_9^+$ *m/z* 81). The alternative to H_3O^+ is used of the NO^+ reagent ion, with low IE(NO) = 9.2 eV [57], mainly reacting via association reactions producing $M.NO^+$ or $(M\text{-}H)^+ + HNO$ ions. However, NO^+ does not react with all VOCs and resonance capturing for association reactions is often slower than for proton transfer, which reduces the detection limit. O_2^+ is able to ionize most VOCs, although the IE(O_2) = 12.1 eV [57] is greatly above most VOCs, frequently resulting in dissociative charge transfer producing multiple fragments. O_2^+ is therefore used as a reagent ion much less frequently.

Last but not least, selectivity and also sensitivity depend on the type and concentration of major components of the gas sample, in which an analyte is diluted. Reagent ions are purposely chosen so their reactivity with the main components of the gas solvent is limited. In reality, H_3O^+, NO^+ and O_2^+ commonly used for CI also react with N_2 and O_2, or CO_2. [260] Their reactions are however often neglected as water vapour is much more influential in the CI system. In the presence of water vapour, all formed ion products of N_2, O_2 and CO_2 quickly react with H_2O via proton transfer or ligand switching. Additionally, H_2O also reacts with reagent ions via an association reaction (as we already pointed out in the description of the PTR-MS instrument). The presence of water in acquired samples is inevitable. Even pure technical gases contain trace levels water impurities. Additionally, because of a dipole moment (μ_{H2O} = 1.85 D) [261], H_2O is much more influential compared to CO or CO_2 (also present in air). *N.B.* water vapour influences all reagent ions, although its presence is most notable for H_3O^+.

The concentration of water vapour in a sample gas depends on the sample sources and may vary from few ppm in an extremely dry sample gas, up to tens of thousands of ppm in gases saturated by water vapour. The pressure of a gas which is saturated with water vapour is very temperature sensitive. In breath analysis, the water concentration of a healthy patient with a body temperature of 36 °C is about 5%. Similar concentrations are seen in tropical forests. At room temperature, the absolute humidity may vary from 1% to 2.5%. The level of water vapour within a sample is important as this directly affects the selectivity and sensitivity of analysis, via a series of secondary reactions:

1, Association reaction with primary ions

All three primary reagent ions, H_3O^+, NO^+ and O_2^+ associate with H_2O forming ion hydrates. In SIFT-MS, for NO^+ and O_2^+, mostly $NO^+.(H_2O)_{1,2}$ and $O_2^+.(H_2O)_{1,2}$ hydrates are seen in the spectra. However, for H_3O^+, much larger hydronium hydrates may be observed, up to $H_3O^+.(H_2O)_4$. In PTR-MS and SIFDT-MS the formation of hydrates is reduced, however not completely removed. The presence of reagent ion hydrates not only reduces the selectivity of the instrument by interfering with product ions with similar *m/z*, but also reduces the concentration of primary reagent ions (which in turn reduces sensitivity of analysis), for samples with higher humidity.

2, Secondary reactions of reagent ion hydrates

Reagent ion hydrates, formed via the association reaction of H_2O and the buffer gas, may often also react with the studied analytes. However, the products of these reactions may not correlate with the primary reaction channels. The possibility of protonated hydronium hydrates to initiate proton transfer is reduced, as proton affinity of water clusters increases with cluster size (see Table 2). A similar reduction in this reactivity applies for the charge transfer process initiated by NO^+ and O_2^+ as well as their respective hydrates. Moreover, reagent ion hydrates often react via ligand switching, forming hydrates of analyte ions:

$$\mathrm{H_3O^+.(H_2O) + M \rightarrow H_3O^+.M + H_2O.} \tag{57}$$

This increases the number of analyte ion products.

3, Secondary reactions of analyte product ions

Product ions also interact with water vapour, forming ion hydrates via a three-body association reaction, in the same way as primary ions:

$$\mathrm{MH^+ + H_2O + N \rightarrow H_3O^+.M + N.} \tag{58}$$

The level of hydration is dependent on the size and molecular structure of the primary ion, hydration level as well as on other parameters as gas temperature and gas pressure. Some molecules do not form hydrates (i.e. monoterpenes [262]) whereas others form hydrates very effectively (i.e. ketones or alcohols [37]). The ion chemistry is very specific for individual product ion hydrates. The formed product ion hydrates may either be stable; undergo additional reactions with H_2O molecules as reverse ligand switching:

$$\mathrm{MH^+.H_2O + H_2O \rightarrow H_3O^+.H_2O + M,} \tag{59}$$

as well as undergo a chemical reaction producing unique ions.

The final reaction pattern is a combination of primary ionization reactions in conjunction with all associated secondary reactions. The influence of individual secondary processes differs for individual reagent ions as well as for different analytes. To illustrate this complexity, Figure 9 shows a full reaction diagram considering all primary and secondary reactions for the reaction between H_3O^+ with a neutral reactant, M, in the presence of water vapour.

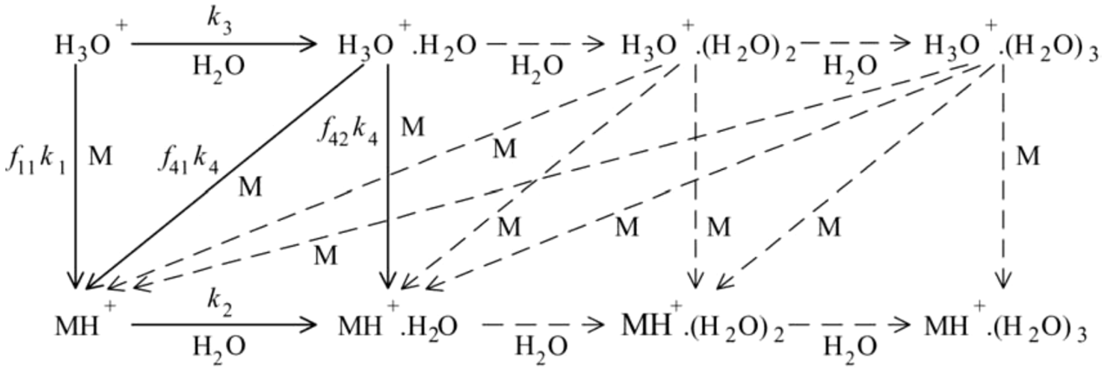

Figure 9 Illustrative reaction diagram of primary and secondary reactions of H_3O^+ with neutral a reactant, M, in the presence of water vapour. [263] Solid line reactions represent moderate humidity levels. Dashed reactions represent saturated water vapour.

It is also necessary to point out, the influence of water vapours on ion chemistry depend also on type of buffer gas and solvent gas components. Formation of water clusters via association is a three-body reaction, requiring a third particle to remove excess energy from the formed nascent complex. Increasing the concentration of two plus atomic molecules (with a high degree of levels of freedom) in the buffer or sample gas may increase the association reaction rate. For example, high concentrations of CO_2 in the sampled gas may significantly accelerate ion hydrates formation.

In conclusion SCIMS ion chemistry uses main ionization reaction channels (first order approximation) to determine the concentration of selected analytes. The presence of secondary reactions, however, induced mainly by water vapour increases the amount of ion products, affecting both sensitivity and selectivity of the analysis. Therefore, for humid samples or environments with rapidly changing humidity, it is also essential to consider the secondary reaction channels and include secondary ion products into the concentration calculation. Thus, careful understanding and analysis of secondary reaction channels is absolutely necessary.

1.5. Objectives of the thesis

The main objective of the ITN project IMPACT was to study the specific limitations of individual SCIMS techniques, to improve their selectivity and sensitivity and to introduce SCIMS to new areas of application. The project itself was divided into three main work groups: ion chemistry, applications and instrumental development. The presented thesis belongs to the ion chemistry work groups; thus, the objectives were defined as follows:

1, Mathematical description of the experimentally obtained dependencies of relative ion signals of product ions, their fragments and hydrates; on water vapour concentration, electrical fields and pressure within the SCIMS tube reactors.

2, Formulation and analytical validation of advanced algorithms resolving mass spectral overlaps of isobaric product and fragment ions, based on two-dimensional data analyses (*m/z* versus the reduced electric field, *E/N*).

3, Characterisation of a Thermal Desorption Unit (TDU) developed for PTR-MS used with SIFT-MS.

4, Formulation and analytical validation of algorithms for analyses of desorption temperature resolved TDU-SIFT-MS data, with improved selectivity.

5, Testing the developed methods in interdisciplinary studies, in clinical breath analysis and environmental science.

By solving the list of stated objectives, a list of expected results should be achieved:

1, Knowledge and data on the variation of SCIMS relative mass spectral ion intensities with humidity and electric fields.

2, New mathematical algorithms for calculations of VOC concentrations from mass spectral SCIMS data, accounting for ion overlaps.

3, Original interdisciplinary results in the areas of breath analysis and environmental science.

During the project, the list of objectives was developed and modified with respect to the scope the project. It must be noted that this list of objectives was formed as part of the official project proposal, written five to six years before thesis submission.

The development of TDU and its coupling with PTR-MS was made at KORE Technology Ltd. (One of the project beneficiaries), in the UK. The TDU was used for the analysis of drugs and other solid samples with low vapour pressures. [254, 264] The company has created and optimized hardware and software for the TDU; now available on the market. Separately, the TDU was developed in Prague by our colleagues previous to the IMPACT project, founded by another GACR national grant and thus will not be included in this thesis. [204] As a result, objectives 3 and 4 were fulfilled without contribution from the author of this thesis. Additionally, both industrial partners of the IMPACT project, KORE Technology and IONICON, have been frequently developing their operational software. One of the features included in their software package is the possibility to determine the composition of a sample by a multi-peak analysis of obtained mass spectra. The method used a pseudoinverse matrix, created from a list of ion products for each compound. The software can thus resolve mass spectral overlaps in a complex sample. Objective No. 2 was thus modified as to provide an analysis of the ion chemistry using two-dimensional data analyses techniques, including gas chromatography.

Therefore, the remaining objectives of the thesis are as follows:

- Investigation of the main limitations of SCIMS techniques with respect to improving sensitivity and selectivity of instruments, by studying the complex ion chemistry within specific SCIMS techniques, mainly focusing on secondary reactions with water.
- Mathematical descriptions of primary and secondary reactions capable of predicting the behaviour of relative ion signals of product ions, their fragments and hydrates, on water vapour concentration, electrical fields and pressure.
- Experimental study of complex ion-molecular reactions relevant for clinical breath analysis, environmental science and other applications related to SCIMS.
- To expand the capabilities of SCIMS analysis to more applications.

In the following chapters we present a summary of the main results, reflecting the individual objectives. Firstly, we introduce the construction of a fast GC pre-separation unit coupled with SIFT-MS, representing an elegant solution for separation of molecular isomers. Secondly, we present the development of a universal numerical simulator of ion-molecular reactions which was used as a tool to supplement our experimental studies. Finally, we present a study of complex ion chemistry on molecules relevant for SCIMS applications, as well as studies further expanding applicability of SCIMS.

2. Construction of fast GC pre-separation for SIFT-MS

Identification of specific isomers in SCIMS is difficult. Isomers (especially structural isomers) react in a similar way with all reagent ions and thus it is difficult to identify them using multiple reagent ion approaches or using high-resolution MS. The same problem occurs even in the presence of an electric field. Product branching ratios for isomers may differ even if products have the same *m/z*. In a complex sample with an unknown mixture of different isomers, quantitative analysis is very difficult and sometimes impossible.

A classic method used to analyse the concentration of different isomers is gas chromatography. The different structure of individual isomers affects their interaction with the active phase of the column. Isomers may be then analysed based on different retention times. [265, 266] A difference in retention time is not guaranteed, but a difference in the molecular structure often leads to differences in the retention time. Classical GC analysis is however time consuming. Based on the type of the column and temperature profile of the analysis, one measurement may take up to an hour to run. This is in contrast to SCIMS techniques, which have built their reputation on real-time fast analysis.

To solve the problem of isomer analysis, we need to make a compromise between the speed of chromatography analysis and its quality. Comparing to classical chromatographic techniques, SCIMS does not require the separation of all molecules presented in the sample. Instead, SCIMS aims for a specific isomer presented in breath or environmental samples, as other molecules can be determined by ion chemistry. Thus, the chromatography coupled to SCIMS may be less specific. The modern solution to this problem used in SCIMS analysis is called fast gas chromatography (fast GC).

Fast GC uses a short column of 5-10 m (compared to 40 m in standard GC) as well as fast temperature ramps (>20°C/min) in order to provide chromatographic analysis in under 5 min. [267] The chromatogram cannot be used to fully determine the composition of the sample, however may be used to help analyse a specific set of isomers. The technique was successfully applied in the analysis of monoterpenes using PTR-MS with a great success. [268, 269] Following previous studies, we developed a fast GC unit to test if the same approach could be applied to SIFT-MS.

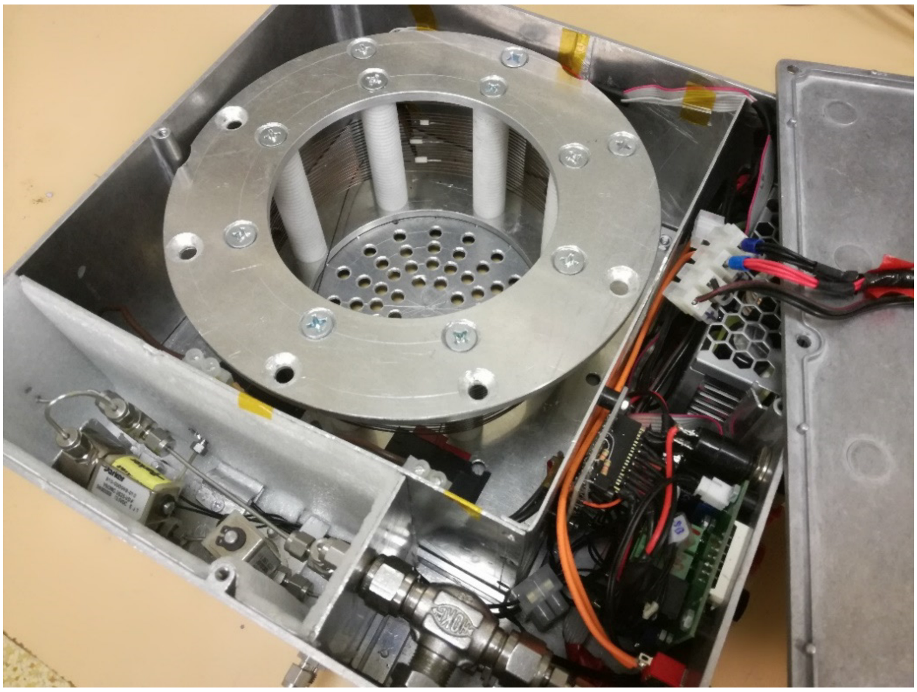

Figure 10 Photograph of the fast GC unit built for the study of individual monoterpenes in gaseous mixtures.

In our solution (see Figure 10), we used two 5 m long metallic GC columns, MXT-1 and MXT-Volatiles, having different active phases of 0.15 µm and 1.15 µm, respectively. Using their own conductivity, both columns were heated from an external power source using joule heating. The study was initiated by ion chemistry and elution times study of individual, most abundant monoterpene isomers: α-pinene, β-pinene, Camphene, Myrcene, 3-carene, R-limonene, α-terpinene and γ-terpinene. These data were later used for analysis of artificially prepared monoterpene mixtures. The selectivity of the obtained chromatogram was further improved by the combined use of H_3O^+ and NO^+ reagent ions; and by analysing the relative ratio of the two main ion products, *m/z* 81 ($C_6H_9^+$) and *m/z* 137 ($C_{10}H_{17}^+$) for H_3O^+; and *m/z* 93 ($C_7H_9^+$) and *m/z* 136 ($C_{10}H_{16}^+$) for NO^+. The obtained knowledge was then applied to the analysis of monoterpene emissions from a series of coniferous biological samples, namely *Picea Pungens Engelm*., *Abies Concolor and Pinus Nigra*.

In this work, we have demonstrated the analytical value the novel combination of fast GC coupled to SIFT-MS. As an enhancement to fast GC systems combined with PTR-MS, we went on to achieve a relatively high LOD (~ 16 ppbv). This is mainly due to the limited sample flow eluting from the column (2-3 sccm) which seems insufficient for SIFT-MS (usually using an order of magnitude more). This could be resolved by using a wider column or by using multiple capillaries in parallel. The use of multiple reagent ions was however a clear advantage as it improved the identification of individual monoterpenes within the chromatogram which was not fully resolved. Finally, the overall benefit of fast GC (not yet stated) is the successful separation of water vapour from the sample. As we observed, the retention time of water is much faster compared to the retention time of the studied monoterpenes. Water vapour is thus evacuated from the flow tube before the analyte of interest is ionized. Consequently, ion chemistry is not significantly affected by system humidity which allows for a systematic use of product branching ratios in future analyses, regardless of sample humidity. This is a very strong benefit of this technique, improving both selectivity and sensitivity of VOC determination in environmental settings.

The full study describing the coupling of fast gas chromatography to selected ion flow tube mass spectrometry for the analysis of individual monoterpenes within mixtures is presented in **Attachment A.1**.

3. Complex model of ion chemistry in SCI-MS

The ion chemistry within the reactor tubes can be very complex. This is because the main ionization channels produce multiple ion products and all main ion reactants and products may react with water vapour in a series of secondary reactions. The presence of secondary reactions increases the complexity of mass spectra, reducing selectivity and sensitivity of the technique. In order to determine the concentration of the analyte, the calculation must consider the ion intensities of all product ions, as well as those produced by secondary reactions. Changes in samples humidity (as well as other components as CO_2) thus affects the presence of secondary ion products. For the successful application of SCIMS in ambient environments where sample humidity may change over time, the secondary reactions must be well understood. For this reason, we have built a numerical simulator capable of simulating the ion chemistry within the reactor flow-tube.

The Kinetics of Ion Molecular Interactions Simulator (KIMI Sim) is a numerical simulator of ion-chemistry found in SCIMS instruments. KIMI was produced to help users understand complex ion-neutral molecule interactions and to simulate the ion and neutral molecule number densities in a flow tube or a drift tube. KIMI may however also be used to simulate various other problems involving ion-molecule interactions. The software was built as a Windows desktop application in the .NET 4.6.1 framework in C#. KIMI uses an interactive graphical interface where the proposed set of ion-molecular reactions may be created. The KIMI then transforms the graphical reaction into a set of kinetic equations that are solved along the central axis of the reactor tube using the classical Runge-Kutta algorithm. [270] Results of the simulation may then be interactively inspected, downloaded or compared with experimental results. The details of how to access the KIMI software are presented at the end of the thesis. (See **Attachment A.7** in the list of attachments.)

The software is composed of two core programs (classes) (see Figure 11). The Main program is responsible for management of software settings; main simulation properties; management of individual reaction species as well as for the interactive graphical interface where the proposed reaction sequence is formed. After definition of all physical properties and the formation of a valid reaction scheme, the main program constructs the calculation, calculating all essential information. Calculation control also allows the user to modify some reaction properties, for example reaction rate constants. Additionally, user may enable a homogenous electric field into the simulation. Furthermore, the calculation control also enables a multidimensional simulation by presenting a range of *E/N* values (or a range of number densities) of one of the reactants. If this option is selected then the simulation will be executed for every value of *E/N* or reactant concentration within the pre-defined range. After initialization of the calculation, the calculation control transforms the reaction objects into a set of differential kinetic equations and solves them along the central axis of the reactor. The calculation is executed by the construction of a "calculation" program, executing a one-step solution (via a differential equation). The process is repeated across selected reaction coordinates. The final data set is stored within a Data management class entity, from where it is accessed through the data plot function. Data plot is also capable of comparing simulation results with experimental data.

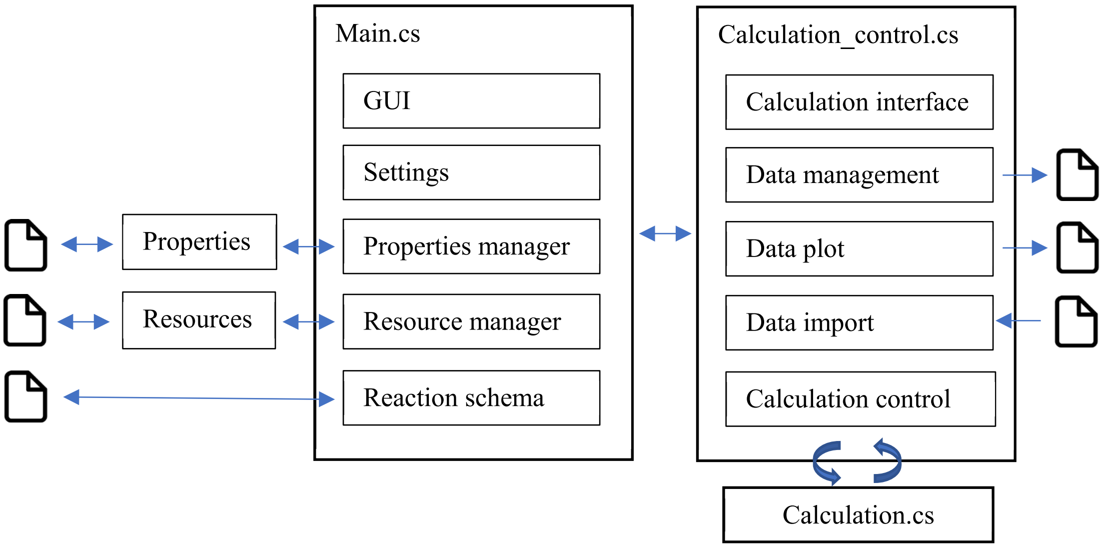

Figure 11 A schematic view of the KIMI main programs and their functionalities.

Before the creation of a reaction scheme, it is necessary to define the reactant and product entities. This may be done via accessing **Resource manager** (Properties → Resource manager, Figure 12) and by collecting a list of particles (ions and neutrals) used in the simulation. Every entity has a defined charge state; name (unique string identifier); chemical formula and a short name. The short name is a short non-unique string, used for the visual representation of the particle. The remaining parameters are required based on the simulation settings. The ion mobility is only required for ions; and only if the simulation incorporates a drift field. The ion mobility may also be set as a function of *E/N*, if necessary. The number density represents the initial number density of particles at the beginning of the simulation. The molar mass is automatically determined from the reaction formula. Diffusion coefficients are necessary if the diffusion effect is enabled in the Diffusion setting; and must signify a diffusion coefficient value representing standard experimental conditions (reactor pressure 1 Torr = 1.33 mbar and temperature 300 K). The diffusion coefficient may be automatically estimated based on the masses of the reaction species, by using a semi-empirical function [136]

$$D_{\mathrm{He}} = 140\ \mathrm{cm}^2\mathrm{s}^{-1} \ln \frac{383}{m/z}. \tag{60}$$

Note that this estimation may only be used when helium is the carrier gas. The error of such an estimation should be less than 50%, although should also be better than 20% for VOCs (and their hydrates). The list of species is stored in the applications setting for later use and may be exported or imported from an external file.

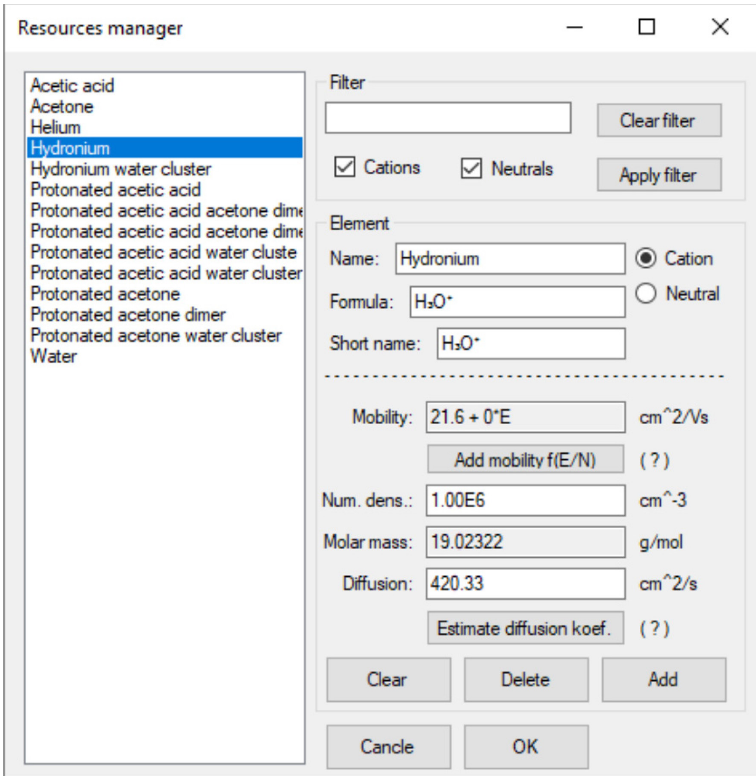

Acetic acid
Acetone
Helium
Hydronium
Hydronium water cluster
Protonated acetic acid
Protonated acetic acid acetone dime
Protonated acetic acid acetone dime
Protonated acetic acid water cluste
Protonated acetic acid water cluster
Protonated acetone
Protonated acetone dimer
Protonated acetone water cluster
Water

☑ Cations ☑ Neutrals

Name: Hydronium
● Cation ○ Neutral
Formula: H_3O^+
Short name: H_3O^+

Mobility: 21.6 + 0*E cm^2/Vs
Num. dens.: 1.00E6 cm^-3
Molar mass: 19.02322 g/mol
Diffusion: 420.33 cm^2/s

Figure 12 Resource manager responsible for the management of individual species within the simulation.

The next step is defining the **Calculation properties** (Properties → Calculation properties, Figure 13). The calculation properties include the general physical properties of the simulation, as well as the main calculation options. The definition of general properties is mandatory for a successful simulation. The carrier gas type allows for the selection of representative neutral species (previously defined in the Resource manager). This is necessary only for the advanced definition of reaction rates, where $k = f(KE_{\mathrm{CM}})$. The carrier gas pressure and temperature are given as the mean value over the gas pressures and temperatures recorded within a reactor. The carrier gas bulk velocity (v_g) and the ion flow velocity (v_i) are parameters which are also crucial for flow-tube simulations.

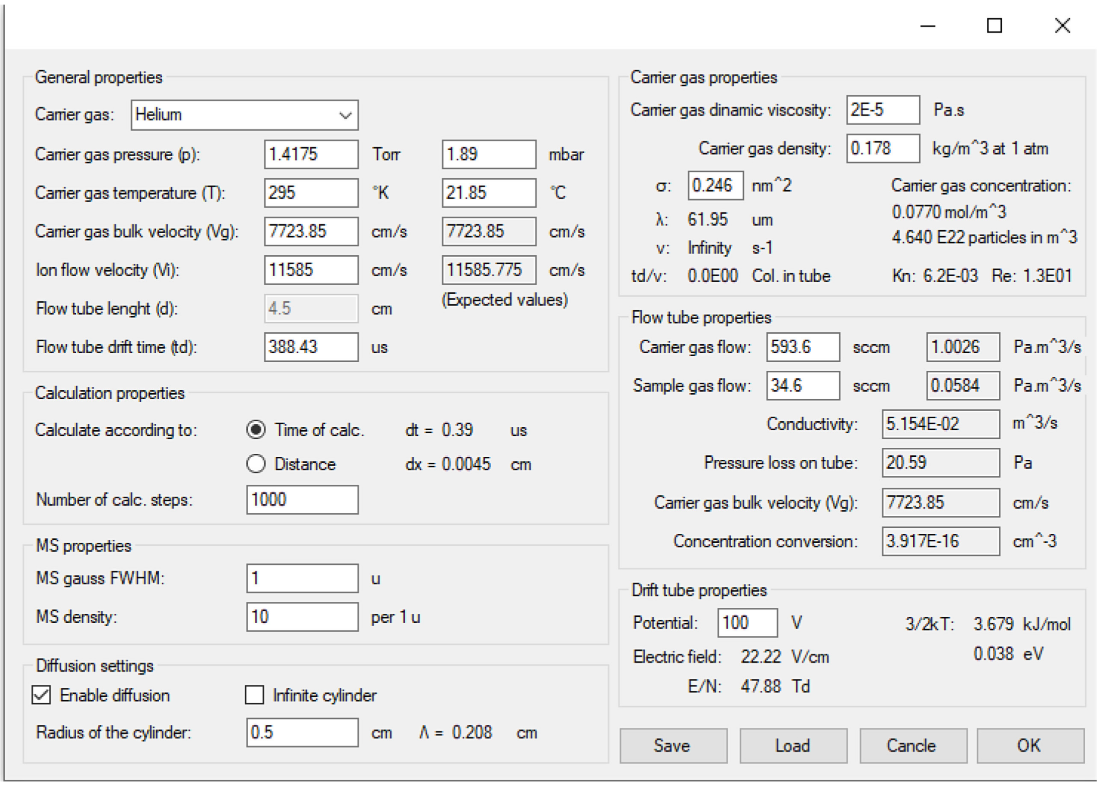
General properties

Carrier gas: Helium

Carrier gas pressure (p): 1.4175 Torr 1.89 mbar

Carrier gas temperature (T): 295 °K 21.85 °C

Carrier gas bulk velocity (Vg): 7723.85 cm/s 7723.85 cm/s

Ion flow velocity (Vi): 11585 cm/s 11585.775 cm/s

Flow tube lenght (d): 4.5 cm (Expected values)

Flow tube drift time (td): 388.43 us

Calculation properties

Calculate according to: ● Time of calc. dt = 0.39 us

○ Distance dx = 0.0045 cm

Number of calc. steps: 1000

MS properties

MS gauss FWHM: 1 u

MS density: 10 per 1 u

Diffusion settings

☑ Enable diffusion ☐ Infinite cylinder

Radius of the cylinder: 0.5 cm Λ = 0.208 cm

Carrier gas properties

Carrier gas dinamic viscosity: 2E-5 Pa.s

Carrier gas density: 0.178 kg/m^3 at 1 atm

σ: 0.246 nm^2

λ: 61.95 um

ν: Infinity s-1

td/ν: 0.0E00 Col. in tube

Carrier gas concentration:
0.0770 mol/m^3
4.640 E22 particles in m^3

Kn: 6.2E-03 Re: 1.3E01

Flow tube properties

Carrier gas flow: 593.6 sccm 1.0026 Pa.m^3/s

Sample gas flow: 34.6 sccm 0.0584 Pa.m^3/s

Conductivity: 5.154E-02 m^3/s

Pressure loss on tube: 20.59 Pa

Carrier gas bulk velocity (Vg): 7723.85 cm/s

Concentration conversion: 3.917E-16 cm^-3

Drift tube properties

Potential: 100 V

Electric field: 22.22 V/cm

E/N: 47.88 Td

3/2kT: 3.679 kJ/mol
0.038 eV

Figure 13 The calculation properties window responsible for the management of physical properties and geometries within the simulation.

The carrier gas bulk velocity represents the mean velocity of the carrier gas flowing in laminar mode through a reactor tube. The ion flow velocity represents the mean velocity of ions carried by carrier gas through the flow tube. For a flow-tube simulation, this value is used to determine the actual reaction time. For drift-tube experiments, this component represents the parasitic ion flow causing an error in the ion drift velocity value calculated. The ion flow velocity (under normal experimental conditions) is expected to be ~ 1.5 × v_g. [23] This is an empirical value based on the ion injection geometry. Ions are injected into a reactor via an orifice situated close to the central axis. Thus, the maximum of the radial ion density distributed is also located on the reactor axis. This density is then reduced via radial ion diffusion. However, the presence of a laminar flow causes the majority of ions (which are centralized on the central reactor axis) to move faster than the ions which already diffused (and are lost) to the reactor wall. The final radial profile of ion velocities is therefore composed of the carrier gas radial velocity $v_g(r)$ and the ion radial density distribution $\rho_0(r)$, $v_g(r) \times \rho_0(r)$. The mean value of ion velocities is thus larger compared to the neutral gas velocity.[1] However, as the gas flow near the injection orifice is not laminar (but somewhat turbulent), it is difficult to properly evaluate this relationship and therefore only the empirical coefficient is applied. The next two parameters, the tube length (d) and the tube drift time (t_d), define the length of the system and are bounded through ion drift velocity. It is therefore necessary to define only one of these parameters. The drift time represents the time a reagent ion takes to pass through the reactor, $t_d = d/v_i$.

In the remaining sections, the user may define whether the reaction differential equation is solved in accordance with the reaction time or the reaction coordinate differential. The number of calculation steps subsequently define the size of the calculation differential. The size of the reaction differential requires specific attention. Too many calculation steps (causing very small reaction differentials) results in long calculation times. Too few calculation steps may cause the numerical method to oscillate, consequently producing false results, especially when large changes in the particle number density is expected. The MS properties define the visual quality of artificially generated MS spectra. The diffusion settings allow the user to define the radius of a reactor and also enable a radial diffusion term to be incorporated into the numerical calculation. The ion diffusion is consequently evaluated using the characteristic diffusion length, Λ, defined as:

---

[1] $v_i(r) = \int v_g(r) \times \rho_i(r,x)\mathrm{d}x$ and than $\overline{v_i(r)} > \overline{v_g(r)}$

$$\Lambda = \sqrt{\frac{1}{\left(\frac{2.405}{R}\right)^2 + \left(\frac{\pi}{L}\right)^2}}, \tag{61}$$

where *R* and *L* represent the radius and length of the cylindrical reactor, respectively. Selecting the option for infinite ciliated systems takes the solution for $L \rightarrow \infty$.

Finally, the calculation properties contain a series of assisting calculations, including those accounting for carrier gas properties; flow and drift tube properties. In the carrier gas properties section, the user may find information on the mean free path of particles in the buffer gas; the Reynold and Knudsen number; and of necessity, the value of the carrier gas number density at defined temperatures and pressures (for specific three body reactions). The flow tube properties also assist in SIFT-MS simulations. Using the reactor geometry and defining the carrier gas and sample gas flow rates (combined with carrier gas properties), the system will calculate the conductivity of the reactor tube and will estimate the reactor pressure loss. This information is useful if a pressure gauge is located on the side of a reactor, as for the simulation a mean reactor tube pressure is used. Finally, the system is able to predict the gas bulk velocity used for the calculation of ion velocities and reaction times (settings dependant):

$$\mathrm{v}_g = \frac{\theta}{pS}\frac{T}{273\ \mathrm{K}}, \tag{62}$$

where θ represents the total gas flow though the reactor tube and *S* is the flow tube surface area. In the drift tube properties section of the program, the user may test the value of *E/N* when a specific electric potential is applied along the reactor axis. In addition, the value of the thermal ion energy is presented. The set of calculation properties may also be exported to an external file.

After definition of the reaction properties as well as the individual reactant and product species, the reaction scheme may be formed by adding individual ions into the reaction grid (see Figure 14). Selecting an empty element of the grid allows the user to associate the grid element with one ion species. To simplify the reaction system, only the short names of ions are presented in the reaction scheme. Two ion species may then be connected together to create a reaction. After establishing this connection, additional parameters of ion-molecule reactions may be defined, including reactions specifications, as well as product neutrals of reaction rates. The reaction rate may be a constant, or as a function of *E/N* or KE_{CM}. The user is free to add and modify any reaction species as well as alter which properties are included in the simulation. Every reaction applied in the scheme is saved and man be reused later. The only limitation is that every used species must be a product of at least one reaction. The reaction scheme may be saved for later use, or loaded from the file. When all ions on the reaction grid are properly connected, the Proceed button is enabled and the Calculation control window can be open.

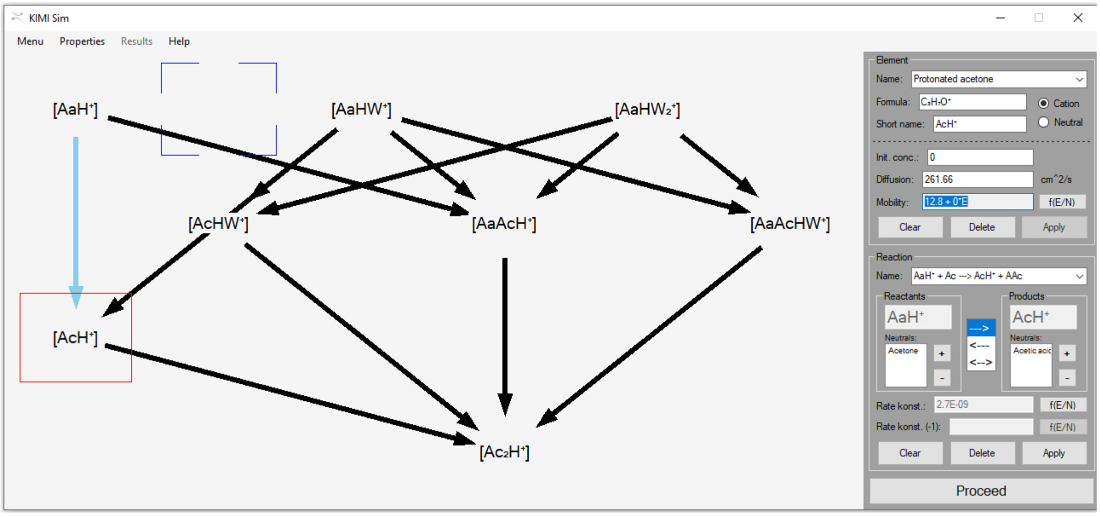

Name: Protonated acetone
Formula: $C_3H_7O^+$
● Cation
○ Neutral
Short name: AcH^+
Init. conc.: 0
Diffusion: 261.66 cm^2/s
Mobility: 12.8 + 0*E

Name: $AaH^+ + Ac \dashrightarrow AcH^+ + AAc$
Reactants: AaH^+
Neutrals: Acetone
---> / <--- / <-->
Products: AcH^+
Neutrals: Acetic acic
Rate konst.: 2.7E-09
Rate konst. (-1):

Figure 14 The Calculation properties window is responsible for the management of physical properties and geometry of simulation.

The **Calculation control** gives access to the simulation properties as well as the reactions and species defined in the reaction grid. Each reaction included together with all ions and neutrals are listed in the overview (see Figure 15). The overview allows for the modification of reaction rate constants or initial number densities before each simulation. If the reaction rate is introduced as a function of *E/N* then the individual parameters of a function may also be modified, although the format of the reaction rate must remain unchanged. One of the implemented features is the possibility of grouping individual species into sub-groups. This allows for the calculation of the relative concentrations of species within the respective sub-groups. This may be used, for example, when studying the relative distribution of reagent and product ions, individually.

Calculation control also enables dynamic changes in the number density of one selected species. If enabled, the simulation will be executed for every defined value.

This option may be used for the study of secondary reactions, simulating the effect of an increase in the water vapour, on the ion chemistry. Similarly, this may be pre-defined for a range of *E/N* values.

Initialization of the simulation triggers a series of processes leading to the transformation of reaction objects into calculation objects. Due to the object-oriented architecture of KIMI, Calculation control has access to objects defined in the Resource manager (if they were introduced into the reaction grid previously). Within the reaction grid, reactions represent the main objects defining relations between ions. During transformation, individual ions and neutrals become the main objects, carrying information about other particle objects and their relation to them. After transformation, a new constructed series of objects follows the format of a kinetic equation (see Figure 16).

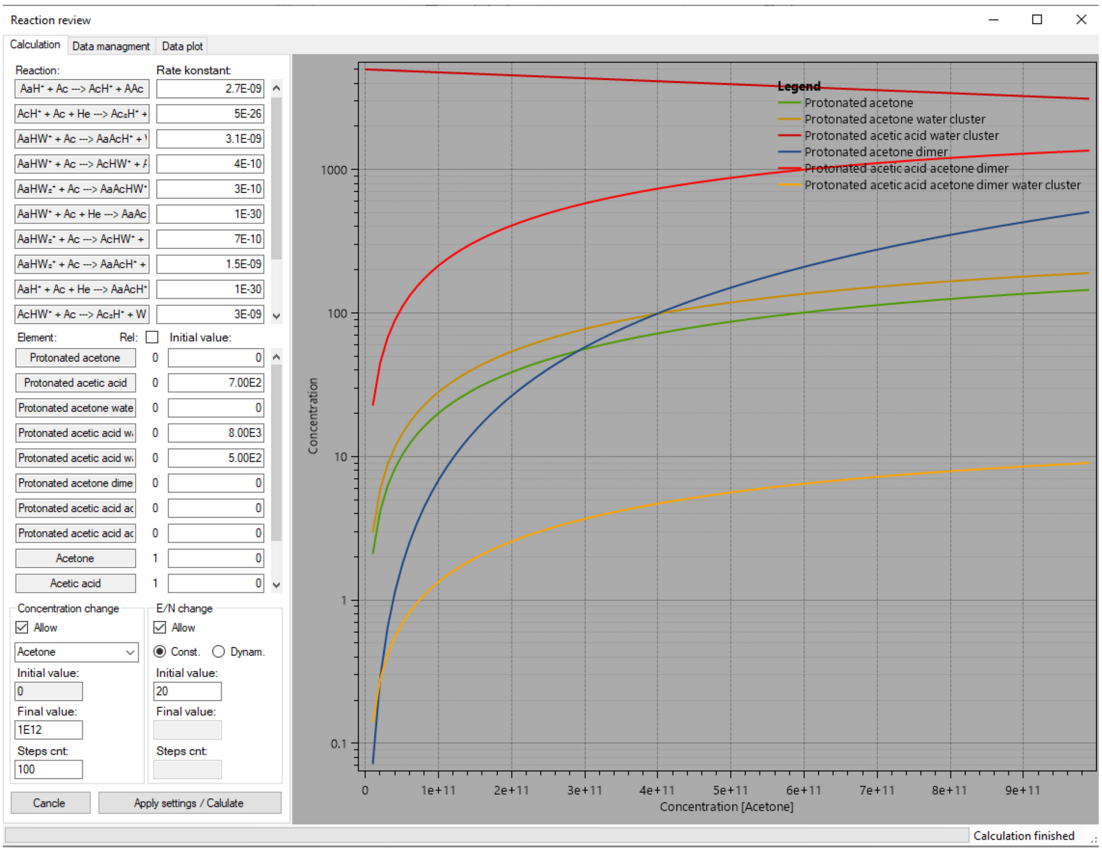

Reaction:	Rate konstant:
AaH^+ + Ac ---> AcH^+ + AAc	2.7E-09
AcH^+ + Ac + He ---> Ac_2H^+ +	5E-26
$AaHW^+$ + Ac ---> $AaAcH^+$ +	3.1E-09
$AaHW^+$ + Ac ---> $AcHW^+$ +	4E-10
$AaHW_2^+$ + Ac ---> AaAcHW	3E-10
$AaHW^+$ + Ac + He ---> AaAc	1E-30
$AaHW_2^+$ + Ac ---> $AcHW^+$ +	7E-10
$AaHW_2^+$ + Ac ---> $AaAcH^+$ +	1.5E-09
AaH^+ + Ac + He ---> AaAcH	1E-30
$AcHW^+$ + Ac ---> Ac_2H^+ + W	3E-09

Rel: ☐

Element:		Initial value:
Protonated acetone	0	0
Protonated acetic acid	0	7.00E2
Protonated acetone wate	0	0
Protonated acetic acid w	0	8.00E3
Protonated acetic acid w	0	5.00E2
Protonated acetone dime	0	0
Protonated acetic acid ac	0	0
Protonated acetic acid ac	0	0
Acetone	1	0
Acetic acid	1	0

Concentration change
☑ Allow
Acetone
Initial value: 0
Final value: 1E12
Steps cnt: 100

E/N change
☑ Allow
● Const. ○ Dynam.
Initial value: 20
Final value:
Steps cnt:

Figure 15 Calculation control window.

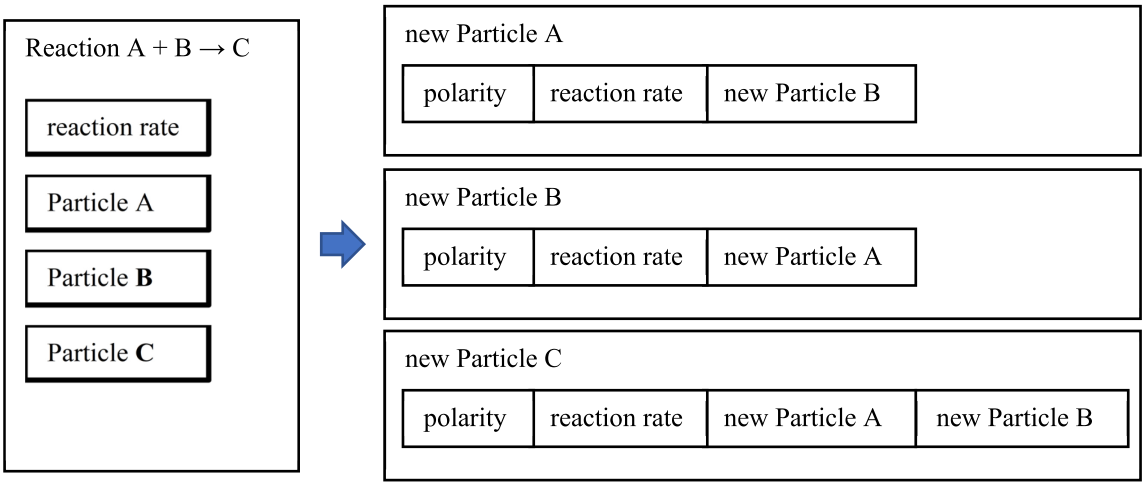

Figure 16 A visualisation of the transformation process. The main reaction object (left) is transformed into a series of calculation objects (left). The new objects are later used by Calculation class to calculate a single step numerical solution of differential kinetic equations.

After data transformation, Calculation control initiates its internal loop. During each iteration**, Calculation control** creates a calculation class, providing a single step solution for a kinetic differential equation, for every particle object. After every iteration, the one step solution of particle number density is stored in memory and is used in the next iteration as a new starting value. The actual differential form of the kinetic equations is also generated within the calculation class, based on the input variables prepared by the Calculation control. This includes the size and type of differential, as well as values of reaction rate or ion mobility for actual *E/N*. At the end of the calculation, differential equations follow the time dependent format for the flow tube (Eq. 39, 40), or the axial coordinate format for the drift-tube (Eq. 53, 54), for constant *E/N*.

Following this, the calculation class program solves the system of differential equations using the classical Runge-Kutta method. This method solves a differential equation as:

$$\frac{\mathrm{d}y}{\mathrm{d}t} = f(t, y), \quad y(t_0) = y_0 \tag{63}$$

where y is an unknown function of t and y_0 is the initial value. Using the discrete parameter $h > 0$, the method estimates the following for $n \geq 0$:

$$y_{n+1} = y_n + \frac{1}{6}h(k_1 + k_2 + k_3 + k_4),$$
$$t_{n+1} = t_n + h, \tag{64}$$

where:

$$\begin{aligned} k_1 &= f(t_n, y_n), \\ k_2 &= f\left(t_n + \frac{h}{2}, y_n + h\frac{k_1}{2}\right), \\ k_3 &= f\left(t_n + \frac{h}{2}, y_n + h\frac{k_2}{2}\right), \\ k_4 &= f(t_n + h, y_n + hk_3). \end{aligned} \tag{65}$$

Thus, the value y_{n+1} is an approximation for $y(t_{n+1})$. In the present solution, y represents the particle number density and h is the time or axial differential. It is important to note that the stability of the numerical solution is related to both $\mathrm{d}y/\mathrm{d}t$ and h. For large changes of y, h needs to be sufficiently small or the solution will be unstable.

All determined values of particle concentration are stored in the **Data storage**, which may be freely accessed by the user. Under the **Data management** list option, the user may browse through previously executed calculations; export them or recover any settings from previous calculations. The user may also import any external experimental data (for comparison with the simulation results). Finally, under the data plot list option, the user may inspect their calculation results and download individual data plots.

The functionality of KIMI was tested on a series of experimental data, produced by SIFT-MS and SIFDT-MS methods. For the initial test, we studied the influence of water vapour concentration on the formation of hydronium hydrates in SIFT-MS. In later work, we conducted similar experiments involving acetone vapours. Both the hydronium reactions with water vapour as well as with acetone are well described in literature. [64, 136, 139, 271] As a result, we used the set of known reaction rate constants as a foundation the for simulation of ion chemistry in the program. Reaction rate constants were subsequently optimised to interpolate experimental data. For the experiment, we used a nalophan bag filled with dry air and acetone for the second study. The humidity of our sample was changed by injecting warm liquid water into the sample bag while the sample gas was introduced into inlet of the SIFT-MS. SIFT-MS is capable of directly calculating the water vapour concentration of sampled gas based on the hydronium hydrates intensity (of c/s) distribution. However, in order to reduce the systematic difference between the experiment and simulation, we decided to use a dimensionless parameter H,

$$\begin{aligned} H &= ln\left(\frac{[\mathrm{H_3O^+}] + [\mathrm{H_3O^+.H_2O}] + [\mathrm{H_3O^+(H_2O)_2}] + \cdots}{[\mathrm{H_3O^+}]}\right) \\ &= ln\left(\frac{i(\mathrm{H_3O^+}) + i(\mathrm{H_3O^+.H_2O}) + i(\mathrm{H_3O^+(H_2O)_2}) + \cdots}{i(\mathrm{H_3O^+})}\right), \end{aligned} \tag{66}$$

representing the logarithm of the ratio between all water related reagent and product ions (hydronium and its respective clusters). These values were linearly dependent on the water vapour concentration in the flow-tube.

Table 3 The list of reactions and reaction rate constants used for the simulation of humid ion chemistry; and its dependence on water vapour concentration in the flow tube. The reaction rates for the three body association reactions are presented as effective two-body reaction rate coefficients. k_{lit} represents data taken from [137].

Reaction	k_{lit} (cm^{3}s^{-1})	k_{KIMI} (cm^{3}s^{-1})
$H_3O^+ + H_2O \rightarrow H_3O^+H_2O$	2.1 x 10^{-11}	1.36 x 10^{-11}
$H_3O^+H_2O + H_2O \rightarrow H_3O^+(H_2O)_2$	5.7 x 10^{-11}	3.23 x 10^{-11}
$H_3O^+(H_2O)_2 + H_2O \rightarrow H_3O^+(H_2O)_3$	6.2 x 10^{-11}	3.1 x 10^{-11}
$H_3O^+(H_2O)_3 \rightarrow H_3O^+(H_2O)_2 + H_2O$		1000 s^{-1}

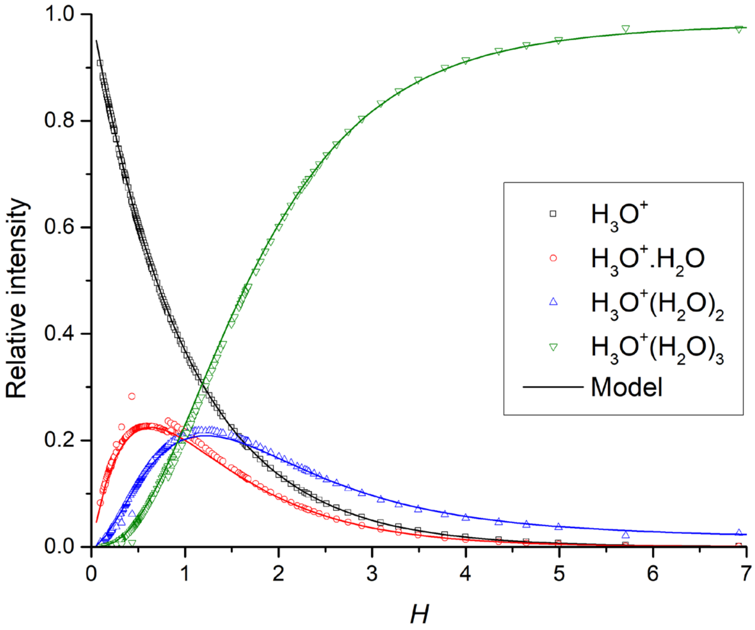

Figure 17 Initial simulation of the formation of hydronium hydrates. Experimental data (in symbols) were interpolated by the set of reactions listed in Table 3.

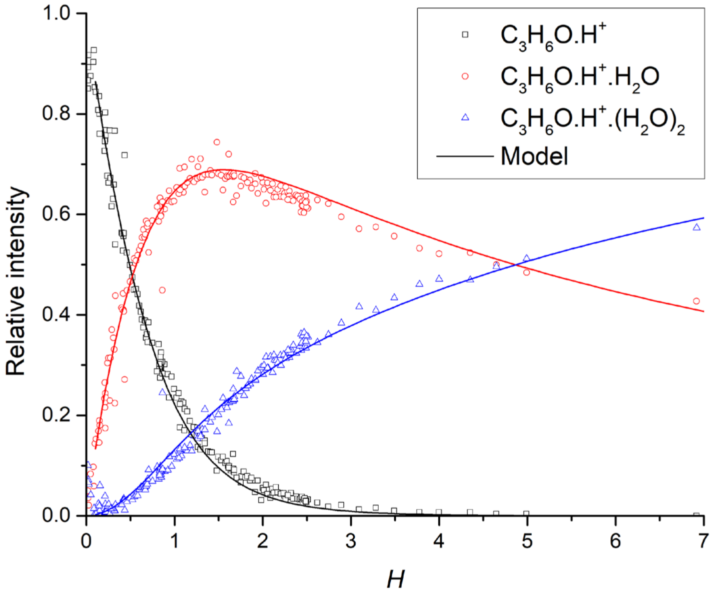

Figure 18 An initial simulation of acetone's ion chemistry under the experimental conditions described in the text. Experimental data (in symbols) were interpolated by the set of reactions shown in Figure 19.

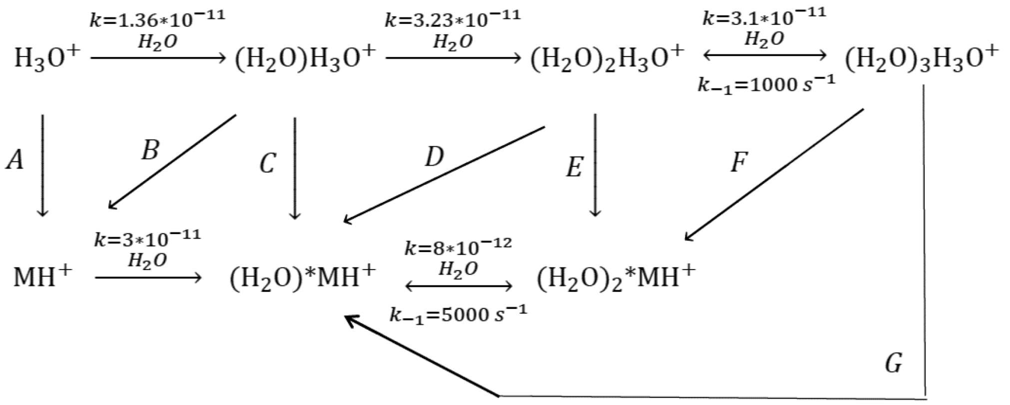

A: $k = 2.7 * 10^{-9}$; $H_3O^+ + M \rightarrow MH^+ + H_2O$
B: $k = 3 * 10^{-9}$; $(H_2O) * H_3O^+ + M \rightarrow MH^+ + 2H_2O$
C: $k = 2 * 10^{-9}$; $(H_2O) * H_3O^+ + M \rightarrow (H_2O) * MH^+ + H_2O$
D: $k = 1 * 10^{-9}$; $(H_2O)_2 * H_3O^+ + M \rightarrow (H_2O) * MH^+ + 2H_2O$
E: $k = 1 * 10^{-10}$; $(H_2O)_2 * H_3O^+ + M \rightarrow (H_2O)_2 * MH^+ + H_2O$
F: $k = 3 * 10^{-9}$; $(H_2O)_3 * H_3O^+ + M \rightarrow (H_2O)_2 * MH^+ + 2H_2O$
G: $k = 1 * 10^{-8}$; $(H_2O)_3 * H_3O^+ + M \rightarrow (H_2O) * MH^+ + 3H_2O$

Figure 19 Schematic visualization of acetone ion chemistry simulated by KIMI. Three body association reactions behave as effective two-body reactions (at a helium number density of [He] = 3.6×10^{16} cm^{-3}). All rate coefficients are in cm^3s^{-1}.

The results of initial tests are presented in Figures 17, 18 and 19. The experiment was carried out under a carrier gas pressure of 1.5 mbar and at a temperature of 295 K. Three body association reactions are presented as effective two-body reaction rate coefficients in cm^3s^{-1} (at a helium number density [He] = 3.6×10^{16} cm^{-3}). The simulation of the acetone ion chemistry presented in this work was directly based on known hydronium ion chemistry. As a starting point we used the reaction rate coefficients from the SIFT-MS library [271], 3.9×10^{-9} cm^3s^{-1} and 3.3×10^{-9} cm^3s^{-1} for channels A and B, respectively (see Figure 19).

Note that all the optimised values of the reaction rates calculated by the simulation were smaller compared to the reference values. This is because at the initial stage of the SIFT-MS system, the radial diffusion of ions was not properly implemented into the KIMI. However, initial tests showed that we are able to simulate complex ion chemical interactions.

Final tests were performed on the ion chemistry of methanol and ethanol with H_3O^+ and NO^+ reagent ions in the presence of an electric field. The references for this system were limited and therefore we optimised the reaction rates only to interpolate experimental data. The primary alcohol molecular reactions were studied by using the SIFDT (2 mbar He; 0.08 mbar air sample; 300 K; reduced field strength *E/N* up to 28 Td; and over a range of sample gas humidity up to 5.5%). The NO^+ reactions resulted in the formation of $(M\text{-}H)^+$ product ions together with NOH neutral molecules, followed by the formation of ion hydrates $(M\text{-}H)^+(H_2O)_{1,2}$. [66] The variation of the percentages of the hydrated product ions depend on both *E/N* and the humidity of the sample. To change the sample humidity, we used an approach identical to the acetone study. From the full set of simulations, we selected one example to demonstrate the ability of KIMI to solve the ion chemistry within a drift tube (Figure 20) simulation. Presented data were obtained for variable *E/N* using high sample humidity. H_2O concentration in the drift tube was ~5×10^{13} cm^{-3}.

The benefit of KIMI is that one is able to simulate a proposed ion chemistry model and subsequently compare it with real-life experimental results. This allows the user to test several ion chemistry theories; to determine effect of individual reaction channels; or to estimate unknown reaction rates. Therefore, we used KIMI Sim to supplement our experimental results of the ion chemistry in several of our publications.

Table 4 The list of reaction and rate constants used for the simulation of humid ion chemistry and its dependence on water vapour concentration in the flow tube. As previously mentioned, the reaction rates for the association reactions are presented as effective two-body reaction rate coefficients.

Reaction	k_{KIMI} (cm^3s^{-1})
$NO^+ + H_2O \rightarrow NO^+.H_2O$	$2 \times 10^{-17} \times KE_{CM,r}^{-3.6}$
$NO^+.H_2O + H_2O \rightarrow NO^+(H_2O)_2$	$8 \times 10^{-17} \times KE_{CM,r}^{-3.6}$
$NO^+ + M \rightarrow (M\text{-}H)^+ + NOH$	3×10^{-9}
$NO^+H_2O + M \rightarrow (M\text{-}H)^+.H_2O + NOH$	3×10^{-9}
$NO^+(H_2O)_2 + M \rightarrow (M\text{-}H)^+(H_2O)_2 + NOH$	3×10^{-9}
$NO^+H_2O + M \rightarrow (M\text{-}H)^+ + H_2O + NOH$	1×10^{-11}
$(M\text{-}H)^+ + H_2O \rightarrow (M\text{-}H)^+.H_2O$	$7 \times 10^{-14} \times KE_{CM,r}^{-2.2}$
$(M\text{-}H)^+.H_2O + H_2O \rightarrow (M\text{-}H)^+(H_2O)_2$	$2.2 \times 10^{-14} \times KE_{CM,r}^{-2.2}$

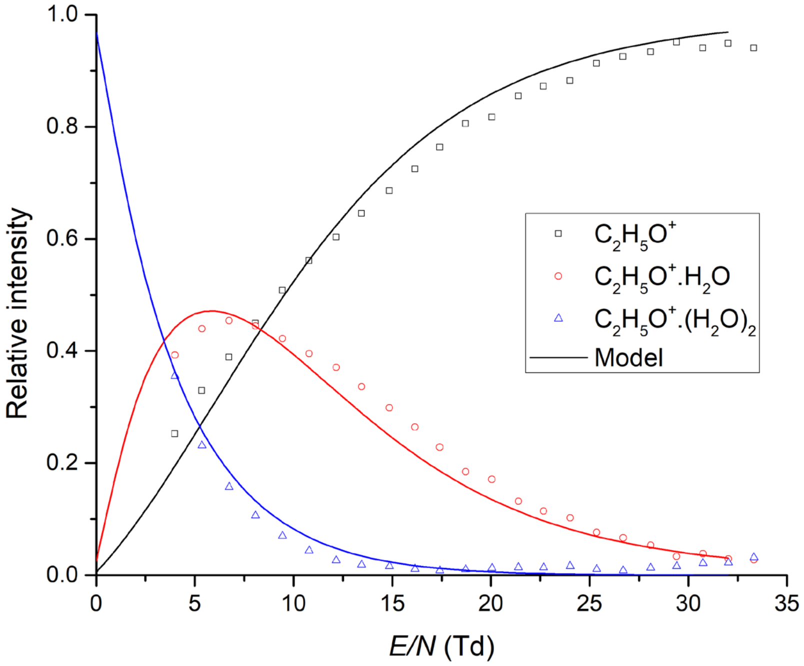

Figure 20 Initial simulation of NO^+ ion chemistry with ethanol. Experimental data (presented as symbols) were interpolated by the set of reactions shown in Table 4.

4. Results

4.1. Complex study of glyoxal ion chemistry

Glyoxal ($C_2H_2O_2$) is the simplest highly reactive dialdehyde. In biological systems, glyoxal is associated with oxidation stress. [272] In the gas phase however, glyoxal may be found as a reaction intermediate in the photo-catalytical reduction of carbon dioxide to methane [273, 274] and also in the earth's atmosphere as a product of the oxidation and photo-oxidation of VOCs (such as toluene, xylene or isoprene) [275-280].

From the stance of chemical ionization, glyoxal represents an analytical challenge as the PA of glyoxal (690 kJ mol^{-1}) estimated by theroretical calculations [281], is simillar to the PA of water (691 kJ mol^{-1}) [57]. Additionaly, neutral glyoxal reacts rapidly with humidity forming a series of oligomers that contribute to the formation of atmospheric aerosol. [272, 282] The ion chemistry of glyoxal with H_3O^+ had been previously studied using SIFT-MS [263, 283], confirming the presence of the proton transfer reaction forming protonated glyoxal. In addition, under increased sample humidity, protonated formaldehyde was also observed. A recent PTR-MS study showed interesting behavior [284] (in contrast to flow tube studies) where the concentration of protonated formaldehyde was very intensive at low humidity, decreasing for higher water vapor concentrations. As none of these studies explained this opposite trend in formation of protonated fornaldehyde, we decided to study this behaviour.

Our study is separated into two parts. Firstly, we investigated glyoxal ion chemistry in the SIFT-MS under variable humidity. This work has already been published and details are in **Attachment A.2**. Secondly, we studied glyoxal's ion chemistry in the presence of an electric field using a PTR-MS as well as a SIFDT-MS instrument. This study has not yet been published, although all details on this work are also available in the manuscript, in **Attachment A.3**.

To summarize, the ion chemistry (for reagent ions in the Profile 3 SIFT-MS: H_3O^+, NO^+ and O_2^+) was investigated, although only H_3O^+ showed a significant change when the water vapour concentration was varied. The high reactivity of neutral glyoxal molecules with water did not allow us to change the humidity of the sample directly.

Instead, we needed to humidify helium carrier gas. Finally, to support study of glyoxal ion chemistry, we also studied the ion chemistry of formaldehyde.

The results confirmed the formation of the protonated glyoxal as the main product ion, as a result of proton transfer from H_3O^+ to glyoxal. An increase in the water concentration leads to the formation of the protonated glyoxal primary hydrate via an association reaction. The protonated glyoxal (primary) hydrate is stable until presented with additional water molecules, resulting in several reaction channels:

$$C_2H_3O_2^+.H_2O + H_2O \leftrightarrow H_3O^+.H_2O + C_2H_2O_2, \tag{67}$$

$$\rightarrow CH_2OH^+ + HCOOH + H_2O, \tag{68}$$

$$C_2H_3O_2^+.H_2O + H_2O + He \rightarrow C_2H_3O_2^+(H_2O)_2 + He. \tag{69}$$

Protonated formaldehyde is formed via the secondary reaction of protonated glyoxal with water (Eq. 68). This assumption was also confirmed by the KIMI simulation, complementing our experimental study.

Additionally, the protonated formaldehyde reacts via a three-body association reaction with water molecules at high system humidity, forming the protonated formaldehyde hydrate. This reaction is of high significance, as the protonated formaldehyde hydrate has the ability to further react with water molecules via a ligand switching reaction into hydronium hydrate:

$$CH_2OH^+ + H_2O + He \rightarrow CH_2OH^+.H_2O + He, \tag{70}$$

$$CH_2OH^+.H_2O + H_2O \rightarrow H_3O^+.H_2O + CH_2O. \tag{71}$$

Reaction 71 is endothermic and relatively slow (5.3×10^{-10} cm^3s^{-1} [285]), however the high number density of water molecules in a humid (up to 3×10^{13} cm^{-3}) reaction equilibrium shifts the system to the production of hydronium hydrate ($H_3O^+.H_2O$). The consequence of this process is a reduction of product ions, characteristic for the detection of glyoxal (when the sample humidity increases).

In conclusion, we clarified that the formation of protonated formaldehyde is caused by the secondary reaction of protonated glyoxal with water vapour. The relative fraction of protonated formaldehyde thus increases with sample humidity. The situation however changes in the presence of an electric field.

Note that the glyoxal ion chemistry was studied using two instruments: the PTR-MS and SIFDT-MS. Important differences in these two methods are found in the type of buffer gas used in these experiments. While the PTR-MS experiments were carried out in N_2, He was used in SIFDT-MS study. This is significant, as the ion mobility differs between the two buffer gases. The ion mobility determined by the SIFDT instrument is also used in the KIMI simulation and therefore the simulation is unsuitable to be compared to empirical PTR-MS results.

The ion chemistry in both experiments at low *E/N* (where the kinetic energy of ions is close to the thermal energy) follows the reaction pathway found in the SIFT-MS (where protonated formaldehyde is formed via the secondary reaction of protonated glyoxal with water vapour). At high *E/N*, protonated formaldehyde is also formed, although via CID reactions:

$$\mathrm{H_3O^+ + C_2H_2O_2 \rightarrow CH_2OH^+ + HCOOH}, \tag{72}$$

$$\mathrm{C_2H_3O_2^+ + BG \rightarrow CH_2OH^+ + CO + BG}, \tag{73}$$

where BG represents the respective N_2 and He buffer gases. The calculation of reaction energies in He shows reaction 72 to be more energetic (KE_{CM} = 0.6 eV at *E/N* 50 Td for Eq. 72; KE_{CM} = 0.08 eV at *E/N* 50 Td for Eq. 73). Nevertheless, reaction 73 also contributes to the formation of protonated formaldehyde. Further theoretical calculations are needed to evaluate the energetics and reaction mechanisms for these two processes.

Using the SIFDT-MS experimental results, supplemented by the numerical simulations of the ion chemistry, we were also able to identify the reactions responsible for the decreasing abundance of protonated formaldehyde at increasing sample humidity. Firstly, the humidity decreases the mobility of the primary H_3O^+ reagent ions, resulting in a decrease in reaction energy (in Eq. 72). This leads to a reduction in the formation of protonated formaldehyde. By increasing the water vapour concentration in the drift tube (from dry up to 6.4×10^{13} cm^{-3} water molecules), we observed a 10% reduction in the reaction energy. However, the numerical simulation of the ion chemistry showed that this reduction of reaction energy is not highly significant. What is more significant is the reverse proton transfer reaction of the primary and secondary product ions with water molecules back to the hydronium ion:

$$\mathrm{C_2H_3O_2^+ + H_2O \rightarrow H_3O^+ + C_2H_2O_2}, \tag{74}$$

$$\mathrm{CH_2OH^+ + H_2O \rightarrow H_3O^+ + CH_2O}. \tag{75}$$

Individual injection of product ions into the humidified drift tube showed that both protonated glyoxal and protonated formaldehyde produce hydronium according to the Arrhenius function. The PA difference between glyoxal and water is almost 0 (based on a theoretical estimation) while the PA differrence between water and formaldehyde is 0.23 eV. [281] [57] This may suggest that reaction 74 proceeds faster compared to reaction 75. The determined ion mobility of protonated formaldehyde is however larger compared to the ion mobility of the protonated glyoxal product ion and consiquenly the relative KE_{CM}. For increasing E/N, the KE_{CM} for Eq. 75 increaseses faster compared to Eq. 74 and tehrefore the reaction rate for Eq. 75 will eventually overtake the reaction rate of Eq. 74. This equlilibrium change is also seenin the ion chemistry of glyoxal at high E/N. An increase of humidity causes protonated formaldehyde to convert into hydronium faster compared to protonated glyoxal. This in turn reduces the concentraion of protonated formaldehyde, relative to protonated glyoxal. Numerical simulations of the proposed reaction mechanisms confirm this behaviour.

It is important to note that the aim of KIMI simulation was not to fully interpolate experimental data, but to explain the chemical mechanisms leading to the experimentally observed data. The simulation uses several approximations covering various reaction parameters. Further theoretical and experimental work is however required (especially for the purposes of fully simulating PTR-MS data).

4.2. Ion chemistry of phthalates studied by SIFT-MS

Phthalates (esters of phthalic acid) are used as plasticizers in the production of plastics. Their negative health effects on human genitalia have however been reported [286, 287]. To date, phthalates have been characterized as endocrine disruptors making this species of chemicals hazardous for pregnant women and children under the age of 3 years. Several of the most dangerous phthalate compounds are under EU regulations [288] or are tracked by the European Chemical Agency (*EHCA*) [289]. For the exception of children's toys, the regulations surrounding phthalates imposed by the EHCA do not cover any other daily plastic products (i.e. plastic containers [290], cosmetics [291], toothbrushes [292] and more). Such plastic products which can be bought in Europe are predominantly manufactured in countries such as China and India where the EHCA (or any other regulatory body) does not prohibit the regulation of phthalate contamination within these plastics. Plastic products imported into the EU should therefore be more controlled.

Several analytical techniques are used for the detection of phthalates; mainly liquid or gas chromatography coupled to mass spectrometry (GC-MS / LC-MS) [120] primarily using electron ionization at 70 eV. The primary product of dissociative ionization which is shown in the mass spectrum is the protonated phthalate anhydride (*m/z* 149), which characteristic for most phthalates [57]. The presence of a phthalate species may be confirmed by the detection of the phthalate anhydride ion; however, mass spectrometry measurements possess poor selectivity (phthalate species dependant). Using chemical ionization, individual phthalate species may be identified. [293] Ion mobility spectrometry (IMS) is a suitable SCI technique for the detection of phthalates. SCIMS techniques may potentially be used for real time analysis and for the accurate detection of phthalate contamination in plastics. The ability to achieve this has already been demonstrated by Michalczuk et al. [150]. As IMS operates near atmospheric pressure, analyte molecules react mainly with hydronium clusters $H_3O^+(H_2O)_n$.

To evaluate the ability of these methods in detecting phthalate species using IMS, one first needs to understand the ion chemistry. To aid us in this understanding, we present a study of several simple phthalates: dimethyl phthalate (DMP), dimethyl isophthalate (DMIP), dimethyl terephthalate (DMTP), diethyl phthalate (DEP), dipropyl phthalate (DPrP) and dibutyl phthalate (DBP); from SIFT-MS experiments. The study focuses on phthalate ion chemistry when these molecules interact with $H_3O^+(H_2O)_n$ primary ions. The respective isomerization effects are also discussed, which compliments the previous work by Michalczuk et al. [150].

A full description of our experiments, results and the corresponding discussion are presented in **Attachment A.4** (as this study has already been published). In this work, the phthalate ion chemistry was studied by using H_3O^+, NO^+ and O_2^+ reagent ions under variable system humidification. Depending on the reagent ion used, the type of interaction occurring between the sample molecule and the bombarding ion may either (primarily) be a proton transfer reaction (H_3O^+)**;** a charge transfer process (O_2^+); or a charge transfer or association process (NO^+).

Previously recorded IMS/MS studies show that the location of ester groups on a benzene core significantly changes the ability for clustering (hydration) of phthalate isomers to hydrate. The 1,2 position (DMP) of an ester group does not provide an accessible angle for hydrogen bonding to occur and does not allow for stable hydrate formation. The presence of phthalate esters on carbons 1 and 3 (DMIP) does however allow for the effective association of two water molecules. The [fully open] 1,4 isomer of phthalate esters (DMTP) effectively binds only one water molecule. These observations were also confirmed in our SIFT-MS studies. The effect of humidity on the ion chemistry is based on two main aspects. The first is the interaction of reagent ion with water molecules, forming water clusters of reagent ions which goes on to affect the ion chemistry. The second aspect is the presence of secondary reactions between products of primary reactions and water molecules. The effect of humidity on the ion chemistry was mainly studied for H_3O^+ reagent ions, where it has the most significant impact.

In our investigation we observed differences between the IMS and SIFT-MS ion chemistry, namely the formation of $(M\text{-}OR)^+$ (characteristic for CI and EI ionization not observed in IMS, presumably, due to the higher pressure). The effect of isomerization on the formation of phthalate hydrates for DMP, DMIP and DMTP has been explained using a computational DFT theoretical approach, showing that the energetic difference between individual states of hydration for *ortho* isomers is very small. Therefore, at a high number density of water molecules, the reaction equilibrium moves in favour of the dominant formation of protonated DMP. The remaining isomers have their energetic minima for the hydration process lower and therefore the formation of protonated hydrates is possible. Finally, we used KIMI simulations to clarify the reaction channels leading to the formation of protonated phthalate hydrates. We confirmed that the hydrates are formed through sequential association reactions of the protonated phthalate entity with water molecule, rather than via ligand switching reaction between hydronium hydrates and neutral phthalates. The presented work helps one to understand the ion chemistry of phthalates in SCIMS and reveals the additional possibilities of differentiating phthalate isomers using their secondary reactivity in the presence of water vapour.

4.3 Study of secondary ligand switching reactions of protonated acetic acid hydrates with acetone

Ligand switching reactions are important ionization mechanisms at atmospheric or near-atmospheric pressure and covers the IMS and SESI analytical techniques. The presence of such processes is crucial for analytical applications. If an analysed sample contains several neutral reactants, the primary ionization reactions between the reagent ions and neutral reactants may also be supplemented by secondary reactions (between the product ions of primary ionization channels and the remaining reactant neutrals). For example, a polar organic molecule, A, reacting via ligand switching with hydronium hydrates

$$\mathrm{H_3O^+(H_2O)_n + A \rightarrow AH^+(H_2O)_n + H_2O} \tag{76}$$

can additionally react with a second polar molecule, M, also via ligand switching, replacing A or forming a proton-bound mixed dimer:

$$\mathrm{AH^+(H_2O)_n + M \rightarrow MH^+(H_2O)_n + A} \tag{77a}$$

$$\mathrm{\rightarrow AH^+(M)(H_2O)_{n-1} + H_2O.} \tag{77b}$$

If the molecule, M, is abundant in the system, secondary ligand switching processes may lead to the replacement of A, forming a symmetrical dimer:

$$\mathrm{AH^+(M)(H_2O)_n + M \rightarrow MH^+M + A +} n\mathrm{H_2O.} \tag{78}$$

This processes clearly complicates analytical methods, decreasing selectivity and sensitivity of particular components in a sample.

Such an effect needs to be considered in SESI-MS studies of exhaled breath. Studies have shown that the concentration of acetic acid in exhaled breath is typically a hundred times lower than the concentration of acetone. [162, 257, 294] In the present work, we studied such effects, specifically looking at the secondary ligand switching reactions between acetic acid hydrates and acetone vapours. The study was carried out using the new generation of SIFDT-MS instrument, (developed at the J. Heyrovsky institute by Dr. Spesyvyi) equipped with an ion source capable of generating protonated hydrates of acetic acid (see Fig 8). In the experiment, hydrated and protonated acetic acid clusters, $CH_3COOH.H^+(H2O)_2$ were generated in the ion source and filtered via an injection filter. These ions were subsequently fragmented via a CID at the entrance of the drift tube, into the hydrated protonated acetic acid entity,

$CH_3COOH.H^+.H_2O$, by using a high kinetic transmission energy for $CH_3COOH.H^+(H2O)_2$ ions in the injection quadrupole. The drift tube operated at a low *E/N* = 14.2 Td was used to study the reaction of hydrated protonated acetic acid with acetone in the presence of a helium carrier gas (at a pressure of 1.9 mbar and temperature of 293 K). This complex experimental study was supplemented by the theoretical DFT calculations of individual protonated hydrates, as well as KIMI simulations of a proposed set of reactions.

This work has already been published and all details may be found in **Attachment A.5**. This case study demonstrates the possibility of instigating study ligand switching reactions in the SIFDT-MS. We also characterised specific ligand switching reactions between protonated acetic acid hydrates and acetone, relevant for breath analysis.

4.4 Real time detection of Arsene and Selene hydrides by SIFT-MS

SCIMS techniques are mainly used for real-time trace analysis of VOCs. However, SCIMS is not limited to only organic analytes, but may also be used for any compound reacting rapidly with one of the primary reagent ions (H_3O^+, NO^+ and O_2^+). In the present study, we investigated the possibility of being able to analyse the inorganic volatile species selenium hydride (SeH_2), arsenic hydride (AsH_3), monomethylarsane (CH_3AsH_2) and dimethylarsane ($(CH_3)_2AsH$). These are all relevant for the detection of Arsenic and Selenic elements in atomizers.

Atomization is a popular method for the trace element analysis of several elements (As, Se, Sb, Sn, …) and is conducted via the generation of volatile hydrides. [295] These are produced from an analyte in the liquid phase, using the reaction between tetrahydridoborate(-1) (TBH) and an acid. This achieves almost 100% conversion (in some cases). During the reaction, the analyte is released into the gaseous phase in form of a volatile hydride where it may be detected by various techniques. It is assumed that the relation between the active hydride species (for example MAs^V) and the volatile hydrides (for example CH_3AsH_2) is explicit (i.e. the specific hydride active species produce specific volatile hydrides). This argument was however questioned by Talmi and Bostick (1975), who suggested that the reaction may be pH dependent. [296]

Generated volatile hydrides are mainly detected by atomic absorption spectrometry. Consequently, volatile hydrides are often decomposed after their generation into atomic species using a quartz tube atomizer, heated up to 900 °C. [297, 298]. Besides standard atomization (decomposing volatiles by heat), plasma dielectric barrier discharge (DBD) atomizers may also be used [299]. In the present study, the SIFT-MS was used to analyse the formation and atomization of selected hydrides in a DBD atomizer. This study was conducted in cooperation with the Institute of Analytical Chemistry of the Czech Academy of Science.

Aside to the volatile hydrides generated from a liquid solution, several other molecules are present in the sample as well: hydrogen gas as a by-product of hydride generation; argon as a carrier gas; water vapour from the sample solution and traces of oxygen penetrating into the generator gas lines. To reduce sample humidity for arsene hydrides, NaOH pellets were introduced into the sample gas line. For selenium hydrides, dryers however cannot be applied, as selenium hydrides, compared to arsenic hydrides, are affected by the presence of a drying agent. The presence of hydrogen gas in the atomizer is crucial as it reacts together with traces of oxygen within the plasma, to produce water. Water consequently influences the property of the DBD discharge, affecting the atomization.

In our study, we first confirmed the formation of the protonated hydrides of all the studied species, in our SIFT-MS. Secondly, we analysed the concentration of the protonated hydrides in the DBD atomizer, together with the formation of secondary products (predominantly H_2O). Finally, we introduced an excess of oxygen gas into the sample to characterize the effect of H_2O on the atomization process in the DBD. As the study has also already been published, all details surrounding this work may be found in **Attachment A.6**.

The present study shows a new application of SCIMS, which goes beyond the detection and analysis of VOCs. We have shown that SIFT-MS, as well as all other SCIMS techniques, may be implemented in the analytical applications of inorganic chemistry. This may either be conducted by direct (or indirect) analysis of inorganic volatile compounds (helping us to understand established analytical procedures, such as atomization).

Conclusion

In conclusion, this thesis discusses the ion chemistry processes used for trace gas analysis carried out by CI-MS techniques, operating in the mbar pressure range. The focus was to understand the limitations of SCIMS techniques; mainly on the aspects of reduced selectivity and sensitivity. Besides many positives (such as high sensitivity, a large dynamic range and a real-time response for most of the VOCs detected), the SCIMS techniques demonstrate limited ability to conduct selective analysis of isomeric molecules. Additionally, water vapour present in the reaction chamber of the instruments (introduced by sample humidity) may reduce sensitivity and selectivity of the analytes, via the secondary reactions of water molecules with ions.

The main objectives of the thesis were to analyse the limitations of these techniques which reduced the sensitivity and selectivity of the SCIMS methods, via the study of complex ion chemistry. This work predominantly focused on secondary reactions with water. Additionally, we aimed to provide a mathematical description of the associated primary and secondary reactions which made it capable to predict the behaviour of the relative ion signals. The mathematical description will be supplemented by an experimental study of complex ion-molecular reactions relevant to typical SCIMS applications (such as breath analysis, environmental science etc.). Finally, we aimed to investigate the new possible applications for SCIMS analysis.

We first presented a unique combination of a fast GC pre-separation unit, coupled to a SIFT-MS experiment. This set-up was developed to try and improve the analytical selectivity of monoterpenes; common isomers in investigated in atmospheric chemistry when studying the formation of secondary organic aerosol; and air quality. In this work, we combined a fast-chromatographic separation technique with the SIFT-MS. As a result, we identified individual isomers of the monoterpene family in under 45 s, using an MXT-1 metallic column in association with the calculation for the ion ratio of the two product ion pairs, generated by H_3O^+ (*m/z* 137 / *m/z* 81) and NO^+ (*m/z* 136 / *m/z* 93). The relative intensities of the fragment ions were shown to be characteristic for the individual monoterpenes. However, we also found that the sample flow rate from the GC column (< 4 sccm) is not sufficient to achieve a sub-ppbv detection limit, which is commonly achieved by fast GC PTR-MS. Interestingly, we also noticed that water vapour has a retention time which is much lower compared to the VOCs detected the samples that we ran. Therefore, fast GC may potentially be used to separate VOCs from sample humidity. This may therefore be a welcomed benefit to the field as water vapour often influences the ion chemistry within these CIMS techniques. In addition, a high humidity within the instrument reduces the selectivity and sensitivity of the methods.

The experimental and mathematical studies conducted of the influence of water vapour on the ion chemistry of the discussed techniques makes-up the main body of this work. We first developed a numerical simulation for the computational investigation of ion-molecule reactions (KIMI) and carried out two sets of experiments. In these experiments we focused on understanding the secondary reactions of product ions with water (the study of the ion chemistry of glyoxal and phthalates).

KIMI is a simple numerical simulator capable of mathematically describing complex reaction systems. The simulator solves a set of differential equations based on a proposed reaction system along the axis of the reactor using the classical Runge-Kutta algorithm. Therefore, KIMI is capable of simulating the ion chemistry which occurs within the SIFT-MS, PTR-MS as well as the SIFDT-MS instruments. To demonstrate its functionality, KIMI was first tested on several simple and well understood reaction systems(i.e. acetone and alcohols), where we observed changes in the product ion distribution. On successfully simulating this chemistry, we later used our KIMI program to investigate more complex reaction systems.

The glyoxal study was divided into two sections. The first part describes the ion chemistry and the associated secondary reactions with water vapour in a flow tube (where we identified the water induced generation of protonated formaldehyde). The second section describes a similar situation for the drift tube, where protonated formaldehyde is also generated; via CID. The aim of the of the drift tube study was to explain the changes in the relative ratios of the main product ions to the protonated formaldehyde and protonated glyoxal ions. Using several experimental techniques together with KIMI, we identified the secondary reactions responsible for the observed changes (primarily induced via secondary reverse proton transfer reactions).

In the study of phthalates, our objective was to describe the ion chemistry of selected phthalates with H_3O^+, NO^+ and O_2^+ reagent ions (as well as the secondary reactions of selected protonated phthalates, with water vapour). The list of selected phthalates included the DMP, DMIP and DMTP isomers. These were chosen to study the effect of varying the position and length of the substituents around the benzene ring on the ion chemistry. The length of the phthalate substituent prominently affects the ion chemistry of charge transfer reactions via the opening of a new rearrangement channel leading to the formation of $(M-(R-2H))^+$ products. The secondary reactions (with water molecules) were also studied for the protonated phthalate molecules. We have demonstrated that protonated phthalates in the *ortho* position do not form hydrides. For the isomers with *meta* and *para* geometries, however, phthalates form hydrides very effectively. For the DMTP isomer, we detected the association of one H_2O molecule to the analyte ion. For DMIP, we detected the clustering of a second H_2O molecule. The hydration does not continue to form any larger clusters, as a strong potential minimum exist only for the specific DMTP and DMIP structures. Finally, we used KIMI to confirm that the protonated phthalate hydrates in the flow tube were formed via the association of water molecules on the protonated phthalate, rather than via ligand switching of the H_2O molecules with hydrated hydronium.

The initial product ions may however (additional to analyte) also react with other abundant neutral molecules in secondary reactions. Subsequently, we studied such reactions between protonated acetic acid hydrates and acetone. This reaction system is interesting as both acetic acid and acetone are abundant and analytically important components in breath analysis. In breath analysis carried out by SESI-MS or IMS techniques in the near-to-atmospheric pressure region of conditions, ion hydrates are formed frequently. As we have shown, hydrates of protonated acetic acid (reflecting the concentration of acetic acid in the sample) undergo secondary ligand switching reactions with acetone. This process leads to the fast formation of the asymmetric proton-bounded dimer $(CH_3COCH_3)H^+(CH_3COOH)$ and ultimately the production of the strongly bound protonated-acetone dimer. This reaction sequence was also simulated using KIMI. This study clearly demonstrates that the presence of highly abundant polar compounds in SESI-MS and IMS may negatively affect the accuracy of quantification of other analytes at low concentrations.

In summary, the presence of secondary reactions complicates the identification and quantification of absolute concentrations of species in SCIMS techniques. The most abundant cause of secondary reactions are water molecules, resulting from sample humidity. Water molecules react with product ions via several secondary reaction channels. In the present work, we identified three secondary reaction channels which were seen to be the most detrimental to accurate analysis of species when using SCIMS techniques:

1. Three-body association reactions forming ion hydrates of both reagent and product ions (Eq. 56).

2. Reverse proton transfer reactions between product ions (or their hydrates) and water molecules (Eq. 59).

3. Reaction channels between product ions and water molecules, producing new and unexpected ions.

The last point reflects the most interesting part of the ion chemistry. An example of point 3 is the formation of protonated formaldehyde from protonated glyoxal via a series of water assisted reactions; or secondary formation of protonated phthalate while using NO^+ reagent ions, via the reaction:

$$\mathrm{M.NO^+ + H_2O \rightarrow MH^+ + HONO.} \tag{79}$$

Additionally, secondary reactions are not only induced by water vapour, but also by other molecules present at sufficiently high concentrations in the reaction chamber. (see study of secondary ligand switching reactions of protonated acetic acid hydrates with acetone, section 4.3).

The effect of the secondary reactions may be minor, but also significant, depending on the analytical situation. So far, we are able to identify three different approaches to reduce the impact of secondary reactions on analysis. The first approach is to carefully increase the effective temperature of the gases in the flow tube (as for example in PTR-MS or SIFDT-MS), as to reduce the formation of ion hydrates. This may however induce both a reverse proton transfer reaction as well as a new reaction channel (as we observed in the glyoxal study). The second approach is to remove the humidity from the sample (either via filters or via pre-separation using the fast GC technique we developed). This however reduces the speed of SCIMS as well as limits its sensitivity. The last approach is an understanding the water-based ion chemistry. This however requires a careful and systematic; theoretical and experimental study of complex reaction systems.

In the final study we pioneered the possibility of using SCIMS for the analysis of inorganic volatile hydrides, produced during atomization. The process of atomization is used to quantify the absolute concentrations of inorganic species of germanium, arsenic, tin etc., primarily in solid samples. The inorganic species are in controlled environments; chemically converted into hydrides. Volatile hydrides are then atomized using a quartz tube or discharge-based atomizers; and are detected via atomic absorption spectrometry. In this study, we investigated the possibility of detecting selected hydrides of selenium and arsenic using SIFT-MS which has in-turn helped us to understand the process of atomisation in dielectric barrier discharge (DBD) under various conditions, much better. The focus of this study was to analyse non-atomised hydrides and subsequently evaluate the effectivity of the atomization process. We have shown that the hydrides are not always atomised; but are often decomposed in the DBD. Additionally, atomization is affected by humidity which is delivered to the atomizer from the sample or is formed in the atomizer via the by-reaction of residual hydrogen and oxygen. The possibility of SCIMS to detect non-atomised hydrides as well as humidity levels is of high interest.

The presented work fulfils the defined objectives of the thesis, as well as the aims of the IMPACT project. The obtained results reported in this thesis have been frequently presented at conferences on the national and international stage. So far, our results have led to the production of 5 high-impact publications; and more publications based on these works are expected to be published soon. The KIMI simulator is still under development but may already be used to assist with ion-molecule interaction research. We believe that the knowledge gained from this work will help to improve the application of current as well as future SCIMS technologies.

List of Tables and Figures

	length l_r, from the injection point up until the end of the flow tube, where neutrals are separated from the ions. Ion-neutral reactions take place along the reaction length (in the flow tube).
Figure 5	A scheme showing the PTR-MS instrument. [144]
Figure 6	Relative intensity of hydrated hydronium clusters $H_3O^+(H_2O)_n$, n = 0,1,2,3 in PTR-MS determined for various E/N values for a sample containing 0.6% humidity (absolute).
Figure 7	The SIFDT-MS instrument; the initial concept. [39]
Figure 8	The SIFDT-MS instrument; the final design. [153] The coloured areas represent individual pressure regions: 5 mbar (yellow), 0.3 mbar (violet), 5×10^{-6} mbar (blue), 1.9 mbar (pink). HC - hollow cathode ion source, SRIG – stacked ring ion guide, OP - octupole, QMF - quadrupole mass filter, VI - Venturi inlet, VDT - Venturi flow-drift tube, GG - gating grid, DTR - drift tube reactor, SNC - ion sampling nose cone, QMA - quadrupole mass analyser, EM - electron multiplier with conversion
Figure 9	Illustrative reaction diagram of primary and secondary reactions of H_3O^+ with neutral a reactant, M, in the presence of water vapour. [263] Solid line reactions represent moderate humidity levels. Dashed reactions represent saturated water vapour.
Figure 10	Photograph of a fast GC unit built for the study of individual monoterpenes in gaseous mixtures.
Figure 11	A schematic view of the KIMI main programs and their functionalities.
Figure 12	Resource manager responsible for management of individual species within the simulation.
Figure 13	The calculation properties window responsible for the management of physical properties and geometries within the simulation.
Figure 14	The Calculation properties window is responsible for the management of physical properties and geometry of simulation.

Figure 15 Calculation control window.

Figure 16 A visualisation of the transformation process. The main reaction object (left) is transformed into a series of calculation objects (left). The new objects are later used by Calculation class to calculate a single step numerical solution of differential kinetic equations.

Figure 17 Initial simulation of the formation of hydronium hydrates. Experimental data (in symbols) were interpolated by the set of reactions listed in Table 3.

Figure 18 An initial simulation of acetone's ion chemistry under the experimental conditions described in the text. Experimental data (in symbols) were interpolated by the set of reactions shown in Figure 19.

Figure 19 Schematic visualization of acetone ion chemistry simulated by KIMI. Three body association reactions behave as effective two-body reactions (at a helium number density of [He] = 3.6×10^{16} cm^{-3}). All rate coefficients are in cm^3s^{-1}.

Figure 20 Initial simulation of NO^+ ion chemistry with ethanol. Experimental data (presented as symbols) were interpolated by the set of reactions shown in Table 4.

List of Abbreviations

APCI	Atmospheric Pressure Chemical Ionization
BDE	Bound Dissociation Energy
CI	Chemical Ionization
CID	Collision Induced Dissociation
CI-MS	Chemical Ionization Mass Spectrometry
DBD	Dielectric Barrier Discharge
DFT	Density Functional Theory
EI-MS	Electron Ionization Mass Spectrometry
FA	Flowing Afterglow
FAIMS	Field Asymmetric Ion Mobility Spectrometry
FDT	Flow-Drift Tube
GC-MS	Gas Chromatography Mass Spectrometry
HIKE-IMS	High Kinetic Energy Ion Mobility Spectrometry
IMS	Ion Mobility Spectrometry
NOAA	National Oceanic and Atmospheric Administration
ppb	parts-per-billion
ppm	parts-per-million
ppq	parts-per-quadrillion
ppt	parts-per-trillion
PTR-MS	Proton Transfer Reaction Mass Spectrometry
SCIMS	Soft Chemical Ionization Mass Spectrometry
SESI	Secondary Electrospray Ionization
SIFDT-MS	Selected Ion Flow-Drift Tube Mass Spectrometry

SIFT	Selected Ion Flow Tube
SIFT-MS	Selected Ion Flow Tube Mass Spectrometry
SRIG	Stacked Ring Ion Guide
ToF-MS	Time-of-Flight Mass Spectrometry
VOCs	Volatile Organic Compounds

List of publications

Lacko M, Wang N, Sovová K, Pásztor P, Španěl P.
Addition of fast gas chromatography to selected ion flow tube mass spectrometry for analysis of individual monoterpenes in mixtures.
Atmospheric Measurement Techniques. 2019. 12(9): 4965-82.

Lacko M, Piel F, Mauracher A, Španěl P.
Chemical ionization of glyoxal and formaldehyde with H_3O^+ ions using SIFT-MS under variable system humidity.
Physical Chemistry Chemical Physics. 2020. 22(18): 10170-10178

Lacko M, Michalczuk B, Matejčík Š, Španěl P.
Ion chemistry of phthalates in selected ion flow tube mass spectrometry: isomeric effects and secondary reactions with water vapour.
Physical Chemistry Chemical Physics. 2020. 22(28): 16345-52.

Spesyvyi A, **Lacko M**, Dryahina K, Smith D, Španěl P.
Ligand Switching Ion Chemistry: An SIFDT Case Study of the Primary and Secondary Reactions of Protonated Acetic Acid Hydrates with Acetone.
Journal of the American Society for Mass Spectrometry. 2021. 32(8): 2251-60.

Kratzer J, **Lacko M**, Dryahina K, Matoušek T, Španěl P, Dědina J.
Atomization of As and Se volatile species in a dielectric barrier discharge atomizer after hydride generation: Fate of analyte studied by selected ion flow tube mass spectrometry.
Analytica chimica acta. 2022. 1190: 339256.

Bibliography

1. Swings, P. and L. Rosenfeld, *Considerations Regarding Interstellar Molecules.* The Astrophysical Journal, 1937. **86**: p. 483-486.
2. McKellar, A., *Evidence for the Molecular Origin of Some Hitherto Unidentified Interstellar Lines.* Publications of the Astronomical Society of the Pacific, 1940. **52**: p. 187.
3. Dalgarno, A. and J. Black, *Molecule formation in the interstellar gas.* Reports on Progress in Physics, 1976. **39**(6): p. 573.
4. Herbst, E. *Molecular ions in interstellar reaction networks*. in *Journal of Physics: Conference Series*. 2005. IOP Publishing.
5. Glosık, J., et al., *The recombination of* H_3^+ *ions with electrons: dependence on partial pressure of* H_2*.* Chemical Physics Letters, 2000. **331**(2-4): p. 209-214.
6. Adams, N.G. and L.M. Babcock, *Advances in gas phase ion chemistry*. Vol. 3. 1998, Greenwich, London: JAI PRESS.
7. Johnson, C.Y., E.B. Meadows, and J.C. Holmes, *Ion composition of the arctic ionosphere.* Journal of Geophysical Research, 1958. **63**(2): p. 443-444.
8. Dickinson, P.H.G. and J. Sayers, *Ion Charge Exchange Reactions in Oxygen Afterglows.* Proceedings of the Physical Society, 1960. **76**(1): p. 137-148.
9. Sayers, J. and D. Smith. *Ion-atom interchange processes*. in *Proc. IIIrd int. conf. on the physics of electronic and atomic collisions*. 1964. Amsterdam.
10. McDaniel, E.W., et al., *Ion-Molecule reactions*. 1970, New York: Wiley.
11. Schmeltekopf, A., et al., *Reaction of atomic oxygen ions with vibrationally excited nitrogen molecules.* Planetary and Space Science, 1967. **15**(3): p. 401-406.
12. Ferguson, E., F. Fehsenfeld, and A. Schmeltekopf, *Flowing afterglow measurements of ion-neutral reactions*, in *Advances in atomic and molecular physics*. 1969, Elsevier. p. 1-56.
13. Bohme, D., in *Interactions between ions and molecules*, P. Ausloos, Editor. 1975, Plenum Press: New York. p. 489-504.
14. Howard, C.J., H.W. Rundle, and F. Kaufman, *Water cluster formation rates of NO+ in He, Ar, N2, and O2 at 296 K.* The Journal of Chemical Physics, 1971. **55**(10): p. 4772-4776.

15. Bolden, R. and N. Twiddy, *A flowing afterglow study of water vapour.* Faraday Discussions of the Chemical Society, 1972. **53**: p. 192-200.

16. Bierbaum, V., M. Golde, and F. Kaufman, *Flowing afterglow studies of hydronium ion clustering including diffusion effects.* The Journal of Chemical Physics, 1976. **65**(7): p. 2715-2724.

17. Liddy, J., C. Freeman, and M. McEwan, *Reactions of* H_3^+ *with XCN where X= H,* CH_3*, Cl, Br, I and CN.* International Journal of Mass Spectrometry and Ion Physics, 1977. **23**(2): p. 153-161.

18. McFarland, M., et al., *Flow‐drift technique for ion mobility and ion‐molecule reaction rate constant measurements. I. Apparatus and mobility measurements.* The Journal of Chemical Physics, 1973. **59**(12): p. 6610-6619.

19. McFarland, M., et al., *Flow‐drift technique for ion mobility and ion‐molecule reaction rate constant measurements. II. Positive ion reactions of* N^+*,* O^+*, and* H_2^+ *with* O_2 *and* O^+ *with* N_2 *from thermal to 2 eV.* The Journal of chemical physics, 1973. **59**(12): p. 6620-6628.

20. McFarland, M., et al., *Flow‐drift technique for ion mobility and ion‐molecule reaction rate constant measurements. III. Negative ion reactions of* O^- *with CO, NO,* H_2*, and* D_2*.* The Journal of Chemical Physics, 1973. **59**(12): p. 6629-6635.

21. Albritton, D., et al., *Effects of ion speed distributions in flow‐drift tube studies of ion‐neutral reactions.* The Journal of Chemical Physics, 1977. **66**(2): p. 410-421.

22. Adams, N. and D. Smith, *The selected ion flow tube (SIFT); a technique for studying ion-neutral reactions.* International Journal of Mass Spectrometry and Ion Physics, 1976. **21**(3-4): p. 349-359.

23. Smith, D. and N. Adams, *The selected ion flow tube (SIFT): studies of ion-neutral reactions.* Advances in atomic and molecular physics, 1988. **24**: p. 1-49.

24. Albritton, D., *Ion-neutral reaction-rate constants measured in flow reactors through 1977.* Atomic data and nuclear data tables, 1978. **22**(1): p. 1-89.

25. Ikezoe, Y., S. Matsuoka, and M. Takebe, *Gas phase ion-molecule reaction rate constants through 1986*. 1987: Ion reaction research group of the Mass spectroscopy society of Japan.

26. Fehsenfeld, F.C., in *Interactions between Ions and Molecules*, P. Ausloos, Editor. 1975, Plenum Press: New York. p. 387-412.

27. Smith, D. and N.G. Adams, *Elementary plasma reactions of environmental interest*, in *Plasma Chemistry I.* 1980, Springer. p. 1-43.

28. Smith, D. and P. Spanel, *Studies of interstellar ion reactions using the SIFT technique: isotope fractionation.* Accounts of chemical research, 1992. **25**(9): p. 414-420.

29. Smith, D. and P. Spanel, *Ions in the terrestrial atmosphere and in interstellar clouds.* Mass Spectrometry Reviews, 1995. **14**(4‐5): p. 255-278.

30. Smith, D. and N. Adams, *Elementary interactions between charged and neutral species in plasmas.* Pure and Applied Chemistry, 1984. **56**(2): p. 175-188.

31. Eiceman, G.A., *Advances in ion mobility spectrometry: 1980–1990.* Critical Reviews in Analytical Chemistry, 1991. **22**(1-2): p. 471-490.

32. Lindinger, W., J. Hirber, and H. Paretzke, *An ion/molecule-reaction mass spectrometer used for on-line trace gas analysis.* International journal of mass spectrometry and ion processes, 1993. **129**: p. 79-88.

33. Phillips, M., *Breath tests in medicine.* Scientific American, 1992. **267**(1): p. 74-79.

34. Smith, D. and P. Španěl, *Application of ion chemistry and the SIFT technique to the quantitative analysis of trace gases in air and on breath.* International Reviews in Physical Chemistry, 1996. **15**(1): p. 231-271.

35. Španěl, P. and D. Smith, *Selected ion flow tube: a technique for quantitative trace gas analysis of air and breath.* Medical and Biological Engineering and Computing, 1996. **34**(6): p. 409-419.

36. Španěl, P. and D. Smith, *A selected ion flow tube study of the reactions of* NO^+ *and* O_2^+ *ions with some organic molecules: The potential for trace gas analysis of air.* The Journal of chemical physics, 1996. **104**(5): p. 1893-1899.

37. Smith, D. and P. Španěl, *Selected ion flow tube mass spectrometry (SIFT‐MS) for on‐line trace gas analysis.* Mass spectrometry reviews, 2005. **24**(5): p. 661-700.

38. Lagg, A., et al., *Applications of proton transfer reactions to gas analysis.* International Journal of Mass Spectrometry and Ion Processes, 1994. **134**(1): p. 55-66.

39. Spesyvyi, A., D. Smith, and P. Španěl, *Selected ion flow-drift tube mass spectrometry: quantification of volatile compounds in air and breath.* Analytical chemistry, 2015. **87**(24): p. 12151-12160.

40. Niessen, W., *Atmospheric pressure ionization in mass spectrometry*, in *Encyclopaedia of spectroscopy and spectrometry*, T.G. Lindon JC, Holmes JL, Editor. 1999, Academic Press: London.

41. Lichvanova, Z., et al., *Using corona discharge-ion mobility spectrometry for detection of 2,4,6-Trichloroanisole.* Talanta, 2014. **127**: p. 239-43.

42. Sabo, M., et al., *Atmospheric pressure corona discharge ionisation and ion mobility spectrometry/mass spectrometry study of the negative corona discharge in high purity oxygen and oxygen/nitrogen mixtures.* International Journal of Mass Spectrometry, 2010. **293**(1-3): p. 23-27.

43. Wu, C., W.F. Siems, and H.H. Hill, *Secondary electrospray ionization ion mobility spectrometry/mass spectrometry of illicit drugs.* Analytical chemistry, 2000. **72**(2): p. 396-403.

44. Field, F.H., *Chemical ionization mass spectrometry.* Accounts of Chemical Research, 1968. **1**(2): p. 42-49.

45. Langevin, M. *Une formule fondamentale de théorie cinétique*. in *Annales de chimie et de physique, Series*. 1905.

46. Jones, J.E., *On the determination of molecular fields.—II. From the equation of state of a gas.* Proceedings of the Royal Society of London. Series A, Containing Papers of a Mathematical and Physical Character, 1924. **106**(738): p. 463-477.

47. Gioumousis, G. and D.P. Stevenson, *Reactions of gaseous molecule ions with gaseous molecules. V. Theory.* The Journal of Chemical Physics, 1958. **29**: p. 294-299.

48. Moran, T.F. and W.H. Hamill, *Cross Sections of Ion‐Permanent‐Dipole Reactions by Mass Spectrometry.* The Journal of Chemical Physics, 1963. **39**(6): p. 1413-1422.

49. Su, T. and M.T. Bowers, *Ion-polar molecule collisions: the effect of ion size on ion-polar molecule rate constants; the parameterization of the average-*

dipole-orientation theory. International Journal of Mass Spectrometry and Ion Physics, 1973. **12**(4): p. 347-356.

50. Bass, L., et al., *Ion-polar molecule collisions. A modification of the average dipole orientation theory: The cos θ model.* Chemical Physics Letters, 1975. **34**(1): p. 119-122.
51. Su, T. and M.T. Bowers, *Parameterization of the average dipole orientation theory: temperature dependence.* International Journal of Mass Spectrometry and ion processes, 1975. **17**: p. 211-212.
52. Ellis, A.M. and C.A. Mayhew, *Proton transfer reaction mass spectrometry: principles and applications*. 2013: John Wiley & Sons.
53. Chesnavich, W.J., T. Su, and M.T. Bowers, *Collisions in a noncentral field: a variational and trajectory investigation of ion–dipole capture.* The Journal of Chemical Physics, 1980. **72**(4): p. 2641-2655.
54. Su, T. and W.J. Chesnavich, *Parametrization of the ion–polar molecule collision rate constant by trajectory calculations.* The Journal of Chemical Physics, 1982. **76**(10): p. 5183-5185.
55. Zhao, J. and R. Zhang, *Proton transfer reaction rate constants between hydronium ion (H_3O^+) and volatile organic compounds.* Atmospheric Environment, 2004. **38**: p. 2177-2185.
56. Bowers, M.T. and D.D. Elleman, *Thermal energy charge transfer reactions of rare-gas ions to methane, ethane, propane, and silane. The importance of franck-condon factors.* Chemical Physics Letters, 1972. **16**(3): p. 486-491.
57. NIST. *NIST WebBook Chemie, NIST Standard Reference Database Number 69*. Available from: http://webbook.nist.gov/chemistry/.
58. Bohme, D.K., G.-I. Mackay, and H. Schiff, *Determination of proton affinities from the kinetics of proton transfer reactions. VII. The proton affinities of O_2, H_2, Kr, O, N_2, Xe, CO_2, CH_4, N_2O, and CO.* The Journal of Chemical Physics, 1980. **73**(10): p. 4976-4986.
59. Lindinger, W., A. Hansel, and A. Jordan, *On-line monitoring of volatile organic compounds at pptv levels by means of proton-transfer-reaction mass spectrometry (PTR-MS) medical applications, food control and environmental research.* International Journal of Mass Spectrometry and Ion Processes, 1998. **173**(3): p. 191-241.

60. Adams, N.G., et al., *Selected ion flow tube study of* NH_4^+ *association and of product switching reactions with a series of organic molecules.* International Journal of Mass Spectrometry, 2003. **223**: p. 459-471.

61. Blake, R.S., et al., *Chemical ionization reaction time-of-flight mass spectrometry: Multi-reagent analysis for determination of trace gas composition.* International Journal of Mass Spectrometry, 2006. **254**(1-2): p. 85-93.

62. Field, F. and F. Lampe, *Reactions of gaseous ions. VI. Hydride ion transfer reactions.* Journal of the American Chemical Society, 1958. **80**(21): p. 5587-5592.

63. Španěl, P. and D. Smith, *SIFT studies of the reactions of* H_3O^+, NO_+ *and* O_2^+ *with several ethers.* International journal of mass spectrometry and ion processes, 1998. **172**(3): p. 239-247.

64. Španěl, P., Y. Ji, and D. Smith, *SIFT studies of the reactions of* H_3O^+, NO_+ *and* O_2^+ *with a series of aldehydes and ketones.* International journal of mass spectrometry and ion processes, 1997. **165**: p. 25-37.

65. Španěl, P. and D. Smith, *Selected ion flow tube studies of the reactions of* H_3O^+, NO_+ *and* O_2^+ *with several amines and some other nitrogen-containing molecules.* International Journal of Mass Spectrometry, 1998. **176**(3): p. 203-211.

66. Spanel, P. and D. Smith, *SIFT studies of the reactions of* H_3O^+, NO_+ *and* O_2^+ *with a series of alcohols.* International journal of mass spectrometry and ion processes, 1997. **167**: p. 375-388.

67. Španěl, P., T. Wang, and D. Smith, *A selected ion flow tube, SIFT, study of the reactions of* H_3O^+, NO_+ *and* O_2^+ *ions with a series of diols.* International Journal of Mass Spectrometry, 2002. **218**(3): p. 227-236.

68. Ŝpaněl, P. and D. Smith, *SIFT studies of the reactions of* H_3O^+, NO_+ *and* O_2^+ *with a series of volatile carboxylic acids and esters.* International journal of mass spectrometry and ion processes, 1998. **172**(1-2): p. 137-147.

69. Harrison, A.G., *Chemical ionization mass spectrometry*. 1992: Routledge.

70. Lau, Y., S. Ikuta, and P. Kebarle, *Thermodynamics and kinetics of the gas-phase reactions* $H_3O^+ (H_2O)_{n-1}$ + *water=* $H_3O^+(H_2O)_n$. Journal of the American Chemical Society, 1982. **104**: p. 1462-1469.

71. Španěl, P., et al., *Analysis of formaldehyde in the headspace of urine from bladder and prostate cancer patients using selected ion flow tube mass spectrometry.* Rapid communications in mass spectrometry, 1999. **13**(14): p. 1354-1359.

72. Lacko, M., et al., *Chemical ionization of glyoxal and formaldehyde with* H_3O^+ *ions using SIFT-MS under variable system humidity.* Phys. Chem. Chem. Phys., 2020. 22(18): 10170-10178

73. Bowers, M.T., *Gas phase ion chemistry, Volume 1.* Vol. 1. 1979: Academic Press.

74. Linden, F., et al., *Is the Reaction of* $C3N^-$ *with* C_2H_2 *a Possible Process for Chain Elongation in Titan's Ionosphere?* The Journal of Physical Chemistry A, 2016. **120**(27): p. 5337-5347.

75. Zymak, I., et al., *Experimental study of the reaction of* O^- *ions with* CO_2 *molecules with different ternary gases at temperatures relevant to the Martian ionosphere.* Icarus, 2020. **354**: p. 114057.

76. Zymak, I., et al., *Experimental study of the reaction of* $NO2^-$ *ions with* CO_2 *molecules at temperatures and energies relevant to the Martian atmosphere.* Icarus, 2020. **335**: p. 113416.

77. Kebarle, P. and S. Chowdhury, *Electron affinities and electron-transfer reactions.* Chemical Reviews, 1987. **87**(3): p. 513-534.

78. Laramee, J., B. Arbogast, and M. Deinzer, *Electron capture negative ion chemical ionization mass spectrometry of 1, 2, 3, 4-tetrachlorodibenzo-p-dioxin.* Analytical chemistry, 1986. **58**(14): p. 2907-2912.

79. Mackay, G., et al., *Rate constants at 297. degree. K for proton-transfer reactions with hydrocyanic acid and acetonitrile. Comparisons with classical theories and exothermicity.* The Journal of Physical Chemistry, 1976. **80**(26): p. 2919-2922.

80. Ellis, H., et al., *Transport properties of gaseous ions over a wide energy range.* Atomic data and nuclear data tables, 1976. **17**(3): p. 177-210.

81. Ellis, H., et al., *Transport properties of gaseous ions over a wide energy range. Part II.* Atomic data and nuclear data tables, 1978. **22**(3): p. 179-217.

82. Ellis, H.W., et al., *Transport properties of gaseous ions over a wide energy range. Part III.* Atomic Data and Nuclear Data Tables, 1984. **31**(1): p. 113-151.

83. Wannier, G.H., *Motion of gaseous ions in strong electric fields.* The Bell System Technical Journal, 1953. **32**(1): p. 170-254.

84. Viehland, L.A. and E. Mason, *Statistical–mechanical theory of gaseous ion–molecule reactions in an electrostatic field.* The Journal of Chemical Physics, 1977. **66**(2): p. 422-434.

85. Su, T., *Parametrization of kinetic energy dependences of ion–polar molecule collision rate constants by trajectory calculations.* The Journal of chemical physics, 1994. **100**(6): p. 4703-4703.

86. Su, T., A. Viggiano, and J.F. Paulson, *The effect of the dipole‐induced dipole potential on ion‐polar molecule collision rate constants.* The Journal of chemical physics, 1992. **96**(7): p. 5550-5551.

87. Bei, H.C., P.K. Bhowmik, and T. Su, *Trajectory calculations of high temperature and kinetic energy dependent ion–polar molecule collision rate constants.* The Journal of chemical physics, 1989. **90**(12): p. 7046-7049.

88. Schmeltekopf, A., E. Ferguson, and F. Fehsenfeld, *Afterglow studies of the reactions* He^+*, He (23S), and* O^+ *with vibrationally excited N2.* The Journal of Chemical Physics, 1968. **48**(7): p. 2966-2973.

89. Bowers, M., et al., *Temperature dependence of ion-molecule collision phenomena: An application of ion cyclotron resonance spectroscopy to the determination of reactive and momentum transfer rate constants.* International Journal of Mass Spectrometry and Ion Physics, 1977. **25**(1): p. 103-116.

90. Dunkin, D., et al., *Ion–Molecule Reaction Studies from 300° to 600° K in a Temperature‐Controlled Flowing Afterglow System.* The Journal of Chemical Physics, 1968. **49**(3): p. 1365-1371.

91. Meot-Ner, M. and F. Field, *Temperature dependences of some fast ion-polar molecule proton transfer and of slow hydride (1-) ion transfer reactions.* Journal of the American Chemical Society, 1975. **97**(8): p. 2014-2017.

92. Lindinger, W., et al., *Translational and internal energy dependences of some ion–neutral reactions.* The Journal of Chemical Physics, 1975. **63**(5): p. 2175-2181.

93. Smith, D. and R. Fouracre, *The temperature dependence of the reaction rate coefficients of* O^+ *ions with molecular oxygen and nitrogen.* Planetary and Space Science, 1968. **16**(2): p. 243-252.

94. Ferguson, E., et al., *Temperature dependence of slow ion–atom interchange reactions.* The Journal of Chemical Physics, 1969. **50**(11): p. 5039-5040.

95. Kebarle, P., *Ion thermochemistry and solvation from gas phase ion equilibria.* Annual Review of Physical Chemistry, 1977. **28**(1): p. 445-476.

96. Pierce, R.C. and R.F. Porter, *Low-temperature chemical ionization mass spectrometry of methane-hydrogen mixtures.* The Journal of Physical Chemistry, 1974. **78**(2): p. 93-97.

97. Abramson, F.P. and J.H. Futrell, *Ion—Molecule Reactions of Methane.* The Journal of Chemical Physics, 1966. **45**(6): p. 1925-1931.

98. Good, A., D.A. Durden, and P. Kebarle, *Ion–molecule reactions in pure nitrogen and nitrogen containing traces of water at total pressures 0.5–4 Torr. Kinetics of clustering reactions forming H+ (H2O) n.* The Journal of Chemical Physics, 1970. **52**(1): p. 212-221.

99. Meot‐Ner, M. and F. Field, *Thermal transitions between collisionally and tight‐complex limited kinetics in the gas phase. Reactions involving carbonium ions.* The Journal of Chemical Physics, 1976. **64**(1): p. 277-281.

100. Perez-Benito, J.F., *Some considerations on the fundamentals of chemical kinetics: steady state, quasi-equilibrium, and transition state theory.* Journal of Chemical Education, 2017. **94**(9): p. 1238-1246.

101. Kassel, L.S., *Studies in homogeneous gas reactions. I.* The Journal of Physical Chemistry, 2002. **32**(2): p. 225-242.

102. Marcus, R.A., *Unimolecular dissociations and free radical recombination reactions.* The Journal of Chemical Physics, 1952. **20**(3): p. 359-364.

103. Callear, A., *Basic RRKM Theory.* Comprehensive Chemical Kinetics, 1983. **24**: p. 333-356.

104. Skinner, G.B. and B. Rabinovitch, *Comparisons of the RRK [Rice-Ramsperger-Kassel] and RRKM [Markus-Rice] theories of thermal unimolecular reaction. Energy distributions and the s parameter.* The Journal of Physical Chemistry, 1972. **76**(17): p. 2418-2424.

105. Durup‐Ferguson, M., et al., *Enhancement of charge‐transfer reaction rate constants by vibrational excitation at kinetic energies below 1 eV.* The Journal of Chemical Physics, 1983. **79**(1): p. 265-272.

106. Viggiano, A. and R.A. Morris, *Rotational and Vibrational Energy Effects on Ion− Molecule Reactivity as Studied by the VT-SIFDT Technique.* The Journal of Physical Chemistry, 1996. **100**(50): p. 19227-19240.

107. Lindinger, W., et al., *Rate constants for the reactions of O_2^+ (a 4Π u) ions with N_2, Ar, CO, CO_2, H_2, and O_2 at relative kinetic energies 0.04–2 eV.* The Journal of Chemical Physics, 1975. **62**(10): p. 4101-4110.

108. Hansel, A., et al., *Energy dependencies of the proton transfer reactions $H_3O^+ + CH_2O \nLeftrightarrow CH_2OH^+ + H_2O$.* International journal of mass spectrometry and ion processes, 1997. **167**: p. 697-703.

109. Smith, S.C., et al., *Unimolecular decomposition of a polyatomic ion in a variable-temperature selected-ion-flow-drift tube: experiment and theoretical interpretation.* International journal of mass spectrometry and ion processes, 1990. **96**(1): p. 77-96.

110. Malásková, M., et al., *Compendium of the reactions of H_3O^+ with selected ketones of relevance to breath analysis using proton transfer reaction mass spectrometry.* Frontiers in chemistry, 2019. **7**: p. 401.

111. Glosik, J., et al., *Energy dependencies of fast reactions of positive ions X^+ with HCl from near thermal to $\approx$ 2 eV center - of - mass collision energy ($X^+ = H^+$, H_2^+, H_3^+, N^+, N_2^+, Ar^+, C^+, CH^+, CH_2^+, CH_3^+, CH_4^+, CH_5^+).* The Journal of chemical physics, 1993. **98**(9): p. 6995-7003.

112. Glosik, J., P. Zakouřil, and W. Lindinger, *Selected ion flow drift tube studies of the reactions of Si^+ (2P) with HCl, H_2O, H2S, and NH_3: Reactions which produce atomic hydrogen.* The Journal of chemical physics, 1995. **103**(15): p. 6490-6497.

113. Zakouril, P., et al., *Selected ion flow drift tube studies of the reactions of S^+ (4S) with CH_4, C_2H_2, C_2H_4, and C_3H_8.* The Journal of Physical Chemistry, 1995. **99**(43): p. 15890-15898.

114. Adams, N. and D. Smith, *SIFDT studies of some CH_3^+ ternary association reactions.* International journal of mass spectrometry and ion processes, 1987. **81**: p. 273-287.

115. Glosik, J., et al., *SIFDT studies of the reactions of C^+, CH^+ and CH_2^+ with HCl and CO_2, and CH_3^+ with HCl.* International journal of mass spectrometry and ion processes, 1993. **129**: p. 131-143.

116. Chiu, Y.h., et al., *Reaction mechanisms and energy disposal in the* $[C_2H_2{:}OCS]^+$ *system: A mode‐selective differential cross section study.* The Journal of chemical physics, 1996. **105**(8): p. 3089-3107.

117. Honma, K., L. Sunderlin, and P. Armentrout, *Reactions of protonated water clusters with deuterated ammonia:* $H(H_2O)^+_n$ *(n= 1–4)+* ND_3*.* International journal of mass spectrometry and ion processes, 1992. **117**: p. 237-259.

118. Fairley, D.A., et al., *Competitive association and charge transfer in the reactions of* NO^+ *with some ketones: a selected ion flow drift tube study.* International journal of mass spectrometry, 1999. **193**(1): p. 35-43.

119. Bartle, K.D. and P. Myers, *History of gas chromatography.* TrAC Trends in Analytical Chemistry, 2002. **21**(9–10): p. 547-557.

120. Russo, M.V., et al., *Extraction and GC-MS analysis of phthalate esters in food matrices: a review.* RSC Adv., 2015. **5**(46): p. 37023-37043.

121. Fialkov, A.B., et al., *Sensitivity and noise in GC–MS: Achieving low limits of detection for difficult analytes.* International journal of mass spectrometry, 2007. **260**(1): p. 31-48.

122. George, C. and H. Prest, *Determination of Phthalate Esters by Positive Chemical Ionization MS with Retention-Time Locked GC.* LCGC NORTH AMERICA, 2002. **20**(2): p. 142-151.

123. Borsdorf, H. and G.A. Eiceman, *Ion mobility spectrometry: principles and applications.* Applied Spectroscopy Reviews, 2006. **41**(4): p. 323-375.

124. Makinen, M.A., O.A. Anttalainen, and M.E. Sillanpää, *Ion mobility spectrometry and its applications in detection of chemical warfare agents*. Anal. Chem, 2010. **82**(83): p. 9594-9600.

125. Guevremont, R., *High-field asymmetric waveform ion mobility spectrometry: a new tool for mass spectrometry.* Journal of Chromatography A, 2004. **1058**(1-2): p. 3-19.

126. Kolakowski, B.M. and Z. Mester, *Review of applications of high-field asymmetric waveform ion mobility spectrometry (FAIMS) and differential mobility spectrometry (DMS).* Analyst, 2007. **132**(9): p. 842-864.

127. Owlstone Medical Ltd, cited 2022; Available from: https://www.owlstonemedical.com/science-technology/faims-technology/.

128. Fenn, J.B., et al., *Electrospray ionization for mass spectrometry of large biomolecules.* Science, 1989. **246**(4926): p. 64-71.

129. Rayleigh, L., *XX. On the equilibrium of liquid conducting masses charged with electricity.* The London, Edinburgh, and Dublin Philosophical Magazine and Journal of Science, 1882. **14**(87): p. 184-186.

130. Španěl, P., M. Pavlik, and D. Smith, *Reactions of H_3O^+ and OH^- ions with some organic molecules; applications to trace gas analysis in air.* International journal of mass spectrometry and ion processes, 1995. **145**(3): p. 177-186.

131. Li, H., M. Xu, and J. Zhu, *Headspace gas monitoring of gut microbiota using targeted and globally optimized targeted secondary electrospray ionization mass spectrometry.* Analytical chemistry, 2018. **91**(1): p. 854-863.

132. Griffiths, W.J., et al., *Electrospray and tandem mass spectrometry in biochemistry.* Biochemical Journal, 2001. **355**(3): p. 545-561.

133. Schlottmann, F., et al., *High Kinetic Energy Ion Mobility Spectrometry (HiKE-IMS) at 40 mbar.* Journal of the American Society for Mass Spectrometry, 2020.

134. Wakelam, V. *KIDA - Kinetic Database for Astrochemistry.* 2012 [cited 2022; Available from: http://kida.obs.u-bordeaux1.fr.

135. Zymak, I., et al., *A pilot study of ion-molecule reactions at temperatures relevant to the atmosphere of Titan.* Origins of Life and Evolution of Biospheres, 2016. **46**(4): p. 533-538.

136. Španěl, P., K. Dryahina, and D. Smith, *A general method for the calculation of absolute trace gas concentrations in air and breath from selected ion flow tube mass spectrometry data.* International Journal of Mass Spectrometry, 2006. **249-250**: p. 230-239.

137. Španěl, P. and D. Smith, *Quantitative selected ion flow tube mass spectrometry: the influence of ionic diffusion and mass discrimination.* Journal of the American Society for Mass Spectrometry, 2001. **12**(7): p. 863-872.

138. Španěl, P. and D. Smith, *Selected ion flow tube mass spectrometry analyses of stable isotopes in water: isotopic composition of H_3O^+ and $H_3O^+(H_2O)_3$ ions in exchange reactions with water vapor.* Journal of the American Society for Mass Spectrometry, 2000. **11**(10): p. 866-875.

139. Dryahina, K. and P. Španěl, *A convenient method for calculation of ionic diffusion coefficients for accurate selected ion flow tube mass spectrometry, SIFT-MS.* International Journal of Mass Spectrometry, 2005. **244**(2-3): p. 148-154.

140. Smith, D., A. Pysanenko, and P. Španěl, *Ionic diffusion and mass discrimination effects in the new generation of short flow tube SIFT-MS instruments.* International Journal of Mass Spectrometry, 2009. **281**(1-2): p. 15-23.

141. Lehnert, A.S., et al., *SIFT-MS optimization for atmospheric trace gas measurements at varying humidity.* Atmos. Meas. Tech., 2020. **13**(7): p. 3507-3520.

142. IONICON ANALYTIK GES.M.B.H. *Benefits of Proton Transfer Reaction - Mass Spectrometry*. 2022; Available from: https://www.ionicon.com/technologies/details/ptr-ms.

143. TOFWERK AG. *Advantages of the Vocus PTR-TOF*. 2022; Available from: https://www.tofwerk.com/products/vocus-ptr-tof/.

144. Amann, A., et al., *Model based determination of detection limits for proton transfer reaction mass spectrometer.* Measurement Science Review, 2010. **10**(6): p. 180-188.

145. Jordan, A., et al., *An online ultra-high sensitivity Proton-transfer-reaction mass-spectrometer combined with switchable reagent ion capability (PTR+SRI−MS).* International Journal of Mass Spectrometry, 2009. **286**(1): p. 32-38.

146. Knighton, W., et al., *Adaptation of a proton transfer reaction mass spectrometer instrument to employ NO$^+$ as reagent ion for the detection of 1, 3‐butadiene in the ambient atmosphere.* Rapid Communications in Mass Spectrometry: An International Journal Devoted to the Rapid Dissemination of Up‐to‐the‐Minute Research in Mass Spectrometry, 2009. **23**(20): p. 3301-3308.

147. Sulzer, P., et al., *From conventional proton-transfer-reaction mass spectrometry (PTR-MS) to universal trace gas analysis.* International Journal of Mass Spectrometry, 2012. **321**: p. 66-70.

148. IONICON ANALYTIK GES.M.B.H. *PTR3-TOF 10K mass spectrometer - Trace VOC-ELVOC Analyzer*. 2022; Available from: https://www.ionicon.com/products/details/ptr3.

149. Keck, L., U. Oeh, and C. Hoeschen, *Corrected equation for the concentrations in the drift tube of a proton transfer reaction-mass spectrometer (PTR-MS).* International Journal of Mass Spectrometry, 2007. **264**(1): p. 92-95.

150. Michalczuk, B., et al., *Isomer and Conformer Selective Atmospheric Pressure Chemical Ionisation of dimethyl phthalate.* Physical Chemistry Chemical Physics, 2019.

151. Wróblewski, T., et al., *Dissociation energies of protonated water clusters.* Radiation Physics and Chemistry, 2003. **68**(1-2): p. 313-318.

152. Spesyvyi, A. and P. Španěl, *Determination of residence times of ions in a resistive glass selected ion flow‐drift tube using the Hadamard transformation.* Rapid Communications in Mass Spectrometry, 2015. **29**(17): p. 1563-1570.

153. Spesyvyi, A., et al., *Ligand Switching Ion Chemistry: An SIFDT Case Study of the Primary and Secondary Reactions of Protonated Acetic Acid Hydrates with Acetone.* Journal of the American Society for Mass Spectrometry, 2021. **32**(8): p. 2251-2260.

154. Phillips, M., et al., *Volatile organic compounds in breath as markers of lung cancer: a cross-sectional study.* The Lancet, 1999. **353**(9168): p. 1930-1933.

155. Syft Technologies. *Voice200 ultra*. 2022; Available from: https://www.syft.com/products.

156. IONICON ANALYTIK GES.M.B.H. *FUSION PTR-TOF 10k - Ultimate*. 2022; Available from: https://www.ionicon.com/products/details/fusion-ptr-tof-10k.

157. Miekisch, W., J.K. Schubert, and G.F. Noeldge-Schomburg, *Diagnostic potential of breath analysis—focus on volatile organic compounds.* Clinica chimica acta, 2004. **347**(1-2): p. 25-39.

158. Španěl, P. and D. Smith, *Progress in SIFT‐MS: Breath analysis and other applications.* Mass spectrometry reviews, 2011. **30**(2): p. 236-267.

159. Bruderer, T., et al., *On-line analysis of exhaled breath: focus review.* Chemical reviews, 2019. **119**(19): p. 10803-10828.

160. Španěl, P. and D. Smith, *Quantification of volatile metabolites in exhaled breath by selected ion flow tube mass spectrometry, SIFT-MS.* Clinical Mass Spectrometry, 2020. **16**: p. 18-24.

161. Storer, M., et al., *Measurement of breath acetone concentrations by selected ion flow tube mass spectrometry in type 2 diabetes.* Journal of Breath Research, 2011. **5**(4): p. 046011.

162. Dryahina, K., et al., *Exhaled breath concentrations of acetic acid vapour in gastro-esophageal reflux disease.* Journal of breath research, 2014. **8**(3): p. 037109.

163. Ratiu, I.-A., et al., *Mass spectrometric techniques for the analysis of volatile organic compounds emitted from bacteria.* Bioanalysis, 2017. **9**(14): p. 1069-1092.

164. Shestivska, V., et al., *Quantification of methyl thiocyanate in the headspace of Pseudomonas aeruginosa cultures and in the breath of cystic fibrosis patients by selected ion flow tube mass spectrometry.* Rapid Communications in Mass Spectrometry, 2011. **25**(17): p. 2459-2467.

165. Shestivska, V., et al., *Variability in the concentrations of volatile metabolites emitted by genotypically different strains of Pseudomonas aeruginosa.* Journal of Applied Microbiology, 2012. **113**(3): p. 701-713.

166. Gilchrist, F.J., et al., *Hydrogen cyanide concentrations in the breath of adult cystic fibrosis patients with and without Pseudomonas aeruginosa infection.* Journal of breath research, 2013. **7**(2): p. 026010.

167. Smith, D., et al., *Breath concentration of acetic acid vapour is elevated in patients with cystic fibrosis.* Journal of breath research, 2016. **10**(2): p. 021002.

168. Davies, S.J., P. Španěl, and D. Smith, *Breath analysis of ammonia, volatile organic compounds and deuterated water vapor in chronic kidney disease and during dialysis.* Bioanalysis, 2014. **6**(6): p. 843-857.

169. Kohl, I., et al., *First observation of a potential non-invasive breath gas biomarker for kidney function.* Journal of breath research, 2013. **7**(1): p. 017110.

170. Eng, K., et al., *Analysis of breath volatile organic compounds in children with chronic liver disease compared to healthy controls.* Journal of breath research, 2015. **9**(2): p. 026002.

171. Lembo, V., et al., *Rapid" breath-print" of liver cirrhosis by Proton Transfer Reaction Time of Flight Mass Spectrometry.* 2013.

172. Smolinska, A., et al., *Profiling of volatile organic compounds in exhaled breath as a strategy to find early predictive signatures of asthma in children.* PloS one, 2014. **9**(4): p. e95668.

173. Kharitonov, S.A. and P.J. Barnes, *Exhaled markers of pulmonary disease.* American journal of respiratory and critical care medicine, 2001. **163**(7): p. 1693-1722.

174. Dryahina, K., et al., *Quantification of pentane in exhaled breath, a potential biomarker of bowel disease, using selected ion flow tube mass spectrometry.* Rapid Communications in Mass Spectrometry, 2013. **27**(17): p. 1983-1992.

175. Lechner, M., et al., *Headspace screening of fluid obtained from the gut during colonoscopy and breath analysis by proton transfer reaction-mass spectrometry: A novel approach in the diagnosis of gastro-intestinal diseases.* International Journal of Mass Spectrometry, 2005. **243**(2): p. 151-154.

176. Harrison, G., et al., *Real‐time breath monitoring of propofol and its volatile metabolites during surgery using a novel mass spectrometric technique: a feasibility study.* British journal of anaesthesia, 2003. **91**(6): p. 797-799.

177. Erhart, S., et al., *3-Heptanone as a potential new marker for valproic acid therapy.* Journal of breath research, 2009. **3**(1): p. 016004.

178. Beauchamp, J., F. Kirsch, and A. Buettner, *Real-time breath gas analysis for pharmacokinetics: monitoring exhaled breath by on-line proton-transfer-reaction mass spectrometry after ingestion of eucalyptol-containing capsules.* Journal of breath research, 2010. **4**(2): p. 026006.

179. Trefz, P., et al., *Drug detection in breath: non-invasive assessment of illicit or pharmaceutical drugs.* Journal of breath research, 2017. **11**(2): p. 024001.

180. Schmidt, F.M., et al., *Background levels and diurnal variations of hydrogen cyanide in breath and emitted from skin.* Journal of breath research, 2011. **5**(4): p. 046004.

181. Moeskops, B., et al., *Real-time trace gas sensing of ethylene, propanal and acetaldehyde from human skin in vivo.* Physiological measurement, 2006. **27**(11): p. 1187.

182. Wisthaler, A. and C.J. Weschler, *Reactions of ozone with human skin lipids: sources of carbonyls, dicarbonyls, and hydroxycarbonyls in indoor air.* Proceedings of the National Academy of Sciences, 2010. **107**(15): p. 6568-6575.

183. Williams, J. and J. Pleil, *Crowd-based breath analysis: assessing behavior, activity, exposures, and emotional response of people in groups.* Journal of breath research, 2016. **10**(3): p. 032001.

184. Wicker, J., et al. *Cinema data mining: The smell of fear*. in *Proceedings of the 21th ACM SIGKDD International Conference on Knowledge Discovery and Data Mining*. 2015.

185. Williams, J., et al., *Cinema audiences reproducibly vary the chemical composition of air during films, by broadcasting scene specific emissions on breath.* Scientific reports, 2016. **6**(1): p. 1-10.

186. Mochalski, P., et al., *Instrumental sensing of trace volatiles—A new promising tool for detecting the presence of entrapped or hidden people.* Journal of breath research, 2018. **12**(2): p. 027107.

187. Giannoukos, S., A. Agapiou, and S. Taylor, *Advances in chemical sensing technologies for VOCs in breath for security/threat assessment, illicit drug detection, and human trafficking activity.* Journal of breath research, 2018. **12**(2): p. 027106.

188. Williams, J., et al., *An atmospheric chemistry interpretation of mass scans obtained from a proton transfer mass spectrometer flown over the tropical rainforest of Surinam.* Journal of Atmospheric Chemistry, 2001. **38**(2): p. 133-166.

189. Crutzen, P., et al., *High spatial and temporal resolution measurements of primary organics and their oxidation products over the tropical forests of Surinam.* Atmospheric Environment, 2000. **34**(8): p. 1161-1165.

190. Warneke, C., et al., *Isoprene and its oxidation products methyl vinyl ketone, methacrolein, and isoprene related peroxides measured online over the tropical rain forest of Surinam in March 1998.* Journal of Atmospheric Chemistry, 2001. **38**(2): p. 167-185.

191. Müller, K., et al., *Biogenic carbonyl compounds within and above a coniferous forest in Germany.* Atmospheric Environment, 2006. **40**: p. 81-91.

192. Rinne, J., et al., *On-line PTR-MS measurements of atmospheric concentrations of volatile organic compounds in a European boreal forest ecosystem.* Boreal environment research, 2005. **10**(5): p. 425-436.

193. Williams, J., et al., *The summertime Boreal forest field measurement intensive (HUMPPA-COPEC-2010): an overview of meteorological and chemical*

influences. Atmospheric Chemistry and Physics, 2011. **11**(20): p. 10599-10618.

194. Ammann, C., et al., *Application of PTR-MS for measurements of biogenic VOC in a deciduous forest.* International Journal of Mass Spectrometry, 2004. **239**(2-3): p. 87-101.

195. Fall, R., et al., *Biogenic C5 VOCs: release from leaves after freeze–thaw wounding and occurrence in air at a high mountain observatory.* Atmospheric Environment, 2001. **35**(22): p. 3905-3916.

196. Karl, T., et al., *High concentrations of reactive biogenic VOCs at a high altitude site in late autumn.* Geophysical Research Letters, 2001. **28**(3): p. 507-510.

197. Fares, S., et al., *Biogenic emissions from Citrus species in California.* Atmospheric Environment, 2011. **45**(27): p. 4557-4568.

198. Misztal, P.K., et al., *Large estragole fluxes from oil palms in Borneo.* Atmospheric Chemistry and Physics, 2010. **10**(9): p. 4343-4358.

199. Misztal, P.K., et al., *Direct ecosystem fluxes of volatile organic compounds from oil palms in South-East Asia.* Atmospheric Chemistry and Physics, 2011. **11**(17): p. 8995-9017.

200. Kammer, J., et al. *Effect of agricultural practices on volatile organic compound (VOC) emissions from winter wheat.* in *8 th International PTR-MS Conference 2019*. 2019.

201. Holzinger, R., et al., *Diurnal cycles and seasonal variation of isoprene and its oxidation products in the tropical savanna atmosphere.* Global Biogeochemical Cycles, 2002. **16**(4): p. 22-1-22-13.

202. Bamberger, I., et al., *BVOC fluxes above mountain grassland.* Biogeosciences, 2010. **7**(5): p. 1413-1424.

203. Davison, B., et al., *Cut-induced VOC emissions from agricultural grasslands.* Plant Biology, 2007. **9**(S 01): p. e60-e68.

204. Sovová, K., et al., *Time-integrated thermal desorption for quantitative SIFT-MS analyses of atmospheric monoterpenes.* Analytical and bioanalytical chemistry, 2019. **411**(14): p. 2997-3007.

205. Bsaibes, S., et al., *Monoterpene Chemical Speciation with High Time Resolution Using a FastGC/PTR-MS: Results from the COV3ER Experiment on Quercus ilex.* Atmosphere, 2020. **11**(7): p. 690.

206. Bsaibes, S., et al., *Variability of hydroxyl radical (OH) reactivity in the Landes maritime pine forest: results from the LANDEX campaign 2017.* Atmospheric Chemistry and Physics, 2020. **20**(3): p. 1277-1300.

207. Yang, Y., et al., *Towards a quantitative understanding of total OH reactivity: A review.* Atmospheric Environment, 2016. **134**: p. 147-161.

208. Ghirardo, A., et al., *Determination of de novo and pool emissions of terpenes from four common boreal/alpine trees by $^{13}CO_2$ labelling and PTR‐MS analysis.* Plant, cell & environment, 2010. **33**(5): p. 781-792.

209. Maleknia, S.D., T.L. Bell, and M.A. Adams, *PTR-MS analysis of reference and plant-emitted volatile organic compounds.* International Journal of Mass Spectrometry, 2007. **262**(3): p. 203-210.

210. Shaw, S.L., et al., *Volatile organic compound emissions from dairy cows and their waste as measured by proton-transfer-reaction mass spectrometry.* Environmental science & technology, 2007. **41**(4): p. 1310-1316.

211. Feilberg, A., et al., *Odorant emissions from intensive pig production measured by online proton-transfer-reaction mass spectrometry.* Environmental Science & Technology, 2010. **44**(15): p. 5894-5900.

212. Hansen, M.J., et al., *Application of proton-transfer-reaction mass spectrometry to the assessment of odorant removal in a biological air cleaner for pig production.* Journal of Agricultural and Food Chemistry, 2012. **60**(10): p. 2599-2606.

213. Sprung, D., et al., *Acetone and acetonitrile in the tropical Indian Ocean boundary layer and free troposphere: Aircraft‐based intercomparison of AP‐CIMS and PTR‐MS measurements.* Journal of Geophysical Research: Atmospheres, 2001. **106**(D22): p. 28511-28527.

214. Sinha, V., et al., *Air-sea fluxes of methanol, acetone, acetaldehyde, isoprene and DMS from a Norwegian fjord following a phytoplankton bloom in a mesocosm experiment.* Atmospheric Chemistry and Physics, 2007. **7**(3): p. 739-755.

215. Williams, J., et al., *Measurements of organic species in air and seawater from the tropical Atlantic.* Geophysical research letters, 2004. **31**(23).

216. Wang, N., et al., *Measurements of carbonyl compounds around the Arabian Peninsula: overview and model comparison.* Atmospheric Chemistry and Physics, 2020. **20**(18): p. 10807-10829.
217. Colomb, A., et al., *Variation of atmospheric volatile organic compounds over the Southern Indian Ocean (30–49 S).* Environmental Chemistry, 2009. **6**(1): p. 70-82.
218. Karl, T., et al., *Use of proton‐transfer‐reaction mass spectrometry to characterize volatile organic compound sources at the La Porte super site during the Texas Air Quality Study 2000.* Journal of Geophysical Research: Atmospheres, 2003. **108**(D16).
219. Filella, I. and J. Penuelas, *Daily, weekly, and seasonal time courses of VOC concentrations in a semi-urban area near Barcelona.* Atmospheric Environment, 2006. **40**(40): p. 7752-7769.
220. MIYAKAWA, Y., S. KATO, and Y. KAJII, *Calibration of the Proton Transfer Reaction Mass Spectrometry (PTR-MS) Instrument for Oxygenated Volatile Organic Compounds (OVOCs) and the Measurement of Ambient Air in Tokyo.* Journal of Japan Society for Atmospheric Environment/Taiki Kankyo Gakkaishi, 2005. **40**(5): p. 209-219.
221. Gros, V., et al., *Volatile organic compounds sources in Paris in spring 2007. Part I: qualitative analysis.* Environmental chemistry, 2011. **8**(1): p. 74-90.
222. Gaimoz, C., et al., *Volatile organic compounds sources in Paris in spring 2007. Part II: source apportionment using positive matrix factorisation.* Environmental chemistry, 2011. **8**(1): p. 91-103.
223. Velasco, E., Pressley, S., Grivicke, R., Allwine, E., Coons, T., Foster, W, *Eddy covariance flux measurements of pollutant gases in urban Mexico City.* Atmospheric Chemistry and Physics, 2009. **9**(19): p. 7325-7342.
224. Herndon, S.C., et al., *Characterization of urban pollutant emission fluxes and ambient concentration distributions using a mobile laboratory with rapid response instrumentation.* Faraday Discussions, 2005. **130**(0): p. 327-339.
225. Jobson, B.T., et al., *On-line analysis of organic compounds in diesel exhaust using a proton transfer reaction mass spectrometer (PTR-MS).* International Journal of Mass Spectrometry, 2005. **245**(1): p. 78-89.

226. Knighton, W.B., et al., *Quantification of aircraft engine hydrocarbon emissions using proton transfer reaction mass spectrometry.* Journal of Propulsion and Power, 2007. **23**(5): p. 949.

227. Herndon, S.C., et al., *Hydrocarbon Emissions from In-Use Commercial Aircraft during Airport Operations.* Environmental Science & Technology, 2006. **40**(14): p. 4406-4413.

228. Akagi, S.K., et al., *Emission factors for open and domestic biomass burning for use in atmospheric models.* Atmos. Chem. Phys., 2011. **11**(9): p. 4039-4072.

229. Wisthaler, A., et al., *Organic trace gas measurements by PTR-MS during INDOEX 1999.* Journal of Geophysical Research: Atmospheres, 2002. **107**(D19): p. INX2 23-1-INX2 23-11.

230. Kolarik, B., et al., *The effect of a photocatalytic air purifier on indoor air quality quantified using different measuring methods.* Building and Environment, 2010. **45**(6): p. 1434-1440.

231. Vesin, A., et al., *Use of the HS-PTR-MS for online measurements of pyrethroids during indoor insecticide treatments.* Analytical and Bioanalytical Chemistry, 2012. **403**(7): p. 1907-1921.

232. Uhde, E. and N. Schulz, *Impact of room fragrance products on indoor air quality.* Atmospheric Environment, 2015. **106**: p. 492-502.

233. Schripp, T., et al., *Application of proton-transfer-reaction-mass-spectrometry for Indoor Air Quality research.* Indoor Air, 2014. **24**(2): p. 178-189.

234. Han, K.H., et al., *Determination of material emission signatures by PTR-MS and their correlations with odor assessments by human subjects.* Indoor Air, 2010. **20**(4): p. 341-354.

235. Syft Technologies. *Cleanroom Monitoring*. 2022; Available from: https://www.syft.com/applications/cleanroom-monitoring.

236. Dryahina, K., D. Smith, and P. Španěl, *Quantification of volatile compounds released by roasted coffee by selected ion flow tube mass spectrometry.* Rapid Communications in Mass Spectrometry, 2018. **32**(9): p. 739-750.

237. Yeretzian, C., et al., *From the green bean to the cup of coffee: investigating coffee roasting by on-line monitoring of volatiles.* European Food Research and Technology, 2002. **214**(2): p. 92-104.

238. Beauchamp, J.D., *Pushing the Boundaries of Dynamic Flavor Analysis with PTR-MS*, in *Dynamic Flavor: Capturing Aroma Using Real-Time Mass Spectrometry*. 2021, American Chemical Society. p. 33-50.

239. Boscaini, E., et al., *Characterization of wine with PTR-MS.* International Journal of Mass Spectrometry, 2004. **239**(2): p. 215-219.

240. Boscaini, E., et al., *Gas Chromatography−Olfactometry (GC-O) and Proton Transfer Reaction−Mass Spectrometry (PTR-MS) Analysis of the Flavor Profile of Grana Padano, Parmigiano Reggiano, and Grana Trentino Cheeses.* Journal of Agricultural and Food Chemistry, 2003. **51**(7): p. 1782-1790.

241. Galle, S.A., et al., *Typicality and Geographical Origin Markers of Protected Origin Cheese from The Netherlands Revealed by PTR-MS.* Journal of Agricultural and Food Chemistry, 2011. **59**(6): p. 2554-2563.

242. Buser, H.R., C. Zanier, and H. Tanner, *Identification of 2, 4, 6-trichloroanisole as a potent compound causing cork taint in wine.* Journal of agricultural and food chemistry, 1982. **30**(2): p. 359-362.

243. Soukoulis, C., et al., *PTR-ToF-MS, A Novel, Rapid, High Sensitivity and Non-Invasive Tool to Monitor Volatile Compound Release During Fruit Post-Harvest Storage: The Case Study of Apple Ripening.* Food and Bioprocess Technology, 2013. **6**(10): p. 2831-2843.

244. Li, H., et al., *Sensory, GC-MS and PTR-ToF-MS profiling of strawberries varying in maturity at harvest with subsequent cold storage.* Postharvest Biology and Technology, 2021. **182**: p. 111719.

245. Soukoulis, C., et al., *Proton transfer reaction time-of-flight mass spectrometry monitoring of the evolution of volatile compounds during lactic acid fermentation of milk.* Rapid Communications in Mass Spectrometry, 2010. **24**(14): p. 2127-2134.

246. Tsevdou, M., et al., *Monitoring the effect of high pressure and transglutaminase treatment of milk on the evolution of flavour compounds during lactic acid fermentation using PTR-ToF-MS.* Food Chemistry, 2013. **138**(4): p. 2159-2167.

247. Capozzi, V., et al., *PTR-MS Characterization of VOCs Associated with Commercial Aromatic Bakery Yeasts of Wine and Beer Origin.* Molecules, 2016. **21**(4): p. 483.

248. Cordell, R.L., et al., *Detection of chemical weapon agents and simulants using chemical ionization reaction time-of-flight mass spectrometry.* Analytical chemistry, 2007. **79**(21): p. 8359-8366.

249. Petersson, F., et al., *Real‐time trace detection and identification of chemical warfare agent simulants using recent advances in proton transfer reaction time‐of‐flight mass spectrometry.* Rapid Communications in Mass Spectrometry: An International Journal Devoted to the Rapid Dissemination of Up‐to‐the‐Minute Research in Mass Spectrometry, 2009. **23**(23): p. 3875-3880.

250. Agarwal, B., et al., *Use of proton transfer reaction time-of-flight mass spectrometry for the analytical detection of illicit and controlled prescription drugs at room temperature via direct headspace sampling.* Analytical and bioanalytical chemistry, 2011. **400**(8): p. 2631-2639.

251. Jürschik, S., et al., *Rapid and facile detection of four date rape drugs in different beverages utilizing proton transfer reaction mass spectrometry (PTR‐MS).* Journal of mass spectrometry, 2012. **47**(9): p. 1092-1097.

252. Sabo, M., M. Malaskova, and Š. Matejčík, *Laser desorption with corona discharge ion mobility spectrometry for direct surface detection of explosives.* Analyst, 2014. **139**(20): p. 5112-5117.

253. Mayhew, C., et al., *Applications of proton transfer reaction time-of-flight mass spectrometry for the sensitive and rapid real-time detection of solid high explosives.* International Journal of Mass Spectrometry, 2010. **289**(1): p. 58-63.

254. González-Méndez, R.n., et al., *Enhancement of compound selectivity using a radio frequency ion-funnel proton transfer reaction mass spectrometer: improved specificity for explosive compounds.* Analytical chemistry, 2016. **88**(21): p. 10624-10630.

255. Sulzer, P., et al., *Applications of switching reagent ions in proton transfer reaction mass spectrometric instruments for the improved selectivity of explosive compounds.* International Journal of Mass Spectrometry, 2013. **354**: p. 123-128.

256. Baur, X., B. Poschadel, and L.T. Budnik, *High frequency of fumigants and other toxic gases in imported freight containers—an underestimated*

occupational and community health risk. Occupational and environmental medicine, 2010. **67**(3): p. 207-212.

257. Pysanenko, A., P. Španěl, and D. Smith, *Analysis of the isobaric compounds propanol, acetic acid and methyl formate in humid air and breath by selected ion flow tube mass spectrometry, SIFT-MS.* International Journal of Mass Spectrometry, 2009. **285**(1-2): p. 42-48.

258. Lacko, M., et al., *Addition of fast gas chromatography to selected ion flow tube mass spectrometry for analysis of individual monoterpenes in mixtures.* Atmospheric Measurement Techniques, 2019. **12**(9): p. 4965-4982.

259. Spesyvyi, A., K. Sovová, and P. Španěl, *In‐tube collision‐induced dissociation for selected ion flow‐drift tube mass spectrometry, SIFDT‐MS: a case study of NO^+ reactions with isomeric monoterpenes.* Rapid Communications in Mass Spectrometry, 2016. **30**(18): p. 2009-2016.

260. Smith, D. and P. Španěl, *Ternary association reactions of H_3O^+, NO^+ and $O_2^{+\bullet}$ with N_2, O_2, CO_2 and H_2O; implications for selected ion flow tube mass spectrometry analyses of air and breath.* Rapid Communications in Mass Spectrometry, 2022. **36**(6): p. e9241.

261. Clough, S.A., et al., *Dipole moment of water from Stark measurements of H_2O, HDO, and D_2O.* The Journal of Chemical Physics, 1973. **59**(5): p. 2254-2259.

262. Wang, T., P. Španěl, and D. Smith, *Selected ion flow tube, SIFT, studies of the reactions of H_3O^+, NO^+ and O_2^+ with eleven $C_{10}H_{16}$ monoterpenes.* Int. J. Mass Spec., 2003. **228**(1): p. 117-126.

263. Michel, E., et al., *A selected ion flow tube study of the reactions of H_3O^+, NO^+ and O_2^+ with methyl vinyl ketone and some atmospherically important aldehydes.* International Journal of Mass Spectrometry, 2005. **244**: p. 50-59.

264. Olivenza-León, D., C.A. Mayhew, and R. González-Méndez, *Selective Reagent Ion Mass Spectrometric Investigations of the Nitroanilines.* Journal of The American Society for Mass Spectrometry, 2019. **30**(11): p. 2259-2266.

265. Roach, J.A., et al., *Chromatographic separation and identification of conjugated linoleic acid isomers.* Analytica Chimica Acta, 2002. **465**(1-2): p. 207-226.

266. Ecker, J., et al., *A rapid GC–MS method for quantification of positional and geometric isomers of fatty acid methyl esters.* Journal of Chromatography B, 2012. **897**: p. 98-104.

267. Matisová, E. and M. Dömötörová, *Fast gas chromatography and its use in trace analysis.* Journal of Chromatography A, 2003. **1000**(1-2): p. 199-221.

268. Materić, D., et al., *Monoterpene separation by coupling proton transfer reaction time-of-flight mass spectrometry with fastGC.* Analytical and bioanalytical chemistry, 2015. **407**(25): p. 7757-7763.

269. Jones, C., et al., *A novel fast gas chromatography method for higher time resolution measurements of speciated monoterpenes in air.* Atmospheric Measurement Techniques, 2014. **7**(5): p. 1259-1275.

270. Runge, C., *Über die numerische Auflösung von Differentialgleichungen.* Mathematische Annalen, 1895. **46**(2): p. 167-178.

271. Spanel, P. and D. Smith, *Advances in on-line absolute trace gas analysis by SIFT-MS.* Current Analytical Chemistry, 2013. **9**(4): p. 525-539.

272. Hazra, M.K., J.S. Francisco, and A. Sinha, *Hydrolysis of glyoxal in water-restricted environments: formation of organic aerosol precursors through formic acid catalysis.* The Journal of Physical Chemistry A, 2014. **118**(23): p. 4095-4105.

273. Shkrob, I.A., et al., *Photoredox reactions and the catalytic cycle for carbon dioxide fixation and methanogenesis on metal oxides.* The Journal of Physical Chemistry C, 2012. **116**(17): p. 9450-9460.

274. Civiš, S., et al., *Photocatalytic transformation of CO_2 to CH_4 and CO on acidic surface of TiO_2 anatase.* Optical Materials, 2016. **56**: p. 80-83.

275. Volkamer, R., U. Platt, and K. Wirtz, *Primary and secondary glyoxal formation from aromatics: experimental evidence for the bicycloalkyl− radical pathway from benzene, toluene, and p-xylene.* The Journal of Physical Chemistry A, 2001. **105**(33): p. 7865-7874.

276. Jang, M. and R.M. Kamens, *Characterization of Secondary Aerosol from the Photooxidation of Toluene in the Presence of NO_x and 1-Propene.* Environmental Science & Technology, 2001. **35**(18): p. 3626-3639.

277. Tuazon, E.C., et al., *Yields of glyoxal and methylglyoxal from the nitrogen oxide (NO_x)-air photooxidations of toluene and m-and p-xylene.* Environmental science & technology, 1984. **18**(12): p. 981-984.

278. Smith, D., T. Kleindienst, and C. McIver, *Primary product distributions from the reaction of OH with m-, p-xylene, 1, 2, 4-and 1, 3, 5-trimethylbenzene.* Journal of Atmospheric Chemistry, 1999. **34**(3): p. 339-364.

279. Yu, J., H.E. Jeffries, and R.M. Le Lacheur, *Identifying airborne carbonyl compounds in isoprene atmospheric photooxidation products by their PFBHA oximes using gas chromatography/ion trap mass spectrometry.* Environmental science & technology, 1995. **29**(8): p. 1923-1932.

280. Yu, J., H.E. Jeffries, and K.G. Sexton, *Atmospheric photooxidation of alkylbenzenes—I. Carbonyl product analyses.* Atmospheric Environment, 1997. **31**(15): p. 2261-2280.

281. Wroblewski, T., et al., *Ab initio and density functional theory calculations of proton affinities for volatile organic compounds.* European Physical Journal-Special Topics, 2007. **144**: p. 191-195.

282. Mattioda, G. and A. Blanc, *Glyoxal*, in *Ullmann's Encyclopedia of Industrial Chemistry*. 2000.

283. Guimbaud, C., et al., *Kinetics of the reactions of acetone and glyoxal with* $O^{-}{}_{2}(+)$ *and* NO^{+} *ions and application to the detection of oxygenated volatile organic compounds in the atmosphere by chemical ionization mass spectrometry.* International Journal of Mass Spectrometry, 2007. **263**(2-3): p. 276-288.

284. Stönner, C., et al., *Glyoxal measurement with a proton transfer reaction time of flight mass spectrometer (PTR‐TOF‐MS): characterization and calibration.* Journal of Mass Spectrometry, 2017. **52**(1): p. 30-35.

285. Bohme, D., G. Mackay, and S.D. Tanner, *An experimental study of the gas-phase kinetics of reactions with hydrated hydronium* (1^{+}) *ions (n= 1-3) at 298 K.* Journal of the American Chemical Society, 1979. **101**(14): p. 3724-3730.

286. Halden, R.U., *Plastics and health risks.* Annu Rev Public Health, 2010. **31**: p. 179-94.

287. Benjamin, S., et al., *A monograph on the remediation of hazardous phthalates.* J Hazard Mater, 2015. **298**: p. 58-72.

288. *DIRECTIVE 2005/84/EC OF THE EUROPEAN PARLIAMENT AND OF THE COUNCIL of 14 December 2005*. 2005: Official Journal of the European Union. p. 40-43.

289. EHCA – European Chemicals Agency, *Candidate List of Substances of Very High Concern of Authorisation*. 2022. Available from: http://echa.europa.eu/candidate-list-table/-/substance/

290. Shen, H.Y., *Simultaneous screening and determination eight phthalates in plastic products for food use by sonication-assisted extraction/GC-MS methods.* Talanta, 2005. **66**(3): p. 734-9.

291. Juhasz, M.L. and E.S. Marmur, *A review of selected chemical additives in cosmetic products.* Dermatol Ther, 2014. **27**(6): p. 317-22.

292. Sadeghi, G., E. Ghaderian, and A. O'Connor, *Determination of Dioctyl phthalate (DEHP) concentration in polyvinylchloride (PVC) plastic parts of toothbrushes.* The Downtown Review, 2015. **1**(2).

293. Jeilani, Y.A., B.H. Cardelino, and V.M. Ibeanusi, *Positive chemical ionization triple-quadrupole mass spectrometry and ab initio computational studies of the multi-pathway fragmentation of phthalates.* J Mass Spectrom, 2010. **45**(6): p. 678-85.

294. Španěl, P., et al., *Breath acetone concentration; biological variability and the influence of diet.* Physiological measurement, 2011. **32**(8): p. N23.

295. Marschner, K., S. Musil, and J.i. Dědina, *Demethylation of Methylated Arsenic Species during Generation of Arsanes with Tetrahydridoborate (1−) in Acidic Media.* Analytical chemistry, 2016. **88**(12): p. 6366-6373.

296. Talmi, Y. and D. Bostick, *Determination of alkylarsenic acids in pesticide and environmental samples by gas chromatography with a microwave emission spectrometric detection system.* Analytical chemistry, 1975. **47**(13): p. 2145-2150.

297. Dedina, J. and D.L. Tsalev, *Hydride generation atomic absorption spectrometry*. Vol. 130. 1995: Wiley.

298. Dędina, J., *Generation of volatile compounds for analytical atomic spectroscopy.* Encyclopedia of Analytical Chemistry: Applications, Theory and Instrumentation, 2006.

299. Duben, O., et al., *Dielectric barrier discharge plasma atomizer for hydride generation atomic absorption spectrometry—Performance evaluation for selenium.* Spectrochimica Acta Part B: Atomic Spectroscopy, 2015. **111**: p. 57-63.

Attachments

Attachment A.1 – Publication and supplement

Lacko M, Wang N, Sovová K, Pásztor P, Španěl P.
Addition of fast gas chromatography to selected ion flow tube mass spectrometry for analysis of individual monoterpenes in mixtures.
Atmospheric Measurement Techniques. 2019. 12(9): 4965-82.

Authors contribution: Contribution of individual authors is stated in the paper.

Attachment A.2 – Publication

Lacko M, Piel F, Mauracher A, Španěl P.
Chemical ionization of glyoxal and formaldehyde with H_3O^+ ions using SIFT-MS under variable system humidity.
Physical Chemistry Chemical Physics. 2020. 22(18): 10170-10178

Authors contribution: Lacko and Piel carried out initial measurements on glyoxal ion chemistry. Results were later supplemented by study of formaldehyde provided by Lacko. Theoretical calculations were done by Lacko and Mauracher. Lacko later simulated experimental data using KIMI Sim. Lacko and Španěl prepared the publication.

Attachment A.3 – Manuscript and supplement

Lacko M, Španěl P, Mayhew Ch, Malásková M, Spesyvyi A.
SIFT-MS and PTR-MS studies of H_3O^+ reaction with glyoxal in presence of water molecules forming protonated formaldehyde at different interaction energies, Manuscript

Authors contribution: Lacko and Malásková carried out the experimenal study of glyoxal on PTR-MS. Lacko and Spesyvyi carried out the experimenal study of glyoxal on SIFDT-MS. Lacko simulated experimental data using KIMI Sim. Lacko, Španěl and Mayhew prepared the manuscript

Attachment A.4 – Publication and supplement

Lacko M, Michalczuk B, Matejčík Š, Španěl P.
Ion chemistry of phthalates in selected ion flow tube mass spectrometry: isomeric effects and secondary reactions with water vapour.
Physical Chemistry Chemical Physics. 2020. 22(28): 16345-52.

Authors contribution: Lacko and Michalczuk carried out the experimenal study. Lacko simulated experimental data using KIMI Sim. Lacko, Španěl and Matejčík prepared the publication.

Attachment A.5 – Publication and supplement

Spesyvyi A, **Lacko M**, Dryahina K, Smith D, Španěl P.
Ligand Switching Ion Chemistry: An SIFDT Case Study of the Primary and Secondary Reactions of Protonated Acetic Acid Hydrates with Acetone.
Journal of the American Society for Mass Spectrometry. 2021. 32(8): 2251-60.

Authors contribution: Spesyvyi carried out the experimenal study, theoretical calculations and preparation of the initial draft. Lacko supported experimental data with simulations of the ion chemistry. All authors later participated on the preparation of the publication.

Attachment A.6 – Publication and supplement

Kratzer J, **Lacko M**, Dryahina K, Matoušek T, Španěl P, Dědina J.
Atomization of As and Se volatile species in a dielectric barrier discharge atomizer after hydride generation: Fate of analyte studied by selected ion flow tube mass spectrometry.
Analytica chimica acta. 2022. 1190: 339256.

Authors contribution: Contribution of individual authors is stated in the paper

Attachment A.7 – KIMI Sim Software

Lacko M. Kinetic of Ion Molecular Interaction Simulator (KIMI Sim). 2022.

The KIMI Sim software is available at https://github.com/Progllar/KIMI-Simulator or in the physical multimedia attached to this work.

In the physical multimedia in the "KIMI Simulator source" file you can find the source code of the program. In the "v2.2.2 KIMI" you can find the build used for latest simulations presented in this work.

Authors contribution: The full code of the KIMI Sim was written by Lacko, except external modules: MassSpectrometry library, OxyPlot.Core library and MwtWinDll library.

Atmos. Meas. Tech., 12, 4965–4982, 2019
https://doi.org/10.5194/amt-12-4965-2019

Atmospheric Measurement Techniques
Open Access

Addition of fast gas chromatography to selected ion flow tube mass spectrometry for analysis of individual monoterpenes in mixtures

Michal Lacko[1,2], Nijing Wang[3], Kristýna Sovová[1], Pavel Pásztor[1], and Patrik Španěl[1]

[1]J. Heyrovský Institute of Physical Chemistry, The Czech Academy of Sciences, Dolejškova 2155/3,
182 23 Prague, Czech Republic
[2]Faculty of Mathematics and Physics, Charles University in Prague, Ke Karlovu 3, 121 16 Prague, Czech Republic
[3]Air Chemistry Department, Max-Planck-Institut für Chemie, Hahn-Meitner-Weg 1, 55128 Mainz, Germany

Correspondence: Michal Lacko (michal.lacko@jh-inst.cas.cz)

Received: 10 January 2019 – Discussion started: 21 March 2019
Revised: 30 July 2019 – Accepted: 13 August 2019 – Published: 13 September 2019

Abstract. Soft chemical ionization mass spectrometry (SCI-MS) techniques can be used to accurately quantify volatile organic compounds (VOCs) in air in real time; however, differentiation of isomers still represents a challenge. A suitable pre-separation technique is thus needed, ideally capable of analyses over a few tens of seconds. To this end, a bespoke fast gas chromatography (GC) instrument with an electrically heated 5 m long metallic capillary column was coupled to selected ion flow tube mass spectrometry (SIFT-MS) measurements. To assess the performance of this combination, a case study of monoterpene isomer ($C_{10}H_{16}$) analyses was carried out. The monoterpenes were quantified by SIFT-MS using H_3O^+ reagent ions (analyte ions $C_{10}H_{17}^+$, m/z 137, and $C_6H_9^+$, m/z 81) and NO^+ reagent ions (analyte ions $C_{10}H_{16}^+$, m/z 136, and $C_7H_9^+$, m/z 93). The combinations of the fragment ion relative intensities obtained using H_3O^+ and NO^+ were shown to be characteristic of the individual monoterpenes. Two non-polar GC columns (Restek Inc.) were tested: the advantage of MXT-1 was shorter retention, whilst the advantage of MXT-Volatiles was better separation. Thus, it is possible to identify components of a monoterpene mixture in less than 45 s using the MXT-1 column and to separate them in less than 180 s using the MXT-Volatiles column. Quality of the separation and the sensitivity of present technique (limit of detection, LOD, ∼ 16 ppbv) was found to be inferior compared to commercially available fast GC solutions coupled with proton transfer reaction mass spectrometry (PTR-MS, LOD ∼ 1 ppbv) due to the limited sample flow through the column. However, using combinations of two reagent ions improved identification of monoterpenes not well resolved by the chromatograms. As an illustrative example, the headspace of needle samples of three conifer species was analysed by both reagent ions and with both columns showing that mainly α-pinene, β-pinene and 3-carene were present. The system can thus be used for direct rapid monitoring of monoterpenes above 20 ppbv, such as applications in laboratory studies of monoterpene standards and leaf headspace analysis. Limitation of the sensitivity due to the total sample flow can be improved using a multi-column pre-separation.

1 Introduction

Monoterpenes, mostly emitted from plants, are very important biogenic volatile organic compounds (BVOCs) in the atmosphere. Due to their high reactivity with atmospheric oxidants such hydroxyl radicals ($OH^\bullet$), oxidation of monoterpenes can lead to tropospheric ozone (O_3) accumulation as well as secondary organic aerosol formation, which can affect human health and contribute to global climate change (Chameides et al., 1992; Fehsenfeld et al., 1992; Kulmala et al., 2004). Although all monoterpenes are comprised of two isoprene units, all of which have the same molecular formula, $C_{10}H_{16}$; their lifetime (inverse to reactivity) for reaction with $OH^\bullet$ and O_3 varies widely, from minutes to days (Atkinson and Arey, 2003) (see Table 1). The values of the total OH reactivity, which is dominated by BVOCs measured in rainforests, have been found to be higher than expected, which could be attributed to undetected monoterpenes or sesquiterpenes (Nolscher et al., 2016). Therefore, it is important to identify and individually quantify these BVOCs at their ambient trace levels.

Standard analytical methods used to identify and quantify volatile organic compounds (VOCs) in air, such as thermal desorption gas chromatography mass spectrometry (TD-GC-MS), are often time-consuming and cannot be used to investigate temporal changes in chemically evolving systems. In contrast, soft chemical ionization mass spectrometry (SCI-MS) techniques, such as selected ion flow tube mass spectrometry (SIFT-MS) (Smith and Španěl, 2011a; Španěl et al., 2006) and proton transfer reaction mass spectrometry (PTR-MS) (Lindinger et al., 1998; Ellis and Mayhew, 2013; Smith and Španěl, 2011b), represent well-established real-time tools for analysing a wide variety of VOCs in ambient air (Amelynck et al., 2013; de Gouw and Warneke, 2007; Malásková et al., 2019; Rinne et al., 2005; Schoon et al., 2003) and in the headspace of biological samples (Shestivska et al., 2011, 2012, 2015). The advantage of SIFT-MS and PTR-MS lies in the possibility of online, real-time analysis obviating sample collection and pre-concentration of VOCs. In these techniques, defined reagent ions (usually H_3O^+, NO^+ or $O_2^{+\bullet}$) interact with trace VOCs present in gas samples introduced into a flow tube or a flow–drift tube. The chemical ionization reactions that produced analyte ions are variously proton transfer, adduct ion formation, charge transfer and hydride ion transfer, principally depending on the type of reagent ions used. This ion chemistry has been thoroughly reviewed in a number of publications (Smith and Španěl, 2005). These ion–molecule reactions are not greatly exothermic, thus few product (analyte) ions result in each reaction that can readily be identified, often just one or two. However, chemically similar molecules with the same atomic composition (structural isomers) usually produce identical analyte ions with similar branching ratios, and therefore the neutral analyte molecules cannot be easily differentiated using SCI-MS alone (Smith et al., 2012). As a result, standard SCI-MS techniques such as SIFT-MS and PTR-MS are limited to reporting concentrations of the sum of monoterpenes presented in the sample, and the composition of the monoterpenes present cannot be determined. However, the reactions of the isomeric molecules may have different rate coefficients with the different reagent ions and lead to product ions at recognizably different branching ratios, depending on their molecular geometry (Jordan et al., 2009; Pysanenko et al., 2009; Španěl and Smith, 1998; Wang et al., 2003). So the concurrent use of the available reagent ions in SIFT-MS analysis can sometimes be used to analyse and identify particular isomers.

Quantitative measurement of monoterpenes is often problematic due to problems of stability of monoterpene mixtures in certified gas standards (Rhoderick and Lin, 2013). Therefore, fresh individual monoterpene standards or monoterpene mixtures can be prepared from liquid standards. To determine an accurate instrument sensitivity to individual monoterpenes, the relative abundance of monoterpene isomers must be known (de Gouw et al., 2003).

Gas chromatography mass spectrometry (GC-MS) coupled with pre-concentration techniques has been developed to successfully identify and quantify different atmospheric monoterpenes (Janson, 1993; Räisänen et al., 2009; Song et al., 2015). However, the requirements of pre-concentration and long cycle time (more than 1 h) are obviously unsuitable for real-time measurements.

A promising approach to the near-real-time analysis of isomeric molecules is to combine both SCI-MS and fast GC methods. Pre-separation provided by fast GC requires short columns with thin active layers, fast temperature ramps, fast injection systems and time resolutions below 5 min (Matisová and Dömötörová, 2003). Materić et al. (2015) established a system using PTR-MS coupled with a fast GC to detect individual monoterpenes and achieved the separation of the six most common monoterpenes at a limit of detection down to 1 ppbv. Pallozzi et al. (2016) then compared a fast CG-PTR time-of-flight (ToF) MS system with traditional GC-MS methods, discussing the limitations of the fast GC peak separation on some BVOCs emitted from plants, including monoterpenes (Pallozzi et al., 2016). The authors then recommended applying longer columns operating with a fast temperature gradient, such as 25 °C min^{-1}. SIFT-MS is also widely used in VOCs analyses (Allardyce et al., 2006; Smith and Španěl, 2011b, 2005b), which has well-defined analytical reaction conditions and the H_3O^+, NO^+ and $O_2^{+\bullet}$ reagent ions can be switched rapidly to analyse time-varying trace gas concentrations in air samples. In the present article, we report experimental developments aimed at selectively analysing individual monoterpenes in mixtures in air using a bespoke fast GC and SIFT-MS combination with H_3O^+ and NO^+ reagent ions. This involved the analysis of both prepared laboratory monoterpene–air mixtures and the headspace of the foliage of different pine trees.

2 Construction of a fast GC device for pre-separation

The experimental setup of the bespoke fast GC setup constructed as an addition to SIFT-MS is shown in Fig. 1. The routing of the sample and the carrier gases was controlled by solenoid valves (Parker VSONC-2S25-VD-F, < 30 m s response), labelled in Fig. 1 as EV1, EV2 and EV3. The needle valve NV1 was used in combination with an overflow relief tube to finely adjust the flow rate of the carrier gas (20–50 sccm from a gas cylinder, regulator set to about 2 bar) so that the air pressure at the column entrance is held just above ambient. The region of the sampling input line, EV2, EV3 and their connection with the column are permanently heated to ~ 60 °C to prevent adsorption of sample gas and vapour and to reduce memory effects.

Three modes of gas flow are possible, as illustrated in Fig. 1.

Table 1. Monoterpenes included in the present study, listed together with their atmospheric lifetime.

Compound	Lifetime for reaction with	Chemical lifetime[d]		Rate constant of $\mathrm{O_3}$	Rate constant of OH
	OH[b] $\mathrm{O_3}$[c]	Day	Night	reaction[e]	reaction[f]
α-pinene	2.6 h 4.6 h	2–3 h	5–30 min	8.7	5.45 ± 0.32
β-pinene	1.8 h 1.1 d	2–3 h	5–30 min	1.5	7.95 ± 0.52
camphene	2.6 h 18 d	nd	nd	9.0[g]	5.33[g]
myrcene	39 min 50 min	40–80 min	5–20 min	49	21.3 ± 1.6
3-carene	1.6 h 11 h	nd	nd	3.8	8.70 ± 0.43
(R)-limonene	49 min 2.0 h	40–80 min	5–20 min	21	16.9 ± 0.5
α-terpinene	23 min 1 min	< 5 min	< 2 min	870	36.0 ± 4.0
γ-terpinene	47 min 2.8 h	nd	nd	14	17.6 ± 1.8

[a] Taken from Atkinson and Arey (2003) unless noted otherwise. [b] Assumed OH radical concentration: 2.0×10^6 molecules $\mathrm{cm^{-3}}$, 12 h daytime average. [c] Assumed $\mathrm{O_3}$ concentration: 7×10^{11} molecules $\mathrm{cm^{-3}}$, 24 h average. [d] Lifetimes are estimated in relation to $[\mathrm{NO_3}] = 10$ pptv, $[\mathrm{O_3}] = 20$ ppb for night and $[\mathrm{OH}] = 10^6$ molecules $\mathrm{cm^3}$, $[\mathrm{O_3}] = 20$ ppb for daylight conditions (Kesselmeier and Staudt, 1999) unless noted otherwise. [e] Rate constants (in units of 10^{-17} $\mathrm{cm^3}$ $\mathrm{molecules^{-1}}$ $\mathrm{s^{-1}}$) for the gas-phase reactions of $\mathrm{O_3}$ with a monoterpenes have been determined at 296 ± 2 K and 740 Torr total pressure of air or $\mathrm{O_2}$ using a combination of absolute and relative rate techniques (Atkinson et al., 1990) unless noted otherwise. [f] Rate constants (in units of 10^{-11} $\mathrm{cm^3}$ $\mathrm{molecules^{-1}}$ $\mathrm{s^{-1}}$) for the gas-phase reactions of the OH radical with monoterpenes have been determined in one atmosphere of air at 294 ± 1 K (Atkinson et al., 1986) unless noted otherwise. [g] Rate constants of k $(\mathrm{OH} + \mathrm{isoprene}) = 1.01 \times 10^{-10}$ $\mathrm{cm^3}$ $\mathrm{molecules^{-1}}$ $\mathrm{s^{-1}}$. $\mathrm{O_3}$ reaction rate constants determined in 10^{-19} $\mathrm{cm^3}$ $\mathrm{molecules^{-1}}$ $\mathrm{s^{-1}}$ units. OH radical reaction rate constants determined in 10^{-11} $\mathrm{cm^3}$ $\mathrm{molecules^{-1}}$ $\mathrm{s^{-1}}$ units (Atkinson et al., 1990). nd: no data.

- *The normal mode*. EV2 is open and both EV1 and EV3 are closed. Carrier gas flows through NV1, partly vented via the overflow relief but mostly into the column. The pressure at the column entrance is just above the ambient atmosphere and a constant flow rate of clean carrier gas (synthetic air or helium) is thus achieved.
- *The sampling mode*. EV1 and EV2 are closed and EV3 is open. Sample air is introduced into the column over a short period (1 to 12 s), after which the normal mode is resumed.
- *The cleaning mode*. All valves are open and the carrier gas taken directly from the cylinder regulator is introduced into the column (higher than normal flow) and purges the sample line via EV3. The overflow relief flow rate is not sufficient to diminish the pressure.

The modes can be switched either manually or remotely by from the SIFT-MS software.

The operation sequence for air sample analysis is as follows: the column is first heated up to 200 °C in the cleaning mode for 3 min prior to commencing the normal mode with an appropriate heating voltage setting (e.g. 15 V as shown in Fig. 2). Whilst the column cools down, a pre-sampling interval (8–10 s sampling mode; see Fig. 2) is applied in order to refill the "dead volume", comprised of the EV3 valve and the sampling inlet by air at its entrance. After the column reaches working temperature and a steady flow of clean carrier gas is established, the sample for actual analysis is introduced by enabling the sampling mode for a selected time period.

In the experiments, two different GC columns were tested. First, a 5 m long nonpolar general-purpose chromatography metallic column MXT-1 (0.28 mm ×0.1 µm active phase, Restek Inc.) uses dry air as the carrier gas. The column was chosen according to the previous PTR-MS fast GC analyses (Romano et al., 2014). Additionally, a second, application-specific column for volatile organic pollutants, MXT-Volatiles (0.28 mm ×1.25 µm active phase, Restek Inc.), was used with helium carrier gas. In order to facilitate direct resistive heating, the coil-shaped stainless steel columns (resistivity $\sim 4.2\ \Omega\ \mathrm{m^{-1}}$) were electrically isolated

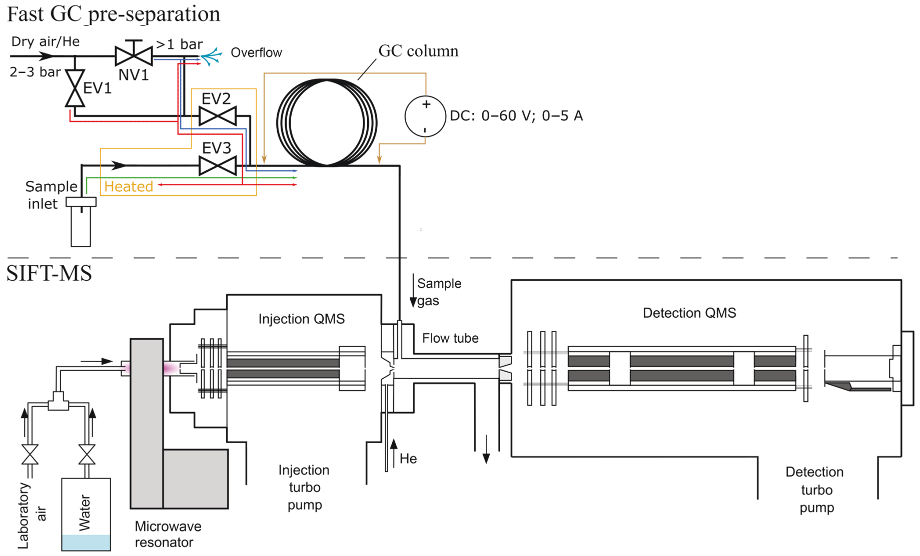

Figure 1. Schematic visualization of the fast GC and SIFT-MS experiment. Coloured lines in the inlet part of the fast CG represent gas flow through the system of valves EV1–3. The blue line traces the “normal mode” regime, the green line represents the “sampling mode” and the red line represents the “cleaning mode”.

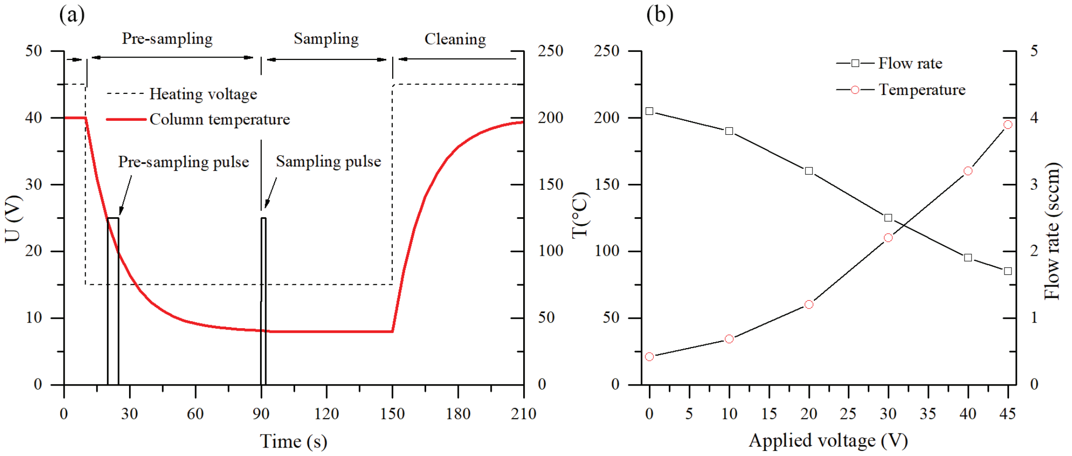

Figure 2. (a) The applied heating voltage (dashed) and the temperature profile of the column (red) during the fast GC cycle. The pulses indicate the opening of valve EV3 during the pre-sampling and the sampling periods. **(b)** The increase in the column temperature and the related decrease in the carrier gas flow rate with the heating voltage.

and connected to a regulated 60 V, 5 A DC power supply. Appearance of cold spots was suppressed by ensuring that the electrical current runs through the entire length of the columns. The temperatures of the columns were monitored by a K-type probe connected to their centres (see the right part of Fig. 2 for the temperature variation with applied voltage). It is interesting to note that the flow of sampled air, established by the pressure difference between ambient atmosphere and the low pressure of the SIFT-MS flow tube, changes with the column temperature due to the variation in the dynamic viscosity of the air (see Fig. 2). This effect can be estimated by direct measurement of the column flow rate and has to be accounted for in the quantification calculation (see Eq. 6).

In the initial tests with the first generic MXT-1 column, the sampling mode duration was fixed at 1.8 s due to SIFT-MS software limitations. For the later tests with the second MXT-Volatiles column, the SIFT-MS operational software was upgraded to provide an arbitrary timing of the sampling mode duration, where 6 or 12 s sampling intervals were used. Sampling was repeated several times to improve signal quality. The GC separation then takes place over typically 60–300 s, whilst the eluent is continuously analysed by SIFT-MS. It is possible to apply a heating ramp during this period.

Several heating ramp profiles were tested (see data for MXT-1 column in Fig. S1 in the Supplement); however, due to the short GC column and relatively long injection time, the monoterpene chromatogram peaks coalesced when the column temperature exceeded 60 °C and it was found that optimal chromatograms were obtained isothermally at 40 °C (15 V heating voltage). Effects of the heating voltage on the retention time and the chromatogram profile are illustrated in Fig. S4 (data for MXT-Volatiles column).

3 SIFT-MS analyses of the eluent

In the present study, a Profile 3 SIFT-MS instrument (Instrument Science, Crewe, UK) was used (Smith et al., 1999). Reagent ions are formed in a microwave discharge through a mixture of water vapour and atmospheric air (see Fig. 1). A mixture of ions is extracted from the discharge and focused into a quadrupole mass filter where they can be analysed according to their mass-to-charge ratio, m/z. Thus, the reagent ions H_3O^+, NO^+ or $O_2^{+\bullet}$ can be selected ($O_2^{+\bullet}$ was not used in the present experiment) and separately injected into flowing helium carrier gas (pressure $p = 1.4$ mbar; temperature $T = 24$ °C). Any internal energy possessed by the reagent ions is rapidly quenched in collisions with helium atoms, leaving a thermalized ion swarm that is convected down the flow tube. Sample gas is introduced into the helium and thermalized swarm at a known flow rate that (in the present experiments) changes with the GC column temperature. The reagent ions react with the VOC molecules in the sample gas during a time period, defined by the known flow speed of the ion swarm and the length of the flow tube. At the end of the flow tube, the ionic products (analyte ions) generated by the analytical ion–molecule reactions are sampled by a pinhole orifice into the analytical quadrupole mass spectrometer. The count rates of the reagent and analyte ions are obtained using a single channel electron multiplier. Thus, full scan (FS) spectra can be obtained over a chosen m/z range to identify the analyte ions or rapidly switched between selected m/z values using the multiple-ion monitoring mode (MIM) (Španěl and Smith, 2011a, 2013). For the present monoterpene study, the FS mode was used for SIFT-MS analyses, whilst the MIM mode was used for the fast GC and SIFT-MS setup. The typical count rate of the reagent ions was one million counts per second (cps) while those for the analyte ions were usually below 1 cps. Switching between the H_3O^+ and NO^+ reagent ions required a few milliseconds, depending mainly on the velocity of the carrier gas (12 000 cm s^{-1}) and the length of the flow tube (5 cm). Therefore, the only limiting factor is the software sampling frequency, which depends on the number of monitored ions but is usually below 1 s.

3.1 Reactions of the H_3O^+ and NO^+ reagent ions with monoterpenes

In the present study, SIFT-MS analyses of monoterpenes were carried out using the previously investigated reactions of monoterpenes with H_3O^+ and NO^+ ions (Schoon et al., 2003; Wang et al., 2003). The H_3O^+ reactions are known to proceed via proton transfer, forming $C_{10}H_{17}^+$ (m/z 137) ions that partially fragments to $C_6H_9^+$ (m/z 81) by the elimination of a C_4H_8 moiety from the nascent ($C_{10}H_{17}{}^{+*}$) excited ion.

$$H_3O^+ + C_{10}H_{16} \rightarrow C_{10}H_{17}^+ + H_2O \qquad \text{(R1a)}$$

$$\rightarrow C_6H_9^+ + C_4H_8 + H_2O \qquad \text{(R1b)}$$

The known values of the proton affinities (PA) of α-pinene, camphene (both 878 kJ mol^{-1}) (Solouki and Szulejko, 2007) and (R)-limonene (875 kJ mol^{-1}) (Fernandez et al., 1998) are well above the PA of water (691 kJ mol^{-1}) (NIST, 2019). The excess energy following proton transfer (almost 2 eV) allows the observed dissociation to occur.

NO^+ reacts with monoterpenes by charge transfer, forming the parent cation $C_{10}H_{16}^{+\bullet}$ (m/z 136) and a number of fragment ions, including $C_7H_9^+$.

$$NO^+ + C_{10}H_{16} \rightarrow C_{10}H_{16}^+ + NO \qquad \text{(R2a)}$$

$$\rightarrow C_7H_9^+ + NOC_3H_7 \qquad \text{(R2b)}$$

The exothermicity of the charge transfer in Reaction 2a is represented by the difference between the ionization energies of the neutral NO (9.26 eV) and that for the particular monoterpene (ranging from 8.07 eV for α-pinene to 8.4 eV for (R)-limonene) (Garcia et al., 2003; NIST, 2019). Other fragment ions, including $C_7H_8^+$, $C_7H_{10}^+$, $C_9H_{13}^+$ and $C_{10}H_{15}^+$, are also seen and the branching ratios between the channels (Reactions 2a to 2b) and other fragments depend on the isomeric structure of the monoterpene (Schoon et al., 2003; Wang et al., 2003). The branching ratios are given in Table S1 in the Supplement. Based on this known ion chemistry, for the present study the monoterpene analysis was accomplished using both the H_3O^+ reagent ions (recording the $C_{10}H_{17}^+$ (m/z 137) and $C_6H_9^+$ (m/z 81) analyte ions) and NO^+ reagent ion (recording the $C_{10}H_{16}^+$ (m/z 136) and $C_7H_9^+$ (m/z 93) analyte ions). To facilitate identification of specific monoterpenes on the basis of the branching ratios of Reactions (1) and (2), the analyte ion signal ratios [m/z 81]/[m/z 137] and [m/z 93]/[m/z 136] were determined under the same conditions as the Profile 3 SIFT-MS instrument as used for the standard monoterpene mixtures. These branching ratios (r), given in Table 2, are discussed in Sect. 4.2.

The interaction of the primary ions with monoterpenes may be affected by the presence of neutral water molecules and thus by different sample humidity. Wang et al. (2003) first reported this phenomenon when observing a change of the product ion signal ratio, r, in the reactions (see Sect. 3.2).

For H_3O^+ reagent ions, this change was significant for β-pinene (r reducing from 0.75 to 0.51), (R)-limonene (0.45 to 0.34) and 3-carene (0.33 to 0.23). For the NO^+ reagent ion, a significant effect was observed only for α-pinene (0.32 to 0.08) and β-pinene (0.25 to 0.05). The decrease in r can be explained by the formation of hydrates in the reagent ions. It can be shown that the PA of monoterpenes is sufficiently high to allow direct proton transfer from $H_3O^+H_2O$ ions.

3.2 Analysis of the product ion intensity ratios

To facilitate assignment of the fast GC elution peaks to specific monoterpenes, mean fragment ion fractions $r_i = f_i/g_i = [m/z\ 81]/[m/z\ 137]$ (or, for NO^+, $r_i = f_i/g_i = [m/z\ 93]/[m/z\ 136]$) were calculated for each interval of retention times t_1 to t_2, as the weighted mean of the product ion signal ratios $\overline{r_w}$:

$$\overline{r_w} = \sum\nolimits_{i=t_1}^{t_2} w_i \frac{f_i}{g_i};\; w_i = \frac{f_i + g_i}{\sum_{i=t_1}^{t_2} f_i + g_i}. \tag{1}$$

The weights (w_i) applied to each of several discrete measurements were based on the total signal count rates of both ions f_i and g_i in order to emphasize the area within the peak. Time intervals t_1 to t_2 were chosen for each isomer as the area of the chromatographic peak where the total ion signal was $> 10\,\%$ of the peak value.

The quality of the ratio estimation was assessed from the variation in the f_i/g_i ratio estimated as

$$\begin{aligned}\sigma_i^2 = \mathrm{Var}(f/g) &\approx \frac{\mu_f^2}{\mu_g^2}\left(\frac{\sigma_f^2}{\mu_f^2} + \frac{\sigma_g^2}{\mu_g^2}\right)\\ &= \frac{\mu_f^2}{\mu_g^2}\left(\frac{f + \sigma_{\mathrm{bg}_f}^2}{\mu_f^2} + \frac{g + \sigma_{\mathrm{bg}_g}^2}{\mu_g^2}\right),\end{aligned} \tag{2}$$

where μ_f and μ_g represent intensities of the selected fragments and σ_f^2 and σ_g^2 are the variances of the μ_f and μ_g intensities, estimated according to the Poisson distribution as the sum of distribution variance equal to the expected value $\lambda = \mu$ and background variance σ_{bg}^2 (Van Kempen and Van Vliet, 2000).

From this variation, the standard error of the weighted mean was calculated as follows:

$$\sigma_{\overline{r_w}} = \sqrt{\sum\nolimits_{i=t_1}^{t_2} w_i^2 \sigma_i^2}. \tag{3}$$

The weighted standard deviation of the f_i/g_i ratios was also routinely calculated as follows:

$$s = \sqrt{\frac{\sum_{i=t_1}^{t_2} w_i \left(\frac{f_i}{g_i} - \overline{r_w}\right)^2}{1 - \sum_{i=t_1}^{t_2} w_i^2}}. \tag{4}$$

3.3 Fast GC and SIFT-MS limits of detection and quantification

The total amount of eluting analyte, C, in each GC peak is determined by SIFT-MS from the area under the curve from the number density of the analyte molecules $[M]$ (Španěl et al., 2006) in the flow tube recorded as a function of time, t, according to the following equation:

$$C = \frac{1}{N_A} \int_0^{t_{\max}} [M] S \mathrm{d}t, \tag{5}$$

where N_A is the Avogadro constant and S is the constant volume flow rate of the sample and carrier gas mixture flowing into the SIFT-MS carrier gas as determined by the pumping speed of the SIFT-MS primary vacuum pump. Note that the flow rate of GC eluent gas does not enter this calculation and does not directly affect the determined amount of analyte expressed in nanomoles, nmol. $[M]$ is calculated by the Profile 3 software according to the SIFT-MS general method for the calculation of absolute trace gas concentrations from the reagent and product ion count rates, the reaction rate constants (see Table S1), and the reaction time considering differential diffusion losses (see Eq. 15 in Španěl et al., 2006).

The amount of neutral analyte (monoterpene) is proportional to its concentration $[A]$ in sampled air and the sampled volume, V, given by the sampling flow rate (usually 3 sccm) and sampling time (1.8 to 12 s) as follows:

$$C = [A] \frac{V}{V_m}, \tag{6}$$

where $[V_m] = 24.0\,\mathrm{L\,mol^{-1}}$ is the molar volume of air at 293 K. Note that the sampled volume, V, calculated from the sampling flow rate and sampling time, changes with the column temperature as mentioned previously. The flow rate needs to be carefully determined by a direct flow measurement.

The limit of detection (LOD) was determined for α-pinene and (R)-limonene from analysis of a calibration curve as 3 times the standard error of the predicted intercept value divided by the slope of the calibration regression line (Graus et al., 2010). α-pinene and (R)-limonene were chosen as they have the lowest and the highest reaction rate constants for proton transfer (2.3 for α-pinene and 2.6 for (R)-limonene, in $10^{-9}\,\mathrm{cm^3\,s^{-1}}$). For a reagent ion the count rate was 10^6 counts $\mathrm{s^{-1}}$, with a 12 s sampling interval and the LOD of the current setup was found to be 16.3 ppbv for α-pinene and 19.5 ppbv for (R)-limonene, using the column temperature 40 °C. For a column temperature 69 °C, the LOD for α-pinene decreased to 6.1 ppbv.

3.4 Reference chemicals and plant samples

All monoterpenes used in the experiments, i.e. (+)–α-pinene (98 %), (+)–β-pinene ($\geq 98.5\,\%$ analytical standard), camphene (95 %), myrcene (≥ 90 % analytical standard), 3-carene (≥ 98.5 % analytical standard), (+)–(R)-limonene (≥ 99.0 % analytical standard), α-terpinene (≥ 95 %) and γ-terpinene (97 %), were purchased from Sigma-Aldrich. Individual monoterpene vapour standards and monoterpene vapour mixtures were prepared using the diffusion tube method (Thompson and Perry, 2009). Thus, for individual standards, about 5 µL of each monoterpene liquid was placed in a 2 mL vial closed by polytetrafluoroethylene (PTFE) septum caps. Each vial was then penetrated with a diffusion tube (0.0625 in. outer diameter × 0.010 in. inner diameter × 5 cm in length PEEK capillary) and placed into a 15 mL glass vial closed by a PTFE septum. The headspace of the 15 mL vial was sampled after stabilization (> 30 min) of the concentration. The humidity of the headspace was typically 1.5 % water vapour by volume, as determined by SIFT-MS. For α-pinene, the vapour concentration was too high and thus it had to be reduced by placing only a much smaller amount of the sample into the 2 mL vial. For the mixture preparations, a similar approach was used in which several vials containing different monoterpenes, penetrated by PEEK capillaries, were placed together into a 500 mL bottle. Note that the concentrations of the individual isomers in the mixture were different due to the variations in the saturated vapour pressures of their liquids. The same mixture was used for H_3O^+ and NO^+ experiments with the MXT-1 column.

To demonstrate the applicability of the fast GC and SIFT-MS analyses to real samples, three different types of coniferous tree needles were prepared: spruce (*Picea pungens*), fir (*Abies concolor*) and pine (*Pinus nigra*) (see Figs. S5–S7). For the first study using the MXT-1 column, the needle samples (0.26 g spruce, 0.42 g fir and 0.32 g pine) were collected in the urban area of Prague (June 2017) and placed into 10 mL vials from which the headspace was sampled 30 min after harvesting. For the later study using the MXT-Volatiles column, pine tree twigs were collected (June 2018) from the same trees (21.8 g spruce, 21.4 g fir and 20.6 g pine). The exposed cuts of the twigs were sealed by wrapping parafilm around the cut. The samples were placed into a Nalophan bag with a volume of approximately 1 L. During the analyses, the analytical laboratory was thermalized to the outdoor temperature (about 30 °C) to reduce thermal shock to the samples. In the laboratory, only a scattered natural light was present.

4 Results and discussion

To investigate if the various monoterpenes in a mixture could be effectively distinguished using SIFT-MS enhanced by the fast GC pre-separation, eight common biogenic monoterpenes were investigated. Individual monoterpene standards were analysed first with both MXT-1 and MXT-Volatiles column to obtain the instrument response in terms of retention times and product ion ratios using the two reagent ions H_3O^+ and NO^+. Then, the separation of monoterpenes was demonstrated through analysis of a prepared monoterpene mixture. Separation of both GC columns was compared using isothermal GC at a temperature of 40 to 45 °C. The elution times of all studied monoterpenes were within 45 s of the total retention time for MXT-1 column and within 180 s for the MXT-Volatiles column. Using the information on the ratios of ion products for the H_3O^+ and NO^+ reactions together with the GC retention times, it was possible to identify the composition of a reference standard mixture. Finally, the same procedure was used to analyse the leaf headspace of three coniferous samples to demonstrate the analysis of real samples.

4.1 Comparison of columns: MXT-1 vs. MXT-Volatiles

In the present experiment both columns were heated isothermally to approximately 40 °C, selected to optimize temperature stability and chromatographic separation (see Fig. S4). For higher temperatures, the monoterpene chromatogram peaks coalesced, while for lower temperatures a significant influence of the lab air temperature fluctuations was apparent. However, even at these optimized conditions for the MXT-1 column, monoterpenes are not fully separated, and thus fast GC with the MXT-1 column alone (at 40 °C) provides only qualitative analysis.

The retention times determined from the chromatograms obtained for individual monoterpenes at 40 °C are given in Table 2 and further supported by Fig. S2. For the MXT-1 column, the apparent difference in retention times observed between the two reagent ions was probably caused by the temperature fluctuations of the column. Whilst the retention times for individual monoterpenes are different, they are not sufficiently stable (i.e. they fluctuate by > 1 s; see Table 2) in the present fast GC device for analyses based only on retention time to be reliable. A noticeable effect of ambient temperature on the rate of passive column cooling was observed, resulting in changes of the column temperature profile and thus in variations in the monoterpene retention times. Therefore, for a longer column and a higher temperature it may be reduced. Use of the MXT-Volatiles column resulted in about 5 times longer retention times and better GC peaks separation at the same operational conditions (flow rate, temperature and pressure), due to the higher efficiency of the 1.25 µm active phase (compared to 0.1 µm for MXT-1 column).

The quality of the separation can be increased by using hydrogen as a carrier gas and by a faster sample injection, as demonstrated by Materić et al. (2015) with fast GC PTR-MS where complete separation of monoterpenes was achieved using the MXT-1 column. As observed for both columns, separation can be improved by decreasing the column temperature (see Figs. 3 and S4); however, this increases the chromatogram width.

The performance of both the MXT-1 and MXT-Volatiles columns were compared by analyses of a gas mixture of eight monoterpenes. For the MXT-1 column, four characteristic GC peaks were identified for both reagent ions, marked as A, B, C, and D with retention times of 17.6, 20.8, 26.3, and ∼ 30 s for H_3O^+ and 17.5, 20.7, 26.3, and ∼ 30 s for NO^+ (see Fig. 4). Based on the retention times obtained for individual monoterpenes (see Table 2 and Fig. S2), peak A is due to co-elution of α-pinene, camphene, and myrcene; peak B is due to the presence of β-pinene exclusively; and peaks C and D are due to the remaining four monoterpenes, mainly 3-carene and (R)-limonene. Note that the individual peak heights are influenced by the monoterpene-saturated vapour pressures (see Table 2). Using the MXT-1 column under these conditions it is not possible to achieve separate GC peaks for individual monoterpenes; however, qualitative analysis is possible.

The MXT-Volatiles column facilitates identification of all monoterpenes present in the mixture for a column temperature close to room temperature (see Fig. 3). For the MXT-Volatiles tests, the sampling mode was extended to 12 s, representing the collection of approximately 0.6 mL of the monoterpene mixture headspace. At a column temperature 40 °C, the monoterpene peaks are well separated; however, α-pinene and camphene are likely to co-elute. It is interesting to note that the chromatogram (see Fig. S4) changes with the temperature of the column and additional peaks appear at higher temperatures, probably as a result of the presence of different conformers. It thus seems that at the column temperature ∼ 45 °C, using 20 V heating voltage (see Fig. 4) in the mixture chromatogram, the small β-pinene is hidden behind the second camphene peak and the α-terpinene peak also disappears (see also the fragmentation analyses later in Sect. 4.2).

4.2 Analysis of product ratio and use of the NO^+ reagent ions

The inadequate separation of monoterpenes due to a short column or high temperature (as for the MXT-1 column) can be mitigated by the analysis of the product ion signal ratios r_i (see Sect. 3.2) and additionally by using an additional reagent ion. It may be possible to improve identification of myrcene or camphene (often co-eluted with α-pinene), as well as of other monoterpenes, by exploiting the different ion chemistry of the NO^+ reagent ions. These data, in combination with H_3O^+ data, allow identification of compounds on the basis of the ratios of four different product ions. The NO^+ reagent ions were used only for the MXT-1 column because full separation of monoterpenes using H_3O^+ reagent ions was not achieved and thus retention time cannot be effectively used as a parameter for their identification. However, as will be shown, use of the NO^+ reagent ions brings additional benefits and thus it may be a valuable source of information even for fully separated chromatograms. Note that the retention times are determined by the fast GC conditions and do not depend on which SIFT-MS reagent ion is used (see Table 2).

The $\overline{r_w}$ values (see Table 2) obtained from the SIFT-MS FS data and the MIM data for the fast GC peaks for most of the isomers are in good agreement. However, the ratios obtained for α-pinene and myrcene are somewhat variable between the FS and MIM data and they also differ somewhat from the literature values (α-pinene from 0.45 to 0.67 for H_3O^+; myrcene from 0.44 to 0.72 for H_3O^+). This may be caused by the different humidities of the samples, as discussed in Sect. 3.1, where it was seen that an increase in humidity lowers the $\overline{r_w}$ values. In the fast GC setup, water retention time is much shorter than the retention time for monoterpenes; thus, water influence on the ion chemistry is negligible for most monoterpenes. α-pinene can be slightly affected as it is the first one presented in the chromatogram. Therefore, only $\overline{r_w}$ values obtained using the fast GC are used for further study. The standard error of the fast GC $\overline{r_w}$ values for individual monoterpenes estimated by Eq. (3) (using the MXT-1 column) is less than 5 % (except 8.6 % for camphene) and is smaller than the observed variability between the analytical methods. The $\overline{r_w}$ values for MXT-Volatiles column were similar to those obtained with MXT-1 column, as expected.

Analysis of $\overline{r_w}$ values can now be used to improve identification of monoterpenes in standard mixtures. For the MXT-1 column, the $\overline{r_w}$ values for peaks A, B, C and D (see Fig. 4) were calculated as 0.49 ± 0.09, 0.63 ± 0.07, 0.45 ± 0.04 and 0.40 ± 0.05, respectively, for H_3O^+ and as 0.21 ± 0.05, 0.21 ± 0.04, 0.27 ± 0.06 and 0.14 ± 0.03 for NO^+. Based on these ratios (using fast GC data from Table 2), peak B could clearly be assigned as β-pinene. However, the remaining peaks contain several isomers and thus the $\overline{r_w}$ values do not provide unique identification. Therefore, the variations in the dynamic profile of r_i needed to be investigated to see if it can provide additional information. The time profile of r_w in the chromatogram is shown in the bottom part of Fig. 4. To recognize trends in these data, Savitzky–Golay smoothing (Savitzky and Golay, 1964) was used (i.e. second-order polynomial across 10 data points (OriginPro 9.0, OriginLab Corporation, Northampton, MA, USA, 2018). Also plotted (grey area in Fig. 4) is the standard deviation of the data points from the smoothed line in the interval of retention times from 15 to 40 s. Note that this standard deviation is greater than the standard error of the data points, possibly due to a lower accuracy of data at the longer retention times. The standard deviation allows assessment of the significance of the changes in $r_i = f_i/g_i$.

According to the elution time, the first chromatographic peak A consists of three monoterpenes: α-pinene, camphene and myrcene. For the H_3O^+ reagent ions, the $\overline{r_w}$ value corresponds to both α-pinene and myrcene, considering the $\overline{r_w}$ value for peak A (0.49) or r_w close to the peak maxima (0.55–0.6). However, a more obvious difference between α-pinene and myrcene is observed using NO^+ reagent ions. The value of the weighted mean ratio for peak A (0.21) is close to the ratio for α-pinene. In the maxima of peak A, however, r_w approaches the value of 0.3, which is close to the value expected for a combination of both these monoterpenes (0.32, considering the data from fast GC measurement

Table 2. Ratios of the H_3O^+ and NO^+ reaction product ion signals and the GC retention times, s, for the eight monoterpenes at a column temperature of 40 °C. Also given are the saturated vapour pressures (Torr). The standard error of the fast GC $\overline{r_w}$ values for individual monoterpenes estimated by Eq. (3) is less than 5 % (except 8.6 % for camphene) and less than ±0.02 overall.

Compound	$[m/z\ 81]/[m/z\ 137]$		$[m/z\ 93]/[m/z\ 136]$		Retention time (s)		
	H_3O^+		NO^+		H_3O^+	NO^+	H_3O^+
Saturated vapour pressure (Torr)	Literature Schoon[a], Wang[b]	Results full scan fast GC MIM	Literature: Schoon[a], Wang[b]	Results full scan fast GC MIM	MXT-1	MXT-1	MXT-Vol
α-pinene 4.75[e]	0.45 0.64	0.67[c] 0.46[d]	0.05 0.09	0.16[c] 0.19[d]	16	14.7	72
camphene 2.50[e]	0.1 0.16	0.14[c] 0.16[d]	0 0.01	– 0.03[d]	17	17.7	83
β-pinene 2.93[e]	0.52 0.67	0.61[c] 0.66[d]	0.03 0.08	0.12[c] 0.17[d]	20.4	22	106
myrcene 2.09[f]	0.44 0.52	0.72[c] 0.51[d]	0.36 0.62	0.72[c] 0.63[d]	18.5	17.8	134
3-carene 3.72[h]	0.24 0.32	0.39[c] 0.35[d]	0.05 0.1	0.12[c] 0.15[d]	25.5	25.6	142
α-terpinene 1.64[h], 1.66[i]	– 0.11	0.14[c] 0.17[d]	–	0.01[c] 0.01[d]	27	25.1	157
(R)-limonene 1.98[g]	0.30 0.43	0.43[c] 0.41[d]	0 0.01	0.03[c] 0.06[d]	27.5	31	170
γ-terpinene 1.07[h], 0.7[j]	– 0.21	0.18[c] 0.16[d]	0.08 0.09	0.08[c] 0.09[d]	40.4	32.5	184

[a] Schoon et al. (2003). [b] Wang et al. (2003). [c] Present result based on SIFT-MS measurement. [d] Present results based on fast GC and SIFT-MS measurement. Saturated vapour pressures in Torr at 25 °C, according to [e] Daubert (1989), [f] Haynes (2014), [g] Yaws (1994), [h] TGSC, [i] Takasago (2011), and at 20 °C, according to [j] Chemical Book (2016).

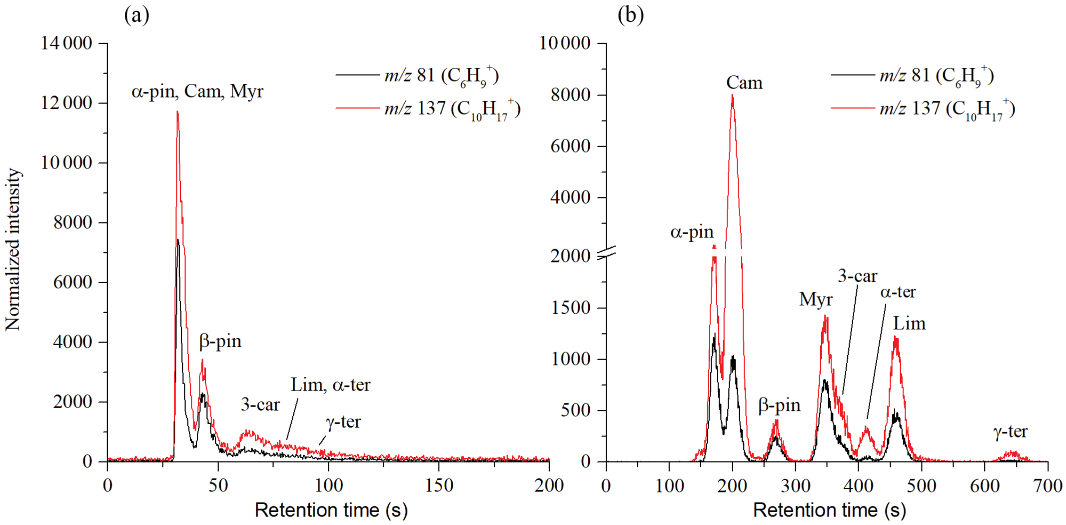

Figure 3. Chromatograms of mixtures of monoterpenes at room temperature obtained using the MXT-1 column **(a)** and the MXT-Volatiles column **(b)**. Chromatogram peaks in the MXT-1 column are not fully separated, but separation takes less than 150 s compared to the 700 s required for the MXT-Volatiles column. The signal intensities are the analyte ion count rates normalized to a H_3O^+ reagent ion count rate of $10^6\ s^{-1}$.

and the vapour pressure in Table 2). For camphene, r_w in the chromatograph did not reach the low values expected for both reagent ions. However, its presence is clearly visible as a dip in r_w situated between peaks A and B. In the absence of camphene, the ratio should linearly move to values characteristic of peak B without any dip. The depth of the dip does not reach the r_w expected for camphene due to the persistent tails of the peaks for both α-pinene and myrcene.

Peak B in the chromatograms is identified as β-pinene by its retention time. The $\overline{r_\mathrm{w}}$ values for the $\mathrm{H_3O^+}$ and $\mathrm{NO^+}$ reagent ions are 0.63 and 0.21, respectively. The r_w values are similar to $\overline{r_\mathrm{w}}$ and slightly higher than the fast GC standard values for β-pinene (see Table 2).

Peaks C and D are not clearly separated in the chromatogram. For the $\mathrm{H_3O^+}$ reagent ions, the $\overline{r_\mathrm{w}}$ value is similar for both peaks; thus, the presence of (R)-limonene, 3-carene or α-terpenine is likely because the $\overline{r_\mathrm{w}}$ values for peaks C (0.45) and D (0.4) are comparable with the analyte signal ratios (see Table 2) for (R)-limonene and 3-carene. A lower r_i for α-terpinene might be interpreted as a dip similar to that for camphene. However, the observed dip in r_i at peak D is not as statistically significant as the dip for camphene, and the vapour pressure for both α- and γ-terpinene is lower than those for the other monoterpenes. Analysis of peaks C and D using the $\mathrm{NO^+}$ reagent ion shows a clearer difference between them. The calculated $\overline{r_\mathrm{w}}$ for peak C (0.27), as well as the maximum r_i (0.35), are, unexpectedly, much higher than for the remaining monoterpenes. This can only be explained by the influence of myrcene or by the presence of impurities in the form of an additional monoterpene in the mixture (for example, ocimene has a high r_i of 0.62; Wang et al., 2003). Amongst the eight monoterpenes, 3-carene has the highest r_i within the retention time of peak C. The second peak D (0.14) can be then associated with (R)-limonene, which has a low r_i (0.06) for $\mathrm{NO^+}$ reagent ions, with some contribution by α-terpinene. The presence of γ-terpenine is not apparent due to its low vapour pressure, but there may be some contribution in the peak D that is much smaller than the contribution by (R)-limonene.

To summarize, combining analyses using both $\mathrm{H_3O^+}$ and $\mathrm{NO^+}$ reagent ions with dynamic variations in r_i allows the identification of α-pinene, camphene and myrcene in peak A and the presence of β-pinene only in peak B. Peak C is characterized as 3-carene and peak D as (R)-limonene and/or α-terpinene. γ-terpenine contributes only weakly due to its low vapour pressure and has no recognizable response in the chromatogram compared to the remaining monoterpenes.

Analysis of the $\overline{r_\mathrm{w}}$ values for the MXT-Volatiles column is simpler due to better separation of peaks. The value of r_i clearly change for different monoterpenes, according to the expected $\overline{r_\mathrm{w}}$ values for individual monoterpenes. The usefulness of the r_i analysis for the MXT-Volatiles column can be observed in the analysis of β-pinene, which is featureless compared to that for camphene. Camphene, additionally, produces a second chromatographic peak, which can be incorrectly associated with β-pinene. Analysis of the r_i shows values below 0.2 for both peak maxima, characteristic of camphene. The presence of β-pinene is visible as an increase in the r_i value up to 0.4 at a retention time of 60 s.

4.3 Tree sample investigation using the MXT-1 column

To test how the fast GC and SIFT-MS combination is applicable for analyses of real botanical samples, VOC emissions were analysed from three fresh coniferous tree needle samples: spruce, fir and pine, as shown in Fig. 5. The analytical MS obtained using a $\mathrm{H_3O^+}$ reagent ion are shown in Fig. S3. Based on the results of the above GC data for standard monoterpene mixtures, the chromatograms were divided into three regions. The first region is characterized by the presence of α-pinene, camphene and myrcene with retention times of between 12 and 18 s, the second region is characterized by the presence of β-pinene with retention times between 18 and 25 s and the third region characterized is by presence of 3-carene and (R)-limonene with retention times between 25 and 40 s. The $\overline{r_\mathrm{w}}$ values were calculated for the specific regions as follows.

Spruce. In the first region of the main peak there was 0.35 ± 0.07 ($\mathrm{H_3O^+}$) and 0.11 ± 0.04 ($\mathrm{NO^+}$). Note that the very low $\overline{r_\mathrm{w}}$ for $\mathrm{NO^+}$ indicates the absence of myrcene. The $\overline{r_\mathrm{w}}$ value for $\mathrm{H_3O^+}$ is lower than expected for β-pinene and higher than expected for camphene. Therefore, the first peak is mainly due to α-pinene, perhaps with a small amount of camphene. In the second region of the main peak there was 0.31 ± 0.07 ($\mathrm{H_3O^+}$) and 0.09 ± 0.08 ($\mathrm{NO^+}$). $\overline{r_\mathrm{w}}$ for $\mathrm{H_3O^+}$ is lower than expected for β-pinene and higher than that for camphene. The signal therefore belongs to the decay of α-pinene. The signal ratio is 0.38 ± 0.14 ($\mathrm{H_3O^+}$); 0.14 ± 0.12 ($\mathrm{NO^+}$) in the third region indicates presence of (R)-limonene or 3-carene.

Fir. The chromatogram shows two large peaks. The calculations of $\overline{r_\mathrm{w}}$ for the first region (0.40 ± 0.04 for $\mathrm{H_3O^+}$ and 0.14 ± 0.04 for $\mathrm{NO^+}$) and for the second region (0.56 ± 0.04 for $\mathrm{H_3O^+}$ and 0.15 ± 0.02 for $\mathrm{NO^+}$) indicate the presence of both α-pinene and β-pinene. The decreasing $\overline{r_\mathrm{w}}$ for the $\mathrm{H_3O^+}$ reagent ions in the last part (0.48 ± 0.06 for $\mathrm{H_3O^+}$ and 0.19 ± 0.05 for $\mathrm{NO^+}$) indicates the presence of 3-carene.

Pine. The chromatogram contains only one peak. $\overline{r_\mathrm{w}}$ is stable for both reagent ions for all retention times (0.55 ± 0.06 for $\mathrm{H_3O^+}$ and 0.21 ± 0.05 for $\mathrm{NO^+}$ for the first sector; 0.57 ± 0.05 for $\mathrm{H_3O^+}$ and 0.22 ± 0.04 for $\mathrm{NO^+}$ for the second sector; 0.57 ± 0.09 for $\mathrm{H_3O^+}$ and 0.22 ± 0.10 for $\mathrm{NO^+}$ for the third sector). Together with the retention time of the peak (16.4 s) this certainly corresponds to α-pinene.

Concentrations of individual monoterpenes were calculated according to the procedure described in Sect. 3.3 for all selected regions. Calculation of monoterpene concentrations depends primarily on the individual reaction rate constants (see Table S1), which change from 2.3 to 2.6 for $\mathrm{H_3O^+}$ and from 2.0 to 2.3 for $\mathrm{NO^+}$ (in units of $10^{-9}\,\mathrm{cm^3\,s^{-1}}$). Incorrect

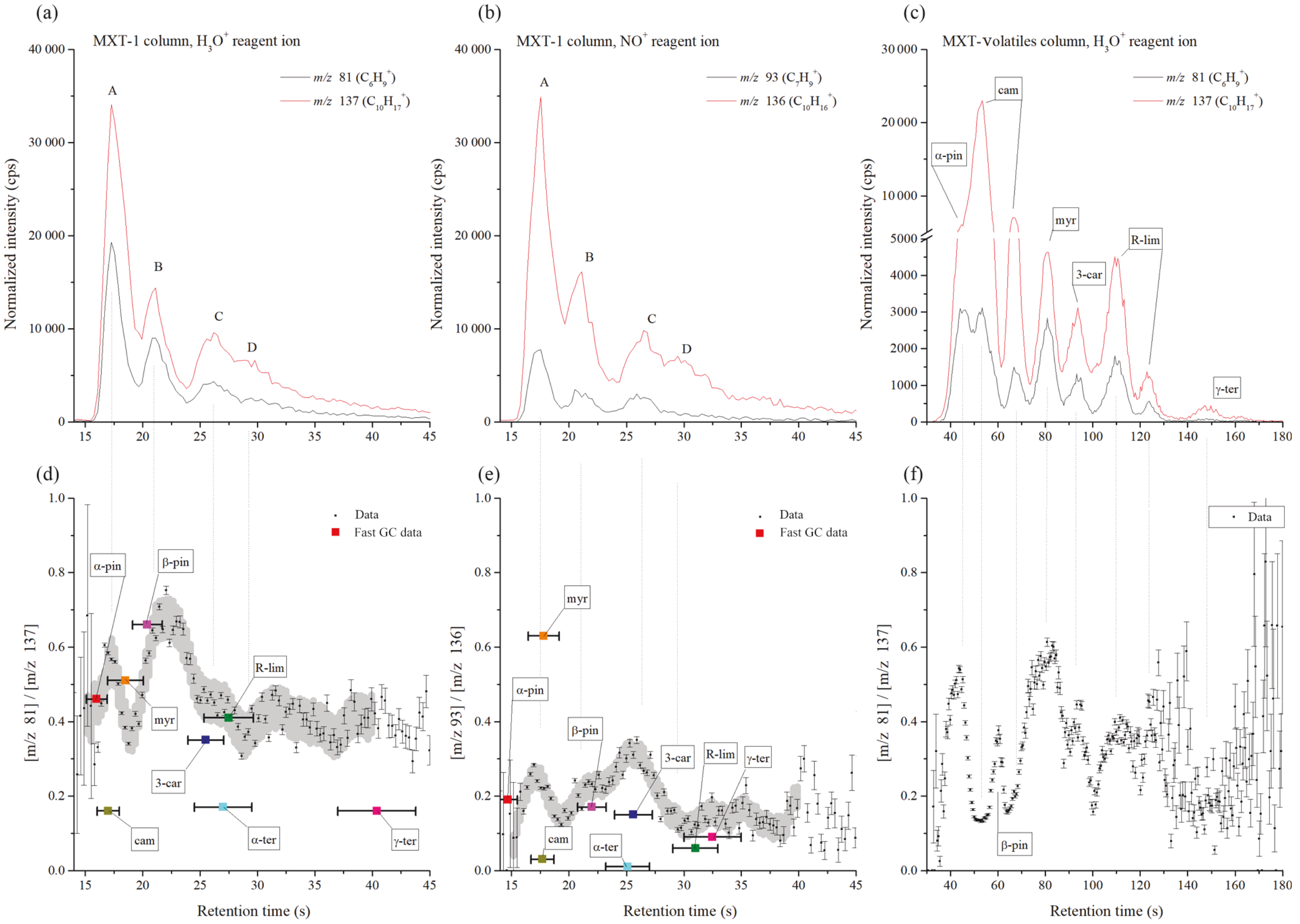

Figure 4. Chromatograms of the mixture of monoterpenes (top row) measured by H_3O^+ **(a)** and NO^+ **(b)** reagent ions, obtained using the MXT-1 column. A, B, C, and D represent characteristic peaks in the chromatogram. For each chromatogram, the product ion signal ratio r_i is presented in the lower figures. The grey data background represents the calculated standard deviation of the data by Savitzky–Golay smoothing between 15 and 40 s. The position and value of the ratio for individual monoterpenes is based on the fast GC MXT-1 measurements presented in Table 1. Note that the retention times are determined by the fast GC conditions and do not depend on which SIFT-MS reagent ion is used. The signal intensities are the analyte ion count rates normalized to a reagent ion count rate of $10^6\ s^{-1}$.

identification of the monoterpene will thus lead to a maximum 20 % error in the concentration calculation. According to the $\overline{r_w}$ values in selected regions, the most representative rate constant was adopted to calculate the monoterpene concentration in the selected region (see Table 3).

4.4 Tree sample analyses using the MXT-Volatiles column

Similar experiments were conducted using the MXT-Volatiles column as well but using a different set of coniferous samples. The retention times for the individual monoterpenes were taken from the standard data obtained at the same column temperature (40 °C). The higher retention times of the MXT-Volatiles provides more accurate peak identification than the MXT-1 analysis does. However, the different sample types resulted in a lower monoterpene concentration and thus the uncertainty of the $\overline{r_w}$ values significantly increased. The headspaces of the prepared tree needles were sampled for 6 s, representing a headspace volume of 0.3 mL. The chromatograms obtained for the spruce, fir and pine samples are shown in Fig. 6 and represent the means of analyte ion count rates from five consecutive runs normalized to a constant reagent ion count rate of $10^6\ s^{-1}$.

Spruce. In the chromatogram, four peaks were observed. The first peak, with a retention time of 68 s, corresponds to α-pinene with $\overline{r_w}$ of 0.60±0.16 for H_3O^+ and 0.24±0.15 for NO^+ reagent ions. The trailing edge of the first peak shows a decrease in $\overline{r_w}$ (0.29 ± 0.11 for H_3O^+ and 0.14 ± 0.26 for NO^+) attributed to a small contribution by camphene. The second peak is attributed to β-pinene and characterized by a retention time of 94 s with $\overline{r_w}$ of 1.05 ± 0.59 for H_3O^+ and 0.50±0.15 for NO^+. The standard deviation in r_w was unfortunately substantial. The position of the third peak is assigned

Table 3. Calculated concentrations of monoterpenes (in ppmv and %) in the headspace over coniferous needles in selected regions of chromatograms obtained using MXT-1 column at column temperature 40 °C, using an injection time of 1.8 s and a column flow of 3 sccm. Rate constant used for the calculation of concentration in selected regions was chosen according to the $\overline{r_\mathrm{w}}$ analysis.

Sample	Concentration (ppmv, %)			
	12–18 s	18–25 s	25–40 s	Sum 12–40 s
Spruce (H_3O^+)	11.0[a], 42 %	9.0[a], 35 %	5.2[c], 5.9[d], 23 %	25.2[a,c], 25.9[a,d]
Spruce (NO^+)	14.5[a], 50 %	6.6[a], 23 %	7.4[c], 7.7[3], 27 %	28.5[a,c], 28.8[a,d]
Fir (H_3O^+)	177[a], 32 %	274[b], 49 %	95[c], 107[d], 19 %	546[a,b,c], 558[a,b,d]
Fir (NO^+)	117[a], 31 %	191[b], 51 %	74[c], 77[d], 18 %	372[a,b,c], 375[a,b,d]
Pine (H_3O^+)	195[a], 55 %	112[a], 31 %	43[c], 49[d], 14 %	350[a,c], 356[a,d]
Pine (NO^+)	128[a], 48 %	100[a], 37 %	38[c], 41[d], 15 %	266[a,c], 269[a,d]

Calculations were performed using the reaction rate constants for [a] α-pinene, [b] β-pinene, [c] (R)-limonene or [d] 3-carene.

to myrcene. The $\overline{r_\mathrm{w}}$ values (0.43 ± 0.25 for H_3O^+, 0.41 ± 0.54 for NO^+) were again imprecise due to the low intensity and do not fully agree with the unique $\overline{r_\mathrm{w}}$ for myrcene (see Table 2). The observed weak peak could therefore be due to monoterpenes other than those eight included in Table 1. The last peak is associated with 3-carene with $\overline{r_\mathrm{w}}$ as 0.48 ± 0.27 for H_3O^+ and 0.16 ± 0.39 for NO^+ reagent ions.

Fir. In the chromatogram, three peaks are present where the first is due to both α-pinene and camphene. Transition of $\overline{r_\mathrm{w}}$ from the left (0.57 ± 0.21 for H_3O^+, 0.23 ± 0.13 for NO^+) to the right (0.22 ± 0.07 for H_3O^+ and 0.04 ± 0.04 for NO^+) part of the first peak is clearly visible on the Fig. 6 in the middle column. The first peak thus consists of two isomers. The second peak is attributed to β-pinene ($\overline{r_\mathrm{w}}$ 0.80 ± 0.21 for H_3O^+ and 0.26 ± 0.19 for NO^+), and the third peak is attributed to 3-carene ($\overline{r_\mathrm{w}}$ 0.39 ± 0.17 for H_3O^+ and 0.15 ± 0.27 for NO^+).

Pine. The chromatogram shows three clear peaks due to α-pinene (0.73 ± 0.13 for H_3O^+ and 0.30 ± 0.04 for NO^+), β-pinene (0.92 ± 0.22 for H_3O^+ and 0.26 ± 0.13 for NO^+) and 3-carene (0.49 ± 0.15 for H_3O^+ and 0.13 ± 0.15 for NO^+) with only a very small and statistically insignificant indication of camphene. The retention times for α-pinene, β-pinene and 3-carene were 69.6, 97 and 141 s, respectively.

The concentrations of individual monoterpenes were calculated according to the procedure described in Sect. 3.3 based on the individual reaction rate constants (see Table S1). Calculated monoterpene concentrations are presented in Table 4.

4.5 Comparison of the tree sample analyses

Some differences are seen between the results from the MXT-1 and MXT-Volatiles columns. The most significant differences are the presence of a camphene peak in the fir sample headspace and the presence of β-pinene and 3-carene in the pine sample headspace when the MXT-Volatiles column was used. However, samples were collected at different times of the year and the character of the samples was also different (only needles for MXT-1 and whole twigs for the MXT-Volatiles analyses). Different sample sources could also cause differences in monoterpene concentration (see Tables 3 and 4).

Additionally, the recorded analyte ions may include interference by ions originating from other BVOCs emitted by the samples, especially when plants are physically damaged, since they emit so-called "leaf aldehydes" such as 2-hexenal and 3-hexenal (Tani et al., 2003). Whilst the reaction of 2-hexenal with H_3O^+ proceeds as a proton transfer forming a product ion at m/z 99 (100 %), it has been found that reaction of *cis*-3-hexenal with H_3O^+ results in H_2O elimination producing a dominant fragment at m/z 81 (Španěl et al., 1997). If these interferences occur, they may eventually lead to the increase and to misinterpretation of the estimated $\overline{r_\mathrm{w}}$ value. To avoid an overlap of 3-hexenal with monoterpenes, it is thus more reliable to use the product or analyte ion at m/z 137 and exclude the m/z 81 ion. Another possibility is to choose NO^+ as a precursor ion, where the product ions of 3-hexenal (m/z 97, 69 and 74) do not overlap with those of monoterpenes (m/z 92, 93 and 136) (Wang et al., 2003). Unfortunately, we did not carry out the fast GC analysis of 3-hexenal, so we do not know if it actually interfered with any of the detected monoterpene peaks.

4.6 Comparison with previous studies

The present experiments indicate that using the fast GC and SIFT-MS combination, it is possible to achieve analysis of monoterpene mixtures. The estimated LODs are as follows: 16.3 ppbv for α-pinene and 19.5 ppbv for (R)-limonene, using the column temperature at 40 °C, and for the column temperature 69 °C, the LOD for α-pinene decreased to 6.1 ppbv. This is inferior to the previously described limit of the detection of up to 1–2 ppbv and full separation achieved by a fast GC-PTR-MS systems (Materić et al., 2015; Pallozzi et al., 2016). The higher LOD of the fast GC and SIFT-MS

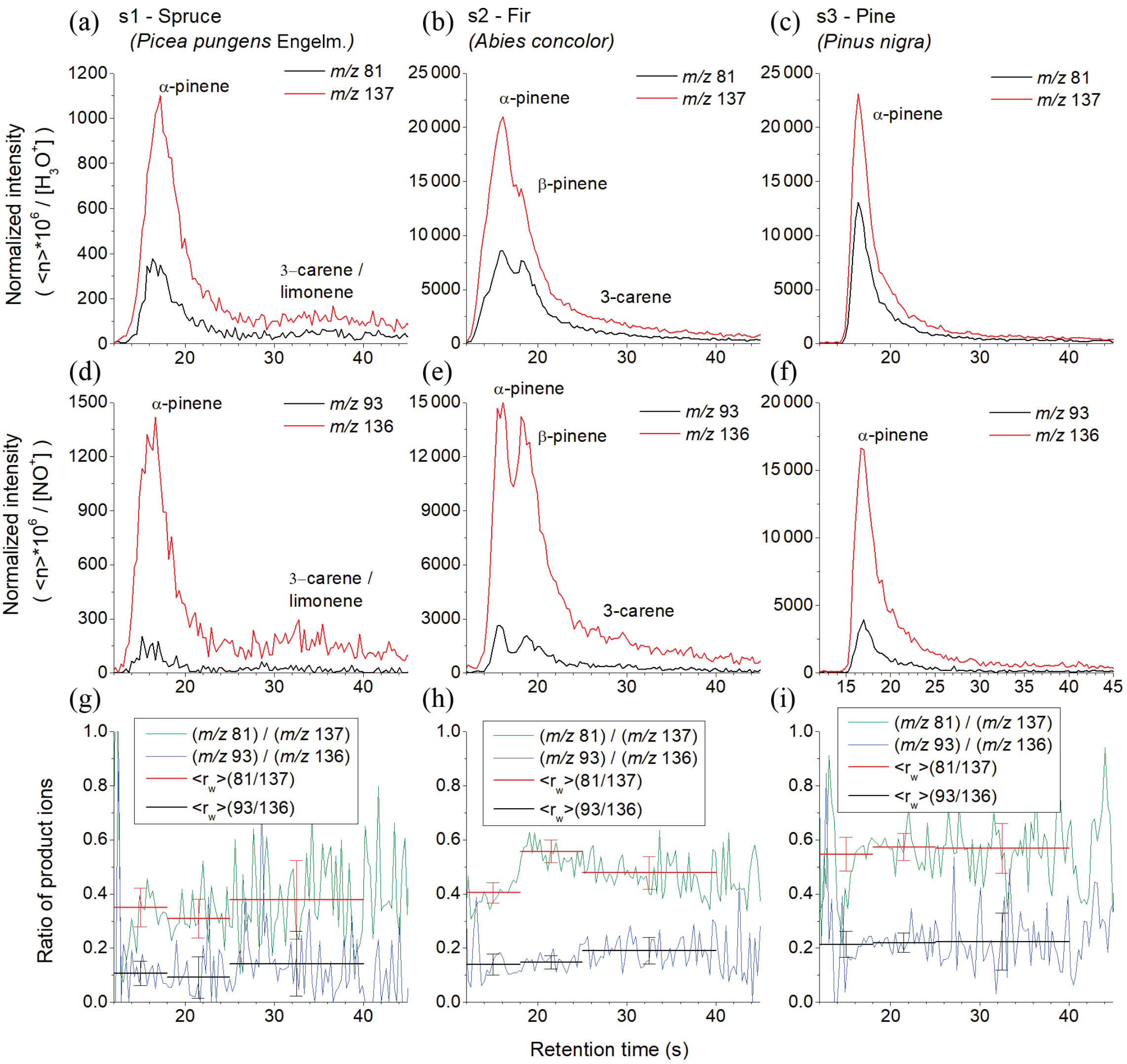

Figure 5. Chromatograms derived using the product ions for the reactions of H_3O^+ **(a, b, c)** and NO^+ **(g, h, i)** reagent ions with monoterpenes obtained for the three investigated pine tree samples (s1, s2 and s3) using the MXT-1 column. The signal intensities are the analyte ion count rates normalized to a reagent ion count rate of $10^6\ s^{-1}$. The black and red curves represent $C_6H_9^+$ (m/z 81) and $C_{10}H_{17}^+$ (m/z 137) product ions for H_3O^+ and $C_7H_9^+$ (m/z 93) and $C_{10}H_{16}^+$ (m/z136) product ions for NO^+ reagent ions. The lower row shows calculated ratios of product ions r_i for both reagent ions (green and blue curves) and for peaks areas calculated $\overline{r_w}$ (red and black).

Table 4. Calculated concentrations of monoterpenes (in ppmv and %) in the headspace of coniferous twigs in selected regions of chromatogram obtained using the MXT-Volatiles column at a column temperature of 40 °C, using an injection time of 6 s and a column flow of 3 sccm.

Sample	Concentration (ppmv, %)				
	α-pinene	Camphene	β-pinene	3-carene	Sum
Spruce (H_3O^+)	0.97, 46 %	0.21, 10 %	0.46, 22 %	0.48, 22 %	2.12
Spruce (NO^+)	0.74, 36 %	0.26, 13 %	0.56, 27 %	0.49, 24 %	2.05
Fir (H_3O^+)	2.51, 31 %	1.46, 18 %	2.9, 36 %	1.17, 15 %	8.04
Fir (NO^+)	1.97, 28 %	1.29, 19 %	2.80, 40 %	0.88, 13 %	6.94
Pine (H_3O^+)	15.5, 65 %	nd	5.95, 25 %	2.29, 10 %	23.74
Pine (NO^+)	13.7, 65 %	nd	5.45, 26 %	1.83, 9 %	20.98

nd: no data.

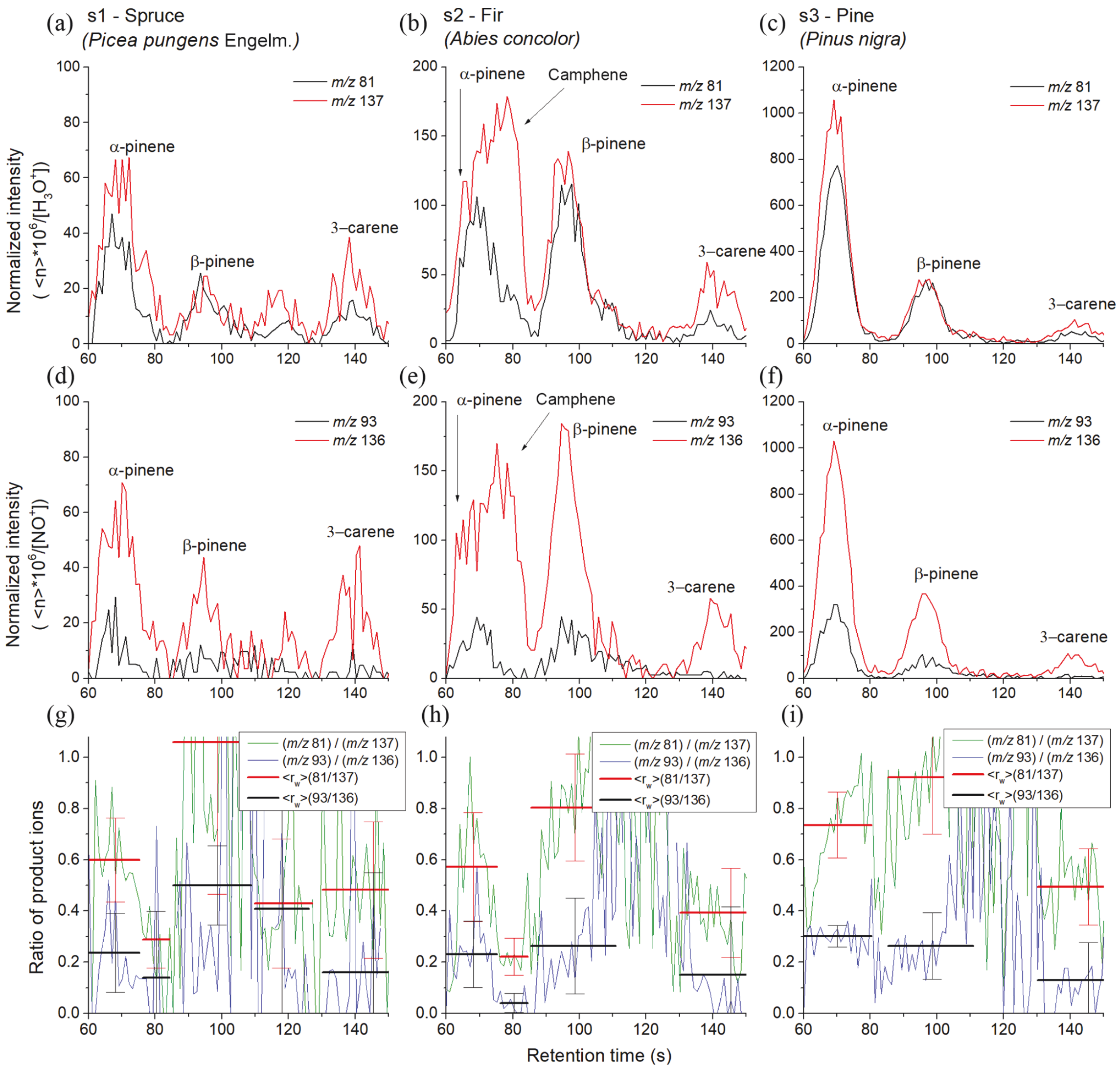

Figure 6. SIFT-MS-selected ion mode, fast GC and SIFT-MS chromatograms for monoterpene emissions from pine tree samples (s1, s2 and s3) obtained using the MXT-Volatiles column. The upper and lower rows were obtained using H_3O^+ and NO^+ reagent ions, respectively. The signal intensities are the analyte ion count rates normalized to a reagent ion count rate of $10^6\ s^{-1}$. The black and red curves stand for monitored ions $C_6H_9^+$ (m/z 81) and $C_{10}H_{17}^+$ (m/z 137) for H_3O^+ reagent ions and $C_7H_9^+$ (m/z 93) and $C_{10}H_{16}^+$ (m/z 136) for NO^+ reagent ions, respectively. The last row shows calculated ratios of product ions r_i for both reagent ions (green and blue curves) and for calculated peaks areas $\overline{r_w}$ (red and black). The signal intensities are the analyte ion count rates normalized to a reagent ion count rate of $10^6\ s^{-1}$.

combination is due to the low flow rate of the sampling gas (∼ 3 sccm) through the fast GC column, which is less than the commonly used 30 sccm. This could be resolved by using a wider column or by using multiple capillaries in parallel.

However, one clear advantage of SIFT-MS analyses is the ability to use three reagent ions that provide different analyte ions. This study has shown that the combination of the data from the two reagent ions, together with the analyses of the product ion signal ratios r_i, can improve the identification of monoterpenes, especially the identification of camphene and myrcene.

Importantly, it must be kept in mind that monoterpenes are not the only BVOCs emitted by plants. The presence of 2-hexenal and 3-hexenal, as already discussed in Sect. 4.5, can be problematical, but the interference from this can be alleviated using NO^+ reagent ions. The same approach may be used to analyse other isomeric or isobaric molecules present in the environment. A further benefit of employing NO^+ reagent ions in atmospheric analysis is the quantification of isoprene, which when using H_3O^+ reagent ion mode suffers mass interference from product ions of other biogenic species, including furan, C5 aldehydes and 2-methylbut-3-en-2-ol (Karl et al., 2012, 2014) as well as the second hydrate of methanol that is also emitted by plants (12 % of global BVOC emissions) (Španěl et al., 1999). Another benefit of using SIFT-MS compared to other techniques is that calculation of VOC concentration in the sample depends only on the known physical constants, reaction rate constants and analyte ion abundance, so complicated calibration procedures are not required.

The results obtained for monoterpene composition in leaf headspace samples agree well with other published studies. Because the emissions from plants depend on various physical parameters, here we only compare monoterpene composition. In a previous study (Mumm et al., 2004) of the volatiles emitted by *Pinus nigra* needles, 35 terpenoid compounds were identified, with the following being most abundant: α-pinene (45 %), β-phellandrene (9 %), limonene (8 %), β-pinene (5 %) and 3-carene (2 %). Holzke et al. (2006) studied diurnal and seasonal variation in monoterpenes and sesquiterpenes from Scots pine. The main monoterpene isomers they observed were α-pinene, β-pinene and 3-carene, which represented 90 % of the total terpene emission. A similar study on monoterpene emissions from boreal Scots pine showed that the most abundant monoterpenes measured above the forest and from the canopy were α-pinene and 3-carene (Räisänen et al., 2009). Kainulainen et al. (1992) investigated the effect of drought and waterlogging stress on monoterpenes released by needles of *Picea abies* (spruce). In the controlled group, the most abundant monoterpenes were camphene (22 %), limonene (14 %), α-pinene (9 %) and myrcene (6 %). In the emissions from southern and central Swedish spruce (Janson, 1993) the following isomers were most abundant: α-pinene (60 %–70 %), camphene (10 %), limonene (10 %) and 3-carene (4 %).

Zavarin et al. (1975) studied cortical oleoresin from *Abies concolor* (fir) that were collected in 43 different localities in order to analyse their composition of monoterpenoid fractions. They concluded that the production of camphene and 3-carene varied geographically. In the study of Pureswaran et al. (2004) they focused on quantitative variations in monoterpenes from four species of conifers, concluding that the four species (Douglas fir, lodgepole pine, interior spruce and interior fir) did not differ qualitatively, but there were significant differences in their quantitative profiles. For example, coastal Douglas fir needle samples contained 10 % of α-pinene, 31 % of Sabinene and 40 % of β-pinene, and in samples of interior Douglas fir the most abundant isomers were bornyl acetate (26 %), camphene (25 %), α-pinene and β-pinene (both 15 %).

In the present headspace study, we detected the presence of α-pinene, β-pinene, camphene and 3-carene, representing common emissions emitted from pine, spruce and fir samples. The present results thus agree with the usually reported composition of monoterpenes emitted from pine trees and their constituent parts.

5 Summary and conclusions

The addition of a fast GC pre-separation stage to SIFT-MS allows analyses of monoterpenes in mixtures at the expense of some loss of sensitivity. The bespoke electrically heated fast GC systems constructed for this study achieved separation in less than 45 s for a 5 m MXT-1 column and less than 180 s for a 5 m MXT-Volatiles column held at 40 °C. However, due to the insufficient GC separation, the analysis was not accurately quantitative, but it can be improved using a longer GC column operating at higher temperature. The identification of individual monoterpenes was aided by using information on the ratios of the product and analyte ion signals of both H_3O^+ and NO^+ reagent ions. It was shown that combining the SIFT-MS product ion ratios and the GC retention times, seven of eight monoterpenes were identified in a prepared mixture using the MXT-Volatiles column. To demonstrate the analytical value of this novel combination of fast GC with SIFT-MS, volatile emissions from spruce, fir and pine samples were analysed. α-pinene was identified together with smaller amounts of β-pinene and 3-carene. A significant contribution of camphene was also observed in the fir sample headspace.

Due to their different OH reactivity, the ability to distinguish individual monoterpenes at high time resolution with fast GC and SIFT-MS has the potential to improve the understanding of the contribution of individual monoterpenes in atmospheric chemistry processes, such as the formation of tropospheric ozone and secondary organic aerosols.

A major limitation of the fast GC and SIFT-MS system described here is the relatively high LOD ($\sim$ 16 ppbv), which currently preclude its application in measurement of monoterpenes in typical ambient concentrations. An additional weakness of the current fast GC setup is its relatively poor temperature stability, caused by a strong dependence on the laboratory ambient temperature. But this can surely be improved by active temperature feedback to control the column temperature. The flow rate through the 5 m long and 0.28 mm internal diameter column was about 10 times lower than the conventional flow rate used in direct SIFT-MS analyses and this resulted in commensurate worsening of the LOD. This could be resolved by using a wider column or by using multiple capillaries in parallel. A clear advantage of SIFT-MS is the ready availability of three different reagent ions to determine different fragmentation ratios for the same retention time to improve the identification of compounds.

Data availability. All data are available upon request from the corresponding author (Michal Lacko).

Supplement. The supplement related to this article is available online at: https://doi.org/10.5194/amt-12-4965-2019-supplement.

Author contributions. ML and NW created the experimental hardware and provided experiments with the MXT-1 column. ML, KS and PP then provided experiments with the MXT-Volatiles column. PS and ML provided data treatment and paper preparation.

Competing interests. The authors declare that they have no conflict of interest.

Acknowledgements. We would like to thank David Smith for his advice and help in the preparation of the manuscript.

Financial support. This project has received funding from the European Union's Horizon 2020 research and innovation programme under the Marie Skłodowska-Curie grant agreement no. 674911. We also gratefully acknowledge partial funding from The Czech Science Foundation (GACR Project No. 17-13157Y).

Review statement. This paper was edited by Yoshiteru Iinuma and reviewed by three anonymous referees.

References

Allardyce, R. A., Langford, V. S., Hill, A. L., and Murdoch, D. R.: Detection of volatile metabolites produced by bacterial growth in blood culture media by selected ion flow tube mass spectrometry (SIFT-MS), J. Microbiol. Meth., 65, 361–365, 2006.

Amelynck, C., Schoon, N., and Dhooghe, F.: SIFT Ion Chemistry Studies Underpinning the Measurement of Volatile Organic Compound Emissions by Vegetation, Curr. Anal. Chem., 9, 540–549, 2013.

Atkinson, R., Aschmann, S. M., and Pitts Jr, J. N.: Rate constants for the gas-phase reactions of the OH radical with a series of monoterpenes at 294 ± 1 K, Int. J. Chem. Kinet., 18, 287–299, 1986.

Atkinson, R., Aschmann, S. M., and Arey, J.: Rate constants for the gas-phase reactions of OH and NO_3 radicals and O_3 with sabinene and camphene at 296 ± 2 K, Atmos. Environ. A-Gen., 24, 2647–2654, 1990.

Atkinson, R., Hasegawa, D., and Aschmann, S. M.: Rate constants for the gas-phase reactions of O_3 with a series of monoterpenes and related compounds at 296 ± 2 K, Int. J. Chem. Kinet., 22, 871–887, 1990.

Atkinson, R. and Arey, J.: Gas-phase tropospheric chemistry of biogenic volatile organic compounds: a review, Atmos. Environ., 37, 197–219, 2003.

Chameides, W., Fehsenfeld, F., Rodgers, M., Cardelino, C., Martinez, J., Parrish, D., Lonneman, W., Lawson, D., Rasmussen, R., and Zimmerman, P.: Ozone precursor relationships in the ambient atmosphere, J. Geophys. Res.-Atmos., 97, 6037–6055, 1992.

ChemicalBook: available at: https://www.chemicalbook.com/ChemicalProductProperty_EN_CB4443087.htm, last access: Januar 2019.

Daubert, T. E.: Physical and thermodynamic properties of pure chemicals: Data compilation Hemisphere Pub. Corp., New York, ISBN 978-0891169482, 2030 pp., 1989.

de Gouw, J. and Warneke, C.: Measurements of volatile organic compounds in the earth's atmosphere using proton transfer reaction mass spectrometry, Mass Spectrom. Rev., 26, 223–257, 2007.

de Gouw, J. A., Goldan, P. D., Warneke, C., Kuster, W. C., Roberts, J. M., Marchewka, M., Bertman, S. B., Pszenny, A. A. P., and Keene, W. C.: Validation of proton transfer reaction mass spectrometry (PTR-MS) measurements of gas-phase organic compounds in the atmosphere during the New England Air Quality Study (NEAQS) in 2002, J. Geophys. Res.-Atmos., 108, https://doi.org/10.1029/2003JD003863, 2003.

Ellis, A. M. and Mayhew, C. A.: Proton transfer reaction mass spectrometry: principles and applications, John Wiley & Sons, ISBN 1-118-68357-9, 368 pp., 2013.

Fehsenfeld, F., Calvert, J., Fall, R., Goldan, P., Guenther, A. B., Hewitt, C. N., Lamb, B., Liu, S., Trainer, M., and Westberg, H.: Emissions of volatile organic compounds from vegetation and the implications for atmospheric chemistry, Global Biogeochem. Cy., 6, 389–430, 1992.

Fernandez, M. T., Williams, C., Mason, R. S., and Cabral, B. J. C.: Experimental and theoretical proton affinity of limonene, J. Chem. Soc., 94, 1427–1430, 1998.

Garcia, G. A., Nahon, L., and Powis, I.: Near-threshold photoionization spectroscopy of the mono-terpenes limonene and carvone, Int. J. Mass Spec., 225, 261–270, 2003.

Graus, M., Müller, M., and Hansel, A.: High resolution PTR-TOF: quantification and formula confirmation of VOC in real time, J. Am. Soc. Mass Spectr., 21, 1037–1044, 2010.

Haynes, W. M.: CRC handbook of chemistry and physics, CRC press, New York, ISBN 978-1-4822-0868-9, 2704 pp., 2014.

Holzke, C., Hoffmann, T., Jaeger, L., Koppmann, R., and Zimmer, W.: Diurnal and seasonal variation of monoterpene and sesquiterpene emissions from Scots pine (*Pinus sylvestris* L.), Atmos. Environ., 40, 3174–3185, 2006.

Janson, R. W.: Monoterpene emissions from Scots pine and Norwegian spruce, J. Geophys. Res.-Atmos., 98, 2839–2850, 1993.

Jordan, A., Haidacher, S., Hanel, G., Hartungen, E., Herbig, J., Märk, L., Schottkowsky, R., Seehauser, H., Sulzer, P., and Märk, T. D.: An online ultra-high sensitivity Proton-transfer-reaction mass-spectrometer combined with switchable reagent ion capability (PTR + SRI − MS), Int. J. Mass Spectr., 286, 32–38, 2009.

Kainulainen, P., Oksanen, J., Palomäki, V., Holopainen, J., and Holopainen, T.: Effect of drought and waterlogging stress on needle monoterpenes of Picea abies, Can. J. Botany, 70, 1613–1616, 1992.

Karl, T., Hansel, A., Cappellin, L., Kaser, L., Herdlinger-Blatt, I., and Jud, W.: Selective measurements of isoprene and 2-methyl-3-buten-2-ol based on NO^+ ionization mass spectrometry, Atmos. Chem. Phys., 12, 11877–11884, https://doi.org/10.5194/acp-12-11877-2012, 2012.

Karl, T., Kaser, L., and Turnipseed, A.: Eddy covariance measurements of isoprene and 232-MBO based on NO^+ time-of-flight mass spectrometry, Int. J. Mass Spectr., 365, 15–19, 2014.

Kesselmeier, J. and Staudt, M.: Biogenic Volatile Organic Compounds (VOC): An Overview on Emission, Physiology and Ecology, J. Atmos. Chem., 33, 23–88, 1999.

Kulmala, M., Suni, T., Lehtinen, K. E. J., Dal Maso, M., Boy, M., Reissell, A., Rannik, Ü., Aalto, P., Keronen, P., Hakola, H., Bäck, J., Hoffmann, T., Vesala, T., and Hari, P.: A new feedback mechanism linking forests, aerosols, and climate, Atmos. Chem. Phys., 4, 557–562, https://doi.org/10.5194/acp-4-557-2004, 2004.

Lindinger, W., Hansel, A., and Jordan, A.: On-line monitoring of volatile organic compounds at pptv levels by means of proton-transfer-reaction mass spectrometry (PTR-MS) medical applications, food control and environmental research, Int. J. Mass Spectrom., 173, 191–241, 1998.

Malásková, M., Henderson, B., Chellayah, P., Ruzsanyi, V., Mochalski, P., Cristescu, S. M., and Mayhew, C. A.: Proton transfer reaction time-of-flight mass spectrometric measurements of volatile compounds contained in peppermint oil capsules of relevance to real-time pharmacokinetic breath studies, J. Breath Res., 13, https://doi.org/10.1088/1752-7163/ab26e2, 2019.

Materić, D., Lanza, M., Sulzer, P., Herbig, J., Bruhn, D., Turner, C., Mason, N., and Gauci, V.: Monoterpene separation by coupling proton transfer reaction time-of-flight mass spectrometry with fast GC, Anal. Bioanal. Chem., 407, 7757–7763, 2015.

Matisová, E. and Dömötörová, M.: Fast gas chromatography and its use in trace analysis, J. Chromatogr. Sci., 1000, 199–221, 2003.

Mumm, R., Tiemann, T., Schulz, S., and Hilker, M.: Analysis of volatiles from black pine (Pinus nigra): significance of wounding and egg deposition by a herbivorous sawfly, Phytochemistry, 65, 3221–3230, 2004.

NIST WebBook Chemie: NIST Standard Reference Database Number 69, U.S. Secretary of Commerce, National Institute of Standards and Technology: Gaithersburg, MD: http://webbook.nist.gov/chemistry/, 2019.

Nolscher, A. C., Yanez-Serrano, A. M., Wolff, S., de Araujo, A. C., Lavric, J. V., Kesselmeier, J., and Williams, J.: Unexpected seasonality in quantity and composition of Amazon rainforest air reactivity, Nat. Commun., 7, 10383, https://doi.org/10.1038/ncomms10383, 2016.

OriginPro 9.0: OriginLab Corporation, One Roundhouse Plaza, Suite 303, Northampton, MA 01060, United States, 1800-969-7720, avaialable at: https://www.originlab.com/, last access: December 2018.

Pallozzi, E., Guidolotti, G., Ciccioli, P., Brilli, F., Feil, S., and Calfapietra, C.: Does the novel fast-GC coupled with PTR-TOF-MS allow a significant advancement in detecting VOC emissions from plants?, Agr. Forest Meteorol., 216, 232–240, 2016.

Pureswaran, D. S., Gries, R., and Borden, J. H.: Quantitative variation in monoterpenes in four species of conifers, Biochem. Syst. Ecol., 32, 1109–1136, 2004.

Pysanenko, A., Španěl, P., and Smith, D.: Analysis of the isobaric compounds propanol, acetic acid and methyl formate in humid air and breath by selected ion flow tube mass spectrometry, SIFT-MS, Int. J. Mass Spectrom., 285, 42–48, 2009.

Räisänen, T., Ryyppö, A., and Kellomäki, S.: Monoterpene emission of a boreal Scots pine (*Pinus sylvestris* L.) forest, Agr. Forest Meteorol., 149, 808–819, 2009.

Rhoderick, G. C. and Lin, J.: Stability assessment of gas mixtures containing monoterpenes in varying cylinder materials and treatments, Anal. Chem., 85, 4675–4685, 2013.

Rinne, J., Ruuskanen, T. M., Reissell, A., Taipale, R., Hakola, H., and Kulmala, M.: On-line PTR-MS measurements of atmospheric concentrations of volatile organic compounds in a European boreal forest ecosystem, Boreal Environ. Res., 10, 425–436, 2005.

Romano, A., Fischer, L., Herbig, J., Campbell-Sills, H., Coulon, J., Lucas, P., Cappellin, L., and Biasioli, F.: Wine analysis by Fast GC proton-transfer reaction-time-of-flight-mass spectrometry, Int. J. Mass Spectrom., 369, 81–86, 2014.

Savitzky, A. and Golay, M. J.: Smoothing and differentiation of data by simplified least squares procedures, Anal. Chem., 36, 1627–1639, 1964.

Schoon, N., Amelynck, C., Vereecken, L., and Arijs, E.: A selected ion flow tube study of the reactions of H_3O^+, NO^+ and O_2^+ with a series of monoterpenes, Int. J. Mass Spectrom., 229, 231–240, 2003.

Shestivska, V., Nemec, A., Dřevínek, P., Sovová, K., Dryahina, K., and Španěl, P.: Quantification of methyl thiocyanate in the headspace of Pseudomonas aeruginosa cultures and in the breath of cystic fibrosis patients by selected ion flow tube mass spectrometry, Rapid Commun. Mass Sp., 25, 2459–2467, 2011.

Shestivska, V., Spanel, P., Dryahina, K., Sovova, K., Smith, D., Musilek, M., and Nemec, A.: Variability in the concentrations of volatile metabolites emitted by genotypically different strains of Pseudomonas aeruginosa, J. Appl. Microbiol., 113, 701–713, 2012.

Shestivska, V., Antonowicz, S. S., Dryahina, K., Kubišta, J., Smith, D., and Španěl, P.: Direct detection and quantification of malondialdehyde vapour in humid air using selected ion flow tube mass spectrometry supported by gas chromatography/mass spectrometry, Rapid Commun. Mass Sp., 29, 1069–1079, 2015.

Smith, D. and Španěl, P.: Selected ion flow tube mass spectrometry (SIFT-MS) for on-line trace gas analysis, Mass Spec. Rev., 24, 661–700, 2005.

Smith, D. and Španěl, P.: Ambient analysis of trace compounds in gaseous media by SIFT-MS, Analyst, 136, 2009–2032, 2011a.

Smith, D., and Španěl, P.: Direct, rapid quantitative analyses of BVOCs using SIFT-MS and PTR-MS obviating sample collection, TrAC Trends in Analytical Chemistry, 30, 945–959, 2011b.

Smith, D., Španěl, P., Holland, T. A., Al Singari, W., and Elder, J. B.: Selected ion flow tube mass spectrometry of urine headspace, Rapid Commun. Mass Sp., 13, 724–729, 1999.

Smith, D., Sovová, K., and Španěl, P.: A selected ion flow tube study of the reactions of H_3O^+, NO^+ and $O_2^{+\bullet}$ with seven isomers of hexanol in support of SIFT-MS, Int. J. Mass Spectrom., 319, 25–30, 2012.

Solouki, T. and Szulejko, J. E.: Bimolecular and unimolecular contributions to the disparate self-chemical ionizations of α-pinene and camphene isomers, J. Am. Soc. Mass Spectr., 18, 2026–2039, 2007.

Song, M., Xia, Y., and Tomasino, E.: Investigation of a Quantitative Method for the Analysis of Chiral Monoterpenes in White Wine by HS-SPME-MDGC-MS of Different Wine Matrices, Molecules, 20, 7359–7378, 2015.

Španěl, P. and Smith, D.: Advances in On-line Absolute Trace Gas Analysis by SIFT-MS, Curr. Anal. Chem., 9, 525–539, 2013.

Španěl, P., Ji, Y., and Smith, D.: SIFT studies of the reactions of H_3O^+, NO^+ and O_2^+ with a series of aldehydes and ketones, Int. J. Mass Spectrom., 165, 25–37, 1997.

Španěl, P. and Smith, D.: Selected ion flow tube studies of the reactions of H_3O^+, NO^+, and O_{2+} with several aromatic and aliphatic hydrocarbons, Int. J. Mass Spectrom., 181, 1–10, 1998.

Španěl, P., Davies, S., and Smith, D.: Quantification of breath isoprene using the selected ion flow tube mass spectrometric analytical method, Rapid Commun. Mass Sp., 13, 1733–1738, 1999.

Španěl, P., Dryahina, K., and Smith, D.: A general method for the calculation of absolute trace gas concentrations in air and breath from selected ion flow tube mass spectrometry data, Int. J. Mass Spectrom., 249, 230–239, 2006.

Takasago: available at: http://www.takasago.com/cgi-bin/pdf/alphaterpinene.pdf, last access: January 2019.

Tani, A., Hayward, S., and Hewitt, C.: Measurement of monoterpenes and related compounds by proton transfer reaction-mass spectrometry (PTR-MS), Int. J. Mass Spectrom., 223, 561–578, 2003.

TGSC: The Good Scents Company Information System: http://www.thegoodscentscompany.com/, last access: January 2019.

Thompson, J. M. and Perry, D. B.: A new system of refillable and uniquely identifiable diffusion tubes for dynamically generating VOC and SVOC standard atmospheres at ppm and ppb concentrations for calibration of field and laboratory measurements, J. Environ. Mon., 11, 1543–1544, 2009.

Van Kempen, G. M. P. and Van Vliet, L. J.: Mean and variance of ratio estimators used in fluorescence ratio imaging, Cytom. Part A, 39, 300–305, 2000.

Wang, T., Španěl, P., and Smith, D.: Selected ion flow tube, SIFT, studies of the reactions of H_3O^+, NO^+ and O_2^+ with eleven $C_{10}H_{16}$ monoterpenes, Int. J. Mass Spec., 228, 117–126, 2003.

Yaws, C. L.: Handbook of Vapor Pressure, Vol 3: C_8–C_{28} Compounds, Gulf Pub Co., Houston, ISBN 978-0884151913, 392 pp., 1994.

Zavarin, E., Snajberk, K., and Fisher, J.: Geographic variability of monoterpenes from cortex of Abies concolor, Biochem. Syst. Ecol., 3, 191–203, 1975.

Supplement of Atmos. Meas. Tech., 12, 4965–4982, 2019
https://doi.org/10.5194/amt-12-4965-2019-supplement

Atmospheric Measurement Techniques
Open Access

Supplement of

Addition of fast gas chromatography to selected ion flow tube mass spectrometry for analysis of individual monoterpenes in mixtures

Michal Lacko et al.

Correspondence to: Michal Lacko (michal.lacko@jh-inst.cas.cz)

Attachment A.1

Table S1: Summary of reaction rate constants and branching ratios of investigated monoterpenes. All presented rate constants have units of 10^{-9}cm^{3}s^{-1}. Only significant products are given, for witch branching ratios are at least 10%.

	H_3O^+			NO^+			$O_2^{+\cdot}$		
	k	*m/z*	Products (b.r.)	*k*	*m/z*	Products (b.r.)	*k*	*m/z*	Products (b.r.)
α-pinene	2.3^{a},	81	$C_6H_9^+$ (30^{a}, 39^{b}),	2.0^{a},	92	$C_7H_8^+$ (16^{b}),	2.0^{a},	92	$C_7H_8^+$ (18^{a}, 22^{b}),
	2.4^{a*}	137	$C_{10}H_{17}^+$ (67^{a}, 61^{b})	2.0^{a*},	136	$C_{10}H_{16}^+$ (85^{a}, 77^{b})	1.9^{a*},	93	$C_7H_9^+$ (52^{a}, 56^{b}),
				2.3^{b}			2.1^{b}	121	$C_9H_{13}^+$ (12^{a}, 12^{b})
β-pinene	2.4^{a},	81	$C_6H_9^+$ (33^{a}, 40^{b}),	2.1^{a},	136	$C_{10}H_{16}^+$ (93^{a}, 89^{b})	2.1^{a},	93	$C_7H_9^+$ (56^{a}, 19^{b}),
	2.6^{a*}	137	$C_{10}H_{17}^+$ (64^{a}, 60^{b})	2.2^{a*},			2.1^{a*},	121	$C_9H_{13}^+$ (49^{b}),
				2.1^{b}			2.0^{b}	136	$C_{10}H_{16}^+$ (11^{a})
R-limonene	2.6^{a},	81	$C_6H_9^+$ (22^{a}, 29^{b}),	2.2^{a},	136	$C_{10}H_{16}^+$ (91^{a}, 89^{b})	2.2^{a},	68	$C_5H_8^+$ (10^{b}),
	2.6^{a*}	137	$C_{10}H_{17}^+$ (73^{a}, 68^{b})	2.2^{a*},			2.1^{a*},	92	$C_7H_8^+$ (10^{b}),
				2.2^{b}			2.2^{b}	93	$C_7H_9^+$ (26^{a}, 30^{b}),
								94	$C_7H_{10}^+$ (11^{a}, 12^{b}),
								107	$C_8H_{11}^+$ (11^{b}),
								121	$C_9H_{13}^+$ (14^{a}, 13^{b}),
								136	$C_{10}H_{16}^+$ (11^{a}, 11^{b})
3-carene	2.3^{a},	81	$C_6H_9^+$ (19^{a}, 24^{b}),	2.1^{a},	136	$C_{10}H_{16}^+$ (86^{a}, 81^{b})	2.0^{a},	92	$C_7H_8^+$ (11^{b}),
	2.4^{a*}	137	$C_{10}H_{17}^+$ (78^{a}, 76^{b})	2.0^{a*},			2.0^{a*},	93	$C_7H_9^+$ (41^{a}, 45^{b}),
				2.2^{b}			1.9^{b}	121	$C_9H_{13}^+$ (20^{a}, 20^{b}),
								136	$C_{10}H_{16}^+$ (14^{a})
myrcene	2.6^{a},	81	$C_6H_9^+$ (26^{a}, 30^{b}),	2.3^{a},	92	$C_7H_8^+$ (11^{b}),	2.2^{a},	69	$C_5H_9^+$ (10^{b}),
	2.7^{a*}	137	$C_{10}H_{17}^+$ (59^{a}, 58^{b})	2.2^{a*},	93	$C_7H_9^+$ (22^{a}, 34^{b}),	2.2^{a*},	92	$C_7H_8^+$ (70^{b}),
				2.2^{b}	136	$C_{10}H_{16}^+$ (61^{a}, 55^{b})	2.2^{b}	93	$C_7H_9^+$ (61^{a})
camphene	2.4^{a},	81	$C_6H_9^+$ (14^{b}),	2.1^{a},	136	$C_{10}H_{16}^+$ (87^{a}, 79^{b}),	2.0^{a},	93	$C_7H_9^+$ (13^{a}, 19^{b}),
	2.6^{a*}	137	$C_{10}H_{17}^+$ (88^{a}, 86^{b})	2.1^{a*},	166	$NO^+C_{10}H_{16}$ (11^{b})	2.1^{a*},	107	$C_8H_{11}^+$ (10^{b}),
				2.3^{b}			2.2^{b}	121	$C_9H_{13}^+$ (44^{a}, 49^{b})
α-terpinene		81	$C_6H_9^+$ (10^{b}),	2.0^{b}	136	$C_{10}H_{16}^+$ (87^{a}, 99^{b}),	2.0^{b}	93	$C_7H_9^+$ (16^{b}),
		137	$C_{10}H_{17}^+$ (87^{b})					121	$C_9H_{13}^+$ (42^{b}),
								136	$C_{10}H_{16}^+$ (33^{b})
γ-terpinene		81	$C_6H_9^+$ (17^{b}),	2.1^{b}	135	$C_{10}H_{15}^+$ (18^{b}),	1.9^{b}	92	$C_7H_8^+$ (12^{b}),
		137	$C_{10}H_{17}^+$ (81^{b})		136	$C_{10}H_{16}^+$ (87^{a}, 75^{b}),		93	$C_7H_9^+$ (46^{b}),
								121	$C_9H_{13}^+$ (21^{b}),
								136	$C_{10}H_{16}^+$ (14^{b})

[a] (Schoon et al., 2003); [b] (Wang et al., 2003); [c] Present result based on SIFT-MS measurements; [d] Present result based on fastGC-SIFT-MS measurements; * theoretical data based on the method of Su and Chesnavitch (Su and Chesnavich, 1982); b.r. stands for branching ratio; Dimension of rate constants is 10^{-9}cm^{3}s^{-1}.

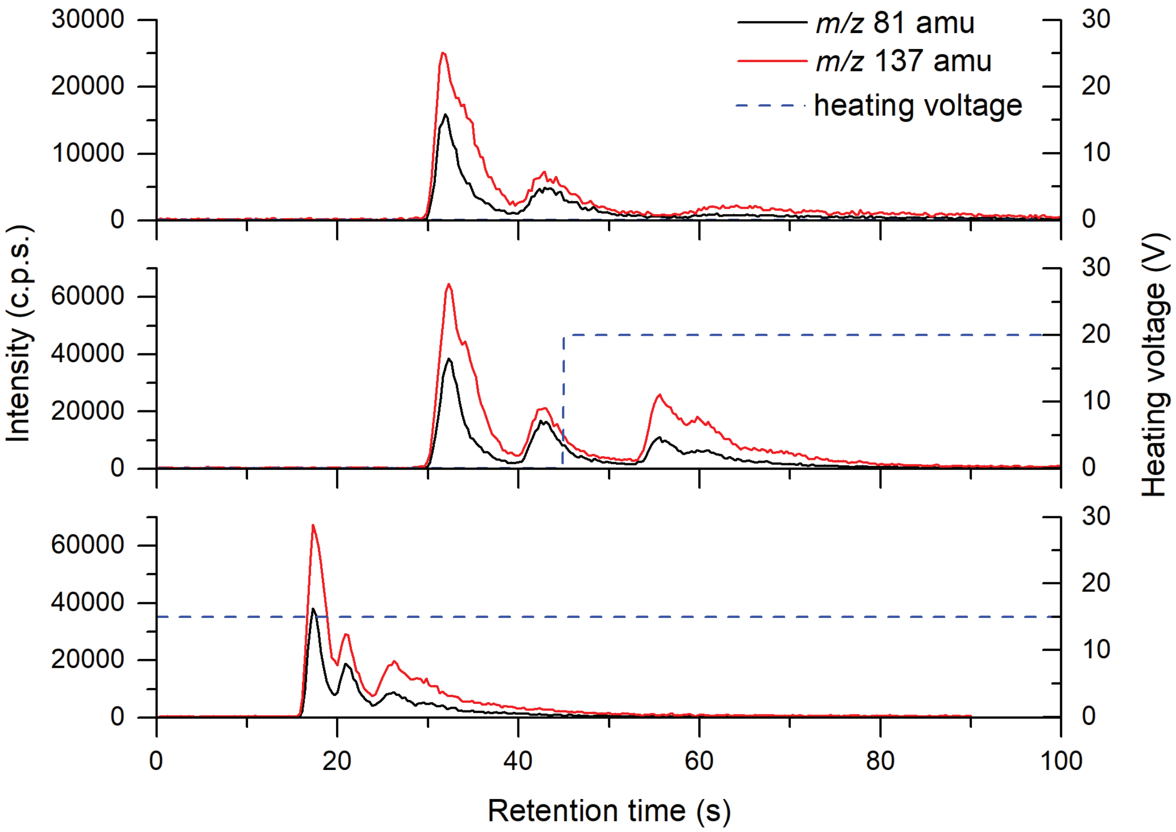

Figure S1: Chromatograms of a monoterpene mixture analysed by the MXT-1 column for different profiles of the heating voltage. Profiles were analysed by SIFT-MS using the H_3O^+ reagent ion.

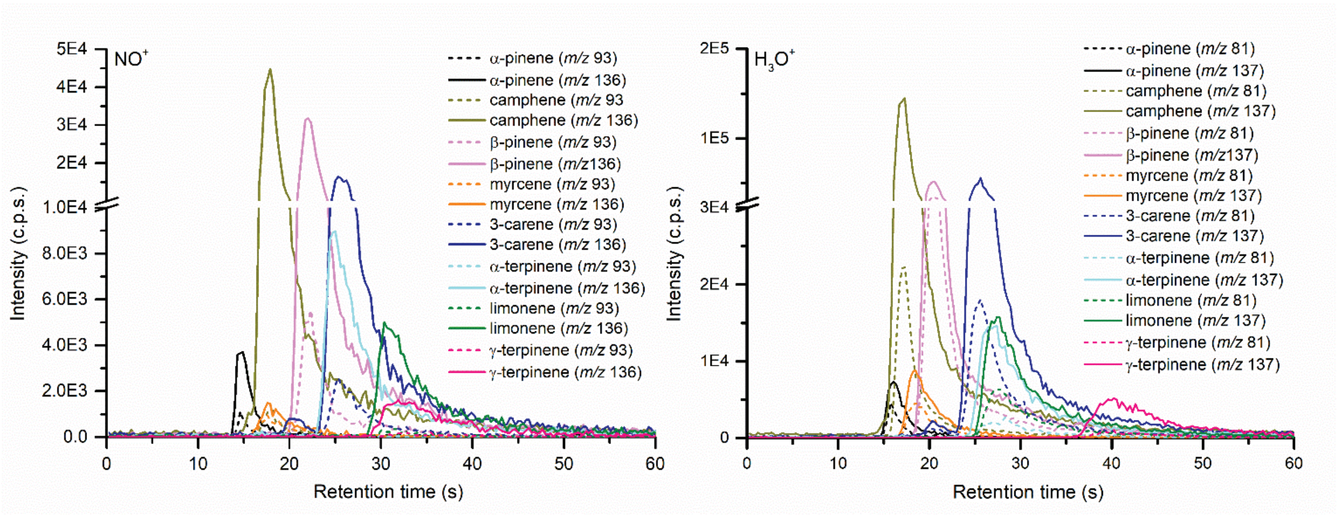

Figure S2: Chromatograms of individual monoterpenes analysed using the MXT-1 column at a constant temperature of column ~40 °C. The profile is associated with the profile shown in the bottom of Figure S1. Profiles were analysed by SIFT-MS using the H_3O^+ reagent ion. Intensity of α-pinene was reduced.

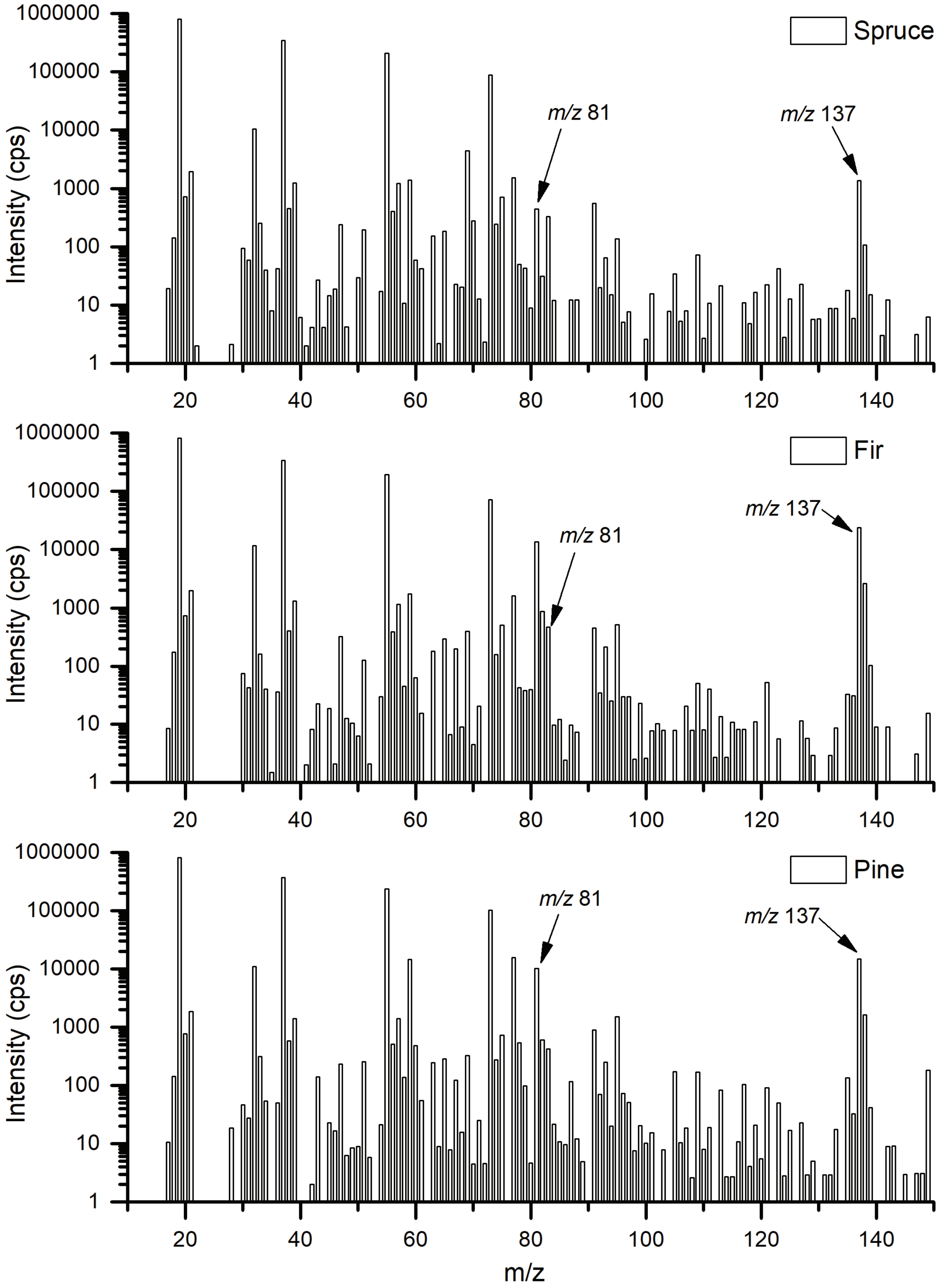

Figure S3: SIFT-MS spectra of coniferous samples analysed by H_3O^+ reagent ions. The marked ions with m/z 81 and m/z 137 were used for analysis of monoterpenes.

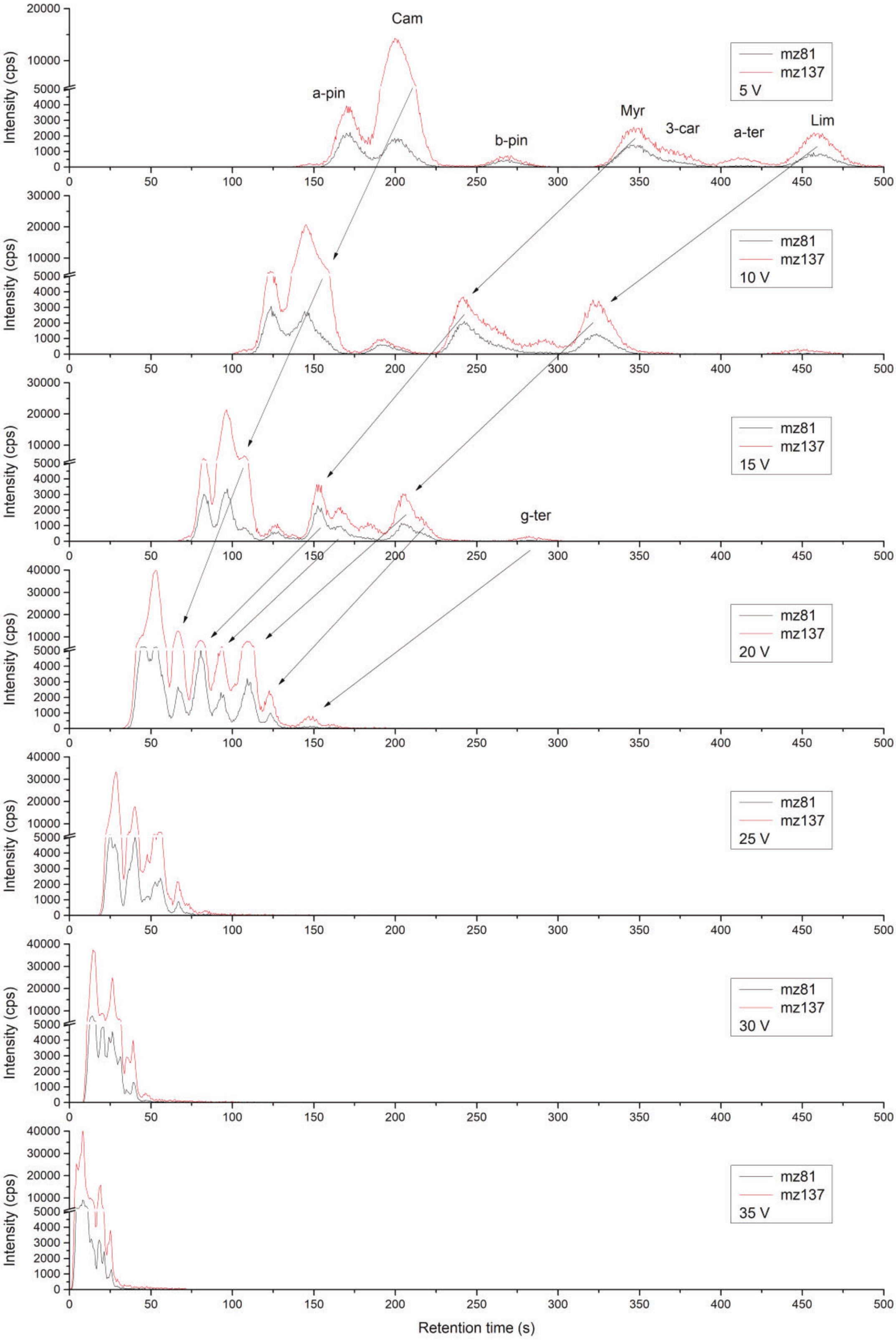

Figure S4: Chromatograms of a monoterpene mixture analysed by the MXT- Volatiles column for different heating voltages. Profiles were analysed by SIFT-MS using the H_3O^+ reagent ion.

Figure S5: Sample no. 1 (Pincea punges)

Figure S6: Sample no. 2 (Abies concolor)

Figure S7: Sample no. 3 (Pinus nigra)

Attachment A.1

References

Schoon, N., Amelynck, C., Vereecken, L., and Arijs, E.: A selected ion flow tube study of the reactions of H_3O^+, NO^+ and O_2^+ with a series of monoterpenes, International Journal of Mass Spectrometry, 229, 231-240, 2003.

Su, T., and Chesnavich, W. J.: Parametrization of the ion–polar molecule collision rate constant by trajectory calculations, The Journal of Chemical Physics, 76, 5183-5185, 1982.

Wang, T., Španěl, P., and Smith, D.: Selected ion flow tube, SIFT, studies of the reactions of H_3O^+, NO^+ and O_2^+ with eleven $C_{10}H_{16}$ monoterpenes, Int. J. Mass Spec., 228, 117-126, 2003.

PCCP

PAPER

View Article Online
View Journal | View Issue

Cite this: *Phys. Chem. Chem. Phys.*, 2020, **22**, 10170

Chemical ionization of glyoxal and formaldehyde with H_3O^+ ions using SIFT-MS under variable system humidity

Michal Lacko, *[ab] Felix Piel, [cde] Andreas Mauracher[d] and Patrik Španěl[a]

Received 17th January 2020,
Accepted 14th April 2020

DOI: 10.1039/d0cp00297f

rsc.li/pccp

Glyoxal ($C_2H_2O_2$) is a highly reactive molecule present at trace levels in specific gaseous environments. For analyses by chemical ionization mass spectrometry, it is important to understand the gas-phase chemistry initiated by reactions of H_3O^+ ions with $C_2H_2O_2$ molecules in the presence of water vapour. This chemistry was studied at variable humidity using a selected ion flow tube, SIFT. The initial step is a proton transfer reaction forming protonated glyoxal $C_2H_3O_2^+$. The second step, in the presence of water vapour, is the association forming $C_2H_3O_2^+(H_2O)$ and interestingly also protonated formaldehyde CH_2OH^+. Hydrated protonated formaldehyde $CH_2OH^+(H_2O)$ was also observed. Relative signals of these four ionic products were studied at the end of the flow tube where the reactions took place during 0.3 ms in helium carrier gas (1.5 mbar, 300 K) as the water vapour number density varied up to 10^{14} cm^{-3}. The data were interpreted using numerical kinetics modelling of the reaction sequences and the mechanisms and kinetics of the reaction steps were characterised. The results thus facilitate SIFT-MS analyses of glyoxal in humid air whilst drawing attention to ion overlaps with formaldehyde products.

1 Introduction

Glyoxal ($C_2H_2O_2$) is the simplest dialdehyde. It can polymerize from an anhydrous monomeric form into a series of oligomers and its vapour is highly reactive, contributing to aerosol formation.[1,2] Glyoxal plays a role in biological processes; it is known to be a cytotoxic metabolite of glucose, a product of lipid peroxidation and a marker of oxidation stress.[3] In addition, recent studies have shown that glyoxal is an intermediate product in the photocatalytic reduction of carbon dioxide to methane.[4,5] It is noteworthy that organic molecules present in the Earth's atmosphere can be transformed into glyoxal by oxidation or photo-oxidation.[6] Such processes were observed for toluene,[7–9] xylene,[8–10] trimethylbenzene,[9,10] isoprene[11] and α-pinene.[12] Daytime atmospheric glyoxal chemistry involves oxidation and may lead to the formation of secondary organic aerosols.[13]

Chemical ionization mass spectrometry (CIMS) is a useful tool for the detection of glyoxal since the high reactivity and short lifetime of glyoxal impede the use of gas chromatography (GC) techniques. Nölscher *et al.* measured the total OH reactivity of tropical forest air and compared it to the reactivity expected from volatile organic compounds (VOCs) determined *via* proton-transfer-reaction mass spectrometry (PTR-MS).[14] The measured OH reactivity exceeded the calculated values, indicating that either PTR-MS underestimated VOC concentrations or that not all relevant species were accounted for. This can also be caused by the different OH reactivity of isomers (which cannot be separated by PTR-MS) or the presence of molecules with high reactivity and low proton affinity (PA) compared to the PA of water (protonated water, H_3O^+, is the most common reagent ion in PTR-MS).

The PA of glyoxal was previously estimated by HF and DFT calculations to be 675 kJ mol^{-1} and 690 kJ mol^{-1}, respectively.[15] Since the PA is very similar to the PA of water (691 kJ mol^{-1}),[16] proton transfer from hydronium (H_3O^+) ions may not proceed at a collisional rate.[17] In addition, the reverse reaction could also take place:

$$H_3O^+ + C_2H_2O_2 \leftrightarrow C_2H_3O_2^+ + H_2O. \qquad (1)$$

CIMS analysis of atmospheric glyoxal can be further hampered by isobaric molecules, *e.g.* acetone or propanal. These are typically present at much higher concentrations, causing signal overlaps. Understanding the ion chemistry may help to distinguish these isobars.

---

[a] *J. Heyrovsky Institute of Physical Chemistry of the CAS, v. v. i, Dolejškova 2155/3, 182 23 Prague, Czech Republic. E-mail: patrik.spanel@jh-inst@cas.cz*
[b] *Charles University, Faculty of Mathematics and Physics, V Holešovičkách 747/2, 180 00 Prague, Czech Republic*
[c] *IONICON Analytik GmbH, Eduard-Bodem-Gasse 3, 6020 Innsbruck, Austria*
[d] *Institut für Ionenphysik und Angewandte Physik, Leopold-Franzens-Universität Innsbruck, Innsbruck 6020, Austria*
[e] *Department of Chemistry, University of Oslo, 0315 Oslo, Norway*

Michel *et al.*[18] previously studied reaction (1) using a selected ion flow tube (SIFT). The reported rate coefficient of 1.9×10^{-9} cm^3 s^{-1} is between the collisional values of the two isomers *trans*-glyoxal (1.3×10^{-9} cm^3 s^{-1}) and *cis*-glyoxal (4.9×10^{-9} cm^3 s^{-1}). In this study, $C_2H_3O_2^+$ was found to decrease with increasing concentration of water vapour in the flow tube whilst protonated glyoxal hydrates did not increase in concentration and minority product ions CH_2OH^+ (*m*/*z* 31) and $CH_2OH^+H_2O$ (*m*/*z* 49) appeared. An increase in glyoxal ion concentration led to the increase of hydrated hydronium ions ($H_3O^+H_2O$, *m*/*z* 37), presumably due to ligand switching reactions. The authors of a reported study[18] concluded that:

"Further experiments are needed to unravel the complex H_3O^+/glyoxal chemistry in the presence of water vapour".

A subsequent study[19] with O_2^+ and NO^+ reagent ions revealed that a combination of NO^+ and H_3O^+ reagent ions is required to unravel individual concentrations of acetone, propanal and glyoxal.

In a recent PTR-MS study,[20] CH_2OH^+ was also observed in addition to $C_2H_3O_2^+$. The ratio of these ions changed, with less CH_2OH^+ produced at increasing water vapour concentrations in the drift tube. The authors excluded the presence of neutral formaldehyde in the reagent mixture but did not discuss the mechanism leading to the formation of protonated formaldehyde. This unusual formation of CH_2OH^+ is a particularly interesting ion chemistry phenomenon. In the SIFT, it increases with water vapour concentration while in PTR-MS it decreases. It is thus important to get insight into the sequences of ion–molecule reactions that can be responsible for this effect.

Thus, we have carried out a detailed SIFT study with the aim to elucidate the influence of humidity on the glyoxal hydronium ion-chemistry. The experimental study was supplemented with the theoretical modelling of ion chemistry considering a sequence of individual ion–molecule reactions. We further studied the ion chemistry of formaldehyde under the same conditions to correctly account for the individual secondary reactions.

2 Experimental

2.1 Materials

Glyoxal was prepared from a 40% glyoxal solution (Sigma-Aldrich) using a method similar to the isolation from glyoxal trimeric dehydrate.[18–21] 10 ml of glyoxal solution was placed into a 250 ml flask and evacuated for 24 hours to remove the bulk of water. The resulting high viscose residuum was crystallised to bis(dioxolane) trimer.[1] Crystals were crushed and covered by a layer of P_2O_5 (Sigma-Aldrich), separated by a 1 cm layer of 1 mm glass beads, to remove any remaining water, and slowly heated up to 150 °C until the yellow-green vapour characteristic for glyoxal appeared by thermal decomposition.[22,23] Glyoxal vapour was re-crystalized in a cold trap, and cooled by dry ice. The glyoxal crystals were stored in a dry ice cooled box to minimise exposure to atmospheric water vapour.

Formaldehyde was prepared by heating a closed vial containing paraformaldehyde powder (Sigma-Aldrich) up to 150 °C. 9 ml of the released formaldehyde vapour was injected into an ∼4 l Nalophan bag, filled with synthetic air (Messer).

2.2 Selected ion flow tube, SIFT

A Profile 3 SIFT-MS instrument (Instrument Science, Crewe, UK, see Fig. 1)[24–26] was used for the ion-chemistry study. Since SIFT-MS is described in detail in the literature, only a brief summary will be given here. A variety of reagent ions (H_3O^+, NO^+ or $O_2^{+\bullet}$) is generated by the introduction of a water vapour/air mixture into a microwave discharge. Reagent ions are selected by a quadrupole mass filter and injected into the 5 cm long flow tube through which a He carrier gas flow was established (p = 1.5 mbar, T = 300 K). The neutral reactant gas mixture is

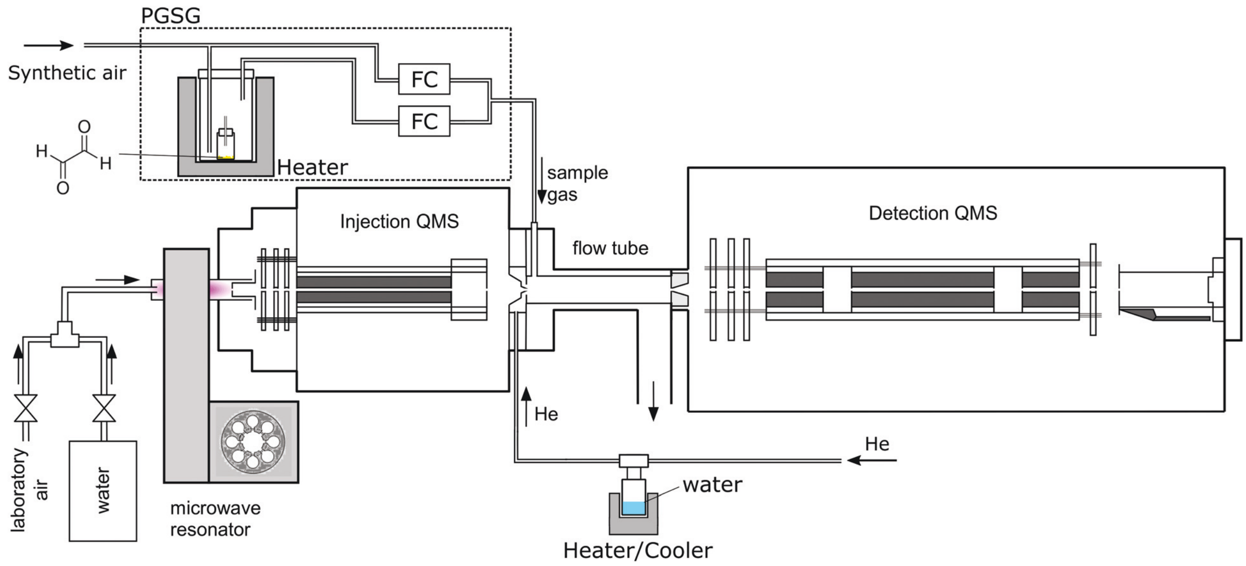

Fig. 1 Scheme of the experimental setup including a PGSG and a SIFT-MS instrument.

injected at a known flow rate into the flow tube, where the ion–molecule reactions take place. Ions are subsequently separated using a quadrupole mass spectrometer and detected *via* a single channel electron multiplier (SCEM).

For glyoxal experiments, 2 mg of glyoxal crystals were placed into a 2 ml glass vial closed by a septum penetrated by a 5 cm long polyether ether ketone capillary (I.D. 0.25 mm), in a diffusion tube configuration.[27] A precision gas standard generator (PGSG; 491M, Kin-Tek) was used at 50 °C to release glyoxal vapour and dilute it with synthetic air to reach the concentration of 15 ppmv, which was then introduced into the flow tube. The humidity of the carrier gas was varied using a reservoir containing 5 ml of water connected to the supply line, thus avoiding the interaction of water with glyoxal prior to its introduction to the SIFT. The water reservoir temperature was slowly increased from −78.5 °C to 60 °C, releasing H_2O number densities in 1.5 mbar of He between 4×10^{12} and 10^{14} cm^{-3} (corresponding to 0.3% to 7.5% sample humidity at a typical SIFT-MS sample flow). To study the influence of He carrier gas on the ion distribution, we varied the flow tube pressure from 0.5 to 2 mbar. Measurements were then carried out at two different water concentrations: $H = 0.03$ (3×10^{12} cm^{-3}) and $H = 0.08$ (1×10^{13} cm^{-3}), see (4), estimated under standard experimental conditions.

For formaldehyde experiments, a 4 l Nalophan bag containing 5 ppmv formaldehyde vapour in synthetic air was used. Humidity was varied by adding a few millilitres of water at room temperature.

The water vapour concentration in the flow tube was determined from the association reactions of (hydrated) H_3O^+ ions with H_2O molecules,

$$H_3O^+(H_2O)_{n-1} + H_2O + He \leftrightarrow H_3O^+(H_2O)_n + He \tag{2}$$

where $n \geq 1$. The H_2O number density in the flow tube $[H_2O]$ was calculated as

$$[H_2O] = \frac{1}{tk_{2\mathrm{eff}}} \ln\frac{[H_3O^+] + [H_3O^+ \cdot H_2O] + [H_3O^+ \cdot (H_2O)_2] + [H_3O^+ \cdot (H_2O)_3]}{[H_3O^+]} \tag{3}$$

where $k_{2\mathrm{eff}}$ is the rate coefficient for reaction (2) ($n = 1$), t is the reaction time, and the symbols in brackets correspond to respective ion count rates. Ion count rates were corrected for mass discrimination and for differential diffusion.[28] To compare the experimental results with the numerical model, it is useful to use the dimensionless logarithmic factor

$$H = \ln\left(\frac{[H_3O^+] + [H_3O^+ \cdot H_2O] + \left[H_3O^+ \cdot (H_2O)_2\right] + \cdots}{[H_3O^+]}\right) \tag{4}$$

as a relative measure of water vapour concentration.

2.3 Numerical model KIMI

To model the ion-chemistry kinetics in a flow tube, we developed the Kinetics of Ion Molecular Interaction software (KIMI; using the Microsoft Visual Studio 2017, NET Framework 4.6.1). KIMI interactively solves sets of kinetic equations that describe the change in reagent and product ion concentrations along the axis of the flow tube and thus model ion concentrations at the end of the flow tube as a function of the reactant concentrations.

The input for the model is generated from a graphical interface that allows drawing reaction pathways and systems involving multiple ionic species. Each species has a defined initial concentration and each reaction path is described by a rate constant k. In addition, diffusion losses of ions are characterised by diffusion coefficients, D_e,[29] and the characteristic radial diffusion length Λ. Concentrations of all species in the reaction system are calculated by solving a set of time dependent differential equations, exemplified by the proton transfer reaction

$$\frac{\mathrm{d}[MH^+]}{\mathrm{d}t} = k[M][H_3O^+] - [MH^+]\frac{D_e}{\Lambda^2} \tag{5}$$

using the Runge–Kutta method.[30,31] In the SIFT, the time coordinate directly corresponds to the axial position due to a constant ion velocity v_i, estimated from the carrier gas velocity v_g as[32]

$$v_i = 1.5 \times v_g \tag{6}$$

v_g can be calculated from the carrier gas flow rate, Φ_C, its pressure, p_g, temperature, T_g (in K) and the internal flow tube diameter d_t as

$$v_g = \frac{\Phi_C}{p_g}\frac{4}{\pi d_t^2}\frac{T_g}{273\ \mathrm{K}}. \tag{7}$$

T_g is assumed to be in equilibrium with the flow tube (usually around 300 K). The pressure is measured at the end of the flow tube. The pressure inside the flow tube is somewhat higher due to its finite conductivity according to the Hagen–Poiseuille equation

$$\Delta p = \frac{8\eta L}{\pi R^4}\frac{\Phi}{\bar{p}}. \tag{8}$$

Under conditions of the experiments ($p = 1.5$ mbar, $T = 300$ K, $\Phi = 880$ sccm, $L = 5$ cm, flow tube radius $R = 0.5$ cm, and the dynamic viscosity of He $\eta = 2 \times 10^{-5}$ Pa s at 300 K), the pressure difference is about 0.3 mbar. To estimate the average flow tube pressure, the measured pressure was thus increased by 0.15 mbar. The total flow rate was measured for several values of pressure in the flow tube. Under typical conditions, the gas bulk velocity according to (7) is equal to 105 m s^{-1} and thus the ion velocity calculated from (6) is 157.5 m s^{-1}. The reaction time for the reaction length $L = 4$ cm corrected by a positive "end correction"[32] $\varepsilon = 0.5$ cm

$$t_r = \frac{L + \varepsilon}{v_i}, \tag{9}$$

is thus 286 μs.

3 Results and discussion

3.1 Experimental observations in the SIFT

The mass spectra (see Fig. 2) showed protonated glyoxal ($C_2H_3O_2^+$, m/z 59) and its water cluster ($C_2H_3O_2^+(H_2O)$, m/z 77). The second water cluster ($C_2H_3O_2^+(H_2O)_2$, m/z 95) appeared only at higher water vapour concentrations. The ion at m/z 31, protonated formaldehyde (CH_2OH^+),[20] was also observed together with its water cluster ($CH_2OH^+(H_2O)$, m/z 49). A small signal at m/z 89 corresponds to the association of protonated formaldehyde and glyoxal ($CH_2OH^+{\cdot}C_2H_2O_2$).

The change in the relative intensities of product ions as a function of relative water vapour concentration H is shown in Fig. 3. For the lowest humidity ($H < 0.1$), protonated glyoxal was dominant (>85%). With increasing humidity $H > 0.4$, protonated formaldehyde concentration rose and became dominant. It is interesting that both hydrated formaldehyde (m/z 49) and hydrated glyoxal (m/z 77) concentration remained below 20%. Water vapour thus removes the glyoxal containing ions and leads to the production of formaldehyde containing ions. This is in stark contrast to analogous acetone ion chemistry that is well understood to terminate under the same conditions in water cluster ions at m/z 77 and m/z 95.[33]

Fig. 3 indicates that protonated formaldehyde is formed when H_3O^+ ions react with $C_2H_2O_2$ at 300 K in the presence of water molecules, without requiring additional collision energy. Glyoxal and formaldehyde have PA($C_2H_2O_2$) = 675 to 690 kJ mol^{-1} [15] and PA(H_2CO) = 713 kJ mol^{-1},[16] both close to the PA of water, PA(H_2O) = 691 kJ mol^{-1},[16] but much lower than the PA of the water dimer, PA($(H_2O)_2$) = 808 kJ mol^{-1}.[34] Therefore, proton transfer is only possible from H_3O^+ (1) but not from $H_3O^+(H_2O)_{1,2,3}$.

Protonated formaldehyde was not observed in the absence of H_2O and thus must be formed in a secondary reaction of protonated glyoxal with water

$$C_2H_3O_2^+ + H_2O \rightarrow H_2COH^+ + HCOOH. \qquad (10)$$

Alternatively, a reaction sequence can occur where an intermediate glyoxal water cluster may be formed by a ligand switching reaction

$$H_3O^+(H_2O) + C_2H_2O_2 \rightarrow C_2H_3O_2^+(H_2O) + H_2O. \qquad (11)$$

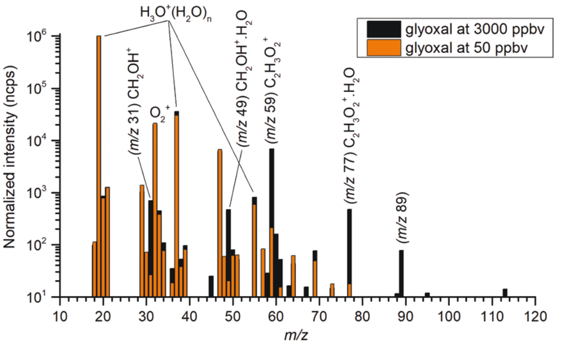

Fig. 2 Mass spectra of products of H_3O^+ reaction with glyoxal, normalized to 10^6 H_3O^+ reagent ions. Glyoxal concentrations are indicated by bar colour. The data were obtained for the lowest attainable water vapour concentration $H = 0.03$ (3×10^{12} cm^{-3}).

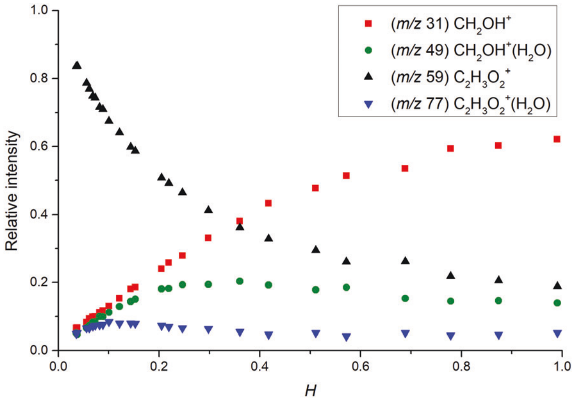

Fig. 3 Change in the relative intensities of product ions of the reaction of H_3O^+ with glyoxal for different carrier gas humidity.

It is also possible that the intermediate glyoxal water cluster is formed by a three-body association reaction

$$C_2H_3O_2^+ + H_2O + He \rightarrow C_2H_3O_2^+(H_2O) + He. \qquad (12)$$

Reaction (11) and (12) may then yield protonated formaldehyde *via* dissociation in a further reaction with H_2O

$$C_2H_3O_2^+(H_2O) + H_2O \rightarrow CH_2OH^+ + HCOOH + H_2O. \qquad (13)$$

Energetics of reactions (10)–(13) were calculated using the B3LYP/6-311G(p,d) level of theory in the Gaussian 09 software package as the change in the sum of the electronic and thermal free energies between optimized geometries of all reactants and products. According to this theory, reaction (10) is exergonic, $\Delta G = -64.81$ kJ mol^{-1}, while reaction (13) is endergonic, $\Delta G = 43.85$ kJ mol^{-1}. However, this can be overcome by internal excitation of the product $C_2H_3O_2^+(H_2O)$ of the highly exergonic reaction (12), $\Delta G = -108.66$ kJ mol^{-1}. Such excitation is unlikely for the endergonic reaction (11) ($\Delta G = 31.4$ kJ mol^{-1}). This set of possible reactions leading to the formation of protonated formaldehyde was numerically modelled to match the experimental data (see below in Section 3.2).

Additional data were also obtained for the NO^+ and $O_2^{+\bullet}$ reactions with $C_2H_2O_2$. It was observed that the NO^+ reaction with glyoxal proceeds *via* charge transfer forming $C_2H_2O_2^{+\bullet}$ (m/z 58) and *via* association forming $C_2H_2O_2NO^+$ (m/z 88). For $H \sim 0.04$, the relative abundance ratio was 0.3 for $C_2H_2O_2^{+\bullet}$ and 0.7 for $C_2H_2O_2NO^+$. For higher humidity ($H > 0.4$), $C_2H_2O_2NO^+$ was dominant (>0.95). $O_2^{+\bullet}$ reacts by charge transfer, forming $C_2H_2O_2^{+\bullet}$ (m/z 58); humidity did not have a significant effect and, interestingly, the CHO^+ fragment (present in the electron ionisation mass spectra[44]) was not observed.

3.2 Numerical simulation of ion chemistry

3.2.1 Distribution of reagent ions. The H_3O^+ reagent ions form $H_3O^+(H_2O)_{1,2,3}$ in a sequence of three-body association reactions (2) with H_2O in helium.[37] The rate coefficients for these reactions obtained in previous studies are given in Table 1.

Table 1 List of the ion–molecule reactions between hydronium ions (H_3O^+) and water or formaldehyde occurring in the flow tube followed by available rate constants

Reaction		Name	k	$k_{reverse}$
Water				
$H_3O^+ + H_2O + He \rightarrow$	$H_3O^+(H_2O) + He$	k_{w1}	$6.65 \times 10^{-28\,a}$ $7.2 \times 10^{-28\,b}$ $5.8 \times 10^{-28\,c}$	
$H_3O^+(H_2O) + H_2O + He \rightarrow$	$H_3O^+(H_2O)_2 + He$	k_{w2}	$1.51 \times 10^{-27\,a}$ $1.59 \times 10^{-27\,c}$	
$H_3O^+(H_2O)_2 + H_2O + He \rightarrow$	$H_3O^+(H_2O)_3 + He$	k_{w3}	$1.50 \times 10^{-27\,a}$ $1.73 \times 10^{-27\,c}$	$4 \times 10^{-15\,a}$
$H_3O^+(H_2O)_3 + H_2O + He \rightarrow$	$H_3O^+(H_2O)_4 + He$	k_{w4}	nd	nd
Formaldehyde				
$H_3O^+ + CH_2O \rightarrow$	$CH_2OH^+ + H_2O$	k_{f1}	$3.4 \times 10^{-9\,de}$ $3.3 \times 10^{-9\,f}$ $3.0 \times 10^{-9\,gi}$	$5.6 \times 10^{-13\,d}$ $2.3 \times 10^{-12\,h}$
$H_3O^+(H_2O) + CH_2O \rightarrow$	$CH_2OH^+(H_2O) + H_2O$	k_{f2}	$3.0 \times 10^{-9\,d}$ $2.3 \times 10^{-9\,f}$	$5.3 \times 10^{-10\,d}$ $3.5 \times 10^{-10\,h}$
$CH_2OH^+ + H_2O + He \rightarrow$	$CH_2OH^+(H_2O) + He$	k_{f3}	$2.3 \times 10^{-27\,g}$ $5.7 \times 10^{-28\,h}$	

Nd – no data. [a] From ref. 35 at 296 K. [b] From ref. 36 at 300 K. [c] From ref. 37 at 298 K. [d] From ref. 38 at 298 K. [e] From ref. 39 at 297 K in H_2. [f] From ref. 40 at 294 K. [g] From ref. 41 at 300 K. [h] From ref. 42 at 300 K and 0.05 eV kinetic energy. [i] From ref. 43 at 300 K. Rate constants of bimolecular reactions are given in $cm^3\ s^{-1}$ and in $cm^6\ s^{-1}$ in the case of three-body reactions.

The distribution of $H_3O^+(H_2O)_{1,2,3}$ in the SIFT is affected by the presence of O_2 and N_2 molecules; in the present experiment, 5% of the carrier gas. A trace amount of an organic sample (glyoxal or formaldehyde) does not affect the distribution. Effective values of $k_{w1,2,3,4}$ under experimental conditions presented herein ($p = 1.5$ mbar, $T = 300$ K, $[H_2O] \cong 10^{12}–10^{14}\ cm^{-3}$, $[He] = 3.62 \times 10^{16}\ cm^{-3}$) were derived by fitting the data shown in Fig. 4 and are given in Table 2. These k values were then used for the modelling of formaldehyde and glyoxal ion chemistry.

3.2.2 Ion chemistry of formaldehyde. Table 1 summarizes the previous studies of the ion chemistry of formaldehyde.[38–43] It is understood that the reverse reaction can take place due to the close PA of water and formaldehyde.[45] A protonated formaldehyde water cluster $CH_2OH^+(H_2O)$ can be formed by ligand switching from the hydronium water cluster $H_3O^+(H_2O)$ with reaction rate k_{f3}. As $[H_2O] \sim 10^{13}\ cm^{-3}$ is much greater than $[CH_2O] \sim 10^{10}\ cm^{-3}$ under the typical SIFT conditions, the reaction equilibrium favours the formation of hydronium water clusters $H_3O^+(H_2O)$ even though the process is slightly endothermic. Fig. 5 illustrates experimental and model results based on the literature values and the model results fitted to the data. Note that the absolute intensities of ions decrease faster with H compared to the model prediction; this may be due to the variation of the formaldehyde concentration with time during the experiment. Thus, the fitting was done to the relative ion intensities that are not affected by this instability. The fitted values ($k_{f1} = 3.0 \times 10^{-9}\ cm^3\ s^{-1}$, $k_{f2} = 5.7 \times 10^{-28}\ cm^6\ s^{-1}$, $k_{f3} = 3.0 \times 10^{-9}\ cm^3\ s^{-1}$, and $k_{f\text{-}3} = 4.0 \times 10^{-10}\ cm^3\ s^{-1}$) were used for the modelling of formaldehyde ion chemistry observed in the glyoxal experiment.

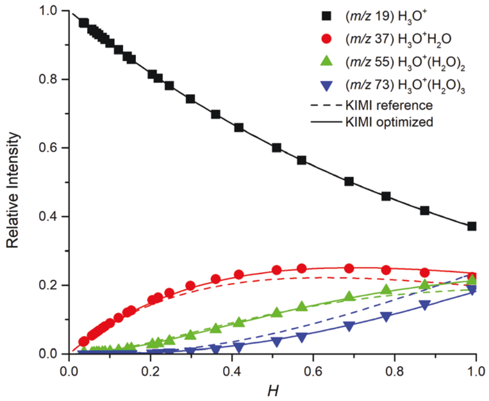

Fig. 4 Relative distribution of water clusters in the SIFT obtained by KIMI (lines) and SIFT analyses (points) of the glyoxal data set. The ion distribution calculated from literature k (dashed lines, ref. 37) does not fit the data well while the effective values given in Table 2 give good fits.

Table 2 List of rate constants (k_n, k_{-n} for reverse reactions) relevant to the formation of hydronium clusters as given in the literature and as obtained by fitting the observed distributions in the present formaldehyde and glyoxal experiments

K	Literature	Formaldehyde	Glyoxal
k_{w1}	$5.80 \times 10^{-28\,b}$	6.80×10^{-28}	7.10×10^{-28}
k_{w2}	$1.59 \times 10^{-27\,b}$	1.59×10^{-27}	1.59×10^{-27}
k_{w3}	$1.73 \times 10^{-27\,b}$	1.40×10^{-27}	1.50×10^{-27}
k_{w4}	$1.00 \times 10^{-28\,a}$	2.50×10^{-29}	3.00×10^{-29}
$k_{w\text{-}3}$	$4.00 \times 10^{-15\,c}$	4.00×10^{-15}	4.00×10^{-15}
$k_{w\text{-}4}$	$1.00 \times 10^{-15\,a}$	1.00×10^{-15}	1.00×10^{-15}

[a] Data added for the initial simulation of the $H_3O^+(H_2O)_4$ cluster with m/z 91. [b] From ref. 37. [c] From ref. 35.

3.2.3 Ion chemistry of glyoxal. Ion kinetics of protonated glyoxal was modelled by considering two possible mechanisms leading to the formation of protonated formaldehyde: (10), or (12) and (13).

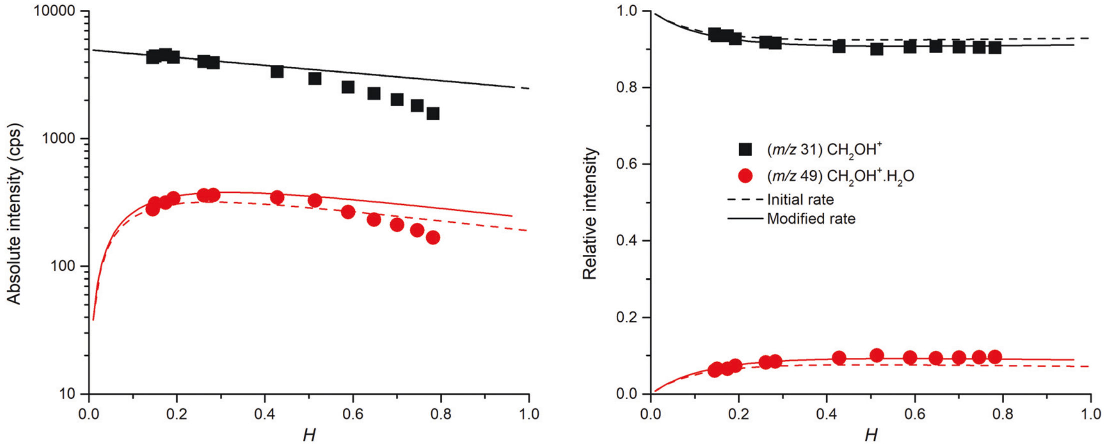

Fig. 5 Absolute (left) and relative (right) intensities of protonated formaldehyde CH_2OH^+ and its water cluster $CH_2OH^+(H_2O)$. The dashed line represents the reference set of selected rate constants.

We were not able to determine the distribution of vibrational energy and potential barriers of the suggested reactions. Hence, we could not estimate whether the amount of internal energy stored within the association product of reaction (12) is

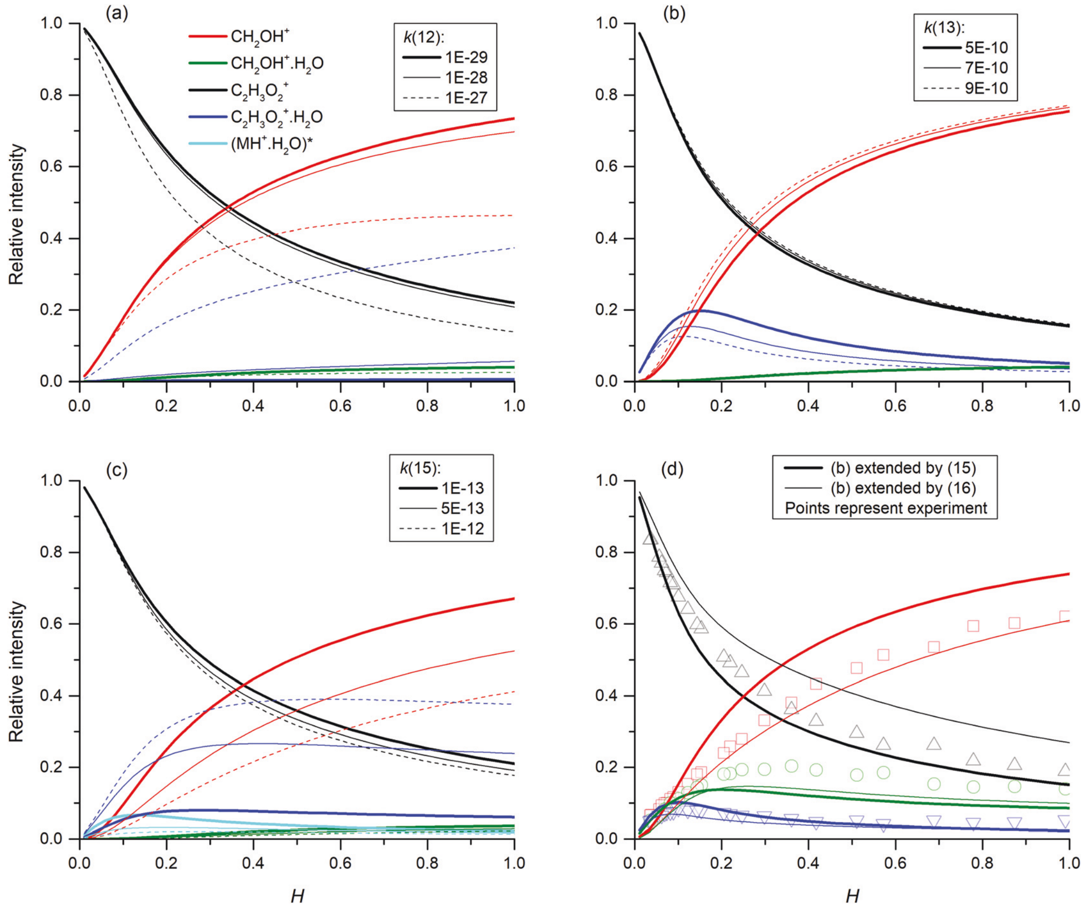

Fig. 6 Numerical modelling of possible reaction channels and their influence on relative ion distribution using different reactions and rate constants. In all presented simulations, protonated glyoxal was formed according to (1), using a reaction rate of 1.35×10^{-9} cm^3 s^{-1} in both directions. (a): reaction (10) fixed at 1×10^{-10} cm^3 s^{-1} and reaction (12) variable (units cm^6 s^{-1}) (b): reaction (12) fixed at 3.7×10^{-27} cm^6 s^{-1} and reaction (13) variable (units cm^3 s^{-1}) (c): reaction sequence (14b) fixed at the association rate 1×10^{-10} cm^3 s^{-1} and the dissociation rate 1×10^{-9} cm^3 s^{-1} to (15) variable. (units cm^3 s^{-1}) (d): reaction (13) at 1×10^{-9} cm^3 s^{-1} followed by (16) at $k = 1 \times 10^{-10}$ cm^3 s^{-1} (thick lines) and reaction (13) at 0.89×10^{-9} cm^3 s^{-1} followed by (17) at 1×10^{-9} cm^3 s^{-1}.

sufficient for reaction (13) to proceed. Thus, the effect of dissociative association was explored numerically, testing whether $C_2H_3O_2^+(H_2O)$ can be formed in an excited state.

Dissociation may be unimolecular:

$$C_2H_3O_2^+ + H_2O \rightarrow C_2H_3O_2^+(H_2O)^* \xrightarrow{\tau} CH_2OH^+ + \text{neutrals} \tag{14a}$$

or induced by a collision with water molecules:

$$C_2H_3O_2^+ + H_2O \rightarrow C_2H_3O_2^+(H_2O)^* \xrightarrow{H_2O} CH_2OH^+ + \text{neutrals}. \tag{14b}$$

However, $C_2H_3O_2^+(H_2O)^*$ can also be stabilized by collision with carrier gas or other neutral molecules and thus form a stable cluster similar to a three-body process:

$$C_2H_3O_2^+(H_2O)^* + He \rightarrow C_2H_3O_2^+(H_2O) + He. \tag{15}$$

The initial increase of $C_2H_3O_2^+(H_2O)$ concentration with H observed in the experiments is followed by a slow decrease for $H > 0.15$ (see Fig. 3). The model explains these observations most appropriately by combining reactions (12) and (13) with rate constants of 10^{-27} cm^6 s^{-1} and 10^{-10} cm^3 s^{-1}, respectively. However, the data can also be modelled by reaction (14b), forming a reaction intermediate $C_2H_3O_2^+(H_2O)^*$ with a rate constant of 10^{-10} cm^3 s^{-1} followed by its reaction with water molecules at 10^{-9} cm^3 s^{-1} and (15) at 10^{-11} cm^3 s^{-1}. Fig. 6 shows model results for several combinations of rate constants.

In addition, reactions (12) and (15) were studied under variable flow tube pressure (see Fig. 7) thus changing the He number density. For two different water concentrations, an increase in the carrier gas pressure leads to a decrease in the formation of protonated formaldehyde ions and a slight increase of $C_2H_3O_2^+(H_2O)$, as expected from (15). However, the water concentration was influenced by He pressure due to different He/H_2O mixing ratios and also the diffusion of ions is accelerated at lower pressures. Therefore, these experiments cannot with certainty confirm three-body reactions, however they do not exclude them, either.

The relative intensities of CH_2OH^+ and $CH_2OH^+(H_2O)$ observed in the glyoxal experiment differ from those observed in the formaldehyde experiment (Section 3.2.2). The association of protonated formaldehyde and water (see k_{f3} in Table 1) alone cannot explain this observation. An additional reaction channel forming hydrated protonated formaldehyde is therefore required. The following two reaction channels describe the relative intensities observed in the glyoxal experiment:

$$C_2H_3O_2^+ + H_2O \rightarrow H_2COH^+(H_2O) + CO, \tag{16}$$

$$C_2H_3O_2^+(H_2O) + H_2O \rightarrow H_2COH^+(H_2O) + HCOOH. \tag{17}$$

Both reactions contribute similarly to the model curve (see Fig. 5d) using rates of 10^{-10} cm^3 s^{-1} and 10^{-9} cm^3 s^{-1} for (16) and (17), respectively. Based on numerical simulations, we cannot favour one of them and even their simultaneous contribution is possible.

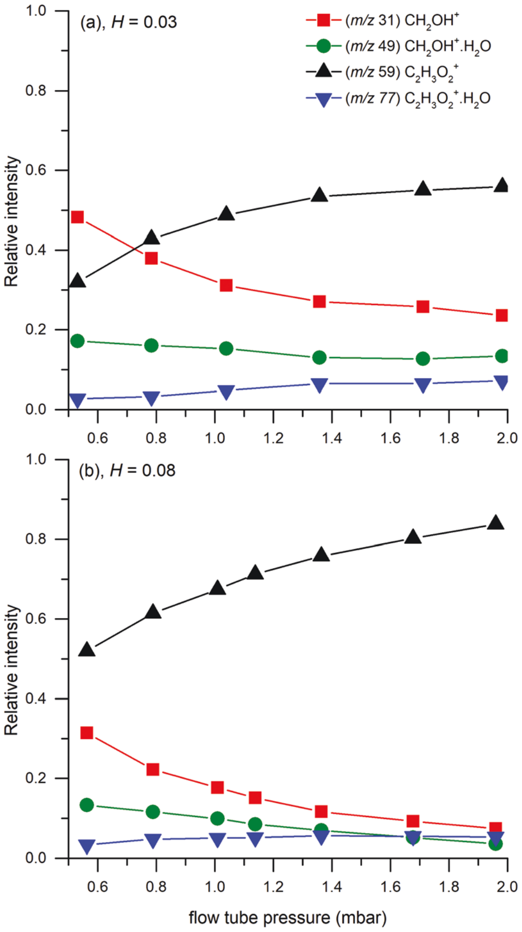

Fig. 7 Relative ion distribution as a function of the flow tube pressure. Experiments were done at H = 0.03 (3 × 10^{12} cm^{-3}) for (a) and H = 0.08 (1 × 10^{13} cm^{-3}) for (b) at 1.5 mbar.

Finally, we have modelled the endothermic ligand switching reaction (11). The high number density of neutral water molecules will shift the equilibrium in the direction of the protonated water dimer. Modelling with different reaction rate constants showed that the reaction does not affect trends in the formation of targeted species. However, it does affect the equilibrium between protonated glyoxal and protonated formaldehyde (see Fig. 8). The ligand switching reaction with water has a significant effect on the total abundance of ions, thus this effect was demonstrated together with the effect of different reaction equilibrium in (1).

The aim of the study was to describe the main reaction channels in the ion chemistry of glyoxal with hydronium in SIFT-MS. The final model of glyoxal ion chemistry consists of thirteen individual kinetic equations, combining the hydronium and formaldehyde ion chemistry given in Table 1 with eqn (1) and (11)–(13) extended by (16) and (17). Even though we carefully considered each rate constant, the final set of rate constants will not be the only solution modelling the experimental observations. It is quite possible that the resulting set can be additionally tuned to better fit the experimental data and the model does not have to be accurate on the absolute

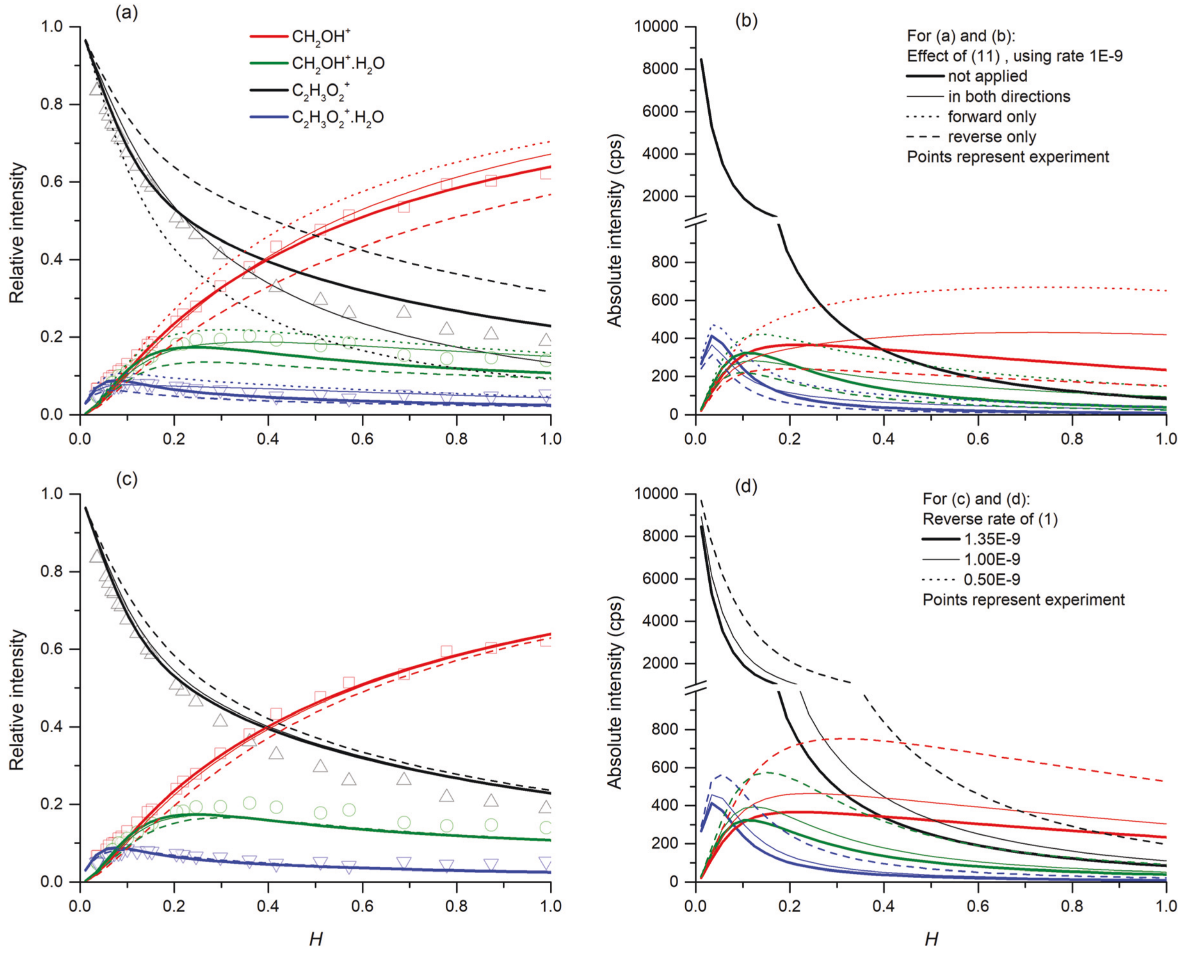

Fig. 8 Influence of (11) (top) and (1) (bottom) on the relative (left) and absolute (right) concentration of ions at the end of the flow tube. The simulation uses (13) ($k = 10^{-9}$ cm^3 s^{-1}) and (12) ($k = 5 \times 10^{-27}$ cm^6 s^{-1}) as the main reaction channels combined with (17) ($k = 8 \times 10^{-10}$ cm^3 s^{-1}). The demonstration of (11) (top) uses a reverse rate of (1) with $k = 1.35 \times 10^{-9}$ cm^3 s^{-1}. The variation of (1) (bottom) does not contain (11). The absolute scale simulation was provided using 10^{10} molecules cm^{-3} glyoxal and 2×10^7 ions per cm^3 hydronium particles as an initial condition.

scale. Nevertheless, the modelling shows the dramatic effect of neutral water concentration on the ion chemistry of glyoxal.

4 Conclusions

We investigated the H_3O^+/glyoxal ion chemistry for variable humidity using a SIFT-MS instrument. The study confirmed the secondary formation of protonated formaldehyde with increasing water concentration. For concentrations over 10^{13} water molecules per cm^3 in the flow tube, the protonated formaldehyde became the dominant product ion. The abundance of total product ions was very sensitive to water concentration, quickly decreasing for higher humidity.

The observed experimental behaviour was described using numerical simulation of ion kinetics. An additional study of hydronium water clusters and formaldehyde ion chemistry was carried out to supplement the study of glyoxal ion formation. The numerical study of glyoxal ion chemistry showed that protonated formaldehyde is formed through the reaction of $C_2H_3O_2^+(H_2O)$ with water molecules. Alternative reaction channels involving water are possible, forming a protonated formaldehyde water cluster $CH_2OH^+(H_2O)$ either from protonated glyoxal (16) or from the protonated glyoxal water cluster (17).

Modifications in the glyoxal interaction with hydronium and hydronium clusters affect the total ion abundance, while changes in the reaction rate with hydronium clusters affect the reaction equilibrium as well. However, in all cases, we may observe a quick dissipation of ion signals for higher water concentration. The ion dissipation is maintained by ligand switching between protonated formaldehyde water cluster $CH_2OH^+(H_2O)$ and neutral water, forming $H_3O^+{\cdot}H_2O$ and neutral formaldehyde. This makes the measurement of glyoxal in moist environments using CIMS particularly difficult. In addition, measurements in moist environments are much more sensitive to the influence of formaldehyde. The amount of protonated formaldehyde produced from glyoxal at H_2O concentrations greater than 10^{13} cm^{-3} corresponds to apparent 5% formaldehyde impurity in glyoxal.

Conflicts of interest

There are no conflicts to declare.

Acknowledgements

This project has received funding from the European Union's Horizon 2020 research and innovation programme under the Marie Skłodowska-Curie grant agreement No 674911.

Notes and references

1 G. Mattioda and A. Blanc, *Glyoxal in Ullmann's Encyclopedia of Industrial Chemistry*, 2000.

2 M. K. Hazra, J. S. Francisco and A. Sinha, *J. Phys. Chem. A*, 2014, **118**, 4095–4105.

3 N. Shangari, W. R. Bruce, R. Poon and P. J. O'Brien, *Biochem. Soc. Trans.*, 2003, **31**, 1390–1393.

4 I. A. Shkrob, T. W. Marin, H. He and P. Zapol, *J. Phys. Chem. C*, 2012, **116**, 9450–9460.

5 S. Civiš, M. Ferus, A. Knížek, P. Kubelik, L. Kavan and M. Zukalova, *Opt. Mater.*, 2016, **56**, 80–83.

6 R. Volkamer, U. Platt and K. Wirtz, *J. Phys. Chem. A*, 2001, **105**, 7865–7874.

7 M. Jang and R. M. Kamens, *Environ. Sci. Technol.*, 2001, **35**, 3626–3639.

8 E. C. Tuazon, R. Atkinson, H. Mac Leod, H. W. Biermann, A. M. Winer, W. P. Carter and J. N. Pitts, *Environ. Sci. Technol.*, 1984, **18**, 981–984.

9 J. Yu, H. E. Jeffries and K. G. Sexton, *Atmos. Environ.*, 1997, **31**, 2261–2280.

10 D. Smith, T. Kleindienst and C. McIver, *J. Atmos. Chem.*, 1999, **34**, 339–364.

11 J. Yu, H. E. Jeffries and R. M. Le Lacheur, *Environ. Sci. Technol.*, 1995, **29**, 1923–1932.

12 J. Fick, L. Pommer, C. Nilsson and B. Andersson, *Atmos. Environ.*, 2003, **37**, 4087–4096.

13 H. Akimoto, *Monogr. Environ., Earth Planets*, 2016, **4**, 1–45.

14 A. C. Nölscher, A. M. Yañez-Serrano, S. Wolff, A. C. de Araujo, J. V. Lavrič, J. Kesselmeier and J. Williams, *Nat. Commun.*, 2016, **7**, 10383.

15 T. Wroblewski, L. Ziemczonek, A. M. Alhasan and G. P. Karwasz, *Eur. Phys. J.-Spec. Top.*, 2007, **144**, 191–195.

16 E. P. L. Hunter and S. G. Lias, *J. Phys. Chem. Ref. Data*, 1998, **27**, 413–656.

17 J. Zhao and R. Zhang, *Atmos. Environ.*, 2004, **38**, 2177–2185.

18 E. Michel, N. Schoon, C. Amelynck, C. Guimbaud, V. Catoire and E. Arijs, *Int. J. Mass Spectrom.*, 2005, **244**, 50–59.

19 C. Guimbaud, V. Catoire, A. Bergeat, E. Michel, N. Schoon, C. Amelynck, D. Labonnette and G. Poulet, *Int. J. Mass Spectrom.*, 2007, **263**, 276–288.

20 C. Stönner, B. Derstroff, T. Klüpfel, J. N. Crowley and J. Williams, *J. Mass Spectrom.*, 2017, **52**, 30–35.

21 R. Volkamer, P. Spietz, J. Burrows and U. Platt, *J. Photochem. Photobiol., A*, 2005, **172**, 35–46.

22 R. A. Lewis and G. G. Hawley, *Hawley's condensed chemical dictionary*, John Wiley & Sons, 2016.

23 D. R. Lide and G. W. A. Milne, *CRC handbook of data on organic compounds*, CRC Press, 1993.

24 P. Španěl and D. Smith, *Med. Biol. Eng. Comput.*, 1996, **34**, 409–419.

25 D. Smith and P. Španěl, *Mass Spectrom. Rev.*, 2005, **24**, 661–700.

26 P. Španěl, K. Dryahina and D. Smith, *Int. J. Mass Spectrom.*, 2006, **249–250**, 230–239.

27 R. Barratt, *Analyst*, 1981, **106**, 817–849.

28 P. Španěl, K. Dryahina and D. Smith, *Int. J. Mass Spectrom.*, 2006, **249**, 230–239.

29 K. Dryahina and P. Španěl, *Int. J. Mass Spectrom.*, 2005, **244**, 148–154.

30 C. Runge, *Mathematische Annalen*, 1895, **46**, 167–178.

31 W. Kutta, *Z. Math. Phys.*, 1901, **46**, 435.

32 D. Smith and N. Adams, *Adv. At. Mol. Phys.*, 1988, **24**, 1–49.

33 D. Smith, P. Spanel and K. Dryahina, *Int. J. Mass Spectrom.*, 2019, **435**, 173–180.

34 D. J. Goebbert and P. G. Wenthold, *Eur. J. Mass Spectrom.*, 2004, **10**, 837–845.

35 V. Bierbaum, M. Golde and F. Kaufman, *J. Chem. Phys.*, 1976, **65**, 2715–2724.

36 R. Bolden and N. Twiddy, *Faraday Discuss. Chem. Soc.*, 1972, **53**, 192–200.

37 P. Španěl and D. Smith, *J. Am. Soc. Mass Spectrom*, 2001, **12**, 863–872.

38 D. Bohme, G. Mackay and S. D. Tanner, *J. Am. Chem. Soc.*, 1979, **101**, 3724–3730.

39 S. D. Tanner, G. I. Mackay and D. K. Bohme, *Can. J. Chem.*, 1979, **57**, 2350–2354.

40 A. J. Midey, S. T. Arnold and A. Viggiano, *J. Phys. Chem. A*, 2000, **104**, 2706–2709.

41 N. Adams, D. Smith and D. Grief, *Int. J. Mass Spectrom. Ion Phys.*, 1978, **26**, 405–415.

42 A. Hansel, W. Singer, A. Wisthaler, M. Schwarzmann and W. Lindinger, *Int. J. Mass Spectrom. Ion Processes*, 1997, **167**, 697–703.

43 Y. Ikezoe, S. Matsuoka and M. Takebe, *Gas phase ion–molecule reaction rate constants through 1986*, Ion reaction research group of the Mass spectroscopy society of Japan, 1987.

44 NIST Chemistry WebBook, NIST Standard Reference Database 69, U.S. Secretary of Commerce, National Institute of Standards and Technology, Gaithersburg, MD, http://webbook.nist.gov/chemistry/, cited November 2019.

45 P. Španěl, D. Smith, T. A. Holland, W. A. Singary and J. B. Elder, *Rapid Commun. Mass Spectrom.*, 1999, **13**, 1354–1359.

SIFT-MS and PTR-MS studies of H_3O^+ reaction with glyoxal in presence of water molecules forming protonated formaldehyde at different interaction energies

Michal Lacko[1,2], Patrik Španěl[1], Chris Mayhew[3], Michaela Malásková[3], Anatoli Spesyvyi[1]

[1] J. Heyrovsky Institute of Physical Chemistry of the CAS, v. v. i, Dolejškova 2155/3, 182 23 Prague 8, Czech Republic

[2] Charles University Prague, Faculty of Mathematics and Physics, Prague, Czech Republic.

[3] Institute for Breath Research, Fakultät für Chemie und Pharmazie, Leopold-Franzens-Universität Innsbruck, Dornbirn, Austria

Abstract

Glyoxal ($C_2H_2O_2$) is the simplest volatile dialdehyde that may be present at trace levels in the air. Detection of glyoxal in the environment using chemical ionisation mass spectrometry (CIMS) can be compromised by the presence of isobaric molecules such as acetone and its high reactivity, mainly with water vapour. In the present work, we studied the reaction of common CIMS regent ions H_3O^+ with glyoxal in the presence of an electric field and at variable humidity. The study was carried out using two CIMS techniques, selected ion flow drift tube mass spectrometry (SIFDT-MS) and proton transfer reaction mass spectrometry (PTR-MS), and the results were compared with numerical simulations. The proton transfer reaction at low water concentrations at low *E/N* results in the formation of protonated glyoxal. At high *E/N,* the formation of protonated formaldehyde is observed. At higher humidity, secondary reactions with H_2O occur and ion chemistry becomes significantly more complicated: At low *E/N*, protonated formaldehyde is formed via a series of secondary reactions involving protonated glyoxal hydride and at high *E/N*, product ions react with H_2O back to form H_3O^+. Consequently, the humidity increase at low *E/N* induces the formation of protonated formaldehyde, whilst at high *E/N,* the observed fraction of protonated formaldehyde decreases.

Introduction

Glyoxal ($C_2H_2O_2$, Ethane-1,2-dione) is the simplest dialdehyde, present as an intermediate in several chemically active systems. It is present in the atmospheric chemistry of biological organic compounds (BVOCs) as a product of oxidation and photo-oxidation of toluene[1-3], xylene[2-4], trimethyl benzene[3, 4], isoprene[5] and α-pinene[6]. Oxidation of glyoxal may generate secondary organic aerosols and thus contribute significantly to daytime atmospheric chemistry [7]. Apart from atmospheric chemistry, glyoxal is also presented in biological systems as a cytotoxic metabolite of glucose, a product of lipid peroxidation or be used as a marker of oxidation stress. [8, 9] Additionally, glyoxal plays an important role as an intermediate in the photocatalytic reduction of carbon dioxide to methane. [10]

As glyoxal is also a volatile organic compound (VOC), its presence can be determined by soft chemical ionisation mass spectrometry (SCIMS). Quantitative determination of glyoxal concentration is, however, challenging. First, glyoxal concentration in the gas sample is often very low and time unstable as neutral glyoxal reacts rapidly with water and polymerises from an anhydrous monomeric form into a series of oligomers.[11, 12] Second, the product of proton transfer chemical ionisation of glyoxal, protonated glyoxal $C_2H_3O_2^+$, interferes with other common BVOCs as protonated acetone ($C_3H_7O^+$). The analysis, therefore, requires high-resolution mass spectrometry instruments. Last, to achieve ionisation, SCIMS techniques primary use proton transfer reaction between hydronium regent ion (H_3O^+) and analyte (M)

$$H_3O^+ + M \rightarrow MH^+ + H_2O. \tag{1}$$

This process requires the proton affinity of analyte *PA*(M) to be lower than the *PA* of water. The difference between proton affinities of glyoxal (calculated as 690.6 kJ/mol and 675.3 kJ/mol [13]) and water (691 kJ/mol [14]) is low. This may reduce the proton transfer reaction rate below the collisional rate and thus reduce the sensitivity of the analysis. [15]

Hydronium ion chemistry with glyoxal was thus studied carefully by several authors using selected ion flow tube mass spectrometry (SIFT-MS) and proton transfer reaction mass spectrometry (PTR-MS), equipped with flow tube and drift tube, respectively. It is important to stress the difference as ion behavior observed in these instruments differs. In SIFT-MS, the proton transfer reaction produces protonated glyoxal as expected from Eq. 1 with a reaction rate of 1.35×10^{-9} $cm^{-3}s^{-1}$ at 297 K. [16, 17] However, as soon as humidity is presented in the flow tube, protonated glyoxal reacts with water vapours in a sequence of secondary reactions into protonated formaldehyde (CH_2OH^+). [18] Thus, the relative concentration of protonated formaldehyde increases with increasing water concentration while the concentration of protonated glyoxal decreases. This reaction sequence will be discussed later in this work more carefully. However, the opposite behaviour was observed in PTR-MS at reduced electric field E/N = 137 Td, where the introduction of humidity decreases the relative abundance of protonated formaldehyde in favour of protonated glyoxal. [19] The formation of protonated formaldehyde in the drift tube at higher E/N is not caused by secondary reactions but presumably by CID. The decrease of protonated formaldehyde abundance is, anyway, unexpected.

The present study aims to understand the ion chemistry initiated by the reaction of hydronium ions with glyoxal molecules in the presence of a homogenous electric field and simultaneously in the presence of humidity. Thus two SCIMS techniques were used: PTR-MS and selected ion flow drift tube mass spectrometry (SIFDT-MS), operating in nitrogen and helium carrier gases, respectively. Experimental results are supplemented by a numerical model of proposed ion chemistry. The results indicate a change in the reaction mechanism with increasing E/N in the drift tube. At low E/N, ion chemistry is primarily driven by secondary reactions of hydrated product ion clusters, while at the high E/N, reverse proton transfer reactions of product ions with water molecules influence the ion chemistry.

Experimental

Glyoxal sample preparation

Glyoxal was prepared from 40% glyoxal solution (CAS: 107-22-2, Sigma-Aldrich) using a method similar to isolation from glyoxal trimeric dehydrate.[16, 17, 19, 20] 10 ml of glyoxal solution was placed in a 250 ml flask and evacuated for 24 hours to remove the bulk of water. The resulting high viscose residuum was crystallised to bis(dioxolane) trimer. [11] Crystals were crushed and covered by a layer of P_2O_5 (Sigma-Aldrich), separated by a 1 cm layer of 1 mm glass beads, to remove any remaining water and slowly heated up to 150°C until the yellow-green vapour characteristic for glyoxal appeared by thermal decomposition [21, 22]. Glyoxal vapour was re-crystalised in a cold trap, cooled by dry ice. The glyoxal crystals were kept in a dry ice-cooled box to minimise exposure to atmospheric water vapour. The glyoxal crystals were stored in a vial placed in a box cooled by dry ice to minimise exposure to atmospheric humidity. Thus, some CO_2 contamination in the experiments may be present.

Proton transfer reaction mass spectrometry (PTR-MS)

The PTR-MS study was carried out using PTR-TOF 8000 apparatus (IONICON Analytik GmbH, Austria). [23, 24] Briefly, $H_3O^+.(H_2O)_n$ (n = 0, 1, 2, …) reagent ions are generated in a hollow cathode discharge in a water vapour atmosphere and transferred to the drift tube via a focusing lens. A series of ring electrodes in the drift tube forms a homogenous electric field, accelerating ions along the central drift tube axis. The distribution of the protonated water clusters in the reaction region depends on the drift tube's E/N value and humidity. Analytes are injected into the drift tube through an inlet pipe. Proton transfer from hydronium to the analyte takes place within the drift tube if the proton affinity (*PA*) of the analyte is higher than that of water ($PA(H_2O)$ = 691 kJ mol^{-1}). Proton transfer can be non-dissociative and dissociative. However, it should be stressed that fragmentation of the protonated molecule can be a barrier-less process and occur spontaneously, or it can be induced by the collision of the reagent ions with the analyte or charged analyte with the buffer gas.

For all measurements, the drift tube was kept at a pressure of 2.3 mbar, with the inlet system and drift tube being maintained at 60°C. The collisional energies of the reagent and product ions were controlled by the value of the reduced electric field, *E/N*. For this study, we kept the drift tube at constant pressure and temperature (and hence constant *N*) and changed the drift tube voltage to alter the value of *E/N*. The drift voltage could be changed from 340 V up to a maximum of 900 V. This corresponds to an *E/N* range from 80 to 210 Td for the applied values of the drift tube pressure and temperature.

The glyoxal sample was prepared by injecting the glyoxal head space into the PTFE bag filled with dry N_2. The bag was either sampled directly (achieving low sample humidity) or mixed with humid N2 (to achieve higher sample humidity) and then sampled afterwards. The mixing point was placed close to the drift tube entering the inlet port to limit the glyoxal neutral reactions with water vapours. Humidified N_2 was prepared using a Liquid Calibration Unit (LCU, IONICON Analytik GmbH, Austria). [25] The LCU generates defined gaseous concentrations from aqueous solutions of volatile and semi-volatile organics. Briefly, a homebuilt liquid flow controller injects a defined flow into a nebuliser (X175, Burgener Research Inc., United Kingdom). The vapourisation of liquid water produces micro-droplets evapourated in a heating chamber maintained at 100°C. The heating chamber is constantly flushed by a buffer N_2 gas, generating a continuous stream of defined humidity. The humidity of the glyoxal sample mixed with humid N_2 and injected into PTR-MS is thus constant. However, it cannot be determined directly. Some portion of humidity can also naturally diffuse from the ion source of the PTR-MS. Therefore, the relative humidity change was determined from the distribution of the hydronium and its associated hydrides $H_3O^+.(H_2O)_n$ (n = 0, 1, 2, …) using a dimension-less parameter *H*, proportional to the absolute humidity in the drift tube, as

$$H_{drift}^{E/N} = ln\left(\frac{[H_3O^+]+[H_3O^+\cdot H_2O]+[H_3O^+\cdot(H_2O)_2]+\cdots}{[H_3O^+]}\right). \qquad (2)$$

The parameter *H* has to be always related to the corresponding *E/N* value. Thus we use $H^{E/N}$ notation.

SIFT-MS instrument [18, 26] was connected to the PTR-MS sampling line for several reference humidity levels (see Supplement, Fig. S1) to relate the *H* value to the absolute sample humidity. In SIFT-MS, the absolute sample humidity can be determined directly. This approach was, however, not used frequently as the additional SIFT-MS sampling flow slightly affects the sample mixing conditions.

Selected ion flow-drift tube mass spectrometry (SIFDT-MS)

Selected ion flow-drift tube mass spectrometry (SIFDT-MS) apparatus was also described previously. We used two versions of the SIFDT-MS apparatus in the present study, equipped with different ion source designs. The remaining parts of the instrument are identical. Compared to the PTR-MS instrument, the drift tube in the SIFDT-MS contains helium carrier gas. Additionally, a modulated signal can be applied to an electrode before the drift tube. It can generate a pulsed ion stream to determine the ion residence time in the drift tube and their velocity, mobility and reaction energies.

Shortly, in the first concept [27], $H_3O(H_2O)_n^+$ reagent ions were generated in a glow cathode discharge operating in a water vapour/ synthetic air mixture. After extraction from the discharge, reagent ions were introduced via ion optics into the quadrupole mass filter. Ions with selected *m/z* are injected into the transition ion optics, supplemented by the shutter grid. The shutter grid modulated the ion transmission by applying the Hadamard modulation. The transition ion optics injected ions into the drift tube reactor (DTR). The ion current, modulated by the Hadamard modulation or continuous stream, entered the drift tube reactor (DTR), a 145 mm long, 10 mm ID, resistive glass tube (PHOTONIS). In the DTR, ions drift along the tube in a homogenous electric field against 150 sccm counterflow of He at 1.4 mbar and gas temperature 24 °C, if not stated otherwise. The voltage across the resistive layer (in the range from 100 to 500 V) created a homogenous electric field (E/N from 10 to 100 Td). At the end of the DTR, ions were introduced via an orifice into the quadrupole mass spectrometer and detected by the electron multiplier with a conversion dynode. Sample gas was introduced into the helium gas stream at the end of the flow-drift tube and carried through by reverse helium flow.

In the modified ion source version [28], a hollow cathode discharge operating in a water vapour/ synthetic air mixture produces $H_3O(H_2O)_n^+$ ions. Ions are then transferred to the stacked ring ion guide (SRIG) housed in the polypropylene vacuum chamber with 5.3 mbar helium buffer gas. Thermalised ions carried by the electric field and helium flow enter the next chamber with 50 mm long octupole (OP), with He pressure of about 0.3 mbar. Using OP, ions are guided through an aperture into the quadrupole mass filter (QMF). Filtered ions are introduced via the Venturi inlet to the small flow-drift tube (VDT), where ions are mixed with He buffer gas and thermalised. At the end of the VDT, a series of three meshes provide the Hadamard modulation of the ion current.

Ions in the electric field move with different velocities based on their mobilities. Thus, ion residence times in the DTR are necessary to estimate ion velocities in laboratory coordinates and later ion-molecule reaction energies and ion mobilities. Ion residence time is determined by applying a pseudo-random Hadamard modulation on a specific electrode of the ion optics in the front of the DTR, reduced by the detector transfer time, determined by applying the same modulation on the ion optics directly after DTR.

Ion velocity is then obtained from the ion residence time (t_r) and known drift tube length (l = 145 mm), adjusted by the carrier gas flow velocity in the drift tube (v_g)

$$v_d = \frac{l}{t_r} - v_g. \tag{3}$$

The mean interaction energy of ions with neutrals, E_r, was calculated using the Wannier equation [29],

$$E_r = \frac{m_n}{(m_n + m_i)}\left(\frac{m_i v_d^2}{2} + \frac{m_c v_d^2}{2}\right) + \frac{3}{2} k_\mathrm{B} T \tag{4}$$

where m_i, m_n and m_c are respectively the masses of the drifting ion, reactant neutral and carrier gas, v_d represents the ion drift velocity, and k_B and T are Boltzmann constant and carrier gas temperature. Reduced ion mobility K_0 was calculated by using the relation

$$K_0 = \frac{v_d}{N_0 \frac{E}{N}}, \tag{5}$$

where $N_0 = 2.6867 \times 10^{25}\ \mathrm{m^{-3}}$ is the gas number density at standard temperature and pressure (STP, 273.15 K and 1.013×10^5 Pa) and E/N is the reduced electric field strength. Note that the ion residence time can be obtained only for reagent ions with sufficiently high intensity. Thus it could not be recorded in every situation due to abundance restrictions.

The study of glyoxal ion chemistry was carried out for each version of the ion source differently, reflecting each concept's strengths. The **first concept** contains simpler ion optics, selecting and transferring ions from the discharge into the DTR while achieving a high ion count (10M cps for hydronium reagent ion detected on the electron multiplier). This allows a comfortable study of the glyoxal ion chemistry; to achieve significant intensities of product ions without reducing the primary ion count rate. Glyoxal headspace was injected into a Nalophan bag filled with He gas. The sample was then introduced at the end of the DTR into the reverse stream of He. The sample flow rate, as well as the He reverse stream flow, were regulated to maintain constant reverse gas flow and DTR pressure. The humidity of the sample was increased by the introduction of an additional Nalophan bag filled with He. Both bags were then simultaneously connected to the sample inlet. Then, a controlled amount of water (1 ml, 3ml, 5 ml) was injected into the second bag, increasing the sample humidity. The hydronium – glyoxal ion chemistry products were thus recorded for various *E/N* and system humidity. We also did an alternative experiment, using synthetic air as the base for the sample headspace. This resulted in an elevated concentration of oxygen and nitrogen molecules in the drift tube to better understand the transition from PTR-MS to SIFDT-MS. In addition, a glyoxal sample was also injected into the discharge, where we observed the formation of previously detected product ions. Ions were then selectively filtered and introduced into DTR to determine the ion mobility for several *E/N* and humidity levels.

Note that application of the Hadamard modulation and determination of the ion residence time requires ions to achieve intensities above 10k cps. Thus, the ion mobility for a specific ion was not determined for all *E/N* values but only when a particular ion was intensive enough. Also, in the first concept, the pressure gauge for the DTR was located on the pumping line, not directly on the DTR. Thus, we expect some deviation between the measured and the real pressure in the DTR. Ion mobility of hydronium (known from literature) was used to calibrate the drift tube pressure by factor 1.3 to compensate for this effect.

The **second concept** using a modified ion source was built to generate various protonated reagent ions. The OP is equipped with a separated inlet from where the gas sample can also be introduced. Introducing sample gas into OP enables proton transfer reactions to occur inside the OP. Product ions can thus be introduced into DTR via a quadrupole filter and studied as primary reagent ions. However, the advanced ion optics reduced the total amount of reagent ions presented in the DTR. Thus, it isn't easy to reconstruct the ion chemistry study executed with the first SIFDT concept, as an increase in the glyoxal sample concentration quickly affects the concertation of primary reagent ions via secondary reactions. Also, note that ions selected via the first quadrupole mass filter enter the VDT with the kinetic energy of 12 eV. This, however, does not affect the experiment as long as fragmentation does not occur because internally excited ions will reach normal temperature energy distribution before they enter DTR.

Anyway, the glyoxal study was carried out similarly to the first SIFDT concept. We also used Nalophan bags filled with He gas and a combination of two bags connected near the SIFDT sample inlet port for humidity studies. Experiments were done at a slightly higher drift tube pressure of 1.8 mbar. The modified ion source allowed us to generate protonated glyoxal and protonated formaldehyde by introducing the glyoxal/helium vapour into the OP chamber through the needle valve, where in reactions with $H_3O(H_2O)_n^+$ those ions were formed. Protonated glyoxal and protonated formaldehyde were then filtered and injected into DTR. By increasing the helium humidity in the DTR, we determined the influence of water vapours on ion chemistry of protonated glyoxal and protonated formaldehyde individually for several *E/N* values. The humidity level was also determined using Eq. 2 and providing reference measurements using SIFT-MS.

KIMI numerical modelling of ion chemistry

Proposed ion chemistry was modelled using numerical ion chemistry simulator KIMI (Kinetic of Ion-Molecular Interaction, using Microsoft Visual Studio 2017, .NET Framework 4.6.1). [18, 30] The simulator interactively solves sets of kinetic equations describing changes of reagent and product ion number densities along the axis of the reactor and thus models ion intensities presented at the end of the flow tube of the drift tube.

The model uses a graphical interface to draw proposed ion chemistry interactively. Graphical input is transferred into a set of differential equations and solved along the axis of the reactor using the classical Runge-Kutta method. [31, 32] The solution represents the profile of ion and neutral number densities and thus models the concertation of ion reactants and products in the reactor.

All particles in the simulation are defined by the initial concentration, reduced ion mobility, μ_0 and the diffusion coefficient [33], D_e, while a separate rate constant k describes every reaction path. Additionally, specific parameters of the reactor are specified; characteristic radial diffusion length Λ, temperature T, pressure p, reactor length L and radius R and the carrier gas velocity v_g.

In the presence of a homogenous electric field, differential equations are constructed from their time-dependent equivalent using the dt = dx/vd substitution, where dt stands for the time differential and dx represents the coordinate differential along the reactor axis and the v_d represents the ion drift velocity.

Differentiation equations can be formed using a model proton transfer reaction between hydronium (H_3O^+) and neutral molecule M, forming protonated MH^+. The time-dependent differential equation describing the concentration evolution of MH^+ takes the form

$$\frac{\mathrm{d}[\mathrm{MH}^+]}{\mathrm{dt}} = k[\mathrm{M}][\mathrm{H_3O}^+] - [\mathrm{MH}^+]\frac{D_e}{\Lambda^2} \tag{6}$$

In the presence of a homogenous electric field, defined by reduced electric field *E/N*, the differential equation takes a new form

$$\frac{\mathrm{d}[\mathrm{MH}^+]}{\mathrm{d}x} = \frac{k(E/N)[\mathrm{M}][\mathrm{H_3O}^+] - [\mathrm{MH}^+]\frac{D_e}{\Lambda^2}}{v_g + \mu_0(E/N)N_0\frac{E}{N}}, \tag{7}$$

where $N_0 = 2.6867 \times 10^{25}$ m^{-3} is the gas number density at normal temperature (273 K) and pressure (1.013×10^5 Pa). The simulation does not account for the longitudinal diffusion, only for the radial diffusion losses.

Results and discussion

The PTR-MS study of glyoxal confirmed the presence of four main ion products (see Supplement, Fig. S2): protonated glyoxal ($C_2H_2O_2.H^+$, *m/z* 59.0321), hydrated protonated glyoxal ($C_2H_4O_3.H^+$, *m/z* 77.0483), protonated formaldehyde ($CH_2O.H^+$, *m/z* 31.0282) and hydrated protonated formaldehyde ($CH_4O_2.H^+$, *m/z* 49.0445). For low *E/N* values, trace amounts of dihydrated protonated glyoxal ($C_2H_6O_4.H^+$, *m/z* 95.0646) and dehydrated protonated formaldehyde ($CH_6O_3.H^+$, *m/z* 67.0608) were also observed. To simplify, we will use only isobaric *m/z* in the text.

The abundance of the main ion products was then carefully recorded for a range of *E/N* values (from 80 Td to 210 Td in 10 Td intervals) at a constant gas pressure in the drift tube and for several water vapour concentrations. The relative intensity of the main ion products can be thus presented in two different plots: (i) as a function of water vapour concentration at constant *E/N* and (ii) as a function applied *E/N* at constant water vapour concentration.

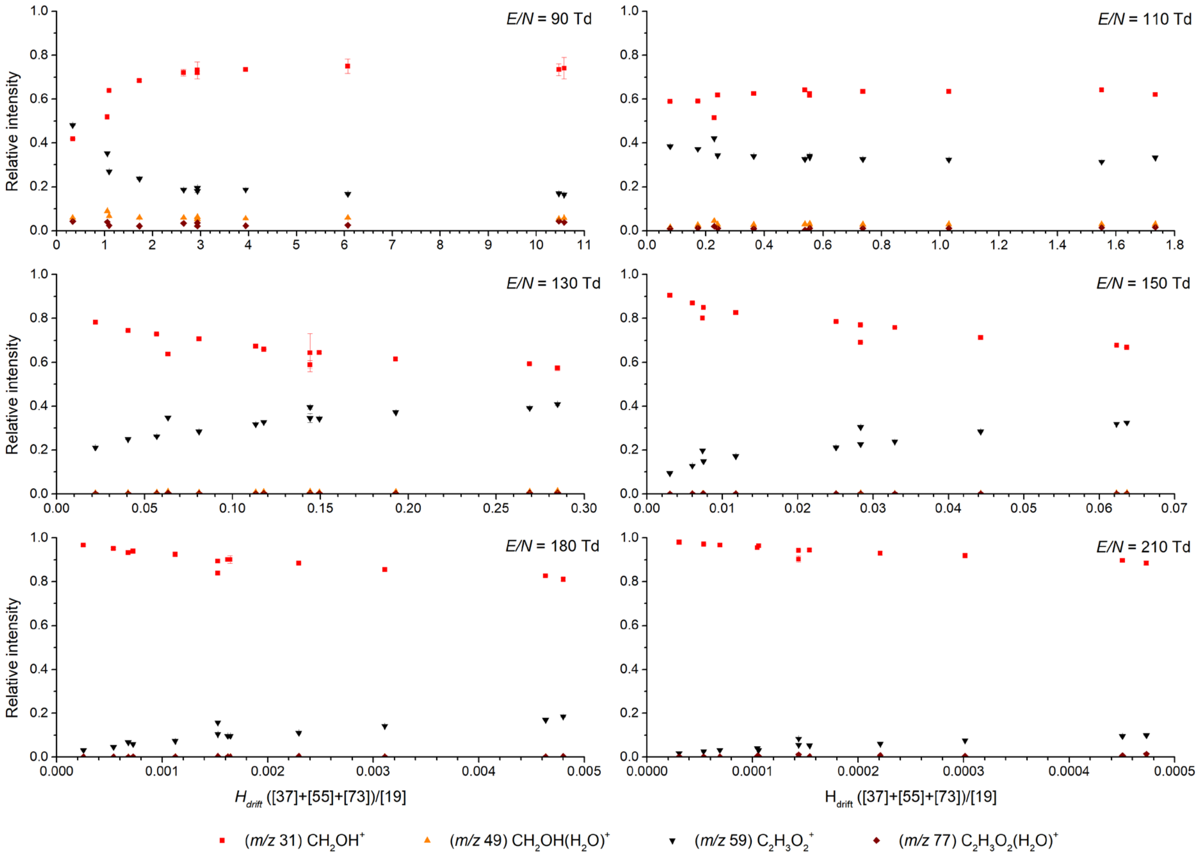

Fig. 1 Relative intensities of main ion products detected for varying water vapour concentration and constant *E/N* value. The water vapour concentration in the drift tube (the x-axis) is determined for each constant value of *E/N* as a dimensionless parameter $H^{E/N}$, described in the experimental.

In the first plot type (see Fig. 1), at constant *E/N* 90 Td, the formation of protonated formaldehyde has a positive trend. This agrees with our previous study of the same reaction system in SIFT-MS, where we concluded protonated formaldehyde to be produced in a secondary reaction of protonated formaldehyde with water molecules. [18] However, the trend converts to negative for E/N 130 Td and above. This observation corresponds with the study of Stönner et al. [19], who also observed the negative trend without explaining it. For high *E/N* 210 Td, the trend is less steep but still negative. The fundamental question is why the trend changes from positive to negative at higher *E/N*.

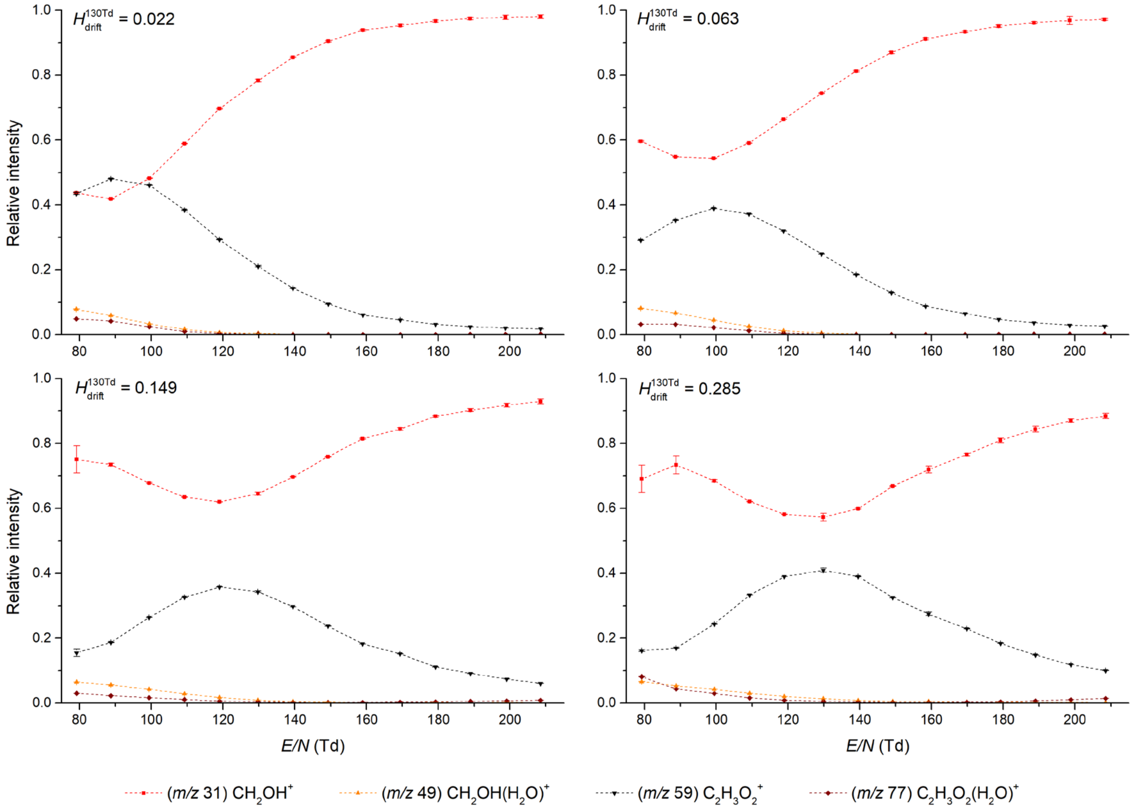

Fig. 2 Relative intensities of main ion products as a function of *E/N*, determined for four selected values of water vapour concentration. Water vapour concentration is defined by the dimensionless parameter *H*, determined at *E/N* 130 Td. Each experimental point represents a mean relative intensity determined in two measuring cycles with a total recording time of 60 s/point.

In the second plot type (see Fig. 2), we present the *E/N* profile of main product ions at four selected levels of water concentration. We can observe a gap in the protonated formaldehyde intensity (*m/z* 31), accompanied by an increased abundance of protonated glyoxal (*m/z* 59) in the form of a "hill" structure, both shifting towards higher *E/N* values as the water vapour content in the drift tube increases. This interesting pattern can be explained by two different processes forming the protonated formaldehyde in the drift tube. First, as stated above and explained by a previous SIFT-MS experiment [18], at low *E/N,* the protonated formaldehyde is mainly produced via a secondary reaction of protonated glyoxal with water vapours (Eq. 8). Thus the profile on the left side of Fig. 2 is affected by increasing water vapour concentration rapidly.

$$\mathrm{H_3O^+} + \mathrm{C_2H_2O_2} \rightarrow \mathrm{C_2H_3O_2^+} + \mathrm{H_2O} \qquad (8a)$$

$$\mathrm{C_2H_3O_2^+} + \mathrm{H_2O} + \mathrm{N_2} \rightarrow \mathrm{C_2H_3O_2^+.H_2O} + \mathrm{N_2} \qquad (8b)$$

$$\mathrm{C_2H_3O_2^+.H_2O} + \mathrm{H_2O} \rightarrow \mathrm{CH_2OH^+} + \mathrm{HCOOH} + \mathrm{H_2O} \qquad (8c)$$

An increase of the *E/N* causes the shift of the reaction equilibrium towards the higher abundance of protonated glyoxal simply by reducing the residence time, decreasing the yield of reactions 3b and 3c.

At higher *E/N*, an additional reaction channel opens, where the protonated formaldehyde is likely formed via collisional induced dissociation (CID) of glyoxal ions with a carrier gas (Eq. 9a) or via direct collision of H_3O^+ with glyoxal neutrals (Eq. 9b).

$$C_2H_3O_2^+ + N_2 \xrightarrow{CID} CH_2OH^+ + CO + N_2 \qquad (9a)$$

$$H_3O^+ + C_2H_2O_2 \xrightarrow{CID} CH_2OH^+ + HCOOH \qquad (9b)$$

The final reaction pattern in Fig. 2 is thus a combination of at least two independent reaction channels. The high-energy CID process seems not to be heavily influenced by the change in the system humidity. However, the rapid response of the low-energy secondary processes on the water concentration forces the "gap" in the final reaction profile to move towards higher *E/N*.

This simple concept, however, does not directly explain the negative trend of the protonated formaldehyde formation at higher *E/N* (see Fig. 1, 130 Td and above). The negative trend can be related to the CID process becoming less effective at higher water vapour concentrations but also to the formation of a new reaction channel induced by the presence of water vapours.

SIFDT-MS experimental study of glyoxal was also carried out to clarify the results. The SIFDT-MS experiment differs from PTR-MS as it uses helium carrier gas. Additionally, it allows us to directly determine the reaction residence time of individual reactant and product ions and thus determine the ion mobility and centre-of-mass reaction energy of involved particles. Note that we used two variations of the SIFDT experiment in the study, as described in the experimental.

First, the ion chemistry study was carried out to compare the effect of helium carrier gas on ion product distribution. The study was also supplemented by varying the system humidity. Note that the *E/N* values used in the SIFDT study (up to 80 Td) are lower compared to the PTR study (up to 210 Td), and the centre-of-mass reaction energy of particles is in a similar range (due to the higher ion mobility of ions in He compare to air) and thus the comparison is reasonable. Aside from the detection of ion product abundance, we also recorded the residence reaction time of primary hydronium reagent ions. The related results are shown in Supplement (Fig. S3-S7). Results agree with the PTR-MS profile, including all the effects stressed above for PTR-MS: strong influence of water vapour concentration on ion chemistry at low *E/N* values, increase of protonated glyoxal abundance for increasing *E/N* as well as the presence of the additional reaction channel forming protonated formaldehyde at higher *E/N*.

Alternatively, we also prepared an experiment where the glyoxal headspace was injected into a bag filled with synthetic air and sampled afterwards. This was done to execute experiments in the He/air mixture where the effect of air neutrals on ion chemistry, bridging between He and air carrier gas, can be studied (see Fig. S8 and S9 in Supplement). Here, the ion product distribution again agrees with previous observations.

Effect of water vapour concentration on reaction equilibrium

To furthermore investigate the effect of increasing water concentration on glyoxal ion chemistry, we independently studied the ion chemistry of main product ions; protonated glyoxal and protonated formaldehyde. This was achieved by introducing the glyoxal headspace into the modified ion source of the SIFDT experiment (see the experimental for details), where protonated formaldehyde and protonated glyoxal were formed. Ions were then selectively introduced into the drift tube via the mass filter. The study was carried out by recording the mass spectra for dry and humidified He carrier gas in the drift tube at three different *E/N* settings.

Choosing protonated glyoxal as the reagent ion while using dry He with $[H_2O] < 1x10^{13}$ cm^{-3}, we observe the expected formation of related product ions (see Fig. 3). At low *E/N* 15.5 Td, the protonated glyoxal is dominant, while a small amount of protonated glyoxal and related hydrides are also formed due to residual water in the system. Increasing the *E/N* to 48 Td results in an increased formation of protonated formaldehyde, as also expected for the CID process in PTR-MS (Eq. 4a):

$$\mathrm{C_2H_3O_2^+ + He \xrightarrow{CID} CH_2OH^+ + CO + He} \tag{10}$$

The water vapour concentration above 6x10^{13} cm^{-3} results in changed ion product distribution. At low *E/N* 14.8 Td, we can observe the expected elevated formation of protonated formaldehyde while the abundance of protonated glyoxal is negligible. Also, a strong pattern of hydronium hydrides $H_3O^+(H_2O)_n$ can also be observed, with $H_3O^+.H_2O$ being dominant. The presence of hydronium hydrides at low *E/N* is not surprising, as its production was also proposed in the previous SIFT-MS study [18].

The reaction sequence forming protonated formaldehyde, as observed in the previous SIFT-MS study, requires the formation of protonated glyoxal hydride, which later reacts with an additional water molecule, forming protonated formaldehyde and acetic acid (similar to Eq. 8). Eq. 8c can eventually proceed in an alternative way and generate hydronium hydride:

$$\mathrm{C_2H_3O_2^+.H_2O + H_2O \rightarrow H_3O^+.H_2O\ + C_2H_2O_2.} \tag{11}$$

Additionally, protonated formaldehyde at a high concentration of water vapours forms protonated formaldehyde hydride, $H_2COH^+.H_2O$. In the following reaction, protonated formaldehyde hydride reacts with an additional water molecule, forming hydronium hydride and neutral formaldehyde:

$$\mathrm{H_2COH^+\ +\ H_2O + He \rightarrow H_2COH^+.H_2O +\ He} \tag{12a}$$

$$\mathrm{H_2COH^+.H_2O\ +\ H_2O \leftrightarrow H_3O^+.H_2O +\ H_2CO} \tag{12b}$$

At present conditions, reaction (12b) has higher reaction rate towards formation of protonated formaldehyde hydride (k_{9b} = 3x10^{-9} cm^{3}s^{-1}) than towards formation of hydronium hydride (k_{-9b} = 4x10^{-10} cm^{3}s^{-1}). However, the high number density of H_2O molecules favours the formation of hydronium hydride even though the process is slightly endothermic [18].

The observed profile of remaining hydronium hydrides in the mass spectrum (*m/z* 55, 73) results from secondary association reactions between $H_3O^+.H_2O$ and water vapours. Increasing the *E/N* to 46 Td led to an increased abundance of protonated glyoxal due to reduced reaction time. Additionally, the hydronium hydride pattern changes as the increased collision energy of hydronium hydrides do not allow the stable population of higher hydronium hydrides. Consequently, increased formation of hydronium is also observed. At *E/N* 77 Td, as expected, CID-generated protonated formaldehyde dominates over protonated glyoxal. However, we also observed a significant amount of hydronium. Hydronium at such high *E/N* cannot result from a previously suggested series of secondary reactions because complex hydronium clusters leading to the formation of hydronium hydride (Eq. 11, 12b) cannot be formed or live long enough to undergo a reaction with a significant reaction rate. Thus, observed hydronium must be produced by reverse proton transfer reaction from protonated glyoxal back to hydronium.

Similarly, we studied the ion chemistry of protonated formaldehyde (see Fig. 4). For dry He and all values of E/N (15.5 Td, 48 Td and 80 Td) we observed only the presence of injected protonated formaldehyde. Elevating the water vapour concentration up to 6x10^{13} cm^{-3} for low *E/N* 14.8 Td resulted in the presence of hydronium hydrides. However, note that the abundance of hydronium hydrides is much smaller relative to the protonated formaldehyde compared to the previous study involving protonated glyoxal. It is then clear that the hydronium hydrides observed in the protonated glyoxal study were formed not mainly by secondary reactions involving protonated formaldehyde (reaction 12b) but rather by secondary reaction of protonated glyoxal hydrides (reaction 11). An additional increase of *E/N* to 46 Td reduces the amount of formed ion hydrides while elevating the formation of hydronium. Further increase of *E/N* to 77 Td also results in rapid formation of hydronium.

The formation of hydronium ions at high *E/N* is an important element in the reaction scheme that was not detected in previous studies due to interference with hydronium reagent ions. The formation of hydronium can be simply rationalised. The PA`s of water, glyoxal as well as formaldehyde are close values (PA (H_2O) = 165.15 kJ/mol, PA(CH_2O) = 170.4 kcal/mol, PA($C_2H_2O_2$) = 165.06 kcal/mol) [13, 34]. Even though we expect the proton transfer from hydronium to glyoxal or formaldehyde to be an exoergic process, however, the reverse reaction is also possible:

$$\mathrm{H_3O^+ + C_2H_2O_2 \leftrightarrow C_2H_3O_2^+ + H_2O} \qquad (13a)$$

$$\mathrm{H_3O^+ + H_2CO \leftrightarrow H_2COH^+ + H_2O} \qquad (13b)$$

At low *E/N* and thus low reaction energies, or in the flow tubes, the reaction equilibrium is towards the formation of protonated glyoxal or formaldehyde, even at elevated number densities of water vapours. This is demonstrated by the small abundance of hydronium in mass spectra recorded for low *E/N* and elevated humidity (Fig. 3 and 4). For higher *E/N*, reaction energy between protonated glyoxal or formaldehyde and neutral water molecules increases, and thus, combined with the high number density of water molecules, hydronium can be formed more rapidly.

If we consider that the reverse reaction 13b proceeds faster than the reaction 13a, we can find a reason for the negative profile of protonated formaldehyde observed in the previous study. Increasing water concentration then reduces the abundance of protonated formaldehyde faster relative to the abundance of protonated glyoxal.

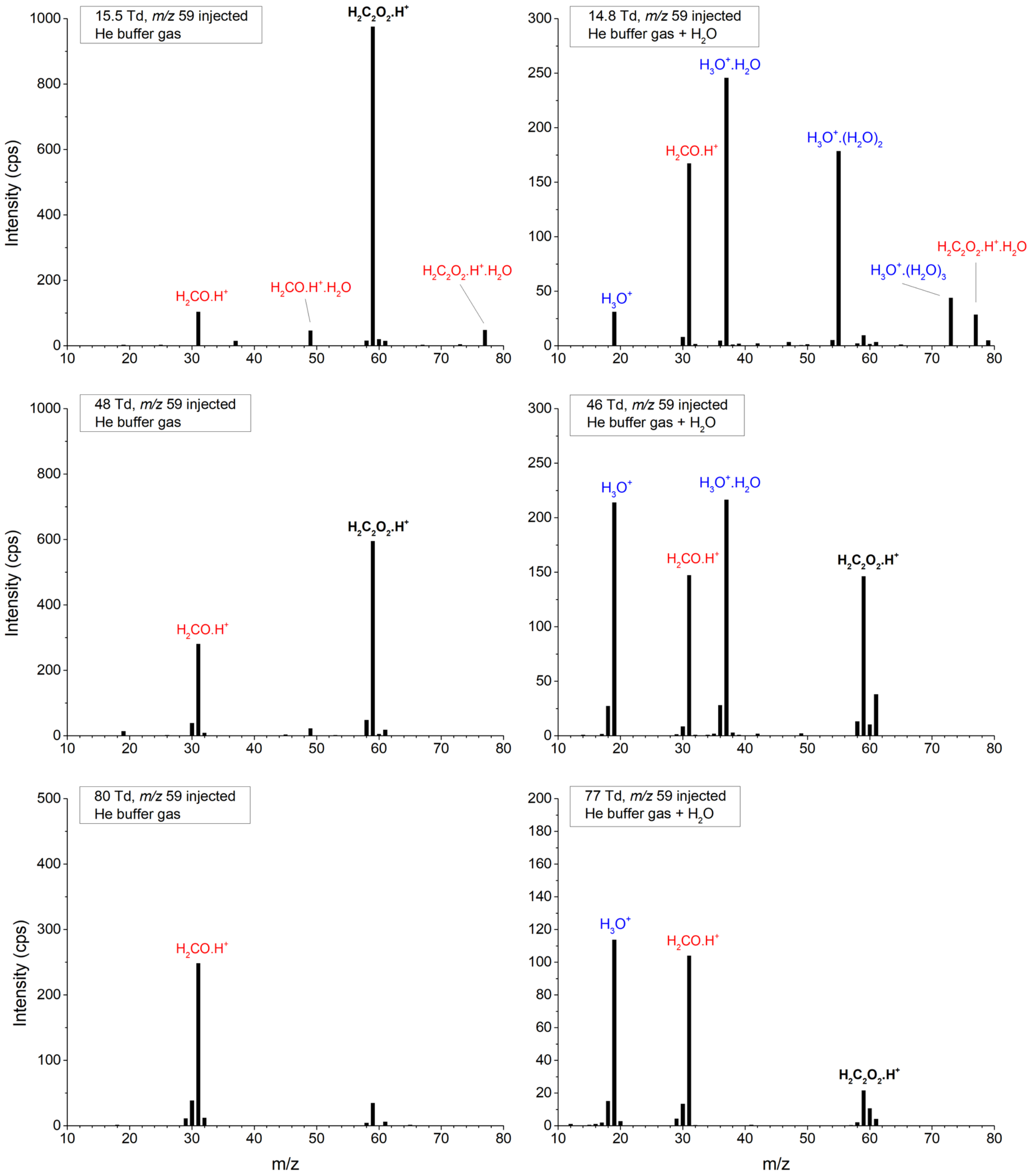

Fig 3: Recorded mass spectra for injection of protonated glyoxal, *m/z* 59, into the drift tube. On the left side, protonated glyoxal was injected into dry He buffer gas. On the right side, He buffer gas also contained water vapours at a concentration of about $[H_2O] = 6 \times 10^{13}$ cm^{-3}.

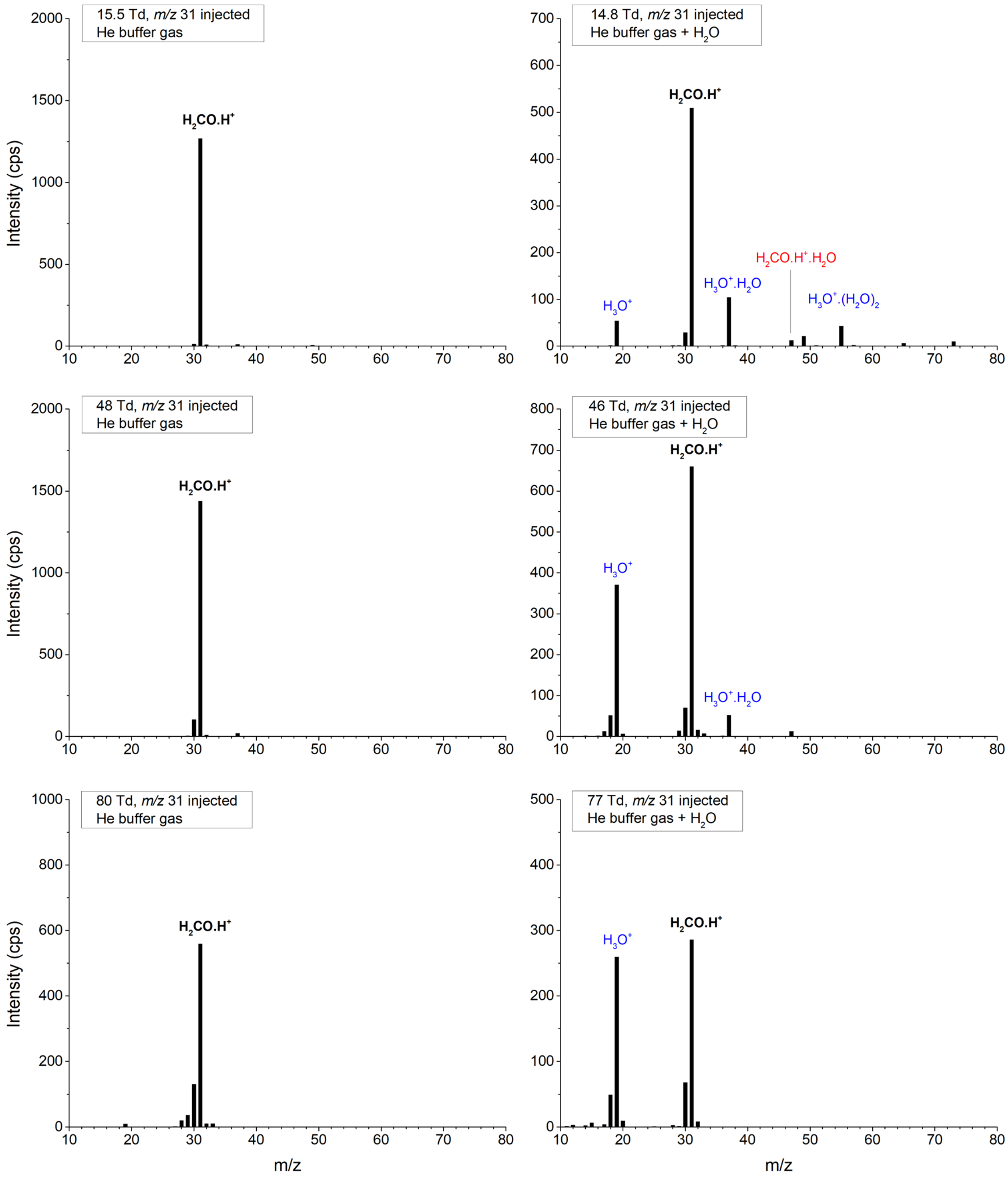

Fig 4: Recorded mass spectra for injection of protonated formaldehyde, *m/z* 31, into the drift tube. On the left side, protonated glyoxal was injected into dry He buffer gas. On the right side, He buffer gas also contained water vapours at a concentration of about [H_2O] = 6 x 10^{13} cm^{-3}.

Ion mobility and reaction energy of ions

Using SIFDT, we determined retention times of hydronium reagent ions for the full range of *E/N* values and dry and humidified He carrier gas $[H_2O] = 6.4x10^{13}$ cm^{-3}. For protonated glyoxal and protonated formaldehyde, we obtained retention times in the range of *E/N* between 10 to 50 Td for dry He and a limited amount of measurements for humidified He. Retention times of protonated formaldehyde and protonated glyoxal hydrides were also obtained only for a limited amount of *E/N* values and only for dry He. The calculated reduced ion mobility values (see Eq. 5) are presented in Supplement (Fig. S10, S11). We observed a decrease of reduced ion mobility for hydronium and protonated glyoxal as system humidity increased. We may expect similar for the remaining ions; however, we did not obtain enough data to confirm.

Additionally, we determined ion collisional reaction energies between ions and individual neutrals using Eq. 4. The reaction energy profiles for the most significant reactions are presented in Fig. 5 (remaining energy profiles can be found in Supplement in Fig S4, S7, S9, S12). First, we can compare individual CID channels proposed in Eq. 10 and Eq. 9b. The reaction energy for direct dissociative proton transfer (Eq. 9b) is higher compared to the CID of protonated glyoxal on helium atoms (Eq. 10). At *E/N* 30 Td, the reaction energy of protonated glyoxal colliding with He is 0.07 eV (0.3 eV for dissociative proton transfer) and at 56 Td is 0.1 eV (0.67 eV for dissociative proton transfer). CID process requires excessive migration of one hydrogen from one C(H)O group to another. Atomic composition of hydronium may assist in rearranging products during direct dissociative proton transfer. CID process was observed to contribute to protonated formaldehyde production. However, we may expect dissociative proton transfer to be significant for the overall reaction process. We may also consider protonated formaldehyde forming via CID of protonated glyoxal on water molecules. This process provides more collisional energy as collisions with He and the atomic composition of water molecules can also assist the rearmament during the reaction. However, the active contribution of this reaction channel would result in increased formation of protonated formaldehyde with an increased concentration of water vapours in the reactor, which is opposite to our experimental observations.

Finally, we discuss the energetics of the reverse proton transfer reactions (Eq. 13), supplementing the CID process at higher *E/N*. Considering available theoretical calculations of *PA*, the *PA* difference between formaldehyde and water is 5.4 kJ/mol (0.23 eV), while for the glyoxal and water, the difference is close to zero. [34] The change in entropy for proton transfer reaction is small thus and can be neglected. At *E/N* 48 Td is the reaction energy of protonated formaldehyde colliding with water molecule 0.28 eV, already exceeding the energy difference necessary for the reverse reaction to occur (see Fig. 5). For protonated glyoxal, the reverse reaction channel is due to the small difference in PA already open. Thus, the reaction rate for reverse reaction (reverse reaction in Eq. 13a) shall be larger than for reaction (reverse reaction in Eq. 13b). However, the reaction energy of protonated formaldehyde quickly increases with *E/N*, and thus the actual reaction rate of reverse proton transfer reaction from protonated formaldehyde can be higher than for protonated glyoxal. In such a situation, protonated glyoxal would be reacting into hydronium faster than protonated glyoxal, and thus with an increasing concentration of water vapours, the abundance of protonated formaldehyde relative to protonated glyoxal would decrease, as observed in the experiment.

The observed decrease of hydronium mobility for elevated humidity of the system can influence proposed reactions, mainly by reducing reaction energy for dissociative proton transfer (Eq. 9b). The decrease of reaction energy caused by mobility reduction is (see Supplement, Fig. S11 and S12), however, relatively small and thus is difficult to estimate if the reduction of protonated formaldehyde abundance is due to reduced hydronium reactivity or reverse proton transfer.

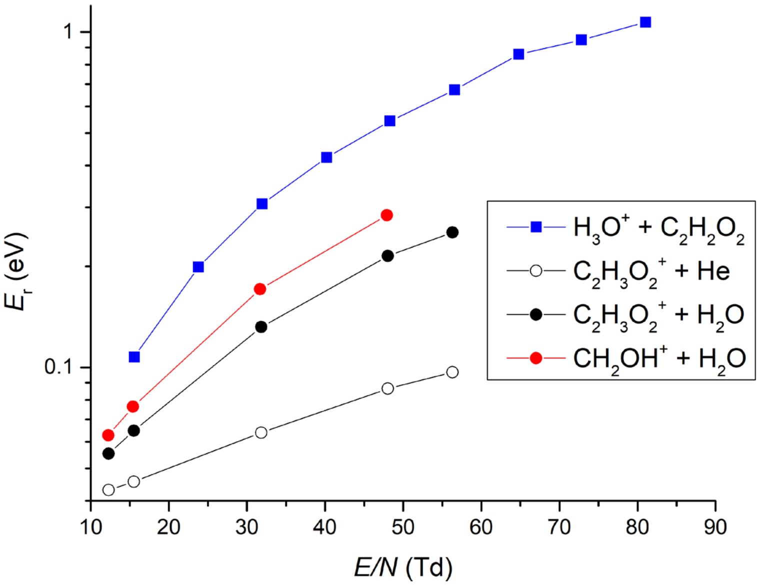

Fig. 5 Center-of-mass reaction energies of selected ions with selected reactant neutrals obtained in SIFDT-MS in dry He buffer gas. The figure stresses the difference between the two possible CID channels: reaction of H_3O^+ with $C_2H_2O_2$ (blue squares, Eq. 9b) and $C_2H_3O_2^+$ with He (open circles, Eq. 10). Also, the difference between protonated glyoxal (black circles, reverse reaction in Eq. 13a) and protonated formaldehyde (red circles, reverse reaction in Eq. 13b) colliding with water molecules during reverse proton transfer reaction.

Simulation of the ion chemistry

Considering proposed reactions, we numerically simulated the ion chemistry in the SIFDT geometry. The simulation aims not to interpolate observed experimental data fully but to reconstruct observed trends and determine the influence of the individual reaction channels on the formation of protonated formaldehyde at various humidity levels. To build up the complete reaction schema, we first reconstructed the data observed for individual injection of protonated formaldehyde and protonated glyoxal into the SIFDT (see Supplement, Simulation 1-3) after we adjusted the remaining reaction channels to reflect the reaction profile observed for the reaction of hydronium with glyoxal (see Supplement, Simulation 4).

Several assumptions were made to build up the reaction schema. The reaction rate of proton transfer from hydronium to glyoxal was constant, k = 1.33x10^{-9} cm^3s^{-1}. Rate constants for all association reactions follow the power-law function $k(E/N) = A/E_r^{-n}$, where A and n were free parameters. Secondary reactions of hydrated clusters were constant. The remaining reaction rates were modeled based on the Arrhenius form k(E/N) = A x exp(-Ea/Er), where A and E_a were free parameters. As initial values for constant reaction rates, we used rates obtained previously in SIFT-MS. [18] For reaction rates following power law, we also applied A based on previous SIFT-MS measurements [18] assuming $k_{SIFT}(T = 297\text{ K}) = k_{SIFDT}(E_r = 0.04\text{ eV})$. Exponent was then adjusted based on the experiment. For reaction rates following the Arrhenius form, A was selected based on the theoretical prediction of the trajectory calculation model of Su [35, 36] and E_a was either taken from previous theoretical calculation [18] or selected based on experimental data. Reaction parameters were first optimised to reflect data observed for injection of protonated formaldehyde (Fig. 4, for simulation, see Fig. S13 in Supplement), followed by optimisation to reflect data observed for injection of protonated glyoxal (Fig. 3, for simulation, see Fig. S14, S15 in Supplement). Finally, we adjusted the remaining reaction to reflect the full reaction pattern of hydronium – glyoxal ion chemistry in He carrier gas (see Supplement, Fig. S3, S5, S6 and S16 for simulation). The full list of reactions, reaction rates and remaining details used for simulation is also presented in the Supplement. The simplified visualisation of simulated ion chemistry is presented in Fig. 6.

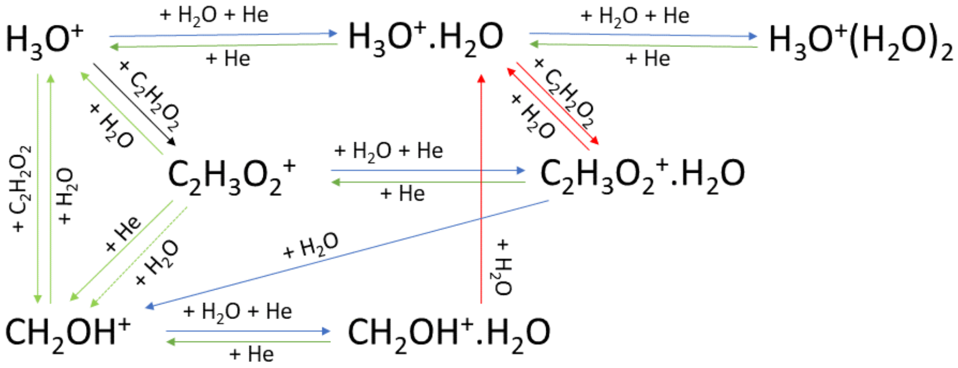

Fig. 6 Simplified visualisation of a simulated reaction sequence for hydronium reaction with glyoxal. The colour of the reaction arrow represents the type of reaction rate used to simulate ion chemistry: black for initial reaction, green for *k*(*E*/*N*) following Arrhenius form, blue for *k*(*E*/*N*) following a power law, red for *k*(*E*/*N*) being constant. The molecules close to the arrows represent reactant neutrals.

In the reaction schema, we expect the protonated formaldehyde to be formed via three possible CID channels: Eq, 9b, Eq. 10 and also via reaction

$$C_2H_3O_2^+ + H_2O \rightarrow CH_2OH^+ + HCOOH. \tag{14}$$

Reaction 14 was not considered yet as it induces the formation of protonated formaldehyde for increasing humidity. However, reaction 14 helps explain the high abundance of protonated formaldehyde observed in Fig. 4 at high humidity (see Simulation 3 in Supplement).

The proposed set of reactions follows the relative ion intensities observed in the experiment (see Simulation 4 in Supplement). Specifically, the model explains the humidity-induced formation of protonated formaldehyde at low *E/N*, increase of protonated glyoxal relative intensity forming "hill" structure for increasing *E/N*, formation of hydronium clusters as well as production of protonated formaldehyde by CID at high *E/N*. The simulation also shows decreasing relative abundance of protonated formaldehyde for elevated humidity. This effect can be achieved as long as reaction 14 is not present, even without decreasing hydronium mobility. Reducing hydronium mobility further increases the negative trend. The effect of reduced ion mobility is, however, smaller than that of reveres proton transfer reactions.

The formation of protonated formaldehyde at high *E/N* was studied further by increasing reaction rates for individual CID and reverse proton transfer reactions. (see Simulation 5 in Supplement) An increase in reaction rates affects reaction equilibrium. However, the location and intensity of the negative trend are mainly defined by the ratio between individual reverse proton transfer reactions (Eq. 13a, 13b). In all simulations, the negative trend increases with increasing *E/N*. In the PTR-MS experiment, we observed the negative trend to be the most significant at *E/N* 130 Td and progressively less effective as *E/N* increases even more. The only reaction channel that may cause such an effect is the reaction in Eq. 14 (see Simulation 6 in Supplement). Therefore, we may assume the reaction in Eq. 14 contributes to the formation of protonated formaldehyde. However, its reaction barrier is energetically above the remaining CID reaction channels, and thus the negative trend in protonated formaldehyde formation is present only in the specific *E/N* region.

Conclusion

We studied the homogenous electric field and humidity effects on hydronium's reaction with neutral glyoxal. The study was carried out using two experiments, PTR-MS and SIFDT-MS, using N_2 and He buffer gas, respectively. The experimental study was supplemented by a numerical simulation of the proposed ion chemistry. Individual results confirmed complex ion chemistry patterns induced by the presence of a homogenous electric field and humidity. At low *E/N*, where reaction energies are close to thermal energy, sample humidity induces a series of secondary reactions between protonated glyoxal and water molecules, forming protonated formaldehyde. An increase of *E/N* reduces the effectivity of secondary reactions (leading to a lower abundance of protonated formaldehyde) and increases the effectiveness of reverse proton transfer reactions. At high *E/N*, protonated formaldehyde is formed via CID, even in a dry buffer gas. However, the presence of humidity can reduce the effectiveness of CID via reduction of ion mobility of reagent ions and secondary reverse proton transfer reactions forming hydronium.

The humidity-induced reduction of CID yield is localised only within a specific range of *E/N*, as long as the reaction of protonated glyoxal with water $C_2H_3O_2^+ + H_2O$ leads to the formation of hydronium. With increasing *E/N,* this reaction may overcome an energy barrier and switch into the formation of protonated formaldehyde and neutral acetic acid, removing the presence negative trend.

This interesting behaviour is possible because PA of all involved molecules, water, glyoxal and formaldehyde, is relatively close and because protonated glyoxal undergoes secondary reactions with water. In common proton transfer reactions occurring in PTR-MS, or other SCIMS instruments, where the gap between PA of water and analyte is more significant and protonated product is less reactive such patterns will not be observed. However, the present work demonstrates that proton transfer reactions may not always be straightforward and that chemical ionisation should be understood before its use for analytical applications.

Acknowledgement

This project has received funding from the European Union's Horizon 2020 research and innovation programme under the Marie Skłodowska-Curie grant agreement No 674911.

References

1. Jang, M. and R.M. Kamens, *Characterisation of Secondary Aerosol from the Photooxidation of Toluene in the Presence of NOx and 1-Propene.* Environmental Science & Technology, 2001. **35**(18): p. 3626-3639.
2. Tuazon, E.C., et al., *Yields of glyoxal and methylglyoxal from the nitrogen oxide (NOx)-air photo-oxidations of toluene and m-and p-xylene.* Environmental science & technology, 1984. **18**(12): p. 981-984.
3. Yu, J., H.E. Jeffries, and K.G. Sexton, *Atmospheric photo-oxidation of alkylbenzenes—I. Carbonyl product analyses.* Atmospheric Environment, 1997. **31**(15): p. 2261-2280.
4. Smith, D., T. Kleindienst, and C. McIver, *Primary product distributions from the reaction of OH with m-, p-xylene, 1, 2, 4-and 1, 3, 5-trimethylbenzene.* Journal of Atmospheric Chemistry, 1999. **34**(3): p. 339-364.

5. Yu, J., H.E. Jeffries, and R.M. Le Lacheur, *Identifying airborne carbonyl compounds in isoprene atmospheric photo-oxidation products by their PFBHA oximes using gas chromatography/ion trap mass spectrometry.* Environmental science & technology, 1995. **29**(8): p. 1923-1932.
6. Fick, J., et al., *Effect of OH radicals, relative humidity, and time on the composition of the products formed in the ozonolysis of α-pinene.* Atmospheric Environment, 2003. **37**(29): p. 4087-4096.
7. Akimoto, H., *Fundamental heterogeneous reaction chemistry related to secondary organic aerosols (SOA) in the atmosphere.* Monographs on Environment, Earth and Planets, 2016. **4**: p. 1-45.
8. Manini, P. and M. d'Ischia, *Aldehydes As Markers of Redox Imbalance in Fanconi Anemia and in Other Oxidative Stress-Related Disorders.* FANCONI ANEMIA AND OXIDATIVE STRESS: p. 69.
9. Shangari, N., et al., *Toxicity of glyoxals - role of oxidative stress, metabolic detoxification and thiamine deficiency.* Biochemical Society Transactions, 2003. **31**(6): p. 1390-1393.
10. Shkrob, I.A., et al., *Photoredox reactions and the catalytic cycle for carbon dioxide fixation and methanogenesis on metal oxides.* The Journal of Physical Chemistry C, 2012. **116**(17): p. 9450-9460.
11. Mattioda, G. and A. Blanc, *Glyoxal*, in *Ullmann's Encyclopedia of Industrial Chemistry*. 2000.
12. Hazra, M.K., J.S. Francisco, and A. Sinha, *Hydrolysis of glyoxal in water-restricted environments: formation of organic aerosol precursors through formic acid catalysis.* The Journal of Physical Chemistry A, 2014. **118**(23): p. 4095-4105.
13. Wroblewski, T., et al., *Ab initio and density functional theory calculations of proton affinities for volatile organic compounds.* European Physical Journal-Special Topics, 2007. **144**: p. 191-195.
14. Hunter, E.P.L. and S.G. Lias, *Evaluated Gas Phase Basicities and Proton Affinities of Molecules: An Update.* Journal of Physical and Chemical Reference Data, 1998. **27**(3): p. 413-656.
15. Zhao, J. and R. Zhang, *Proton transfer reaction rate constants between hydronium ion (H 3 O+) and volatile organic compounds.* Atmospheric Environment, 2004. **38**: p. 2177-2185.
16. Michel, E., et al., *A selected ion flow tube study of the reactions of H 3 O+, NO+ and O 2+ with methyl vinyl ketone and some atmospherically important aldehydes.* International Journal of Mass Spectrometry, 2005. **244**: p. 50-59.
17. Guimbaud, C., et al., *Kinetics of the reactions of acetone and glyoxal with O-2(+) and NO+ ions and application to the detection of oxygenated volatile organic compounds in the atmosphere by chemical ionisation mass spectrometry.* International Journal of Mass Spectrometry, 2007. **263**(2-3): p. 276-288.
18. Lacko, M., et al., *Chemical ionisation of glyoxal and formaldehyde with H_3O^+ ions using SIFT-MS under variable system humidity.* Phys. Chem. Chem. Phys., 2020.
19. Stönner, C., et al., *Glyoxal measurement with a proton transfer reaction time of flight mass spectrometer (PTR-TOF-MS): characterisation and calibration.* Journal of Mass Spectrometry, 2017. **52**(1): p. 30-35.
20. Volkamer, R., et al., *High-resolution absorption cross-section of glyoxal in the UV-vis and IR spectral ranges.* Journal of Photochemistry and Photobiology a-Chemistry, 2005. **172**(1): p. 35-46.
21. Lewis, R.A. and G.G. Hawley, *Hawley's condensed chemical dictionary*. 2016: John Wiley & Sons.
22. Lide, D.R. and G.W.A. Milne, *CRC handbook of data on organic compounds*. 1993: CRC Press.
23. Jordan, A., et al., *An online ultra-high sensitivity Proton-transfer-reaction mass-spectrometer combined with switchable reagent ion capability (PTR+SRI−MS).* International Journal of Mass Spectrometry, 2009. **286**(1): p. 32-38.
24. Graus, M., M. Müller, and A. Hansel, *High resolution PTR-TOF: quantification and formula confirmation of VOC in real time.* Journal of the American Society for Mass Spectrometry, 2011. **21**(6): p. 1037-1044.
25. Fischer, L., et al. *The LCU: versatile trace gas calibration*. in *CONFERENCE SERIES*. 2013.

26. Smith, D. and P. Španěl, *Selected ion flow tube mass spectrometry (SIFT-MS) for on-line trace gas analysis.* Mass spectrometry reviews, 2005. **24**(5): p. 661-700.
27. Spesyvyi, A., D. Smith, and P. Španěl, *Selected ion flow-drift tube mass spectrometry: quantification of volatile compounds in air and breath.* Analytical chemistry, 2015. **87**(24): p. 12151-12160.
28. Spesyvyi, A., et al., *Ligand Switching Ion Chemistry: An SIFDT Case Study of the Primary and Secondary Reactions of Protonated Acetic Acid Hydrates with Acetone.* Journal of the American Society for Mass Spectrometry, 2021. **32**(8): p. 2251-2260.
29. Wannier, G.H., *Motion of gaseous ions in strong electric fields.* The Bell System Technical Journal, 1953. **32**(1): p. 170-254.
30. Lacko, M., *Kinetic of Ion Molecular Ineraction Simulator (KIMI Sim)*. 2021: https://github.com/Progllar/KIMI-Simulator.
31. Kutta, W., *Beitrag zur näherungweisen Integration totaler Differentialgleichungen.* Z. Math. Phys., 1901. **46**: p. 435.
32. Runge, C., *Über die numerische Auflösung von Differentialgleichungen.* Mathematische Annalen, 1895. **46**(2): p. 167-178.
33. Dryahina, K. and P. Španěl, *A convenient method for calculation of ionic diffusion coefficients for accurate selected ion flow tube mass spectrometry, SIFT-MS.* International Journal of Mass Spectrometry, 2005. **244**(2-3): p. 148-154.
34. NIST. *NIST WebBook Chemie, NIST Standard Reference Database Number 69*. Available from: http://webbook.nist.gov/chemistry/.
35. Su, T. and W.J. Chesnavich, *Parametrisation of the ion–polar molecule collision rate constant by trajectory calculations.* The Journal of Chemical Physics, 1982. **76**(10): p. 5183-5185.
36. Su, T., *Parametrisation of kinetic energy dependences of ion–polar molecule collision rate constants by trajectory calculations.* The Journal of chemical physics, 1994. **100**(6): p. 4703-4703.

Supplement of: SIFT-MS and PTR-MS studies of H_3O^+ reaction with glyoxal in presence of water molecules forming protonated formaldehyde at different interaction energies

Michal Lacko[1,2], Patrik Španěl[1], Chris Mayhew[3], Michaela Malásková[3], Anatoli Spesyvyi[1]

[1] J. Heyrovsky Institute of Physical Chemistry of the CAS, v. v. i, Dolejškova 2155/3, 182 23 Prague 8, Czech Republic

[2] Charles University Prague, Faculty of Mathematics and Physics, Prague, Czech Republic.

[3] Institute for Breath Research, Fakultät für Chemie und Pharmazie, Leopold-Franzens-Universität Innsbruck, Dornbirn, Austria

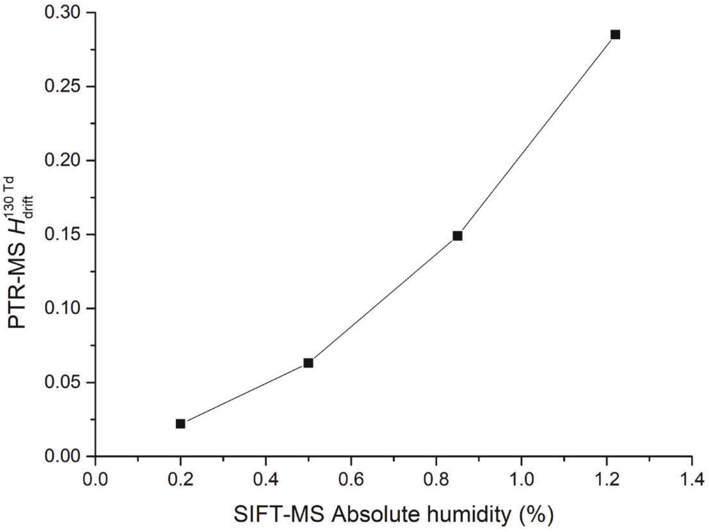

Fig S1: Correlation between absolute humidity of the glyoxal sample, determined by SIFT-MS , and humidity parameter *H* obtained from the distribution of hydronium water clusters in PTR-MS at *E/N* 130 Td.

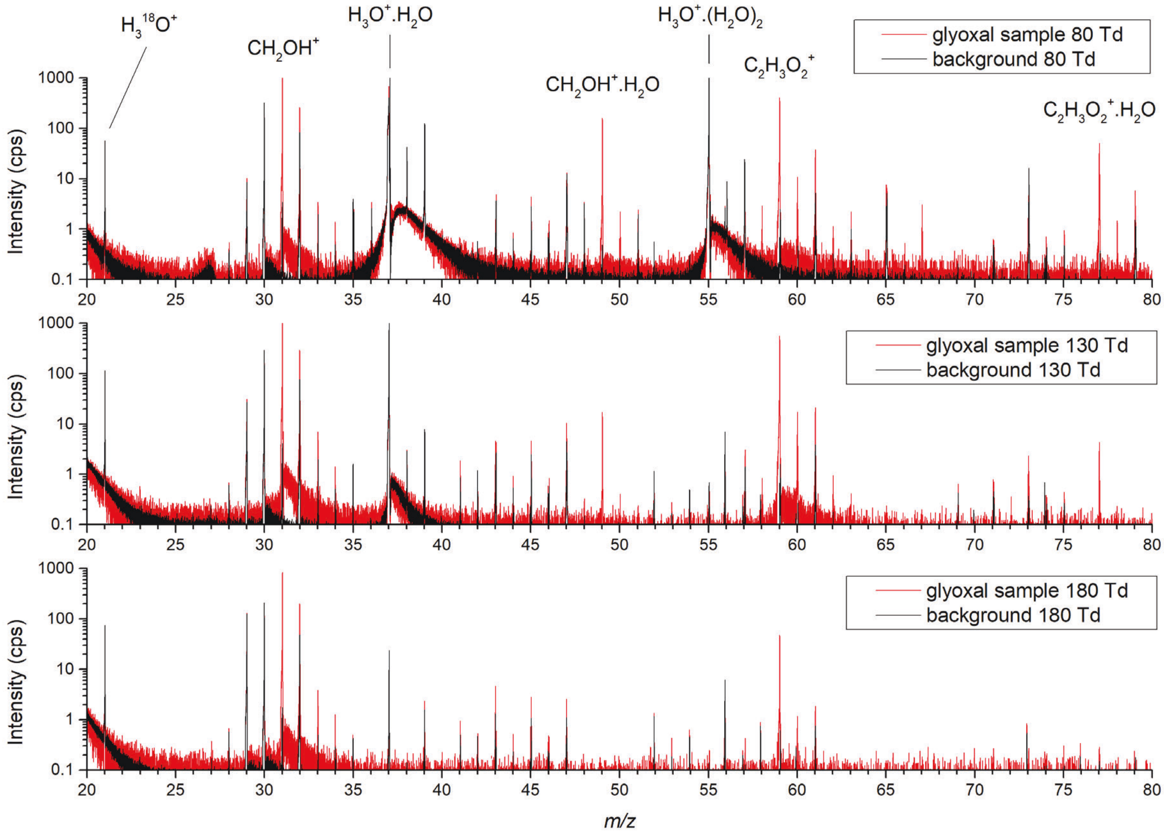

Fig S2: Mass spectra of dry glyoxal sample obtained for three different *E/N*.

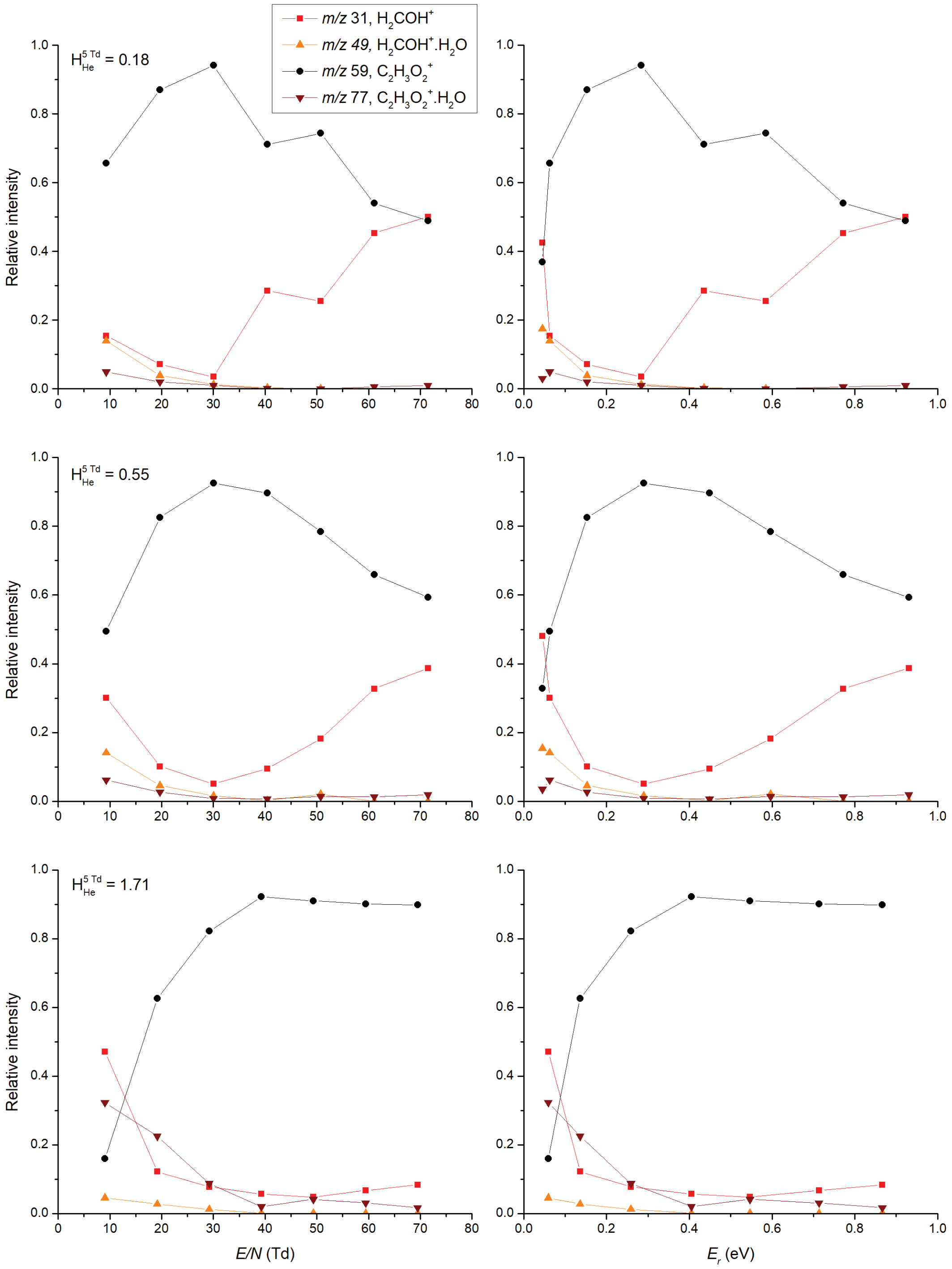

Fig S3: Relative intensities of glyoxal ion products obtained for different system humidity in He carrier gas using first SIFDT-MS experimental concept. The values on the left side are shown as a function of *E/N*. Data on the right side are shown as a function of reaction energy between H_3O^+ ion and neutral glyoxal molecule (Eq. 4).

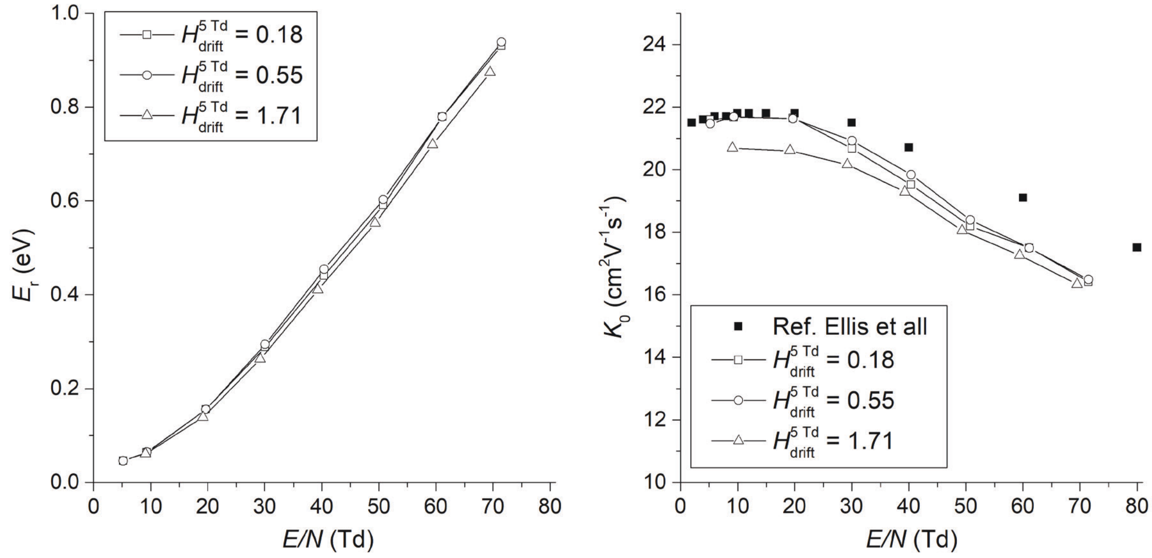

Fig S4: Reaction energy and ion mobility of H_3O^+ ions determined for different system humidity using first SIFDT-MS experimental concept. The reaction energy is determined between H_3O^+ ion and glyoxal neutrals (Eq. 4). The ion mobility is calculated using Eq. 5. The ion mobility data are compared with data obtained by Ellis et all [1].

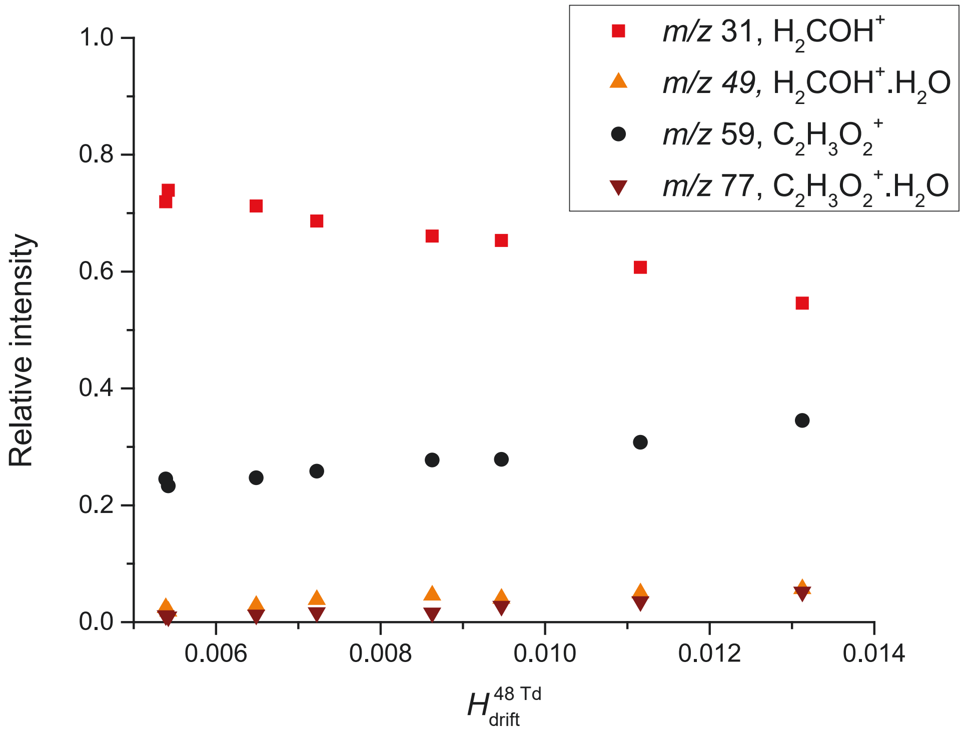

Fig S5: Relative intensities of glyoxal ion products determined at variable system humidity at constant *E/N* 48 Td in He using first SIFDT-MS experimental concept. The data show decrease production of protonated formaldehyde for increasing system humidity.

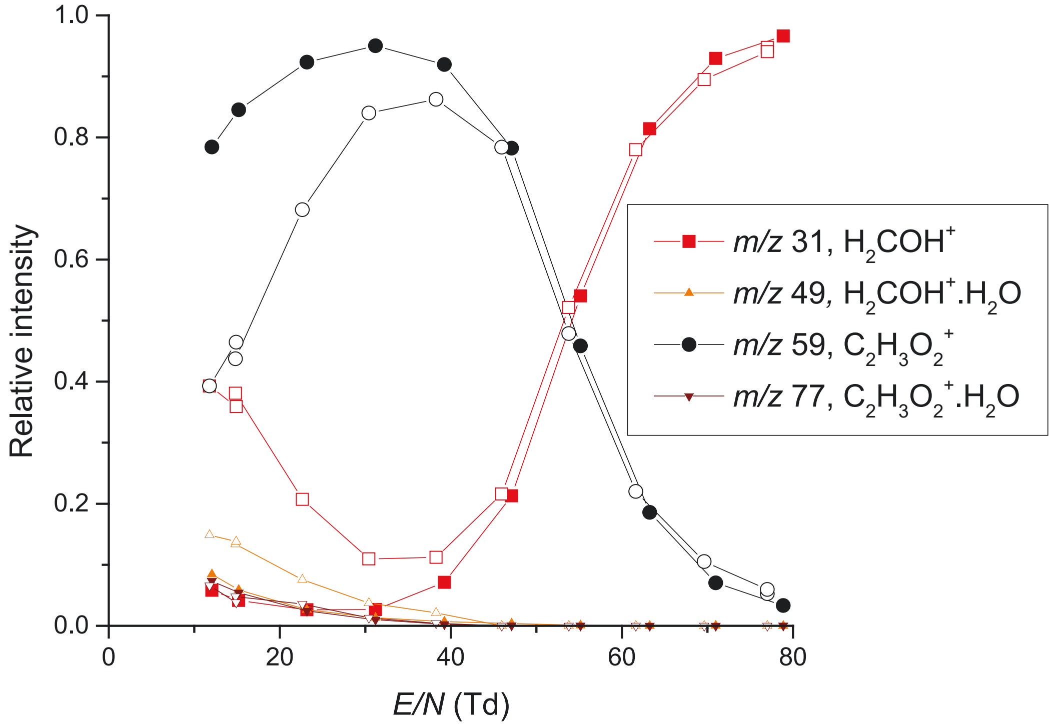

Fig S6: Relative intensities of glyoxal ion products obtained for different system humidity in He carrier gas using second SIFDT-MS experimental concept. Solid symbols represent the data obtained for pure He carrier gas. Open symbols represent He carrier gas with water concentration [H_2O] = 4.5×10^{13} cm^{-3}.

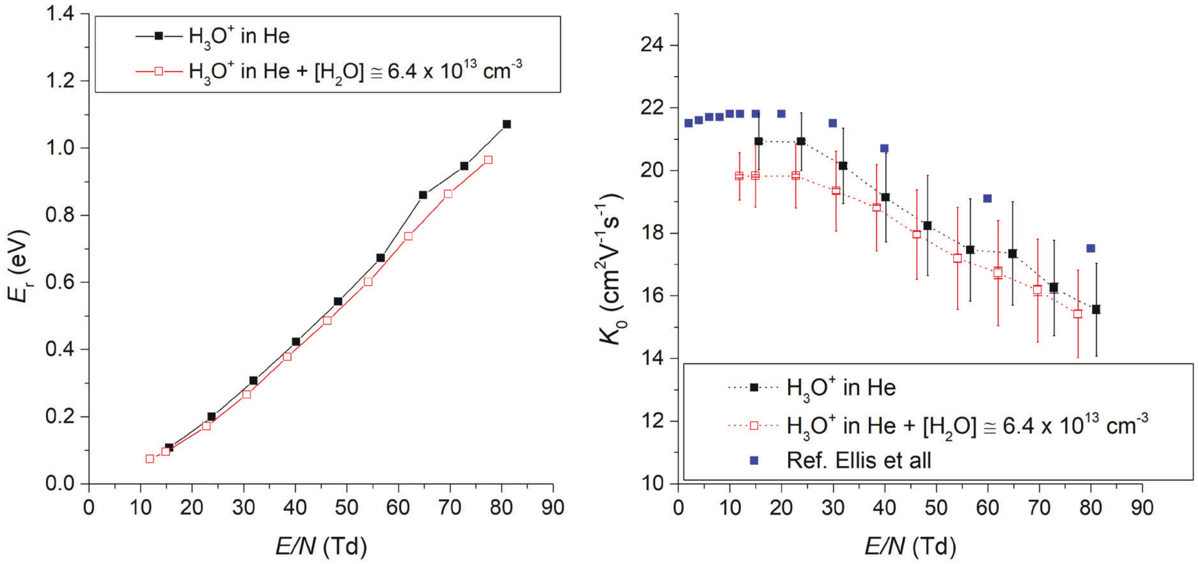

Fig S7: Reaction energy and ion mobility of H_3O^+ ions determined for different system humidity using second SIFDT-MS experimental concept. The reaction energy is determined between H_3O^+ ion and glyoxal neutrals (Eq. 4). The ion mobility is calculated using Eq. 5. The ion mobility data are compared with data obtained by Ellis et all [1].

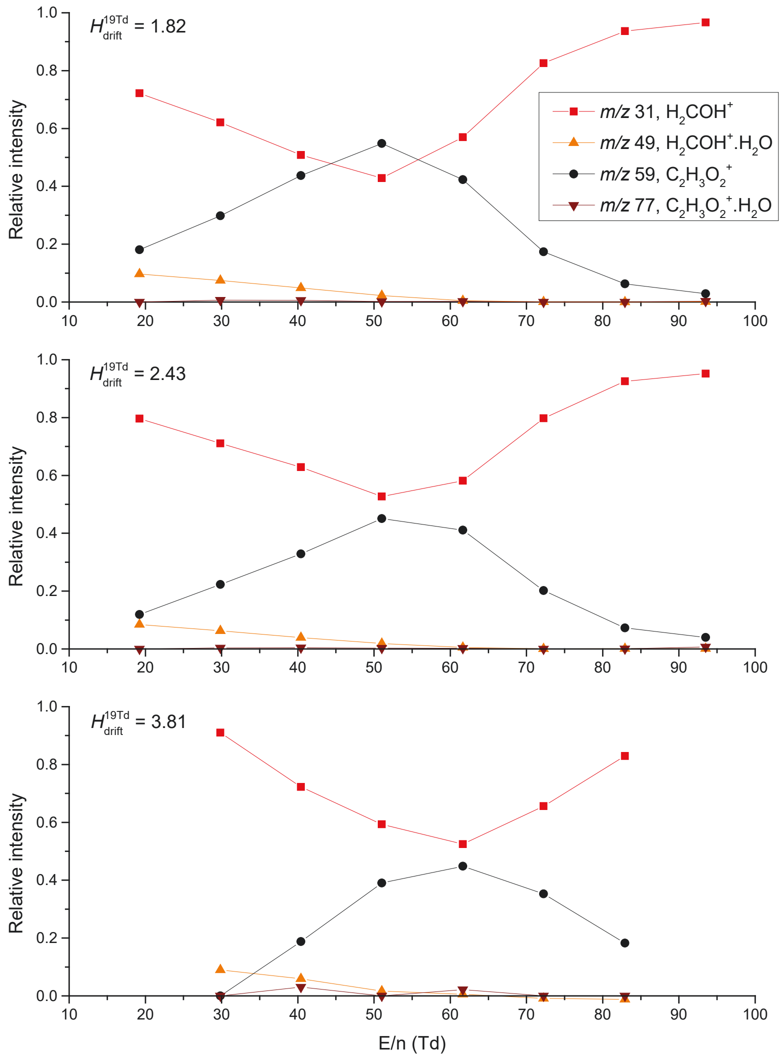

Fig S8: Relative intensities of glyoxal ion products obtained for different system humidity in He carrier gas using first SIFDT-MS experimental concept, while the injected glyoxal sample was diluted in dry air instead of He.

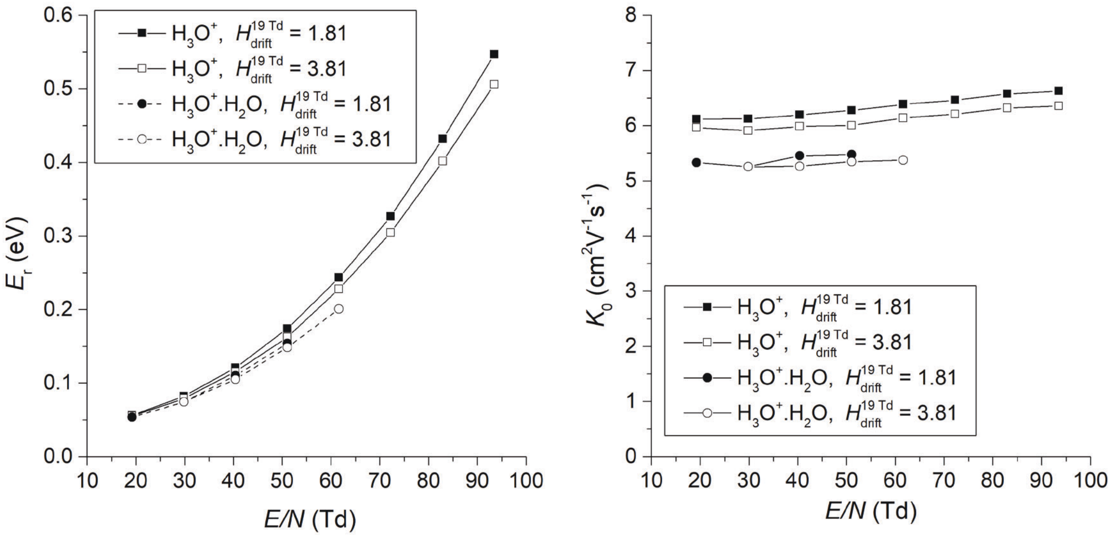

Fig S9: Determined reaction energy and ion mobility of H_3O^+ and $H_3O^+H_2O$ ions for different system humidity using first SIFDT-MS experimental concept. The reaction energy is determined between respective ion and glyoxal neutrals (Eq. 4). The ion mobility is calculated using Eq. 5.

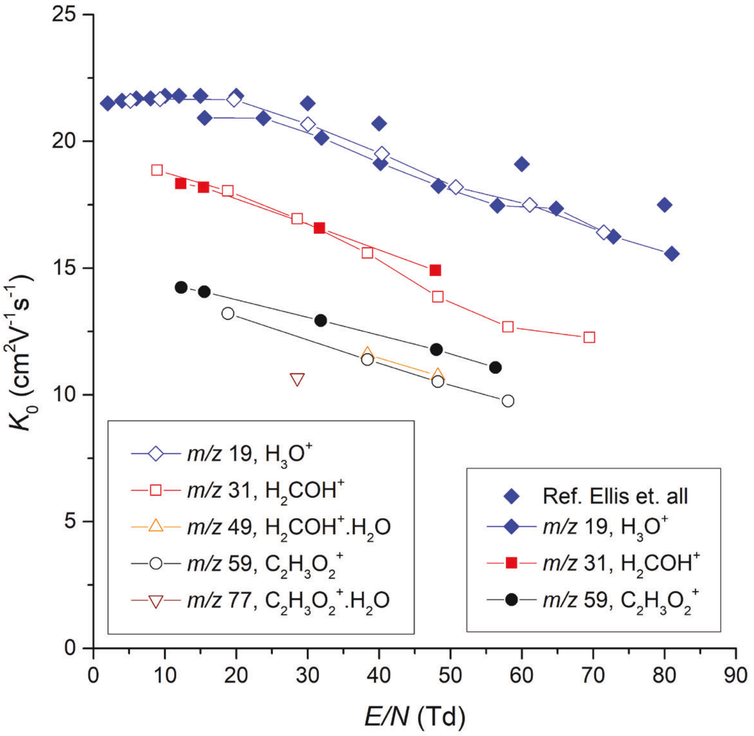

Fig S10: Ion mobilities of selected ions obtained by the first (open symbols) and second (solid symbols) concept of SIFDT-MS experiment determined in dry He carrier gas. Individual ions were generated before the SIFDT-MS first mass filter (see Experimental part). The ion mobility data are compared with data obtained by Ellis et all [1].

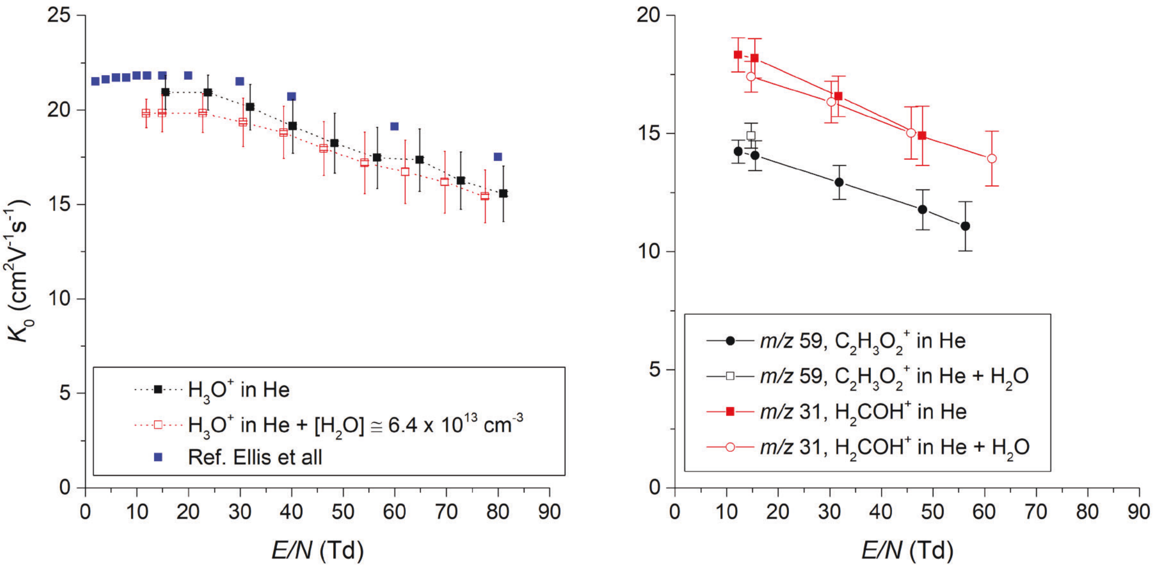

Fig S11: Influence of humidity on ion mobility determined by second SIFDT-MS experimental concept. Ions were generated in the ion source and selectively injected into DTR occupied by dry He or He containing water vapours at concentration [H_2O] ≅ 6.4 x 10^{13} cm^{-3}. The H_3O^+ ion mobility data are compared with data obtained by Ellis et all [1].

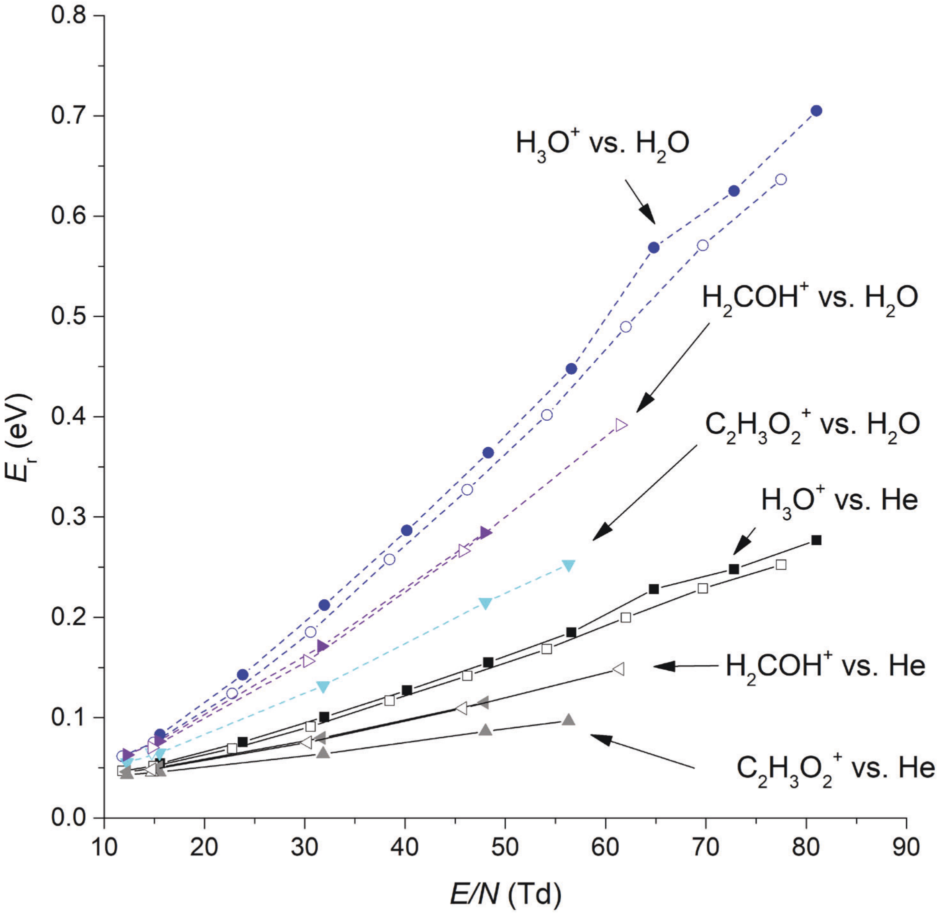

Fig. S12 Calculated reaction energies (Eq. 4) between selected ions and neutrals (He or H_2O) using ion retention times obtained in the second SIFDT-MS experimental concept. The full symbols represent energies obtained for dry He and open symbols represent He containing also water vapours $[H_2O] \cong 6.4 \times 10^{13}$ cm^{-3}.

Simulation of ion chemistry

Table S1 Ion mobilities of involved ions determined by SIFDT-MS in He carrier gas used for the simulations. The ion mobilities are presented as functions of *E/N* in form $K_0(E/N) = K(0)*(1 + A \times (E/N)^2 + B \times (E/N)^4)$. Ion mobilities were determined for dry He based on measurements presented in Fig. S10 and S11. Ion mobility of hydronium was also determined for He containing $[H_2O] \cong 6.4 \times 10^{13}$ cm^{-3}. For hydrides of protonated glyoxal and formaldehyde, functions have reduced form due to limited number of measurements.

Ion	μ(0)	A	B
H_3O^+	21.72	-7.23E-05	4.64E-09
H_3O^+ in humid He	20.16	-5.41E-05	2.53E-09
$H_3O^+.H_2O$	17.39	-8.85E-05	8.68E-09
$H_3O^+.(H_2O)_2$	13.88	-9.66E-05	2.10E-09
CH_2OH^+	18.89	-1.37E-04	1.30E-08
$CH_2OH^+.H_2O$	11.62	-4.31E-06	-9.91E-09
$C_2H_3O_2^+$	14.33	-1.36 E-05	1.59E-08
$C_2H_3O_2^+.H_2O$	10.67	0	0

Simulation case 1: *Injection of protonated formaldehyde into humid He.*

Reaction	Reaction rate
H_3O^+ + H_2O + He <-->> $H_3O^+.H_2O$ + He	5E-31/Er(E/N)^2.5
H_3O^+ + H_2O + He <<--> $H_3O^+.H_2O$ + He	1.2E-09*EXP[-1.25/Er(E/N)]
$H_3O^+.H_2O$ + He + H_2O <-->> $H_3O(H_2O)_2^+$ + He	8E-31/Er(E/N)^2.5
$H_3O^+.H_2O$ + He + H_2O <<--> $H_3O(H_2O)_2^+$ + He	1.2E-09*EXP[-0.91/Er(E/N)]
CH_3O^+ + H_2O ---> H_3O^+ + H_2CO	**3.3E-10*EXP[-0.3/Er(E/N)]**
CH_3O^+ + H_2O + He <-->> $CH_3O^+.H_2O$ + He	1.14E-28/Er(E/N)^0.5
CH_3O^+ + H_2O + He <<--> $CH_3O^+.H_2O$ + He	3E-09*EXP[-1.2/Er(E/N)]
$CH_3O^+.H_2O$ + H_2O <-->> $H_3O^+.H_2O$ + H_2CO	5E-10
$CH_3O^+.H_2O$ + H_2O <<--> $H_3O^+.H_2O$ + H_2CO	3E-09

Ion	Initial concentration (cm^{-3})	Diffusion coefficient (cm^2s^{-1})
H_3O^+	0	420.33
$H_3O^+.H_2O$	0	327.05
$H_3O(H_2O)_2^+$	0	271.56
CH_3O^+	1000	351.81
$CH_3O^+.H_2O$	0	287.73
H_2O	6E+13	-
He	4.52E+16	-

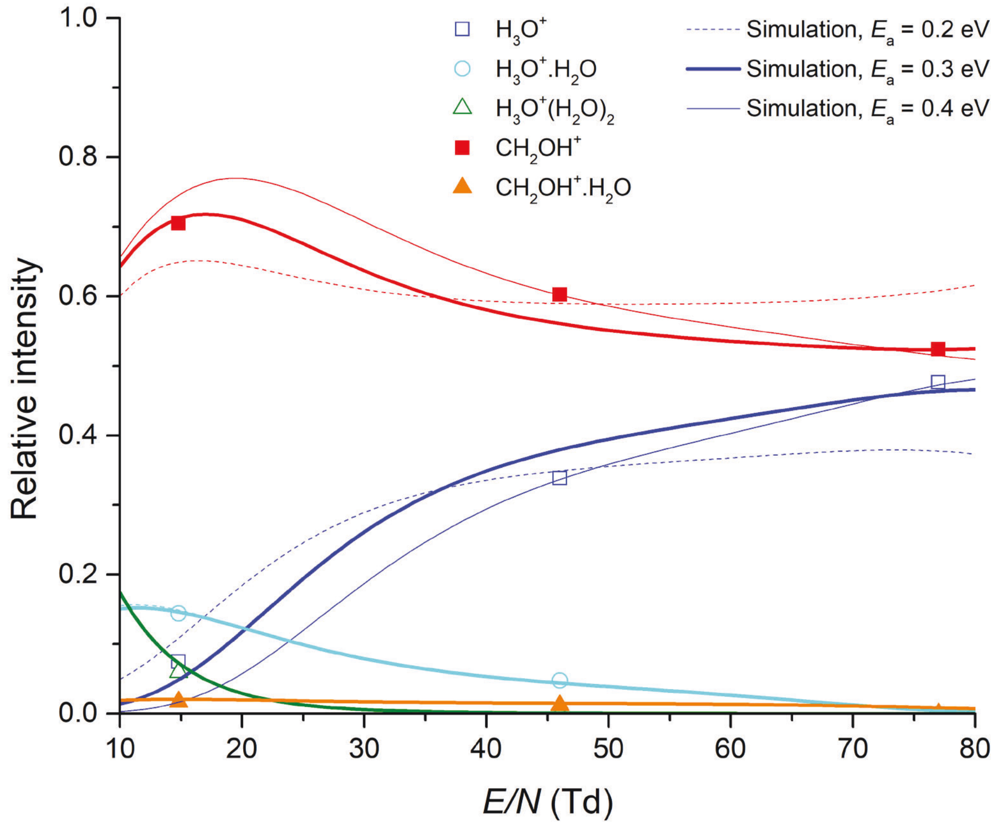

Fig. S13 Simulation of protonated formaldehyde ion chemistry in SIFDT-MS, injected into He carrier gas containing water vapours. The solid points represent experimental data obtained from Fig. 4. Lines represent specific simulations, where we changed reaction rate of reverse proton transfer CH_3O^+ + H_2O to 2E-10*EXP[-0.2/Er(E/N)] (dotted line), 3.3E-10*EXP[-0.3/Er(E/N)] (thick line) and 4.2E-10*EXP[-0.4/Er(E/N)] (thin line).

Simulation case 2: *Injection of protonated glyoxal into dry He.*

Reaction	**Reaction rate**
$H_3O^+ + H_2O + He$ <-->> $H_3O^+.H_2O + He$	5E-31/Er(E/N)^2.5
$H_3O^+ + H_2O + He$ <<--> $H_3O^+.H_2O + He$	1.2E-09*EXP[-1.25/Er(E/N)]
$H_3O^+.H_2O + He + H_2O$ <-->> $H_3O(H_2O)_2^+ + He$	8E-31/Er(E/N)^2.5
$H_3O^+.H_2O + He + H_2O$ <<--> $H_3O(H_2O)_2^+ + He$	1.2E-09*EXP[-0.91/Er(E/N)]
$CH_3O^+ + H_2O$ ---> $H_3O^+ + H_2CO$	3.3E-10*EXP[-0.3/Er(E/N)]
$CH_3O^+ + H_2O + He$ <-->> $CH_3O^+.H_2O + He$	1.14E-28/Er(E/N)^0.5
$CH_3O^+ + H_2O + He$ <<--> $CH_3O^+.H_2O + He$	3E-09*EXP[-1.2/Er(E/N)]
$CH_3O^+.H_2O + H_2O$ <-->> $H_3O^+.H_2O + H_2CO$	5E-10
$CH_3O^+.H_2O + H_2O$ <<--> $H_3O^+.H_2O + H_2CO$	3E-09
$C_2H_3O_2^+ + He$ ---> $CH_3O^+ + He + CO$	**8.5E-12*EXP[-0.38/Er(E/N)]**
$C_2H_3O_2^+ + H_2O + He$ <-->> $C_2H_3O_2^+.H_2O + He$	1E-27/Er(E/N)^0.5
$C_2H_3O_2^+ + H_2O + He$ <<--> $C_2H_3O_2^+.H_2O + He$	2E-09*EXP[-1.13/Er(E/N)]
$C_2H_3O_2^+.H_2O + H_2O$ <-->> $H_3O^+.H_2O + C_2H_2O_2$	1E-09
$C_2H_3O_2^+.H_2O + H_2O$ <<--> $H_3O^+.H_2O + C_2H_2O_2$	1E-09
$C_2H_3O_2^+.H_2O + H_2O$ ---> $CH_3O^+.H_2O + HCOOH$	8E-10

Ion	**Initial concentration (cm^{-3})**	**Diffusion coefficient (cm^2s^{-1})**
H_3O^+	0	420.33
$H_3O^+.H_2O$	0	327.05
$H_3O(H_2O)_2^+$	0	271.56
CH_3O^+	0	351.81
$CH_3O^+.H_2O$	0	287.73
$C_2H_3O_2^+$	10000	351.81
$C_2H_3O_2^+.H_2O$	0	224.48
H_2O	1E+13	-
He	4.52E+16	-

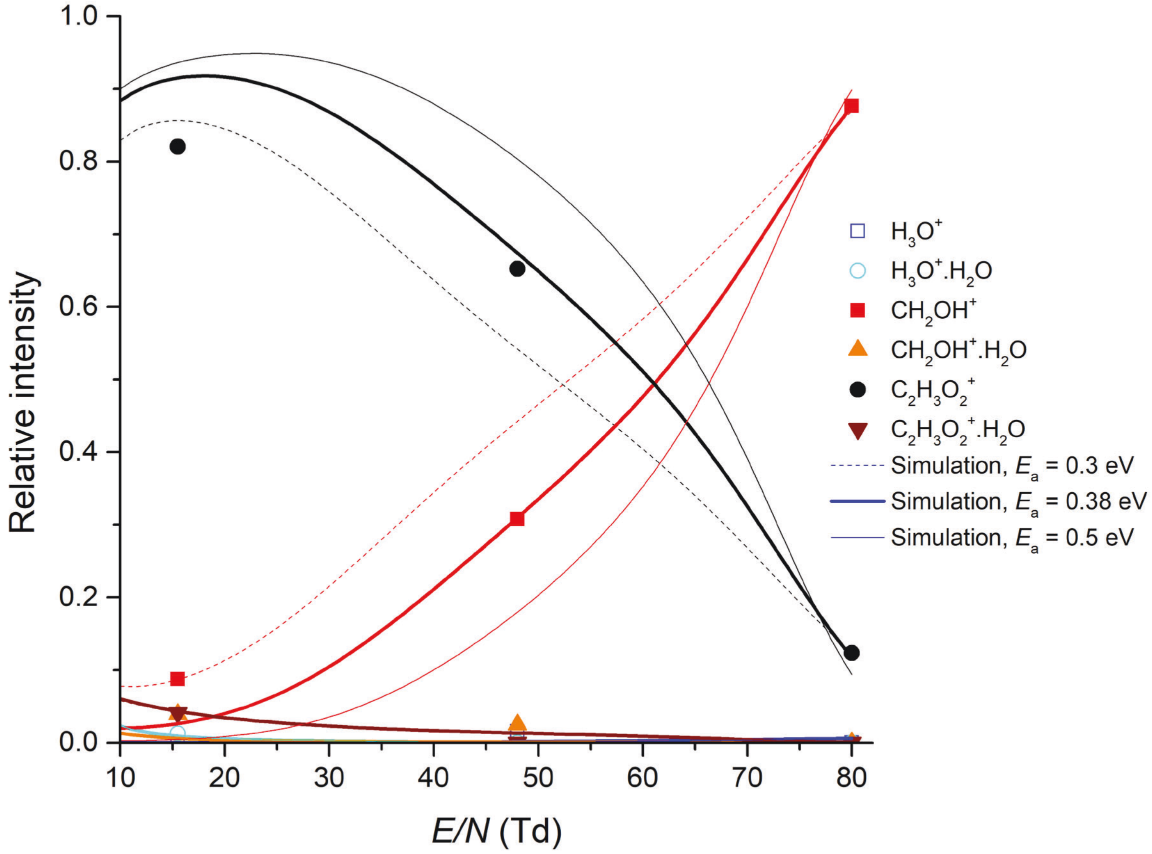

Fig. S14 Simulation of protonated formaldehyde ion chemistry in SIFDT-MS, injected into He carrier gas. The solid points represent experimental data obtained from Fig. 3. Lines represent specific simulations, where we changed reaction rate of CID channel $C_2H_3O_2^+$ + He to 5E-12*EXP[-0.3/Er(E/N)] (dotted line), 8.5E-12*EXP[-0.38/Er(E/N)] (thick line) and 2E-11*EXP[-0.5/Er(E/N)] (thin line).

Attachment A.3

Simulation case 3: *Injection of protonated glyoxal into humid He.*

Reaction	**Reaction rate**
H_3O^+ + H_2O + He <-->> $H_3O^+.H_2O$ + He	5E-31/Er(E/N)^2.5
H_3O^+ + H_2O + He <<--> $H_3O^+.H_2O$ + He	1.2E-09*EXP[-1.25/Er(E/N)]
$H_3O^+.H_2O$ + He + H_2O <-->> $H_3O(H_2O)_2^+$ + He	8E-31/Er(E/N)^2.5
$H_3O^+.H_2O$ + He + H_2O <<--> $H_3O(H_2O)_2^+$ + He	1.2E-09*EXP[-0.91/Er(E/N)]
CH_3O^+ + H_2O ---> H_3O^+ + H_2CO	3.3E-10*EXP[-0.3/Er(E/N)]
CH_3O^+ + H_2O + He <-->> $CH_3O^+.H_2O$ + He	1.14E-28/Er(E/N)^0.5
CH_3O^+ + H_2O + He <<--> $CH_3O^+.H_2O$ + He	3E-09*EXP[-1.2/Er(E/N)]
$CH_3O^+.H_2O$ + H_2O <-->> $H_3O^+.H_2O$ + H_2CO	5E-10
$CH_3O^+.H_2O$ + H_2O <<--> $H_3O^+.H_2O$ + H_2CO	3E-09
$C_2H_3O_2^+$ + He ---> CH_3O^+ + He + CO	8.5E-12*EXP[-0.38/Er(E/N)]
$C_2H_3O_2^+$ + H_2O + He <-->> $C_2H_3O_2^+.H_2O$ + He	7E-28/Er(E/N)^0.5
$C_2H_3O_2^+$ + H_2O + He <<--> $C_2H_3O_2^+.H_2O$ + He	3E-09*EXP[-1.13/Er(E/N)]
$C_2H_3O_2^+.H_2O$ + H_2O <-->> $H_3O^+.H_2O$ + $C_2H_2O_2$	1.6E-09
$C_2H_3O_2^+.H_2O$ + H_2O ---> CH_3O^+ + HCOOH + H_2O	1.78E-10/Er(E/N)^0.5
$C_2H_3O_2^+$ + H_2O ---> H_3O^+ + $C_2H_2O_2$	3E-10*EXP[-0.3/Er(E/N)]
$C_2H_3O_2^+$ + H_2O ---> CH_3O^+ + HCOOH	3E-09*EXP[-1/Er(E/N)]

Ion	**Initial concentration (cm^{-3})**	**Diffusion coefficient (cm^2s^{-1})**
H_3O^+	0	420.33
$H_3O^+.H_2O$	0	327.05
$H_3O(H_2O)_2^+$	0	271.56
CH_3O^+	0	351.81
$CH_3O^+.H_2O$	0	287.73
$C_2H_3O_2^+$	10000	351.81
$C_2H_3O_2^+.H_2O$	0	224.48
H_2O	6E+13	-
He	4.52E+16	-

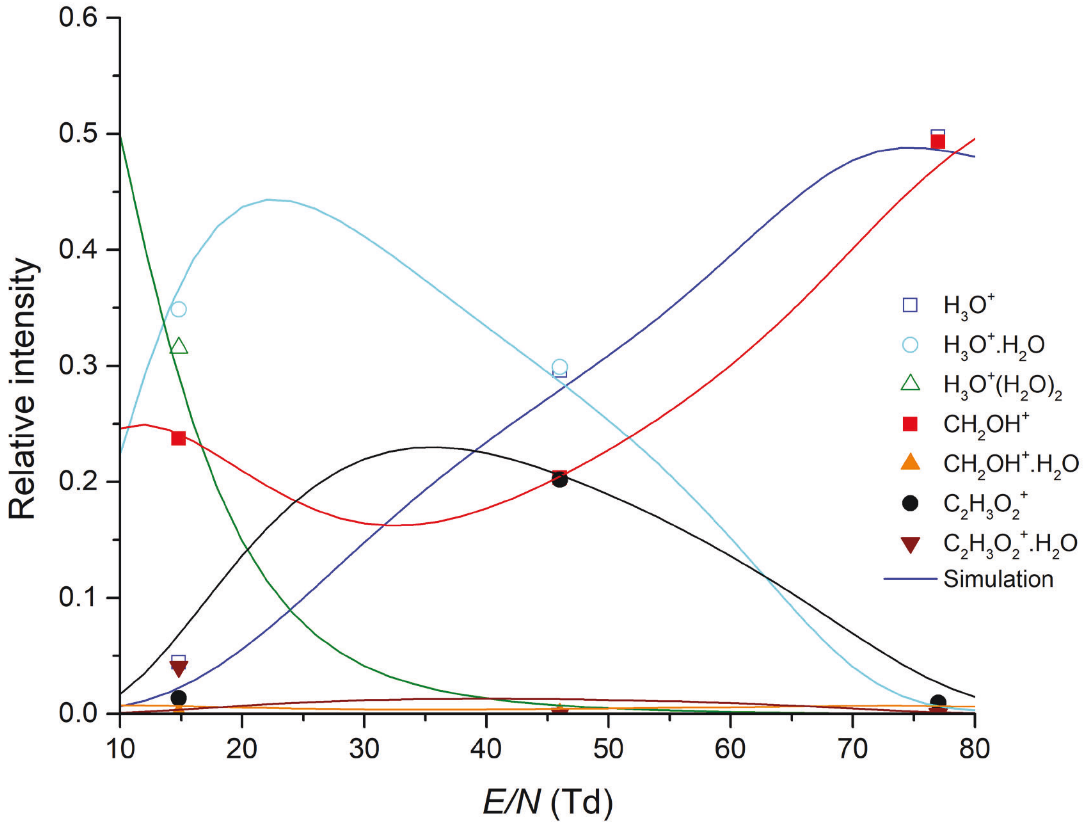

Fig. S15 Simulation of protonated formaldehyde ion chemistry in SIFDT-MS, injected into He carrier gas. The solid points represent experimental data obtained from Fig. 3. Lines represent optimised simulation profile.

***Simulation case 4:** Full ion chemistry simulation. Injection of hydronium ions into dry and humid He carrier gas containing glyoxal molecules*

Reaction	Reaction rate
$H_3O^+ + H_2O + He$ <-->> $H_3O^+.H_2O + He$	5E-31/Er(E/N)^2.5
$H_3O^+ + H_2O + He$ <<--> $H_3O^+.H_2O + He$	1.2E-09*EXP[-1.25/Er(E/N)]
$H_3O^+.H_2O + He + H_2O$ <-->> $H_3O(H_2O)_2^+ + He$	8E-31/Er(E/N)^2.5
$H_3O^+.H_2O + He + H_2O$ <<--> $H_3O(H_2O)_2^+ + He$	1.2E-09*EXP[-0.91/Er(E/N)]
$CH_3O^+ + H_2O$ ---> $H_3O^+ + H_2CO$	3.3E-10*EXP[-0.3/Er(E/N)]
$CH_3O^+ + H_2O + He$ <-->> $CH_3O^+.H_2O + He$	1.14E-28/Er(E/N)^0.5
$CH_3O^+ + H_2O + He$ <<--> $CH_3O^+.H_2O + He$	3E-09*EXP[-1.2/Er(E/N)]
$CH_3O^+.H_2O + H_2O$ <-->> $H_3O^+.H_2O + H_2CO$	5E-10
$CH_3O^+.H_2O + H_2O$ <<--> $H_3O^+.H_2O + H_2CO$	3E-09
$C_2H_3O_2^+ + He$ ---> $CH_3O^+ + He + CO$	8.5E-12*EXP[-0.38/Er(E/N)]
$C_2H_3O_2^+ + H_2O + He$ <-->> $C_2H_3O_2^+.H_2O + He$	7E-28/Er(E/N)^0.5
$C_2H_3O_2^+ + H_2O + He$ <<--> $C_2H_3O_2^+.H_2O + He$	3E-09*EXP[-1.13/Er(E/N)]
$C_2H_3O_2^+.H_2O + H_2O$ <-->> $H_3O^+.H_2O + C_2H_2O_2$	1.6E-09
$C_2H_3O_2^+.H_2O + H_2O$ <<--> $H_3O^+.H_2O + C_2H_2O_2$	1E-09
$C_2H_3O_2^+.H_2O + H_2O$ ---> $CH_3O^+ + HCOOH + H_2O$	1.78E-10/Er(E/N)^0.5
$C_2H_3O_2^+ + H_2O$ ---> $CH_3O^+ + HCOOH$	**3E-09*EXP[-1/Er(E/N)]**
$H_3O^+ + C_2H_2O_2$ <-->> $C_2H_3O_2^+ + H_2O$	1.33E-09(1-Exp(-1/Er(E/N)))
$H_3O^+ + C_2H_2O_2$ <<--> $C_2H_3O_2^+ + H_2O$	3E-10*EXP[-0.3/Er(E/N)]
$H_3O^+ + C_2H_2O_2$ ---> $CH_3O^+ + HCOOH$	1.33E-09*EXP[-1/Er(E/N)]

Ion	Initial concentration (cm^{-3})	Diffusion coefficient (cm^{2}s^{-1})
H_3O^+	1E6	420.33
$H_3O^+.H_2O$	0	327.05
$H_3O(H_2O)_2^+$	0	271.56
CH_3O^+	0	351.81
$CH_3O^+.H_2O$	0	287.73
$C_2H_3O_2^+$	1E8	351.81
$C_2H_3O_2^+.H_2O$	0	224.48
H_2O	**6.4E+13**	-
He	4.37E+16	-

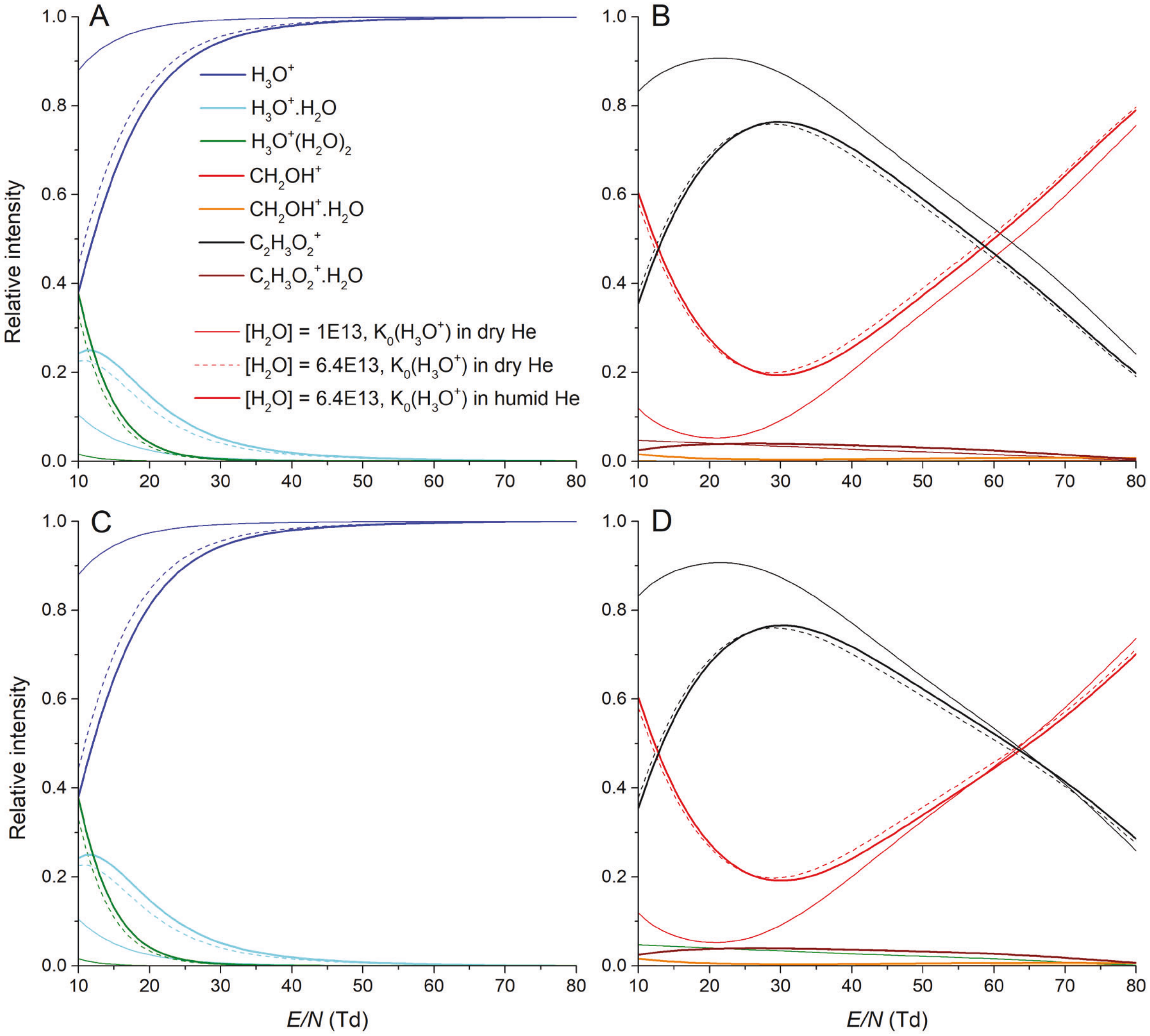

Fig. S16 Simulation of hydronium ion chemistry with glyoxal in SIFDT-MS. The top (A,B) and bottom (C,D) represents two different simulations, where on top the reaction $C_2H_3O_2^+ + H_2O \text{--->} CH_3O^+ +$ HCOOH is enabled while on bottom the reaction disabled. The left side (A, C) represents respective relative ion intensity of hydronium hydrates. The right side (B, D) shows relative ion intensities of product ions. Individual line types represent different initial conditions for the simulation. For solid line, low water concentration $[H_2O]$ = 1E13 was used together with hydronium ion mobility determined for dry He. The dashed line represents increased water vapour concentration to $[H_2O]$ = 6.4E13 while we still using hydronium ion mobility determined for dry He. Last, the thick line shows the scenario where water vapours concentration is still high, $[H_2O]$ = 6.4E13, while hydronium ion mobility is properly adjusted with respect to water vapour concentration.

Simulation case 5: *Full ion chemistry simulation. Injection of hydronium ions into dry and humid He carrier gas containing glyoxal molecules. In this simulation we determine effect of selected reactions on formation of protonated formaldehyde at high E/N, while not considering reaction* $C_2H_3O_2^+$ + H_2O ---> CH_3O^+ + HCOOH.

Reaction	**Reaction rate**
H_3O^+ + H_2O + He <-->> $H_3O^+.H_2O$ + He	5E-31/Er(E/N)^2.5
H_3O^+ + H_2O + He <<--> $H_3O^+.H_2O$ + He	1.2E-09*EXP[-1.25/Er(E/N)]
$H_3O^+.H_2O$ + He + H_2O <-->> $H_3O(H_2O)_2^+$ + He	8E-31/Er(E/N)^2.5
$H_3O^+.H_2O$ + He + H_2O <<--> $H_3O(H_2O)_2^+$ + He	1.2E-09*EXP[-0.91/Er(E/N)]
CH_3O^+ + H_2O ---> H_3O^+ + H_2CO	**3.3E-10*EXP[-0.3/Er(E/N)]**
CH_3O^+ + H_2O + He <-->> $CH_3O^+.H_2O$ + He	1.14E-28/Er(E/N)^0.5
CH_3O^+ + H_2O + He <<--> $CH_3O^+.H_2O$ + He	3E-09*EXP[-1.2/Er(E/N)]
$CH_3O^+.H_2O$ + H_2O <-->> $H_3O^+.H_2O$ + H_2CO	5E-10
$CH_3O^+.H_2O$ + H_2O <<--> $H_3O^+.H_2O$ + H_2CO	3E-09
$C_2H_3O_2^+$ + He ---> CH_3O^+ + He + CO	**8.5E-12*EXP[-0.38/Er(E/N)]**
$C_2H_3O_2^+$ + H_2O + He <-->> $C_2H_3O_2^+.H_2O$ + He	7E-28/Er(E/N)^0.5
$C_2H_3O_2^+$ + H_2O + He <<--> $C_2H_3O_2^+.H_2O$ + He	3E-09*EXP[-1.13/Er(E/N)]
$C_2H_3O_2^+.H_2O$ + H_2O <-->> $H_3O^+.H_2O$ + $C_2H_2O_2$	1.6E-09
$C_2H_3O_2^+.H_2O$ + H_2O <<--> $H_3O^+.H_2O$ + $C_2H_2O_2$	1E-09
$C_2H_3O_2^+.H_2O$ + H_2O ---> CH_3O^+ + HCOOH + H_2O	1.78E-10/Er(E/N)^0.5
H_3O^+ + $C_2H_2O_2$ <-->> $C_2H_3O_2^+$ + H_2O	1.33E-09(1-Exp(-1/Er(E/N)))
H_3O^+ + $C_2H_2O_2$ <<--> $C_2H_3O_2^+$ + H_2O	**3E-10*EXP[-0.3/Er(E/N)]**
H_3O^+ + $C_2H_2O_2$ ---> CH_3O^+ + HCOOH	**1.33E-09*EXP[-1/Er(E/N)]**

Ion	**Initial concentration (cm^{-3})**	**Diffusion coefficient (cm^2s^{-1})**
H_3O^+	1E6	420.33
$H_3O^+.H_2O$	0	327.05
$H_3O(H_2O)_2^+$	0	271.56
CH_3O^+	0	351.81
$CH_3O^+.H_2O$	0	287.73
$C_2H_3O_2^+$	1E8	351.81
$C_2H_3O_2^+.H_2O$	0	224.48
H_2O	**6.4E+13**	-
He	4.37E+16	-

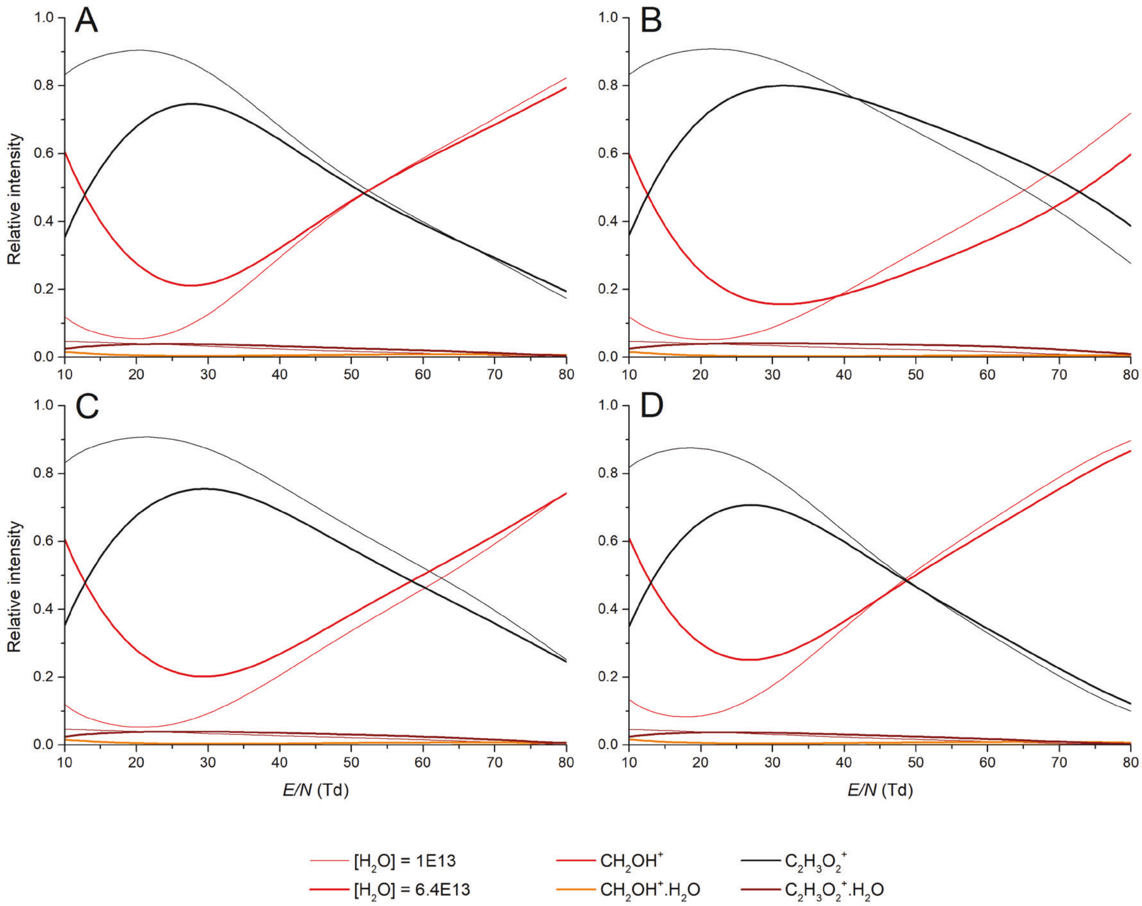

Fig. S17 Simulation of hydronium ion chemistry with glyoxal in SIFDT-MS, showing influence of individual selected reaction channels on negative trend in protonated formaldehyde formation at high *E/N*. In each simulation (A-D), only one specific reaction channel was changed by factor of 3 compare to simulation case 4:

A: H_3O^+ + $C_2H_2O_2$ ---> CH_3O^+ + HCOOH changed to 3E-09*EXP[-1/Er(E/N)]
B: CH_3O^+ + H_2O ---> H_3O^+ + H_2CO changed to 1E-09*EXP[-0.3/Er(E/N)]
C: H_3O^+ + $C_2H_2O_2$ <<--> $C_2H_3O_2^+$ + H_2O changed to 9E-10*EXP[-0.3/Er(E/N)]
D: $C_2H_3O_2^+$ + He ---> CH_3O^+ + He + CO changed to 2.6E-11*EXP[-0.38/Er(E/N)]

The thin line represents solution for He humidity [H_2O] = 1E13, thick line is for [H_2O] = 6.41E13. Mobility of hydronium ions was changed according to He humidity.

Simulation case 6: *Full ion chemistry simulation. Injection of hydronium ions into dry and humid He carrier gas containing glyoxal molecules. Effect of* $C_2H_3O_2^+$ + H_2O ---> CH_3O^+ + HCOOH *reaction*

Reaction	**Reaction rate**
H_3O^+ + H_2O + He <-->> $H_3O^+.H_2O$ + He	5E-31/Er(E/N)^2.5
H_3O^+ + H_2O + He <<--> $H_3O^+.H_2O$ + He	1.2E-09*EXP[-1.25/Er(E/N)]
$H_3O^+.H_2O$ + He + H_2O <-->> $H_3O(H_2O)_2^+$ + He	8E-31/Er(E/N)^2.5
$H_3O^+.H_2O$ + He + H_2O <<--> $H_3O(H_2O)_2^+$ + He	1.2E-09*EXP[-0.91/Er(E/N)]
CH_3O^+ + H_2O ---> H_3O^+ + H_2CO	3.3E-10*EXP[-0.3/Er(E/N)]
CH_3O^+ + H_2O + He <-->> $CH_3O^+.H_2O$ + He	1.14E-28/Er(E/N)^0.5
CH_3O^+ + H_2O + He <<--> $CH_3O^+.H_2O$ + He	3E-09*EXP[-1.2/Er(E/N)]
$CH_3O^+.H_2O$ + H_2O <-->> $H_3O^+.H_2O$ + H_2CO	5E-10
$CH_3O^+.H_2O$ + H_2O <<--> $H_3O^+.H_2O$ + H_2CO	3E-09
$C_2H_3O_2^+$ + He ---> CH_3O^+ + He + CO	8.5E-12*EXP[-0.38/Er(E/N)]
$C_2H_3O_2^+$ + H_2O + He <-->> $C_2H_3O_2^+.H_2O$ + He	7E-28/Er(E/N)^0.5
$C_2H_3O_2^+$ + H_2O + He <<--> $C_2H_3O_2^+.H_2O$ + He	3E-09*EXP[-1.13/Er(E/N)]
$C_2H_3O_2^+.H_2O$ + H_2O <-->> $H_3O^+.H_2O$ + $C_2H_2O_2$	1.6E-09
$C_2H_3O_2^+.H_2O$ + H_2O <<--> $H_3O^+.H_2O$ + $C_2H_2O_2$	1E-09
$C_2H_3O_2^+.H_2O$ + H_2O ---> CH_3O^+ + HCOOH + H_2O	1.78E-10/Er(E/N)^0.5
$C_2H_3O_2^+$ + H_2O ---> CH_3O^+ + HCOOH	**1E-09*EXP[-1.5/Er(E/N)]**
H_3O^+ + $C_2H_2O_2$ <-->> $C_2H_3O_2^+$ + H_2O	1.33E-09(1-Exp(-1/Er(E/N)))
H_3O^+ + $C_2H_2O_2$ <<--> $C_2H_3O_2^+$ + H_2O	3E-10*EXP[-0.3/Er(E/N)]
H_3O^+ + $C_2H_2O_2$ ---> CH_3O^+ + HCOOH	1.33E-09*EXP[-1/Er(E/N)]

Ion	**Initial concentration (cm^{-3})**	**Diffusion coefficient (cm^2s^{-1})**
H_3O^+	1E6	420.33
$H_3O^+.H_2O$	0	327.05
$H_3O(H_2O)_2^+$	0	271.56
CH_3O^+	0	351.81
$CH_3O^+.H_2O$	0	287.73
$C_2H_3O_2^+$	1E8	351.81
$C_2H_3O_2^+.H_2O$	0	224.48
H_2O	**6.4E+13**	-
He	4.37E+16	-

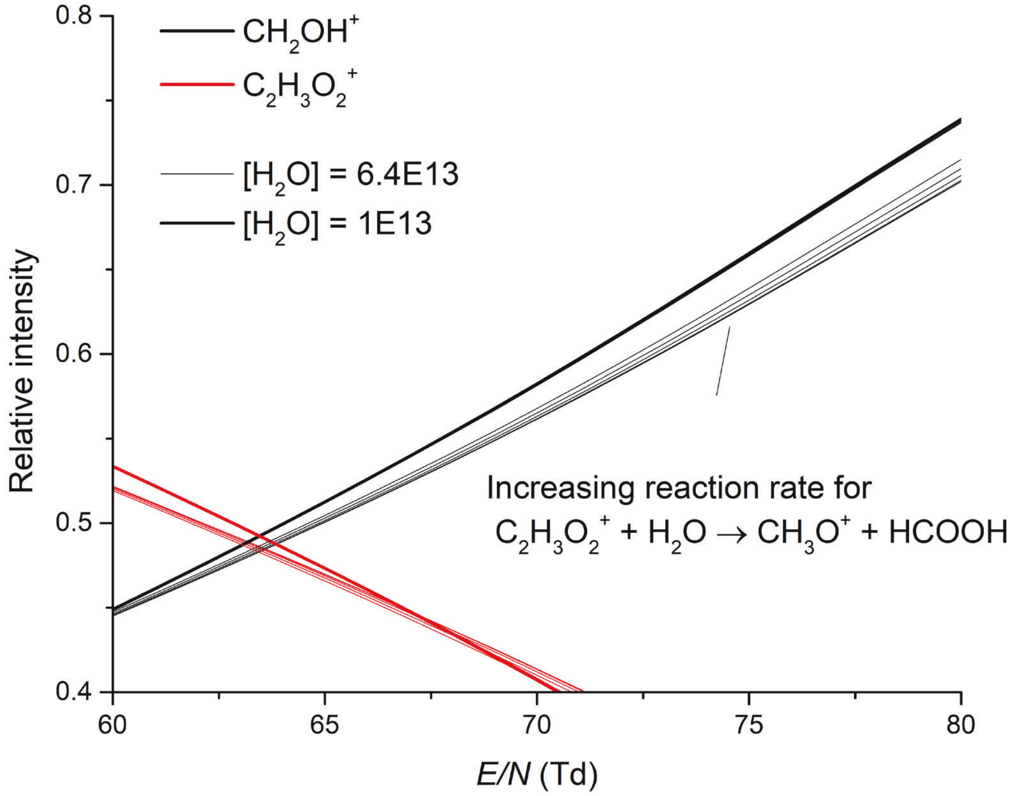

Fig. S18 Simulation of hydronium ion chemistry with glyoxal in SIFDT-MS, showing reduction of negative trend of protonated formaldehyde formation at high *E/N* via reaction $C_2H_3O_2^+ + H_2O$ ---> CH_3O^+ + HCOOH. Compare to simulation case 4, we increased *E*a to 1.5 followed by slow increase of first reaction rate coefficient A from 5E11 to 1E9. This results into steady decrease of protonated formaldehyde negative trend.

References

1. Ellis, H., et al., *Transport properties of gaseous ions over a wide energy range. Part II.* Atomic data and nuclear data tables, 1978. **22**(3): p. 179-217.

PCCP

PAPER

View Article Online
View Journal | View Issue

Cite this: *Phys. Chem. Chem. Phys.*, 2020, **22**, 16345

Ion chemistry of phthalates in selected ion flow tube mass spectrometry: isomeric effects and secondary reactions with water vapour†

Michal Lacko, *[a,b] Bartosz Michalczuk, [c] Štefan Matejčík [c] and
Patrik Španěl [a]

Phthalates are widely industrially used and their toxicity is of serious environmental and public health concern. Chemical ionization (CI) analytical techniques offer the potential to detect and monitor traces of phthalate vapours in air or sample headspace in real time. Promising techniques include selected ion flow tube mass spectrometry (SIFT-MS), proton transfer reaction mass spectrometry (PTR-MS) and ion mobility spectrometry (IMS). To facilitate such analyses, reactions of H_3O^+, O_2^+ and NO^+ reagent ions with phthalate molecules need to be understood. Thus, the ion chemistry of dimethyl phthalate isomers (dimethyl phthalate, DMP – *ortho*; dimethyl isophthalate, DMIP – *meta*; dimethyl terephthalate, DMTP – *para*), diethyl phthalate (DEP), dipropyl phthalate (DPP) and dibutyl phthalate (DBP) was studied by SIFT-MS. Reactions of H_3O^+, O_2^+ and NO^+ with these phthalate molecules M were found to produce the characteristic primary ion products MH^+, M^+ and MNO^+, respectively. In addition, a dissociation process forming the $(M{-}OR)^+$ fragment was observed. For phthalates with longer alkyl chains, mainly DPP and DBP, a secondary dissociation channel triggered by the McLafferty rearrangement was also observed. However, this is dominant only for the more energetic O_2^+ reactions with phthalates, additionally resulting in a recognisable formation of the protonated phthalate anhydride. For the NO^+ reagent ions, the McLafferty rearrangement makes only a minor contribution and for H_3O^+, it was not observed. Experiments on the effect of water vapour on this ion chemistry have shown that protonated DMIP and DMTP efficiently associate with H_2O forming the $DMIP{\cdot}H^+H_2O$, $DMIP{\cdot}H^+(H_2O)_2$ and $DMTP{\cdot}H^+H_2O$ cluster ions, whilst the protonated *ortho* DMP isomer as well as other *ortho* phthalates DEP, DPP and DBP does not associate with H_2O. The results indicate that the degree of hydration can be used to identify specific phthalate isomers in CI.

Received 31st January 2020,
Accepted 18th June 2020

DOI: 10.1039/d0cp00538j

rsc.li/pccp

Introduction

Phthalates (esters of phthalic acid) are used in the production of plastics as plasticizers and their environmental and health impacts are now well understood. Phthalates are characterized as endocrine disruptors that represent a major hazard for pregnant women and children under 3 years.[1,2] Several of the most dangerous phthalates (diethylhexyl phthalate, dibutyl phthalate, benzylbutyl phthalate, diisononyl phthalate, diisodecyl phthalate, and di-*n*-octyl phthalate) are regulated by EU regulations[3] or tracked by the European Chemical Agency.[4] However, these regulations only cover toys and are not concerned with other daily products. Phthalates can thus be present in plastic containers,[5] cosmetics[6] and toothbrushes.[7] Phthalates were additionally detected in indoor air and dust[8] or in seawater.[9] Further risk of exposure to phthalates may also arise from the import of products from countries without regulations in place.

Several analytical techniques are used for the detection of phthalates, mainly based on gas chromatography – mass spectrometry using electron ionization, EI, at 70 eV.[10,11] The notable feature observed in phthalate mass spectra is a common fragment ion of the protonated phthalate anhydride with the mass to charge ratio *m*/*z* 149. This mass peak is characteristic for most phthalates with longer alkyl substituents. Whilst the appearance of the *m*/*z* 149 peak is a good indicator for the presence of phthalate, the selectivity between the different phthalate compounds by EI is limited. Chemical ionization (CI) combined with liquid chromatography has been shown to provide better selectivity between different phthalates.[12]

---

[a] *J. Heyrovský Institute of Physical Chemistry of the CAS, v. v. i. Dolejškova 2155/3, 182 23 Prague, Czech Republic. E-mail: patrik.spanel@jh-inst@cas.cz*
[b] *Charles University, Faculty of Mathematics and Physics, V Holešovičkách 747/2, 180 00 Prague, Czech Republic*
[c] *Comenius University in Bratislava, Faculty of Mathematics, Physics and Informatics, Mlynska dolina, 84248 Bratislava, Slovakia*

† Electronic supplementary information (ESI) available. See DOI: 10.1039/d0cp00538j

The aim of the present study is to investigate the possibilities of analyzing phthalate vapours *via* proton transfer reaction mass spectrometry (PTR-MS) and selected ion flow tube mass spectrometry (SIFT-MS). These techniques are mainly used in the real time detection of VOCs present at trace levels[13] and were successfully applied in several analytical applications including breath research, food flavour analysis, environmental monitoring and homeland security.[14–16] It is, therefore, important to understand the ion chemistry of phthalates related to SIFT-MS and PTR-MS not only to facilitate their analyses, but also to gain insight into the reaction mechanism by observing trends in changes of reactivity with the phthalate molecule size and structure. Recently, atmospheric pressure chemical ionization (APCI) and ion mobility spectrometry (IMS) were combined to study dimethyl phthalate isomers showing interesting selective behaviour in the formation of protonated phthalate water clusters where the *ortho* orientation of phthalate esters does not form water clusters whilst the other two conformers do.[17]

In the present study, we have investigated the H_3O^+, NO^+ and O_2^+ ion reactions with dimethyl phthalate (DMP), dimethyl iso-phthalate (DMIP), dimethyl terephthalate (DMTP), diethyl phthalate (DEP), dipropyl phthalate (DPP) and dibutyl phthalate (DBP) *via* SIFT-MS. Secondary reactions of the protonated products with neutral water molecules were also studied in order to gain an understanding of formation of their water clusters.

Experiment

SIFT experiments

The SIFT experiments[22] were carried out using a Profile 3 instrument (Instrument Science, Crewe, UK). The H_3O^+, NO^+ and O_2^+ reagent ions were generated in a microwave discharge. One reagent ion type was mass selected using a quadrupole mass filter at a time and injected into the 5 cm long flow tube where a constant laminar flow of helium carrier gas was established at a total pressure of 1.5 mbar and a temperature of 300 K. Synthetic air containing the controlled amounts of neutral reagent vapours (phthalates and water vapour) was introduced into the flow tube by an inlet port located 1 cm downstream from the ion injector at a flow rate of 20 mL min^{-1}. Depending on the type of the reagent ions, the ionization of phthalate molecules (M) may occur at thermal energy *via* several channels: proton transfer typical for reaction with H_3O^+ reagent ions

$$H_3O^+ + M \rightarrow MH^+ + H_2O, \quad (1)$$

charge transfer, characteristic for O_2^+ reagent ions

$$O_2^+ + M \rightarrow M^+ + O_2, \quad (2)$$

and association forming an ion adduct, typical for primary reactions with NO^+ reagent ions or secondary reactions of ions with water

$$NO^+ + M + He \rightarrow MNO^+ + He. \quad (3)$$

The product ions were sampled at the end of the flow tube, mass analysed using the downstream quadrupole mass filter and detected using an electron multiplier. Data were collected from full scan mass spectra (MS) and the multi-ion monitoring (MIM) mode was used to monitor the product ion distribution during the controlled humidity change.

Gases and chemicals

The investigated phthalates DMP (dimethyl phthalate, CAS: 131-11-3), DMIP (dimethyl isophthalate, CAS: 1459-93-4), DMTP (dimethyl terephthalate, CAS: 120-61-6), DEP (diethyl phthalate, CAS: 84-66-2), DPP (dipropyl phthalate, CAS: 131-16-8) and DBP (dibutyl phthalate, CAS: 84-74-2) were purchased from Sigma-Aldrich as reagents with stated 99% purity.

To characterize the product ion composition *via* mass spectrometry, a few mg of phthalate sample was placed at the bottom of a 15 mL glass vial closed by aluminium foil and heated up to T = 370 K. The volume of the vial containing phthalate vapours was then sampled directly *via* SIFT-MS. The humidification of the sample was difficult in this setup. Thus, we carried out the measurements only with synthetic and laboratory air.

To confirm the identity of the product ions, phthalate vapours were also deposited on the inner surface of a 2 m long, 0.25 mm ID polyether ether ketone (PEEK) capillary heated up to T = 360 K. This capillary was then flushed by a flow rate of 20 mL min^{-1} of pure synthetic air. This approach allowed the suppression of highly volatile impurities and the spectra so obtained were much cleaner, containing only the clean phthalate product ion peaks. Peaks that disappeared (*i.e.* m/z 57, 75 and 93 in DDP using H_3O^+, see the ESI†) were considered to originate from volatile impurities.

To study the influence of humidity on phthalate ion chemistry, we used the diffusion tube method.[23] A few mg of phthalate sample was placed in a 2 mL vial closed by polytetrafluoroethylene (PTFE) septum caps penetrated with a diffusion tube (1/16″ OD × 0.25 mm ID × 5 cm length PEEK capillary). The 2 mL vial was then placed in a 15 mL glass vial closed by a PTFE septum. The headspace of the 15 mL vial was sampled directly *via* SIFT-MS. Individual samples were heated up to T = 370 K to enhance their evaporation. Synthetic air was used to refill the air in the vial sampled *via* SIFT-MS. The humidity of synthetic air was controlled using an in-line water reservoir using the diffusion tube method. The water temperature within the reservoir was varied between T = 77 K and T = 350 K. The resulting water vapor concentration ranged from 10^{12} to 10^{14} molecules per cm^3. These water vapor concentrations were estimated according to the hydronium water cluster distribution *via* SIFT-MS as described elsewhere.[24,25] The relative value of the water vapor concentration is calculated using the following dimensionless logarithmic factor

$$H = \ln\left(\frac{[H_3O^+] + [H_3O^+ \cdot H_2O] + [H_3O^+ \cdot (H_2O)_2] + \cdots}{[H_3O^+]}\right) \quad (4)$$

Eqn (4) allows us to better compare the obtained experimental results.

Results and discussion

Molecular properties

The properties of three DMP isomer molecules and of the DEP molecule are given in Table 1. The quantification of DMP isomers using chemical ionization in the H_3O^+ reactions is feasible as their proton affinity (PA) is > 1.5 eV that of water molecules (PA(H_2O) = 7.2 eV[26]). Note that proton transfer is possible also from the hydrated hydronium ion as PA(($H_2O)_2$) = 8.56 eV.[17] In addition, charge transfer from O_2^+ is also possible due to the ionisation potential being lower than that of O_2. As the PA of all three DMP isomers exceeds the PA of H_2O, the rate constant for proton transfer (k) is equal to the collisional rate constant (k_c).[27] The k_c can be calculated for the H_3O^+ reactions using the parametrised trajectory formulation described by Su and Chesnavich[18] (see Table 1) using the polarizabilities and dipole moments of the molecules. These parameters were obtained by quantum chemical calculations (ωb97xd/6-311+G(2d,p)) related to previous IMS studies of these DMP isomers.[17]

Ion molecule reaction products

Using the SIFT method, we have studied the ion chemistry of individual DMP isomers, DEP, DMP and DBP using H_3O^+, NO^+ and O_2^+ reagent ions. The observed ion products are summarized in Table 2. All H_3O^+ reactions led to the formation of protonated phthalates (1) and a loss of one alkyloxy substituent (OR, where R stands for alkyl radicals). This dissociation channel, forming $(M–OR)^+$ ions, was observed for all phthalate reactions. Protonated phthalate anhydride (m/z 149, $PhA{\cdot}H^+$) was a minor product only for DPP and DBP.

For the NO^+ reactions, association (reaction (3)) was observed for all phthalates except DBP, where the adduct mass exceeded the upper limit of the downstream quadrupole mass filter (m/z 300). $DBP{\cdot}NO^+$ is likely to be a dominant product (as for the smaller phthalates) and thus the product ratio cannot be determined and only the upper limits are given in Table 2. The protonated molecule MH^+ was observed for all phthalates and, as will be discussed later, we consider this to be a product of the $M{\cdot}NO^+$ secondary reaction with water vapour. Other fragments including protonated phthalate anhydride and $(M–(R–2H))^+$ were detected with low intensity.

Table 1 Summary of the ionization energies (IEs) and the proton affinities (PAs) of reactants together with estimated rate coefficients for reactions of H_3O^+

Molecule	m (u)	IE (eV)	PA (eV)	α (10^{-24} cm^3)	μ (D)	k_c (H_3O^+) (10^{-9} cm^3 s^{-1})
DMP	194	9.64[a]	9.7[c]	23.99[c]	0.26[c]	2.82
DMIP	194	9.84[a]	8.74,[b] 8.77[c]	24.84[c]	1.9[c]	3.63
DMTP	194	9.78[a]	8.74,[b] 8.74[c]	28.71[c]	0[c]	3.02
DEP	222	nd	nd	~23[d]	nd	nd
DPrP	250	nd	nd	nd	nd	nd
DBP	278	nd	nd	nd	nd	nd

Presented also are the monoisotopic molecular weight, m, in atomic units u, polarizability α, in units of 10^{-24} cm^3 and permanent dipole moment μ, in Debye, D. The values of α and μ are taken from a report by Michalczuk *et al.*,[17] based on private communications and post analysis of their data at the ωb97xd/6-311+G(2d,p) level of theory. The collision rate coefficient k_c was calculated according to the parameterised trajectory formulation put forth by Su and Chesnavich.[18] For additional references: [a] Ref. 19. [b] Ref. 20. [c] Ref. 17. [d] ChemSpider predicted properties,[21] nd – no data.

Finally, O_2^+ reactions proceeded *via* charge transfer (reaction (2)). The molecular ion is dominant only for the *ortho* and *para* DMP isomers. The $(M–OR)^+$ ion fragment was formed for all DMP isomers. The production of $(M–(R–2H))^+$ becomes dominant for phthalates with longer alkyl chains, and it is accompanied by the formation of protonated phthalic acid (m/z 167, $(PhA{\cdot}H + H_2O)^+$) and protonated phthalate anhydride (m/z 149, $PhA{\cdot}H^+$).

The observed ion chemistry may be compared with previous studies of chemical ionization reactions of phthalates, using CI reagents such as methane and isobutane,[28] methane and ammonia[12] and methane.[29] Chemical ionisation reactions involving isobutane and ammonia were found to produce mostly the protonated phthalate ions. For methane, the CI reaction leads to protonated phthalate anhydrides (m/z 149) since the PA of methane (5.6 eV) is much lower than the PAs of phthalates. Note that in electron ionization,[30] this ion (m/z 149) is also often dominant. The formation of protonated phthalate anhydride was well explained by theoretical calculations of Jeilani *et al.* studying protonated[29] and ionised[31] phthalates. Protonated phthalate anhydride is generated from protonated phthalates *via* two pathways, initiated by the dissociation of alkyl or alcohol:

$$MH^+ \rightarrow [M–OR]^+ + HOR \qquad (5)$$

$$MH^+ \rightarrow [M–(R–2H)]^+ + (R–H) \qquad (6)$$

First, the loss of an alcohol molecule (5), common for all phthalates, leads to the formation of protonated phthalate anhydride directly. The second reaction (6) proceeds *via* a McLafferty rearrangement,[32] which requires a C_2 or longer alkyl ligand to be present in the phthalate ester group. From there, formation of the $(M–(R–2H))^+$ fragment leads to protonated phthalic acid (m/z 167, $(PhA{\cdot}H + H_2O)^+$) and then to m/z 149 by H_2O loss. The change of the free energy for the case of DBP favours reaction (6) by 12.2 kJ mol^{-1}[31] as calculated at the B3LYP/6-311G(d,p) level of theory.

Both pathways were identified in the CI spectra of most phthalates before; $(M–OR)^+$ ions are often more intense than $(M–(R–2H))^+$ ions and the intensity of the $(M–OR)^+$ fragment decreases with increasing alkyl chain length.[12] In contrast to these previous studies, in our present results, only traces of the specific products related to the McLafferty rearrangement were observed for DMIP and DBP. For phthalates with longer alkyl chains, even though the calculations indicated the McLafferty rearrangement to be energetically more favourable, the loss of alcohol is a much faster process when H_3O^+ or methane ions are used.

Similar pathways were described for phthalate ions produced by EI[30,31]

$$M^+ \rightarrow [M–OR]^+ + OR \qquad (7)$$

$$M^+ \rightarrow [M–(R–2H)]^+ + (R–2H) \qquad (8)$$

and these agree with the observed charge transfer reactions (2) of O_2^+ reagent ions. The McLafferty rearrangement occurs for

Table 2 Ion products of phthalates interacting with H_3O^+, NO^+ and O_2^+ reagent ions obtained *via* SIFT-MS. R stands for an alkyl substituent variating for different phthalates and PhA stands for the phthalate anhydride. Experiments were carried out in synthetic air. The ions in italic are products of secondary ion interaction with water vapour[a]

	H_3O^+			NO^+			O_2^+		
Compound (vapour pressure)	*m/z*	br	Ion	*m/z*	br	Ion	*m/z*	br	Ion
DMP (4.1^{a}) 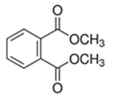	163	75%	$(DMP–OR)^+$	163	86%	$(DMP–OR)^+$	163	83%	$(DMP–OR)^+$
	195	25%	$DMP{\cdot}H^+$	195	2%	$\mathit{DMP{\cdot}H}^{+}$	194	17%	DMP^+
				224	11%	$DMP{\cdot}NO^+$			
DMIP (12.8^{a}) 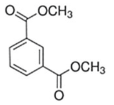	163	8%	$(DMIP–OR)^+$	163	63%	$(DMIP–OR)^+$	163	39%	$(DMIP–OR)^+$
	181	1%	$(DMIP{\cdot}H\text{-}CH_2)^+$	195	9%	$\mathit{DMIP{\cdot}H}^{+}$	194	61%	$DMIP^+$
	195	82%	$DMIP{\cdot}H^+$	224	28%	$DMIP{\cdot}NO^+$			
	213	9%	$\mathit{DMIP{\cdot}H}^{+}\mathit{{\cdot}H_2O}$						
DMTP (14.1^{a}) 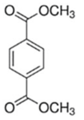	163	11%	$(DMTP–OR)^+$	163	79%	$(DMTP–OR)^+$	163	26%	$(DMTP–OR)^+$
	195	82%	$DMTP{\cdot}H^+$	195	9%	$\mathit{DMTP{\cdot}H}^{+}$	194	74%	$DMTP^+$
	213	7%	$DMTP{\cdot}H^+{\cdot}H_2O$	224	11%	$DMTP{\cdot}NO^+$			
DEP (2.8^{b}) 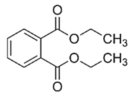	177	36%	$(DEP–OR)^+$	177	31%	$(DEP–OR)^+$	149	11%	$PhA{\cdot}H^+$
	223	64%	$DEP{\cdot}H^+$	223	3%	$\mathit{DEP{\cdot}H}^{+}$	167	5%	$(PhA{\cdot}H + H_2O)^+$
				252	66%	$DEP{\cdot}NO^+$	177	53%	$(DEP–OR)^+$
							195	6%	$(DEP–(R–2H))^+$
							222	24%	DEP^+
DPP (0.18^{c}) 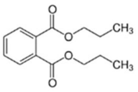	149	1%	$PhA{\cdot}H^+$	149	1%	$PhA{\cdot}H^+$	149	24%	$PhA{\cdot}H^+$
	163	1%	$(DPP–OR)^+$	191	21%	$(DPP–OR)^+$	167	6%	$(PhA{\cdot}H + H_2O)^+$
	191	15%	$DPP{\cdot}H^+$	209	2%	$(DPP–(R–2H))^+$	191	15%	$(DPP–OR)^+$
	251	83%		251	3%	$\mathit{DPP{\cdot}H}^{+}$	209	47%	$(DPP–(R–2H))^+$
				280	73%	$DPP{\cdot}NO^+$	250	8%	DPP^+
DBP (0.027^{d}) 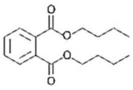	149	6%	$PhA{\cdot}H^+$	178	$<12\%$	$PhA{\cdot}NO^+$	149	24%	$PhA{\cdot}H^+$
	167	2%	$(PhA{\cdot}H + H_2O)^+$	205	$<52\%$	$(DBP–OR)^+$	167	7%	$(PhA{\cdot}H + H_2O)^+$
	205	9%	$(DBP–OR)^+$	223	$<4\%$	$(DBP–(R–2H))^+$	205	13%	$(DBP - OR)^+$
	279	83%	$DBP{\cdot}H^+$	279	$<32\%$	$\mathit{DBP{\cdot}H}^{+}$	223	34%	$(DBP–(R–2H))^+$
				308	?*	$DBP{\cdot}NO^+$	278	22%	DBP^+

[a] br – branching ratio, vapour pressure is stated in units of 10^{-3} mbar at 25 °C according to (a) Daubert and Thomas,[33] (b) Hinckley *et al.*,[34] (c) EPA[35] and (d) Donovan.[36] * *m/z* 308 is out of the *m/z* range of SIFT-MS.

DEP, and becomes dominant for DPP and DBP. For DBP, the activation energy calculated by B3LYP/6-311G(d,p)[31] for (8) is only 23 kJ mol^{-1}, and it is 97.3 kJ mol^{-1} to produce $PhA{\cdot}H^+$. The loss of alkoxyl requires 42.3 kJ mol^{-1} for (7), and 130 kJ mol^{-1} is required to produce $PhA{\cdot}H^+$. Our present studies follow this precedence, and fragments related to (8) can be observed for DEP and become dominant for DPP and DBP.

In the NO^+ CI reactions, the observed $(M–OR)^+$ fragments cannot result from the dissociative charge transfer, as IE(NO) = 9.26 eV[26] is below the IE of DMP isomers and must proceed by the formation of a neutral RONO product from the reaction intermediate MNO^+. A similar process was observed previously for the $M{\cdot}C_2H_5^+$ adducts.[29] In our present studies, the only observed fragment adduct ion was $PhA{\cdot}NO^+$ resulting from the NO^+ reaction with DBP. An interesting observation is the presence of a small amount of $(M–(R–2H))^+$ fragments, as these are typical for McLafferty rearrangement. For $M{\cdot}C_2H_5^+$ adducts, this rearrangement occurred in a reaction sequence after the initial dissociation of an alkyl substituent, while in the present study, it is a separate NO^+ reaction channel. The presence of protonated phthalate was also observed for $M{\cdot}C_2H_5^+$ adducts and it was explained by the dissociation of neutral C_2H_4 obtained from the adduct. This process is not possible for NO^+ ions. However, the protonated phthalate can be formed *via* secondary reactions with water vapour, which will be explained later.

Secondary reactions with water vapour

In the second part of the work, we have studied the influence of humidity on the ion chemistry of individual phthalates by changing the water vapour concentration within the flow tube. The presence of water vapour affects the ion chemistry in several ways. First, the reagent ions form water clusters and this changes their facility to ionise other organic molecules. In SIFT-MS, H_3O^+ reagent ions are the most affected, where reactions

$$H_3O^+(H_2O)_{n-1} + H_2O + He \leftrightarrow H_3O^+(H_2O)_n + He \qquad (9)$$

can form clusters with n up to 4. This effect is illustrated in Fig. 1, showing the relative distribution of hydronium water clusters as a function of water vapour concentration. Second, water clusters formed from protonated organic molecules may lead to complicated ion chemistry, compromising SIFT-MS selectivity and detection limits. Finally, at higher concentrations, water vapour may increase the rate of adduct formation.

The influence of water vapour on ion chemistry has been investigated in the present experiments for all reagent ions. For the NO^+ reagent ions, we observed an increase in the relative intensity for the MH^+ ions (by 5–10%) with water vapour concentration. This MH^+ intensity is too great to be produced by proton transfer from the ($\sim$1%) amount of H_3O^+ ions present in the flow tube together with the NO^+ ions. Based on

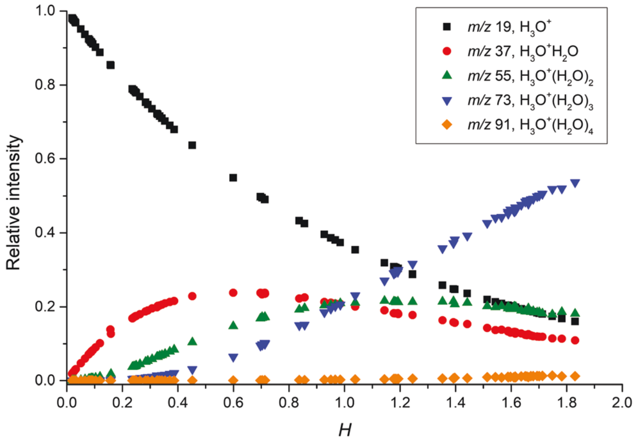

Fig. 1 Relative distribution of hydronium reagent ions based on different water concentrations in the flow tube.

its increase with water vapour concentration, we suggest that it can be produced *via* a secondary reaction with the phthalate–NO^+ adduct.

$$M{\cdot}NO^+ + H_2O \rightarrow MH^+ + HONO \qquad (10)$$

Reaction (10) can only take place if the proton affinity of phthalate (M) sufficiently exceeds the NO^+ affinity, as the notional reaction

$$NO^+ + H_2O \rightarrow H^+ + HONO \qquad (11)$$

is 711 kJ mol^{-1} endothermic.[26] The proton affinity is known only for the DMP isomers (see Table 1) while the NO^+ affinity can only be estimated. The typical NO^+ affinities[37] of organic molecules range from 100 to 200 kJ mol^{-1}. A linear correlation between PA and NO^+ affinity can be used, but it depends on whether the NO^+ association gives a σ or π complex.[37] For DMP, such a correlation estimates a NO^+ affinity of 169 kJ mol^{-1} for the σ complex (222.6 kJ mol^{-1} for π). Both these estimates are well below the PA(DMP) = 935.9 kJ mol^{-1} and render reaction (10) exothermic by 56.3 (or 2.7) kJ mol^{-1}. For the *meta* and *para* isomers, reaction (10) would be endothermic by 4.7 (or 39.4) kJ mol^{-1}. Despite this, the high number density of water molecules in the carrier gas (10^{12}–10^{14} cm^{-3}) can shift the reaction equilibrium in favour of MH^+ production.

Finally, the secondary reactions of the O_2^+ products can be discussed. A notable effect was observed only for DEP, DPP and DBP. Increasing the water vapour concentration led to a decrease in the fragmentation rate of the protonated phthalate anhydride (*m*/*z* 149) by 5–10%, compensated by an increase of protonated phthalate acid (*m*/*z* 167) intensity.

For the H_3O^+ reagent ions, the change in the relative distribution of the phthalate product ions for different water vapour concentrations is shown in Fig. 2. The formation of protonated phthalate water clusters depends strongly on the location of esters in the phthalate structure. In the *ortho* position, protonated phthalate hydrates are not produced at all. However, for DMIP (phthalate ester in the *meta* position),

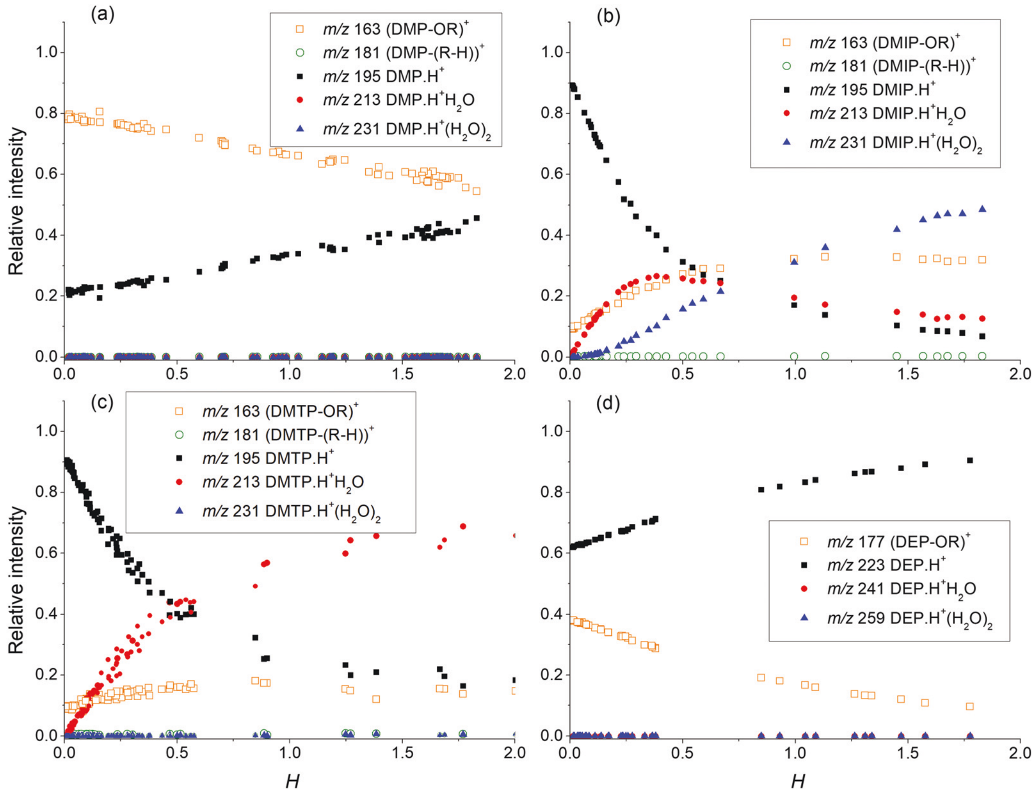

Fig. 2 Relative ion ratio between the observed products of phthalate molecules (a) DMP, (b) DMIP, (c) DMTP, and (d) DEP based on the relative water concentration in the flow tube *H*.

Table 3 Calculated changes of Gibbs free energies for individual proton transfer reactions and adduct formation reactions of DMP isomers (M) with different reagent ions. Data taken from ref. 17

Reagent ion	Products	DMP (eV)	DMIP (eV)	DMTP (eV)
H_3O^+	$MH^+ + H_2O$	−2.445	−1.678	−1.572
$H_3O^+(H_2O)$	$MH_3O^+ + H_2O$	−1.283	**−0.908**	**−0.793**
	$MH^+ + (H_2O)_2$	−1.156	−0.389	−0.282
$H_3O^+(H_2O)_2$	$MH_2OH_3O^+ + H_2O$	−0.627	**−0.756**	−0.338
	$MH_3O^+ + (H_2O)_2$	−0.560	−0.184	−0.070
	$MH^+ + (H_2O)_3$	−0.513	0.255	0.361
$H_3O^+(H_2O)_3$	$M(H_2O)_2H_3O^+ + H_2O$	−0.156	−0.579	−0.204
	$MH_2OH_3O^+ + (H_2O)_2$	−0.076	−0.205	0.213
	$MH_3O^+ + (H_2O)_3$	−0.089	0.286	0.401
	$MH^+ + (H_2O)_4$	−0.124	0.642	0.728

the formation of protonated phthalate water clusters can proceed to a degree of up to two water molecules per ion. Finally, for DMTP (phthalate esters in the *para* position), only one water molecule is observed to be attached to the protonated DMTP. The observed trend agrees with the APCI-IMS study of DMP isomers that was theoretically explained.[17] For DMP·H$^+$, the proton is located between the two carboxyl oxygens of phthalate esters, independent of the amount of H_2O molecules.

The formation of the protonated DMP hydrates is energetically possible (see Table 3). However, due to the minimal energy difference between the individual hydration states and high number density of water molecules, equilibrium will be established through ligand switching reactions

$$MH^+(H_2O)_{n-1} + H_2O \leftrightarrow MH^+ + n(H_2O) \quad (12)$$

where $n > 0$, in favour of the protonated phthalate. For DMIP and DMTP isomers, the formation of H_2O adducts is favoured, due to the deeper energetic minimum for DMIP·H_3O^+, DMIP·$H_3O^+H_2O$ and DMTP·H_3O^+ formation. This is in excellent agreement with our observation. Data in Table 1 indicate that the protonated phthalate clusters may achieve even higher levels of hydration, however the direct formation of individual ions *via* primary switching reactions

$$H_3O(H_2O)_{n-1} + M \leftrightarrow MH^+(H_2O)_{m-n} + n(H_2O) \quad (13)$$

where $n, m > 0$ becomes inefficient for higher hydronium water clusters. Additional hydration is possible due to the secondary association reactions of phthalate ions with water molecules

$$MH^+(H_2O)_{n-1} + H_2O + He \leftrightarrow MH^+(H_2O)_n + He \quad (14)$$

where $n > 0$.

Using the numerical simulation software KIMI developed by the first author of this paper,[38] it is possible to model the contribution of the individual reactions taking place in SIFT. Taking into account the relative ion distribution of protonated phthalate ions (Fig. 3), it is possible to interpret the observed

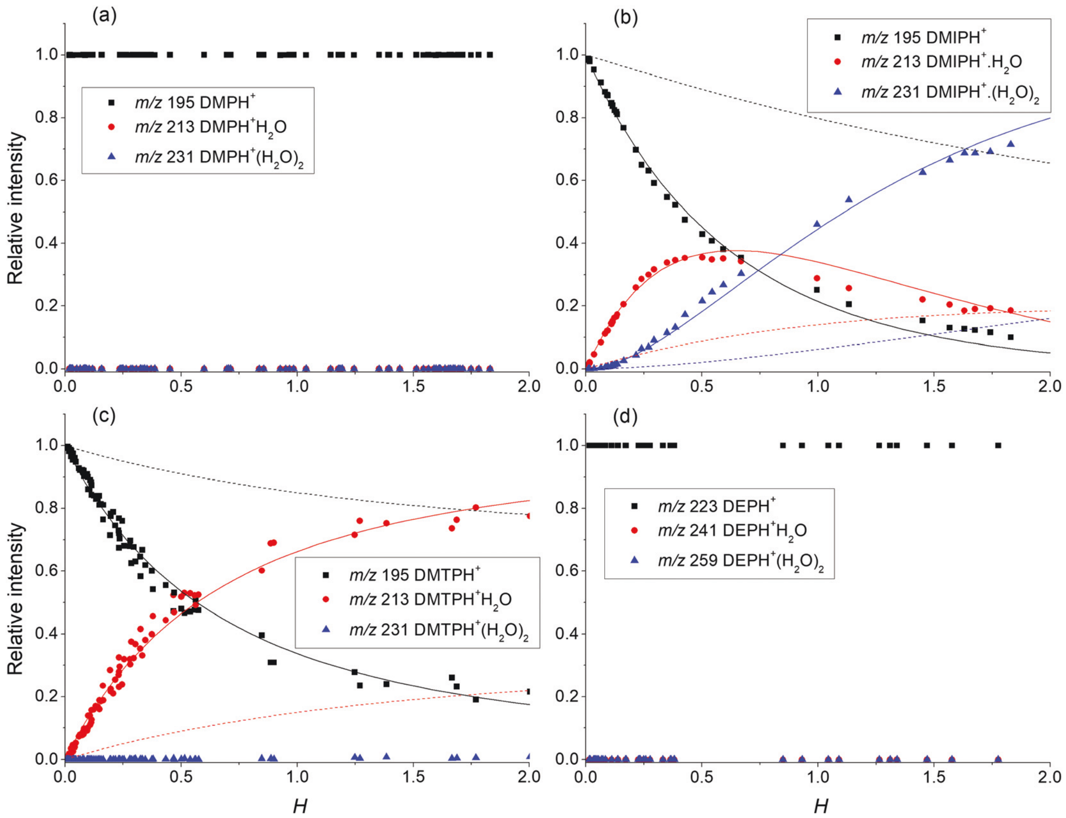

Fig. 3 Relative ion ratio between the protonated phthalate molecules (a) DMP, (b) DMIP, (c) DMTP, and (d) DEP, and their water clusters based on the relative water concentrations in the flow tube *H*. The relative distributions of DMIP and DMTP are supplemented by the simulation of ion kinetics using KIMI (ref. 38). The dash line represents a solution containing only proton transfer and adduct formation from hydronium clusters (reaction (13)). The solid line represents the previous solution obtained by the association of protonated phthalates with water (reaction (14)).

profile considering only proton transfer from hydronium reagent ions (H_3O^+) and secondary interaction of protonated phthalates with water according to (14). Thus, in CI, where multiple hydronium water clusters as reagent ions are present, higher protonated phthalate water clusters will be formed mainly by the hydration of smaller water clusters rather than by direct switching reactions of $H_3O^+(H_2O)_n$. This agrees with previous SIFT results for a series of aldehydes.[39] Finally, formation of the $(M–OR)^+$ fragment is affected by different concentrations of water vapour in SIFT as well. Fig. 2 shows a similar trend for DMP and DEP, where dissociation at higher water concentrations decreases as hydronium ions are replaced by less reactive hydronium water clusters. For DPP, DBP and DMTP, the dissociation was not affected by the presence of water vapour. The opposite trend can be observed for DMIP, where fragmentation rates increase with water vapour concentration. As the reactivity for higher hydronium water clusters decreases with the level of hydration, increased fragmentation can be explained by an additional secondary reaction. This reaction is probably initiated by the formation of a protonated phthalate–water complex, observed only for DMIP and DMTP, in a specific electronic state providing specific repulsive potential leading to

$$[MH^+(H_2O)_{n-1}]^\# \rightarrow (M–OR)^+ + HOR\cdot(H_2O)_n \qquad (15)$$

where $n > 1$. As we cannot determine details of this process, further study is required to fully understand this reaction.

Conclusions

New data were obtained on the kinetics of reactions involving H_3O^+, NO^+ and O_2^+ ions with phthalate isomers DMP, DMIP and DMTP, DEP, DPP and DBP, including information on the primary and some secondary ion products using SIFT at different concentrations of water vapour. Different ion–molecule reaction channels were observed for the individual reagent ions, including a characteristic dissociation channel forming $(M–OR)^+$ ions. This dissociation channel has been observed in previous CI and EI studies for several phthalates and its dominance can be explained for the DMP isomers and DEP by the short length of the alkyl substituents. For DPP and DBP containing longer alkyl chains, products characteristic of the McLafferty rearrangement were dominant only for the O_2^+ reagent ions.

A strong effect of the DMP isomeric structure on the formation of the protonated phthalate water clusters was revealed. For the *ortho* DMP molecules, hydration of protonated molecules is not effective due to the small energy difference between the individual hydration levels. The high number density of water molecules moves the reaction equilibrium in favour of the dominant formation of protonated DMP.

For the DMIP and DMTP isomers, the energy levels for water cluster formation are more different, facilitating the formation of $DMIP\cdot H_3O^+$, $DMIP\cdot H_3O^+H_2O$ and $DMTP\cdot H_3O^+$ water clusters. Using numerical simulation, we show that under the given SIFT conditions, phthalate water clusters are preferably formed by sequential hydration of protonated phthalates (14) rather than by direct ligand switching from hydronium water clusters (13). An increasing fragmentation rate at increasing water vapour concentrations observed for DMIP indicates the presence of an additional dissociation channel, producing $(M–OR)^+$ fragments from the generated protonated phthalate clusters. For DMP and DEP (phthalate esters in the *ortho* position), the protonated phthalate water clusters are not observed and the dissociation rate decreases with increasing water vapour concentration.

This detailed SIFT study of ion chemistry thus demonstrated that it is possible to analyse phthalates using different SIFT-MS ionization mechanisms. In addition, the humidity of the sample does not affect the ion chemistry for the studied *ortho* phthalates. As the proton is located between the two carboxyl oxygens of phthalate esters, the same effect is expected for the other phthalates as well. The effect of humidity on DMIP and DMTP can be additionally used to differentiate individual phthalate isomers *via* SIFT-MS.

Conflicts of interest

There are no conflicts to declare.

Acknowledgements

We would like to thank P. Papp for quantum chemical calculations (ωb97xd/6-311+G(2d,p)) of polarizabilities and dipole moments of the DMP isomers. This project has received funding from the European Union's Horizon 2020 research and innovation programme under the Marie Skłodowska-Curie grant agreement no. 674911.

Notes and references

1 R. U. Halden, *Annu. Rev. Public Health*, 2010, **31**, 179–194.
2 S. Benjamin, S. Pradeep, M. S. Josh, S. Kumar and E. Masai, *J. Hazard. Mater.*, 2015, **298**, 58–72.
3 Directive 2005/84/EC of the European Parliament and of the Council of 14 December 2005, Official Journal of the European Union, 2005, L 344, 40–43.
4 See http://echa.europa.eu/candidate-list-table/-/substance/ for EHCA – European Chemicals Agency, Candidate List of Substances of Very High Concern of Authorisation.
5 H. Y. Shen, *Talanta*, 2005, **66**, 734–739.
6 M. L. Juhasz and E. S. Marmur, *Dermatol. Ther.*, 2014, **27**, 317–322.
7 G. Sadeghi, E. Ghaderian and A. O'Connor, *The Downtown Review*, 2015, **1**, 2.
8 D. Kashyap and T. Agarwal, *Sci. Total Environ.*, 2018, **635**, 817–827.
9 A. Paluselli, V. Fauvelle, N. Schmidt, F. Galgani, S. Net and R. Sempéré, *Sci. Total Environ.*, 2018, **621**, 578–587.
10 M. V. Russo, P. Avino, L. Perugini and I. Notardonato, *RSC Adv.*, 2015, **5**, 37023–37043.

11 J. Fischer, K. Ventura, B. Prokeš and P. Jandera, *Chromatographia*, 1993, **37**, 47–50.
12 C. George and H. Prest, *LCGC North Am.*, 2002, **20**, 142–151.
13 D. Smith and P. Španěl, *TrAC, Trends Anal. Chem.*, 2011, **30**, 945–959.
14 D. Smith and P. Španěl, *Analyst*, 2011, **136**, 2009–2032.
15 W. Lindinger, A. Hansel and A. Jordan, *Int. J. Mass Spectrom. Ion Processes*, 1998, **173**, 191–241.
16 R. N. González-Méndez, P. Watts, D. Olivenza-León, D. F. Reich, S. J. Mullock, C. A. Corlett, S. Cairns, P. Hickey, M. Brookes and C. A. Mayhew, *Anal. Chem.*, 2016, **88**, 10624–10630.
17 B. Michalczuk, L. Moravsky, P. Papp, P. Mach, M. Sabo and S. Matejcik, *Phys. Chem. Chem. Phys.*, 2019, **21**, 13679–13685.
18 T. Su and W. J. Chesnavich, *J. Chem. Phys.*, 1982, **76**, 5183–5185.
19 W. F. Kuhn, *J. Chem. Phys.*, 1968, **49**, 5550.
20 E. P. L. Hunter and S. G. Lias, *J. Phys. Chem. Ref. Data*, 1998, **27**, 413–656.
21 ChemSpider, Diethyl phthalate, Properties, Predicted – ACD/Labs, http://www.chemspider.com/Chemical-Structure.13837303.html?rid=aa9741f9-550c-4b10-8ab7-478a749dba82, accessed 10/24, 2019.
22 D. Smith and P. Španěl, *Mass Spectrom. Rev.*, 2005, **24**, 661–700.
23 J. M. Thompson and D. B. Perry, *J. Environ. Monit.*, 2009, **11**, 1543–1544.
24 P. Španěl and D. Smith, *Rapid Commun. Mass Spectrom.*, 2001, **15**, 563–569.
25 P. Spanel and D. Smith, *Curr. Anal. Chem.*, 2013, **9**, 525–539.
26 NIST Chemistry WebBook, NIST Standard Reference Database 69, U.S. Secretary of Commerce, National Institute of Standards and Technology, http://webbook.nist.gov/chemistry/, cited November 2018.
27 G. Bouchoux, J. Y. Salpin and D. Leblanc, *Int. J. Mass Spectrom. Ion Processes*, 1996, **153**, 37–48.
28 H. Fales, G. Milne and R. Nicholson, *Anal. Chem.*, 1971, **43**, 1785–1789.
29 Y. A. Jeilani, B. H. Cardelino and V. M. Ibeanusi, *J. Mass Spectrom.*, 2010, **45**, 678–685.
30 M. Lacko, P. Papp and Š. Matejčík, *J. Chem. Phys.*, 2018, **148**, 214305.
31 Y. A. Jeilani, B. H. Cardelino and V. M. Ibeanusi, *J. Am. Soc. Mass Spectrom*, 2011, **22**, 1999–2010.
32 F. W. McLaffrety and F. Tureček, *Interpretation of Mass Spectra*, University science books, Sausalito, 1993.
33 T. E. Daubert, *Physical and thermodynamic properties of pure chemicals*, Data compilation Hemisphere Pub. Corp., New York, 1989.
34 D. A. Hinckley, T. F. Bidleman, W. T. Foreman and J. R. Tuschall, *J. Chem. Eng. Data*, 1990, **35**, 232–237.
35 United States Environmental Protection Agency, Dipropyl phthalate – Summary, https://comptox.epa.gov/dashboard/dsstoxdb/results?search=DTXSID5031133#properties, cited March 2020.
36 S. F. Donovan, *J. Chromatogr. A*, 1996, **749**, 123–129.
37 F. Cacace, G. De Petris and F. Pepi, *Proc. Natl. Acad. Sci. U. S. A.*, 1997, **94**, 3507–3512.
38 M. Lacko, F. Piel, A. Mauracher and P. Španěl, *Phys. Chem. Chem. Phys.*, 2020, **22**, 10170–10178, DOI: 10.1039/d0cp00297f.
39 D. Smith, T. W. E. Chippendale and P. Španěl, *Rapid Commun. Mass Spectrom.*, 2014, **28**, 1917–1928.

Ion chemistry of phthalates in selected ion flow tube mass spectrometry: isomeric effects and secondary reactions with water vapor

M. Lacko,[a,b] B. Michalczuk[c], Š. Matejčík[c] and P. Španěl[a]

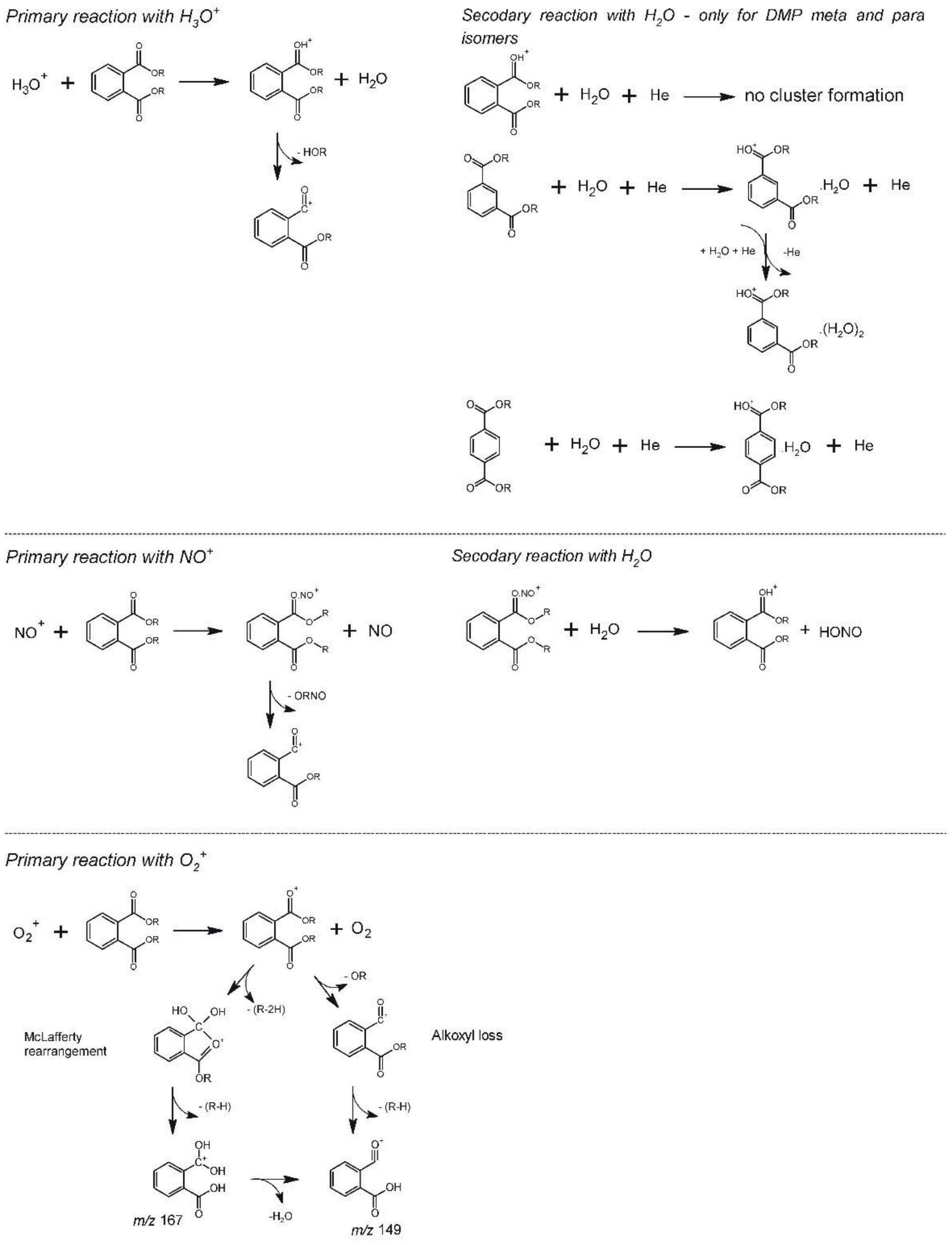

Scheme S1: Mass spectrum of DBP using H_3O^+ reagent ions. Selected peaks presented during the direct sampling of DPB headspace are not related to the DBP ion chemistry.

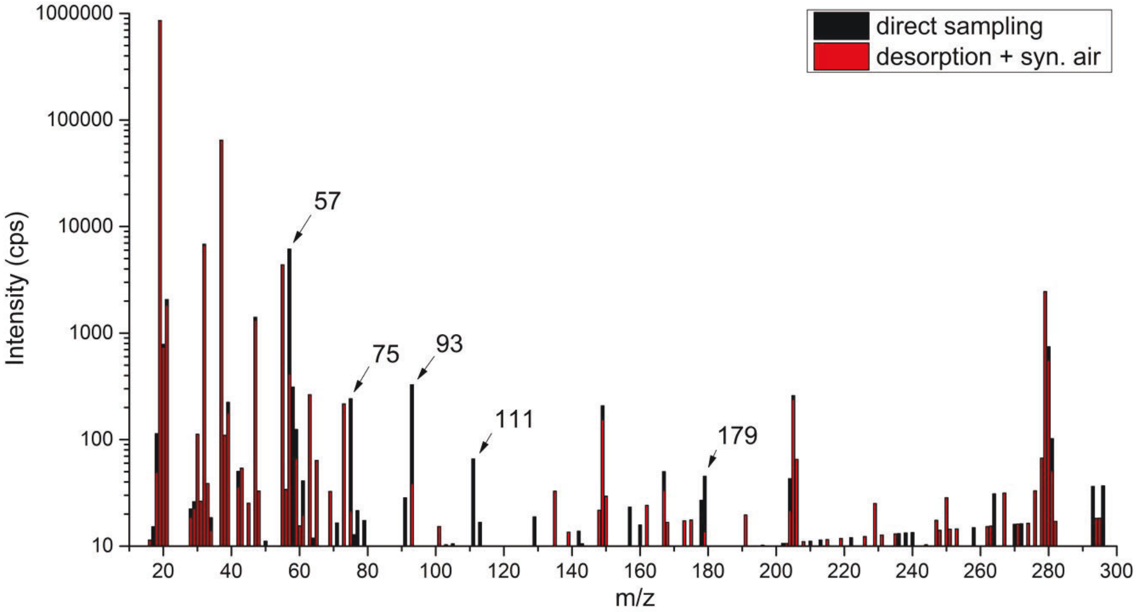

Figure S1: Mass spectrum of DBP using H_3O^+ reagent ions. Selected peaks presented during the direct sampling of DPB headspace are not related to the DBP ion chemistry.

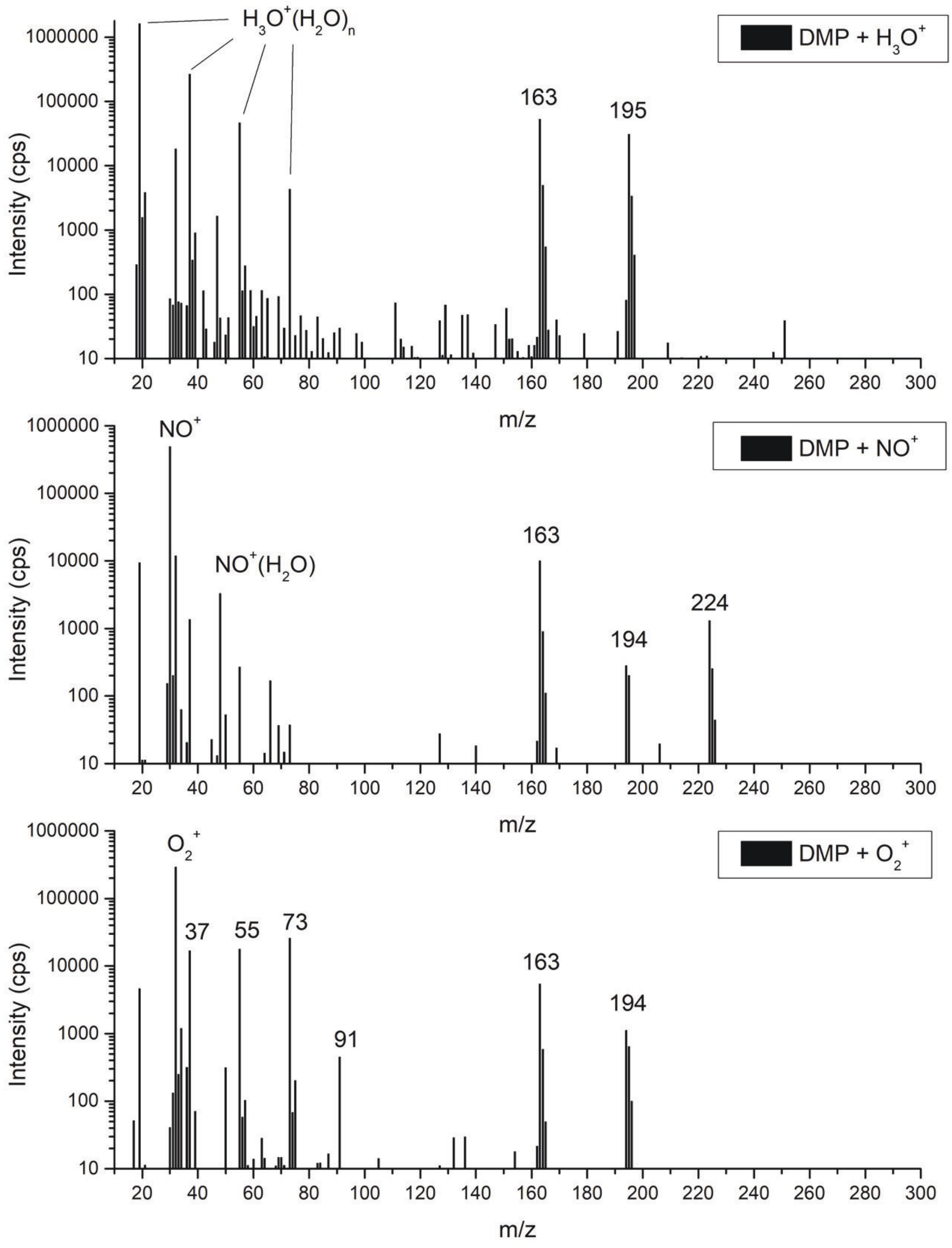

Figure S2: Mass spectrum of DMP using H_3O^+, NO^+ and O_2^+ reagent ions.

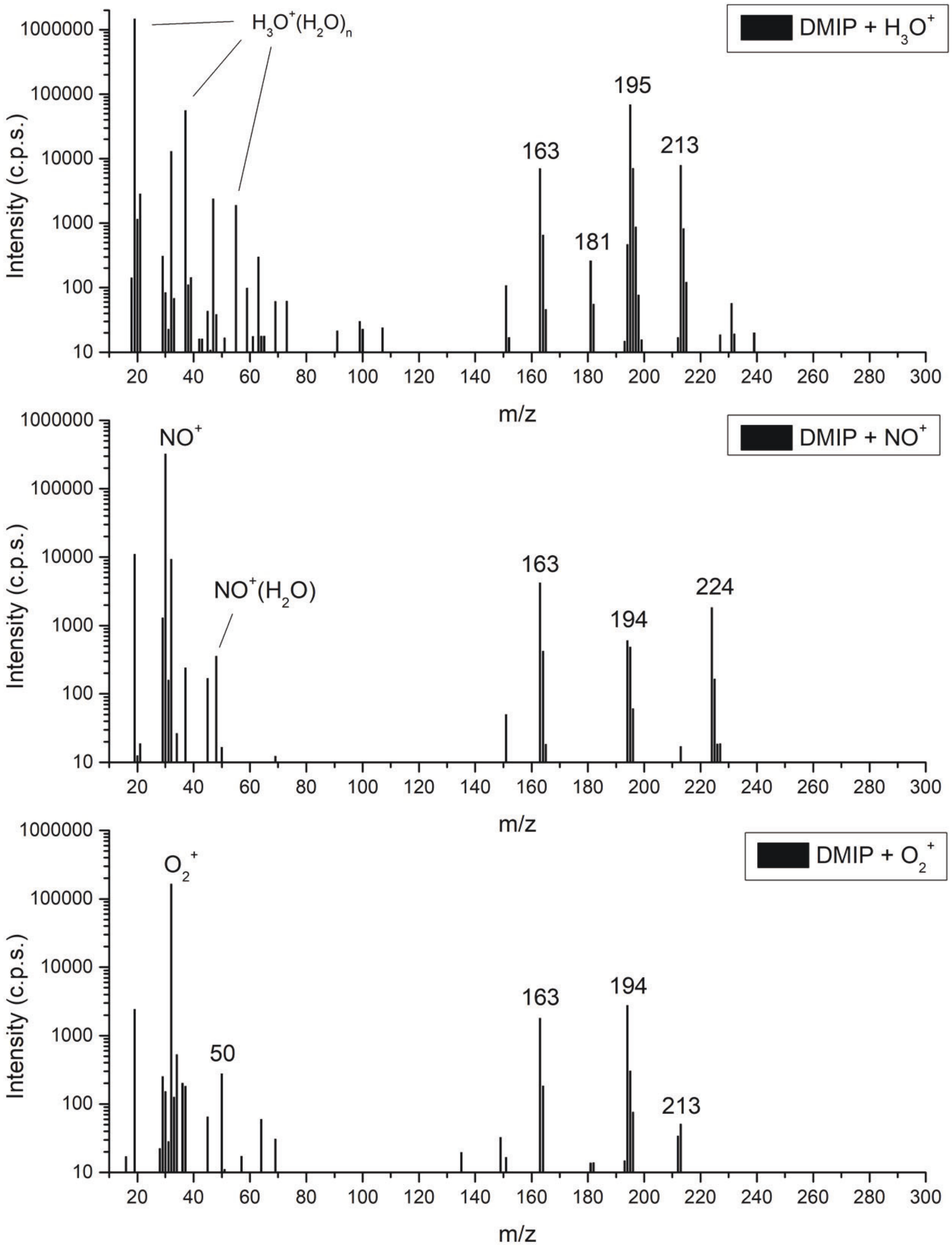

Figure S3: Mass spectrum of DMIP using H_3O^+, NO^+ and O_2^+ reagent ions.

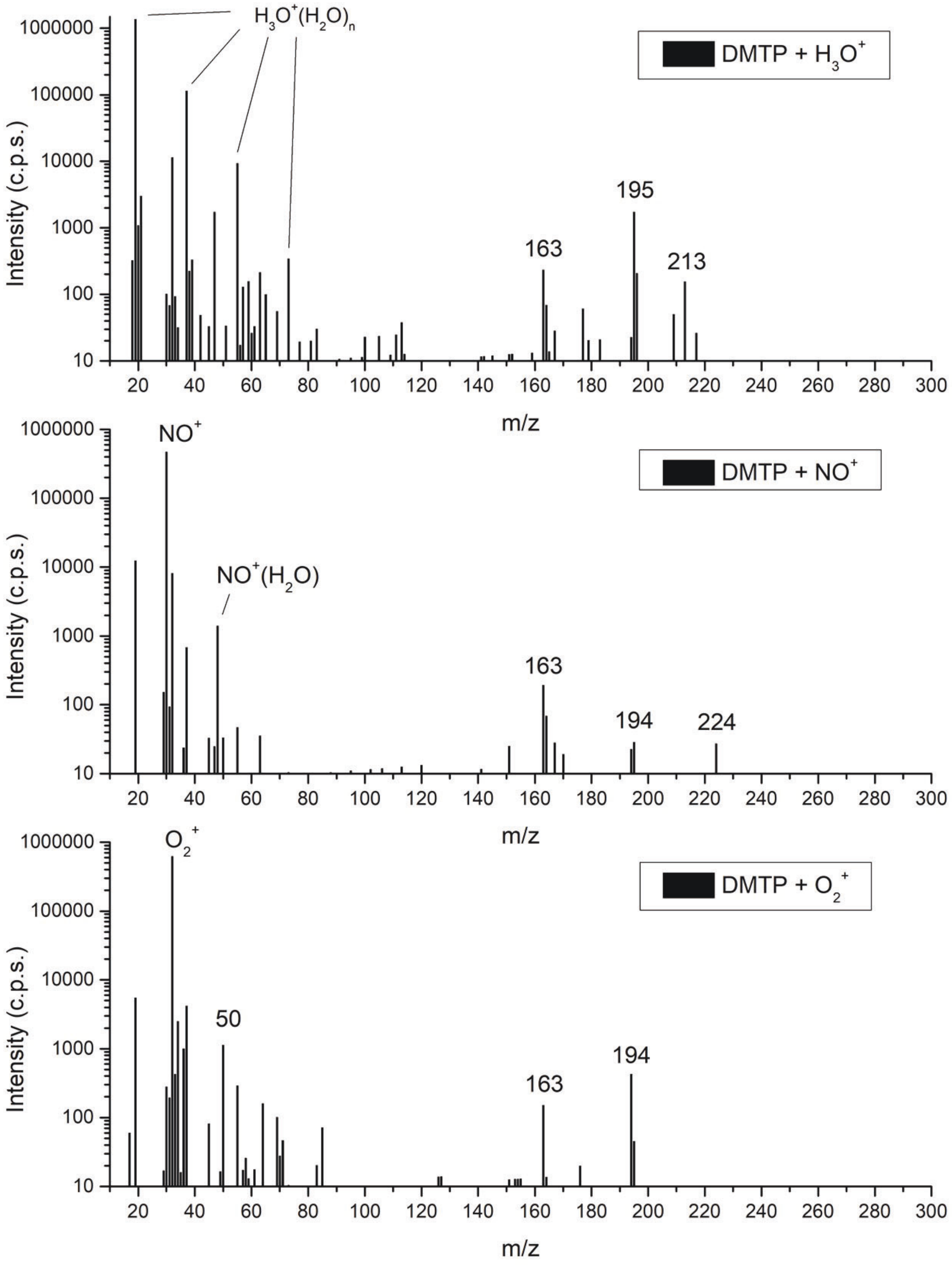

Figure S4: Mass spectrum of DMTP using H_3O^+, NO^+ and O_2^+ reagent ions.

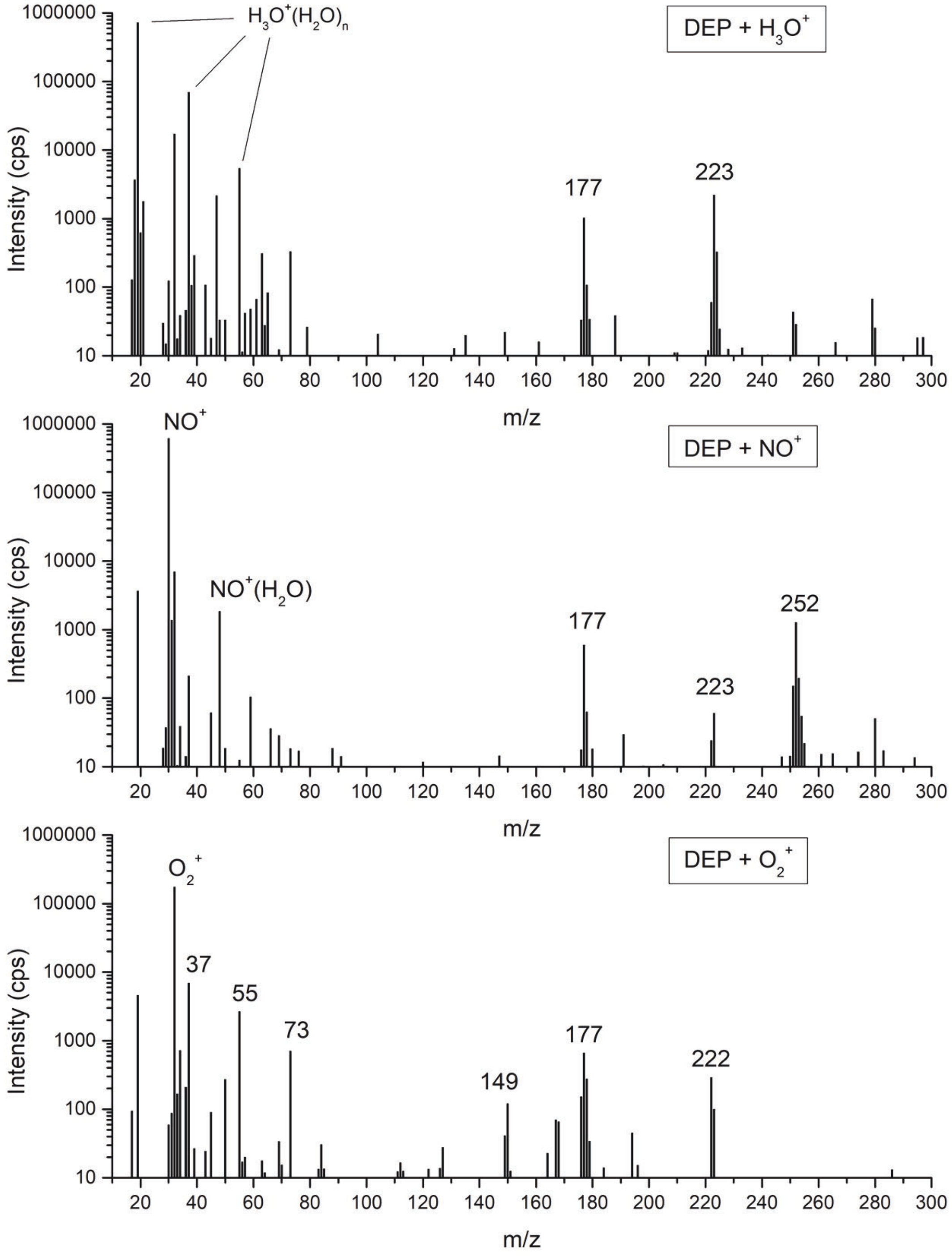

Figure S5: Mass spectrum of DEP using H_3O^+, NO^+ and O_2^+ reagent ions.

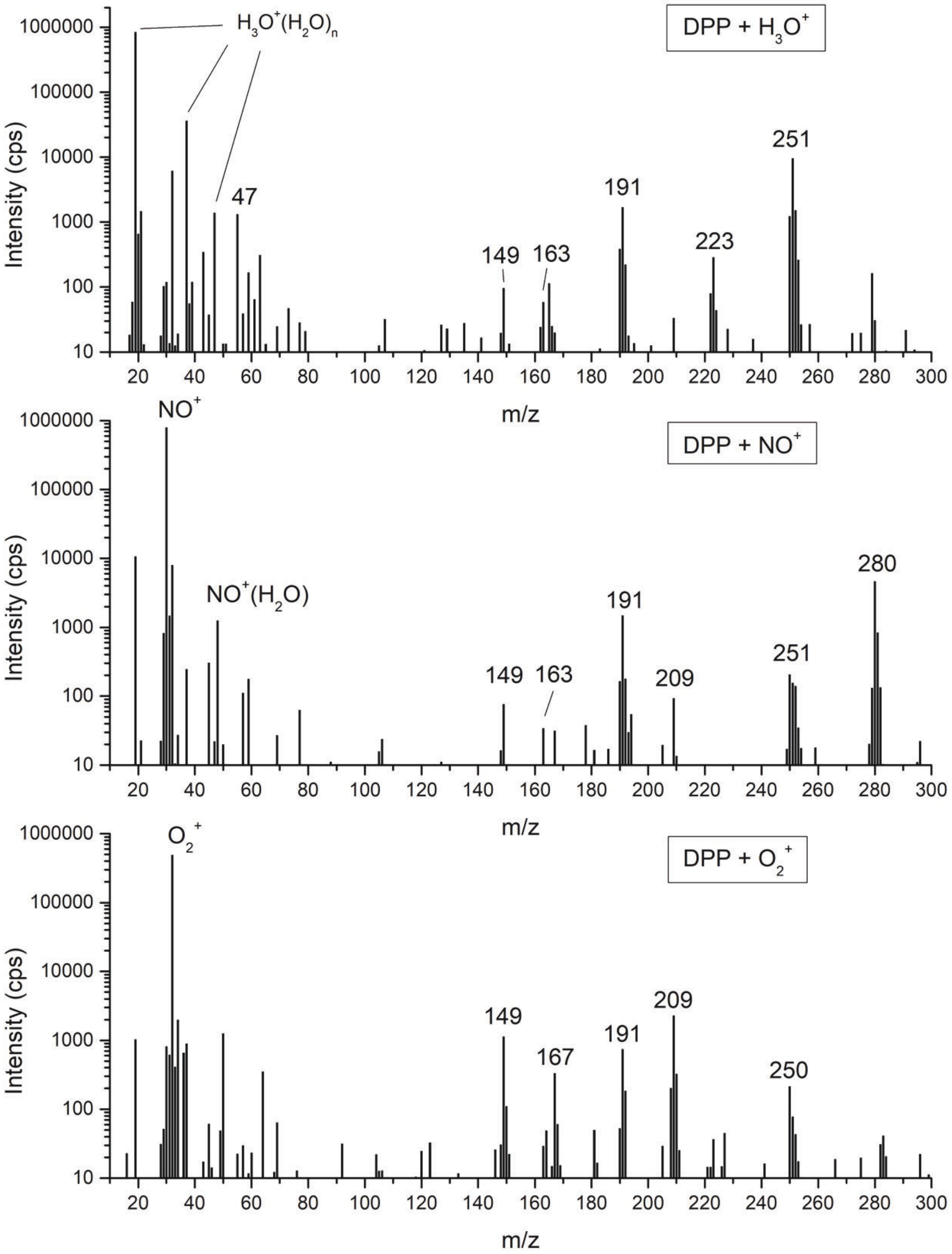

Figure S6: Mass spectrum of DPP using H_3O^+, NO^+ and O_2^+ reagent ions.

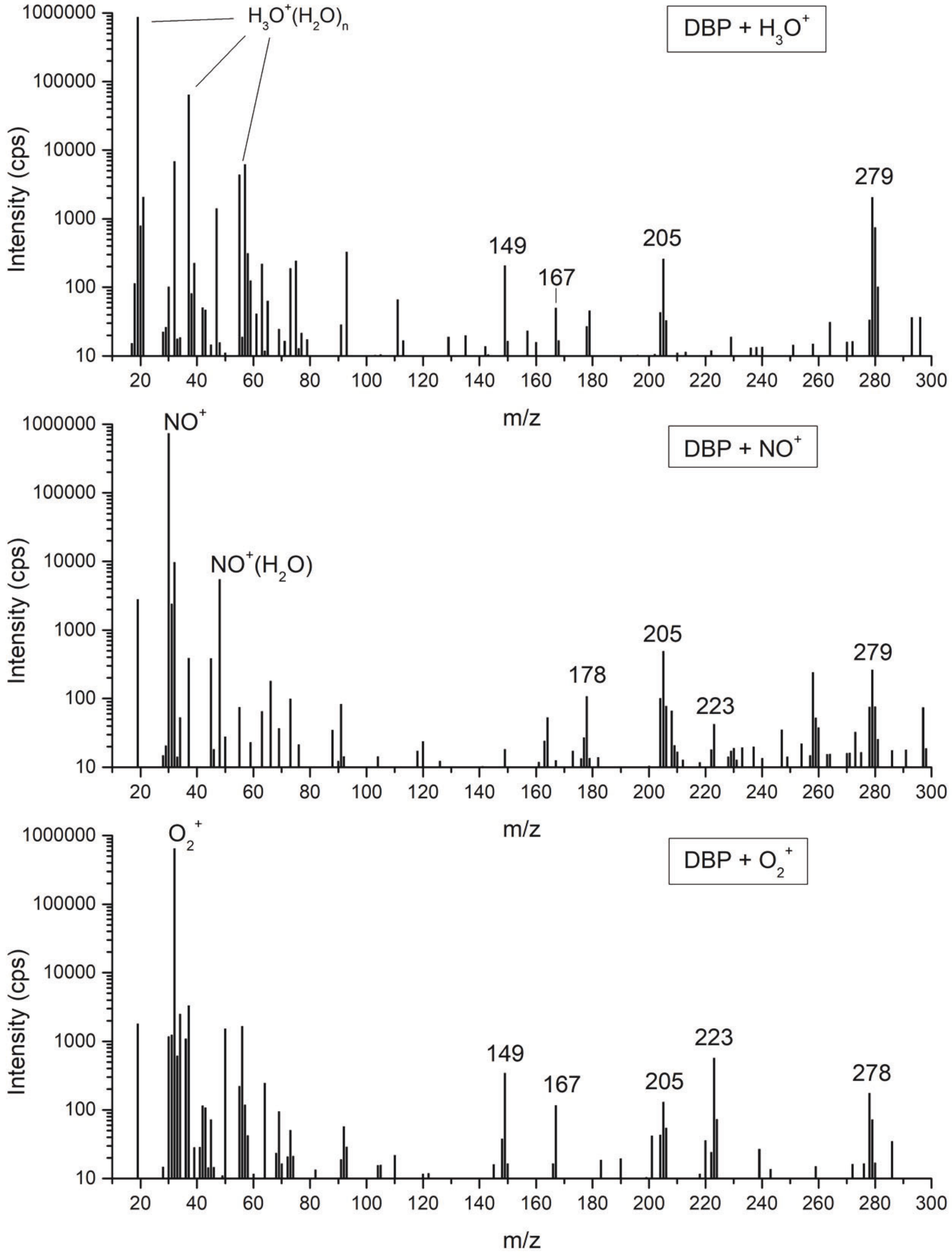

Figure S7: Mass spectrum of DBP using H_3O^+, NO^+ and O_2^+ reagent ions.

ACS Partner Journal

Journal of the American Society for Mass Spectrometry

pubs.acs.org/jasms

Research Article

Ligand Switching Ion Chemistry: An SIFDT Case Study of the Primary and Secondary Reactions of Protonated Acetic Acid Hydrates with Acetone

Anatolii Spesyvyi,* Michal Lacko, Kseniya Dryahina, David Smith, and Patrik Španěl

Cite This: *J. Am. Soc. Mass Spectrom.* 2021, 32, 2251−2260

Read Online

ACCESS | Metrics & More | Article Recommendations | Supporting Information

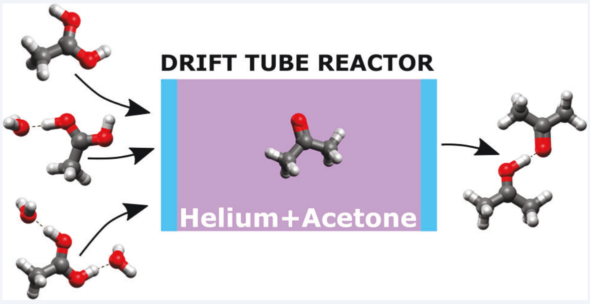

ABSTRACT: A study was performed of the reactions of protonated acetic acid hydrates, $CH_3COOHH^+(H_2O)_n$, with acetone molecules, CH_3COCH_3, using a selected ion flow-drift tube (SIFDT). The rationale for this study is that hydrated protonated organic molecules are major product ions in secondary electrospray ionization mass spectrometry (SESI-MS) and ion mobility spectrometry (IMS). Yet the formation and reactivity of these hydrates are only poorly understood, and kinetics data are only sparse. The existing SIFDT instrument in our laboratory was upgraded to include an octupole ion guide and a separate drift tube by which hydrated protonated ions can be selectively injected into the drift tube reactor and their reactions with molecules studied under controlled conditions. This case study shows that, in these hydrated ion reactions with acetone molecules, the dominant reaction process is ligand switching producing mostly proton-bound dimer ions $(CH_3COCH_3)H^+(CH_3COOH)$, with minor branching into $(CH_3COCH_3)H^+(H_2O)$. This switching reaction was observed to proceed at the collisional rate, while other studied hydrated ions reacted more slowly. An attempt is made to understand the reaction mechanisms and the structures of the reaction intermediate ions at the molecular level. Secondary switching reactions of the asymmetric proton-bound dimer ions lead to a formation of strongly bound symmetrical dimers $(CH_3COCH_3)_2H^+$, the terminating ion in this ion chemistry. These results strongly suggest that, in SESI-MS and IMS, the presence of a polar compound, like acetone in exhaled breath, can suppress the analyte ions of low concentration compounds like acetic acid thus compromising their quantification.

INTRODUCTION

Ion molecule reactions of the type $AB^+ + M \rightarrow AM^+ + B$ are usually classified as ligand switching reactions.[1−3] This process is frequently observed in atmospheric and near-atmospheric pressure humid air in which the cation composition is dominated by hydrated (cluster) cations, for example

$$H_3O^+(H_2O)_n + A \rightarrow AH^+(H_2O)_n + H_2O \tag{1}$$

Such reactions govern the ion chemistry important for chemical ionization in the analytical techniques of secondary electrospray ionization mass spectrometry (SESI-MS)[4−7] and ion mobility spectrometry (IMS).[8−10] There have been few studies of these reactions considering their dominance in the above systems.[2,11,12] One notable study involving $H_3O^+H_2O_{(1,2,3)}$ reactions was performed more than two decades ago,[2] which showed switching occurred rapidly between these H_3O^+ hydrates and oxygen-bearing polar organic molecules, A, such as alcohols, aldehydes, carboxylic acids, and ketones, but such reactions are very slow for hydrocarbons.

There were only a few previous studies of the specific further reactions of the $AH^+(H_2O)_n$ ions with polar molecules M in IMS,[13−15] yet they are involved in SESI-MS,[5,6] for example

$$AH^+(H_2O)_n + M \rightarrow AH^+(M)(H_2O)_{n-1} + H_2O \tag{2a}$$

$$\rightarrow MH^+(H_2O)_n + A \tag{2b}$$

These reactions produce proton-bound mixed dimers or hydrated protonated M. When the concentration of M is high enough, secondary reactions can occur that replace the H_2O molecules, and even replace the molecule A, forming the symmetrical dimer.

$$AH^+(M)(H_2O)_n + M \rightarrow MH^+M + A + nH_2O \tag{3}$$

Received: May 28, 2021
Revised: July 6, 2021
Accepted: July 7, 2021
Published: July 20, 2021

https://doi.org/10.1021/jasms.1c00174

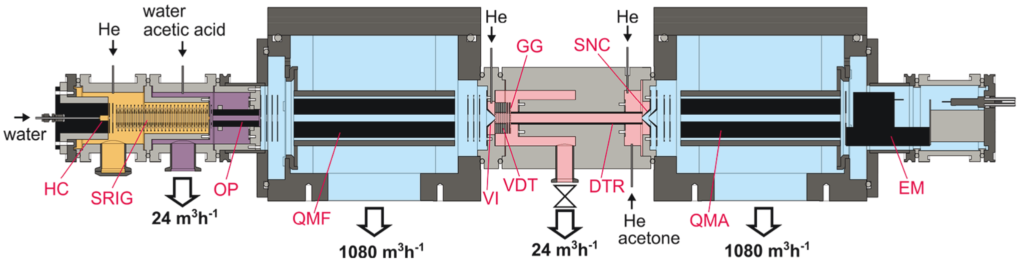

Figure 1. A SIFDT apparatus scheme with the designated input gas flows and indicated pumping arrangement. The dark gray parts are metal chambers; light gray indicates polypropylene chambers. The gas pressures in the different sectors are marked with colors: 5 mbar (yellow), 0.3 mbar (violet,) 5×10^{-6} mbar (blue), 1.9 mbar (pink). Also indicated are the hollow cathode ion source (HC), the stacked ring ion guide (SRIG), the octupole (OP), the quadrupole mass filter (QMF), the Venturi inlet (VI), the Venturi flow-drift tube (VDT), the gating grid (GG), the drift tube reactor (DTR), the ion sampling nose cone (SNC), the quadrupole mass analyzer (QMA), and the electron multiplier with conversion dynode (EM).

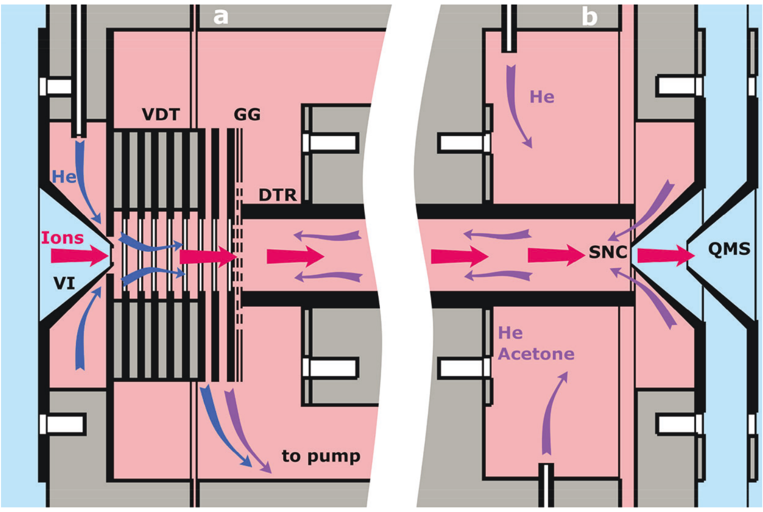

Figure 2. A detailed schematic view of the VDT (a) and SNC (b) regions with designated gas and ion flows.

Clearly, in mixtures of polar molecules A and M, whatever their type, ligand switching ion chemistry can become very complicated, and an analysis by SESI-MS and IMS will be difficult. This is even more so if the rate coefficients for the reactions are not known. To better understand the kinetics of such complex reaction systems, we initiated wide-ranging experimental studies of ligand switching reactions using our recently developed selected ion flow-drift tube (SIFDT) instrument,[16] by which it is possible to selectively inject hydrated cluster ions into a relatively low-pressure flow-drift tube reactor. As a beginning and as a case study, we chose to investigate the reactions of protonated acetic acid monohydrate $C_2H_4O_2H^+(H_2O)$ with acetone molecules, C_3H_6O, and the subsequent secondary reactions of the primary product ions of this reaction with acetone molecules. The rationalization for the choice of these compounds lies in a desire to accurately measure their concentrations simultaneously in exhaled breath using SESI-MS. Preliminary studies using SIFT-MS have shown that, in exhaled breath, the acetic acid concentrations is typically at a few parts per billion by volume (ppbv), whereas acetone is measured at hundreds of ppbv.[17−19] The major uncertainty that must be addressed is whether or not the higher concentration of acetone interferes with an analysis of the much lower acetic acid concentration due to possible interference by the ligand switching reactions described above.

EXPERIMENTAL SECTION

Selected Ion Flow-Drift Tube, SIFDT. All experiments were conducted on the SIFDT instrument that has been described in earlier publications[16,20] but with an upgraded ion source that facilitates a hydrated reagent ions production by a chemical ionization. A schematic representation of the SIFDT highlighting the modifications needed for the present study is shown in Figure 1.

Water vapor is introduced into the hollow cathode (HC) discharge where $H_3O^+(H_2O)_n$ ions are produced. These ions are directed toward the stacked ring ion guide (SRIG) housed in a polypropylene vacuum chamber containing a helium buffer gas at a pressure of 5 mbar. The SRIG is 100 mm long and comprises several 0.5 mm thick stainless steel electrodes, with 10 mm ID central apertures that are spaced by 1.5 mm. A sinusoidal voltage of opposite phase (4.5 MHz frequency and 200 V peak-to-peak) is applied to alternating SRIG electrodes from a homemade radio-frequency (RF) power supply based on the Ivo Cermak design.[21] Direct-current (DC) voltages establishing the electrical drift field (E = 25 V cm^{-1}) for the SRIG are provided by a resistor divider network powered via two inductor chokes from an external supply. A stainless steel disk with a 4 mm central aperture is placed at the end of the SRIG. Ions directed by the *E* field and helium flow enter the next chamber into an octupole (OP) ion guide 50 mm long, 3 mm field radius, at a helium pressure of ~0.3 mbar. This chamber is evacuated through the booster port of an Edwards nEXT300 turbomolecular pump. The OP is powered by an RF sinusoidal voltage, 7.9 MHz frequency, 400 V peak-to-peak using an RF power supply of the same design as that for the SRIG. The ions are guided via the OP to the disk with a 2 mm central aperture into a quadrupole mass filter (QMF). The filtered ions are introduced via the Venturi inlet (VI) to the short 15 mm Venturi flow-drift tube (VDT) with $E = 3$ V cm^{-1}, which consists of stainless steel electrodes 0.5 mm thick with 10 mm central apertures isolated by polytetrafluoroethylene (PTFE) spacers of thickness 1.5 mm. The last two ring electrodes of the VDT (see Figure 2) are not constrained with spacers, which would restrict the pumping out of the He carrier gas. A precise ion current modulation can be accomplished by a stack of three thin (0.1 mm) steel hexagonal (0.6 mm side) grids, a similar approach that is used in low-pressure ion mobility spectrometry.[22] The first grid is connected to the last electrode of the VDT, the second gating grid (GG) is connected to a pulse generator, and the third grid is connected to the entrance to the drift tube reactor (DTR). These grids are spaced by 0.4 mm insulators. The ion arrival time distributions (ATD) at the downstream detector can thus be recorded using a single pulse or Hadamard sequence modulation of the GG.[23]

The DTR, in which the ion−molecule reactions occur, is in the form of a resistive glass tube 145 mm long, 10 mm ID, as supplied by Photonis. At the end of this DTR is a sampling nose cone (SNC) with a central 0.5 mm orifice through which reagent and product ions are sampled into the quadrupole mass analyzer (QMA) and detected by the electron multiplier with a conversion dynode. A helium buffer gas and the sample gas are introduced into the DTR near to the SNC and pumped along the DTR and exit before they can enter the VDT. This (counter) flow is in opposition to the direction of ion drift due to the axial *E*-field, which ensures that the composition of gas in DTR is homogeneous and is not affected by any gas from the VDT (see Figure 2). The DTR chamber is pumped by the valve-regulated booster port of an Edwards nEXT300 turbomolecular pump (see Figure 1).

Experimental Setup for the Present Studies. For the present experiments the DTR entrance potential was fixed at 100 V, the exit potential at 3 V, the helium pressure at 1.9 mbar, and the room temperature at 20 °C. All electrode potentials upstream of the DTR were referenced to the DTR entrance potential. Thus, the ratio of the electric field strength *E* to the gas number density in the drift tube reactor (DTR), *N*, that is, the reduced electric field, *E*/*N*, was held at 14.2 Townsend (1 Td = 10^{-17} V cm^2). This value was chosen as the smallest practically usable *E*/*N* from the viewpoint of a trade-off between a sufficient QMA ion signal intensity for kinetics measurements and being as close as possible to thermalized conditions in the ion-chemical reactor (see quantitative estimates later).

Hydrated protonated acetic acid reagent ions were produced in reactions of $H_3O(H_2O)_n^+$ cluster ions with acetic acid molecules following the introduction of acetic acid/water vapor into the OP chamber through a needle valve (see typical QMF spectra in Figure S1). The dihydrate ion $C_2H_4O_2H^+(H_2O)_2$ at *m*/*z* 97 was selected by the QMF and injected into the DTR. A potential difference of ~12 V between OP and VI corresponds to the kinetic energy of ions injected to VDT of 12 eV, which results in a collisional induced dissociation of the hydrated ions on helium atoms prior to entering the VDT. Note that at the *E*/*N* of 14.2 Td no fragmentation was observed to take place in DTR or SNC as checked by lowering the *E*/*N*. The main dissociation product ion was the ion of interest, the monohydrate $C_2H_4O_2H^+(H_2O)$ at *m*/*z* 79 (~90%) together with a small fraction of protonated acetic acid $C_2H_4O_2H^+$ at *m*/*z* 61 (5%) and some residual dihydrate at *m*/*z* 97 (5%) (see Figure S2a). For additional experiments, the protonated acetone monohydrate $C_3H_6OH^+(H_2O)$ (QMF at *m*/*z* 77) was prepared by introducing acetone/water vapor into the OP chamber, and this hydrate was injected into the DTR together with some fraction of $C_3H_6OH^+$ at *m*/*z* 59 as formed by partial collision-induced dissociation (CID). To inject the proton-bound dimer of acetone and acetic acid, $C_3H_6OH^+C_2H_4O_2$ (QMF at *m*/*z* 119), an acetone/acetic acid/water vapor mixture was introduced into the OP chamber.

In order to study the reactions of the various injected cluster ions with acetone molecules, a sample gas consisting of mixtures of acetone in helium (helium is also the buffer gas) was prepared in Nalophan bags at a concentration ~0.5% by volume and introduced at known, variable flow rates into the DTR via a needle valve and a mass flow meter. There are two contraflows of clean He introduced: one through the VI and the other one introduced near to the exit of DTR, each at a flow rate of 75 sccm. Thus, the VDT contained only pure He, and the DTR contained a defined mixture of He with acetone vapor allowing accurate molecule reaction kinetics studies under well-defined conditions. Note that the injected ions were thermalized via He collisions in the VDT prior to entering the DTR. The sample gas flow rate was limited to a maximum of 1.6 sccm to keep the pressure in the DTR relatively undisturbed (1.91−1.94 mbar).

Computational Details. All quantum-chemistry calculations were performed using ORCA 4.2.1 software.[24] Molecular geometries were first optimized using the following density functional theory (DFT) method: RKS BP86 RI SVP def2/J[25] with D3BJ correction[26] and then optimized again using the TZVPP basis set instead of SVP (see visualized[27] geometries Figure S6). The latter level of theory was also used to calculate vibrational frequencies and thermodynamic quantities for normal temperature and pressure (298.15 K, 1 atm). Note that the initial guessed geometries for $C_3H_6OH^+$-$C_2H_4O_2(H_2O)$ and some other clusters were obtained by the ab initio molecular dynamics (AIMD) module of ORCA with DFT: BLYP D3 def2-SVP level of theory as the total energy minima. The geometries were checked for imaginary frequencies, and additional optimization was performed if such were present.

Then the E_{MDCI} energy (Single-Point Energy) calculation for the final geometry was performed at the DLPNO-CCSD(T)[24] cc-pVQZ[28] cc-pVQZ/C[29] level of theory. For each ion and each neutral molecule, Gibbs free energy, G_{298}, was calculated by combining the DFT calculations $(G - E_{\mathrm{el}})_{\mathrm{DFT}}$ with the single-point electron energy for the same geometry E_{MDCI}. The thermochemistry of the reactions was then calculated as a difference of Gibbs free energies between products and reactants, ΔG_{298}.To test whether the selected levels of theory provide appropriate energetics, the method was benchmarked on the known proton affinities of water, acetic acid, and

https://doi.org/10.1021/jasms.1c00174
J. Am. Soc. Mass Spectrom. 2021, 32, 2251−2260

Table 1. Results Obtained for Reagent Ions Listed for Ion Residence Time in the DTR (t_r), Ion Mobility (K), Reduced Ion Mobility (K_0), Mean Ion-Acetone Molecule Interaction Energy (E_r), Measured Rate Coefficient (k_{exp}) with Standard Deviations and Capture Rate Coefficient (k_{Su})

ion	m/z	t_r, μs	K, cm^2 V^{-1} s^{-1}	K_0, cm^2 V^{-1} s^{-1}	E_r, eV	k_{exp}, 10^{-9} cm^3 s^{-1}	k_{Su}, 10^{-9} cm^3 s^{-1}
H_3O^+	19	179	12341	21.6	0.10		3.6
$C_3H_6OH^+$	59	305	7331	12.8	0.08	1.5 ± 0.1[a]	2.6
$C_2H_4O_2H^+$	61	281	7950	13.9	0.08	2.7 ± 0.3	2.5
$C_3H_6OH^+(H_2O)$	77	362	6217	10.9	0.07	1.8 ± 0.1	2.5
$C_2H_4O_2H^+(H_2O)$	79	339	6614	11.6	0.07	2.4 ± 0.1	2.4
$C_2H_4O_2H^+(H_2O)_2$	97	404	5593	9.8	0.07	1.3 ± 0.2	2.4
$(C_3H_6O)_2H^+$	117	482	4722	8.2			
$C_3H_6OH^+C_2H_4O_2$	119	462	4912	8.6	0.06	1.2 ± 0.1	2.3

[a] Effective bimolecular rate coefficient for a three-body association reaction of protonated acetone ions with acetone molecules forming the proton-bound dimer $(C_3H_6O)_2H^+$.

acetone calculated as 690.1, 787.7, and 812.4 kJ/mol, which closely correspond to the values from the National Institute of Standards and Technology (NIST) library: 691, 783.7, 812 kJ/mol.[30]

Numerical Modeling of Reaction Kinetics. To model the proposed set of ion-molecular reactions in the DTR, we used the Kinetic of Ion Molecular Interaction Simulator (KIMI) developed by Lacko et al.[31−33] In KIMI, the set of differential equations describing the kinetics of an ion−molecule reaction system is numerically solved using the classical Runge−Kutta method,[34,35] providing the simulation of development of reagent and product ion concentrations along the DTR central axis space coordinate x, for a variable reactant (acetone) concentration.

All ion species included in the model are characterized by their initial concentration, reduced ion mobility, K_0, and their diffusion coefficient[36] D_e. The reaction paths are described by rate coefficient k. In the presence of a homogeneous electric field, the concentrations of all involved particles are calculated by solving a set of one-dimensional x-coordinate dependent differential equations (where $x = 0$ represents the reagent ion entrance, and $x = L = 14.5$ cm represents the end of DTR). Differential equations can be exemplified[32] by that describing a proton transfer reaction between H_3O^+ and M forming MH^+ as

$$\frac{d[MH^+]}{dx} = \frac{k(E/N)[M][H_3O^+] - [MH^+]\frac{D_e}{\Lambda^2}}{v_g + K_0(E/N)N_0\frac{E}{N}} \qquad (4)$$

Here, v_g is the carrier gas velocity, $K_0(E/N)$ is the reduced ion mobility[37] of the MH^+ ion, and $k(E/N)$ is the reaction rate coefficient, both at the specific E/N in the DTR, $N_0 = 2.6867 \times 10^{25}$ m^{-3} is the gas number density at standard temperature and pressure (STP, 273.15 K and 1.013×10^5 Pa), and Λ is the characteristic radial diffusion length.[32] The k values for the system of reactions were optimized to fit the model output to the experimental results.

RESULTS AND DISCUSSION

Experimental Determination of Reaction Rate Coefficients. As is common for flow tube and flow-drift tube experiments, reaction rate coefficients k and product ion distributions were determined by monitoring the decay rate of the reagent ion and the relative signal levels of the reaction product ions by using the downstream MS/detection system as the concentration (number density) of the reactant molecules in the reactor was varied. To obtain k, the reaction (residence) time t_r of the ions is required. In the thermalized SIFT experiments, t_r is traditionally obtained from the flow speed of the carrier gas with some correction to the speed of the reagent and product ions.[38] But in flow-drift tubes the presence of the E-field constrains the various reagent and product ions to move in the field direction at different speeds that are dependent on E/N and their respective mobility. If the mobility of each ion species is known as a function of E/N, the residence time can be calculated. Such data are not available for all the cluster ions involved in these SIFDT studies in He under particular energies (see Table 1). Thus, ion residence times in the DTR needed to be obtained experimentally for all ions involved in this study. From such measurements, ion−molecule interaction energies and mobility values for each ion can also be obtained. The arrival time distributions (ATD) were recorded using a Hadamard modulation of the GG voltage, as described previously[23] and exemplified in Figure 3. These ATDs also include the time needed for ions to transit the QMA to the EM detector, and this shorter time needs to be accounted for to accurately define ion residence times. These flight times were measured in the same manner by applying a Hadamard modulation to the SNC (see the ATDs in Figure S3 and Figure S4). Mean interaction energies of ions with acetone molecules, E_r, were then calculated using the Wannier equation.[39] Ion mobility, K, and reduced ion mobility K_0, corresponding to STP, were calculated from the ion speeds.[37] These parameters

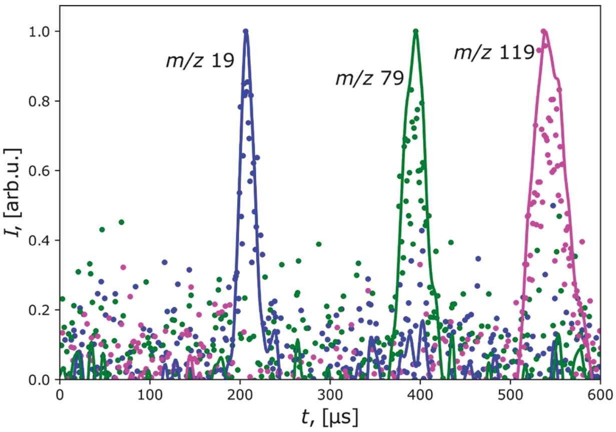

Figure 3. Superimposed arrival time distributions of ions at m/z 19, 79, and 119 measured using the Hadamard modulation method: the data points are experimental values, and the lines are obtained by smoothing with a Gaussian filter.

https://doi.org/10.1021/jasms.1c00174
J. Am. Soc. Mass Spectrom. 2021, 32, 2251−2260

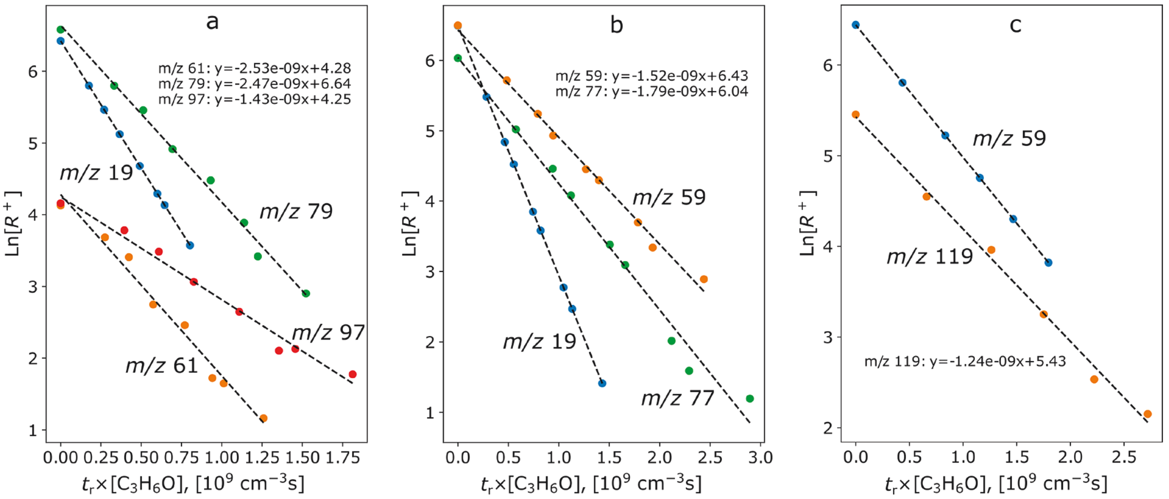

Figure 4. Exemplar plots of reagent ion decays with increase of acetone number density in the DTR multiplied by the corresponding reaction time from which reaction rate coefficients are defined by the slopes of the linear regression fits when the QMF is switched: (a) between *m/z* 19 and 97; (b) between *m/z* 19 and 77; (c) between *m/z* 59 and 119.

are required for the numerical simulation of the ion−molecule reaction kinetics (see eq 4 and later discussion), and they are given in Table 1.

As mentioned above, the determination of the *k* values requires the number density of the reactant neutral molecules (in this case acetone) in the DTR. This was obtained from a simultaneous measurement of the H_3O^+ decay rate in DTR at different acetone/helium mixtures, the measured t_r for H_3O^+ ions, and the rate coefficient for the H_3O^+/acetone proton transfer reaction k_a (3.6×10^{-9} cm^3 s^{-1}) theoretically calculated at the appropriate *T*, E_r.[40] In practice, this was achieved by rapidly switching the QMF between H_3O^+ and the reagent ion (e.g., *m/z* 97), dwelling for 100 ms at each setting to allow the count rates, c/s, for each ion to be accumulated. Thus, from semilogarithmic decay plots of ion intensities in the DTR measured by the QMA/detection system, the acetone number density, [M], in the DTR was calculated[41] as

$$[\mathrm{M}] = \frac{1}{k_a t_r}\ln(I/I_0) \tag{5}$$

where t_r is the reaction time for H_3O^+ ions, and *I* and I_0 are the reagent ion intensity with and without acetone in the reactor. Sample decay plots for the H_3O^+/acetone reaction are shown in Figure 4. Note that the abscissa is plotted as the product of the ion residence time t_r and the acetone molecule number density [M]. When the acetone concentration at each sample flow rate and t_r for each reagent ion are known, the reaction rate coefficients with acetone molecules can be obtained.

Now, the QMF is set to pass the protonated acetic acid dihydrate $C_2H_4O_2H^+(H_2O)_2$ at *m/z* 97 when a partial collisional dissociation results in ions $C_2H_4O_2H^+$ at *m/z* 61 and $C_2H_4O_2H^+(H_2O)$ at *m/z* 79 together with some nondissociated ions at *m/z* 97 that pass through the Venturi inlet into the 15 mm long VDT, where they thermalize in collisions with helium buffer/carrier gas atoms. Then these ions pass via the GGs into the 145 mm DTR and drift, due to the *E*-field, toward the SNC and into the QMA/EM for analysis and detection. The measured intensity of $C_2H_4O_2H^+(H_2O)$ (*m/z* 79) constituted ∼90% of the total ion signal, and those of $C_2H_4O_2H^+$ (*m/z* 61) and $C_2H_4O_2H^+(H_2O)_2$ (*m/z* 97) constituted ∼5% each. The decay curves obtained are given in Figure 4a, from the linear slopes of which the rate coefficients for the reactions of the particular ions with acetone molecules are obtained. Then a similar approach was used to measure the rate coefficients for the reactions of protonated acetone at *m/z* 59 and its hydrate at *m/z* 77 with acetone molecules, and the decay curves obtained are shown in Figure 4b.

Finally, to measure the rate coefficient for the reactions of the mixed proton-bound dimer of acetone and acetic acid, $C_3H_6OH^+C_2H_4O_2$ (*m/z* 119), with acetone, the QMF was rapidly switched between *m/z* 59 and 119. The decay plots are shown in Figure 4c. Note that *m/z* 59 was used, because *m/z* 19 reacted away and was not available in the OP chamber when acetone and acetic acid were introduced in sufficient amounts to produce *m/z* 119. So, the earlier measured effective binary rate coefficient of 1.5×10^{-9} cm^3 s^{-1} for the ternary association reaction of *m/z* 59 with acetone molecules (producing the acetone dimer ion at *m/z* 117) was used to calculate the acetone number densities.

All the measured decay plots are available in Figure S5. The derived rate coefficients for all of the reactions are given in Table 1 as k_{exp} values in the usual units (i.e., cm^3 s^{-1}). The estimated uncertainty of the derived absolute rate coefficients is at most ±30% for this method. The uncertainty of the relative values is smaller, typically less than 10%, as indicated by the standard deviations of multiple measurements given in Table 1.

It is instructive to compare k_{exp} with the theoretical values according to Su,[40] given in Table 1 as k_{Su}, which predict the capture rate coefficients at which the reaction intermediate complex is formed. In the case of switching reactions, the complex can either dissociate to various products or back to reactants, which explains why some $k_{exp} < k_{Su}$. To gain further insight into the nature of these ion-chemical reactions, it is important to identify the ion products of the reactions. This aspect of this study is considered in the next sections, where the kinetics and energetics of the reactions, and possible branching ratios of the ion products, are discussed.

Experimental Product Ion Distributions. To obtain the experimental product ion distributions for specific reactions,

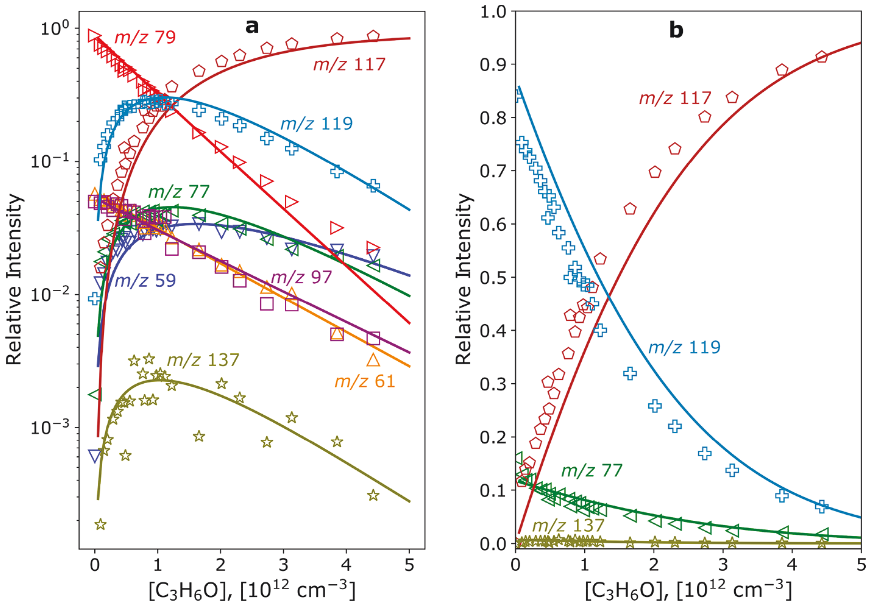

Figure 5. (a) Dependence of the relative reactant and product ion intensities on the acetone molecule number density in the DTR. (b) Dependence of the selected product ion percentages on acetone molecule number density in the DTR. The experimental results for each *m/z* are shown as data points, and the corresponding kinetic model dependencies are shown as solid lines.

Table 2. Gibbs Free Energy Differences, ΔG_{298}, from Quantum-Chemistry Calculations for the Reactions of the Ions Indicated with Acetone Molecules, C_3H_6O[a]

N	reagent ion	*m/z*	product ions	*m/z*	ΔG_{298}, kJ/mol
1	$C_2H_4O_2H^+$	61	$C_3H_6OH^+ + C_2H_4O_2$	59	−23.5
2			$C_2H_4O_2H^+(C_3H_6O)$	119	−97.9
3	$C_2H_4O_2H^+(H_2O)$	79	$C_2H_4O_2H^+(C_3H_6O) + H_2O$	119	−38.2
4			$C_3H_6OH^+(H_2O) + C_2H_4O_2$	77	−18.5
5			$C_3H_6OH^+C_2H_4O_2(H_2O)$	137	-(44.5 to 62.6)
6			$C_3H_6OH^+ + H_2O + C_2H_4O_2$	59	+36.1
7			$C_3H_6OH^+ + C_2H_4O_2(H_2O)$	59	+7.3
8	$C_2H_4O_2H^+(H_2O)_2$	97	$C_3H_6OH^+C_2H_4O_2(H_2O) + H_2O$	137	-(3.3 to 21.4)
9			$C_2H_4O_2H^+(C_3H_6O) + 2H_2O$	119	−0.2
10			$C_3H_6OH^+(H_2O) + C_2H_4O_2 + H_2O$	77	+19.5
11			$C_3H_6OH^+(H_2O) + C_2H_4O_2(H_2O)$	77	+26
12	$C_3H_6OH^+C_2H_4O_2$	119	$C_3H_6OH^+(C_3H_6O) + C_2H_4O_2$	117	−14.7
13	$C_3H_6OH^+(H_2O)$	77	$C_3H_6OH^+(C_3H_6O) + H_2O$	117	−34.4
14	$C_3H_6OH^+$	59	$C_3H_6OH^+(C_3H_6O)$	117	−89
15	$C_3H_6OH^+C_2H_4O_2(H_2O)$	137	$C_3H_6OH^+(C_3H_6O) + C_2H_4O_2 + H_2O$	117	−11.6 to +6.5

[a] The values in round parentheses represent ranges for the different geometries that are considered for the *m/z* 137 complex.

full scan mass spectra at the QMA for different acetone number densities in the DTR were recorded (see Figure S2). Then the selected ion intensities for the injected reagent ions (*m/z* 61, 79, 97) and the reaction product ions (*m/z* 59, 77, 117, 119, 137) were recorded as the flow rate of the acetone/helium mixture (from a Nalophan bag) was varied. The primary product ion branching ratios were determined in the limit of zero flow, as described in detail for numerous reactions previously studied by the SIFT method.[42] This method reveals the primary reaction products and any secondary reaction products (see Figure 5b). Two bag samples were used: the first contained the same composition as that used for the rate coefficient measurement with the defined acetone number density to flow rate ratio (from the known H_3O^+ proton transfer reaction); the second contained a lower concentration of acetone in the helium to facilitate the identification of the relative product ion signals in the limit of zero acetone concentration (no secondary reactions). Note that the carrier/buffer gas in the DTR is essentially dry, and so free H_2O molecules are not significantly involved in the ion chemistry discussed below.

Typical experimental data are given (in Figure 5), which show the primary reactant and product ions observed when the major reagent ion, monohydrated protonated acetic acid, $C_2H_4O_2H^+(H_2O)$ at *m/z* 79, together with minor breakup product ions $C_2H_4O_2H^+$ at *m/z* 61 and its dihydrate $C_2H_4O_2H^+(H_2O)_2$ at *m/z* 97, react with acetone molecules. The linearity of the plots for the (injected) primary reagent ions is clear. The products of these ion−molecule reactions are given in the following equations.

The direct proton transfer reaction.

$$C_2H_4O_2H^+ + C_3H_6O \rightarrow C_3H_6OH^+ + C_2H_4O_2 \quad (6)$$

This can occur because the proton affinity (PA) of acetone (812 kJ/mol) exceeds that of acetic acid (783.7 kJ/mol),[30] the single product being protonated acetone at m/z 59, which can be seen in Figure 5. The experimentally observed bimolecular rate coefficient for the reaction k_{exp} is equal to the collisional rate coefficient k_{Su}, as indicated in Table 1.

The reaction of the dominant reagent ion, $C_2H_4O_2H^+(H_2O)$, with acetone proceeds as

$$C_2H_4O_2H^+H_2O + C_3H_6O$$
$$\rightarrow C_3H_6OH^+C_2H_4O_2 + H_2O \quad (7a)$$
$$\rightarrow C_3H_6OH^+(H_2O) + C_2H_4O_2 \quad (7b)$$

Both reaction channels involve ligand switching, for (7a) the water molecule being replaced by an acetone molecule and for (7b) the acetic acid molecule being replaced by an acetone molecule. The experimental data in Figure 5 indicate the rapid rise of the product ion at m/z 119, which is the mixed proton-bound dimer (7a) together with ~15% of product ion at m/z 77, hydrated protonated acetone (7b). This overall ligand switching reaction is facile and has a k_{exp} value close to the k_{Su} value (Table 1). The negative ΔG_{298} values for both channels (Table 2) support the observation that this reaction proceeds rapidly. A possible mechanism of the branching in this reaction is discussed further in a later section.

The reaction of the dihydrate of protonated acetic acid, m/z 97, most probably proceeds thus:

$$C_2H_4O_2H^+(H_2O)_2 + C_3H_6O$$
$$\rightarrow C_3H_6OH^+(H_2O)C_2H_4O_2 + H_2O \quad (8a)$$
$$\rightarrow C_3H_6OH^+C_2H_4O_2 + 2H_2O \quad (8b)$$

One of the H_2O molecules is replaced by a C_3H_6O molecule by ligand switching (8a). This is supported by the lowest Gibbs free energy, ΔG_{298}, as listed in Table 2 for the potential product channels. Additional loss (evaporation) of H_2O from the product (8b) is also possible, and according to the data in Table 2 it is exoergic. As can be seen in Table 1, the k_{exp} for reaction (8) is ~60% of k_{Su}. This somewhat lower reaction efficiency could be due to steric hindrance by the additional H_2O molecule.

The obvious decay of the common product ions of reactions (7) and (8), specifically, the mixed proton-bound dimer ion, indicates that it reacts with acetone molecules by ligand switching to form the symmetrical proton-bound dimer ion at m/z 117:

$$C_3H_6OH^+C_2H_4O_2 + C_3H_6O \rightarrow (C_3H_6O)_2H^+ + C_2H_4O_2 \quad (9)$$

The measured k_{exp} for this switching reaction is ~50% of k_{Su} (Table 1), even though this switching reaction is clearly exoergic (Table 2). Again, this is most probably due to either steric hindrance or because a mutual alignment of the approaching acetone molecule and the dimer ion is needed to facilitate the switching within the intermediate ion/molecule complex. This symmetrical proton-bound dimer of acetone is the terminating ion in this complex chemistry, as can be seen in Figure 5. It must also be noted that this dimer ion can be formed by the termolecular reaction of protonated acetone (produced in reaction 6) with acetone molecules mediated by the (otherwise inert) helium carrier/buffer atoms, thus:

$$C_3H_6OH^+ + C_3H_6O + He \rightarrow (C_3H_6O)_2H^+ + He \quad (10)$$

In the experiment, the rate coefficient for this reaction (Figure 4c) was measured as an effective bimolecular reaction with coefficient k_{2eff}, shown in Table 1 as 1.5×10^{-9} cm^3 s^{-1}, which is clearly lower than the collisional rate coefficient. The equivalent termolecular association rate coefficient, k_3 $(=k_{2eff}/[X])$, where [X] is the number density of the stabilizing He atoms in the DTR, is calculated as 3.2×10^{-26} cm^6 s^{-1}, which is in the high range of termolecular reactions.[43] However, the contribution of this production route to the overall production of the symmetrical dimer is small compared to that of reaction 9 because the signal at m/z 59 is much smaller than the signal at m/z 119.

Kinetic Models from Numerical Simulation. The present experimental data can be satisfactorily modeled by two possible approaches:

(i) Simply treat reaction (7) as an immediate binary reaction with an acetone molecule, which proceeds at the collisional rate with a calculated binary rate coefficient $k = 2.8 \times 10^{-9}$ cm^3 s^{-1}.

(ii) A two-step reaction in which an intermediate complex (m/z 137) is formed in association of $C_2H_4O_2H^+(H_2O)$ (m/z 79) with acetone that dissociates into m/z 119 (7a, lifetime 4 μs) and m/z 77 (7b, lifetime 29 μs) corresponding to the experimental branching ratio of 88%−12%.

The $C_3H_6OH^+(H_2O)$ (m/z 77) and $C_3H_6OH^+C_2H_4O_2$ (m/z 119) products in both scenarios then undergo a secondary reaction with acetone molecules resulting in $(C_3H_6O)_2H^+$ (m/z 117). The result of scenario (ii) of the kinetic model as fitted to the experimental date is shown in Figure 5 as solid lines. Further details of the kinetics modeling are in the Supporting Information.

Branching in the $C_2H_4O_2H^+(H_2O)$ Reaction with Acetone Molecules. The observed small intensities of $C_3H_6OH^+C_2H_4O_2(H_2O)$ at m/z 137, together with the kinetic model, suggest that reaction (7) occurs via the formation of a long-lived intermediate complex from which either H_2O or $C_2H_4O_2$ can evaporate. This would result in $C_3H_6OH^+C_2H_4O_2$ (7a) or $C_3H_6OH^+(H_2O)$ (7b). Similar mechanisms have been discussed in the literature that relate to studies of the reactions of proton-bound acetic acid dimers with different bases.[44] To gain further insight into these processes, AIMD simulations were performed. Thus, the acetone molecule was placed near to the $C_2H_4O_2H^+(H_2O)$ ion at three attacking sites, specifically, adjacent to the proton, the methyl radical, and the water molecule, and the simulations were run for 5 ps at two Berendsen thermostat algorithm temperatures, 293 K (room temperature) and 853 K, which is equivalent to a mean interaction energy of 0.073 eV that corresponds to the operating value of E/N of 14.2 Td. Note that these temperatures are only qualitative and that the Berendsen thermostat temperature is not directly equivalent to the interaction energy E_r (Table 1). The resulting sampled and optimized geometries of the reaction intermediate complex shown in Figure 6 can be described and grouped as proton-bound clusters (a, b), hydronium-bound clusters (c, d, f), and a cyclic cluster (e).

https://doi.org/10.1021/jasms.1c00174
J. Am. Soc. Mass Spectrom. 2021, 32, 2251−2260

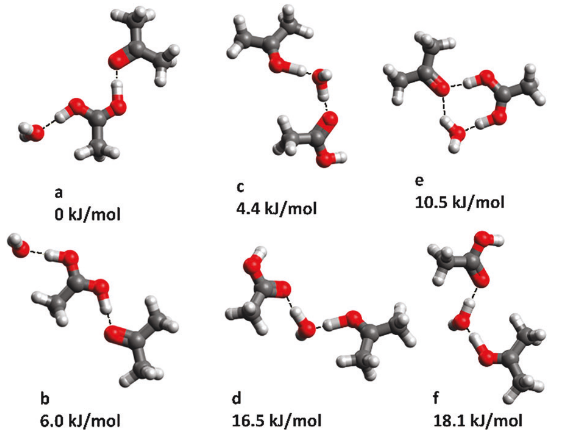

Figure 6. The $C_3H_6OH^+C_2H_4O_2(H_2O)$ geometries from AIMD with the Gibbs free energies relative to the lowest-energy configuration. The attacking sites and Berendsen thermostat temperatures are as follows: (a) proton, 293 K; (b) proton, 853 K; (c) methyl, 293 K; (d) methyl, 853 K; (e) water, 293 K; (f) water, 853 K. The lines indicate hydrogen bonds.

These geometries represent possible arrangements of the intermediate complex of reaction (7). Their structure can indicate corresponding dissociation products: (a) and (b) will likely result in a proton-bound mixed dimer $C_3H_6OH^+C_2H_4O_2$ (7a), and (c), (d) and (f) will dissociate to the protonated acetone hydrate $C_3H_6OH^+(H_2O)$ (7b). The configuration (e) could result in both products.

It is useful to explain this dissociation considering the concept of gas-phase ion affinity (IA), defined as a negative enthalpy change for the association reaction of a given ion with a given molecule. Thus, the H_3O^+ affinity of M is defined as $-\Delta H$ of the reaction

$$M + H_3O^+ \rightarrow M(H_3O^+) \qquad (11)$$

The present calculations give IA[H_3O^+] for acetone as 216.5 kJ/mol and for acetic acid as 197.1 kJ/mol. Thus, when the reaction intermediate complexes (c), (d), and (f) dissociate, the H_3O^+ ion is likely to be bound to a molecule with a higher H_3O^+ affinity, acetone in this case. A similar calculation of the IA of protonated acetic acid to water and to acetone molecules M can be done considering reaction

$$M + C_2H_4O_2H^+ \rightarrow M(C_2H_4O_2H^+) \qquad (12)$$

This gives IA[$C_2H_4O_2H^+$] for water as 99.4 kJ/mol, and for acetone it is 144.1 kJ/mol, explaining why the structures (a) and (b) dissociate to form the proton-bound mixed dimer ion $C_3H_6OH^+C_2H_4O_2$.

■ CONCLUSIONS

A new technique has been developed by upgrading an SIFDT instrument[16,20,45,46] to allow the generation of a wide variety of cluster cations via a newly introduced octupole ion guide followed by m/z filtering by a QMF. This enables experimental studies of kinetics of cluster ion formation and reactivity. The new technique has an advantage over the established experimental techniques like SIFT and SIFDT in that it allows the generation of cluster ions at purities and intensities sufficient for studies of their reactions with volatile compounds. Thus, the features of cluster ion reactions with molecules can now be explored in a controlled way to unravel some of the mysteries of ligand switching ion−molecule reactions important in SESI-MS and IMS and also in the terrestrial troposphere.[47]

As an initial case study of the potential and utility of this modified SIFDT instrument, the reactions of the mono- and dihydrates of protonated acetic acid with acetone molecules have been studied at a low E/N close to the thermalized situation. Actually, the dihydrate of protonated acetic acid molecules, $C_2H_4O_2H^+(H_2O)_2$, at m/z 97 was selected by the QMF and largely dissociated before reacting in the DTR. The reagent ion composition was not pure, being seen by the downstream QMA to be $C_2H_4O_2H^+H_2O$ at m/z 79 (90%) and ∼5% of $C_2H_4O_2H^+$ at m/z 61 and ∼5% of the undissociated primary ion at m/z 97. Thus, it is seen that protonated acetic acid monohydrate reacts with acetone molecules at close to the collisional rate by ligand switching, forming 85% of the asymmetric proton-bound dimer of acetic acid and acetone, $C_3H_6OH^+C_2H_4O_2$, together with 15% of the protonated acetone monohydrate $C_3H_6OH^+(H_2O)$. This observed product branching can be rationalized by considering possible geometrical configurations of the intermediate reaction complex that result from different sites of attack by the acetone neutral molecule.

Following these reactions, it was observed that both product ions undergo secondary ligand switching reactions with acetone to produce a symmetrical proton-bound acetone dimer, $(C_3H_6O)_2H^+$, this ion being more strongly bound than its precursor ions and, thus, the terminating ion in this complex chemistry. Some of these switching reactions proceed at rates somewhat smaller than the upper-limit collisional rates, with coefficients $k < k_c$ (see Table 1). Such a lowering of the reaction rate may be greater for heavily hydrated ions that occur in system like SESI-MS and IMS ion sources, possibly due to a more effective steric hindrance. To verify this assumption, further experiments would be needed. Yet ligand switching will remain the dominant reaction process. This interaction between trace gas analyte molecules and cluster ions in humid matrices could result in the suppression of analyte ions[4] by more abundant molecules leading to an inaccurate quantification and possible misinterpretations of the results. An example of this is the trace concentration of acetic acid and the much larger concentration of acetone in humid exhaled breath, which can compromise the analysis of acetic acid unless switching reactions described in this paper are accounted for.

These initial exploratory studies can now be extended using our modified SIFDT instrument to involve other major polar compounds present in humid exhaled breath, such as ammonia, methanol, and ethanol, in order to further probe the nature of cluster ion−molecule reactions and, in particular, the ligand switching phenomenon.

■ ASSOCIATED CONTENT

SI Supporting Information

The Supporting Information is available free of charge at https://pubs.acs.org/doi/10.1021/jasms.1c00174.

> Mass spectra of ion composition in the OP chamber; mass spectra of ion distributions in the DTR at different acetone abundances; plots of arrival time distributions; semilogarithmic decay plots for the reaction rate coefficient determinations; graphic representation of

the ion geometries; details of the numerical modeling of reaction kinetics (PDF)

AUTHOR INFORMATION

Corresponding Author

Anatolii Spesyvyi — *J. Heyrovský Institute of Physical Chemistry of the Czech Academy of Sciences, 18223 Prague 8, Czech Republic;* orcid.org/0000-0003-0220-0519; Email: anatolii.spesyvyi@jh-inst.cas.cz

Authors

Michal Lacko — *J. Heyrovský Institute of Physical Chemistry of the Czech Academy of Sciences, 18223 Prague 8, Czech Republic; Faculty of Mathematics and Physics, Charles University, 18000 Prague 8, Czech Republic*

Kseniya Dryahina — *J. Heyrovský Institute of Physical Chemistry of the Czech Academy of Sciences, 18223 Prague 8, Czech Republic*

David Smith — *J. Heyrovský Institute of Physical Chemistry of the Czech Academy of Sciences, 18223 Prague 8, Czech Republic*

Patrik Španěl — *J. Heyrovský Institute of Physical Chemistry of the Czech Academy of Sciences, 18223 Prague 8, Czech Republic*

Complete contact information is available at: https://pubs.acs.org/10.1021/jasms.1c00174

Notes

The authors declare no competing financial interest.

ACKNOWLEDGMENTS

The authors gratefully acknowledge partial financial support from the Czech Science Foundation (GACR; Project No. 18-12902S and No. 21-25486S). A.S. also thanks J. Kubišta for help with the RF generator design and K. Sovová for organizational support during the SIFDT instrument upgrade.

REFERENCES

(1) Bohme, D. K.; Mackay, G. I.; Tanner, S. D. Experimental-Study of the Gas-Phase Kinetics of Reactions with Hydrated H_3O^+ Ions (N = 1−3) at 298-K. *J. Am. Chem. Soc.* **1979**, *101* (14), 3724−3730.

(2) Španěl, P.; Smith, D. Reactions of hydrated hydronium ions and hydrated hydroxide ions, with some hydrocarbons and oxygen-bearing organic-molecules. *J. Phys. Chem.* **1995**, *99* (42), 15551−15556.

(3) Klee, S.; Albrecht, S.; Derpmann, V.; Kersten, H.; Benter, T. Generation of ion-bound solvent clusters as reactant ions in dopant-assisted APPI and APLI. *Anal. Bioanal. Chem.* **2013**, *405* (22), 6933−6951.

(4) Lan, J.; Kaeslin, J.; Greter, G.; Zenobi, R. Minimizing ion competition boosts volatile metabolome coverage by secondary electrospray ionization orbitrap mass spectrometry. *Anal. Chim. Acta* **2021**, *1150*, 338209.

(5) Dryahina, K.; Som, S.; Smith, D.; Spanel, P., Reagent and analyte ion hydrates in secondary electrospray ionization mass spectrometry (SESI-MS), their equilibrium distributions and dehydration in an ion transfer capillary: Modelling and experiments. *Rapid Commun. Mass Spectrom.* **2021**, *35* (7). DOI: 10.1002/rcm.9047

(6) Rioseras, A. T.; Gaugg, M. T.; Martinez-Lozano Sinues, P. Secondary electrospray ionization proceeds via gas-phase chemical ionization. *Anal. Methods* **2017**, *9* (34), 5052−5057.

(7) Som, S.; Kubišta, J.; Dryahina, K.; Španěl, P. Parallel secondary electrospray ionisation mass spectrometry and selected ion flow tube mass spectrometry quantification of trace amounts of volatile ketones. *Rapid Commun. Mass Spectrom.* **2021**, *35* (4), No. e8981.

(8) Allers, M.; Kirk, A. T.; Schaefer, C.; Schlottmann, F.; Zimmermann, S., Formation of positive product ions from substances with low proton affinity in high kinetic energy ion mobility spectrometry. *Rapid Commun. Mass Spectrom.* **2021**, *35* (4). DOI: 10.1002/rcm.8998

(9) Jurado-Campos, N.; Garrido-Delgado, B.; Martinez-Haya, B.; Eiceman, G. A.; Arce, L. Stability of proton-bound clusters of alkyl alcohols, aldehydes and ketones in Ion Mobility Spectrometry. *Talanta* **2018**, *185*, 299−308.

(10) Valadbeigi, Y.; Ilbeigi, V.; Michalczuk, B.; Sabo, M.; Matejcik, S. Effect of Basicity and Structure on the Hydration of Protonated Molecules, Proton-Bound Dimer and Cluster Formation: An Ion Mobility-Time of Flight Mass Spectrometry and Theoretical Study. *J. Am. Soc. Mass Spectrom.* **2019**, *30* (7), 1242−1253.

(11) Midey, A. J.; Williams, S.; Arnold, S. T.; Viggiano, A. A. Reactions of $H_3O^+(H_2O)_{(0,1)}$ with alkylbenzenes from 298 to 1200 K. *J. Phys. Chem. A* **2002**, *106* (48), 11726−11738.

(12) Williams, T. L.; Adams, N. G.; Babcock, L. M. Selected ion flow tube studies of $H_3O^+(H_2O)_{(0,1)}$ reactions with sulfides and thiols. *Int. J. Mass Spectrom. Ion Processes* **1998**, *172* (1−2), 149−159.

(13) Ewing, R. G.; Eiceman, G. A.; Stone, J. A. Proton-bound cluster ions in ion mobility spectrometry. *Int. J. Mass Spectrom.* **1999**, *193* (1), 57−68.

(14) Puton, J.; Augustyniak, D.; Perycz, U.; Witkiewicz, Z. Conservation of dimer peak intensity in ion mobility spectrometers with ketone-doped carrier gas. *Int. J. Mass Spectrom.* **2014**, *373*, 43−49.

(15) Puton, J.; Holopainen, S. I.; Makinen, M. A.; Sillanpaa, M. E. T. Quantitative Response of IMS Detector for Mixtures Containing Two Active Components. *Anal. Chem.* **2012**, *84* (21), 9131−9138.

(16) Spesyvyi, A.; Smith, D.; Španěl, P. Selected Ion Flow-Drift Tube Mass Spectrometry: Quantification of Volatile Compounds in Air and Breath. *Anal. Chem.* **2015**, *87* (24), 12151−12160.

(17) Dryahina, K.; Pospisilova, V.; Sovova, K.; Shestivska, V.; Kubista, J.; Spesyvyi, A.; Pehal, F.; Turzikova, J.; Votruba, J.; Spanel, P. Exhaled breath concentrations of acetic acid vapour in gastro-esophageal reflux disease. *J. Breath Res.* **2014**, *8* (3), 037109.

(18) Pysanenko, A.; Španěl, P.; Smith, D. Analysis of the isobaric compounds propanol, acetic acid and methyl formate in humid air and breath by selected ion flow tube mass spectrometry, SIFT-MS. *Int. J. Mass Spectrom.* **2009**, *285* (1−2), 42−48.

(19) Spanel, P.; Dryahina, K.; Rejskova, A.; Chippendale, T. W. E.; Smith, D. Breath acetone concentration; biological variability and the influence of diet. *Physiol Meas* **2011**, *32* (8), N23−N31.

(20) Spesyvyi, A.; Smith, D.; Spanel, P. Ion chemistry at elevated ion−molecule interaction energies in a selected ion flow-drift tube: reactions of H_3O^+, NO^+ and $O_2{}^{\cdot+}$ with saturated aliphatic ketones. *Phys. Chem. Chem. Phys.* **2017**, *19* (47), 31714−31723.

(21) Cermak, I. Compact radio-frequency power supply for ion and particle guides and traps. *Rev. Sci. Instrum.* **2005**, *76* (6), 063302.

(22) Langejuergen, J.; Allers, M.; Oermann, J.; Kirk, A.; Zimmermann, S. Quantitative Detection of Benzene in Toluene- and Xylene-Rich Atmospheres Using High-Kinetic-Energy Ion Mobility Spectrometry (IMS). *Anal. Chem.* **2014**, *86* (23), 11841−11846.

(23) Spesyvyi, A.; Spanel, P. Determination of residence times of ions in a resistive glass selected ion flow-drift tube using the Hadamard transformation. *Rapid Commun. Mass Spectrom.* **2015**, *29* (17), 1563−1570.

(24) Guo, Y.; Riplinger, C.; Becker, U.; Liakos, D. G.; Minenkov, Y.; Cavallo, L.; Neese, F. Communication: An improved linear scaling perturbative triples correction for the domain based local pair-natural orbital based singles and doubles coupled cluster method [DLPNO-CCSD(T)]. *J. Chem. Phys.* **2018**, *148* (1), 011101.

(25) Weigend, F. Accurate Coulomb-fitting basis sets for H to Rn. *Phys. Chem. Chem. Phys.* **2006**, *8* (9), 1057−1065.

(26) Grimme, S.; Ehrlich, S.; Goerigk, L. Effect of the Damping Function in Dispersion Corrected Density Functional Theory. *J. Comput. Chem.* **2011**, *32* (7), 1456−1465.

(27) Hanwell, M. D.; Curtis, D. E.; Lonie, D. C.; Vandermeersch, T.; Zurek, E.; Hutchison, G. R., Avogadro: an advanced semantic chemical editor, visualization, and analysis platform. *J. Cheminf.* **2012** *4*. DOI: 10.1186/1758-2946-4-17

(28) Dunning, T. H. Gaussian-Basis Sets for Use in Correlated Molecular Calculations.1. The Atoms Boron through Neon and Hydrogen. *J. Chem. Phys.* **1989**, *90* (2), 1007−1023.

(29) Weigend, F.; Kohn, A.; Hattig, C. Efficient use of the correlation consistent basis sets in resolution of the identity MP2 calculations. *J. Chem. Phys.* **2002**, *116* (8), 3175−3183.

(30) Hunter, E. P. L.; Lias, S. G. Evaluated Gas Phase Basicities and Proton Affinities of Molecules: An Update. *J. Phys. Chem. Ref. Data* **1998**, *27* (3), 413−656.

(31) Lacko, M.; Michalczuk, B.; Matejcik, S.; Spanel, P. Ion chemistry of phthalates in selected ion flow tube mass spectrometry: isomeric effects and secondary reactions with water vapour. *Phys. Chem. Chem. Phys.* **2020**, *22* (28), 16345−16352.

(32) Lacko, M.; Piel, F.; Mauracher, A.; Španěl, P. Chemical ionization of glyoxal and formaldehyde with H_3O^+ ions using SIFT-MS under variable system humidity. *Phys. Chem. Chem. Phys.* **2020**, *22*, 10170.

(33) Lacko, M. Kinetic of Ion Molecular Interaction Simulator (KIMI Sim), 2.2.2; https://github.com/Progllar/KIMI-Simulator, 2021, accessed 12/05/2021.

(34) Kutta, W. Beitrag zur näherungweisen Integration totaler Differentialgleichungen. *Z. Math. Phys.* **1901**, *46*, 435.

(35) Runge, C. Über die numerische Auflösung von Differentialgleichungen. *Mathematische Annalen* **1895**, *46* (2), 167−178.

(36) Dryahina, K.; Španěl, P. A convenient method for calculation of ionic diffusion coefficients for accurate selected ion flow tube mass spectrometry, SIFT-MS. *Int. J. Mass Spectrom.* **2005**, *244* (2−3), 148−154.

(37) Thomson, G. M.; Schummers, J. H.; James, D. R.; Graham, E.; Gatland, I. R.; Flannery, M. R.; Mcdaniel, E. W. Mobility, Diffusion, and Clustering of K^+ Ions in Gases. *J. Chem. Phys.* **1973**, *58* (6), 2402−2411.

(38) Španěl, P.; Dryahina, K.; Smith, D. A general method for the calculation of absolute trace gas concentrations in air and breath from selected ion flow tube mass spectrometry data. *Int. J. Mass Spectrom.* **2006**, *249*, 230−239.

(39) Wannier, G. H. Motion of Gaseous Ions in Strong Electric Fields. *Bell Syst. Tech. J.* **1953**, *32* (1), 170−254.

(40) Su, T. Parametrization of Kinetic-Energy Dependences of Ion Polar Molecule Collision Rate Constants by Trajectory Calculations. *J. Chem. Phys.* **1994**, *100* (6), 4703−4703.

(41) Spesyvyi, A.; Sovova, K.; Smith, D.; Spanel, P. Increase of the Charge Transfer Rate Coefficients for NO^+ and $O_2^{\cdot+}$ Reactions with Isoprene Molecules at Elevated Interaction Energies. *J. Phys. Chem. A* **2018**, *122* (51), 9733−9737.

(42) Adams, N. G.; Smith, D. Selected ion flow tube (SIFT) - technique for studying ion-neutral reactions. *Int. J. Mass Spectrom. Ion Phys.* **1976**, *21* (3−4), 349−359.

(43) Ikezoe, Y.; Matsuoka, S.; Takebe, M.; Viggiano, A. *Gas Phase Ion−Molecule Reaction Rate Constants Through 1986;* Maruzen: Tokyo, Japan, 1987.

(44) Feng, W. Y.; Lifshitz, C. Reactions of protonated acetic acid clusters $(CH_3COOH)_nH^{(+)}$ (n = 1−3). *J. Mass Spectrom.* **1995**, *30* (12), 1179.

(45) Spesyvyi, A.; Španěl, P.; Sovova, K. Styrene radical cations for chemical ionization mass spectrometry analyses of monoterpene hydrocarbons. *Rapid Commun. Mass Spectrom.* **2019**, *33* (24), 1870−1876.

(46) Spesyvyi, A.; Sovova, K.; Španěl, P. In-tube collision-induced dissociation for selected ion flow-drift tube mass spectrometry, SIFDT-MS: a case study of NO^+ reactions with isomeric monoterpenes. *Rapid Commun. Mass Spectrom.* **2016**, *30* (18), 2009−2016.

(47) Aplin, K. L.; Harrison, R. G. Ions in the Atmosphere. In *Encyclopedia of Atmospheric Sciences*, 2nd ed.; Pyle, J., Zhang, F., Eds.; Academic Press: Oxford, UK, 2015; pp 9−13.

Supporting Information

Ligand Switching Ion Chemistry: An SIFDT Case Study of the Primary and Secondary Reactions of Protonated Acetic Acid Hydrates with Acetone

Anatolii Spesyvyi*[1], Michal Lacko[1,2], Kseniya Dryahina[1], David Smith[1], Patrik Španěl[1]

[1] J. Heyrovský Institute of Physical Chemistry of the Czech Academy of Sciences, Dolejškova 2155/3, 18223 Prague 8, Czech Republic

[2] Charles University, Faculty of Mathematics and Physics, V Holešovičkách 747/2, 18000 Prague 8, Czech Republic

Corresponding author: Anatolii Spesyvyi, J. Heyrovský Institute of Physical Chemistry of the Czech Academy of Sciences, Dolejškova 3, Prague 8, 18223, Czech Republic, +420 26605 2112

Email: anatolii.spesyvyi@jh-inst.cas.cz

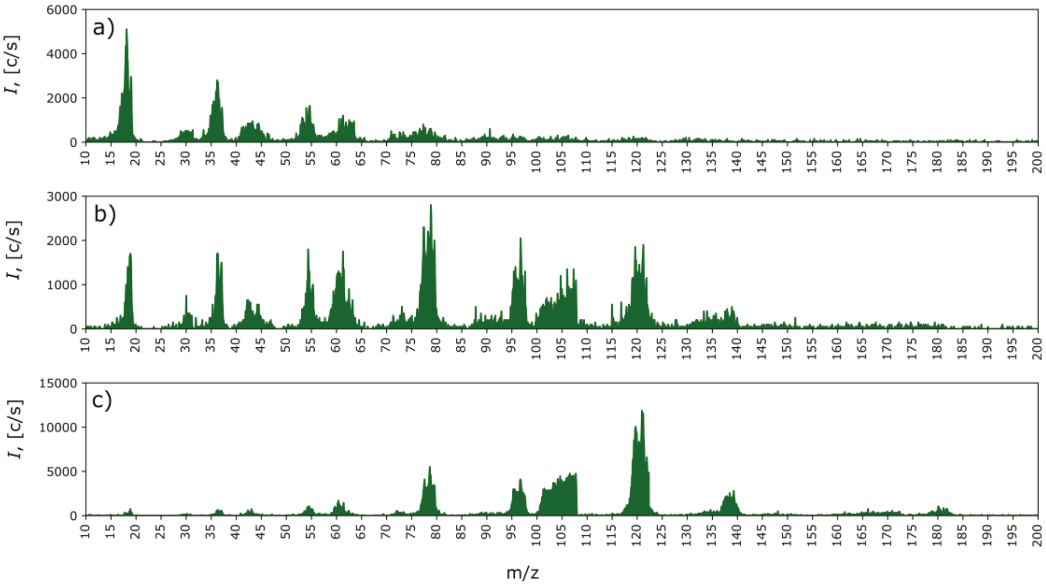

Figure S1. Mass spectra scans by QMF demonstrating ion composition after OP at different abundances of introduced acetic acid/water vapour in OP chamber: valve is closed (a), small amount (b) and valve fully open (c). It can be noticed that ions shift from $H_3O^+(H_2O)_n$ to protonated acetic acid hydrates and protonated acetic acid dimer. The signal in the region *m/z* 100 – 108 is likely an instrumental artefact.

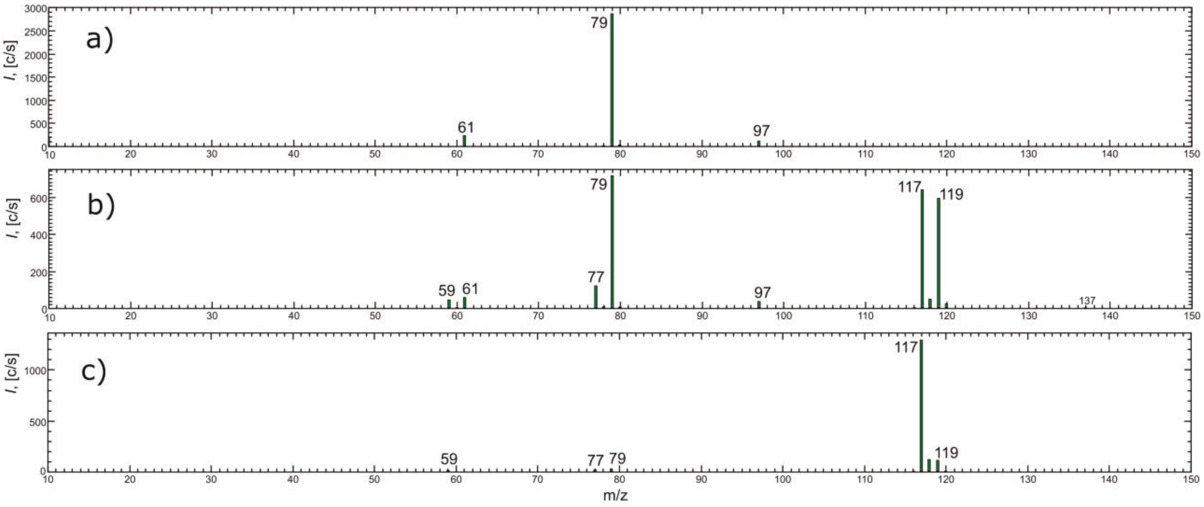

Figure S2. Mass spectral scans by QMA showing ion distributions in the DTR when *m/z* 97 is filtered by QMF and injected at different abundances of acetone into the DTR: a) no acetone; b) small amount; c) maximum amount.

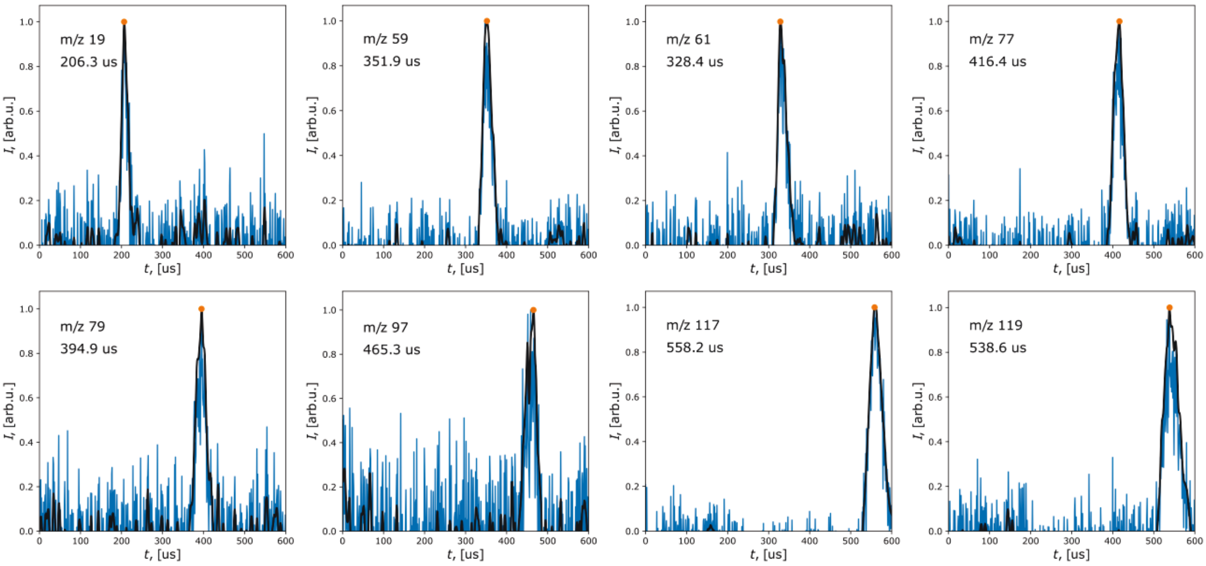

Figure S3. Arrival time distributions of the studied ions obtained using the Hadamard modulation on GM before the DTR.

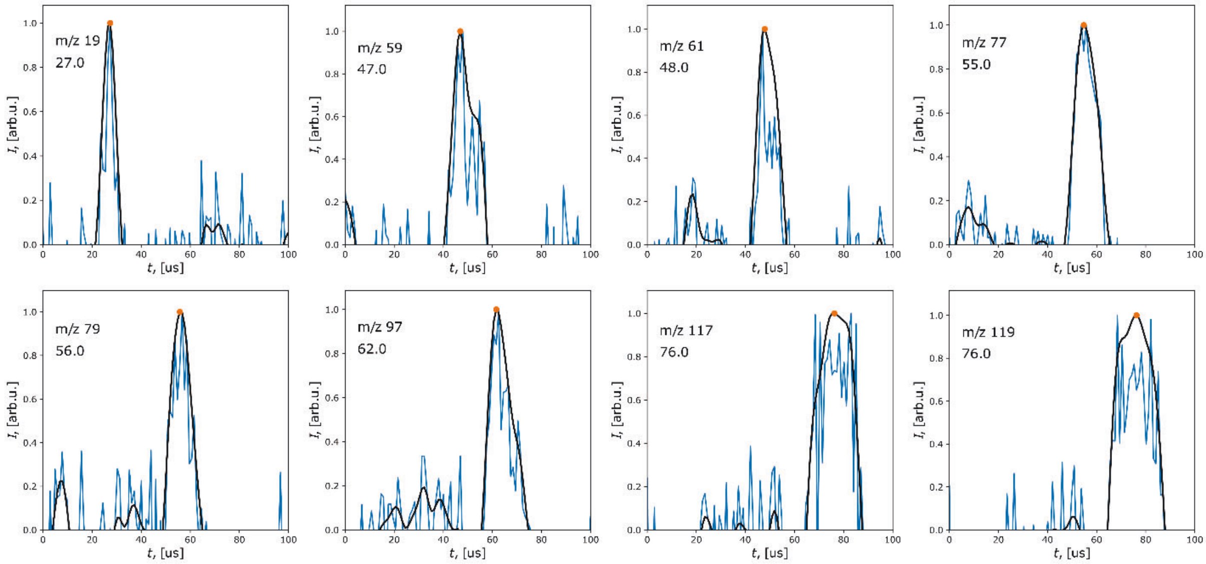

Figure S4. Arrival time distributions of the studied ions obtained using the Hadamard modulation on SNC before the QMA.

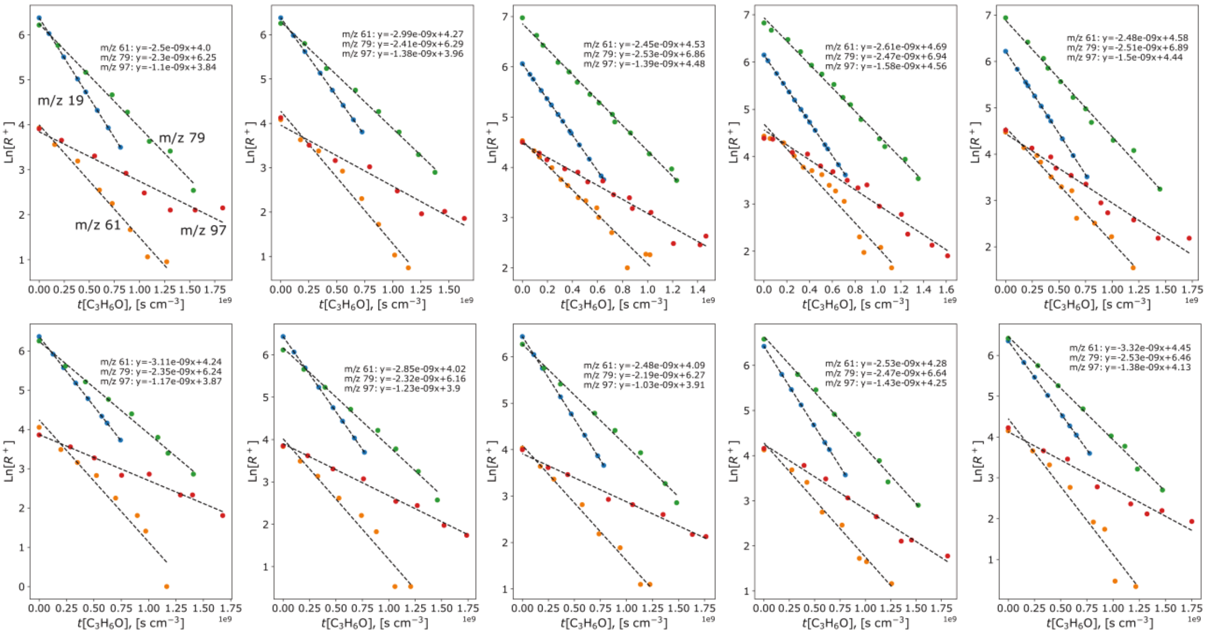

Figure S5. Semi logarithmic decay plots used to estimate the reaction rate coefficients for *m/z* 61, *m/z* 79 and *m/z* 97 with acetone.

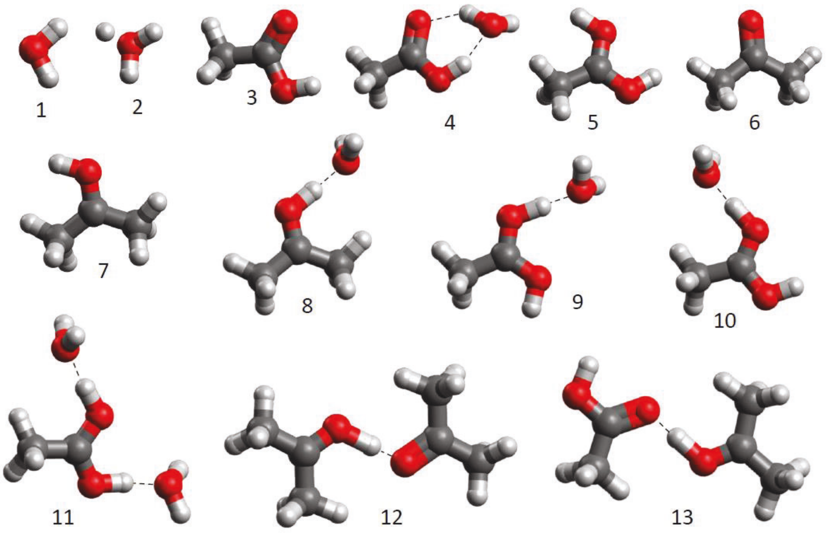

Figure S6. Geometries of ions and molecules from the DFT optimizations used to calculate the reaction thermochemistry: H_2O (1), H_3O^+ (2), $C_2H_4O_2$ (3), $C_2H_4O_2$ (H2O) (4), $C_2H_4O_2H^+$ (5), C_3H_6O (6), $C_3H_6OH^+$ (7), $C_3H_6OH^+(H_2O)$ (8), $C_2H_4O_2H^+(H_2O)$ (9, 10), $C_2H_4O_2H^+(H_2O)_2$ (11), $C_2H_4O_2H^+(C_3H_6O)$ (12), $C_3H_6OH^+(C_3H_6O)$ (13).

Reaction kinetics modelling

The numerical modelling of the proposed ion chemistry was based on the experimental data of relative ion intensities obtained for increasing acetone concentration (*Fig. 5 in the paper*). It is important to note that the secondary reactions with water molecules were not included as the experiment was done in dry helium buffer gas.

Firstly, we have optimized the decay of the three primary ions - protonated acetic acid (*m/z* 61), hydrated protonated acetic acid (*m/z* 79) and dihydrated protonated acetic acid (*m/z* 97) - based on the experimental determination of the total reaction rates (*Table 1 in the paper*). Initial concentrations (in cm^{-3}) of reagent ions were set to be 5E2, 8E3 and 5E2 for protonated acetic acid (*m/z* 61), hydrated protonated acetic acid (*m/z* 79) and dihydrated protonated acetic acid (*m/z* 97), respectively, to correspond with the ion count rate observed at zero acetone concentration. Total reaction rates of regent ions were than optimized to fit the experimental data. (see Fig. S7) The optimized values of the total reaction rates were used for further simulations.

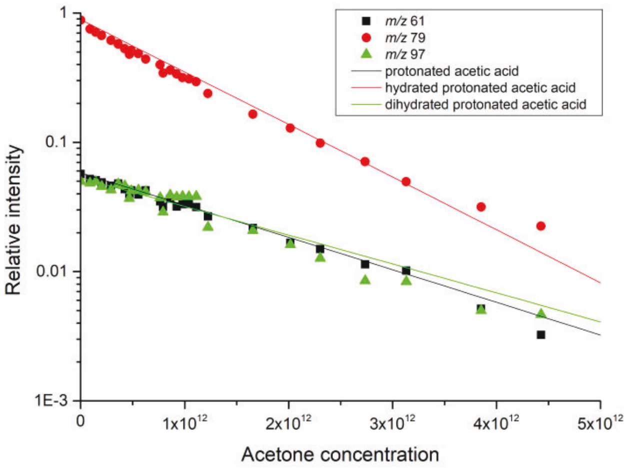

Figure S7. A model of relative reagent ions intensities as functions of the acetone concentration. The optimized total reaction rate coefficients are 2.1, 2.9 and 1.3 (all in 10^{-9} cm^{3}s^{-1}) for protonated acetic acid, hydrated protonated acetic acid and dihydrated protonated acetic acid, respectively, reacting with acetone. Presented data are relative to all ions involved in the simulation or experimental data set.

Simulations of protonated acetone channel

Protonated acetone is primarily formed via proton transfer between protonated acetic acid and acetone. The theoretical calculations, however, suggest that protonated acetic acid can also react via three body reaction with carrier gas forming $CH_3COOHH^+CH_3COCH_3$ ion with *m/z* 119. Finally, protonated acetone in secondary reaction with acetone forms protonated acetone dimer with *m/z* 117, with experimentally determined binary reaction rate coefficient 1.5x10^{-9} cm^{3}s^{-1}. The simulation presented in Fig. S8 (left) shows that the formation of protonated acetone cannot be explained only by proton transfer reaction of protonated acetic acid as this reaction alone underestimate the detected abundance of protonated acetone ions. Thus, we supplemented the formation of protonated acetone by additional channel:

$CH_3COOH^+.H_2O + CH_3COCH_3 \rightarrow CH_3COCH_3H^+ + CH_3COOH.H_2O$

This reaction is in theoretical calculation slightly endergonic, however only small reaction rate (1x10^{-10} cm^{3}s^{-1}) is required to fit the observed formation of protonated acetone.

The theoretical calculation also suggests the protonated acetic acid can react with acetone by a three-body reaction with helium carrier gas, forming the mixed proton-bound dimer with *m/z* 119. This process has a minor effect on formation of the mixed proton-bound dimer with *m/z* 119, as this ion is effectively produced by other channels discussed later. To investigate the effect of this channel, we used two different reaction rates, 0.22 and 2.15, x10^{-26} cm^{6}s^{-1}, representing the bimolecular reaction rates 0.1 and 1, 10^{-9} cm^{3}s^{-1}. The lower value of reaction rate does not significantly affect the proposed reaction schema. The higher value of reaction rate requires enhancement of the hydrated protonated acetic acid reactivity producing protonated acetone.

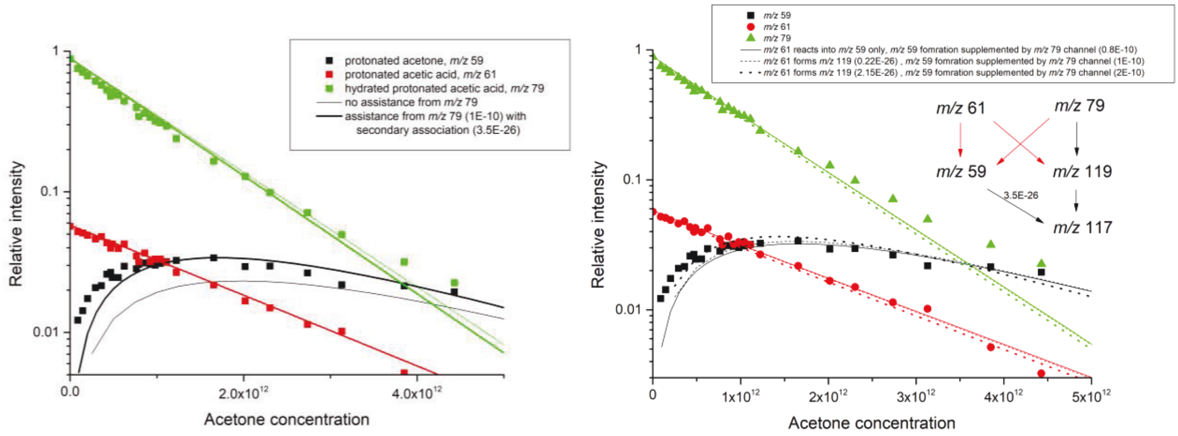

Figure S8. Modelling of the protonated acetone channel. Left in thin line is the formation of protonated acetone only from protonated acetic acid at its full reactivity, 2.9x10^{-9} cm^{3}s^{-1}, supplemented by a secondary reaction with acetone, forming protonated acetone dimers at 3.22x10^{-26} cm^{6}s^{-1} (corresponding to a bimolecular reaction rate 1.5x10^{-9} cm^{3}s^{-1}). The thick line indicates the protonated acetone also produced from hydrated protonated acetic acid via reaction with acetone at 1x10^{-10} cm^{3}s^{-1}. Reaction rate for the secondary reaction of protonated acetone forming protonated acetone dimer was slightly increased to 3.5x10^{-26} cm^{6}s^{-1}. On the right side we additionally added tree body reaction of protonated acetic acid and acetone forming the mixed proton-bound dimer with *m/z* 119. Two reaction rates to this channel were considered: 0.22 and 2.15, x10^{-26} cm^{-6}s^{-1}, representing the bimolecular reaction rates 0.1 and 1x10^{-9} cm^{3}s^{-1}. Presence of this channel requires higher reaction rate of hydrated protonated acetic acid forming protonated acetone to maintain the level of observed protonated acetone.

Simulation of the main reaction channels

The main reaction channels in the simulation are those initiated by the reaction of hydrated protonated acetic acid with acetone, producing hydrated protonated acetone with *m/z* 77 and the mixed proton-bound dimer with *m/z* 119, followed by the secondary reactions generating protonated acetone dimer with *m/z* 117. Considering the theoretical calculations and the experimentally obtained reaction rates for *m/z* 77 and *m/z* 119 ions, we proposed following reaction schemas that could represent the observed data.

RS1. Direct formation of *m/z* 77 and *m/z* 119 ions. Both ions are formed directly via bimolecular reaction of hydrated protonated acetic acid with acetone.

RS2. Formation via stable *m/z* 137 intermediate. Reaction of hydrated protonated acetic acid with acetone result into formation of stable *m/z* 137 ion that may spontaneously (or by collisions with carrier gas) dissociate into *m/z* 77 and *m/z* 119 ions.

RS3. Formation via quasi-stable m/z 137 intermediate. Reaction of hydrated protonated acetic acid with acetone result into formation of quasi-stable *m/z* 137 intermediate, that may spontaneously dissociate into *m/z* 77 and *m/z* 119 ions or be stabilised by collisions with helium carrier gas into stable *m/z* 137 ion.

For the first reaction scenario (RS1), a direct formation of *m/z* 77 and *m/z* 119 ions, we assume that both ions are formed rapidly via reaction (7). The proposed simulation is shown in Fig. S9, using reaction rates $0.3\text{x}10^{-9}$ cm^3s^{-1} and $2.5\text{x}10^{-9}$ cm^3s^{-1} for generation of hydrated protonated acetone (*m/z* 77) and the mixed proton-bound dimer (*m/z* 119), respectively. The secondary reaction rate coefficients for both ions with acetone have been experimentally estimated as $1.8\text{x}10^{-9}$ cm^3s^{-1} and $1.2\text{x}10^{-9}$ cm^3s^{-1}, respectively. However, in the simulation the secondary reaction of the mixed proton-bound dimer (*m/z* 119) had to be increased up to $1.8\text{x}10^{-9}$ cm^3s^{-1} to follow the abundance of *m/z* 117 and *m/z* 119.

The formation of the hydrated mixed proton-bound dimer (*m/z* 137) is provided via the following reaction channels: *a*, by reaction of dihydrated protonated acetic acid with acetone and *b*, by three body reaction of hydrated protonated acid with acetone stabilised by helium. In the first scenario, we assume formation of *m/z* 137 at variation of low reaction rates, up to $2.5\text{x}10^{-10}$ cm^3s^{-1} for ligand switching reaction of dihydrated protonated acetic acid with acetone and up to $5\text{x}10^{-28}$ cm^6s^{-1} for three-body association of hydrated protonated acetic acid with acetone. This scenario represents the observed profile of *m/z* 137 well, assuming the ion undergo a secondary reaction with acetone at reaction rate $2\text{x}10^{-9}$ cm^3s^{-1}. The product of this secondary reaction can be the mixed proton-bound dimer (*m/z* 119) or the protonated acetone dimer (*m/z* 117). The profile of either presented product ion is not highly affected as the abundance of the *m/z* 137 is very low. The reaction of ion with *m/z* 137 with acetone is necessary as the spontaneous dissociation, triggered for example by collisions with neutrals, does not represent the observed profile well (see the red line in Fig. S10, left). Note that due to low reaction rate of dihydrated protonated acetic acid (*m/z* 97) with acetone forming the hydrated mixed proton-bound dimer (*m/z* 137), another reaction with acetone, leading into formation of the mixed proton-bound dimer (*m/z* 119), was use to maintain its total reactivity.

In the second scenario, the three-body reaction of hydrated protonated acetic acid with acetone stabilised by helium remained at the previous level, to $3\text{x}10^{-28}$ cm^6s^{-1}, however we assume the second channel of dihydrated protonated acetic acid reacting with acetone leads only to formation of *m/z* 137. In this scenario, the formed ion with *m/z* 137 cannot react by secondary reaction with acetone, as the reaction rate of such reaction would be unrealistically high. Thus, we assume it may be consumed only via mono-molecular self-dissociation process, triggered by collision with gas or other neutrals: *m/z* 137 -> *m/z* 119 + H_2O. The model profiles (see Fig .S10, right) correspond to the experimental data using the reaction rate 20000 s^{-1}.

Due to low abundance of the *m/z* 137 ion, it is difficult to favour either scenario as both can be used to describe the formation of *m/z* 137.

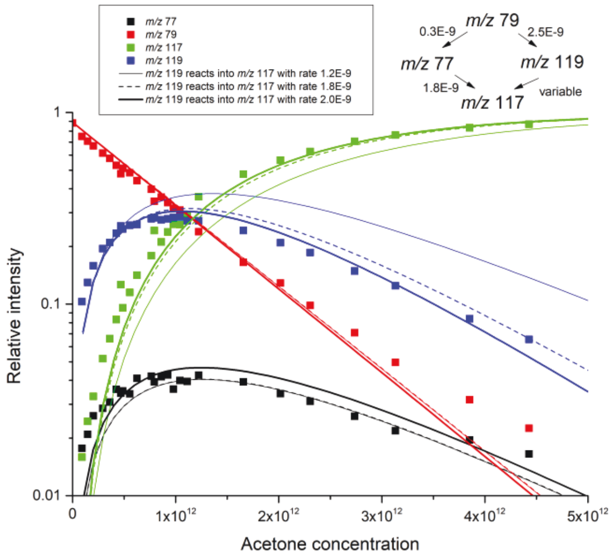

Figure S9. Modelling of the main reaction channel for hydrated protonated acetone (*m/z* 77) and the mixed proton-bound dimer (*m/z* 119) via direct formation from hydrated protonated acetic acid (*m/z* 79). The total reactivity of hydrated protonated acetic acid is reduced to 2.8x10^{-9} cm^{3}s^{-1} due to another reaction forming *m/z* 137 ion described later. The selected rate coefficients 0.3x10^{-9} cm^{3}s^{-1} and 2.5x10^{-9} cm^{3}s^{-1} well describe the generation of hydrated protonated acetone (*m/z* 77) and the mixed proton-bound dimer (*m/z* 119). Both ions further react with acetone, forming protonated acetone dimer (*m/z* 117) what is the ultimate product of the reaction sequence. The experimentally obtained reaction rate for the secondary reaction of the mixed proton-bound dimer (*m/z* 119), determined as 1.2x10^{-9} cm^{3}s^{-1} needs to be increased up to 1.8x10^{-9} cm^{3}s^{-1} in order to interpolate observed data.

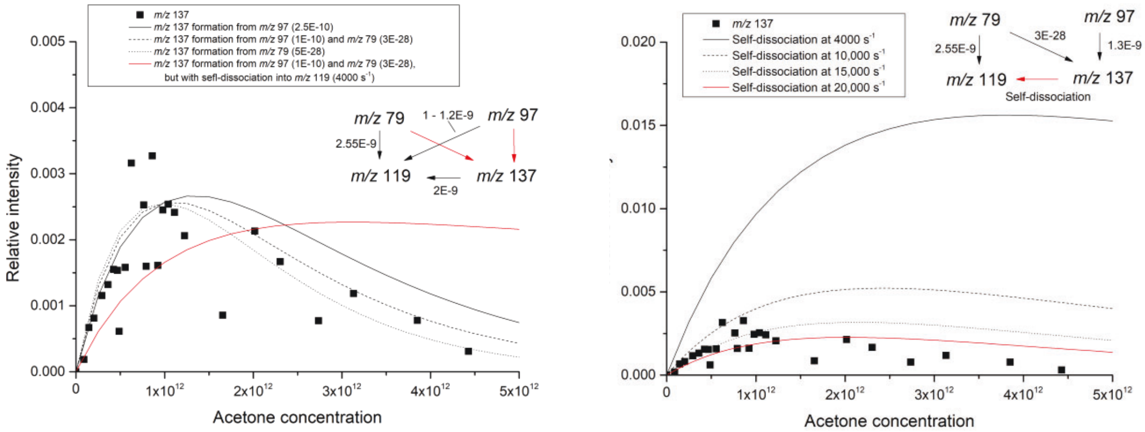

Figure S10. Simulation of the hydrated mixed proton-bound dimer (*m/z* 137). Left, using a variation of low reaction rates of *m/z* 79 and *m/z* 97 with acetone. The hydrated mixed proton-bound dimer may then react with acetone into *m/z* 119 or *m/z* 117 (due to low abundance of *m/z* 137, both products are possible). In red line, the secondary reaction is replaced by self-dissociation channel, not requiring acetone to react with *m/z* 137. Right, for the higher reaction rates. The rate coefficient for ligand switching reaction of dihydrated protonated acetic acid with acetone is significantly increased to 1.3x10^{-9} cm^{3}s^{-1}. We do not assume the *m/z* 137 ion secondary reaction with acetone, as those would need to be unrealistically fast. Instead, we simulated mono-molecular self-dissociation process, triggered by collision with gas or other neutrals: *m/z* 137 -> *m/z* 119 + H_2O.

For the second reaction scenario (RS2) we assume the reaction of hydrated protonated acetic acid with acetone results into formation of stable m/z 137 ion that may spontaneously (or by collisions with carrier gas) dissociate into *m/z* 77 and *m/z* 119 ions. Those ions will, as in the previous simulation, react in a secondary reaction with acetone, forming protonated acetone dimer (*m/z* 117). In the present setup (see Fig. S11), intermediate ion (*m/z* 137) is formed rapidly from three-body association of hydrated protonated acetic acid (*m/z* 79) with acetone and helium at reaction rate 6x10^{-26} cm^{6}s^{-1} and also from a ligand switching reaction of dihydrated protonated acetic acid (*m/z* 97) with acetone at reaction rate 1.3x10^{-9} cm^{3}s^{-1}. Reaction rate of hydrated protonated acetic acid (*m/z* 79) correspond to the bimolecular reaction rate 2.8 x10^{-9} cm^{3}s^{-1}. Formed intermediate ion with *m/z* 137 than spontaneously dissociate into main fragments hydrated protonated acetone (*m/z* 77) and the mixed proton-bound dimer (*m/z* 119) with reaction rate coefficients 35000 s^{-1} and 250000 s^{-1}, respectively. Reaction coefficients were optimised to correspond with observed abundance of involved ions: *m/z* 137, *m/z* 77 and *m/z* 119. Formed hydrated protonated acetone (*m/z* 77) and the mixed proton-bound dimer (*m/z* 119) undergo a secondary reaction with acetone, resulting into the formation of protonated acetone dimer (*m/z* 117). Also in this situation, we initiated the simulation by experimentally obtained values of both secondary reactions. However, the secondary reaction of the mixed proton-bound dimer (*m/z* 119) had to be optimised and increased to value 1.8x10^{-9} cm^{3}s^{-1} to reflect the decay of the *m/z* 119 and the intensity of the *m/z* 117.

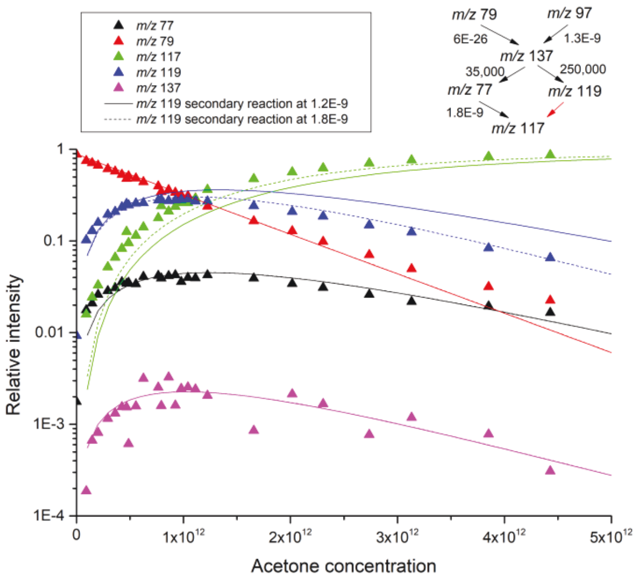

Figure S11. Modelling of the main reaction channel for hydrated protonated acetone (*m/z* 77) and the mixed proton-bound dimer (*m/z* 119) via formation of stable intermediate ion with *m/z* 137. In the figure, the two line types represent simulation using different reaction rates for secondary reaction of the mixed proton-bound dimer (*m/z* 119) with acetone, 1.2x10^{-9} cm^{3}s^{-1} (solid line) and 1.8x10^{-9} cm^{3}s^{-1} (dash line).

Finally, for the third reaction scenario (RS3), we considered the similar situation as the one above but the intermediate ion with *m/z* 137 was generated in a quasi-stable state, form where it may dissociate into hydrated protonated acetone (*m/z* 77) and the mixed proton-bound dimer (*m/z* 119) or it may stabilise into a stable ion with *m/z* 137. In the Fig. S12 we can compare difference between this and previous situation. Stabilisation of the ion with *m/z* 137 would mean it will no more spontaneously dissociate. Thus, the only reaction available is the reaction of *m/z* 137 with acetone, forming protonated acetone dimer. As this reaction is unlikely to take place, the abundance of ion with *m/z* 137 will not correspond to the observed profile.

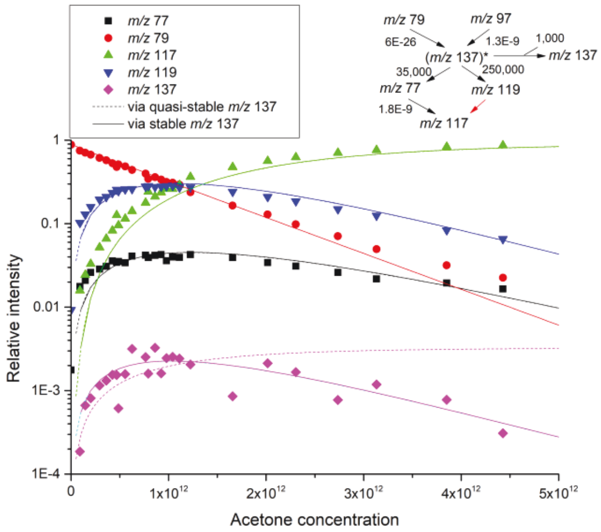

Figure S12. A comparison between formation of stable (solid) and quasi-stable (dashed) intermediate ion with *m/z* 137. Simulated profile of ion with *m/z* 137 generated from the quasi-stable ion with *m/z* 137 does not correspond with the observed experimental profile. Additional reaction would be required (as in Fig. S10) to bend the tail of the dashed line so it would correspond to the experimental data.

The experimental data can be fitted using two approaches: via a direct formation of hydrated protonated acetone (*m/z* 77) and the mixed proton-bound dimer (*m/z* 119) from reaction of hydrated protonated acetic acid (*m/z* 79) and acetone and also via formation of intermediate ion with *m/z* 137 from reaction of hydrated protonated acetic acid (*m/z* 79), which will dissociate into hydrated protonated acetone (*m/z* 77) and the mixed proton-bound dimer (*m/z* 119). Both solutions describe the experimental ion profiles well (see Fig. S13). The second situation contains fewer reaction channels as both reagent ions hydrated protonated acetic acid (*m/z* 79) and dihydrated protonated acetic acid (*m/z* 97) react with acetone into *m/z* 137. Secondary reactions of both ion products with acetone, hydrated protonated acetone (*m/z* 77) and the mixed proton-bound dimer (*m/z* 119) occur at reaction rates close to experimental, however, for the mixed proton-bound dimer (*m/z* 119) the secondary reaction needs to be increased to $1.8\text{x}10^{-9}$ cm^3s^{-1} to represent the observed formation of protonated acetone dimer (*m/z* 117).

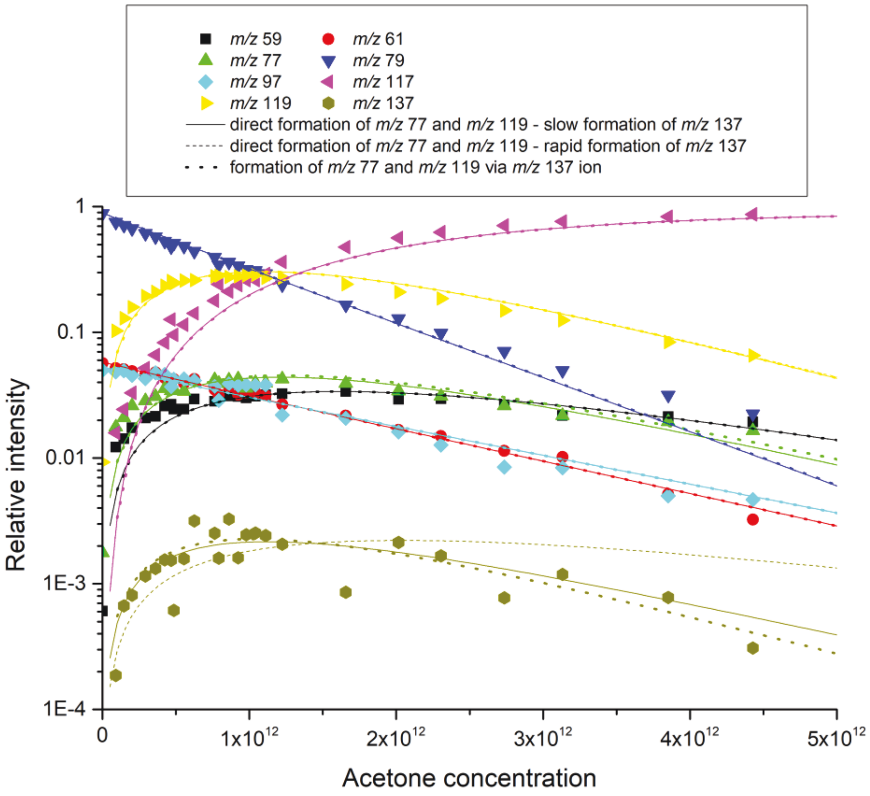

Figure S13. Comparison between individual solutions: Solution 1 – direct formation of *m/z* 77 and *m/z* 119 with slow formation of *m/z* 137, Solution 2 - direct formation of *m/z* 77 and *m/z* 119 with rapid formation of *m/z* 137, Solution 3 - formation of *m/z* 77 and *m/z* 119 via *m/z* 137 ion. Details of all solutions are collected in individual logs.

Model parameters

Table S1. Ions and their properties used in the simulation

Molecule	Initial Concentration (cm^{-3})	Reduced mobility (cm^2/Vs)	Mass (Da)	Diffusion coefficient (cm^2/s)
He	4.67E+16	0	4.002602	
C_3H_6O	0	0	58.07914	
$C_2H_4O_2(H_2O)$	0	0	78.06724	
$C_2H_4O_2$	0	0	60.05196	
$C_2H_4O_2H^+$	500	13.9	61.0599	257.07
$C_3H_6OH^+C_2H_4O_2$	0	8.6	119.13904	163.48
$C_2H_4O_2H^+(H_2O)(C_3H_6O)$	0	8	137.15432	143.77
$C_2H_4O_2H^+(H_2O)_2$	500	9.8	97.09046	192.13
$C_3H_6OH^+$	0	12.8	59.08708	261.66
$C_3H_6OH^+(C_3H_6O)$	0	8.2	117.16622	165.82
$C_3H_6OH^+(H_2O)$	0	10.9	77.10236	224.41
$C_2H_4O_2H^+(H_2O)$	8000	11.6	79.07518	220.87

Table S2. Solution 1 – direct formation of *m/z* 77 and *m/z* 119 with slow formation of *m/z* 137

Reaction	Rate coefficient
$C_2H_4O_2H^+ + C_3H_6O \rightarrow C_3H_6OH^+ + C_2H_4O_2$	2x10^{-9}
$C_3H_6OH^+ + C_3H_6O + He \rightarrow C_3H_6OH^+(C_3H_6O) + He$	3.5x10^{-26}
$C_2H_4O_2H^+(H_2O) + C_3H_6O \rightarrow C_3H_6OH^+C_2H_4O_2 + H_2O$	2.45x10^{-9}
$C_2H_4O_2H^+(H_2O) + C_3H_6O \rightarrow C_3H_6OH^+(H_2O) + C_2H_4O_2$	3.5x10^{-10}
$C_2H_4O_2H^+(H_2O)_2 + C_3H_6O \rightarrow C_2H_4O_2H^+(H_2O)(C_3H_6O) + H_2O$	1x10^{-10}
$C_2H_4O_2H^+(H_2O)_2 + C_3H_6O \rightarrow C_3H_6OH^+C_2H_4O_2 + 2H_2O$	1.2x10^{-9}
$C_3H_6OH^+(H_2O) + C_3H_6O \rightarrow C_3H_6OH^+(C_3H_6O) + H_2O$	1.8x10^{-9}
$C_3H_6OH^+C_2H_4O_2 + C_3H_6O \rightarrow C_3H_6OH^+(C_3H_6O) + C_2H_4O_2$	1.8x10^{-9}
$C_2H_4O_2H^+ + C_3H_6O + He \rightarrow C_3H_6OH^+C_2H_4O_2 + He$	2.2x10^{-27}
$C_2H_4O_2H^+(H_2O) + C_3H_6O \rightarrow C_3H_6OH^+ + C_2H_4O_2(H_2O)$	1x10^{-10}
$C_2H_4O_2H^+(H_2O) + C_3H_6O + He \rightarrow C_2H_4O_2H^+(H_2O)(C_3H_6O) + He$	2.15x10^{-28}
$C_2H_4O_2H^+(H_2O)(C_3H_6O) + C_3H_6O \rightarrow C_3H_6OH^+C_2H_4O_2 + H_2O + C_3H_6O$	2x10^{-9}

Table S3. Solution 2 - direct formation of *m/z* 77 and *m/z* 119 with rapid formation of *m/z* 137

Reaction	Rate coefficient
$C_2H_4O_2H^+ + C_3H_6O \rightarrow C_3H_6OH^+ + C_2H_4O_2$	$2x10^{-9}$
$C_3H_6OH^+ + C_3H_6O + He \rightarrow C_3H_6OH^+(C_3H_6O) + He$	$3.5x10^{-26}$
$C_2H_4O_2H^+(H_2O) + C_3H_6O \rightarrow C_3H_6OH^+C_2H_4O_2 + H_2O$	$2.45x10^{-9}$
$C_2H_4O_2H^+(H_2O) + C_3H_6O \rightarrow C_3H_6OH^+(H_2O) + C_2H_4O_2$	$3.5x10^{-10}$
$C_2H_4O_2H^+(H_2O)_2 + C_3H_6O \rightarrow C_2H_4O_2H^+(H_2O)(C_3H_6O) + H_2O$	$1.3x10^{-9}$
$C_3H_6OH^+(H_2O) + C_3H_6O \rightarrow C_3H_6OH^+(C_3H_6O) + H_2O$	$1.8x10^{-9}$
$C_3H_6OH^+C_2H_4O_2 + C_3H_6O \rightarrow C_3H_6OH^+(C_3H_6O) + C_2H_4O_2$	$1.8x10^{-9}$
$C_2H_4O_2H^+ + C_3H_6O + He \rightarrow C_3H_6OH^+C_2H_4O_2 + He$	$2.2x10^{-27}$
$C_2H_4O_2H^+(H_2O) + C_3H_6O \rightarrow C_3H_6OH^+ + C_2H_4O_2(H_2O)$	$1x10^{-10}$
$C_2H_4O_2H^+(H_2O) + C_3H_6O + He \rightarrow C_2H_4O_2H^+(H_2O)(C_3H_6O) + He$	$2.15x10^{-28}$
$C_2H_4O_2H^+(H_2O)(C_3H_6O) \rightarrow C_3H_6OH^+C_2H_4O_2 + H_2O$	20000

Table S4. Solution 3 - formation of *m/z* 77 and *m/z* 119 via *m/z* 137 ion

Reaction	Rate coefficient
$C_2H_4O_2H^+ + C_3H_6O \rightarrow C_3H_6OH^+ + C_2H_4O_2$	$2x10^{-9}$
$C_3H_6OH^+ + C_3H_6O + He \rightarrow C_3H_6OH^+(C_3H_6O) + He$	$3.5x10^{-26}$
$C_2H_4O_2H^+(H_2O)_2 + C_3H_6O \rightarrow C_2H_4O_2H^+(H_2O)(C_3H_6O) + H_2O$	$1.3x10^{-9}$
$C_3H_6OH^+(H_2O) + C_3H_6O \rightarrow C_3H_6OH^+(C_3H_6O) + H_2O$	$1.8x10^{-9}$
$C_3H_6OH^+C_2H_4O_2 + C_3H_6O \rightarrow C_3H_6OH^+(C_3H_6O) + C_2H_4O_2$	$1.8x10^{-9}$
$C_2H_4O_2H^+ + C_3H_6O + He \rightarrow C_3H_6OH^+C_2H_4O_2 + He$	$2.2x10^{-27}$
$C_2H_4O_2H^+(H_2O) + C_3H_6O \rightarrow C_3H_6OH^+ + C_2H_4O_2(H_2O)$	$1x10^{-10}$
$C_2H_4O_2H^+(H_2O) + C_3H_6O + He \rightarrow C_2H_4O_2H^+(H_2O)(C_3H_6O) + He$	$6x10^{-26}$
$C_2H_4O_2H^+(H_2O)(C_3H_6O) \rightarrow C_3H_6OH^+C_2H_4O_2 + H_2O$	250000
$C_2H_4O_2H^+(H_2O)(C_3H_6O) \rightarrow C_3H_6OH^+(H_2O) + C_2H_4O_2$	35000

Analytica Chimica Acta 1190 (2022) 339256

Contents lists available at ScienceDirect

Analytica Chimica Acta

journal homepage: www.elsevier.com/locate/aca

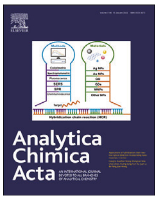

Atomization of As and Se volatile species in a dielectric barrier discharge atomizer after hydride generation: Fate of analyte studied by selected ion flow tube mass spectrometry

Jan Kratzer [a], [*], Michal Lacko [b], [c], Kseniya Dryahina [b], Tomáš Matoušek [a], Patrik Španěl [b], Jiří Dědina [a]

[a] Institute of Analytical Chemistry of the Czech Academy of Sciences, Veveří 97, 602 00, Brno, Czech Republic
[b] J. Heyrovský Institute of Physical Chemistry of the Czech Academy of Sciences, Dolejškova 2155/3, 182 23, Prague 8, Czech Republic
[c] Charles University, Faculty of Mathematics and Physics, V Holešovičkách 747/2, 180 00, Prague, Czech Republic

HIGHLIGHTS

- Atomization of volatile As and Se species in a DBD plasma atomizer was studied.
- Its efficiency was assessed by selected ion flow tube mass spectrometry (SIFT-MS).
- 100% atomization efficiency found for AsH_3, CH_3AsH_2,$(CH_3)_2AsH$; while 80% for SeH_2.
- SIFT-MS also enables quantitative determination of gas phase water vapor content.
- This information is crucial for maximum performance of low power DBD plasmas.

GRAPHICAL ABSTRACT

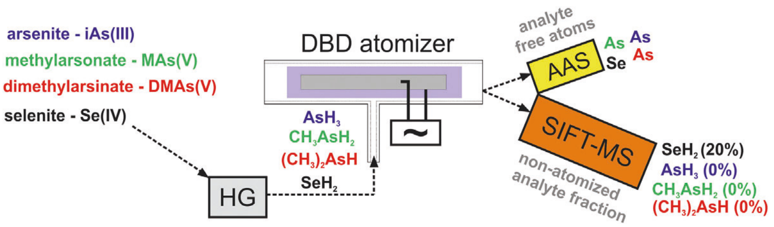

ARTICLE INFO

Article history:
Received 9 September 2021
Received in revised form
29 October 2021
Accepted 4 November 2021
Available online 9 November 2021

Keywords:
Dielectric barrier discharge atomizer
Hydride generation
Arsenic species
Selenium hydride
Selected ion flow tube mass spectrometry
Atomization mechanism

ABSTRACT

Atomization of hydrides and their methylated analogues in a dielectric barrier discharge (DBD) plasma atomizer was investigated. Selected ion flow tube mass spectrometry (SIFT-MS) was chosen as a detector being capable of selective detection of non-atomized original volatile species allowing thus direct quantification of atomization efficiency. Selenium hydride (SeH_2) and three volatile arsenic species, namely arsenic hydride (AsH_3), monomethylarsane (CH_3AsH_2) and dimethylarsane ($(CH_3)_2AsH$), were selected as model analytes. The mechanistic study performed contributes to understanding of the atomization processes in atomic absorption spectrometry (AAS). The presented results are compatible with a complete atomization of arsenic hydride as well as its methylated analogues and with atomization efficiency of SeH_2 below 80%. Using AsH_3 as a model analyte and a combination of AAS and SIFT-MS detectors has revealed that the hydride is not atomized, but decomposed in the DBD atomizer in absence of hydrogen fraction in the carrier gas. Apart from investigation of analyte atomization, the SIFT-MS detector is capable of quantitative determination of water vapor content being either transported to, or produced in the atomizer. This information is crucial especially in the case of the low-power/

---

[*] Corresponding author.
E-mail address: jkratzer@biomed.cas.cz (J. Kratzer).

https://doi.org/10.1016/j.aca.2021.339256

temperature DBD atomizer since its performance is sensitive to the amount of water vapor introduced into the plasma.

1. Introduction

Some elements, including those highly important from toxicological and environmental (As, Hg, Cd, Pb, Sn, Sb, Te, Ge, Bi) or biological (Se) point of view can be converted to volatile hydrides prior to their spectrometric detection. Hydride generation (HG) is thus a derivatization and sample introduction technique [1–3] that helps to overcome many problems arising during sample introduction prior to spectrometric detection. Firstly, sample introduction efficiency is improved 10 to 20-times compared to liquid nebulization and better limits of detection (LOD) are reached [1–3]. Secondly, analyte separation from sample matrix during HG step results in a reduced risk of interference. HG can be coupled to virtually any of the atomic spectrometric detectors. Atomic absorption spectrometry (AAS) is still the daily workhorse in trace element analysis offering affordable instrumentation, method robustness and operator friendliness. Moreover, if coupled with preceding HG step, the detection limits reached by AAS detector can meet the desired values at reasonable expenses.

Quartz tube atomizers (QTA) heated externally are the most common hydride atomizers in AAS including their advanced modifications such as multiple microflame quartz tube atomizer (MMQTA) [1–3]. However, the dielectric barrier discharge (DBD) can also be effectively employed for hydride atomization in AAS as proven recently [4–6]. A systematic research on DBD based hydride atomizers in AAS was performed by Kratzer et al., who investigated atomization of As [7], Se [8], Sb [9], Te [10], Bi [11], Sn [12] and Pb [13] hydrides in a DBD atomizer and compared its performance to the most common hydride atomizers, *i.e.* QTA or MMQTA, respectively.

From the DBD atomization point of view, the hydride forming elements can be obviously divided into two groups. As, Se, Sb and Te represent elements which hydrides can be easily and efficiently atomized providing high sensitivity and low LODs. On the contrary, atomization of Sn, Bi, and Pb hydrides in DBD is challenging reaching significantly worse sensitivity and impaired LODs. Even more interesting is the sensitivity comparison, under optimum atomization conditions, between the novel DBD atomizers and the conventional (MM)QTAs for individual elements. Sensitivity in (MM)QTA among the seven elements differs at maximum by a factor of three, reaching from 0.66 $s\ ng^{-1}$ for Te [10] down to 0.21 $s\ ng^{-1}$ for Pb [13]. On the contrary, the difference in sensitivity among the elements reaches a factor of 16 in the DBD. The highest sensitivity 0.48 $s\ ng^{-1}$ was reached for As [7] while the lowest was found for Sn (0.03 $s\ ng^{-1}$) [12] and Pb (0.04 $s\ ng^{-1}$) [13]. This difference in sensitivity clearly indicates the need for deeper understanding of atomization processes and atomization efficiency in DBD atomizers which is essential for further development of their designs in order to reach maximum performance. Atomization efficiency and the fate of free atoms are crucial parameters affecting atomizer sensitivity for given analyte.

Mechanistic studies performed so far focused on the atomization processes of Se [14], Bi [15], As [16], Sn [17], Pb [13] and Te [10] hydrides in plane-parallel DBD atomizers. A combination of different approaches and spectroscopic methods was employed with focus on quantification of atomization efficiency and free atoms distribution in the optical path. They were combined with additional spectroscopic measurements allowing quantification of analyte deposition in the atomizer during/after atomization step as well as spatial distribution mapping of these deposits. On the contrary, also the analyte fraction leaving the atomizer after volatile species atomization was monitored in order to assess the retention/outflow ratio for individual analytes to be correlated with analyte behavior in AAS.

Significant differences in behavior among the analytes were found. Strong interaction of Bi with the inner surface of the DBD atomizer was confirmed with >90% of Bi deposited in the optical arm [15]. This fraction was only around 30% for Se indicating longer life-time of Se free atoms [14]. Temporally and spatially resolved OES measurements have shown that AsH_3 is atomized and excited in the plane-parallel DBD atomizer across the whole discharge channel which explains its good sensitivity in AAS measurements [16]. Analogous OES measurements have revealed that the major part of Sn is atomized close to the walls of the atomizer [17]. Thus, the probability of the decay of analyte atoms by deposition at the quartz surface of the DBD atomizer increases. A mechanistic study by laser induced fluorescence (LIF) has been performed to visualize the spatial distribution of free Pb atoms in the DBD atomizer as well as to quantify plumbane atomization efficiency [13]. Free Pb atoms were present only in the central region of the DBD atomizer and plumbane atomization efficiency was quantified only to 23 ± 7% [13]. Analogous measurement by LIF were performed for Te reaching diametrically opposed results [10]. Free Te atoms were identified all over the length of the optical arm while atomization efficiency reached 100 ± 7% [10]. The results of mechanistic studies correlate well with the observations made in AAS. This accentuates the importance of understanding the atomization processes to achieve wider applicability and better performance of the DBD atomizers.

The methods leading to direct quantification of atomization efficiency such as LIF should be naturally preferred to other methods providing just the clues to the atomization behavior such as assessment of the deposited/passed through analyte fractions without being specific to the chemical structure of analyte species. However, the quantification of atomization efficiency of As and Se hydrides by LIF is not easily feasible because of the lack of appropriate laser dyes to produce suitable wavelength for the excitation scheme of LIF measurement. Since As and Se belong to analytically important elements, alternative approaches were searched for to investigate atomization efficiency of As and Se volatile compounds in the DBD and QTA atomizers.

As a consequence, selected ion flow tube mass spectrometry (SIFT-MS) was tested for the first time in this work as a tool to analyze As and Se hydride species at the outlet of DBD atomizer to get unique information on the atomization efficiency. SIFT-MS is an analytical technique using chemical ionization mass spectrometry (CI-MS) to determine trace concentrations of molecules in real time [18]. This technique uses reagent ions (H_3O^+, NO^+ or O_2^+) to softly ionize analyte molecules, whilst excluding the main air components (N_2, O_2). Thus, SIFT-MS is widely used for rapid quantification of volatile compounds in complex systems, such as breath, environmental air or food emissions [18,19]. SIFT-MS is not limited to organic analytes, but can be used for any compound rapidly reacting with one of the reagent ions. Volatile hydrides, AsH_3 and

SeH_2, have proton affinity 747.9 kJ mol^{-1} and 707.8 kJ mol^{-1}, respectively [20], which makes them suitable to undergo a proton transfer reaction with hydronium, as proton affinity of water is lower (691 kJ mol^{-1}). The protonated hydrides formed in these reactions can thus be used for quantitative analysis of these compounds by SIFT-MS. The operational range of SIFT-MS highly depends on the reaction rate between primary reagent ions and target neutral molecules. For reactions exothermic by more that 10 kJ mol^{-1}, as in the case of selected hydrides, reaction rates tend to be close to the collisional rates and thus the operating range is from ppbv levels up to several hundreds of ppmv [18]. Thus the SIFT-MS technique can be used for a direct in-line analysis of volatile hydrides and potentially also other reaction products presented in atomizers.

Liquid standards containing arsenite – iAs(III), methylarsonate – MAs(V), dimethylarsinate DMAs(V) and selenite – Se(IV) were employed to generate the volatile species: AsH_3, CH_3AsH_2, $(CH_3)_2AsH$ and SeH_2 which atomization mechanism and efficiency in a DBD atomizer was investigated. To the best of our knowledge, this is the first attempt to use SIFT-MS to investigate atomization processes in the atomizers employed in AAS.

2. Experimental

2.1. Chemicals

All reagents were of analytical reagent grade or higher purity. Deionized water (<0.1 μS cm^{-1}, Ultrapur, Watrex, USA) was used to prepare solutions. Working Se standards were prepared from 1000 mg l^{-1} Se stock solution (Fluka, Germany) by dilution in 1 mol l^{-1} HCl (Merck, Germany). Stock solutions of 1000 mg l^{-1} As were prepared for iAs(III), MAs(V) and DMAs(V) in deionized water using the following compounds: As_2O_3 (Lachema, Czech Republic); $Na_2CH_3AsO_3 \cdot 6H_2O$ (Chem. Service, USA); $(CH_3)_2As(O)OH$ (Strem Chemicals, Inc., USA) by dilution in 0.7 mol l^{-1} HNO_3. The reductant was a solution of $NaBH_4$ (≥97%, Sigma Aldrich, Germany) stabilized by KOH (Merck, Germany), prepared fresh daily. The NaOH pellets (p.a., Penta, Czech Republic) were used as a filling of a dryer cartridge for water vapor and aerosol removal. Nitric acid (65%, p.a., Lach-Ner, Czech Republic) was used to clean the DBD atomizers if necessary. Compressed gases Ar (99.996%), H_2 (99.95%) and O_2 (99.5%) were produced by SIAD Czech, Ltd. If explicitly stated, AsH_3 mixture in Ar from a cylinder was employed instead of AsH_3 produced by chemical hydride generation from iAs(III). The mixture was provided by SIAD Czech, Ltd. with certified content of 200 ± 17 ppbv AsH_3.

2.2. Generation of volatile species

2.2.1. Hydride generator

The in-house made hydride generator consisted of three channels serving for introduction of blank/standard and reductant solutions, as well as draining waste propelled by a peristaltic pump (Ismatec, Germany). A three way-valve was used to switch between blank and sample solution introduction. Two PEEK T-pieces connected to 1.0 mm (i.d.) Teflon tubings were used to merge the reductant solution with the acid solution, employing 75 ml min^{-1} Ar as carrier gas which flow rate was controlled by a mass flow controller (Cole-Parmer, USA). In the quartz gas-liquid separator (GLS) with a forced outlet volatile species generated were directed to the atomizer/detector, while liquid waste was drained from the bottom. In all experiments, sample, reductant and waste flow rates were 4.2, 1.2 and 8.5 ml min^{-1}, respectively. A scheme of the hydride generator is presented in Supplementary data, Fig. S1.

2.2.2. Generation of As volatile species

Experimental conditions for hydride generation of volatile arsenic species, *i.e.* AsH_3, CH_3AsH_2 and $(CH_3)_2AsH$, were: carrier acid/blank was 0.7 mol l^{-1} HNO_3 while the reductant was 1% $NaBH_4$ in 0.1% KOH. Analyte concentration in the standard solutions was, if not stated otherwise, 100 ng ml^{-1} for iAs(III) as well as MAs(V) and 200 ng ml^{-1} for DMAs(V). If explicitly stated, the carrier acid/blank was replaced by 1 mol l^{-1} HCl. A dryer based on a polypropylene cartridge (100 mm long, 15 mm i.d.) filled with solid sodium hydroxide pellets (further termed as NaOH dryer) was inserted downstream the GLS in all experiments with As volatile species. Such a NaOH dryer was found effective to prevent aerosol droplets and water vapor to enter the atomizers while allowing the volatile As species to pass through without losses [21]. The amount of H_2 produced in the hydride generator from the $NaBH_4$ decomposition was measured volumetrically as 19 ml min^{-1}.

If explicitly stated (experiments presented in section 3.5), AsH_3 mixture in Ar from a cylinder was employed as a source of arsane instead of hydride generator. Such an experimental arrangement was chosen to introduce arsane into DBD without production of co-generated hydrogen. The flow rate of the gas mixture (200 ppbv AsH_3 in Ar) was controlled by a mass flow controller (Cole-Parmer, USA) and kept at 100 ml min^{-1}.

2.2.3. Generation of Se hydride

Experimental conditions for selenium hydride generation were: carrier acid/blank 1 mol l^{-1} HCl while the reductant was 0.5% $NaBH_4$ in 0.4% KOH. The amount of H_2 produced in the hydride generator from the $NaBH_4$ decomposition was measured volumetrically as 11 ml min^{-1}. NaOH dryer was not employed in measurements with Se since it retains apart from water vapor also SeH_2 quantitatively [13]. Concentration in the standard solution was 250 ng ml^{-1} Se(IV) if not otherwise stated.

2.2.4. Quantification of the hydride generation efficiency

The HG efficiency was assessed by a comparison of ICP-MS/MS signals of nebulized known amounts of Se and As species standard solutions and the signals of volatile As species and Se introduced from hydride generator. See the Supplementary data, section 1.1, for detailed description of the procedure.

2.3. DBD atomizer

The design of the DBD atomizer was similar to that used in previous studies [7–17] consisting of an (i) optical arm in which the plasma is sustained and an (ii) inlet arm. The optical arm was fused together from quartz microscope slides (15 × 75 × 1 mm) and two quartz spacers (3 × 75 × 3 mm) purchased from UQG Optics Ltd., England. It was thus 75 mm long with a 7 mm × 3 mm rectangular internal cross-section. Two copper electrodes (50 mm long; 5 mm wide; 0.15 mm thick) were glued to the central part of the outer surface of the microscope slides and their surfaces covered with an insulating layer of epoxy resin to avoid surface discharge across the outer body of the chamber. The DBD electrodes were coupled to a power supply generating a sinusoidal waveform frequency (excitation frequency 28.5 kHz) and a high voltage transformer, both fabricated by Lifetech (Czech Republic) and described previously [7–17]. The inlet arm was fused to the center of one of the quartz spacers of the optical arm in the right angle being realized by a quartz tube (20 mm long, 2 mm inner diameter (i.d.), 4 mm outer diameter (o.d.)). The DBD atomizer was housed in a supporting frame of high density polyvinyl chloride (PVC) which protected the DBD chamber from mechanical damage. A computer fan was attached to the bottom of the DBD chamber to provide air cooling. The high voltage and power employed reached 17.5 kV (17 W) for atomization of As species and 15.0 kV (14 W) for selenium hydride, respectively. The DBD atomizers were cleaned prior to their first use with 10% (v/v) HNO_3 for 10 min and subsequently flushed with deionized water. The atomizer was then allowed to dry at room temperature.

2.4. SIFT-MS detector

The inlet arm of the DBD atomizer was blocked for actual SIFT-MS measurements. As a consequence, the gas phase from the hydride generator was introduced to the left end of the optical arm through a PTFE plug. The right end of the optical arm was open to the ambient atmosphere and served for gas phase sampling into the SIFT-MS detector through the sampling capillary which protruded ca 3 mm into the optical arm. See Supplementary data, Fig. S2A for illustration of the experimental set-up. If explicitly stated (section 3.5) the hydride generator was replaced by a gaseous mixture containing arsane in Ar from a cylinder (200 ppbv AsH_3 in Ar at a flow rate of 100 ml min^{-1}).

In this study, a *Profile 3* SIFT-MS instrument (Instrument Science, Crewe, UK) was used [22–24]. Reagent ions (hydronium, H_3O^+ for the presented results) are generated in a microwave discharge in a mixture of water vapor and laboratory air. The reagent ions are electro-statically extracted from the ion source and introduced into a quadrupole mass filter. Ions with selected *m/z* are injected into a 5 cm long flow tube and mixed with helium carrier gas flowing through the flow tube at pressure $p = 1.5$ mbar and temperature $T = 305$ K. A laminar flow of He carries reagent ions along the drift tube where they quickly thermalize. Sample gas is introduced into the He stream at a known constant flow rate (usually 30 ml min^{-1}, as measured by Agilent Technologies model 5067-0223 flowmeter) *via* a sample inlet located 1 cm downstream after the reagent ion injection orifice. In the presence of helium, selected reagent ions react with sample gas *via* several possible reaction channels. For the hydronium reagent ions, chemical ionization is mainly achieved *via* proton transfer reaction

$$H_3O^+ + M \rightarrow MH^+ + H_2O,$$

where M represents an analyte molecule with proton affinity above the proton affinity of water (691 kJ mol^{-1}) [20]. Sometimes the MH^+ product may dissociate into energetically favoured fragments, as is often the case for alcohols or esters [23]. The reagent ions and the reaction product ions are at the end of the flow tube introduced into a quadrupole mass spectrometer and detected *via* a single channel electron multiplier.

In the present work we used the SIFT-MS apparatus in two modes. First, a classical full MS scanning of the quadrupole mass spectrometer was performed to determine the presence of all product ions. Second, a multi-ion monitoring (MIM) mode, switching between selected reagent and product ions in a short interval (300 ms for each selected ion) was used for monitoring the abundance of the selected ions over time. In the current work, we monitored the reagent ion (H_3O^+; *m/z* 19) as well as its adducts with one to three water molecules ($H_3O^+(H_2O)_n$; n = 1, 2, 3; *m/z* 37, 55, 73) and one or more protonated hydride products, resulting into MIM time resolution of ~2 s. The ions monitored in this work are summarized in Table 1.

To estimate the absolute water concentration, we monitored the three-body association reaction between hydronium reagent ions and neutral water molecules assisted by helium, resulting into formation of hydronium water clusters $H_3O^+(H_2O)_n$, n = 1,2,3. The absolute water concentration was than determined using the known three-body reaction constant for the association process, 7.2×10^{-28} cm^{6}s^{-1}, transformed into the corresponding second reaction order rate constant 2.28×10^{-11} cm^{3}s^{-1} at the flow tube pressure 1.5 mbar and temperature 305 K [25].

Table 1
Species and masses detected in SIFT-MS.

Target analyte	SIFT-MS detected ion	Monitored ions (*m/z*)
water vapor	$H_3O^+(H_2O)_{0,1,2,3}$	19,37,55,73
AsH_3	$[^{75}AsH_3 + H]^+$	79
CH_3AsH_2	$[H_3CAsH_2+ H]^+$	93
$(CH_3)_2AsH$	$[(H_3C)_2AsH + H]^+$	107
SeH_2	$[^{80}SeH_2 + H]^+$	83

2.5. AAS detector

The inlet arm of the DBD atomizer serves in AAS experiments to gaseous phase introduction from the hydride generator. AAS measurements were employed in the experimental configuration depicted in Supplementary data, Fig. S2B to check the hydride generator performance as well as the sensitivity of DBD atomizers in preliminary experiments (see section 3.1). Moreover, they were used to investigate the effect of hydrogen on AsH_3 atomization (see section 3.5). A GBC model SavantAA atomic absorption spectrometer (GBC, Australia) was employed without background correction. A Photron As boosted hollow cathode lamp (superlamp) operated at 193.7 nm analytical line with 2.0 nm spectral bandpass and a lamp current of 20 mA (boost current 7–15 mA) while a Photron Se superlamp operated at 196.0 nm analytical line with 1.0 nm spectral bandpass and a lamp current of 18 mA (boost current 23 mA).

2.6. OES detector

A miniature fiber optics UV-VIS spectrometer, model BLACK-Comet C (StellarNet Inc., USA) equipped with a concave grating covering a range of 183–850 nm and armored solarization resistant 1000 μm fibre optic cable (F1000-UVVIS-SR-1) was employed to acquire emission spectra using SpectraWiz software version 5.33 (StellarNet Inc., USA) in experimental configuration as depicted in Supplementary data, Fig. S2C. The detector integration time was 250 ms with 10 spectra to be averaged. The spectra were recorded in end-on-view mode. The optical fiber was positioned in the longitudinal axis of the DBD *ca* 20 mm far from one of the outlets of the quartz body of the plasma channel.

3. Results and discussion

3.1. Preliminary results – generation efficiency and sensitivity in AAS

Measurement sensitivity, observed in AAS for the volatile species investigated, is summarized in Table 2 together with generation efficiencies of the species as determined by ICP-MS/MS. See the Supplementary data, section 2.1 for details. Relating sensitivities of all arsanes to their generation efficiencies determined by ICP-MS/MS (Table 2) indicates that atomization efficiencies of individual arsanes do not differ substantially. In order to get deeper insights into atomization processes and to estimate the atomization efficiency, SIFT-MS experiments were performed which results are further interpreted in sections 3.2–3.5.

3.2. Quantification of water vapor content by SIFT-MS

Due to their low-power and low-temperature nature the DBDs are extremely sensitive to discharge gas composition and moisture content. Carrier gas composition, especially hydrogen fraction in

Table 2
Sensitivities reached for examined species by HG-DBD-AAS. Generation efficiencies of the species investigated as quantified by ICP-MS/MS.

Analyte species liquid phase	gaseous phase	AAS sensitivity (DBD) s ng^{-1}	Generation efficiency, %
iAs(III)	AsH_3	0.50 ± 0.01	90 ± 2
MAs(V)	CH_3AsH_2	0.48 ± 0.01	70 ± 2
DMAs(V)	$(CH_3)_2AsH_2$	0.27 ± 0.01	35 ± 2
Se(IV)	SeH_2	0.33 ± 0.01	76 ± 2

the discharge gas as well as the amount of co-generated aerosol and water vapor are definitely dictated by HG conditions (reductant and carrier acid concentration and their flow rates) as well as generator and gas-liquid separator designs. However, the amount of water vapor produced can be effectively reduced downstream the GLS by an appropriate dryer. Water molecules as well as other molecular impurities in the discharge gas (*e.g.* N_2) possess many rotational and vibrational energetic levels which give the accelerated electrons in the discharge the chance to deposit their energy very efficiently as well as trigger new reaction channels in plasma *via* formation of highly reactive H_3O^+ or OH^- species. A high extent of water vapor can lead to significant quenching of the plasma and in extreme cases to the extinction of the discharge.

The water vapor content in the gas phase was quantified by SIFT-MS under the experimental conditions employed for HG of As species, *i.e.* with the dryer (see section 2.2.2) and SeH_2 for which NaOH dryer cannot be employed due to quantitative retention of analyte (see section 2.2.3 for details). The HG of blank was running in both experiments while the gas phase was sampled either at the outlet of the dryer or directly at the exit of the gas-liquid separator. In the first experiment with the dryer included the water vapor content in the gas phase reached 0.160 ± 0.001%. The water vapor content in the second experiment (without the dryer) increased significantly to 2.0%. The latter value is close to the absolute humidity of the air reaching 2.2% at 20 °C.

Following experiment was performed in order to investigate also the effects of the plasma discharge and oxygen content on the water vapor content in the DBD atmosphere. The apparatus was operated under conditions employed for HG of AsH_3 (see section 2.2.2), the NaOH dryer was incorporated while generation of blank was performed. The signal in SIFT-MS was continuously monitored.

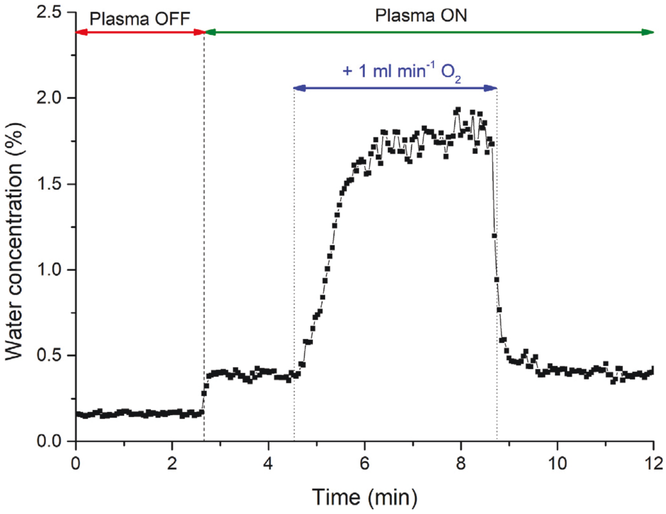

Fig. 1. Effects of the plasma discharge and oxygen content on water vapor production in the DBD atomizer quantified by SIFT-MS. HG conditions as used for As; NaOH dryer included; DBD discharge was off and on (18 kV, equal to 14 W) as indicated. No oxygen added or 1 ml min^{-1} O_2 admixed to discharge gas as indicated.

Three different experimental conditions were investigated as depicted in Fig. 1. Firstly, the DBD discharge was switched off while the hydride generator was running (blank measurement) with gaseous phase passing through the NaOH dryer. The water vapor content in the gaseous phase reached 0.16% as already discussed above. Secondly, the DBD discharge was switched on. The content of water vapor increased to 0.390 ± 0.003% indicating plasma-driven production of water vapor by reaction of oxygen traces with hydrogen excess produced in the hydride generator (see Fig. 1). Subsequently, a flow rate of 1 ml min^{-1} O_2 from a cylinder was admixed to the carrier gas (upstream the GLS) while all the other experimental parameters remained unchanged. The water vapor content increased to 1.77 ± 0.01% (see Fig. 1) indicating the reaction between oxygen and hydrogen in the DBD discharge is likely quantitative. Finally, the flow rate of oxygen to the DBD atomizer was stopped while the discharge and hydride generator were still in operation. The water vapor content decreased to a value of 0.40%, which is well comparable to the result observed under the same conditions before (0.39%). In principle, also oxygen contaminant level in the carrier/discharge gas can be deduced from SIFT-MS experiments from the values of water vapor content in presence and absence of the DBD plasma assuming the quantitative conversion of oxygen traces to water vapor in excess of hydrogen in the presence of the plasma while expecting no reaction between O_2 and H_2 in absence of the plasma.

Comparing the results of water vapor content in the DBD in presence/absence of the dryer the effectiveness of various dryers can be estimated in this manner. Unfortunately, selection of an appropriate dryer is analyte-dependent. Thus, there is no a universal dryer to be compatible with all potential analytes since analyte losses in the dryer compartment have to be prevented. Also the significance of the positive effect of the dryer on analyte signal in AAS is different among the elements. The use of NaOH dryer improves As signal in DBD atomizer (introduced as AsH_3) by 15% [7] while the same dryer enhances Sn response (generated as SnH_4) three-times in the same DBD atomizer [12]. Neither arsane, nor the stannane are retained (lost) in the NaOH based dryer [7,12]. Searching for a proper dryer is a complex but important task with DBD atomizers. Knowledge of the water vapor content in the gas phase together with approaches to its effective elimination is crucial for reaching the best sensitivity in DBD. SIFT-MS has been proven a useful tool to quantify water vapor content in the discharge gas and to investigate the efficacy of various dryers. Alternatively, the performance of the dryer can be studied by optical emission spectroscopy (OES), since the intensity of OH band at 309 nm can be employed as a rough measure of water vapor content in the discharge gas as well. The results making use of this approach are discussed in Supplementary data, section 2.2 and Fig. S3.

3.3. *Atomization of As and Se hydrides*

3.3.1. *Measurement concept*

Initially, SIFT-MS measurements in the full MS scan mode have been performed (see section 2.4 for details). They allowed identification of all product ions being produced under given experimental conditions, thus originating from generation of either analyte standard or blank in both absence and presence of the DBD plasma. The detailed interpretation of the experiments performed in the full MS scan mode can be found in Supplementary data, section 2.3 and Fig. S4.

Based on these measurements the dominant and important analyte ions were subsequently selected which signal development over longer period of time was investigated in the multi-ion monitoring (MIM) mode of the SIFT-MS instrument (see section 2.4 for details). The results reached by SIFT-MS measurements in the MIM mode for individual species studied are discussed below exploring the effects of experimental conditions such as standard/blank introduction and DBD plasma presence/absence on their signals. The experimental sequence (plasma conditions) as well as introduction of either a standard solution or a blank can be seen intuitively in the figures. They are indicated by green (plasma on) and red (plasma off) horizontal arrows. The time periods for analyte standard or blank introduction can be distinguished by blue (analyte) and grey (blank) arrows, respectively.

3.3.2. *As hydride*

The results for AsH_3 generated from a 100 ng ml^{-1} iAs(III) are depicted in Fig. 2A with the signal monitored at *m/z* 79 corresponding to $[^{75}AsH_3 + H]^+$ since this is the only reaction product originating from AsH_3 in the SIFT-MS source as discussed in Supplementary data, section 2.3 (see also Fig. S4A). Employing the SIFT-MS detector, the signal from a standard or a blank solution was investigated in presence or absence of the plasma in the DBD atomizer. Signal at *m/z* 79, corresponding to AsH_3 presence at the outlet of the DBD atomizer, can only be clearly detected when iAs(III) standard is introduced and when the DBD plasma is off (Fig. 2A). Arsane is obviously not atomized under such conditions and can be quantitatively detected by SIFT-MS. The signal in SIFT-MS immediately drops as soon as the DBD plasma is switched on to the same „background“ signal for standard or for blank (Fig. 2A). The same observations were made in full mass spectrum mode of the SIFT-MS measurements for which analyte signal was detected only in absence of the DBD plasma and not in its presence (compare Figs. S4A and S4E). The fact that the signal of original volatile analyte molecule is not detected by SIFT-MS does not necessarily mean it had been atomized since the analyte molecule could have been significantly changed in other ways, *e.g.* being decomposed forming analyte dimers, oxides, *etc.* [3].

The present interpretation of the data is based on our experience with AAS measurements proving arsane atomization in the DBD under experimental conditions employed [7,8,14,16]. Free As atoms produced in the atomizer do not decay to form arsane even though thermodynamic equilibrium calculations indicate that As_2 and AsH_3 should prevail among species formed by decay of free As atoms (see Ref. [3] and references therein).

3.3.3. *Se hydride*

Analogous experiment was performed also for Se employing 250 ng ml^{-1} Se standard solution. Protonated hydride (selane) is the only reaction product originating from SeH_2 in the SIFT-MS source as discussed in Supplementary data, section 2.3. Its signal is however distributed among several Se isotopes with relative intensities corresponding to their natural abundance (see Fig. S4D). Since ^{80}Se is the most abundant isotope, the most intensive signal at *m/z* 83 related to $^{80}SeH_3^+$ was selected for further investigations. Fig. 2B shows clearly that the behavior of SeH_2 is different compared to AsH_3. The highest signal of SeH_2, was found in absence of DBD plasma during the introduction of Se standard into the hydride generator, similar as in case of arsenic measurements. The signal height decreased just to 22 ± 3% when the DBD plasma was switched on (Fig. 2B). Apart from the measurements in the MIM mode of the SIFT-MS, the same observations were made also in the full MS scan mode of the same instrument (Fig. S4H).

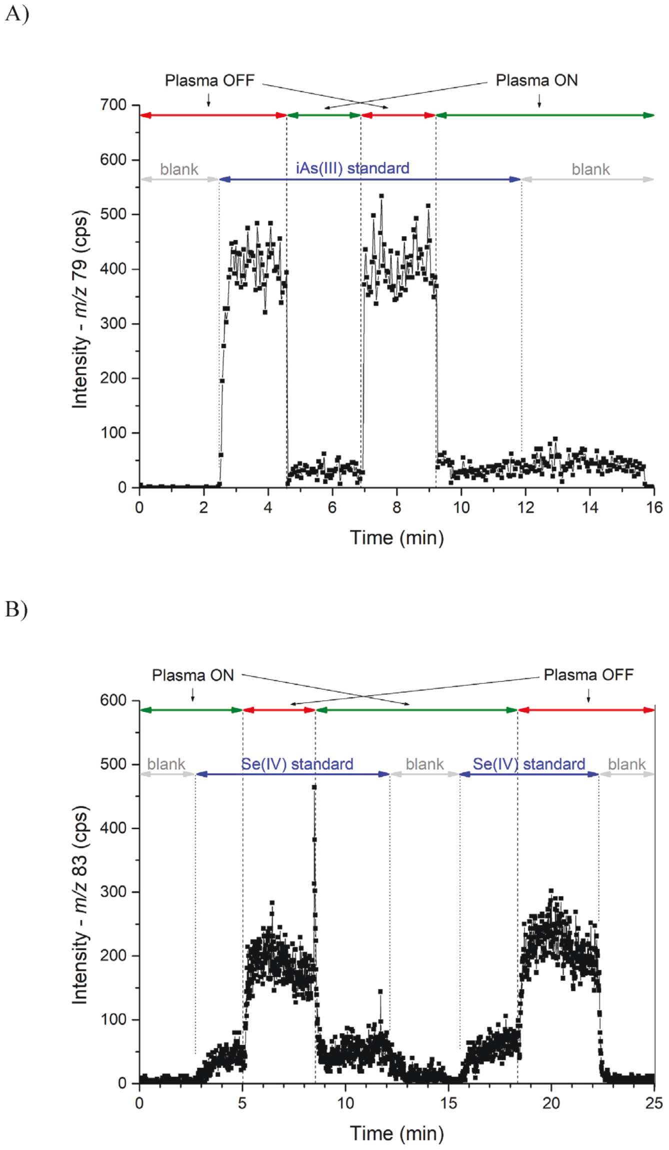

Fig. 2. SIFT-MS signals of analyte hydrides and blanks in the DBD atomizer in presence and absence of the plasma. A) AsH_3 generated from 100 ng ml^{-1} iAs (III); B) SeH_2 generated from 250 ng ml^{-1} Se(IV). Generation and atomization conditions as described in the text.

3.3.4. *Interpretation of the results*

The data on atomization efficiency in DBD received for both hydride forming elements by SIFT-MS in this work agree with the results published recently based on independent spectroscopic methods. In our previous work [7] 100% arsane atomization efficiency in the DBD was estimated, based on AAS measurements. This agrees well with another observation confirmed by OES with high resolution in time and space that free As atoms exist all over the discharge area, *i.e.* along the full length of DBD electrodes [16]. On the contrary, the AAS sensitivity for selane detection in the DBD was 25% lower than in QTA [8]. This could be explained by 75% atomization efficiency in the DBD. Incomplete selane atomization in the DBD atomizer was confirmed by direct analysis in real time mass spectrometry (DART-MS) measurements in which ca 30% fraction of SeH_2 was detected (as $[HSe]^-$) in the gaseous phase at the outlet of DBD with plasma switched on [14]. This result is in concordance with 22% SeH_2 fraction being non-atomized in DBD as found in this work by SIFT-MS. The presence of SeH_2 at the confines could be, in principle, explained by two scenarios. First explanation assumes a complete SeH_2 atomization in the DBD atomizer, but followed by partial (ca 20–30%) re-synthesis of selane due to reactions of free Se atoms with hydrogen. According to the second scenario, the atomization of SeH_2 in the DBD atomizer is incomplete reaching only the efficiency of 70–80%.

3.4. Atomization of methyl-substituted As hydrides

Analogous experiments as described above for binary hydrides were performed also for CH_3AsH_2 and $(CH_3)_2AsH$. Their protonated molecules were found to be the only species produced in the SIFT-MS source as discussed in Supplementary data, section 2.3. As a consequence, HG of CH_3AsH_2 resulted in production of $CH_3AsH_3^+$ which signal was monitored at *m/z* 93 (see Fig. S4B) while HG of $(CH_3)_2AsH$ led to production of $(CH_3)_2AsH_2^+$ (*m/z* 107) as depicted in Fig. S4C.

The behavior of both methylated arsane species is the same. Analyte signal can only be detected if the plasma is switched off providing standard solution is introduced into the hydride generator. No analyte signal is detected in SIFT-MS when the DBD is switched on indicating efficient atomization of methylarsane (Fig. S5A) and dimethylarsane (Fig. S5B) in the DBD. The same conclusion can be deduced from the measurements performed in the full MS scan mode (Figs. S4F and S4G). There is no difference in the signal with DBD switched on regardless standard solution or blank are introduced into the hydride generator (see Figs. S5A and B).

Effort was also made to monitor other As species with lower degree of methylation that could be formed in the DBD as products of partial decomposition (de-methylation) since the atomization is believed to be a stepwise reaction [1]. The decomposition of $(CH_3)_2AsH$ and CH_3AsH_2, respectively, *via* a loss of a methyl group followed by its substitution with H radical could in principle result in formation of CH_3AsH_2 and AsH_3. To check this, signals of CH_3AsH_2 and AsH_3 were also monitored in SIFT-MS during investigation of $(CH_3)_2AsH$ in the MIM mode. For the same reason, signal of AsH_3 was watched by SIFT-MS simultaneously with CH_3AsH_2 measurements. Neither of these attempts was successful. These observations are also supported by the full MS scans presented in Figs. S4F and S4G. These observations indicate that atomization of both methylated As species investigated, CH_3AsH_2 and $(CH_3)_2AsH$, proceeds in the DBD atomizer analogously to atomization of arsane. It appears that there are no stable decomposition products of these species.

When combined with the results from AAS measurements, the observations made in the MIM mode of SIFT-MS measurements presented in sections 3.3 and 3.4 lead to the conclusions that AsH_3 and its methylated analogues, CH_3AsH_2 and $(CH_3)_2AsH$, produced by hydride generation, are completely atomized in the DBD atomizer since no signal was detected in SIFT-MS when the DBD plasma was on. The same conclusions can be drawn from full mass spectra acquired by SIFT-MS (Supplementary data, section 2.3 and Fig. S4).

3.5. Atomization of As hydride in absence of hydrogen

The hydride generation step always produces hydrogen, as a side-product of $NaBH_4$ hydrolysis in acidic environment. Hydrogen presence is a requisite for analyte atomization in DBD atomizers (holds true also for QTA) [1,26]. Under conditions employed in this work for arsane generation, the resulting hydrogen flow rate is 19 ml min^{-1}.

To investigate atomization in the absence of hydrogen, H_2 must be removed from the gaseous phase, *e.g.* by cryogenic trapping [1]. Another approach, chosen also in this study, is to sample analyte from a cylinder. The aim of the present measurements was to employ SIFT-MS to understand the mechanism of the processes taking place in the DBD atomizer in absence of hydrogen. In other words to explain whether the absence of free atoms proven by AAS measurements in the absence of hydrogen in atomizer (see below) is due to the fact the analyte molecule (i) remains untouched, or (ii) analyte molecule is decomposed through a reaction pathway that does not result in free atom formation. Hydrogen free arsane mixture in Ar was used as a model analyte (see section 2.1 for details). The first hypothesis (i) would allow detection of analyte (arsane) signal in SIFT-MS. The second (ii) would result in absence of SIFT-MS signal.

The effect of presence and absence of the DBD plasma on the signal of protonated arsane molecule as detected by SIFT-MS is depicted in Fig. S6A in Supplementary data. Arsane was introduced continuously from the gas cylinder, thus in absence of hydrogen, into the DBD while the DBD plasma was alternately swiched off and on as indicated. Arsane could be detected only in the time periods when the plasma was switched off as can be clearly seen from Fig. S6A.

The measurements with AAS detection have revealed that arsenic atoms cannot be detected if arsane is introduced into the running DBD without hydrogen. The effect of hydrogen flow rate between 0 and 20 ml min^{-1} admixed to reaction mixture (100 ml min^{-1}) introduced from the cylinder on As signal in AAS was investigated: arsenic signal cannot be detected in absence of hydrogen, increasing steeply up to hydrogen flow rate 5 ml min^{-1} H_2 and then leveling off, see Fig. S6B in Supplementary data. Hence, hydrogen produced in the hydride generator is sufficient for efficient atomization.

The combination of SIFT-MS and AAS detectors has undoubtedly proven that arsane is not atomized but decomposed in absence of hydrogen in the DBD. The detectors employed do not allow to decide whether the decomposition products are deposited on the inner DBD walls or they are transported outside the confines of the DBD atomizer.

4. Conclusions

SIFT-MS has been shown as a reliable method belonging to the portfolio of spectroscopic techniques suited for mechanistic studies of atomization processes in AAS. The presented results are compatible with a complete atomization of arsane and its methylated analogues in the DBD atomizer and with *ca* 80% atomization efficiency of selane. Moreover, SIFT-MS is also a valuable tool to quantify the water vapor content in the DBD atomizer which is an important parameter to be controlled in order to reach maximum DBD performance. SIFT-MS can be thus proposed as a proper detector to assess the feasibility of gas phase dryers testing as shown in this work. Additionally, the elegant and user-friendly way of online water vapor content monitoring in the gas phase is not limited to the field of hydride generation, but can be made use of universally in other industrial, environmental or medical applications for which the determination of absolute humidity in gas phase is requested.

This has been the first application of SIFT-MS to mechanistic studies in the field of volatile species atomization in hydride atomizers employed in AAS. Its proof-of-concept has been undoubtedly demonstrated. Despite the difference in atomization efficiency between As and Se that is lower for the latter element, both arsane and selane represent the group of hydrides being effectively atomized in DBD. These observations reached by SIFT-MS in the recent study are in excellent agreement with our previous results reached by various spectroscopic techniques [14,16]. Due to the complexity of the studied processes a broad range of spectroscopic probes has to be employed to explore their mechanisms. Some of the approaches give only indirect evidence of the atomization processes while the others such as LIF [10,13], spatiotemporally resolved OES [16,17] and last but not least SIFT-MS, as demonstrated in this work, enable direct observation of analyte fate allowing straightforward interpretation of the data. All the data on arsane and selane atomization collected so far are rather cohesive providing a detailed insight into their mechanism. Further experiments are in progress to employ SIFT-MS to investigate atomization mechanisms of other hydride forming elements in the DBD atomizers, especially those suffering from impaired sensitivity, such as Sn or Pb.

Understanding the mechanisms of atomization of volatile species in DBD plasmas together with the knowledge of the effectiveness of these processes is crucial for further development in the field of DBD plasmas as well as their application as atomizers or excitation devices in routine measurements employing atomic spectrometric detectors [4–6].

CRediT authorship contribution statement

Jan Kratzer: Conceptualization, Investigation, Data curation, Resources, Writing – original draft. **Michal Lacko:** Investigation, Methodology, Data curation, Validation, Formal analysis, Writing – original draft. **Kseniya Dryahina:** Investigation, Methodology, Data curation. **Tomáš Matoušek:** Investigation, Methodology, Data curation. **Patrik Španěl:** Conceptualization, Methodology, Resources, Supervision. **Jiří Dědina:** Conceptualization, Investigation, Data curation, Validation.

Declaration of competing interest

The authors declare that they have no known competing financial interests or personal relationships that could have appeared to influence the work reported in this paper.

Acknowledgment

This research has been supported by the Czech Science Foundation under contract 21-05285S (partial funding for the SIFT-MS laboratory is acknowledged from contract 21-25486S) and by the Czech Academy of Sciences, Institute of Analytical Chemistry (Institutional Research Plan no. RVO: 68081715).

Appendix A. Supplementary data

Supplementary data to this article can be found online at https://doi.org/10.1016/j.aca.2021.339256.

References

[1] J. Dědina, D.L. Tsalev, Hydride Generation Atomic Absorption Spectrometry, John Wiley & Sons, Inc., Chichester, 1995.
[2] J. Dědina, Generation of Volatile Compounds for Analytical Atomic Spectroscopy, John Wiley and Sons Ltd., Chichester, 2010.
[3] J. Dědina, Atomization of volatile compounds for atomic absorption and atomic fluorescence spectrometry: on the way towards the ideal atomizer, Spectrochim. Acta, Part B 62 (2007) 846–872.
[4] S. Brandt, A. Schütz, F.D. Klute, J. Kratzer, J. Franzke, Dielectric barrier discharges applied for optical spectrometry, Spectrochim. Acta, Part B 123 (2016) 6–32.
[5] S. Liu, Y.L. Yu, J.H. Wang, Advances in discharge-based microplasmas for the analysis of trace species by atomic spectrometry, J. Anal. At. Spectrom. 32 (2017) 2118–2126.
[6] G. Niu, A. Knodel, S. Burhenn, S. Brandt, J. Franzke, Review: miniature dielectric barrier discharge (DBD) in analytical spectrometry, Anal. Chim. Acta 1147 (2021) 211–239.
[7] P. Novák, J. Dědina, J. Kratzer, Preconcentration and atomization of arsane in a dielectric barrier discharge with detection by atomic absorption spectrometry, Anal. Chem. 88 (2016) 6064–6070.
[8] O. Duben, J. Boušek, J. Dědina, J. Kratzer, Dielectric barrier discharge plasma atomizer for hydride generation atomic absorption spectrometry—performance evaluation for selenium, Spectrochim. Acta, Part B 111 (2015) 57–63.
[9] P. Zurynková, J. Dědina, J. Kratzer, Trace determination of antimony by hydride generation atomic absorption spectrometry with analyte preconcentration/atomization in a dielectric barrier discharge atomizer, Anal. Chim. Acta 1010 (2018) 11–19.
[10] K. Bufková, S. Musil, J. Kratzer, P. Dvořák, M. Mrkvičková, J. Voráč, J. Dědina J, Generation of tellurium hydride and its atomization in a dielectric barrier discharge for atomic absorption spectrometry, Spectrochim. Acta, Part B 171 (2020) 105947.
[11] J. Kratzer, J. Boušek, R.E. Sturgeon, Z. Mester, J. Dědina, Determination of bismuth by dielectric barrier discharge atomic absorption spectrometry coupled with hydride generation: method optimization and evaluation of analytical performance, Anal. Chem. 86 (2014) 9620–9625.
[12] L. Juhászová, S. Burhenn, L. Sagapova, J. Franzke, J. Dědina, J. Kratzer, Hydride generation atomic absorption spectrometry with a dielectric barrier discharge atomizer: method optimization and evaluation of analytical performance for tin, Spectrochim. Acta, Part B 158 (2019) 105630.
[13] M. Albrecht, M. Mrkvičková, J. Hraníček, J. Voráč, P. Dvořák, J. Dědina, J. Kratzer, Atomization of lead hydride in a dielectric barrier discharge atomizer: optimized for atomic absorption spectrometry and studied by laser-induced fluorescence, Spectrochim. Acta, Part B 166 (2020) 105819.
[14] J. Kratzer, S. Musil, K. Marschner, M. Svoboda, T. Matoušek, Z. Mester, R. Sturgeon, J. Dědina, Behavior of selenium hydride in heated quartz tube and dielectric barrier discharge atomizers, Anal. Chim. Acta 1028 (2018) 11–21.
[15] J. Kratzer, O. Zelina, M. Svoboda, R. Sturgeon, Z. Mester, J. Dědina, Atomization of bismuthane in a dielectric barrier discharge: a mechanistic study, Anal. Chem. 88 (2016) 1804–1811.
[16] S. Burhenn, J. Kratzer, F.D. Klute, J. Dědina, J. Franzke, Atomization of arsenic hydride in a planar dielectric barrier discharge: behavior of as atoms studied by temporally and spatially resolved optical emission spectrometry, Spectrochim. Acta, Part B 152 (2019) 68–73.
[17] S. Burhenn, J. Kratzer, J. Dědina, J. Franzke, Influences of voltage shape and discharge gas on the temporally and spatially resolved emission characteristics of tin in a planar dielectric barrier discharge, Spectrochim. Acta, Part B 161 (2019) 105695.
[18] D. Smith, P. Španěl, Selected ion flow tube mass spectrometry (SIFT-MS) for on-line trace gas analysis, Mass Spec. Rev. 24 (2005) 661–700.
[19] D. Smith, P. Španěl, Ambient analysis of trace compounds in gaseous media by SIFT-MS, Analyst 136 (2011) 2009–2032.
[20] NIST WebBook Chemie, NIST Standard Reference Database Number 69. Available from: http://webbook.nist.gov/chemistry/.
[21] P. Taurková, M. Svoboda, S. Musil, T. Matoušek, Loss of di- and trimethylarsine on Nafion membrane dryers following hydride generation, J. Anal. At. Spectrom. 26 (2011) 220–223.
[22] P. Španěl, D. Smith, Selected ion flow tube: a technique for quantitative trace gas analysis of air and breath, Med. Biol. Eng. Comput. 34 (1996) 409–419.
[23] D. Smith, P. Španěl, Selected ion flow tube mass spectrometry (SIFT-MS) for on-line trace gas analysis, Mass Spectrom. Rev. 24 (2005) 661–700.
[24] P. Španěl, K. Dryahina, D. Smith, A general method for the calculation of absolute trace gas concentrations in air and breath from selected ion flow tube mass spectrometry data, Int. J. Mass Spectrom. 249–250 (2006) 230–239.
[25] R.C. Bolden, N.D. Twiddy, A flowing afterglow study of water vapour, Faraday Discuss. Chem. Soc. 53 (1972) 192–200.
[26] P. Dvořák, M. Talába, J. Kratzer, J. Dědina, Radical theory of hydride atomization confirmed after four decades – determination of H radicals in the quartz hydride atomizer by two-photon absorption laser-induced fluorescence, Chem. Sci. 10 (2019) 3643–3648.

Attachment A.6

Supporting Information (SI)

Atomization of As and Se volatile species in a dielectric barrier discharge atomizer after hydride generation: fate of analyte studied by selected ion flow tube mass spectrometry

Jan Kratzer[a]*, Michal Lacko[b,c], Kseniya Dryahina[b], Tomáš Matoušek[a], Patrik Španěl[b], Jiří Dědina[a]

[a]Institute of Analytical Chemistry of the Czech Academy of Sciences, Veveří 97, 602 00 Brno, Czech Republic. E-mail: jkratzer@biomed.cas.cz

[b]J. Heyrovský Institute of Physical Chemistry of the Czech Academy of Sciences, Dolejškova 2155/3, 182 23 Prague 8, Czech Republic.

[c]Charles University, Faculty of Mathematics and Physics, V Holešovičkách 747/2, 180 00 Prague, Czech Republic

Table of Contents

1. Experimental

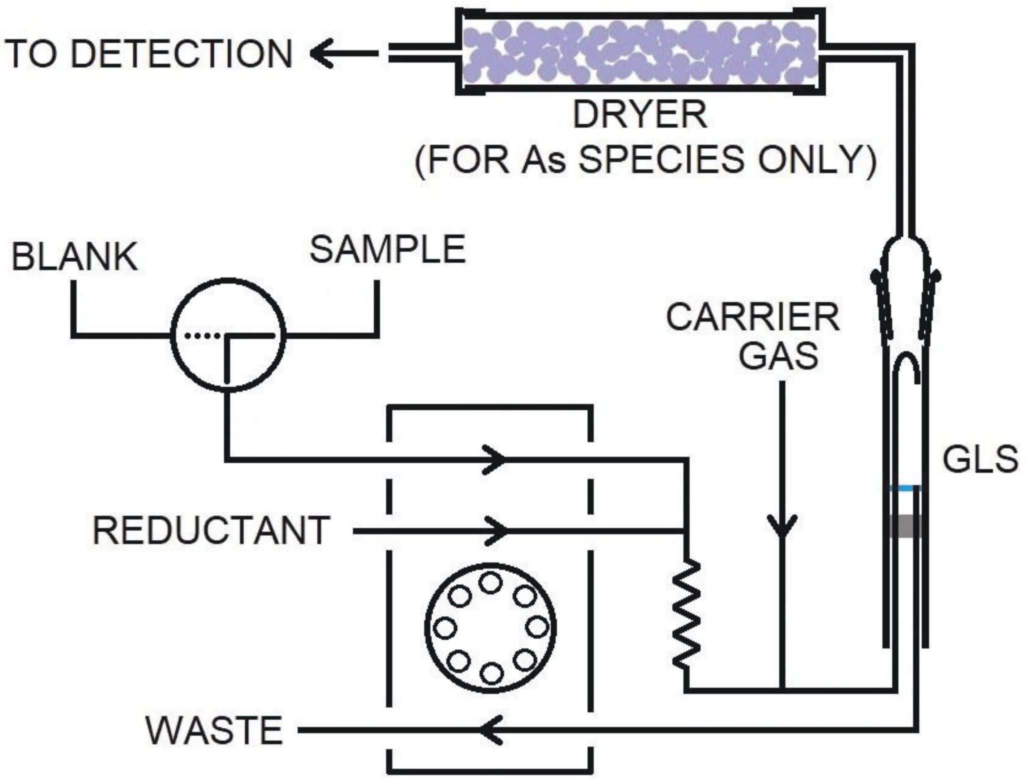

Figure S1 Scheme of the hydride generator employed.

Attachment A.6

1.1 Quantification of the hydride generation efficiency

Hydride generation efficiencies of As and Se hydrides as well as CH_3AsH_2 and $(CH_3)_2AsH$ were quantified by means of ICP-MS/MS from comparison of the slopes of calibration curves obtained with nebulization of respective liquid standards to those obtained with hydride generation (HG). The same approach is detailed in our previous publications.[1-5] Special attention was paid to maintain the same plasma conditions for both nebulization and gaseous phase introduction.[6] Therefore, HG from blank solution was on when recording nebulization signals while nebulization blank solution was introduced to the nebulizer when recording the signals for volatile species from HG. Flow of carrier gas with volatilized analyte from HG was introduced by a PTFE T-piece into the make-up gas line of the ICP-MS/MS spectrometer.

A 8900 ICP-MS/MS spectrometer (Agilent, Japan) was used. The configuration of the instrument consisted of a double-pass spray chamber and MicroMist nebulizer. The operating parameters were 1550 W RF power, 0.60 l min^{-1} Ar nebulizer gas, 0.6 l min^{-1} Ar make-up gas and 32% O_2 reaction cell gas. 100 ng ml^{-1} Te(VI) solution and 10 ng ml^{-1} of Rh and Y in 2% HNO_3 (m v^{-1}) were co-nebulized as internal standards to provide robust wet plasma conditions. Measurements were carried out with O_2 in the reaction cell in a mass-shift mode. Thus As and Se as analytes as well as Y, Rh, and Te as internal standards were measured as $^{75}As^{16}O^+$ (*m/z* 91), $^{78}Se^{16}O^+$ (*m/z* 94) and $^{125}Te^{16}O^+$ (*m/z* 141), $^{103}Rh^{16}O^+$ (*m/z* 119) and $^{89}Y^{16}O^+$ (*m/z* 105), respectively.

Signals were corrected for drift on Y signal (*m/z* 105) as internal standard. Signals (counts per ng) from nebulization of 100 ng ml^{-1} and 200 ng ml^{-1} of iAs(III) and Se(IV), respectively, were compared with the signals obtained by HG of 1 ng ml^{-1} solutions of iAs(III), MAs(V) and Se(IV) and 2 ng ml^{-1} DMAs(V), respectively. HG conditions were similar to those described in sections 2.2.2 and 2.2.3 corresponding also to SIFT-MS experiments. 10 ng ml^{-1} Y and Rh in 2% HNO_3 was used as nebulization blank.

For determination of nebulized solution mass, a dynamic mass flow approach was applied.[3,7] Shortly, a test solution (100 ng ml^{-1} of As and Te and 10 ng ml^{-1} of Rh and Y in 2% HNO_3) was continuously nebulized and the waste solution from the spray chamber returned back into a container. The weight loss of the container, corresponding to a mass of solution nebulized, was monitored on analytical balance over 120 min of operation. Nebulization efficiency was assessed as 5.6 ±0.1%.

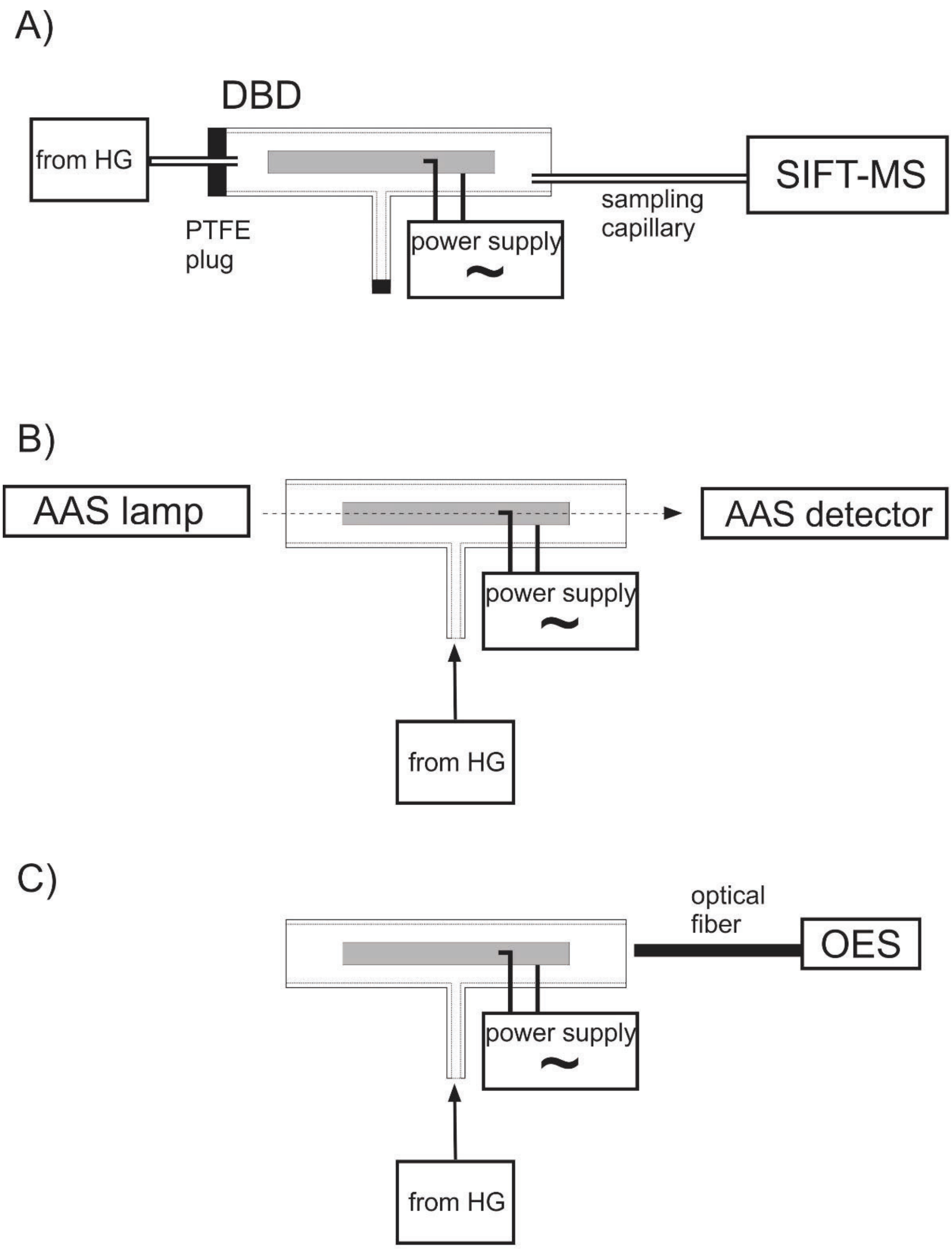

Figure S2 Measurement configurations employed for A) SIFT-MS; B) AAS and C) OES detection.

2. Results and discussion

2.1 Preliminary results – generation efficiency and sensitivity in AAS

Conditions of generation of all volatile species and their atomization are described in sections 2.2 and 2.3, respectively. Atomizer sensitivity was checked prior to SIFT-MS measurements by AAS. The same DBD pieces as employed for sensitivity check were later used in the SIFT-MS experiments. Hydride generation was performed from a liquid standard (10 ng ml^{-1} analyte concentration) in triplicate.

Since generation of binary hydrides is commonly performed from HCl medium rather than HNO_3 which was employed in this work to avoid de-methylation of CH_3AsH_2 and $(CH_3)_2AsH$ as recommended in our earlier study[8], the first experiment performed was to compare the efficiency of arsane generation from HNO_3 and HCl. The generation efficiency was quantified by ICP-MS/MS, see section 1.1 in Supporting Information for the description of the experimental approach employed. Arsane generation efficiency was quantified to 90 ± 2 % from both acids. Virtually the same sensitivity of 0.50 ± 0.01 s ng^{-1} was reached for both acids in AAS measurements proving again indirectly the fact the generation efficiencies of arsane are equal from HNO_3 and HCl media. As a consequence, the data interpretation regarding arsane atomization discussed throughout this work are valid also for more common HCl environment.

The sensitivity observed in AAS for all As volatile species and for Se hydride is summarized in Table 2. The values for arsane and selane are consistent with the values reported in our previous studies proving their robustness. Sensitivity for As detection by HG-DBD-AAS reached in this work, 0.50 ± 0.01 s ng^{-1}, agrees well with the values of 0.48 ± 0.01 s ng^{-1} and 0.44 ± 0.02 s ng^{-1} As, respectively reached in our earlier works.[9,10] Analogously, sensitivity value for Se determination found in this work (0.33 ± 0.01 s ng^{-1}) is in accord with those of 0.32 ± 0.01 s ng^{-1} and 0.38 ± 0.02 s ng^{-1} Se, respectively reported previously.[11,12]

2.2 Investigation of water vapor content by OES

It should be noted that this approach is, in contrast to SIFT-MS, rather qualitative than quantitative. For illustration, emission spectrum of the DBD plasma discharge under HG conditions used for arsenic species, i.e. using discharge gas composition consisting of 75 ml min^{-1} Ar and 19 ml min^{-1} of co-generated H_2, is depicted in Figure S3. Emission spectra were recorded by a miniature fiber optics spectrometer (see section 2.6 and Figure S2C for description of the experimental arrangement) in the wavelength range between 200 and 850 nm. Two blank spectra depicted in Figure S3 differ from each other only by presence of the NaOH dryer downstream the GLS. Measurements of As emission spectra recorded from a DBD discharge after hydride generation were discussed in our previous work[13], but OES has not been employed to investigate the effect of water vapor content on emission spectrum. Ar emission lines (Ar I) are clearly detected in the region 690-850 nm. A broad continuum between 200 to 400 nm is related to dissociation of molecular hydrogen. Several emission lines can be detected on the top of this continuum, namely the OH band at 309 nm and lines representing the N_2 second positive system at 337 and 357 nm, respectively. As expected, the OH emission band is significantly (ca 5-times) more intense in absence of the dryer compared to its presence (see inset in Figure S3). Both spectra were recorded shortly one after another keeping the same detector integration time (250 ms). Emission spectrum is more intense in the whole wavelength range if the dryer is present. This feature can be also explained by lower water vapor content in the discharge since the plasma is less quenched in presence of the dryer.

The water vapor content determined by SIFT-MS under the same experimental conditions was 2.0% and 0.16%, respectively, in absence and presence of the dryer (see section 3.2). The difference between the results observed by OES (5-times higher signal with the dryer) and SIFT-MS (13-times lower water content with the dryer) might be explained by the fact that also the sensitivity of the emission measurements is dependent on water vapor concentration as discussed above and can be clearly seen for hydrogen dissociation continuum. The sensitivity is impaired at higher water vapor concentration levels preventing thus from direct comparisons of emission lines intensities without further corrections. The advantage of the SIFT-MS is the fact that absolute value of water vapor content in the gaseous phase can be determined.

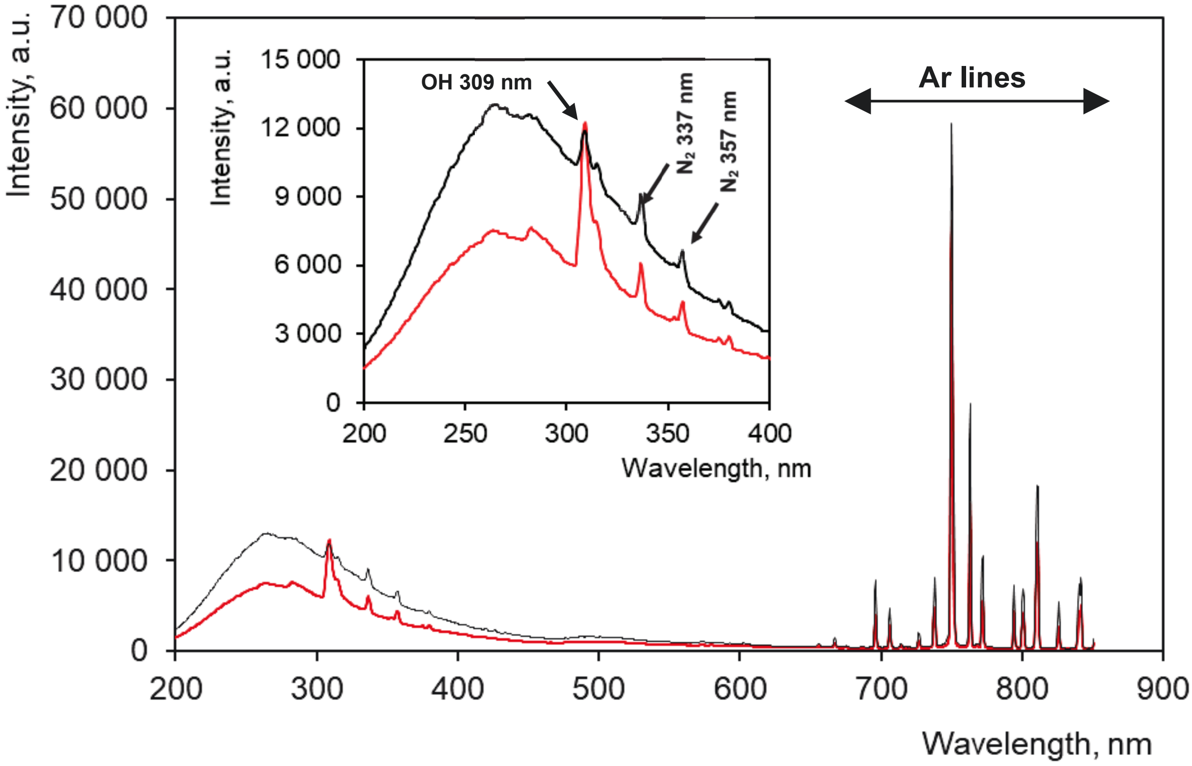

Figure S3 Emission spectra of the DBD discharge operated at HG conditions for As species generation (discharge gas composition: 75 ml min^{-1} Ar + 19 ml min^{-1} H_2) without any dryer (red line) and in presence of NaOH dryer (black line). Both spectra are for blank (no As species introduced). Detector integration time 250 ms, 10 spectra to be averaged.

2.3 SIFT-MS ion chemistry study

The chemistry of ion reactions of the gas phase species investigated (AsH_3, CH_3AsH_2, $(CH_3)_2AsH$, SeH_2) with hydronium in the SIFT source was not published previously. As a consequence, mass spectra were recorded for individual hydrides being always compared with corresponding blank measurements employing apparatus arrangement depicted in the Figure S2A while the mode of the SIFT-MS measurement was set to the classical full MS scanning (see section 2.4 for details). Moreover, such measurements have been performed firstly in absence of the plasma in the DBD atomizer, to be subsequently followed by the set of experiments with DBD plasma switched on. The results of all experiments are summarized in Figure S4. It must be highlighted that slightly higher concentrations of analyte species standard solutions were used in these measurements compared to the experiments in MIM mode of SIFT-MS in order to acquire the signals high enough for clear demonstration of ion chemistry.

Only protonated water clusters ($H_2O^+(H_2O)_n$; n = 0, 1, 2, 3) can be detected when hydride generation of a blank solution was performed in absence of the DBD plasma (red signals in Figures S4A-D). Interestingly, the signal of hydronium hydrated with the highest (n = 3) amount of water molecules (*m/z* 73) can only be seen under the experimental conditions when no gas phase dryer was employed which is in perfect agreement with the results observed during investigations of water vapor content (section 3.2 and Supporting Information, section 2.2).

According to the expectations, the signals of protonated water clusters were accompanied by protonated molecules of respective analyte hydrides in the presence of hydride generation from a standard solution in absence of the DBD plasma (black signals in Figures S4A-D). As a consequence, AsH_4^+ can be clearly identified when AsH_3 was generated from iAs(III) standard solution (Figure S4A); $CH_3AsH_3^+$ is identified after HG from MAs(V) standard solution (Figure S4B) and $(CH_3)_2AsH_2^+$ was found for HG from DMAs(V) standard (Figure S4C). The mass spectrum for SeH_2 (Figure S4D) contains more peaks, due to the isotopic pattern of selenium, but all of them belong to SeH_3^+. These experiments revealed the ions to be further investigated for individual analytes in the multiple-ion monitoring (MIM) mode of the measurement. Their results are in detail discussed in sections 3.3 to 3.5 and Figures 2 and S5.

Subsequently, the same set of experiments was performed but the DBD plasma was switched on. The results are summarized in Figures S4E-H. The mass spectra of hydride generation from a blank solution in the presence of DBD plasma (red signals Figures S4E-H) remain qualitatively the same as those in the absence of DBD plasma (red signals in Figures S4A-D). On the contrary, significant changes in the results were observed when hydride generation from standard solutions was performed in the presence of DBD plasma. In case of all As species investigated the signals of protonated analyte hydride products, *i.e.* AsH_4^+ (Figure S4E); $CH_3AsH_3^+$ (Figure S4F) and $(CH_3)_2AsH_2^+$ (Figure S4G) were absent due to their active atomization in the DBD plasma. Compared to blank MS, no additional peaks corresponding to *e.g.* decomposition of methylated As species by loss of one or two methyl groups, are present. It can be concluded that atomization of As species in the DBD plasma generate species not detected/detectable by SIFT-MS. The behavior of selenium hydride was different. Some signal of protonated selane, although significantly suppressed, could still be detected even in the presence of the DBD plasma (Figure S4H).

Effort was made to search also for other potential reaction pathways and decomposition products of the species at higher *m/z* (up to *m/z* 600) since protonated dimers and n-mers might be produced by analyte hydride interaction with DBD plasma. Similar reactions were recently described for As species in the DART-MS source.[14] However, such species were not identified (data not shown) for any of the analytes investigated.

The mass spectra measured and discussed in this section are well suited for identification of the important analyte structures to be further investigated. Their behavior was subsequently studied in the multiple-ion monitoring (MIM) mode of the SIFT-MS measurements that enables reaching higher sensitivity and better precision as well as allows monitoring of signal over a longer period of time. The results of SIFT-MS measurements in the MIM mode are in detail interpreted in sections 3.3 to 3.5 and Figures 2 and S5.

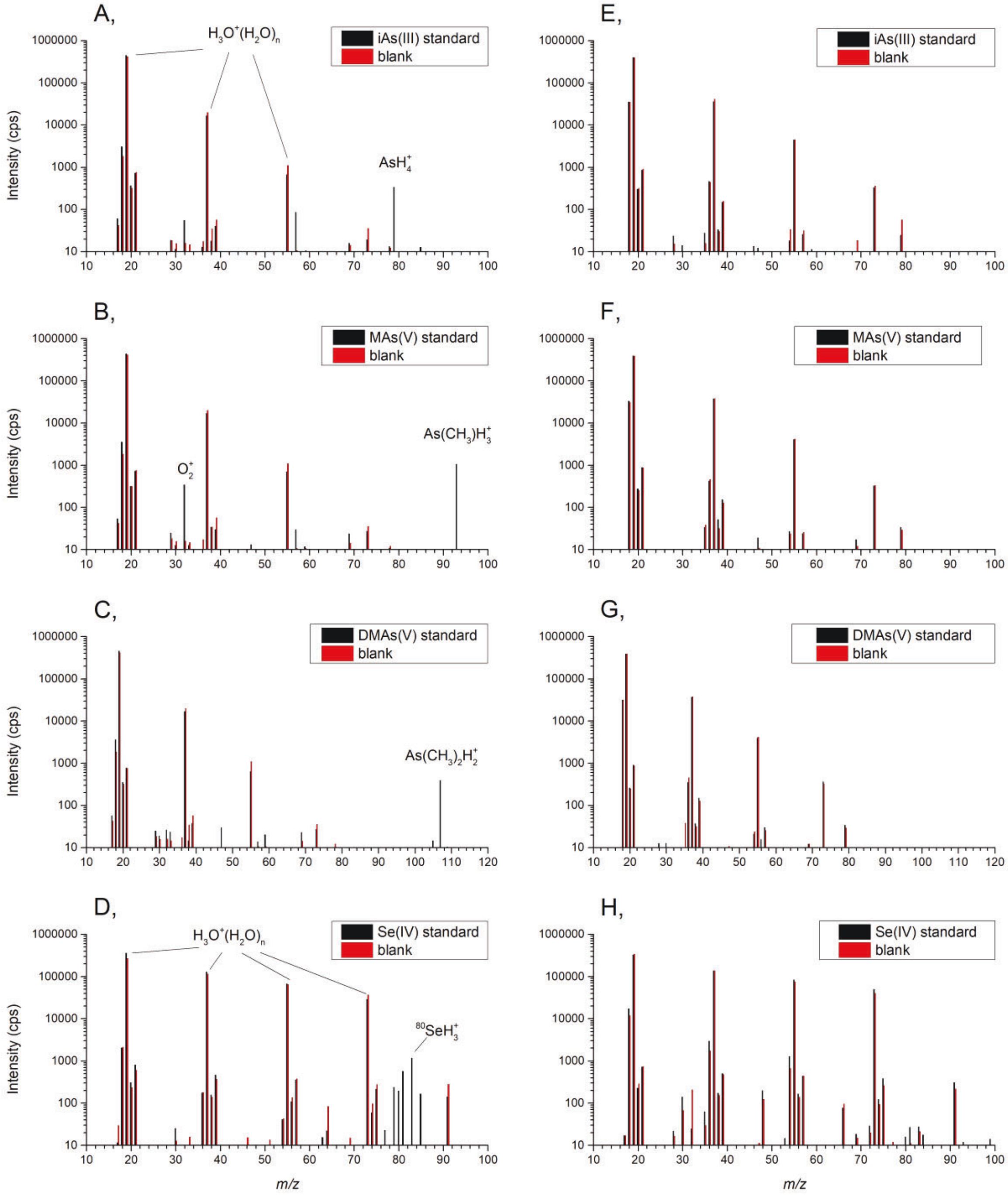

Figure S4 Mass spectra (MS) of individual hydrides.

On the left (A-D): MS of volatile analyte species (black) and MS of blank (red). DBD plasma switched off. Concentration of the species in the standard solutions prior to HG: A) 1 µg l^{-1} iAs(III); B) 2 µg l^{-1} MAs(V), C) 0.6 µg l^{-1} DMAs(V); D) 1 µg l^{-1} Se(IV).

On the right (E-H): MS of volatile analyte species (black) and MS of blank (red). DBD plasma switched on. Concentration of the species in the standard solutions prior to HG: E) 0.1 µg l^{-1} iAs(III); F) 0.1 µg l^{-1} MAs(V) ; G) 0.2 µg l^{-1} DMAs(V); H) 1 µg l^{-1} Se(IV).

2.4 Atomization of methyl-substituted As hydrides

A)

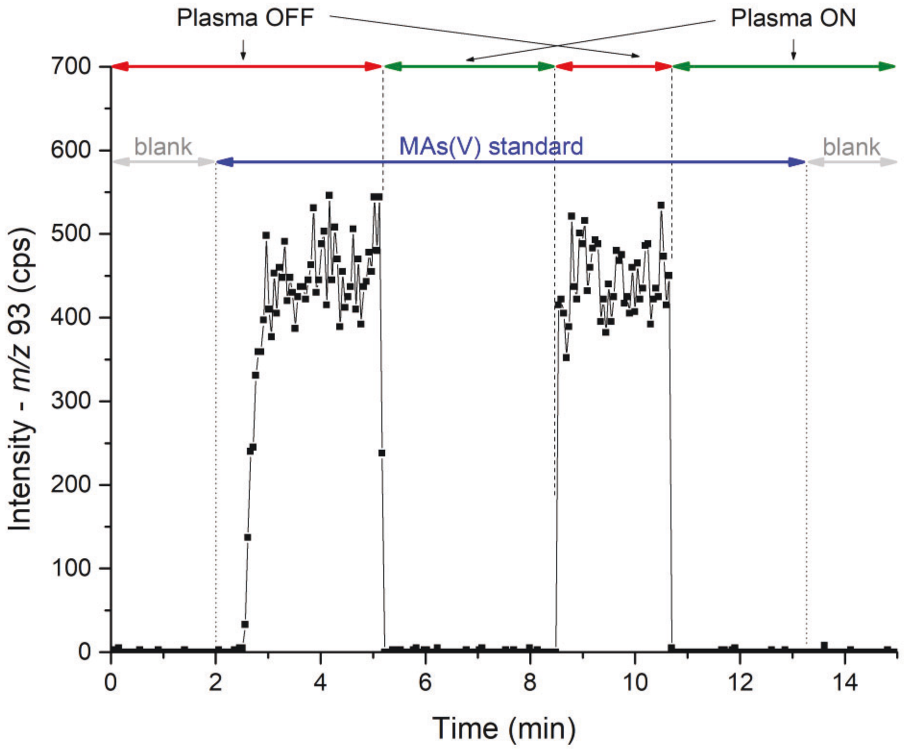

B)

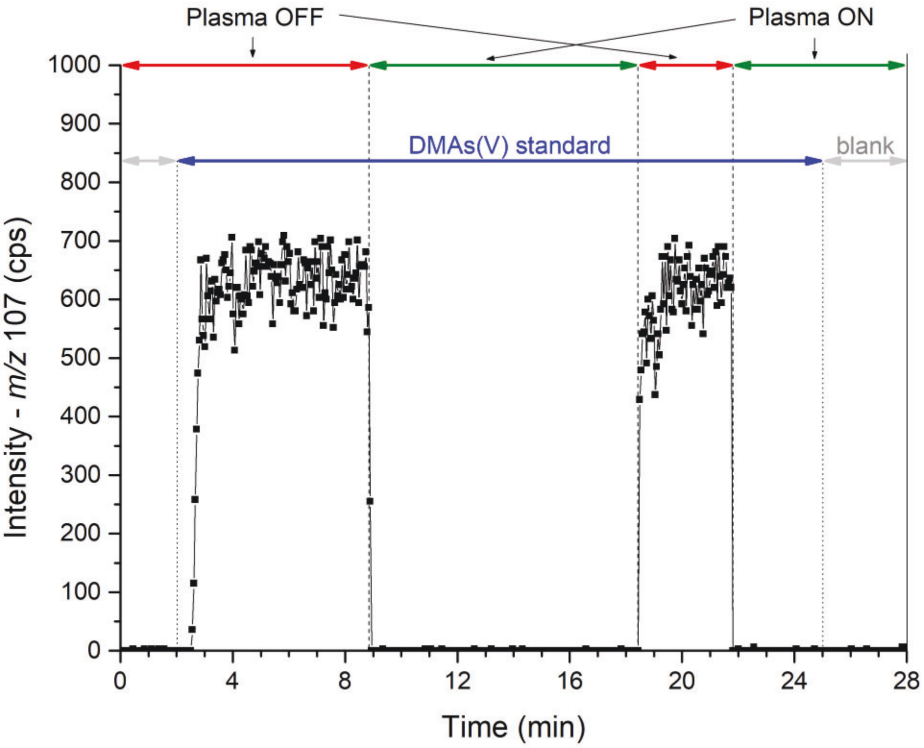

Figure S5 SIFT-MS signals of methyl-substituted arsanes and blanks in the DBD atomizer in presence and absence of the plasma. A) CH_3AsH_2 generated from 100 ng ml^{-1} MAs(V); B) $(CH_3)_2AsH$ generated from 200 ng ml^{-1} DMAs(V); Generation and atomization conditions as described on the text.

2.5 Atomization of As hydride in absence of hydrogen

A)

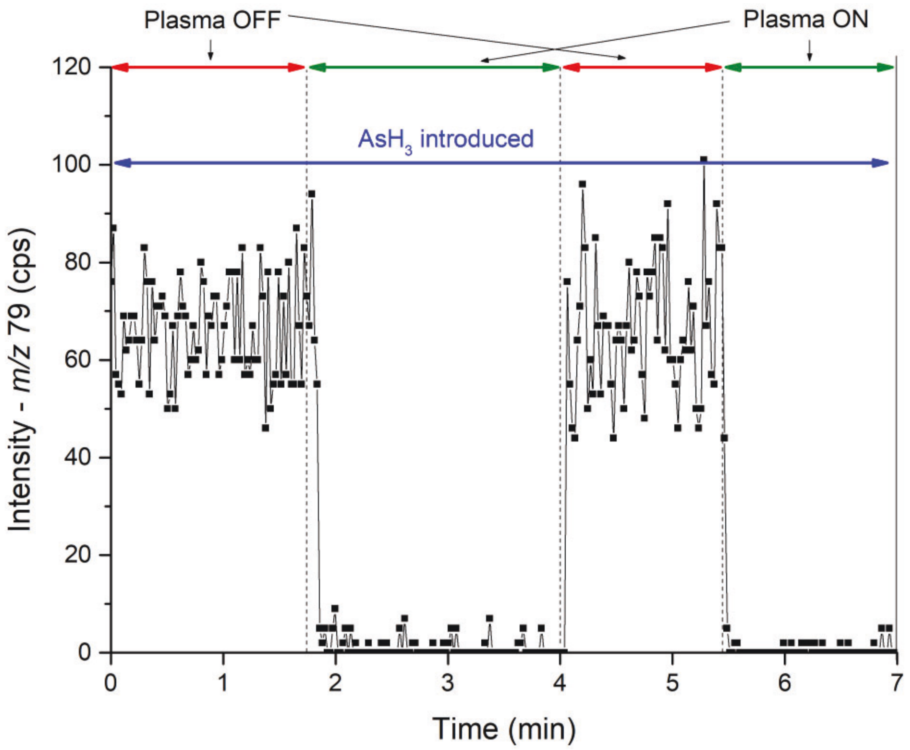

B)

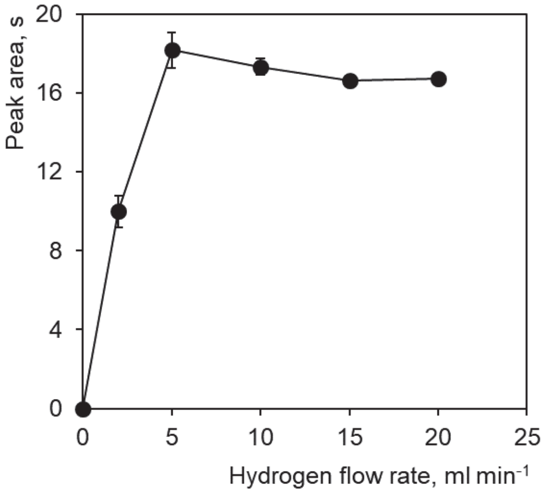

Figure S6 A) SIFT-MS signal of AsH_3 (mixture in Ar from cylinder) in absence of hydrogen B) Effect of hydrogen on signal in AAS

References

(1) Nováková, E.; Horová, K.; Červený, V.; Hraníček, J.; Musil, S. *J. Anal. At. Spectrom.* **2020**, 35, 1380–1388.

(2) Bufková, K.; Musil, S.; Kratzer, J.; Dvořák, P.; Mrkvičková, M.; Voráč, J.; Dědina, J. *Spectrochim. Acta Part B* **2020**, 171, 105947.

(3) Vyhnanovský, J.; Strugeon, R. E.; Musil, S. *Anal.Chem.* **2019**, 91, 13306–13312.

(4) Vyhnanovský, J.; Yildiz, D.; Štádlerová, B.; Musil, S. *Microchem. J.* **2021**, 164, 105997.

(5) Sagapova, L.; Musil, S.; Kodríková, B.; Kratzer, J. *Anal. Chim. Acta* **2021**, 1168, 338601.

(6) Matoušek, T. *Anal. Bioanal. Chem.* **2007**, 388, 763-767

(7) Cuello-Nunez, S.; Abad-Alvaro, I.; Bartczak, D.; del Castillo Busto, M. E.; Ramsay, D. A.; Pellegrino, F.; Goenaga-Infante, H. *J. Anal. At. Spectrom.* **2020**, 35, 1832-1839.

(8) Marschner, K.; Musil, S.; Dědina, J. *Anal. Chem.* **2016**, 88, 6366–6373.

(9) Novák, P.; Dědina, J.; Kratzer, J. *Anal. Chem.* **2016**, 88 (11), 6064-6070.

(10) Burhenn, S.; Kratzer, J.; Klute, F.D.; Dědina, J.; Franzke, J. *Spectrochim. Acta Part B* **2019**, 152, 68-73.

(11) Duben, O.; Boušek, J.; Dědina, J.; Kratzer, J. *Spectrochim. Acta Part B* **2015**, 111, 57-63.

(12) Kratzer, J.; Musil, S.; Marschner, K.; Svoboda, M.; Matoušek, T.; Mester, Z.; Sturgeon, R.; Dědina, J. *Anal. Chim. Acta* **2018**, 1028, 11-21.

(13) Straka, M.; Burhenn, S.; Marschner, K.; Brandt, S.; Marggraf, U.; Dědina, J.; Franzke, J.; Kratzer, J. *Spectrochim. Acta Part B* **2018**, 146, 69-76.

(14) Matoušek, T.; Kratzer, J.; Sturgeon, R.; Mester, Z.; Musil, S. *Anal. Bioanal. Chem.* **2021**, 13, 3443-3453.